

**Spectroscopy, Electrochemistry and Photochemistry of
Phenylazonaphthalene Dyes**

Chad Quentin Bullivant

PhD

2010

**Spectroscopy, Electrochemistry and Photochemistry of
Phenylazonaphthalene Dyes**

by

Chad Quentin Bullivant

A Thesis Submitted to The University of York for the
Degree of Doctor of Philosophy

Department of Chemistry
The University of York

July 2010

Abstract

The spectroscopy, electrochemistry and photochemistry of seven 2-(4-R-phenylazo)naphthalene-4,8-disulfonate dyes (R-Span dyes), were studied to report on their structure and reactivity in water. The dyes differ in their structure by only the R substituent attached to the phenyl ring, representing a range of electron-donating and electron-withdrawing substituents; most studies were carried out on OH-Span.

A combination of UV/Visible, NMR, Raman and IR spectroscopy together with DFT calculations has shown that the dyes are planar in their stable *trans*-isomer form. The spectra were found to be sensitive to the R substituent and generally they show good correlations with Hammett σ_p substituent constants. The structures of OH-Span ($pK_a = 7.98$) and NH_2 -Span ($pK_a = 2.88$) are pH dependent, and none of the dyes show aggregation at $\leq 3 \times 10^{-2} \text{ mol dm}^{-3}$.

Spectroelectrochemistry and controlled potential electrolysis studies showed that OH-Span undergoes an irreversible four electron reduction process, where detailed product analysis showed that naphthyl and phenyl fragments of the dye are produced due to azo bond scission; similar results were observed for the other R-Span dyes. Dyes containing electron-donating R substituents are more resistant to reduction, whereas dyes containing electron-withdrawing R substituents are more resistant to oxidation.

The stability of the R-Span dyes was assessed by reaction with photoinitiator generated 2-hydroxy-2-propyl radicals to study reductive fading. Time-resolved studies were carried out on OH-Span:photoinitiator solutions and rate constants for electron transfer to produce the dye radical anion and subsequent disproportionation were found to be 6.00×10^9 and $5.00 \times 10^8 \text{ dm}^3 \text{ mol}^{-1} \text{ s}^{-1}$, respectively. The detailed product analysis identified the naphthyl fragment of the dye, which was also observed for other R-Span dyes, indicating that the reduction mechanism occurs via disproportionation resulting in azo bond scission.

The R-Span dyes show *trans* to *cis* photoisomerisation, and NH_2 -, OH-, OMe- and NHAc-Span showed complete *cis* to *trans* thermal back reactions within ca. 30 ms, 35 μs , 11 days and 1 day, respectively.

Contents

Abstract	i
Contents	iii
List of Figures	ix
List of Tables	xxxi
Abbreviations and Symbols	xxxix
Acknowledgements	xliii

Chapter 1 Introduction

1.1 Introduction to dyes.....	1
1.1.1 Colour and the perception of colour.....	1
1.1.2 Colorants.....	2
1.1.2.1 Azo dyes.....	2
1.1.2.2 Carbonyl dyes.....	4
1.1.2.3 Phthalocyanine dyes.....	5
1.1.2.4 Pigments.....	5
1.2 Ink-jet printing.....	6
1.2.1 Historical overview.....	6
1.2.2 Ink-jet printers.....	6
1.2.2.1 Continuous.....	7
1.2.2.2 Drop-on-demand.....	8
1.2.3 Ink-jet inks.....	9
1.2.4 Ink-jet paper.....	9
1.2.5 Printing quality.....	10
1.3 Techniques.....	11
1.3.1 Electronic spectroscopy.....	11
1.3.2 Vibrational spectroscopy.....	14
1.3.3 Nuclear magnetic resonance spectroscopy.....	16
1.3.4 Electrochemistry.....	19
1.3.5 High performance liquid chromatography.....	21
1.3.6 Liquid chromatography mass spectrometry.....	21

1.3.7 Time-resolved UV/Visible absorption spectroscopy.....	22
1.3.8 DFT calculations.....	22
1.4 Aims.....	24
1.5 References.....	26

Chapter 2 Experimental

2.1 Materials.....	29
2.2 Sample preparation.....	30
2.3 Instrumentation.....	31
2.3.1 UV/Visible absorption and emission spectroscopy.....	31
2.3.2 Raman spectroscopy.....	31
2.3.3 Infrared spectroscopy.....	32
2.3.4 NMR spectroscopy.....	32
2.3.4.1 Structural studies.....	32
2.3.4.2 Product studies.....	32
2.3.5 Electrochemical studies.....	34
2.3.5.1 Cyclic voltammetry.....	34
2.3.5.2 Spectroelectrochemistry.....	34
2.3.5.3 Controlled potential electrolysis.....	35
2.3.6 Photochemical studies.....	35
2.3.6.1 Steady-state studies.....	35
2.3.6.2 Time-resolved studies.....	36
2.3.7 HPLC analysis.....	37
2.3.8 LC-MS analysis.....	37
2.4 DFT calculations.....	38
2.5 Data manipulation.....	38
2.6 References.....	39

Chapter 3 Structure

3.1 Introduction.....	41
3.1.1 General.....	41
3.1.1.1 Azo-hydrazone tautomerism.....	41
3.1.1.2 Aggregation.....	42
3.1.1.3 Hydrogen bonding.....	44
3.1.2 Azobenzenes.....	45
3.1.2.1 Structure.....	45
3.1.2.2 Isomerisation.....	46
3.1.2.3 Substituent effect.....	46
3.1.2.4 pH dependence.....	47
3.1.3 Phenylazonaphthalenes.....	51
3.1.3.1 Structure.....	51
3.1.4 Aims.....	52
3.2 Results, analysis and discussion.....	53
3.2.1 UV/Visible absorption spectroscopy.....	53
3.2.1.1 pH dependence.....	53
3.2.1.2 Spectra of all dyes at set pH values.....	56
3.2.1.3 Concentration dependence.....	61
3.2.1.4 Solvent dependence.....	62
3.2.2 DFT calculations.....	63
3.2.2.1 Optimised geometries.....	63
3.2.2.2 Electronic structure.....	68
3.2.2.3 Atomic charges.....	71
3.2.3 NMR spectroscopy.....	74
3.2.3.1 NH ₂ -Span.....	74
3.2.3.2 OH-Span.....	78
3.2.3.3 All R-Span dyes.....	80
3.2.4 Vibrational spectroscopy.....	85
3.2.4.1 General experimental conditions.....	85
3.2.4.2 OH-Span.....	87
3.2.4.3 All R-Span dyes.....	94
3.2.4.4 OH-Span pH dependence.....	100

3.2.5 Protonation of NH ₂ -Span.....	102
3.2.5.1 UV/Visible absorption spectroscopy.....	103
3.2.5.2 DFT Calculations.....	111
3.2.5.3 NMR spectroscopy.....	111
3.2.5.4 Raman spectroscopy.....	114
3.2.6 Summary.....	118
3.3 Conclusions.....	123
3.4 References.....	124

Chapter 4 Electrochemistry

4.1 Introduction.....	129
4.1.1 Electrochemical techniques.....	129
4.1.2 Electron transfer processes.....	130
4.1.3 Substituent effect.....	133
4.1.4 Aims.....	135
4.2 Results, analysis and discussion.....	136
4.2.1 OH-Span.....	137
4.2.1.1 Cyclic voltammetry.....	137
4.2.1.2 Spectroelectrochemistry.....	138
4.2.1.3 Controlled potential electrolysis reduction.....	140
4.2.1.4 Product analysis.....	141
4.2.2 Other R-Span dyes.....	159
4.2.2.1 Spectroelectrochemistry.....	159
4.2.2.2 Controlled potential electrolysis reduction.....	164
4.2.2.3 Product analysis.....	165
4.2.3 Summary.....	174
4.2.3.1 Reduction.....	174
4.2.3.2 Substituent effect.....	176
4.2.3.3 Oxidation.....	180
4.3 Conclusions.....	181
4.4 References.....	183

Chapter 5 Photochemistry

5.1 Introduction.....	185
5.1.1 Isomerisation.....	186
5.1.1.1 Azobenzene.....	186
5.1.1.2 Phenylazonaphthalene.....	187
5.1.2 Reactivity.....	189
5.1.2.1 Photo-oxidation.....	190
5.1.2.2 Photo-reduction.....	191
5.1.2.3 Photoinitiators.....	192
5.1.3 Aims.....	196
5.2 Results, analysis and discussion.....	196
5.2.1 OH-Span.....	198
5.2.1.1 Steady-state studies.....	198
5.2.1.2 Time-resolved studies.....	227
5.2.2 Other R-Span dyes.....	237
5.2.2.1 Dyes alone.....	238
5.2.2.2 Dyes with photoinitiator.....	249
5.2.3 Summary.....	262
5.3 Conclusions.....	264
5.4 References.....	265

Chapter 6 Conclusions and future work

6.1 Conclusions.....	269
6.1.1 Techniques.....	272
6.1.2 Dye structure.....	273
6.1.3 Dye reactivity.....	273
6.1.3.1 Reduction.....	273
6.1.3.2 Oxidation.....	274
6.1.3.1 Photoisomeriation.....	274
6.2 Future work.....	274

Appendices

Appendix 1 Structure

A1.1 Non-linear regression analysis on spectrometric pH titration data.....	277
A1.2 Solvent dependence data.....	283
A1.3 DFT calculations.....	284
A1.3.1 Optimisations.....	284
A1.3.2 Electronic structure.....	286
A1.4 NMR spectroscopy.....	291
A1.5 Vibrational spectroscopy.....	308
A1.5.1 Short term photoalteration.....	308
A1.5.2 Supplementary figures.....	310
A1.6 Protonation of NH ₂ -Span.....	316

Appendix 2 Electrochemistry

A2.1 Supplementary CV data.....	319
A2.2 Spectroelectrochemical fit.....	319
A2.3 Supplementary CPE data.....	322
A2.4 Supplementary HPLC data.....	323

Appendix 3 Photochemistry

A3.1 Kinetic rate laws.....	327
A3.2 Supplementary TRVIS data.....	328

Appendix 4 Computational data CD.....	329
--	------------

List of Figures

Chapter 1 Introduction

Figure 1.1 Generic synthesis of an azo dye.....	2
Figure 1.2 Structure of 1,4-benzoquinone and 9,10-anthraquinone.....	5
Figure 1.3 An example of a phthalocyanine dye, Direct Blue 86.....	5
Figure 1.4 Pigment Red 49.....	6
Figure 1.5 Continuous ink-jet: A binary-deflection system.....	7
Figure 1.6 Continuous ink-jet: A multiple-deflection system.....	7
Figure 1.7 Drop-on-demand roof-shooter thermal ink-jet.....	8
Figure 1.8 Structure of cellulose as a polymer of β -glucose.....	10
Figure 1.9 Ground and excited electronic and vibrational energy levels.....	13
Figure 1.10 Jablonski diagram of the routes of excitation and decay of electronic states; abs = absorption, ic = internal conversion, isc = intersystem crossing, f = fluorescence, p = phosphorescence, vr = vibrational relaxation.....	14
Figure 1.11 Transitions between vibrational energy levels that are observed in IR and Raman spectra.....	16
Figure 1.12 Effect of a magnetic field on a degenerate nuclei with $I = \frac{1}{2}$.	
Figure 1.13 Structures of the “pure” dyes NH ₂ -Span, OH-Span, OMe-Span, NHAc-Span and the “impure” dyes H-Span, Br-Span and CN-Span, all shown without their sodium counter ions in the <i>trans</i> form.....	17

Chapter 2 Experimental

Figure 2.1 Spectroelectrochemical cell.....	35
--	----

Chapter 3 Structure

Figure 3.1 Azo-hydrazone tautomerism in a 1-hydroxy-2-phenylazonaphthalene system.....	42
Figure 3.2 Common types of dimer.....	43

Figure 3.3 Exciton splitting for dimers of various geometries indicative of different shifts in the UV/Visible absorption spectrum.....	43
Figure 3.4 Structures of Direct Blue 1 (Top) Acid Red 1 (Bottom).....	44
Figure 3.5 <i>Trans</i> - and <i>cis</i> -azobenzene, together with numbering system.....	45
Figure 3.6 X, Y substituted 4,4'-azobenzene.....	47
Figure 3.7 4-hydroxyazobenzene-modified cyclodextrins, where CD represents cyclodextrin.....	48
Figure 3.8 Phenolate-phenol equilibrium of 4-hydroxyazobenzene-modified cyclodextrins.....	48
Figure 3.9 Protonation of 4-aminoazobenzene, together with the resonance structure of the azonium tautomer.	49
Figure 3.10 Protonation of Methyl Orange.....	49
Figure 3.11 Possible protonation sites and tautomerisation of 4- <i>N,N</i> -dimethylamino-4-aminoazobenzene.....	50
Figure 3.12 Structure of 1-phenylazonaphthalene (1) and 2-phenylazonaphthalene (2).....	51
Figure 3.13 Structure of 4,4'-substituted 1-phenylazonaphthalene.....	52
Figure 3.14 Left: UV/Visible absorption spectra of aqueous OH-Span at $5 \times 10^{-5} \text{ mol dm}^{-3}$; the arrows indicate changes with increasing pH over a range of pH ca. 2 to 12. Right: pH curves analysed using equation 3.3 at 363 and 457 nm.....	54
Figure 3.15 Left: UV/Visible absorption spectra of aqueous NH ₂ -Span at $5 \times 10^{-5} \text{ mol dm}^{-3}$; the arrows indicate changes with increasing pH over a range of pH ca. 2 to 12. Right: pH curves analysed using equation 3.3 at 398 and 518 nm.....	54
Figure 3.16 Deprotonation of OH-Span.....	55
Figure 3.17 UV/Vis absorption spectra of all R-Span dyes in water ($1 \times 10^{-3} \text{ mol dm}^{-3}$); pH adjusted to 5.2, 12 and 1.2 for -OH, O ⁻ and p-NH ₂ , respectively; dashed line gives peak position for H-Span; O ⁻ -Span spectrum truncated at 210 nm due to KOH features at short wavelength.....	57
Figure 3.18 HPLC chromatograms of all R-Span dyes recorded at 254 nm.....	59

Figure 3.19 UV/Vis absorption spectra of all R-Span dyes as HPLC components in water obtained at retention times given in Table 3.6; dashed line represents peak position for H-Span.....	60
Figure 3.20 Left: UV/Vis absorption spectrum of OH-Span (3×10^{-2} and 5×10^{-5} mol dm ⁻³) in water at pH 2 and 12. Right: UV/Vis absorption spectrum of NH ₂ -Span (3×10^{-2} and 5×10^{-5} mol dm ⁻³) in water at pH 7.....	61
Figure 3.21 UV-visible absorption spectra of OH, O ⁻ and NH ₂ -Span in DMSO, water and ethanol at 5×10^{-5} mol dm ⁻³	62
Figure 3.22 Optimised structures of R-Span dyes along with their numbering systems. (<i>Original in colour</i>).....	64
Figure 3.23 Resonance structures of R-Span dyes where X = electron donating substituent and Y = electron withdrawing substituent.....	66
Figure 3.24 Expansion of phenyl ring of NH ₂ -Span. (<i>Original in colour</i>).....	67
Figure 3.25 Calculated HOMO-1, HOMO, LUMO, LUMO+1 and energy difference (LUMO-HOMO) for H-Span, OH-Span and CN-Span. (<i>Original in colour</i>).....	68
Figure 3.26 Calculated changes in electron density on excitation to the first (bottom) and second (top) excited states for H-Span (left) and OH-Span (middle) and CN-Span (right). Blue and white regions represent a decrease and increase in electron density on excitation, respectively. (<i>Original in colour</i>).....	70
Figure 3.27 Pictorial representation of calculated Mulliken atomic charges of all R-Span dyes; red regions represent positive charge; blue regions represent negative charge; 1 Å radius per unit charge; position 14 shown for H-Span common for all dyes and NHAc-Span numbering system shown. (<i>Original in colour</i>).....	73
Figure 3.28 Aromatic region ¹ H NMR spectrum of NH ₂ -Span in DMSO-d ₆ (top) and D ₂ O (bottom).....	76
Figure 3.29 ¹³ C NMR spectrum of NH ₂ -Span in DMSO-d ₆ (top) and D ₂ O (bottom).....	76
Figure 3.30 Structure of NH ₂ -Span with the numbering system used for NMR assignments.....	77

Figure 3.31 COSY and NOESY interactions for NH ₂ -Span in DMSO-d ₆ and D ₂ O.....	77
Figure 3.32 Aromatic region ¹ H NMR spectrum of OH-Span in D ₂ O; pD 5.2 (top, 700 MHz), unadjusted (middle, 500 MHz) and pD 12.0 (bottom, 400 MHz).....	79
Figure 3.33 Structure of OH-Span with the numbering system used for NMR assignments.....	79
Figure 3.34 R-Span dyes numbering system used for NMR assignments.....	81
Figure 3.35 Left: Aromatic region ¹ H NMR spectra for all R-Span dyes in D ₂ O; Right Calculated ¹ H NMR spectra for all R-Span dyes.....	82
Figure 3.36 Left: Aromatic region ¹³ C NMR spectra for all R-Span dyes in D ₂ O; Right Calculated ¹³ C NMR spectra for all R-Span dyes.....	83
Figure 3.37 UV/Vis absorption spectra of all R-Span dyes as prepared in water (left) and as pure HPLC components (right) in water; dashed lines show Raman excitation wavelengths.....	86
Figure 3.38 Experimental Raman spectra of OH-Span in water (4 × 10 ⁻⁴ mol dm ⁻³) with 350.6, 413.1 and 514.5 nm excitation, experimental IR spectra of OH-Span in water (saturated), experimental Raman spectra of NAPDAD (solid) and APOL in water (1 × 10 ⁻³ mol dm ⁻³) with 514.5 nm excitation; all with their calculated spectra.....	90
Figure 3.39 Structure of NAPDAD and selected calculated normal mode vibrations of NAPDAD that match those from OH-Span. (<i>Original in colour</i>).....	92
Figure 3.40 Structure of APOL and selected calculated normal mode vibrations of APOL that match those from OH-Span. (<i>Original in colour</i>).....	92
Figure 3.41 Selected calculated normal mode vibrations of OH-Span. (<i>Original in colour</i>).....	93
Figure 3.42 Experimental Raman spectra of R-Span (4 × 10 ⁻⁴ mol dm ⁻³) in water with 514.5 nm excitation, and their calculated spectra.....	95
Figure 3.43 Experimental Raman spectra of NH ₂ -, OH- and NHAc-Span (4 × 10 ⁻⁴ mol dm ⁻³) in water with 413.1 nm excitation.....	98
Figure 3.44 Experimental Raman spectra of NH ₂ -, OH-, OMe- and NHAc-Span (4 × 10 ⁻⁴ mol dm ⁻³) in water with 350.6 nm excitation.....	98

Figure 3.45 UV/Vis absorption spectrum of O ⁻ -Span (4×10^{-4} mol dm ⁻³) in water at pH 12; dashed lines show Raman excitation wavelengths.....	100
Figure 3.46 Experimental Raman spectra of O ⁻ -Span (4×10^{-4} mol dm ⁻³) in water at pH 12 with 350.6, 413.1 and 514.5 nm excitation.....	100
Figure 3.47 Resonance structure of the O ⁻ -Span.....	102
Figure 3.48 UV/Visible absorption spectra of aqueous NH ₂ -Span and P-NH ₂ -Span at 5×10^{-5} mol dm ⁻³ at ca. pH 7 and pH 1.8, respectively.....	103
Figure 3.49 Possible protonation scheme for NH ₂ -Span.....	103
Figure 3.50 Optimised structures of the azonium and ammonium tautomer of P-NH ₂ -Span dyes along with the numbering system. (<i>Original in colour</i>).....	104
Figure 3.51 Pictorial representation of Mulliken atomic charges of the azonium and ammonium tautomers of P-NH ₂ -Span; red regions represent positive charge, blue regions represent negative charge; 1 Å radius per unit charge. (<i>Original in colour</i>).....	104
Figure 3.52 Calculated HOMO-1, HOMO, LUMO, LUMO+1 and energy differences (LUMO-HOMO) for azonium and ammonium tautomers of P-NH ₂ -Span. (<i>Original in colour</i>).....	106
Figure 3.53 Calculated changes in electron density on excitation to the third (top), second (middle) and first (bottom) excited states for the azonium (left) and ammonium (right) tautomer of P-NH ₂ -Span. Blue and white regions represent a decrease and increase in electron density on excitation, respectively. (<i>Original in colour</i>).....	107
Figure 3.54 Resonance structure of the azonium tautomer of P-NH ₂ -Span.	109
Figure 3.55 Aromatic region ¹ H NMR spectra of P-NH ₂ -Span in D ₂ O/DCl at pD 2.0 (top), the calculated az tautomer (middle) and am tautomer (bottom) of P-NH ₂ -Span.....	112
Figure 3.56 ¹³ C NMR spectra of P-NH ₂ -Span D ₂ O/DCl at pD 2.0 (top), the calculated az tautomer (middle) and am tautomer (bottom) of P-NH ₂ -Span.....	113
Figure 3.57 UV/Vis absorption spectrum of P-NH ₂ -Span in water (4×10^{-4} mol dm ⁻³) at pH 2.0; dashed line represents Raman excitation wavelength.....	116

Figure 3.58 Experimental Raman spectra of P-NH ₂ -Span in water at pH 2.0 with 514.5 and 350.6 nm excitation and calculated Raman spectra of the azonium and ammonium tautomers of P-NH ₂ -Span.....	116
Figure 3.59 Resonance structure of NH ₂ -Span.....	118
Figure 3.60 Left: Experimental and calculated wavelength (λ_{\max}) vs <i>para</i> Hammett constant σ_p for the R-Span dye series, Right: Experimental and calculated ¹ H NMR position of H13/15 vs <i>para</i> Hammett constant σ_p for the R-Span dye series.....	121
Figure 3.61 Experimental and calculated ¹³ C NMR position of C13/15 (left) and C14 (right) vs <i>para</i> Hammett constant σ_p for the R-Span dye series.....	121
Figure 3.62 Calculated Mulliken atomic charge of C2, C11 and C14 vs <i>para</i> Hammett constant σ_p for the R-Span dye series.....	121
Figure 3.63 Structure of chlorotriazine-Span dye.....	122
Figure 3.64 Experimental Raman spectra of R-Span (4×10^{-4} mol dm ⁻³) in water with 514.5 nm excitation focused on the three main regions of interest, dashed lines indicate the position of H-Span.....	122

Chapter 4 Electrochemistry

Figure 4.1 Structure of Orange II.....	130
Figure 4.2 Four electron reduction of Orange II by zerovalent Iron.....	130
Figure 4.3 Two-step four-electron reduction of Orange I via disproportionation...	131
Figure 4.4 Proposed two-step four-electron reduction of Methyl Red.....	132
Figure 4.5 Proposed four-electron reduction of 4-hydroxyazobenzene via N-N bond scission.....	132
Figure 4.6 One-Step two-electron reduction of azobenzene.....	133
Figure 4.7 Structures of 4-dimethylaminoazobenzene and 4-aminoazobenzene.....	133
Figure 4.8 One-Step two-electron reduction of substituted azobenzenes, where R= NH ₂ , OH, OMe, H and Br.....	134
Figure 4.9 Half wave potential for the reduction of substituted azobenzenes where R= NH ₂ , OH, OMe, H and Br in aqueous dioxane vs their Hammett substituent constants σ_p	134

Figure 4.10 One-Step two-electron reduction of 1-(4-Nitrophenylazo)-2-naphthol.	135
Figure 4.11 Cyclic voltammogram of OH-Span (1×10^{-3} mol dm ⁻³) in pH 5.2 sodium acetate buffer solution recorded with a sweep rate of 10 mV s ⁻¹	137
Figure 4.12 Left: UV/Visible absorption spectra of OH-Span (5×10^{-4} mol dm ⁻³) in pH 5.2 sodium acetate buffer solution; the arrow indicates the change with decreasing potential over a range of 0 to -1.2 V (vs Ag wire) and with the overall difference spectrum (final – initial) shown. Right: Potential curve analysed using equation 4.1 at 363 nm, where n = 0.45.....	139
Figure 4.13 Left: UV/Visible absorption spectra of OH-Span (5×10^{-4} mol dm ⁻³) in pH 5.2 sodium acetate buffer solution; the arrow indicates the change with increasing potential over a range of 0 to +1.0 V (vs Ag wire) and with the overall difference spectrum (final – initial) shown. Right: Potential curve analysed using equation 4.1 at 363 nm where n = 0.39.....	139
Figure 4.14 CPE reduction on OH-Span (8×10^{-4} mol dm ⁻³) in pH 5.2 sodium acetate buffer solution over 30 min at a potential of -1.2 V (vs Ag/AgCl) Left: Current-time profile, Right: Charge-time profile.....	140
Figure 4.15 HPLC chromatograms of OH-Span (8×10^{-4} mol dm ⁻³) before (top) and after (bottom) CPE reduction. Inserts show the expansions of the HPLC chromatogram of each component.....	142
Figure 4.16 Top: UV/Visible absorption spectrum of OH-Span (8×10^{-4} mol dm ⁻³) before CPE reduction at an elution time of 12.22 min. Bottom: UV/Visible absorption spectra of Components A, B and C after CPE reduction at retention times of 2.43, 3.87 and 4.26 min.....	142
Figure 4.17 Left: Negative ion ESI mass spectrum of OH-Span with a retention time of 12.12 min. Middle: Negative ion MS/MS-1 mass spectrum of the ion with 407.0 m/z. Right: Negative ion MS/MS-2 mass spectrum on the ion with 327.0 m/z.....	143
Figure 4.18 Structure of [OH-Span + H ⁺] corresponding to base peak at 407.0 m/z and its observed fragmentations.....	143
Figure 4.19 Left: Negative ion ESI mass spectrum of component A formed after CPE of OH-Span with a retention time of 2.32 min. Right: Negative ion MS/MS-1 mass spectrum on the ion with 302.0 m/z.....	144

Figure 4.20 Left: Aromatic region ^1H NMR (700 MHz) DOSY display OH-Span at $5 \times 10^{-3} \text{ mol dm}^{-3}$ and pD 5.2. Right: Histogram of all components in DOSY display.....	146
Figure 4.21 Left: Aromatic region ^1H NMR (700 MHz) DOSY display of components E, F and G formed after CPE reduction of OH-Span at $5 \times 10^{-3} \text{ mol dm}^{-3}$ and pD 5.2. Right: Histogram of all components in DOSY display.....	146
Figure 4.22 Proposed two-step four-electron reduction of OH-Span producing NAPDAD and APOL (numbering system shown).....	147
Figure 4.23 Left: UV/Visible absorption spectra of aqueous NAPDAD at $5 \times 10^{-5} \text{ mol dm}^{-3}$; the arrows indicate changes with increasing pH over a range of pH 2 to 12. Right: pH curve analysed using equation 3.3 (Chapter 3) at 242 nm.....	148
Figure 4.24 UV/Visible absorption spectrum of NAPDAD (left) and APOL (right) in water and in pH 5.2 sodium acetate buffer solution, both at $5 \times 10^{-5} \text{ mol dm}^{-3}$	148
Figure 4.25 HPLC chromatogram of NAPDAD (top) and APOL (bottom) both at $1 \times 10^{-3} \text{ mol dm}^{-3}$. Inserts show expansions of the regions of the HPLC chromatogram of each component.....	150
Figure 4.26 UV/Visible absorption spectra of NAPDAD (left) and APOL (right) both at $1 \times 10^{-3} \text{ mol dm}^{-3}$ at retention times of 2.41, 3.87 and 4.26 min, respectively.....	150
Figure 4.27 Left: Negative ion ESI mass spectrum of NAPDAD with a retention time of 2.41 min. middle: Negative ion MS/MS-1 mass spectrum on the ion with 302.0 m/z. Right: Structure of $[\text{NAPDAD} + \text{H}^+]^-$ corresponding to base peak at 302.0 m/z and its observed fragmentation.....	151
Figure 4.28 Left: Positive ion ESI mass spectrum of APOL with a retention time of 3.71 min. Right: Structure of $[\text{APOL} + \text{H}^+]^+$ corresponding to base peak at 110.1 m/z.....	151
Figure 4.29 Left: Aromatic region ^1H NMR (700 MHz) DOSY display of NAPDAD (top), APOL (bottom) at $5 \times 10^{-3} \text{ mol dm}^{-3}$ and pD 5.2. Right: Histogram of all components in DOSY display.....	153

Figure 4.30 Left: Aromatic region ^1H NMR (700 MHz) DOSY display of a mixture of APOL, NAPDAD and OH-Span mixture at $5 \times 10^{-3} \text{ mol dm}^{-3}$ and pD 5.2. Right: Histogram of all components in DOSY display.....	154
Figure 4.31 Hydrolysis of hydrazine-dye-intermediate to produce hydroquinone.....	154
Figure 4.32 Left: Aromatic region ^1H NMR (700 MHz) DOSY display of 1,4-hydroquinone at $1 \times 10^{-3} \text{ mol dm}^{-3}$ and pD 5.2. Right: Histogram of all components in DOSY display.....	154
Figure 4.33 Left: UV/Visible absorption spectra of NH_2 -Span ($5 \times 10^{-4} \text{ mol dm}^{-3}$) in pH 5.2 sodium acetate buffer solution; the arrow indicates the change with decreasing potential over a range of 0 to -1.0 V (vs Ag wire) and with the overall difference spectrum (final – initial) shown. Right: Potential curve analysed using equation 4.1 at 401 nm where $n = 0.79$	160
Figure 4.34 Left: UV/Visible absorption spectra of NH_2 -Span ($5 \times 10^{-4} \text{ mol dm}^{-3}$) in pH 5.2 sodium acetate buffer solution; the arrow indicates the change with increasing potential over a range of 0 to +1.0 V (vs Ag wire) and with the overall difference spectrum (final – initial) shown. Right: Potential curve analysed using equation 4.1 at 401 nm where $n = 0.85$	160
Figure 4.35 Left: UV/Visible absorption spectra of NHAc -Span ($5 \times 10^{-4} \text{ mol dm}^{-3}$) in pH 5.2 sodium acetate buffer solution; the arrow indicates the change with decreasing potential over a range of 0 to -1.2 V (vs Ag wire) and with the overall difference spectrum (final – initial) shown. Right: Potential curve analysed using equation 4.1 at 362 nm where $n = 0.40$	161
Figure 4.36 Left: UV/Visible absorption spectra of NHAc -Span ($5 \times 10^{-4} \text{ mol dm}^{-3}$) in pH 5.2 sodium acetate buffer solution; arrow indicates the change with increasing potential over a range of 0 to +1.0 V (vs Ag wire) and with the overall difference spectrum (final – initial) shown. Right: Potential curve analysed using equation 4.1 at 362 nm where $n = 0.53$	161
Figure 4.37 Left: UV/Visible absorption spectra of OMe -Span ($5 \times 10^{-4} \text{ mol dm}^{-3}$) in pH 5.2 sodium acetate buffer solution; the arrow indicates the change with decreasing potential over a range of 0 to -1.0 V (vs Ag wire) and with the overall difference spectrum (final – initial) shown. Right: Potential curve analysed using equation 4.1 at 364 nm where $n = 1.05$	162

Figure 4.38 Left: UV/Visible absorption spectra of H-Span (5×10^{-4} mol dm ⁻³) in pH 5.2 sodium acetate buffer solution; the arrow indicates the change with decreasing potential over a range of 0 to -1.0 V (vs Ag wire) and with the overall difference spectrum (final – initial) shown. Right: Potential curve analysed using equation 4.1 at 331 nm where $n = 0.36$	162
Figure 4.39 Left: UV/Visible absorption spectra of Br-Span (5×10^{-4} mol dm ⁻³) in pH 5.2 sodium acetate buffer solution; the arrow indicates the change with decreasing potential over a range of 0 to -0.9 V (vs Ag wire) and with the overall difference spectrum (final – initial) shown. Right: Potential curve analysed using equation 4.1 at 341 nm where $n = 0.68$	163
Figure 4.40 Left: UV/Visible absorption spectra of CN-Span (5×10^{-4} mol dm ⁻³) in pH 5.2 sodium acetate buffer solution; the arrow indicates the change with decreasing potential over a range of 0 to -0.9 V (vs Ag wire) and with the overall difference spectrum (final – initial) shown. Right: Potential curve analysed using equation 4.1 at 337 nm where $n = 0.37$	163
Figure 4.41 CPE reduction on NH ₂ -Span (8×10^{-4} mol dm ⁻³) in pH 5.2 sodium acetate buffer solution over 30 min at a potential of -1.2 V (vs Ag/AgCl) Left: Current-time profile, Right: Charge-time profile.....	165
Figure 4.42 CPE on NHAc-Span (8×10^{-4} mol dm ⁻³) in pH 5.2 sodium acetate buffer solution over 30 min at a potential of -1.2 V (vs Ag/AgCl) Left: Current-time profile, Right: Charge-time profile.....	165
Figure 4.43 HPLC chromatograms of NH ₂ -Span (8×10^{-4} mol dm ⁻³) before (top) and after (bottom) CPE reduction. Inserts show the expansions of the HPLC chromatogram of each component.....	167
Figure 4.44 Top: UV/Visible absorption spectrum of NH ₂ -Span (8×10^{-4} mol dm ⁻³) before CPE reduction at an elution time of 10.72 min. Bottom: UV/Visible absorption spectra of Components A' and B' after CPE reduction at retention times of 2.41, 3.65 min.....	167
Figure 4.45 Structure of DAB.....	168
Figure 4.46 HPLC chromatogram DAB at 1×10^{-3} mol dm ⁻³ and pH 5.2. Insert: UV/Visible absorption spectra of DAB at retention time of 3.64 min.....	168

Figure 4.47 Left: UV/Visible absorption spectra of aqueous DAB at $5 \times 10^{-5} \text{ mol dm}^{-3}$ over a pH range of pH 2 to 12. Right: pH curve analysed using a multi pK_a equation (Appendix 1 equation A1.42) at 230 and 284 nm.....	168
Figure 4.48 Protonation of DAB; pK_a of 2.72 and 5.35 in water, pK_{a3} is non-reversible, hence a chemical effect.....	168
Figure 4.49 HPLC chromatograms of NHAc-Span ($8 \times 10^{-4} \text{ mol dm}^{-3}$) before (top) and after (bottom) CPE reduction. Inserts show expansion of selected regions of the HPLC chromatogram of components at ca. 3 and 6 min.....	171
Figure 4.50 Top: UV/Visible absorption spectrum of NHAc-Span ($8 \times 10^{-4} \text{ mol dm}^{-3}$) before CPE at an elution time of 14.89 min. Bottom: UV/Visible absorption spectra of Components A'', B'', C'', D'' and E'' after CPE at retention times of 2.36, 3.05, 3.77, 6.27, 10.28 min.....	171
Figure 4.51 Structure of APA.....	172
Figure 4.52 HPLC chromatogram APA at $1 \times 10^{-3} \text{ mol dm}^{-3}$ and pH 5.2. Insert: UV/Visible absorption spectra of APA at retention time of 10.26 min.....	172
Figure 4.53 Left: UV/Visible absorption spectra of aqueous APA at $5 \times 10^{-5} \text{ mol dm}^{-3}$; the arrows indicate changes with increasing pH over a range of pH 2 to 12. Right: pH curve analysed using equation 3.3 (Chapter 3) at 240 and 252 nm.....	172
Figure 4.54 Protonation of APA; pK_a of 4.39 in water.....	172
Figure 4.55 UV/Visible absorption product spectra formed after the spectroelectrochemical reduction of the R-Span dyes; dashed line represents the absorption band of NAPDAD at 353 nm.....	175
Figure 4.56 Fitted curves of the spectroelectrochemical reduction of the R-Span dyes analysed by equation 4.1. (<i>Original in colour</i>).....	177
Figure 4.57 Estimated reduction potentials for R-Span dyes in pH 5.2 sodium acetate buffer solution vs <i>para</i> substituent Hammett constants, σ_p and σ_p^- and their fits to a straight line.....	178
Figure 4.58 Calculated Mulliken atomic charges for $\text{N}\alpha$ and $\text{N}\beta$ for the R-Span dyes vs; Left: <i>Para</i> substituent Hammett σ_p constants and Right: <i>Para</i> substituent Hammett $\sigma_p \sigma_p^-$ constants and their fits to a straight line.....	179

Figure 4.59 Estimated reduction potentials for R-Span dyes in pH 5.2 sodium acetate buffer solution vs calculated Mulliken atomic charges for $N\alpha$ and $N\beta$ for the R-Span dyes and their fits to a straight line.....	180
Figure 4.60 Generic two-step four-electron reduction of R-Span producing NAPDAD and R-aminobenzene.....	182

Chapter 5 Photochemistry

Figure 5.1 Jablonski diagram of the routes of excitation and decay of electronic states; abs = absorption, ic = internal conversion, isc = intersystem crossing, f = fluorescence, p = phosphorescence, vr = vibrational relaxation.....	185
Figure 5.2 <i>Trans</i> - and <i>cis</i> -azobenzene, together with numbering system.....	186
Figure 5.3 Mechanism of azobenzene isomerisation.....	187
Figure 5.4 Structure of 4,4'-substituted 1-phenylazonaphthalene.....	188
Figure 5.5 <i>Trans</i> - and <i>cis</i> -NHMe-Span, together with numbering system.....	189
Figure 5.6 Reaction mechanism, of singlet oxygen with 4-aryl azo-1-naphthol.....	190
Figure 5.7 Photo-reduction of azobenzene.....	192
Figure 5.8 Top: Irradiation of the photoinitiator (2-hydroxy-4'- (2-hydroxyethoxy)-2-methylpropiophenone) resulting in the formation of benzoyl and 2-hydroxy-2-propyl radicals. Middle: Hydrogen atom transfer between benzoyl and 2-hydroxy-2-propyl radicals to produce H-benzaldehyde (4-(2-hydroxy-ethoxy)-benzaldehyde) and acetone. Bottom: Reaction of benzoyl radicals with oxygen to produce H-benzoic acid (4-(2-hydroxyethoxy) benzoic acid).....	193
Figure 5.9 Proposed one-electron reduction mechanism of Orange II by 2-hydroxy-2-propyl radicals.....	194
Figure 5.10 Proposed one-electron oxidation mechanism of Orange II.....	195
Figure 5.11 UV/Visible absorption spectra of OH-Span alone in pH 5.2 sodium acetate buffer solution at $5 \times 10^{-5} \text{ mol dm}^{-3}$ before and after 30 light pulses.....	198
Figure 5.12 UV/Visible absorption spectra obtained on irradiation of photoinitiator in pH 5.2 sodium acetate buffer solution at $5 \times 10^{-5} \text{ mol dm}^{-3}$ under nitrogen (left) and air (right) over 30 light pulses, with arrows indicating changes and with the overall difference spectrum (final – initial) shown.....	199

Figure 5.13 HPLC chromatogram of photoinitiator alone (5×10^{-5} mol dm ⁻³) under air before (top) and after (bottom) 30 light pulses.....	200
Figure 5.14 Top: UV/Visible absorption spectra of photoinitiator (5×10^{-5} mol dm ⁻³) before irradiation. Bottom: UV/Visible absorption spectra of H-benzoic acid (left), photoinitiator (PI) product (right) formed after 30 light pulses.....	200
Figure 5.15 HPLC chromatogram of photoinitiator alone (5×10^{-5} mol dm ⁻³) under nitrogen before (top) and after (bottom) 30 light pulses.....	202
Figure 5.16 Top: UV/Visible absorption spectra of photoinitiator (5×10^{-5} mol dm ⁻³) before irradiation. Bottom: UV/Visible absorption spectra of H-benzoic acid (left), photoinitiator product (middle) and H-benzaldehyde (right) formed after 30 light pulses.....	202
Figure 5.17 Left: Positive ion ESI mass spectrum of photoinitiator with a retention time of 24.83 min. Middle: Positive ion MS/MS-1 mass spectrum of the ion with 224.9 m/z. Right: Structure of $[\text{PI} + \text{H}^+]^+$ corresponding to base peak at 224.9 m/z.....	203
Figure 5.18 Left: Negative ion ESI mass spectrum of component H-benzoic acid formed after irradiation of photoinitiator alone with a retention time of 12.17 min. Right: Structure of $[\text{H-Benzoic acid} - \text{H}^+]^-$ corresponding to base peak at 181.2 m/z.....	203
Figure 5.19 Left ¹ H NMR (700 MHz) DOSY display of photoinitiator alone before (top) and after 50 light pulses (bottom) at 5×10^{-4} mol dm ⁻³ at pD 5.2 under nitrogen. Right: Histogram of all components in DOSY display.....	206
Figure 5.20 Possible components present after the irradiation of photoinitiator alone under nitrogen after 50 light pulses, where PIP = photoinitiator product, HEB = H-benzaldehyde and R and R' are unknown.....	208
Figure 5.21 Irradiation of 1:1 (left) and 1:10 (right) OH-Span:photoinitiator (5×10^{-4} mol dm ⁻³ dye concentration) in pH 5.2 sodium acetate buffer solution under nitrogen over 30 light pulses; arrows indicate changes with increasing light pulse, with the overall difference spectrum (final – initial) shown.....	210

Figure 5.22 Irradiation of 1:1 (left) and 1:10 (right) OH-Span:photoinitiator (5×10^{-4} mol dm ⁻³ dye concentration) in pH 5.2 sodium acetate buffer solution under air over 30 light pulses; arrows indicate changes with increasing light pulse, with the overall difference spectrum (final – initial) shown.....	210
Figure 5.23 Normalised absorbance at 363 nm as a function of light pulse for 1:1 and 1:10 H-Span:photoinitiator in pH 5.2 sodium acetate buffer solution under nitrogen (left) and air (right).....	211
Figure 5.24 HPLC chromatogram of 1:1 OH-Span:photoinitiator (5×10^{-4} mol dm ⁻³ dye concentration) under nitrogen before (top) and after (bottom) 50 light pulses.....	213
Figure 5.25 HPLC chromatogram of 1:10 OH-Span:photoinitiator (5×10^{-4} mol dm ⁻³ dye concentration) under nitrogen before (top) and after (bottom) 50 light pulses.....	213
Figure 5.26 UV/Visible absorption spectra of components identified from 1:10 OH-Span:photoinitiator (5×10^{-4} mol dm ⁻³ dye concentration) under nitrogen after 50 light pulses.....	214
Figure 5.27 Left: ESI mass spectrum of component A, D and E with a retention times of 2.32, 10.40 and 10.55 min, respectively, formed after irradiation of 1:10 OH-Span:photoinitiator. Right: MS/MS-1 mass spectrum on the base peak ion of each component.....	215
Figure 5.28 Left: ESI mass spectrum of component F, K and Q with a retention time of 10.81, 14.65 and 21.05 min, respectively, formed after irradiation of 1:10 OH-Span:photoinitiator. Middle: MS/MS-1 mass spectrum on the base peak ion of each component. Right: MS/MS-2 mass spectrum of each component.....	216
Figure 5.29 HPLC chromatogram of 1:1 NAPDAD:photoinitiator (both at 5×10^{-4} mol dm ⁻³) at pH 5.2 under nitrogen before (top) and after (bottom) 50 light pulses.....	219
Figure 5.30 Top: UV/Visible absorption spectra of 1:1 NAPDAD:photoinitiator before irradiation. Bottom: UV/Visible absorption spectra of components formed after 50 light pulses.....	219
Figure 5.31 HPLC chromatogram of 1:1 APOL:photoinitiator (both at 5×10^{-4} mol dm ⁻³) at pH 5.2 under nitrogen before (top) and after (bottom) 50 light pulses.....	220

Figure 5.32 Top: UV/Visible absorption spectra of 1:1 APOL:photoinitiator before irradiation. Bottom: UV/Visible absorption spectra of components formed after 50 light pulses.....	220
Figure 5.33 Left: ^1H NMR (700 MHz) DOSY display of 1:1 OH-Span:photoinitiator before (top) and after 50 light pulses (bottom) at $5 \times 10^{-4} \text{ mol dm}^{-3}$ at pD 5.2 under nitrogen (D = Dye P = Photoinitiator). Right: Histogram of all components in DOSY display.....	224
Figure 5.34 Possible components from the irradiation of 1:1 OH-Span:photoinitiator after 50 light pulses under nitrogen. For component *, R' contains *P.....	226
Figure 5.35 TRVIS spectra of OH-Span alone ($4 \times 10^{-4} \text{ mol dm}^{-3}$) in pH 5.2 sodium acetate buffer solution, 150, 300, 600 1250 and 3500 ns after excitation; arrows indicate changes with time.....	228
Figure 5.36 TRVIS kinetic traces of OH-Span alone ($4 \times 10^{-4} \text{ mol dm}^{-3}$) in pH 5.2 sodium acetate buffer solution at 360 and 460 nm, fitted using equation 5.7.....	228
Figure 5.37 Isomerisation of OH-Span.....	228
Figure 5.38 TRVIS kinetic traces of photoinitiator alone ($1 \times 10^{-3} \text{ mol dm}^{-3}$) in pH 5.2 sodium acetate buffer solution under nitrogen analysed at 410 nm, fitted using equation 5.7.....	229
Figure 5.39 TRVIS spectra of 1:10 OH-Span:photoinitiator ($1 \times 10^{-4} \text{ mol dm}^{-3}$ dye concentration) in pH 5.2 sodium acetate buffer solution under nitrogen, 325 ns after excitation.....	230
Figure 5.40 TRVIS spectra of 1:10 OH-Span:photoinitiator ($1 \times 10^{-4} \text{ mol dm}^{-3}$ dye concentration) in pH 5.2 sodium acetate buffer solution under nitrogen, 1.30, 3.50, 6.50, 15.00, 45.00 and 85.00 μs after excitation.....	230
Figure 5.41 TRVIS kinetic traces of 1:10 OH-Span:photoinitiator ($1 \times 10^{-4} \text{ mol dm}^{-3}$ dye concentration) in pH 5.2 sodium acetate buffer solution under nitrogen at 360 and 490 nm.....	230
Figure 5.42 TRVIS kinetic traces of OH-Span alone and 1:10 OH-Span:photoinitiator (all $1 \times 10^{-4} \text{ mol dm}^{-3}$ dye concentration) in pH 5.2 sodium acetate buffer solution under nitrogen at 360 nm.....	231

Figure 5.43 TRVIS kinetics of 1:10 OH-Span:photoinitiator (1×10^{-4} mol dm ⁻³ dye concentration) in pH 5.2 sodium acetate buffer solution at 360 nm (left) and 490 nm (right) together with modelled overall contribution (solid line) alongside Dye ^{•-} (dashed line) and Dye (dotted line) contributions.....	235
Figure 5.44 OH-Span radical anion spectrum (solid line), produced by addition of OH-Span bleach (dashed line) at a concentration of ca. 2.01×10^{-5} mol dm ⁻³ to the TRVIS spectra at 45 μ s.....	236
Figure 5.45 Proposed reduction of OH-Span in the presence of 2-hydroxy- 2-propyl radicals.....	237
Figure 5.46 UV/Visible absorption spectra of NH ₂ -Span (left) and CN-Span (Right) alone in water at 5×10^{-5} mol dm ⁻³ before and after 30 light pulses.....	238
Figure 5.47 UV/Visible absorption spectra of O ⁻ -Span alone in pH 11 sodium acetate buffer solution at 5×10^{-5} mol dm ⁻³ before and after 30 light pulses.....	238
Figure 5.48 TRVIS spectra of NH ₂ -Span alone (4×10^{-4} mol dm ⁻³) in water, 1.0, 2.5, 4.5, 14.5 and 30.0 ms after excitation.....	239
Figure 5.49 TRVIS Kinetic traces of NH ₂ -Span alone (4×10^{-4} mol dm ⁻³) in water at 400 nm.....	240
Figure 5.50 TRVIS spectra of CN-Span alone (4×10^{-4} mol dm ⁻³) in water, 0.1, 0.5, 1.0, 2.0 and 4.0 ms after excitation.....	240
Figure 5.51 TRVIS Kinetic traces of CN-Span alone (4×10^{-4} mol dm ⁻³) in water at 400 nm.....	240
Figure 5.52 UV/Visible absorption spectra of OMe-Span (left) and NHAc-Span (Right) alone in water at 1×10^{-4} mol dm ⁻³ before and after 1 and 30 light pulses, with the overall difference spectrum (final – initial) shown.....	242
Figure 5.53 HPLC chromatogram of a OMe-Span sample (40% dye, 60 % NaCl).	242
Figure 5.54 Left: Negative ion ESI mass spectrum of <i>cis</i> -OMe-Span with a retention time of 12.41 min. Right: Negative ion ESI mass spectrum of <i>trans</i> - OMe-Span with a retention time of 19.29 min.....	242
Figure 5.55 Optimised structures of <i>cis</i> -OMe-Span (left) and <i>cis</i> -NHAc-Span (right) along with the numbering system. (<i>Original in colour</i>).....	243
Figure 5.56 Aromatic and non-aromatic region ¹ H NMR spectrum of OMe-Span (top) and NHAc-Span (bottom) both at 1×10^{-4} mol dm ⁻³ after 30 light pulses.....	243

Figure 5.57 Calculated UV/Visible absorption spectrum of <i>cis</i> -OMe-Span (left) and <i>cis</i> -NHAc-Span (right).....	244
Figure 5.58 Left: UV/Visible absorption spectra of OMe-Span (1×10^{-4} mol dm ⁻³) in water recorded for 28 days after 30 light pulses at 21 °C, Right: Single exponential fit at 363 nm.....	246
Figure 5.59 Left: UV/Visible absorption spectra of NHAc-Span (1×10^{-4} mol dm ⁻³) in water recorded for 32 hr after 30 light pulses at 21 °C Right: Single exponential fit at 363 nm.....	246
Figure 5.60 TRVIS spectra from OMe-Span (left) and NHAc-Span (right) Alone (4×10^{-4} mol dm ⁻³) in water, 20, 40, 120, 250 and 600 ms after excitation...	247
Figure 5.61 TRVIS Kinetic traces for OMe-Span alone (left) and NHAc-Span (right) alone (4×10^{-4} mol dm ⁻³) in water at 360 nm.....	247
Figure 5.62 Structure of a reactive dye where R is a reactive group.....	248
Figure 5.63 Irradiation of 1:1 (left) and 1:10 (right) O ⁻ -Span:photoinitiator in pH 11 phosphate buffer solution under nitrogen over 30 light pulses; arrows indicate changes with increasing light pulse, with the overall difference spectrum (final – initial) shown.....	250
Figure 5.64 Irradiation of 1:1 (left) and 1:10 (right) O ⁻ -Span:photoinitiator in pH 11 phosphate buffer solution under air over 30 light pulses; arrows indicate changes with increasing light pulse, with the overall difference spectrum (final – initial) shown.....	250
Figure 5.65 Irradiation of 1:1 (left) and 1:10 (right) NH ₂ -Span:photoinitiator in water under nitrogen over 30 light pulses; arrows indicate changes with increasing light pulse, with the overall difference spectrum (final – initial) shown.....	251
Figure 5.66 Irradiation of 1:1 (left) and 1:10 (right) NH ₂ -Span:photoinitiator in water under air over 30 light pulses; arrows indicate changes with flash, with the overall difference spectrum (final – initial) shown.....	251
Figure 5.67 Irradiation of 1:1 (left) and 1:10 (right) NHAc-Span:photoinitiator in water under nitrogen over 30 light pulses; arrows indicate changes with increasing light pulse, with the overall difference spectrum (final – initial) shown.....	252
Figure 5.68 Irradiation of 1:1 (left) and 1:10 (right) NHAc-Span:photoinitiator under air over 30 light pulses; arrows indicate changes with increasing light pulse, with the overall difference spectrum (final – initial) shown.....	252

Figure 5.69 Normalised absorbance at 457 nm as a function of light pulse for 1:1 and 1:10 H-Span:photoinitiator in pH 11 phosphate buffer solution under nitrogen (left) and air (right).....	253
Figure 5.70 Normalised absorbance at 401 nm as a function of light pulse for 1:1 and 1:10 NH ₂ -Span:photoinitiator under nitrogen (left) and air (right).....	253
Figure 5.71 Normalised absorbance at 364 nm as a function of light pulse for 1:1 and 1:10 NHAc-Span:photoinitiator under nitrogen (left) and air (right).....	253
Figure 5.72 HPLC chromatogram of 1:10 O ⁻ -Span:photoinitiator (5 × 10 ⁻⁵ mol dm ⁻³ dye concentration) under nitrogen before (top) and after (bottom) 30 light pulses.....	255
Figure 5.73 HPLC chromatogram of 1:10 O ⁻ -Span:photoinitiator (5 × 10 ⁻⁵ mol dm ⁻³ dye concentration) under nitrogen before (top) and after (bottom) 30 light pulses.....	255
Figure 5.74 UV/Visible absorption spectra of each component formed from 1:10 O ⁻ -Span:photoinitiator (5 × 10 ⁻⁵ mol dm ⁻³ dye concentration) under nitrogen after 30 light pulses.....	256
Figure 5.75 HPLC chromatogram of 1:1 NH ₂ -Span:photoinitiator (5 × 10 ⁻⁵ mol dm ⁻³ dye concentration) under nitrogen before (top) and after (bottom) 30 light pulses.....	257
Figure 5.76 HPLC chromatogram of 1:10 NH ₂ -Span:photoinitiator (5 × 10 ⁻⁵ mol dm ⁻³ dye concentration) under nitrogen before (top) and after (bottom) 30 light pulses.....	258
Figure 5.77 UV/Visible absorption spectra of each component formed from 1:10 NH ₂ -Span:photoinitiator (5 × 10 ⁻⁵ mol dm ⁻³ dye concentration) under nitrogen after 30 light pulses.....	258
Figure 5.78 HPLC chromatogram of 1:11 NHAc-Span:photoinitiator (5 × 10 ⁻⁵ mol dm ⁻³ dye concentration) under nitrogen before (top) and after (bottom) 30 light pulses.....	259
Figure 5.79 HPLC chromatogram of 1:10 NHAc-Span:photoinitiator (5 × 10 ⁻⁵ mol dm ⁻³ dye concentration) under nitrogen before (top) and after (bottom) 30 light pulses.....	260

Figure 5.80 UV/Visible absorption spectra of each component formed from 1:10 NHAc-Span:photoinitiator (5×10^{-5} mol dm ⁻³ dye concentration) under nitrogen after 30 light pulses.....	260
---	-----

Appendices

Appendix 1 Structure

Figure A1.1 Profile of NHAc-Span in DMSO, water and ethanol at 5×10^{-5} mol dm ⁻³	283
Figure A1.2 Calculated HOMO-1, HOMO, LUMO, LUMO+1 and energy difference for NH ₂ -Span, NHAc-Span, OMe-Span and Br-Span. (<i>Original in colour</i>).....	286
Figure A1.3 Calculated changes in electron density on excitation of the first (top) and second (bottom) excited states for H-Span (left) and OH-Span (middle) and NH ₂ -Span right). Blue and white regions represent a decrease and increase in electron density on excitation, respectively. (<i>Original in colour</i>).....	287
Figure A1.4 3 rd excited state of NH ₂ -Span. (<i>Original in colour</i>).....	288
Figure A1.5 Aromatic region ¹ H NMR spectrum of OH-Span in DMSO-d ₆ (top) and D ₂ O (bottom).....	292
Figure A1.6 ¹³ C NMR spectrum of OH-Span in DMSO-d ₆ (top) and D ₂ O (bottom).....	292
Figure A1.7 Structure of OH-Span with the numbering system used for NMR assignments.....	293
Figure A1.8 COSY and NOESY interactions for OH-Span in DMSO-d ₆ and D ₂ O.....	293
Figure A1.9 Aromatic region ¹ H NMR spectrum of NHAc-Span in DMSO-d ₆ (top) and D ₂ O (bottom).....	295
Figure A1.10 ¹³ C NMR spectrum of NHAc-Span in DMSO-d ₆ (top) and D ₂ O (bottom).....	295
Figure A1.11 Structure of NHAc-Span with the numbering system used for NMR assignments.....	296
Figure A1.12 COSY and NOESY interactions for NHAc-Span in DMSO-d ₆ and D ₂ O.....	296

Figure A1.13 Aromatic region ^1H NMR spectrum of OMe-Span in DMSO- d_6 (top) and D_2O (bottom).....	298
Figure A1.14 ^{13}C NMR spectrum of OMe-Span in DMSO- d_6 (top) and D_2O (bottom).....	298
Figure A1.15 Structure of OMe-Span with the numbering system used for NMR assignments.....	299
Figure A1.16 COSY and NOESY interactions for OMe-Span in DMSO- d_6 and D_2O	299
Figure A1.17 Aromatic region ^1H NMR spectrum of H-Span in D_2O	301
Figure A1.18 ^{13}C NMR spectrum of H-Span D_2O	301
Figure A1.19 Structure of H-Span with the numbering system used for NMR assignments.....	302
Figure A1.20 COSY and NOESY interactions for H-Span in D_2O	302
Figure A1.21 Aromatic region ^1H NMR spectrum of Br-Span in D_2O	303
Figure A1.22 ^{13}C NMR spectrum of Br-Span D_2O	303
Figure A1.23 Structure of Br-Span with the numbering system used for NMR assignments.....	304
Figure A1.24 COSY and NOESY interactions for Br-Span in D_2O	304
Figure A1.25 Aromatic region ^1H NMR spectrum of CN-Span in D_2O	305
Figure A1.26 ^{13}C NMR spectrum of CN-Span D_2O	305
Figure A1.27 Structure of CN-Span with the numbering system used for NMR assignments.....	306
Figure A1.28 COSY and NOESY interactions for CN-Span in D_2O	306
Figure A1.29 Dependence on the normalised Raman intensity S' for a square beam model on the photoalteration factor F	308
Figure A1.30 Selected calculated normal mode vibrations of NH_2 -Span. (Original in colour).....	310
Figure A1.31 Selected calculated normal mode vibrations of OMe-Span. (Original in colour).....	311
Figure A1.32 Selected calculated normal mode vibrations of NHAc -Span. (Original in colour).....	312
Figure A1.33 Selected calculated normal mode vibrations of H-Span. (Original in colour).....	313

Figure A1.34 Selected calculated normal mode vibrations of Br-Span. (Original in colour).....	314
Figure A1.35 Selected calculated normal mode vibrations of CN-Span. (Original in colour).....	315
Figure A1.36 Selected calculated normal mode vibrations of the azonium tautomer of P-NH ₂ -Span. (Original in colour).....	317
Figure A1.37 Selected calculated normal mode vibrations of the ammonium tautomer of P-NH ₂ -Span. (Original in colour).....	318

Appendix 2 Electrochemistry

Figure A2.1 Cyclic voltammograms of 0.5 mol dm ⁻³ sodium acetate pH 5.2 buffer solution recorded with a sweep rate of 10 mV s ⁻¹ ; Left: Reduction, Right: Oxidation.....	319
Figure A2.2 Left: UV/Visible absorption spectra of OH-Span (5 × 10 ⁻⁴ mol dm ⁻³) in pH 5.2 sodium acetate buffer solution. Right: Potential curve analysed using equation A2.11 at 363 nm with different values of n, where E ⁰ is set at -0.749 V...	321
Figure A2.3 CPE reduction on pH 5.2 sodium acetate buffer solution (0.5 mol dm ⁻³) over 30 min at a potential of -1.2 V (vs Ag/AgCl) Left: Current-time profile, Right: Charge-time profile.....	322
Figure A2.4 HPLC chromatograms of NAPDAD (1 × 10 ⁻³ mol dm ⁻³) over a injection volume range of between 1 and 25 µl analysed at 254 nm.....	323
Figure A2.5 HPLC chromatograms of APOL (1 × 10 ⁻³ mol dm ⁻³) analysed at 254 nm with both the sample and eluting system of pH 4.6 (left) and pH 5.2 (right).....	323
Figure A2.6 HPLC chromatograms of NAPDAD over a concentration range of between 1 × 10 ⁻³ and 1 × 10 ⁻⁴ mol dm ⁻³ analysed at 254 nm with 25 µl injection....	324
Figure A2.7 HPLC chromatograms of APOL over a concentration range of Between 1 × 10 ⁻³ and 1 × 10 ⁻⁴ mol dm ⁻³ analysed at 254 nm with 25 µl injection....	324
Figure A2.8 Concentration calibration curve for NAPDAD (left) and APOL (right) over a concentration range of between 1 × 10 ⁻³ and 1 × 10 ⁻⁴ mol dm ⁻³ analysed at 254 nm both with 25 µl injection volumes.....	325

Figure A2.9 HPLC chromatograms of DAB over a concentration range of Between 1×10^{-3} and 1×10^{-4} mol dm ⁻³ analysed at 254 nm.....	325
Figure A2.10 HPLC chromatograms of APA over a concentration range of between 1×10^{-3} and 1×10^{-4} mol dm ⁻³ analysed at 254 nm.....	326
Figure A2.11 Concentration calibration curve for DAB (left) and APA (right) over a concentration range of between 1×10^{-3} and 1×10^{-4} mol dm ⁻³ analysed at 254 nm both with 25 µl injection volumes.....	326

Appendix 3 Photochemistry

Figure A3.1 TRVIS spectra of 1:30 OH-Span:photoinitiator (1×10^{-4} mol dm ⁻³ dye concentration) in pH 5.2 sodium acetate buffer solution, 300 ns after excitation.....	328
Figure A3.2 TRVIS spectra of 1:30 OH-Span:photoinitiator (1×10^{-4} mol dm ⁻³ dye concentration) in pH 5.2 sodium acetate buffer solution, 0.65, 1.30, 2.50, 6.50, 45.00 and 85.00 µs after excitation.....	328

List of Tables

Chapter 1 Introduction

Table 1.1 Wavelength range showing absorbed and observed colours.....	2
Table 1.2 Types of azo dyes.....	3
Table 1.3 Typical composition of a dye based ink-jet ink	9
Table 1.4 <i>Para</i> substituent Hammett σ_p , σ_p^+ and σ_p^- constants for the R-Span dye series.....	25

Chapter 3 Structure

Table 3.1 Experimental (in d_6 -benzene) and calculated ^1H NMR chemical shifts (ppm) for <i>trans</i> - and <i>cis</i> -azobenzene.....	46
Table 3.2 Main absorption bands (λ_{max} / nm) and (ϵ_{max} / $\text{dm}^3 \text{mol}^{-1} \text{cm}^{-1}$) of substituted 4,4'-azobenzenes in ethanol, and selected Raman bands (cm^{-1}) in CCl_4	47
Table 3.3 Spectral data of 4,4'-substituted 1-phenylazonaphthalene.....	52
Table 3.4 <i>Para</i> substituent Hammett σ_p constants for the R-Span dye series.....	53
Table 3.5 UV/Visible absorption band positions (λ_{max} / nm) and absorption coefficients ($\epsilon / 10^4 \text{dm}^3 \text{mol}^{-1} \text{cm}^{-1}$) of R-Span dyes in water ($1 \times 10^{-3} \text{mol dm}^{-3}$)...	58
Table 3.6 Retention times of pure R-Span dye components.....	59
Table 3.7 UV-visible absorption band positions (λ_{max} / nm) and absorption coefficients ($\epsilon / 10^4 \text{dm}^3 \text{mol}^{-1} \text{cm}^{-1}$) of OH-, O ⁻ -, NH ₂ - and NHAc-Span in DMSO, water and ethanol at $5 \times 10^{-5} \text{mol dm}^{-3}$	62
Table 3.8 Selected bond lengths (\AA) of the optimised structures; differences ($\Delta / 0.001 \text{\AA}$) given for bond lengths from the values of H-Span.....	65
Table 3.9 Bond angles ($^\circ$) of the optimised structures; differences (Δ) given for angle from the values of H-Span.....	65
Table 3.10 Calculated orbital contributions, transition energies (E), wavelengths (λ), and oscillator strengths (f) for the first and second excited state of H-Span, OH-Span and CN-Span.....	70
Table 3.11 Comparison of experimental band positions (λ / nm) to calculated	

HOMO to LUMO transition wavelengths (λ / nm) and second excited state transition wavelengths (λ /nm) for all R-Span dyes.....	71
Table 3.12 Calculated Mulliken atomic charges (q) from the optimised structures; differences (Δ / 0.001 q) given from the values of H-Span.....	72
Table 3.13 ^1H and ^{13}C NMR chemical shifts (ppm) of NH_2 -Span in DMSO- d_6 and D_2O , along with calculated values.....	77
Table 3.14 ^1H chemical shifts (ppm) of OH-Span at pD 5.2, unadjusted and pD 12.0, and an estimate of the % of OH in the unadjusted sample.....	79
Table 3.15 Experimental and calculated ^1H NMR chemical shifts (δ /ppm) in the aromatic region for all R-Span dyes; differences (Δ) given for chemical shifts from the values of H-Span.....	82
Table 3.16 Experimental and calculated ^{13}C NMR chemical shifts (δ /ppm) in the aromatic region for all R-Span dyes; differences (Δ) given for chemical shifts from the values of H-Span.....	84
Table 3.17 Raman and IR band positions (cm^{-1}) of OH-Span in water, calculated band positions and normal mode assignments together with matching NAPDAD and APOL assignments.....	91
Table 3.18 Raman band positions (cm^{-1}) of R-Span dyes in water on 514.5 nm excitation and their assignments.....	96
Table 3.19 Experimental ($\lambda_{\text{ex}} = 514.5$ nm in water) and calculated Raman band positions (cm^{-1}) of H-Span with differences from other R-Span dyes.....	97
Table 3.20 Raman band positions (cm^{-1}) of NH_2 -, OH-, OMe-, NHAc-Span in water with 413.1 or 350.6 nm excitation.....	99
Table 3.21 Experimental Raman band positions (cm^{-1}) of O^- -Span in water on 514.5, 413.1 and 350.6 nm excitation, together with differenced (Δ) from H and OH-Span at 514.5 nm.....	101
Table 3.22 Calculated bond lengths (\AA), bond angles ($^\circ$) and Mulliken atomic charges (q) of the azonium and ammonium tautomer of P-azo NH_2 -Span; differences (ΔAz and ΔAm / 0.001 \AA) given for bond lengths, bond angles ($^\circ$) and atomic charges (q / 0.001) from the values of NH_2 -Span.....	105
Table 3.23 Calculated transition energies (E), wavelengths (λ), and oscillator strengths (f) for the first, second and third excited states of the azonium and ammonium tautomer of P- NH_2 -Span.....	108

Table 3.24 ^1H and ^{13}C NMR chemical shifts (ppm) of P-NH ₂ -Span in D ₂ O at pD 2.0 and calculated ^1H and ^{13}C NMR chemical shifts (ppm) of the az and am tautomer.....	113
Table 3.25 Experimental and calculated ^1H and ^{13}C NMR chemical shifts (δ / ppm) in the aromatic region for NH ₂ -Span (NH ₂) and P-NH ₂ -Span (P); with differences (Δ) given for chemical shifts from the values of NH ₂ -Span.....	114
Table 3.26 Experimental Raman band positions (cm ⁻¹) of P-NH ₂ -Span in water, calculated band positions, intensities and matching normal mode assignments for the azonium and ammonium tautomers.....	117
Table 3.27 Selected experimental (λ_{max} / nm, ϵ / 10 ⁴ dm ³ mol ⁻¹ cm ⁻¹ , δ / ppm) and calculated (λ_{max} / nm, Charge / q, Bond length / Å) structural features of R-Span dye series related to their Hammett <i>para</i> substituent constants.....	120

Chapter 4 Electrochemistry

Table 4.1 Hammett constants σ_p and Half-wave potential $E_{1/2}$ for hydrazine formation for substituted azobenzenes where R= NH ₂ , OH, OMe, H and Br in aqueous dioxane.....	134
Table 4.2 UV/Visible absorption band positions of NAPDAD and APOL in water and in pH 5.2 sodium acetate buffer solution, both at 5×10^{-5} mol dm ⁻³	149
Table 4.3 Retention times (RT / min), peaks integrations (PI) and UV/Visible absorption band positions (λ / nm) from HPLC and Retention times (RT / min), base peak ions (BP / m/z) and fragment ions (F / m/z) of components before and after CPE of OH-Span (8×10^{-4} mol dm ⁻³) and the model compounds NAPDAD (1×10^{-3} mol dm ⁻³) and APOL (1×10^{-3} mol dm ⁻³).....	156
Table 4.4 ^1H chemical shifts (ppm), apparent diffusion coefficient per splitting ($D_{\text{All}} / 10^{-10}$ m ² s ⁻¹), mean apparent diffusion coefficient per component ($D_{\text{mean}} / 10^{-10}$ m ² s ⁻¹) and calculated diffusion coefficient ($D_{\text{Calculated}} / 10^{-10}$ m ² s ⁻¹) for OH-Span, NAPDAD, APOL and HQ and ^1H chemical shifts (ppm), apparent diffusion coefficient per splitting ($D_{\text{All}} / 10^{-10}$ m ² s ⁻¹), mean apparent diffusion coefficient per component ($D_{\text{mean}} / 10^{-10}$ m ² s ⁻¹) and concentrations (Conc / 10 ⁻⁴ mol dm ⁻³) for each component (Comp) formed after CPE reduction...	157

Table 4.5 Estimated radius (R_H) from DFT structures and diffusion coefficients (D) for APOL, NAPDAD and OH-Span.....	158
Table 4.6 The estimated reduction and oxidation potentials for R-Span dyes in pH 5.2 sodium acetate buffer solution.....	164
Table 4.7 Retention times (RT / min), peak integrations (PI) and UV/Visible absorption band positions (λ / nm) from HPLC and Retention times (RT / min components before and after CPE reduction of NH_2 -Span (8×10^{-4} mol dm^{-3}) and DAB (1×10^{-3} mol dm^{-3}).....	169
Table 4.8 Retention times (RT / min), peak integrations (PI) and UV/Visible absorption band positions (λ / nm) from HPLC and Retention times (RT / min components before and after CPE of $NHAc$ -Span (8×10^{-4} mol dm^{-3}) and compound APA (1×10^{-3} mol dm^{-3}).....	173
Table 4.9 Estimated reduction potentials (vs Ag wire) for the start (E_1), (E_2), potential range (Δ) and a measure of the slope (n) in which reduction is occurring for R-Span dyes in pH 5.2 sodium acetate buffer solution.....	177
Table 4.10 <i>Para</i> substituent Hammett σ_p and σ_p^- constants and the estimated reduction potentials for R-Span dyes in pH 5.2 sodium acetate buffer solution.....	178
Table 4.11 <i>Para</i> substituent Hammett σ_p and σ_p^- constants and the calculated Mulliken atomic charges (q) for the R-Span dyes.....	179

Chapter 5 Photochemistry

Table 5.1 Isomeric composition in the photostationary state at 366 nm (determined by HPLC analysis) and first-order rate constant (k) of the thermal <i>cis</i> to <i>trans</i> isomerisation of substituted 1-phenylazonaphthalenes in benzene at 30 °C.....	188
Table 5.2 1H NMR chemical shifts (ppm) of the <i>cis</i> and <i>trans</i> forms of $NHMe$ -Span in $DMSO-d_6$ and differences (Δ) between them.....	189
Table 5.3 Retention times (RT / min), peak integrations (PI) and UV/Visible absorption band positions (λ \ nm) of each component before and after 30 light pulses for photoinitiator under air.....	201

Table 5.4 Retention times (RT / min), peaks integrations (PI) and UV/Visible absorption band positions (λ / nm) from HPLC and Retention times (RT / min), base peak ions (BP / m/z) and fragment ions (F / m/z) of components before and after 30 light pulses on photoinitiator alone (5×10^{-5} mol dm ⁻³).....	204
Table 5.5 ¹ H chemical shifts (ppm), apparent diffusion coefficient per Splitting ($D_{All} / 10^{-10}$ m ² s ⁻¹), mean apparent diffusion coefficient per component ($D_{mean} / 10^{-10}$ m ² s ⁻¹) and concentration (Concn / 10 ⁻⁴ mol dm ⁻³) of each component of photoinitiator alone before and after irradiation under nitrogen.....	207
Table 5.6 Retention times (RT / min), peaks integrations (P), concentrations (Conc / 10 ⁻⁴ mol dm ⁻³) and UV/Visible absorption band positions (λ / nm) from HPLC and Retention times (RT / min), base peak ions (BP / m/z) and fragment ions (F / m/z) of components before and after 50 light pulses on 1:1 and 1:10 OH-Span:photoinitiator in pH 5.2 sodium acetate buffer solution under nitrogen.....	217
Table 5.7 Retention times (RT / min), peak integrations (PI), concentrations (Concn / 10 ⁻⁴ mol dm ⁻³) and UV/Visible absorption band positions (λ / nm) of each component before and after 50 light pulses for 1:1 APOL:photoinitiator and 1:1 NAPDAD:photoinitiator under nitrogen.....	221
Table 5.8 ¹ H chemical shifts (ppm), apparent diffusion coefficient per splitting ($D_{All} / 10^{-10}$ m ² s ⁻¹), mean apparent diffusion coefficient per component ($D_{mean} / 10^{-10}$ m ² s ⁻¹) and concentration (Concn / 10 ⁻⁴ mol dm ⁻³) of each component of OH-Span:photoinitiator alone before and after irradiation under nitrogen.....	225
Table 5.9 Calculated concentration of initial $\cdot C(CH_3)_2OH$ (mol dm ⁻³) and estimated molar absorption coefficient ($\epsilon / dm^3 mol^{-1} cm^{-1}$) the modelled values of rate constants ($k / dm^3 mol^{-1} s^{-1}$) at 21 °C, from equations A1-A8.....	234
Table 5.10 ¹ H NMR chemical shifts (ppm) of OMe-Span and NHAc-Span after 30 light pulses in D ₂ O, together with their calculated <i>cis</i> positions and differences between the <i>cis</i> and <i>trans</i> forms.....	244
Table 5.11 Retention times (RT / min), peak integrations (PI), concentrations (Concn / 10 ⁻⁵ mol dm ⁻³) and UV/Visible absorption band positions (λ / nm) of each component before and after 30 light pulses for 1:1 and 1:10 O ⁻ -Span:photoinitiator under nitrogen.....	257

Table 5.12 Retention times (RT / min), peak integrations (PI), concentrations (Concn / 10^{-5} mol dm ⁻³) and UV/Visible absorption band positions (λ / nm) of each component before and after 30 light pulses for 1:1 and 1:10 NH ₂ -Span:photoinitiator under nitrogen.....	259
Table 5.13 Retention times (RT / min), peak integrations (PI), concentrations (Concn / 10^{-5} mol dm ⁻³) and UV/Visible absorption band positions (λ / nm) of each component before and after 30 light pulses for 1:1 and 1:10 NHAc-Span:photoinitiator under nitrogen.....	261
Table 5.14 Hammett σ_p and σ_p^- constants and rate constants (k / s ⁻¹) for the <i>cis-trans</i> thermal back reaction of NH ₂ -, OH-, OMe and NHAc-Span.....	262

Appendices

Appendix 1 Structure

Table A1.1 Bond lengths (\AA) of the optimised structures; differences (Δ) given for bond lengths (10^{-3} \AA) from the values of H-Span.....	284
Table A1.2 Bond angles ($^\circ$) of the optimised structures; differences (Δ) given for angles ($^\circ$) from the values of H-Span.....	285
Table A1.3 Calculated transition energies (E), wavelengths (λ), and oscillator strengths (f) for the excited states of NH ₂ -Span.....	288
Table A1.4 Calculated transition energies (E), wavelengths (λ), and oscillator strengths (f) for the excited states of OH-Span.....	288
Table A1.5 Calculated transition energies (E), wavelengths (λ), and oscillator strengths (f) for the excited states of OMe-Span.....	289
Table A1.6 Calculated transition energies (E), wavelengths (λ), and oscillator strengths (f) for the excited states of NHAc-Span.....	289
Table A1.7 Calculated transition energies (E), wavelengths (λ), and oscillator strengths (f) for the excited states of H-Span.....	289
Table A1.8 Calculated transition energies (E), wavelengths (λ), and oscillator strengths (f) for the excited states of Br-Span.....	290
Table A1.9 Calculated transition energies (E), wavelengths (λ), and oscillator strengths (f) for the excited states of CN-Span.....	290

Table A1.10 Calculated dipole moments (D) for the ground state, 1 st and 2 nd excited states of the R-Span dye series.....	290
Table A1.11 HSQC and HMBC of NH ₂ -Span in DMSO-d ₆ , ● direct attachment	
○ adjacent attachment.....	291
Table A1.12 HSQC and HMBC of NH ₂ -Span in D ₂ O, ● direct attachment	
○ adjacent attachment.....	291
Table A1.13 ¹ H and ¹³ C NMR chemical shifts (ppm) of OH-Span in DMSO-d ₆ and D ₂ O.....	293
Table A1.14 HSQC and HMBC of OH-Span in DMSO-d ₆ , ● direct attachment	
○ adjacent attachment.....	294
Table A1.15 HSQC and HMBC of OH-Span in D ₂ O, ● direct attachment	
○ adjacent attachment.....	294
Table A1.16 ¹ H and ¹³ C NMR chemical shifts (ppm) of NHAc-Span in DMSO-d ₆ and D ₂ O.....	296
Table A1.17 HSQC and HMBC of NHAc-Span in DMSO-d ₆ , ● direct attachment	
○ adjacent attachment.....	297
Table A1.18 HSQC and HMBC of NHAc-Span in D ₂ O, ● direct attachment	
○ adjacent attachment.....	297
Table A1.19 ¹ H and ¹³ C NMR chemical shifts (ppm) of OMe-Span in DMSO-d ₆ and D ₂ O.....	299
Table A1.20 HSQC and HMBC of OMe-Span in DMSO-d ₆ , ● direct attachment	
○ adjacent attachment.....	300
Table A1.21 HSQC and HMBC of OMe-Span in D ₂ O, ● direct attachment	
○ adjacent attachment.....	300
Table A1.22 ¹ H and ¹³ C NMR chemical shifts (ppm) of H-Span in D ₂ O.....	302
Table A1.23 HSQC and HMBC of H-Span in D ₂ O, ● direct attachment	
○ adjacent attachment.....	303
Table A1.24 ¹ H and ¹³ C NMR chemical shifts (ppm) of Br-Span in D ₂ O.....	304
Table A1.25 HSQC and HMBC of Br-Span in D ₂ O, ● direct attachment	
○ adjacent attachment.....	305
Table A1.26 ¹ H and ¹³ C NMR chemical shifts (ppm) of CN-Span in D ₂ O.....	306
Table A1.27 HSQC and HMBC of CN-Span in D ₂ O, ● direct attachment	
○ adjacent attachment.....	307

Table A1.28 Experimental conditions, laser power (P / mW), beam radius ($\omega / \mu\text{m}$), sample flow rate ($v / \text{cm s}^{-1}$) and molar absorption ($\epsilon / \text{dm}^3 \text{cm}^{-1} \text{cm}^{-1}$) coefficient for assessment of photoalteration on Raman spectra with an excitation wavelength of 514.5 nm and a total collection time of 3600 s by calculating F and S' as given in equation A1.45.....	309
Table A1.29 Calculated transition energies (E), wavelengths (λ), and oscillator strengths (f) for the excited states of the Hydrazone tautomer of P-NH ₂ -Span.....	316
Table A1.30 Calculated transition energies (E), wavelengths (λ), and oscillator strengths (f) for the excited states for the Azo tautomer of P-NH ₂ -Span..	316

Abbreviations and Symbols

Am	Ammonium
Ag / AgCl	Saturated silver/ silver chloride reference electrode
APA	N-(4-aminophenyl)acetamide
APOL	4-aminophenol
Az	Azonium
B3LYP	Becke 3-style-parameter-term with Lee, Yang, Parr exchange
BP	Base peak
Calc	Calculated
COSY	CORrelated SpectroscopY
CPE	Controlled Potential Electrolysis
CV	Cyclic Voltammetry
δ	Chemical shift; bend
D	Diffusion coefficient
Δ	Change; Difference
DAB	1,4-diaminobenzene
DFT	Density Functional Theory
DMSO	Dimethyl sulfoxide
DOSY	Diffusion Ordered SpectroscopY
E	Energy; Potential
ϵ	Molar absorption coefficient
EPR	Electron Paramagnetic Resonance
ESI	ElectroSpray Ionisation
Exp	Experimental
f	Oscillator Strength; fluorescence
F	Fragment
FID	Free Induction Decay
FT	Fourier Transform
GC	Gas chromatography
GIAO	Gauge Invariant Atomic Orbitals
HEB	4-(2-hydroxyethoxy) benzaldehyde
HMQC	Heteronuclear Multiple Quantum Coherence

HOMO	Highest Occupied Molecular Orbital
HPLC	High-Performance Liquid Chromatography
HQ	1,4-hydroquinone
HSQC	Heteronuclear Single Quantum Coherence
ic	Internal conversion
IR	Infrared
isc	Intersystem crossing
l	Pathlength
LC-MS	Liquid Chromatography-Mass Spectrometry
LCQ	Liquid Chromatography Quadrapole
LUMO	Lowest Unoccupied Molecular Orbital
m	medium
MO	Molecular Orbital
MS/MS-1	Mass spectrum first fragment
MS/MS-2	Mass spectrum second fragment
nap	Naphthyl
NAPDAD	2-naphthylamine-4,8-disulfonate
NMR	Nuclear Magnetic Resonance
NOESY	Nuclear Overhauser Effect Spectroscopy
NRP	Non-Radical Products
P	Power
p	Phosphorescence
PFG	Pulsed Field Gradient
ph	Phenyl
PI	Photoinitiator
PIP	Photoinitiator Product
ppm	Parts per million
q	Mulliken atomic charge
Q	Total charge
R	Radius; Substituent
ro	rocking motion
R-Span	2-(4-R-phenylazo)naphthalene-4,8-disulfonate dyes
RT	Retention time
σ	Hammett constant

s	strong
S_0	Electronic ground singlet state
S_n	Electronic excited singlet states
sc	scissor motion
sh	shoulder
SHE	Standard Hydrogen Electrode
SCE	Saturated Calomel Electrode
T_n	Electronic excited triplet states
TMS	Tetramethylsilane
TRVIS	Time-Resolved UV/Visible Absorption Spectroscopy
TSP	sodium 3-(trimethylsilyl)propionate-2,2,3,3-d ₄
UV	Ultraviolet
λ	Wavelength
v	Vibrational quantum number
v	stretch
vw	very weak
vr	Vibrational relaxation
vs	very strong
w	weak

Acknowledgements

I would like to say thanks for all those people who have helped and supported me during this research, culminating in the production of this thesis. Firstly, I would like to thank my two supervisors, Dr John Moore and Prof. John Lindsay Smith, for their help, support and guidance throughout this project. A special thanks goes to Dr Laurence Abbott for his invaluable practical support and for his computational knowledge throughout all of this project. I would also like to say thanks to Dr David Atkinson, a previous member of the group for getting me started on this project.

I would like to thank Fujifilm Imaging Colorants Ltd for synthesising and purifying the dyes and along with the EPSRC for funding this project. I would like to thank Dr Thomas Paul for his guidance during this project.

There are many people who I would like to thank for the assistance and support they have provided throughout this project and for their practical support. Ms Heather Fish for measurement of NMR spectra for structural studies, Dr David Williamson for measurement of NMR spectra for product studies and Dr Trevor Dransfield for LC-MS training and support. Thanks also goes to Steve Hau and Mike Keogh from stores.

I thank those project students, Simon Roper, James Wallington-Smith and John-Michael Warner who I have worked with at some point during this project.

Chapter 1 Introduction

This brief introduction and review will consider the properties of dyes which are of key importance to the dye industry, including the types and variants of colourants used as outlined in section 1.1 and an historical account of ink-jet printing as outlined in section 1.2.¹⁻³ The techniques used in this research are introduced in section 1.3, and the aims of the work are introduced in section 1.4.

The dyes studied here (introduced in section 1.4) have been identified by Fujifilm Imaging Colorants Ltd as models for potential colourants that may be used in ink-jet inks. The majority of research carried out previously on azo colourants has been where the hydrazone tautomer dominates whereas the azo tautomer dominates for the dyes studied in this research; within this set a variety of substituents are attached to the chromophore, with properties which range from electron-donating through to electron-withdrawing. Various relevant spectroscopic and analytical techniques will be used to determine their structure and stability (e.g. under a variety of reaction conditions) from which their suitability for ink-jet printing applications can be evaluated.

1.1 Introduction to dyes

1.1.1 Colour and the perception of colour

Colour⁴⁻⁶ is perceived by the brain when light interacts with the human eye. The sensitivity of the human eye to different wavelengths, which give rise to the perception of different colours, is governed by a collection of light-sensitive rods and cones cells located in the retina. Light that reaches the retina has often been transmitted or reflected from observable objects, and Table 1.1 gives a list of absorbed and complementary observed colours in the visible region of 400 to 700 nm.⁴ Colour may also be described in terms of: hue, the dominant wavelength based on the tristimulus theory of colour; chroma, the density or intensity of the colour which can be modified by the grey scale (the gradual transition from very pale to deep colours); value, the brightness of the colour.⁶

Table 1.1 Wavelength range showing absorbed and observed colours.⁴

Wavelength range / nm	Absorbed colour	Observed colour
400–435	Violet	Greenish – yellow
435–480	Blue	Yellow
480–490	Greenish – blue	Orange
490–500	Bluish – green	Red
500–560	Green	Purple
560–580	Yellowish – green	Violet
580–595	Yellow	Blue
595–605	Orange	Greenish – blue
605–750	Red	Bluish – green

1.1.2 Colourants

The common types of colourants^{1,4,5} that are used as a component of ink-jet inks are classified according to common chemical structural features, and they include azo, carbonyl and phthalocyanine dyes alongside associated pigments.^{4,5}

1.1.2.1 Azo dyes

Azo dyes^{4,5} contain the common structural feature of an azo linkage (-N=N-) in which the colour observed is due to extended conjugation of groups attached to this linkage. The normal method of synthesising azo dyes is through diazotisation of a primary aromatic amine with sodium nitrite under acidic and low temperature conditions. The diazonium salt produced is reacted by azo coupling to produce the azo compound, as shown in Figure 1.1. In this way it is possible to synthesise monoazo, bisazo, disperse, mordant, acidic, reactive, cationic, direct, solvent and food dyes, and examples of these are given in Table 1.2.^{4,6}

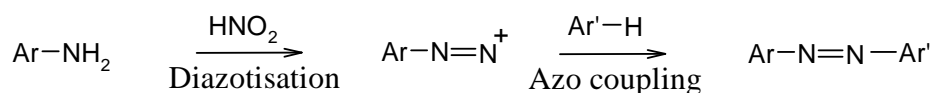
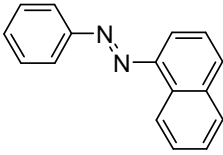
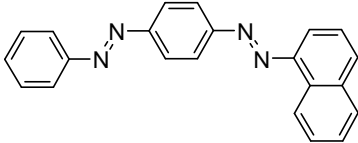
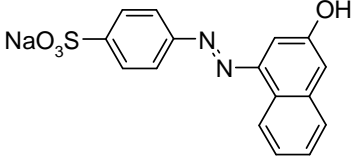
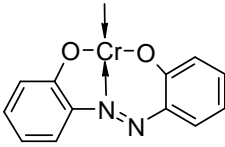
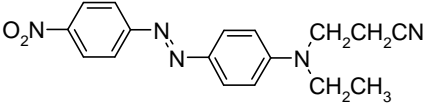
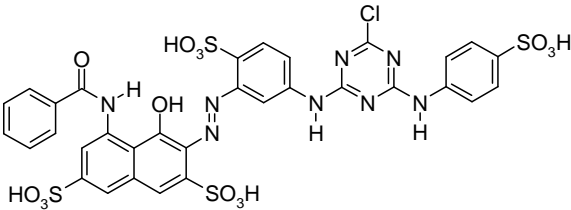
**Figure 1.1** Generic synthesis of an azo dye.

Table 1.2 Types of azo dyes.⁴⁻⁸

Azo dye	Example structure	Comment
Monoazo		Monoazo dyes contain a single azo linkage.
Bisazo		Bisazo dyes contain two azo linkages.
Acidic		Acidic dyes typically contain a sulfonate or carboxylate group which aids the water solubilisation of the dye and application to a fibre.
Mordant		Transition metals can form very stable complexes with complexing azo dyes; this can result in superior fastness properties on a fibre.
Disperse		Disperse dyes have a relatively low solubility in water and therefore can be applied to hydrophobic fibres.
Reactive		Here a reactive functional group, monochlorotriazinyl is attached to the dye can chemically react with another functional group in the fibre and result in a chemical bond.

Azo dye	Example structure	Comment
Cationic		Cationic dyes are water soluble and can be applied to cellulose. They have a poor light fastness. Also used in the textile industry because they have a high affinity for acrylic fibres.
Direct		Direct dyes consist of large molecules which are long, narrow and planar with functional groups that give high affinity with cellulose through a combination of van der Waals forces, dipolar and hydrogen bonding.
Solvent		Solvent dyes are used in ink where the carrier medium is non-aqueous.

1.1.2.2 Carbonyl dyes

Carbonyl dyes⁴⁻⁶ have the common structural feature of containing a carbonyl (C=O) group, which can extend the conjugation within the dye, for example with the aromatic rings. Anthraquinones form the largest subdivision, with others including indigoids, benzodifuranones, coumarins, naphthalimides, quinacridones, perylenes, perinones and diketopyrrolopyrroles. Carbonyl dyes are reported to be more suited to high-performance colourants due to their superior lightfastness, when compared with azo dyes. Carbonyl dyes however have increased manufacturing costs due to their multistep syntheses.⁴

A benzoquinone or anthraquinone group as shown in Figure 1.2 form the most common bases for carbonyl dyes.

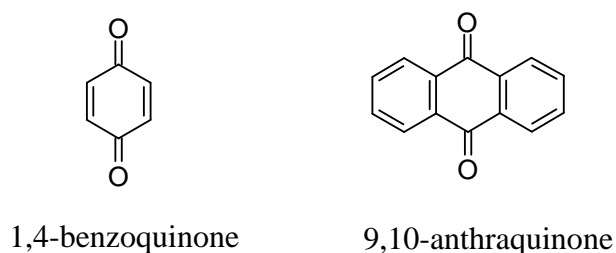


Figure 1.2 Structure of 1,4-benzoquinone and 9,10-anthraquinone.

1.1.2.3 Phthalocyanine dyes

An example of a phthalocyanine dye⁶ is given in Figure 1.3. Phthalocyanines are structurally related to porphyrin derivatives and are aromatic and highly stable. They generally show highly intense blue and green colours.

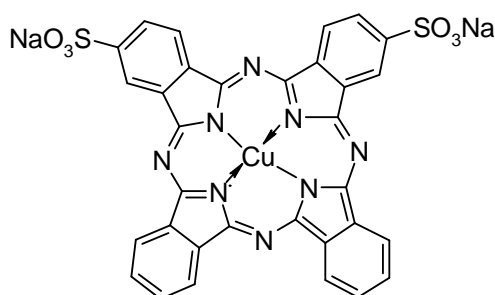


Figure 1.3 An example of a phthalocyanine dye, Direct Blue 86.⁶

1.1.2.4 Pigments

Unlike dyes, pigments are insoluble; organic pigments are usually less stable than their inorganic counterparts, but provide brighter and more intense colours.⁴ The level of dispersion on or within the media that the pigments are applied to directly relates to their chemical and physical properties. Azo pigments, for example Pigment Red 49 as shown in Figure 1.4, exhibit good lightfastness due to intramolecular hydrogen bonding,

but weak intermolecular forces result in poor solvent resistance, resulting in leaching to the solvent.^{4,5}

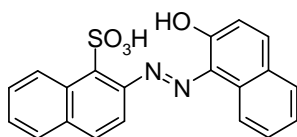


Figure 1.4 Pigment Red 49.

1.2 Ink-jet printing

1.2.1 Historical overview

In 1878 Lord Rayleigh described the mechanism by which a liquid stream breaks up into droplets.⁹ The first patented ink-jet recording device, using Rayleigh's mechanism, was developed by Rune Elmqvist of Siemens in 1951.¹⁰ The early 1960s saw the development of continuous ink-jet technology by Richard Sweet¹¹ of Stanford University which was later adapted by IBM in the 1970s for their printers. The late 1970s saw the first use of drop-on-demand ink-jet printing methods as discovered by Steven Zoltan.¹⁰ Development was further increased in 1979 by Canon who developed bubble jet printing and Hewlett-Packard who developed thermal ink-jet printing heralding the first successful low cost ink-jet printer. Their low cost, quietness and relatively good print quality was a revelation when compared with the noisy impact dot matrix printers.¹²

1.2.2 Ink-jet printers

Common ink-jet printing methods include continuous³ and drop-on-demand^{1,3,13} printing, with the latter being subdivided into thermal and piezoelectric.^{2,14}

1.2.2.1 Continuous

In continuous ink-jet printing,³ the process by which an ink can flow onto paper is through a binary deflection system as shown in Figure 1.5 or a multiple deflection system as shown in Figure 1.6. In both types the ink-jet droplets are generated by the drop generator and pass through the charge electrodes. In a binary system both charged and uncharged ink droplets travel through the high voltage deflection plate. It is here that the charged ink droplets are deflected, collected and re-circulated via the gutter. The uncharged ink droplets are allowed to travel through to the paper. In the multiple-deflection system the charged ink droplets are deflected at different levels and thereafter travel through to the paper.³

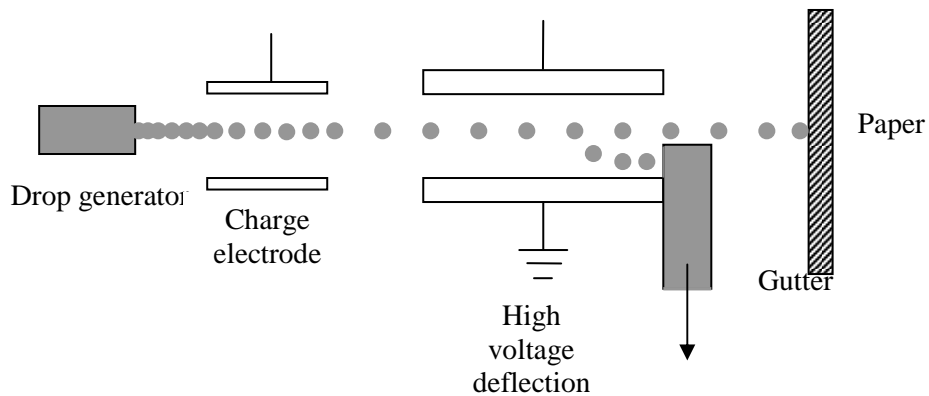


Figure 1.5 Continuous ink-jet: A binary-deflection system.³

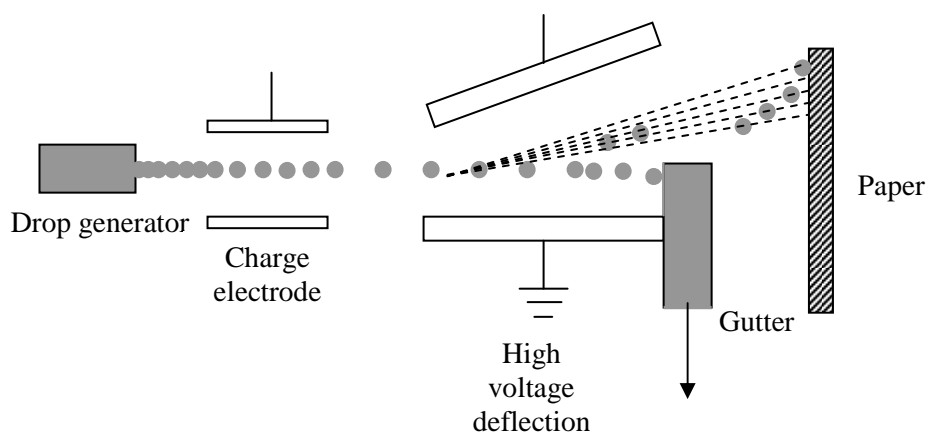


Figure 1.6 Continuous ink-jet: A multiple-deflection system.³

1.2.2.2 Drop-on-demand

Thermal ink-jet printing is the most successful and most widely used printing method in the home.³ In a thermal drop-on-demand printer as shown in Figure 1.7 there is a heater that heats the ink up to 300 °C within a pressure chamber creating an ink-jet bubble by evaporation. This bubble presses the ink out of the orifice, after which the heating stops causing the vapour inside the bubble to condense. This condensing bubble and the surface tension draws fresh ink into the chamber allowing a drop by drop flow of the ink onto the paper.^{3,15}

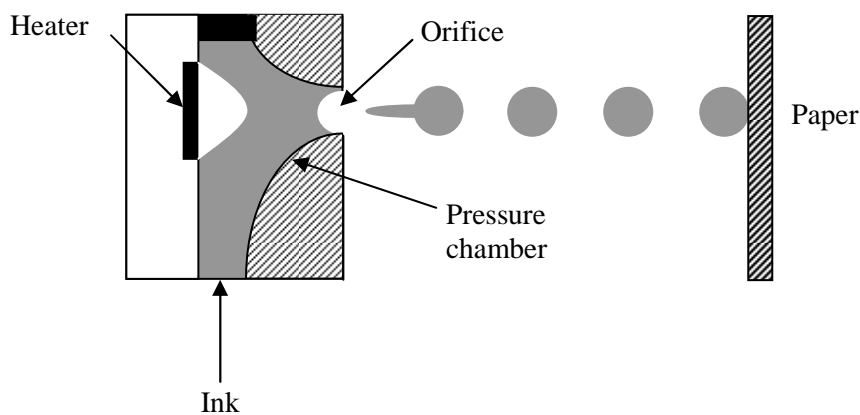


Figure 1.7 Drop-on-demand roof-shooter thermal ink-jet.³

Piezoelectric ink-jet printing methods^{2,3,14} are more widely used in industry than in the home as they give accurate printing and can be used with a wide variety of organic solvents. Piezoelectric printers are classified as squeeze, bend, push or shear types relating to the mode of ink movement.^{2,3} Rather than a heating element, there is now a piezoelectric material behind each nozzle. When a voltage is applied an electric field produces a pressure wave on the ink-jet ink, forcing it through the nozzle. The four piezoelectric types allow for a wide range of inks to be used.

1.2.3 Ink-jet inks

The typical composition of an ink-jet ink is shown in Table 1.3.^{1,3,13,16-18}

Table 1.3 Typical composition of a dye based ink-jet ink.¹

Component	Composition (%)	Properties
Water soluble dye	~ 3–6	usually anionic and coloured
Water	~ 70–80	a good solvent for the thermal ink-jet process, safe and low in cost
Humectant	~ 5–10	prevents evaporation of water from the printhead when idle, a typical example is ethane-1,2-diol.
Surfactant	~ 1	enhances the contact with the surface, a common example is Surfynol 465
Penetrant	~ 2–10	lowers the surface tension of the inks allowing them to diffuse onto a surface very quickly, pentane-1,5-diol is commonly used

The ideal properties of the whole ink-jet ink are that it is non-toxic, non-flammable, thermally stable and quick drying to be used in the printing process. Other types of ink formulations include: phase-change inks, which change phase with temperature; solvent-based inks, commonly used for printing onto glass, plastic or metal; oil-based inks; UV curable inks; hot-melt and reactive based inks.³

1.2.4 Ink-jet paper

The medium¹⁶ used often determines the finish that is required; for example, photographic media require a rapid dry time, high print resolution and glossy finish to give bright and vibrant colours. The medium of current choice is a microporous surface which has a faster drying time but a lower light fastness than a swellable polymer type surface.¹⁶

General printing methods use paper, of which cellulose is the major constituent. Cellophane (a processed form of cellulose) is often used to mimic paper for the scientific studies of dyes,¹⁹⁻²² and Figure 1.8 shows the simplified structure of cellulose as a long-chain polymeric polysaccharide of β -glucose.⁴ It can be seen that cellulose has hydroxyl groups by which intermolecular hydrogen bonds can form with a dye molecule. Its open structure also allows a dye molecule to enter within its structure.

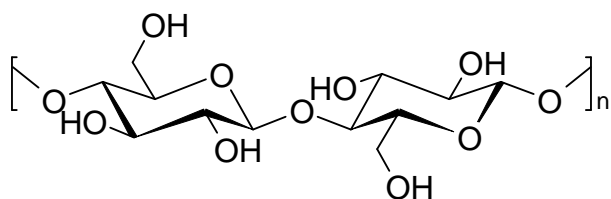


Figure 1.8 Structure of cellulose as a polymer of β -glucose.

1.2.5 Printing quality

Printing quality^{1,15,16,18} is ultimately the most important aspect of the whole printing method, and is determined by the hue, chroma and value of the ink-jet ink, by the resolution (dots per millimetre), by the number of grey levels, and by the transition between pale and dark colours. Ideally one would like to use very small ink-jet ink droplets, while maintaining an efficient printing process. Using small ink-jet droplets is advantages to give the best grey-scale properties, which describes the gradual transition from the lightest to darkest shade of colour by allowing control of droplets within a unit area. In addition to size pale magenta and cyan inks can also aid the grey scale properties by building up layers.¹⁶

1.3 Techniques

The following section outlines in brief both the theory and practical aspects of the spectroscopic, electrochemical and photochemical techniques used in this research.

1.3.1 Electronic spectroscopy

UV/Visible absorption spectroscopy is used to gain information on electronic transitions within a molecule. Upon absorption of a photon of light in the ultraviolet or visible region, an electron in one orbital becomes excited to a higher orbital corresponding to a transition from the ground to an excited electronic state of the molecule.

A typical UV/Visible absorption spectrometer usually records over the region of 190 – 900 nm using a deuterium lamp for the UV region and a tungsten lamp for the visible region. Radiation from the lamps passes through a fixed slit and into a monochromator where light is dispersed by a diffraction grating. In a double beam instrument as used in this work, an optical chopper allows the specifically chosen wavelength of light to pass through both the reference and sample cell.²³

In general, the transmittance (T) is the ratio of the intensity of emerging (I) to incident (I_0) light, and the absorbance (A) of the sample is calculated using Equation 1.1.

$$A = -\log T = -\log \left(\frac{I}{I_0} \right) \quad (1.1)$$

The Beer-Lambert law as shown in Equation 1.2 is used to relate absorbance to sample concentration ($c / \text{mol dm}^{-3}$), molar absorption coefficient ($\epsilon / \text{mol}^{-1} \text{ dm}^3 \text{ cm}^{-1}$) and the pathlength of the cell (l / cm).

$$A = \epsilon cl \quad (1.2)$$

The molar absorption coefficient gives a measure of the intensity of absorption which is dependent on a combination of spin, orbital and nuclear selection rules. Transitions between states are governed by whether there is a change of spin upon excitation, and in general only transitions between states of the same multiplicities are observed for small organic molecules. The orbital selection rule can be considered in terms of the symmetry of the orbitals and states arising from them and so depends on molecular structure and also the spatial overlap of the orbitals. The nuclear selection rule depends on the vibrational overlap integral, indicating how well the vibrational wavefunction of the two states overlap. The higher the molar absorption coefficients at a particular wavelength the stronger the colour observed.

Electronic transitions within a molecule are accompanied by vibrational transitions which influence the profile of the overall spectrum observed as shown in Figure 1.9. The Franck-Condon principle describes that, as a result of nuclei being much more massive than electrons, an electronic transition occurs much more rapidly than the nuclei can respond. At room temperature the lowest occupied vibrational energy level ($v' = 0$) is the most highly populated, and the most probable geometry is at the equilibrium separation of the nuclei. Upon excitation there is a vertical transition without a change in geometry (S_0 to S_1) as shown in Figure 1.9 from $v' = 0$ to $v'' = 4$. The square of the vibrational overlap integral between the ground and excited states gives a measure of the intensity of the vibronic transition. The broadness of the absorption spectrum will depend on the number of accessible vibrational levels in the excited state of the molecule as a result of the change in geometry on excitation.²⁴ In general, spectra recorded in the gaseous phase or an organic solvent often show resolved vibrational fine structure, in water however this is not usually observed due to dipole interactions.

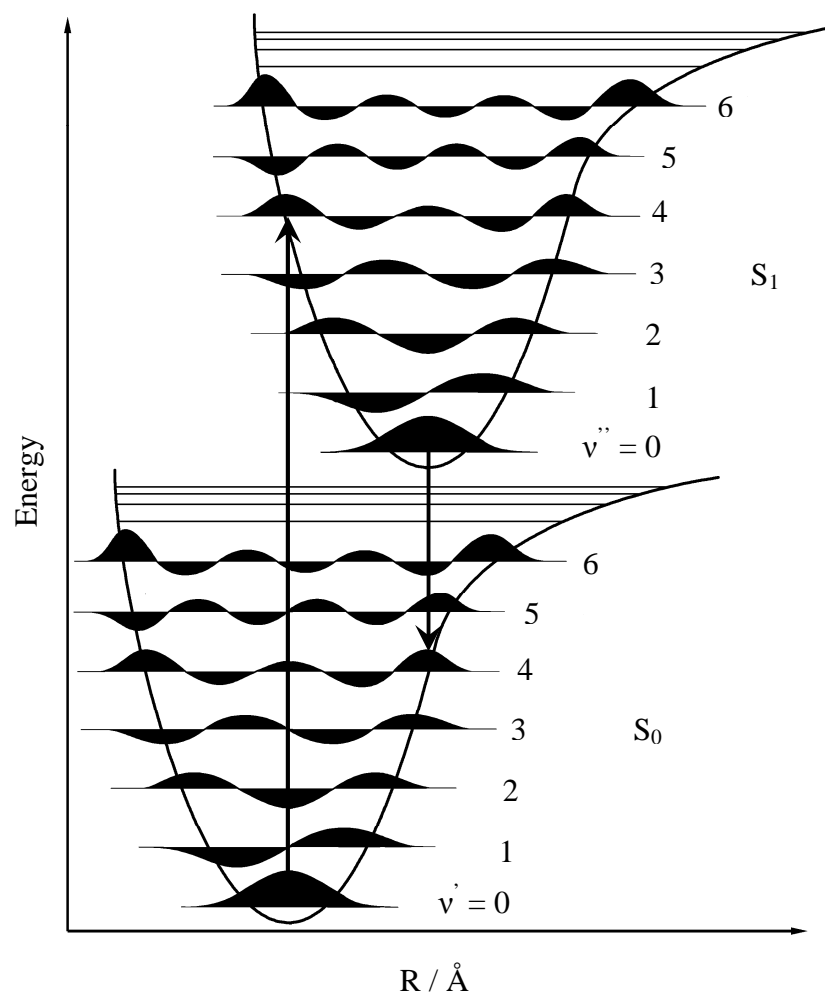


Figure 1.9 Ground and excited electronic and vibrational energy levels.

UV/Visible emission spectroscopy is used to gain information on excited states. An excited state of a molecule can decay through radiative and non-radiative pathways as shown by the Jablonski diagram in Figure 1.10. The use of a fluorimeter allows for the measurement of fluorescence and phosphorescence spectra, giving energy gaps and quantum yields which allows for the determination of the fate of the excited states and some information on the pathways by which they decay.

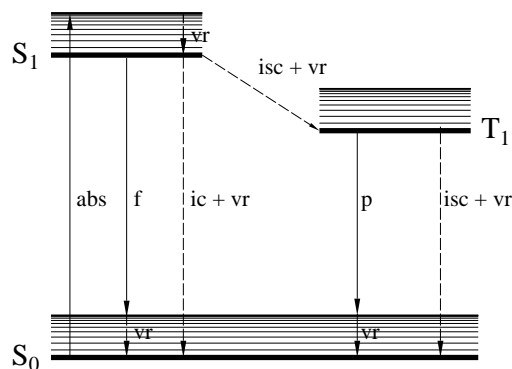


Figure 1.10 Jablonski diagram of the routes of excitation and decay of electronic states; abs = absorption, ic = internal conversion, isc = intersystem crossing, f = fluorescence, p = phosphorescence, vr = vibrational relaxation.

A fluorimeter typically uses a xenon arc lamp and records over a range of 250–700 nm. Two monochromators are utilised allowing the user to record both emission and excitation spectra. In emission mode, the absorption band at longest wavelength is usually selected by the excitation monochromator, although a change in excitation wavelength should not generally change the profile of the emission spectrum.²⁵ The emission monochromator is used to scan across a predefined wavelength range producing an emission spectrum. In excitation mode, the wavelength of emission is selected by the emission monochromator. The excitation monochromator is used to scan across a predefined wavelength range to produce an excitation spectrum.²⁶

1.3.2 Vibrational spectroscopy

In this work, both IR and Raman spectroscopic techniques were used to study molecular vibrations. For non-linear molecules such as organic dyes, after taking into account for rotation and translational motion there are $3N - 6$ normal modes. In general for large molecules, vibrations are commonly seen across the whole structure as a combination of bends and stretches which are observed experimentally as bands arising from a series of normal modes. The frequencies observed experimentally are determined by the masses and specific force constants assigned to the molecular motion; in general these are higher for stretching than bending motion. Both spectroscopic techniques are briefly described below.

IR spectroscopy generally covers the 400–4000 cm^{-1} region of the electromagnetic spectrum and experimentally observes the absorption of a photon in this region by a molecule. For a normal mode to be IR active there must be a change in dipole moment of the molecule upon vibration.²⁷ In an IR spectrum, vibrational transitions are generally observed due to a change in vibrational state corresponding to a fundamental transition from $v = 0$ to $v = 1$ as shown in Figure 1.11.

Raman spectroscopy is a complementary technique in which a monochromatic light source (typically a laser) produces photons which are scattered by molecules the types of which are shown in Figure 1.11. If the frequency of the scattered light is the same as the incident light then Rayleigh scattering has occurred. If the frequency of scattered light is different from that of the incident light then Raman scattering has occurred. Stokes Raman scattering occurs when the frequency of scattered light is lower than that of the incident light. Anti-Stokes Raman scattering occurs when the frequency of scattered light is higher than the incident light, and this can be observed when an incident photon interacts with a molecule that is in an excited vibrational state. For a motion in a normal mode to be Raman active there must be a change in molecular polarisability upon vibration.²⁷ In a Raman spectrum vibrational transitions are observed due to a change in state corresponding to a transition from $v = 0$ to a higher vibrational state.

The Raman effect is weak, and only about 1 in 10^{10} incident photons undergo Raman scattering.²⁸ As absorption of radiation is commonly more likely than scattering, if a molecule or impurities fluoresce readily then this can easily mask the Raman signal and make it more difficult to observe. The resonance Raman technique is often utilised to enhance Raman scattering, in which the incident frequency of light is chosen to correspond to that of an electronic transition. Under these conditions, vibrational transitions that are coupled to electronic transitions will be enhanced. Resonance Raman spectroscopy is often utilised for organic dyes with extended chromophores allowing for enhancement with their electronic transitions. Unfortunately the resonance Raman technique does have the disadvantage of enhancing any fluorescence in the sample.²⁸

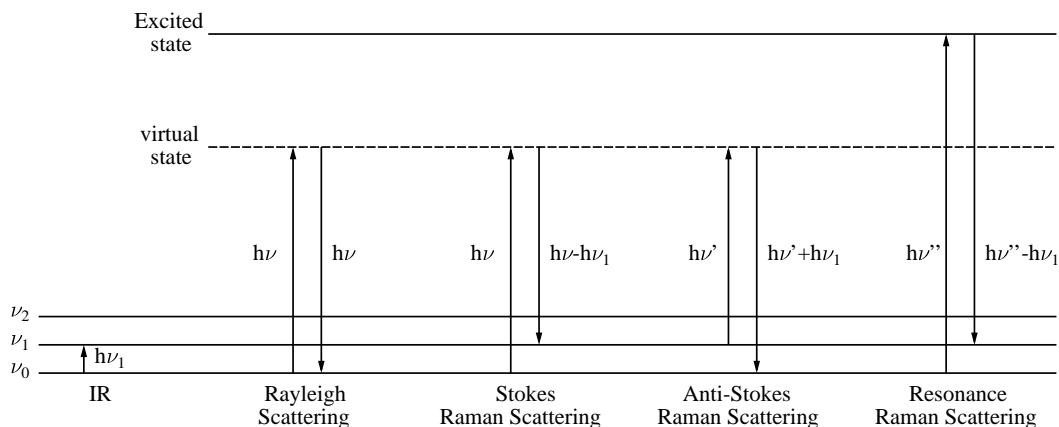


Figure 1.11 Transitions between vibrational energy levels that are observed in IR and Raman spectra.

Lasers are utilised in recording Raman spectra because they provide a highly monochromatic, polarised and directional light source with a high power range.²⁹ The tunability of some lasers used allows for different resonant conditions to be explored. Although Raman is a complementary technique to IR spectroscopy it has several advantages. One of the main advantages is that aqueous samples of organic dyes can be studied more easily because water strongly absorbs across the infrared region whereas the Raman effect for water is weak and therefore does not mask the vibrational signal to the same degree.

1.3.3 Nuclear magnetic resonance spectroscopy

NMR spectroscopy is a common analytical technique used for the elucidation of structure and molecular interactions, and in this work ^1H and ^{13}C NMR have been used.

Nuclei have an associated spin quantum number I and magnetic moment ($\mu / \text{J T}^{-1}$),³⁰ and can orientate themselves $2I + 1$ different ways in an applied magnetic field. Figure 1.12 shows the effect of the interaction between magnetic field (B_0 / T) and μ of ^1H and ^{13}C nuclei which both have an $I = 1/2$; the once degenerate state now has two orientations that differ in energy. The energy difference between the two levels corresponds to the Larmor frequency (ν_0 / s^{-1}) and upon the application of a radiofrequency pulse at ν_0 a transition results from α to β states.³¹

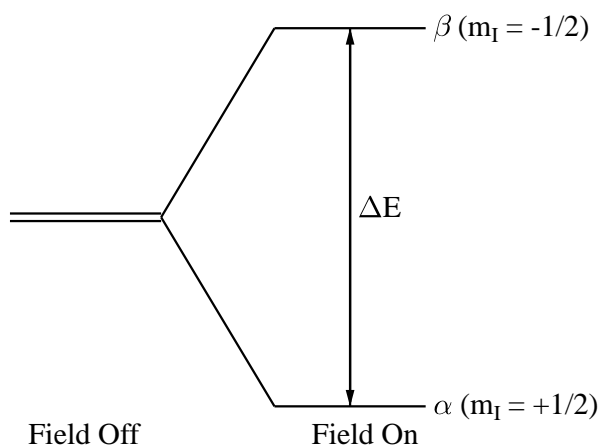


Figure 1.12 Effect of a magnetic field on a degenerate nuclei with $I = \frac{1}{2}$.

In reality ν_0 , is affected by the creation of local magnetic fields caused by either the electron cloud surrounding the nuclei or by neighbouring molecules, which will change the energy between α and β states.³¹ Experimentally, the frequency for a specific nucleus is represented by the chemical shift (δ) scale which is related to the difference between the resonance frequency of the specific nucleus observed (ν) and a reference (ν^0) (which is usually an internal standard or solvent) and is shown in Equation 1.3.³¹

$$\delta = \frac{\nu - \nu^0}{\nu^0} \times 10^6 \quad (1.3)$$

In modern Fourier Transform (FT) NMR spectrometers, after irradiating with a short pulse of radiofrequency radiation, the emission as a result of relaxation is detected as a function of time, and this Free Induction Decay (FID) can then be Fourier transformed to produce an NMR spectrum.³²

Each signal peak in an NMR spectrum has an intensity which can be integrated to give a ratio of the number of nuclei in the same environment to that in another. This is a very useful feature in for example ^1H NMR, where CH, CH₂ and CH₃ groups can be easily distinguished.

Fine structure is commonly observed in ^1H NMR spectra and in a few cases in ^{13}C NMR spectra as the result of neighbouring magnetic nuclei modifying the resonant

frequency of another by contributing to its local magnetic field. The magnitude of the spin-spin interactions is given by the coupling constant J , and importantly this is independent of the applied magnetic field. In general, for a given proton giving rise to a signal surrounded by n non-equivalent protons there will be $(n + 1)$ lines for that signal seen in the spectra and the intensities of these lines are given by Pascal's triangle.³³ This is a very useful feature in elucidating a structure by understanding which atoms neighbour each other.

COrelated Spectroscopy (COSY) and Nuclear Overhauser Effect Spectroscopy (NOESY) are two-dimensional NMR techniques that are used in this work in helping in the assignment of ^1H spectra. COSY is a multiple pulse sequence technique used to determine all the protons that couple together.³³ The normal ^1H NMR spectrum is represented on x and y axis, the cross peaks that are off the diagonal represent neighbouring protons that couple to each other. NOESY is the study of through-space interactions between neighbouring nuclei. Upon irradiation of a specific nucleus using a radiofrequency pulse at its resonance frequency, the signals from neighbouring nuclei become perturbed,³³ and the cross-peaks given from neighbouring protons that are close in space.

Heteronuclear Single Quantum Coherence (HSQC) and Heteronuclear Multiple Bond Coherence (HMBC) are two-dimensional NMR techniques that are used to determine those protons that are directly attached to a carbon and those protons that are adjacent to carbon, usually two to four bonds away, allowing for structural determination.

For a sample containing a mixture of components, its NMR spectrum can often be difficult to interpret, hence methods have been and are still in the process of being developed. One such method is Diffusion Ordered Spectroscopy (DOSY),³⁴⁻³⁷ and the use of this method allows separation of NMR signals from each individual species based on their diffusion coefficients. The diffusion coefficient ($D / \text{m}^2 \text{s}^{-1}$) is a property that is dependent on the size of the species, specifically the hydrodynamic radius (R_H / m) using Stokes-Einstein equation as shown in Equation 1.4, where k ($\text{m}^2 \text{kg s}^{-2} \text{K}^{-1}$) is the Boltzmann constant, T (K) is temperature and η ($\text{kg m}^{-1} \text{s}^{-1}$) is the solvent viscosity.

$$D = \frac{kT}{6\pi\eta R_H} \quad (1.4)$$

DOSY spectra are recorded as a function of pulsed field gradient (PFG), these 1D spectra are then converted to a 2D spectrum by fitting the decay of the signal as a function of the square of the PFG amplitude. The Stejskal-Tanner equation³⁸ as shown in Equation 1.5, describes the decay of the signal in an ideal pulsed field gradient, where S (arbitrary units) is the signal amplitude, S_0 (arbitrary units) is the signal amplitude had there been no diffusion, D ($\text{m}^2 \text{s}^{-1}$) is the diffusion coefficient, δ (s) is the gradient pulse width, γ ($\text{s}^{-1} \text{T}^{-1}$) is the magnetogyric ratio, g (T m^{-1}) is the gradient amplitude and Δ (s) is the diffusion time.

$$S = S_0 e^{-D\gamma^2\delta^2g^2\Delta} \quad (1.5)$$

In this work it is the application of the DOSY technique that is of interest rather than its development. So far the reported use of the technique has mainly been limited to test samples, rather than to chemical applications of the type reported in this work.

1.3.4 Electrochemistry

Electrochemistry is a branch of chemistry that studies electron transfer processes at electrodes. In a redox reaction, species that lose electrons are oxidised and species that gain electrons are reduced. A simple electrochemical cell comprises two electrodes usually made from a metal or graphite, the anode and the cathode, submersed into an electrolyte.³⁹ Oxidation takes place at the anode and reduction at the cathode, with the flow of current travelling from anode to cathode.²³ Often a reference is used that has a standard electrode potential E^\ominus that all other potentials are compared to, commonly the standard hydrogen electrode (SHE) is used as it produces a reproducible electrode potential scale.²³

The application of the Nernst equation, as shown in Equation 1.6, relates the applied potential E to the potential of the electrochemical reaction E^\ominus , where R ($8.314 \text{ J K}^{-1} \text{ mol}^{-1}$) is the molar gas constant, T (K) is the temperature, n is the number

of electrons transferred in the electrochemical process, F (96485 C mol^{-1}) is the Faraday constant and K is the equilibrium constant which is defined by the ratio of the activities of reducing and oxidising species as shown in Equation 1.7.

$$E = E^\ominus - \left(\frac{RT}{nF} \right) \ln K \quad (1.6)$$

$$K = \frac{a_{\text{red}}}{a_{\text{ox}}} \quad (1.7)$$

Cyclic voltammetry is commonly used to measure redox properties of a system.⁴⁰ It is a method by which the voltage is changed as function of time and continually cycles back and forth, and as such the current is measured as a function of voltage. Upon approaching the reduction or oxidation potential of the analyte, the current rapidly increases.

Controlled potential electrolysis (CPE) is an electrochemical technique in which a constant potential is applied to bulk solutions to determine the number of electrons transferred through electron transfer processes, by measuring the current and therefore charge during the process.⁴¹

Spectroelectrochemistry is an electrochemical technique in which UV/Visible absorption spectra are recorded as a function of potential which allows for the observation of spectral changes that occur during electron transfer processes.⁴²

1.3.5 High performance liquid chromatography

High Performance Liquid Chromatography (HPLC) is an analytical technique that is commonly used to separate species which can then be identified by such methods such as UV/Visible absorption spectroscopy and mass spectrometry.

In a typical HPLC machine^{23,26,43} small sample volumes (ca. 5–500 μl) are injected into a mobile phase of choice. The mobile phase is sparged with an inert gas such as helium and an isocratic or gradient elution scheme is used in which the composition is changed as a function of time. A pump is used to maintain a constant flow rate of the mobile phase of ca. 0.1–10 ml min^{-1} through the column containing the stationary phase. Silica is a commonly used stationary phase with particle sizes of ca. 3–10 μm , in a 3–30 cm length and 1–10 mm diameter column. Detection of components eluting at different retention times is often made by spectroscopy using a diode array UV/Visible absorption spectrometer. HPLC chromatograms can be displayed using a fixed UV or visible wavelength for detection.

In this work, reverse-phase chromatography has been used, which uses a column where octadecyl (C_{18}) groups are bonded to the silica surface, creating a non-polar stationary phase. In using a more polar mobile phase than the stationary phase, the most polar components from the injected sample elute first.

1.3.6 Liquid chromatography mass spectrometry

Liquid chromatography mass spectrometry (LC-MS) utilises the HPLC separation of components in a mixture which are then detected by mass. To increase the sensitivity to ion detection, which is low due to the large volume in the mobile phase, the flow rate through the column is slowed compared with that optimised for spectroscopic detection allowing a smaller volume of mobile phase into the mass analyser.

Organic dyes containing sulfonate groups, as used in this study, are usually analysed for mass detection with soft ionisation techniques due to having an overall negative charge. One such soft ionisation technique is electrospray ionisation (ESI)⁴⁴ in which a fine mist of the mobile phase, carrying the components to be analysed, is ionised. Where positive

ion mode is used parent ions due to $[M + H^+]^+$ are detected and where negative ion mode is used parent ions due to $[M - H^+]^-$ are detected.

Fragmentation of the parent ion provides useful information about the structure of the parent species. The process by which specific ions are selected and fragmented is called Tandem Mass Spectrometry (MS-MS) using a triple quadrupole. In the first quadrupole a specific ion is selected, in the second quadrupole the ions are accelerated and allowed to collide with inert atoms such as helium; the fragment ions formed as a result of collisionally activated dissociation (CAD) are then detected in the third quadrupole.

1.3.7 Time-resolved UV/Visible absorption spectroscopy

Processes that occur on short time-scales can be studied using pulsed laser methods allowing their spectroscopic and kinetic properties to be determined. Time-resolved UV/Visible absorption spectroscopy (TRVIS) is a method by which the transient absorption of a species can be recorded as a function of time with methods available from the femtosecond to the second timescale.^{45,46} A pump-probe technique is often employed where a pump laser creates an excited state or induces a chemical reaction which can then be probed. Arc lamps are commonly employed as probes as they can be used to observe over a large wavelength range.

1.3.8 DFT calculations

Computational calculations are very useful to experimental chemists to aid in the interpretation of data by simulating structures and mechanisms. Calculations are based on electronic structure methods that aim to solve the Schrödinger equation as shown in Equation 1.8, where H , Ψ and E are the Hamiltonian operator, wavefunction and total energy of the system studied, respectively.⁴⁷ For most applications the system is too large to give an exact solution to the Schrödinger equation. Various methods are therefore used to simplify this problem; semi-empirical methods use experimentally derived parameters and ab initio methods use first principles.

$$H\psi = E\psi \quad (1.8)$$

Density functional theory (DFT) is now a commonly used electronic structure method that attempts to take into account the effect of electron correlations between neighbouring atoms using an iterative approach to approximate the Schrödinger equation. This is done by modelling the total energy of the system as given in Equation 1.9,⁴⁸ where E^T accounts for the kinetic energy of the electrons; E^V accounts for the potential energy resulting from the nuclear-electron attraction and nuclear-nuclear repulsion; E^J accounts for the potential energy resulting from the electron-electron repulsion; E^{XC} is the exchange-correlation term corresponding to the remaining electron-electron interaction. In the last term, it is the correlation that corresponds to interactions between electrons of different spins that is unknown; hence local density approximations (LDA) have been introduced. The B3LYP function used in this work is a hybrid functional that mixes the exchange energy that is represented by Becke with the correlation energy as formulated by Lee, Yang and Parr.⁴⁹

$$E = E^T + E^V + E^J + E^{XC} \quad (1.9)$$

In order to model a system correctly, a suitable basis set must be chosen. The basis set is a mathematical description of the orbitals. The larger the basis set the less restrictions on where the electrons are located, however the length of computational time increases. The STO-3G basis set describes the minimal basis set for an atom by modelling them using Slater type orbitals using three gaussian functions. In this work a 6-31G(d) basis set models each atom by using six gaussian functions for each core orbital and a combination of three and one gaussian functions for each valence orbital, this allows for the addition of polarisation to hydrogens and heavy atoms allowing for accurate energy calculations, and hence molecular properties can be predicted with more certainty.⁴⁸

1.4 Aims

A series of seven 2-(4-R-phenylazo)naphthalene-4,8-disulfonate dyes (R-Span), where R = NH₂, OH, OMe, NHAc, H, Br and CN as shown in Figure 1.13, have been synthesised by Fujifilm Imaging Colorants Ltd as models for potential dyes for use in ink-jet inks. The overall aim of this project was to study the structure and reactivity of these R-Span dyes in aqueous solution.

The first main aim was to study the structural properties of the R-Span dyes and the influence of the R substituent using a range of spectroscopic and computational techniques, and these results are reported and discussed in Chapter 3. The second main aim was to study the substituent effect on the reactivity of the R-Span dyes by electrochemical and photochemical methods, focusing on reduction and using various analytical techniques to identify products and mechanisms. Electrochemically induced reactions of the R-Span dyes are reported and discussed in Chapter 4. Photochemically induced reactions are reported and discussed in Chapter 5, including two types of study; in one case, a photoinitiator was used to create radicals to react with the R-Span dyes, and in the other the direct photochemistry of the R-Span dyes was studied.

In this work, one of the main aims was to study the effect of the *para*-R substituent on structure and reactivity, and the effect can be considered alongside Hammett constants, σ_p (as given in Table 1.4), which give an indication of the total electronic effect of the substituent *para*-R attached to a benzene ring. In general, a negative σ_p indicates an electron donating substituent and a positive σ_p indicates an electron withdrawing substituent, useful when considering structure. σ_p^+ and σ_p^- are a series of values⁵⁰ (Table 1.4) that have been produced to account for the direct resonance of an R substituent with a reaction site, a useful property when considering reactivity; in general σ_p^+ values can be considered when positive charge develops at the reaction centre and σ_p^- values a negative charge developing at the reaction centre. Where data are presented for all R-Span dyes in this study, they are given in the order of their *para*-R σ_p Hammett constants.

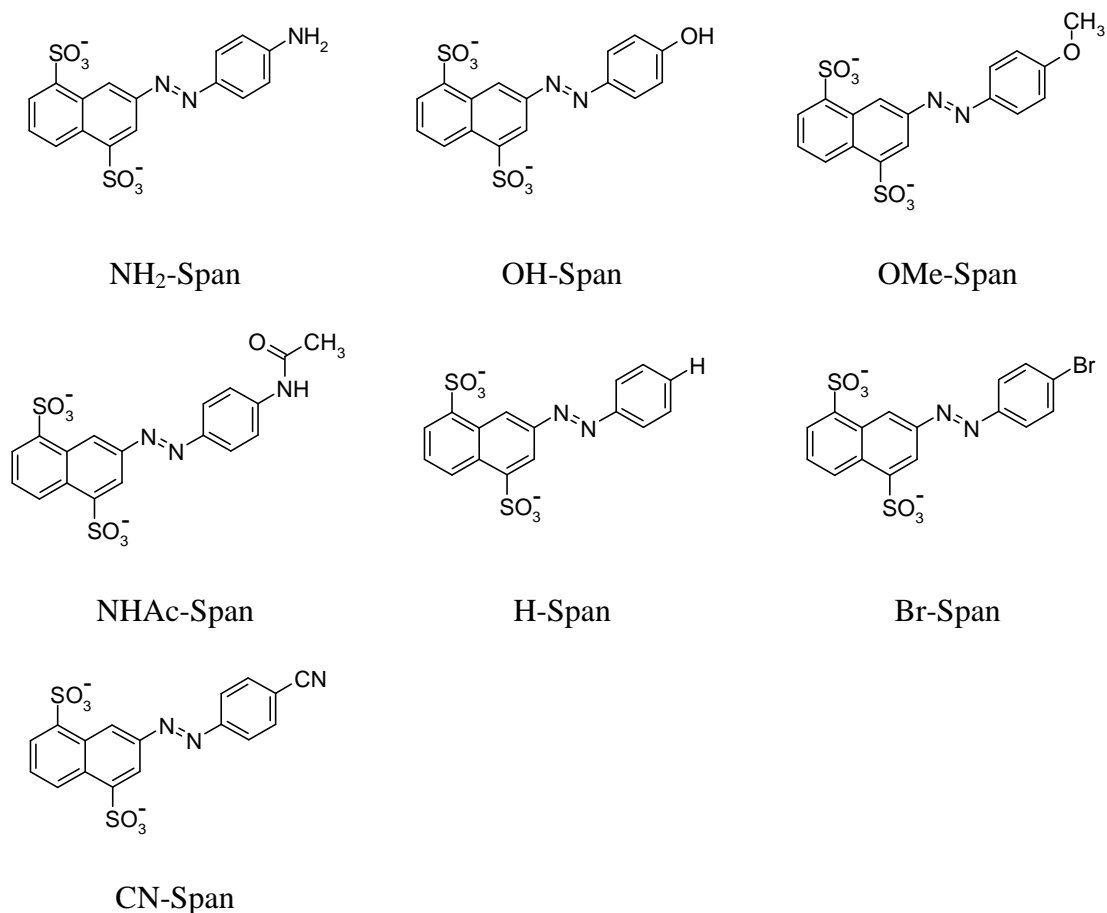


Figure 1.13 Structures of the “pure” dyes NH_2 -Span, OH-Span, OMe-Span, NHAc-Span and the “impure” dyes H-Span, Br-Span and CN-Span, all shown without their sodium counter ions in the *trans* form (see Chapter 2).

Table 1.4 *Para* substituent Hammett σ_p , σ_p^+ and σ_p^- constants for the R-Span dye series.⁵⁰

Substituent	-NH ₂	-OH	-OMe	-NHAc	-H	-Br	-CN
σ_p	-0.66	-0.37	-0.27	0.00	0.00	+0.23	+0.66
σ_p^+	-1.30	-0.92	-0.78	-0.60	0.00	+0.15	+0.66
σ_p^-	-0.15	-0.37	-0.26	-0.46	0.00	+0.25	+1.00

1.5 References

1. Gregory, P. *Chem. Br.* **2001**, *36*, 39-42.
2. Brunahl, J.; Grishin, A. M. *Sens. Actuators, A* **2002**, *101*, 371-382.
3. Le, H. P. *J. Imaging Sci. Technol.* **1998**, *42*, 49-62.
4. Christie, R. M. *Colour Chemistry*. RSC Paperbacks: Cambridge, 2001.
5. Allen, R. L. M. *Colour Chemistry*. Nelson: London, 1971.
6. Zollinger, H. *Color Chemistry*. 3rd ed.; Wiley-VCH: Switzerland, 2003.
7. Abrahart, E. N. *Dyes and their Intermediates*. 2nd ed.; Edward Arnold: London, 1977.
8. Gregory, P. *High Technology Applications of Organic Colourants*. Plenum Press: New York. 1991.
9. Rayleigh, F. R. S. *Proc. London Math. Soc.* **1878**, *10*, 4-13.
10. Elmqvist, R. U.S. Patent 2,566,443, 1951.
11. Sweet, R. G. U.S. Patent 3,596,275, 1971.
12. Zoltan, S. I. U.S. Patent 3,683,212, 1976.
13. Yoon, C.; Choi, J. H.; Koob, B. C.; Jeong, Y. D. *Color Technol.* **2005**, *121*, 13-17.
14. de Jong, J.; de Bruin, G.; Reinten, H.; van den Berg, M.; Wijshoff, H.; Versluis, M.; Lohse, D. *J. Acoust. Soc. Am.* **2006**, *120*, 1257-1265.
15. Park, J.; Moon, J. *Langmuir* **2006**, *22*, 3506-3513.
16. Gregory, P. *Opt. Laser Technol.* **2006**, *38*, 306-314.
17. Curry, S. A.; Portig, H. *IBM J. Res. Dev.* **1977**, *21*, 10-14.
18. Buehner, W. L.; Hill, J. D.; Williams, T. H.; Woods, J. W. *IBM J. Res. Dev.* **1977**, *21*, 2-9.
19. Bird, J.; Brough, N.; Dixon, S.; Batchelor, S. N. *J. Phys. Chem. B* **2006**, *110*, 19557-19561.
20. Abbott, L. C.; Batchelor, S. N.; Jansen, L.; Oakes, J.; Lindsay Smith, J. R.; Moore, J. N. *New J. Chem.* **2004**, *28*, 815-821.
21. Abbott, L. C.; Batchelor, S. N.; Oakes, J.; Lindsay Smith, J. R.; Moore, J. N. *J. Phys. Chem. B* **2004**, *108*, 13726-13735.
22. Abbott, L. C.; MacFaul, P.; Jansen, L.; Oakes, J.; Lindsay Smith, J. R.; Moore, J. N. *Dyes Pigm.* **2001**, *48*, 49-56.
23. Skoog, D. A.; West, D. M.; Holler, F. J. *Fundamentals of Analytical Chemistry*. 7th ed.; Saunders College Publishing: New York. 1991.

24. Atkins, P. *The Elements of Physical Chemistry*. 3rd ed.; Oxford University Press: Oxford. 2001.
25. Kasha, M. *Discuss. Faraday Doc.*, **1950**, 9, 14-19.
26. Harris, D. C. *Quantitative Chemical Analysis*. 4th ed.; W. H. Freeman & Co: New York. 1995.
27. Banwell, C. N; McCash, E. M. *Fundamentals of Molecular Spectroscopy*. 4th ed.; McGraw-Hill Book Company: London. 1994.
28. McCreery, R. L. Raman Spectroscopy for Chemical Analysis. In *Chemical Analysis*. Wiley: New York, 2000; Volume 157.
29. Wolverson, D. Raman Spectroscopy. In *Introduction to Laser Spectroscopy*. Andrews, D. L.; Demidov, A. A.; Eds.; Plenum Press: New York. 1995.
30. Günther, H. *NMR Spectroscopy*. 2nd ed.; John Wiley and Sons Ltd: Chichester. 1995.
31. Atkins, P. *Physical Chemistry*. 6th ed.; Oxford University Press: Oxford. 2000.
32. Anderson, R. J.; Bendell, D. J.; Groundwater, P. W. *Organic Spectroscopic Analysis*. The Royal Society of Chemistry: Cambridge. 2004.
33. Kemp, W. *NMR in Chemistry A Multinuclear Approach*. Macmillan Education Ltd: London. 1986.
34. Stilbs, P. *Prog. Nucl. Magn. Reson. Spectrosc.* **1987**, 19, 1-45.
35. Morris, K. F.; Johnson, C. S. *J. Am. Chem. Soc.* **1992**, 114, 3139-3141.
36. Morris, K. F.; Johnson, C. S. *J. Am. Chem. Soc.* **1993**, 115, 4291-4299.
37. Johnson, C. S. *Prog. Nucl. Magn. Reson. Spectrosc.* **1999**, 34, 203-256.
38. Tanner, J. E.; Stejskal, E. O. *J. Phys. Chem.* **1965**, 42, 288-292.
39. Hamann, C. H.; Hamnett, A.; Vielstich, W. *Electrochemistry*. Wiley-VCH: Chichester. 1998.
40. Brett, C. M. A; Brett, M. O. B. *Electrochemistry Principles, Methods and Applications*. Oxford University Press: 1994.
41. Speiser, B. *Organic Electrochemistry*. Schäfer, H. J.; Ed Wiley-VCH: Weinheim, 2003. Volume 3.
42. Salbeck, J. *Anal. Chem.*, **1993**, 65, 2169-2173.
43. Cox, G. B. Conventional Coulmn Systems: Instrumentation and Current Practise. In *Techniques in Liquid Chromatography*. C. F. Simpson.; Ed.; Wiley Heyden: Chichester. 1982.

44. *Electrospray Ionisation Mass Spectrometry Fundamentals Instrumentation and Applications*. Cole, R. B.; Ed.; John Wiley and Sons Inc.: Chichester. 1997.
45. Jones, W. J. High Sensitivity Picosecond Spectroscopy. In *Introduction to Laser Spectroscopy*. Andrews, D. L.; Demidov, A. A.; Eds.; Plenum Press: New York. 1995.
46. Andrews, D. L. *Lasers in Chemistry*. 3rd ed; Springer: London. 1997.
47. Young, D. *Computational Chemistry A Practical Guide for Applying Techniques to Real World Problems*. John Wiley and Sons Inc.: Chichester. 2001.
48. Foresmann, J. B.; Frisch, A. *Exploring Chemistry with Electronic Structure Methods*. 2nd ed; Gaussian Inc. Pittsburgh. 1996.
49. Stephens, P. J.; Devlin, F. J.; Chadalowski, C. F.; Frisch, M. J. *J. Phys. Chem.*, **1994**, 98, 11623-11627.
50. Hansch, C.; Leo, A.; Taft, R. W. *Chem. Rev.* **1991**, 91, 165-195.

Chapter 2 Experimental

2.1 Materials

The approximate quantities of dyes supplied were: OH-Span 400 mg, NH₂-Span 150 mg, NHAc-Span 150 mg, OMe-Span 50 mg, H-Span 40 mg, Br-Span 40 mg and CN-Span 30 mg. Due to its greater quantity, more detailed work was generally carried out on OH-Span. All the R-Span dyes were used as received from Fujifilm Imaging Colorants Ltd without any further purification. All R-Span dyes are implied as being in the *trans* form unless mentioned otherwise and they were supplied as the sodium salt; in this work, the name R-Span refers to the dianion without counter-ions. Fujifilm spent a considerable amount of time and effort in synthesising and purifying these dyes, and the quantities received reflect the purification difficulties for each dye, with the main aim of maximising purity rather than yield.

Samples of OH-Span, NH₂-Span, NHAc-Span and OMe-Span had an organic purity confirmed to be ca. 98% by NMR spectroscopy and HPLC, and these are termed “pure” dyes in this work. The combined inorganic impurities including water and salt content for all the pure dyes were obtained by Fujifilm Imaging Colorants Ltd from either Karl-Fischer titration (w/w) or by elemental analysis, and were 22%, 14%, 20% and 17% for OH-Span, NH₂-Span, NHAc-Span and OMe-Span, respectively.

Samples of H-Span, Br-Span and CN-Span had a organic purity confirmed to be 49%, 71% and 83%, respectively, by NMR spectroscopy and HPLC and are termed “impure” dyes in this work. The impure dyes showed various organic impurities giving resonances in both the aromatic and aliphatic regions of the NMR spectra and extra peaks in the HPLC chromatograms. There was insufficient quantity of material available for the inorganic impurities of the impure dyes to be determined.

In the literature the inorganic impurity content of azo dyes is not often considered in concentration calculations, and concentrations are reported here without correction of any impurity.

The model compound 2-naphthylamine-4,8-disulfonic acid disodium salt (NAPDAD, 98%) was used as received from ABCR. D₂O (99.9% D), DMSO-d₆ (99.9% D), DMSO (spectroscopic grade), potassium hydroxide (90+%), hydrochloric acid (37% ACS reagent grade), deuterium hydrochloride (35% wt. in 99% D D₂O), sodium deuterioxide (40% wt. in 99%+ D D₂O), disodium hydrogen phosphate (99%), acetic acid (99.7% ACS reagent grade), the model compounds 4-aminophenol (APOL, 95%), 1,4-diaminobenzene (DAB 99%), N-(4-aminophenyl)acetamide (APA 99%), 1,4-hydroquinone and the photoinitiator 2-hydroxy-4'-(2-hydroxyethoxy)-2-methylpropiophenone (98%) were used as received from Aldrich. Sodium acetate (analytical grade), ammonium acetate (100%), sodium hydroxide (98%), ethanol (analytical grade) and acetonitrile (HPLC grade) were used as received from Fisher Scientific. Sodium acetate-d₃ (95% D), acetic acid-d₄ (95% D) and sodium 3-(trimethylsilyl)propionate-2,2,3,3-d₄ (TSP 99% D) were used as received from Goss scientific.

2.2 Sample preparation

Stock solutions of the azo dyes at concentrations of typically 1×10^{-3} mol dm⁻³ were made up in 25 cm³ volumetric flasks. Sonication followed by observation under a lamp was used to check that all the solid dye had dissolved. Subsequent dilutions, where necessary, were made from the stock solution using a 1.00 cm³ micropipette.

All experiments were conducted at room temperature (ca. 19 °C) unless stated otherwise.

2.3 Instrumentation

2.3.1 UV/Visible absorption and emission spectroscopy

UV/Visible absorption spectra were recorded using a Hitachi U-3010 spectrometer with a scan speed of 300 nm min^{-1} and a slitwidth of 2 nm, using matching quartz cuvette cells of pathlength 1 or 10 mm. The appropriate solvent was used for reference.

For spectrophotometric pH titrations, aqueous dye solutions ($5 \times 10^{-5} \text{ mol dm}^{-3}$) were adjusted to pH 2 using concentrated HCl and made up to a volume of 250 cm^3 . While constantly stirred in a conical flask, aliquots of between 0.05 and 5 cm^3 of 0.5 mol dm^{-3} KOH were added to adjust the pH and a UV/Visible absorption spectrum was recorded after each addition, with samples thermostatically controlled at $25 \text{ }^\circ\text{C}$. The pH was recorded using an Oakton double junction, glass bodied probe (35801-79) with a working range of pH 2 to 12.

Corrected UV/Visible emission spectra were recorded using a Hitachi F-4500 spectrofluorimeter with a photomultiplier voltage of 950 V, a spectral slitwidth of 10 nm and a scan speed of 60 nm min^{-1} . Solution samples (ca. $4.5 \times 10^{-6} \text{ mol dm}^{-3}$) were studied with right-angled illumination in a 1 cm pathlength cell and with an absorbance of < 0.1 at the excitation wavelength to minimise self-absorption.

2.3.2 Raman spectroscopy

The Raman apparatus in York has been described in detail previously.¹ Raman spectra were recorded with excitation wavelengths of 514.5 nm (Spectra Physics 2025 argon ion laser), 413.1 nm or 350.6 nm (Coherent Innova 90 krypton ion laser).

Scattered light was collected at 90° to the incident beam, dispersed in a Spex 1403 double monochromator with a $30 \text{ }\mu\text{m}$ slitwidth and detected using a nitrogen-cooled charge coupled device. The resolution was ca. 3, 5 and 7 cm^{-1} and accuracy was ± 2 , 4 and 6 cm^{-1} (all ± 1 pixel) for 514.5, 413.1 and 350.6 nm excitation, respectively. Solution samples (ca. $4 \times 10^{-4} \text{ mol dm}^{-3}$) were held in a capped spinning quartz cell and

spectra recorded as multiple 300 s exposures to give a total acquisition time of 20–60 min. Any fluorescence background was removed, and the spectra were calibrated against the Raman spectra of 1,4-dioxane or acetone.

Sample integrity was monitored by recording UV/Visible absorption spectra and HPLC chromatograms before and after acquisition, as well as monitoring Raman spectra during data collection.

2.3.3 Infrared spectroscopy

Infrared spectra of OH-Span (5×10^{-2} mol dm⁻³) were recorded using a Nicolet Avatar 360 FTIR spectrometer with 516 scans and a resolution of 4 cm⁻¹, and ratioed against the solvent / background spectrum. Spectra were recorded using a demountable cell with CaF₂ windows and a 6 μm Teflon spacer.

2.3.4 NMR spectroscopy

2.3.4.1 Structural studies

1D and 2D (COSY, NOESY, HSQC and HMBC) ¹H (500 MHz) and ¹³C (125 MHz) spectra were recorded at 300 K by Ms. Heather Fish using a Bruker AV500 spectrometer. 1D ¹H (400 MHz) spectra were also recorded without assistance at 300 K using a Bruker AV400 spectrometer. Solutions were prepared in 1 cm³ D₂O and 0.75 cm³ DMSO-d₆ (3×10^{-2} mol dm⁻³).

2.3.4.2 Product studies

1D and 2D (COSY, NOESY, DOSY) ¹H (700 MHz) spectra were recorded at 298 K with the assistance of Dr. David Williamson using a Bruker AV700 spectrometer fitted with a broadband inverse (BBI) probe with an actively shielded Z-gradient. Solutions were prepared in a pH 5.2 deuterated sodium acetate buffer solution² and transferred to a 5 mm diameter NMR tube with a Young's tap. Where possible sodium

3-(trimethylsilyl)propionate-2,2,3,3-d₄ (TSP) (5×10^{-5} mol dm⁻³) was added to use as a chemical shift reference.

¹H NMR spectra were recorded using the established Bruker zg pulse sequence for model compounds, and the zgesgp pulse sequence with water suppression (using excitation sculpting with gradients)³ was used for photochemical and electrochemical samples which was chosen to maximise the signal-to-noise. Data were acquired using between 4 and 256 scans with a relaxation delay varying between 1 to 20 s. Long relaxation delays (20 s) were required to provide accurate integrations for OH-Span and NAPDAD with long T₁ values (longitudinal relaxation times).

DOSY was carried out using a pulsed field gradient NMR (PFG-NMR) with either the ledbpgp2s pulse sequence,⁴ which is a 2D sequence for diffusion measurement using spin-echo and a longitudinal eddy current delay of 5 ms (LED), or the stebpgp1s19 pulse sequence,⁴ which is a 2D sequence for diffusion measurement using stimulated echoes with bipolar gradients under water suppression with presaturation chosen to maximise the signal-to-noise ratio. Data were acquired using between 64 and 512 scans with a diffusion time of ca. 50 ms tailored such that the noise was ca. 10% of the maximum signal, to provide the best data to fit to an exponential decay.

DOSY spectral analysis was performed using DoseyToolbox Version 0.4 (MATLAB script)⁵ where standard 1D (F₂ dimension) processing was followed by reference deconvolution,⁶ and FIDDLE⁷ was used on each of the spectra to optimise the line-shape to aid DOSY processing. Upon DOSY (F₁ dimension) processing of the 1D spectra, exponential fitting to two components per peak was obtained by peak picking the 1D spectra with 100 tries per peak and a diffusion coefficient range of 0 – 20×10^{-10} m² s⁻¹ (recorded over 64 steps).

2.3.5 Electrochemical studies

2.3.5.1 Cyclic voltammetry

An EG&G Princeton Applied Research potentiostat (model 273) was used to control the potential in conjunction with its associated software to record the voltage and current. The cyclic voltammetry cell consists of a three-electrode modified round-bottom flask with a 3 mm Pt-disc working electrode, a Pt wire counter electrode, and a Ag/AgCl reference electrode enclosed in a glass tube containing saturated KCl. A 1×10^{-3} mol dm^{-3} solution of OH-Span was made up in 0.5 mol dm^{-3} pH 5.2 sodium acetate buffer solution and purged beforehand by nitrogen for 20 min and kept under an atmosphere of flowing nitrogen throughout the experiment. A scan rate of 10 mV s^{-1} was used.

2.3.5.2 Spectroelectrochemistry

An Oxford Electronics potentiostat was used to control the potential. The spectroelectrochemical cell (shown in Figure 2.1) consists of a working electrode of Pt gauze with dimensions of 2.1×0.9 cm contained within a 1 mm pathlength quartz cell, a counter electrode of Pt wire and a reference electrode of Ag wire. The dye solution (5×10^{-4} mol dm^{-3}) was purged by nitrogen and transferred via a cannula through a septum into the cell (which had previously been purged by nitrogen for 20 min) so that solution covered the working electrode. The potential of the cell was stepped at 0.1 V intervals and left for 10 min, after which a UV/Visible absorption spectrum was recorded.

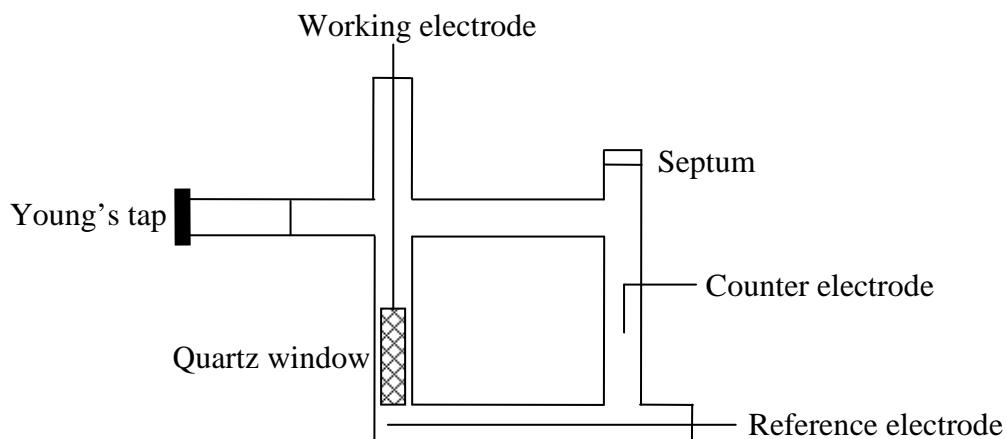


Figure 2.1 Spectroelectrochemical cell

2.3.5.3 Controlled potential electrolysis

An EG&G Princeton Applied Research potentiostat (model 273) was used to control the potential in conjunction with a PMD-1208FS D/A converter to record the current and voltage at 0.5 s intervals using in-house software. A three-electrode Bioanalytical Systems (BASi) bulk electrolysis cell was used consisting of a 75 cm³ glass beaker which contained a reticulated vitreous carbon working electrode, a platinum counter electrode enclosed in a small glass tube with a sintered disc at the bottom, a Ag/AgCl reference electrode containing 3 mol dm⁻³ aqueous sodium chloride, a PTFE tube to purge the sample under nitrogen, and a small magnetic stirrer bar at the bottom.

To determine the number of electrons used per molecule during the electrochemical process, 50 cm³ of dye (8×10^{-4} mol dm⁻³) and then 50 cm³ of buffer (0.5 mol dm⁻³) purged by nitrogen throughout were reduced over 30 min at a fixed potential of -1.2 V.

2.3.6 Photochemical studies

2.3.6.1 Steady-state studies

Steady-state studies of photochemical reactions were monitored by UV/Visible absorption spectroscopy. 1:1 and 1:10 R-Span:photoinitiator were purged under an

atmosphere of nitrogen or air for 20 min before starting the experiment. Solutions were irradiated in a 1 cm pathlength quartz cell attached to a Young's tap using a Cobra 450AF flashgun which was held directly against the window of the cell.

2.3.6.2 Time-resolved studies

TRVIS studies were performed on R-Span alone and on OH-Span:photoinitiator solutions by using a 308 nm, 12 ns pulse width XeCl excimer laser (MSX-250) providing ca. 3 mJ of laser energy at the sample. The sample was probed using the output from a 250 W Xe arc lamp, which was pulsed when using observation times of $\leq 50 \mu\text{s}$. The lamp was not pulsed at observation times of $\geq 50 \mu\text{s}$ and was under automated shutter control when using observation times of $\leq 20 \text{ ms}$, beyond which the shutter was under manual control. The probe beam was analysed using a monochromator (Applied Photophysics Laser Kinetic spectrometer), with a slit width of 0.6 – 1.0 mm giving a spectral resolution of 2.4 – 4.0 nm, and detected using a photomultiplier tube (Hamamatsu R928). A digital oscilloscope (Tektronix TDS 520) recorded 2500 data points, using a 50 Ω terminator for observations times $\leq 50 \mu\text{s}$ and a 1 or 10 k Ω terminator for observation times of $\geq 50 \mu\text{s}$. Typically data was collected over 8 laser pulses and averaged.

Dye alone studies were carried out in a 1 cm pathlength quartz cell under air. OH-Span:photoinitiator studies were carried out in a 1 mm pathlength cell attached to a flow system using a peristaltic pump. A fresh solution from a sample reservoir was flowed into the cell in between each laser pulse, and data collected from static samples.

Kinetic traces were recorded as a function of voltage vs time at 10 nm wavelength intervals, conversion of voltage to absorbance as a function of time (ΔA) was calculated by equation 2.1 by averaging the voltage (V) during the first 80 % of the pre-trigger period to give V_0 . Transient absorption spectra were produced point by point by averaging ΔA at various delay times from the kinetic traces.

$$\Delta A = \log_{10} \left(\frac{V_0}{V} \right) \quad (2.1)$$

2.3.7 HPLC analysis

HPLC analysis was performed using a Hewlett Packard HP1090 chromatograph with a Phenomenex C₁₈ reverse phase column held at 40 °C. Three solvent reservoirs were used, containing: A, 7×10^{-2} mol dm⁻³ pH 5.2 ammonium acetate buffer solution; B, water; C, acetonitrile. A binary mobile phase of A and C was used with a flow rate of 1 cm³ min⁻¹. The mobile phase was kept at 98:2 A:C for the first 5 min, it was then ramped up linearly to 70:30 A:C over the next 25 min, and kept constant for 1 min before being ramped back down to 98:2 A:C over the next 10 min to clean the column. Reservoir B was used for cleaning the column at the end of the day. An auto-sampler was used with an injection volume of 25 µl with the components eluting off the column being identified by UV/Visible absorption using a diode array detector with a 6 mm pathlength flow cell.

2.3.8 LC-MS analysis

LC-MS analysis was carried out using a Finnigan MAT LCQ ion trap mass spectrometer with an Electrospray Ionisation (ESI) source, using both positive or negative ion mode, and operated using Finnigan Navigator software version 1.2. The system comprises a Thermo Separations AS auto sampler, P4000 gradient pump and a UV2000 UV/Vis detector (Thermo quest). Reverse phase separation was carried out by using a Phenomenex C₁₈ reverse phase column. Three solvent reservoirs were used, containing: A, 1×10^{-2} mol dm⁻³ pH 5.2 sodium acetate buffer solution; B, water; C, acetonitrile. A binary mobile phase of A and C was used with a flow rate of 0.7 cm³ min⁻¹. The mobile phase was kept at 98:2 A:C for the first 5 min, it was then ramped up linearly to 70:30 A:C over the next 25 min, and kept constant for 1 min before being ramped back down to 98:2 A:C over the next 10 min to clean the column. Reservoir B was used to clean the column at end of the day. Mass spectrometer conditions used were: capillary temperature 250 °C, source voltage 3.5 kV, source current 100 µA, sheath gas flow 90 (arbitrary units) and auxiliary gas flow 50 (arbitrary units). Recorded masses are accurate to ± 0.5 Da. MS/MS conditions used an isolation width of 1 m/z of the base peak ion in either positive or negative ion mode using a collision energy of 28 eV.

2.4 DFT calculations

All DFT calculations were carried out using the Gaussian 03 software package⁸ on a PC running Linux. Initially an AM1 semi-empirical optimisation was calculated on *trans*-H-Span from which fully optimised structures for all *trans*-dyes were calculated using the B3LYP DFT functional and the 6-31G(d) basis set. Molekel (version 4.3)⁹ and Molden software¹⁰ packages were used to view the optimised structures.

The GIAO method¹¹ was applied to the optimised structures to calculate their ¹H and ¹³C NMR chemical shifts, which are reported relative to those of tetramethylsilane (TMS) calculated at the same level of theory (giving chemical shifts of ¹H 32.18 ppm and ¹³C 189.675 ppm).

The frontier molecular orbitals were obtained from the output file of the optimised structures and were viewed in Molekel. Excited state structures were calculated using time-dependent DFT using the B3LYP functional and 6-31G(d) basis set.

Vibrational wavenumbers were calculated using the B3LYP DFT / 6-31G(d) level of theory and were scaled by a factor of 0.9614.¹² The IR and Raman spectra were created by applying a Gaussian profile with a 5 cm⁻¹ linewidth (full width at half maximum) using in-house software. For clarity the spectra presented have been scaled relative to experimental data.

2.5 Data manipulation

Generally spectra were processed using Grams 32AI software (Galactic industries). All 1D spectral analysis was performed using Bruker TOPSPIN 2.0 software. LC-MS data were processed using Finnigan Navigator software version 1.2. Non-linear regression analysis was performed using SPSS for windows version 16.0 (SPSS Inc.) and values are reported with 95 % confidence limits. Kinetic modelling software written in-house by Dr L. C. Abbott was applied with a model mechanism to analyse the TRVIS data of the OH-Span:photoinitiator solutions to calculate concentrations of species as a function of time.

2.6 References

1. Abbott, L. C. D.Phil. Thesis, University of York, 1998
2. Marshall, A. G. *Biophysical Chemistry*; John Wiley & Sons. Canada, 1978
3. Hwang, T. L.; Shaka, A. J. *J. Magn. Reson., A* **1995**, *112*, 275-279.
4. Wu, A. H.; Chen, A. D.; Johnson, C. S. *J. Magn. Reson., A* **1995**, *115*, 260-264.
5. Nilsson, N. *J. Magn. Reson.* **2009**, *200*, 296-302.
6. Metz, K. R.; Lam, M. M.; Webb, A. G. *Concepts Magn. Reson.* **2000**, *12*, 21-42
7. Morris, G. A.; Barjat, H.; Horne, T. J. *Prog. Nucl. Magn. Reson. Spectrosc.* **1997**, *31*, 197-257.
8. Frisch, M. J.; Trucks, G. W.; Schlegel, H. B.; Scuseria, G. E.; Robb, M. A.; Cheeseman, J. R.; Montgomery, J. A., Jr.; Vreven, T.; Kudin, K. N.; Burant, J. C.; Millam, J. M.; Iyengar, S. S.; Tomasi, J.; Barone, V.; Mennucci, B.; Cossi, M.; Scalmani, G.; Rega, N.; Petersson, G. A.; Nakatsuji, H.; Hada, M.; Ehara, M.; Toyota, K.; Fukuda, R.; Hasegawa, J.; Ishida, M.; Nakajima, T.; Honda, Y.; Kitao, O.; Nakai, H.; Klene, M.; Li, X.; Knox, J. E.; Hratchian, H. P.; Cross, J. B.; Adamo, C.; Jaramillo, J.; Gomperts, R.; Stratmann, R. E.; Yazyev, O.; Austin, A. J.; Cammi, R.; Pomelli, C.; Ochterski, J. W.; Ayala, P. Y.; Morokuma, K.; Voth, G. A.; Salvador, P.; Dannenberg, J. J.; Zakrzewski, V. G.; Dapprich, S.; Daniels, A. D.; Strain, M. C.; Farkas, O.; Malick, D. K.; Rabuck, A. D.; Raghavachari, K.; Foresman, J. B.; Ortiz, J. V.; Cui, Q.; Baboul, A. G.; Clifford, S.; Cioslowski, J.; Stefanov, B. B.; Liu, G.; Liashenko, A.; Piskorz, P.; Komaromi, I.; Martin, R. L.; Fox, D. J.; Keith, T.; Al-Laham, M. A.; Peng, C. Y.; Nanayakkara, A.; Challacombe, M.; Gill, P. M. W.; Johnson, B. G.; Chen, W.; Wong, M. W.; Gonzalez, C.; Pople, J. A. *Gaussian 03*, Revision B.05; Gaussian, Inc.: Pittsburgh, PA, 2003.
9. Portmann, S.; Luthi, H. P. *Chimia* **2000**, *54*, 766-770.
10. Schaftenaar, G.; Noordik, J. H. *J. Comput. Aid. Mol. Des.*, **2000**, *14*, 123-134.
11. Wolinski, K.; Hinton, J. F.; Pulay, P. *J. Am. Chem. Soc.*, **1990** *112*, 8251-8260.
12. Scott, A. P., Radom, L. *J. Phys. Chem.*, **1999**, 16502-16513.

Chapter 3 Structure

3.1 Introduction

The introduction to this chapter begins with a general overview of structural studies of azo dyes, specifically, azo-hydrazone tautomerism, aggregation, hydrogen bonding and pH dependence. There is then a focus on the structure of azobenzenes and phenylazonaphthalenes established in the literature all of which are useful in this work. The specific aims of the structural studies of the R-Span dyes reported in this chapter conclude the section.

3.1.1 General

In general, relatively few crystal structures have been reported for azo dyes due to difficulty in their crystallisation.¹⁻¹³ Various spectroscopic techniques have been used to study the structure of azo dyes in solution, for example, UV/Visible spectroscopy, NMR spectroscopy, Raman spectroscopy and IR spectroscopy.¹⁴⁻³⁸ Computational techniques^{19,30,39-41} have become a very useful tool in interpreting these experimental results and they have been employed in the research reported here.

For most dyes it is important that they are soluble in water in order to be a component for an ink-jet ink, and this is usually achieved by having a sulfonic acid group often present as the sodium salt within the structure; in water these groups dissociate, giving the sulfonate anion.

3.1.1.1 Azo-hydrazone tautomerism

Azo-hydrazone tautomerism^{24,40-46} commonly occurs in dyes that have a hydroxyl group adjacent or opposite to the azo group, usually on a naphthalene ring. Figure 3.1 shows the dynamic equilibrium that is set up between the two tautomers where there is a hydroxyl group adjacent to the azo group, which is favoured as a result of a strong intramolecular hydrogen bond, locking it as the hydrazone form. It is known that substituents attached to the phenyl ring can alter the position of the tautomer

equilibrium. An electron-donating substituent on the phenyl ring can stabilise the azo tautomer whereas an electron-withdrawing substituent favours the hydrazone tautomer.^{42,46} Azo-hydrazone tautomerism can be observed by UV/visible absorption, NMR and Raman spectroscopy.^{14,15,24,25,43}

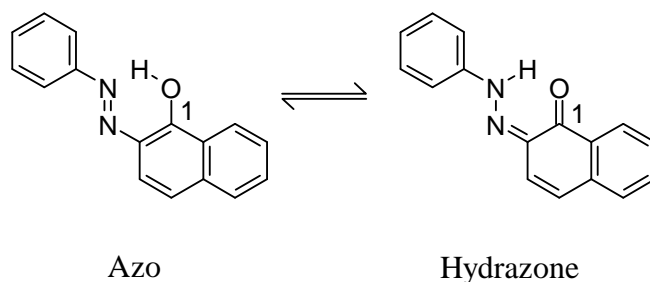


Figure 3.1 Azo-hydrazone tautomerism in a 1-hydroxy-2-phenylazonaphthalene system.

3.1.1.2 Aggregation

Aggregation is another phenomenon commonly seen for azo dyes.^{19-23,37,47} Equation 3.1 shows an example of an aggregation equation.



Aggregation is often characterised by a UV/Vis absorption spectrum in which changes in the relative heights or band shapes as a function of dye concentration can be used to calculate dimerisation and higher aggregation constants.¹⁷⁻²² Possible interactions that can occur between monomers are by π - π stacking, van der Waals forces and intermolecular hydrogen bonding. The hydrophobic effect can often explain aggregation, as monomer dyes are surrounded by water molecules in the form of hydrated anions;^{17,20} upon increasing the concentration of dye the monomers initially dimerise, as a result the water molecules surrounding them are released and thereby increasing the entropy of the system.^{17,19,30,46} Their formation may be described in terms of their orientations as a parallel dimer (H-type), head-to-tail dimer (J-type) or an oblique type dimer as shown in Figure 3.2.^{20-22,48,49}

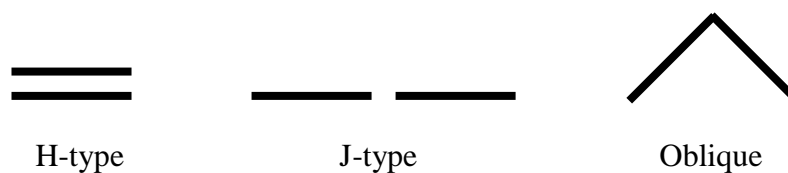


Figure 3.2 Common types of dimer.

The application of exciton theory^{48,49} has predicted that an excited monomer state splits into two levels when dimerisation occurs. The spectral shift observed upon dimerisation is determined by the geometry of the dimer as shown in Figure 3.3.⁴⁸⁻⁵⁰ For an H-type dimer, a blue shift is observed with respect to the monomer because the transition to the lowest energy excited state is forbidden. In the J-type, the transition to the highest energy excited state is forbidden resulting in a red shift being observed with respect to the monomer. For the oblique dimer the transitions to both excited dimer states become allowed.

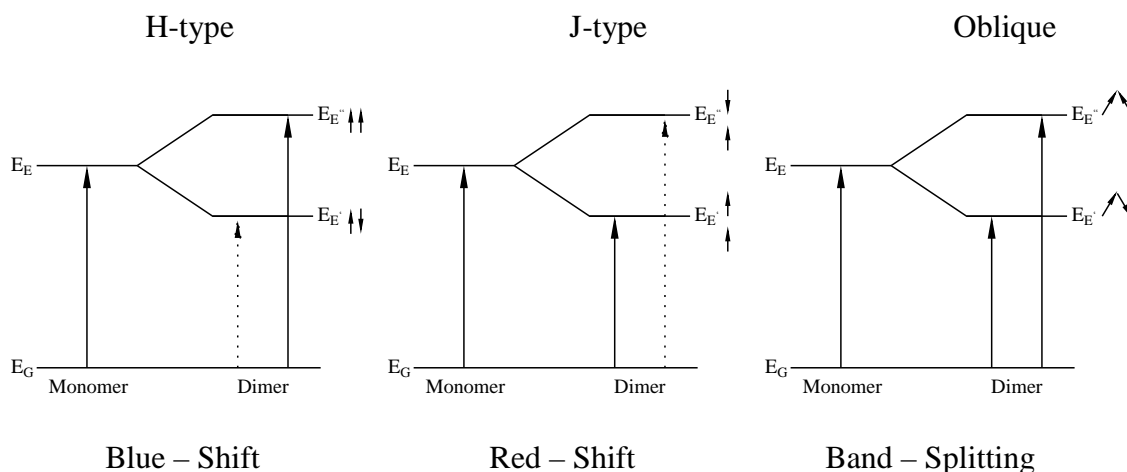


Figure 3.3 Exciton splitting for dimers of various geometries indicative of different shifts in the UV/Visible absorption spectrum.⁴⁸⁻⁵⁰

NMR spectroscopy can also be used to study azo dye aggregation;^{14,15,17-20,23} upon π - π stacking there is often a change in the local magnetic field, which can be observed as a change in the chemical shift in the NMR spectrum. In dyes such as Direct Blue 1¹⁵ and arylazo-1-naphthols (for example Acid Red 1),¹⁹ as shown in Figure 3.4, relatively large upfield shifts have been observed with increasing dye concentration for those protons attached to the biphenyl or phenyl ring, respectively, consistent with π - π stacking due to an increase in electron density from the adjacent aromatic ring.

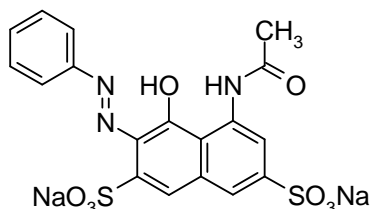
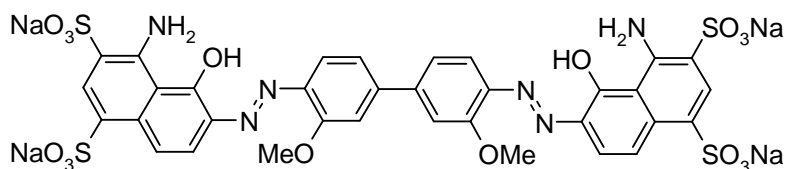


Figure 3.4 Structures of Direct Blue 1 (Top) Acid Red 1 (Bottom).

3.1.1.3 Hydrogen bonding

Intramolecular hydrogen bonding is commonly seen for arylazonaphthol dyes due to a hydrogen bond donor adjacent to the azo linkage (Figure 3.1).^{19,25,30} For purely azo dye systems such as those studied here, intramolecular hydrogen bonding is less likely but may arise due to R substituents within the molecule, such as an acetamide group. Where X-ray crystallography data are unavailable, DFT calculations can give an estimated hydrogen bonding distance between an electropositive H atom and an electronegative Y atom containing a lone pair of electrons which can then be compared with the sum of their van der Waals radii.¹⁴ Intermolecular hydrogen bonding may be observed from aggregation between dye molecules or from solvation, where solvation offers competitive interactions.¹⁶

3.1.2 Azobenzenes

Figure 3.5 shows the structure of *trans*- and *cis*-azobenzene; where azobenzene is named without the prefix in this thesis, it is implied to be in the *trans* form.

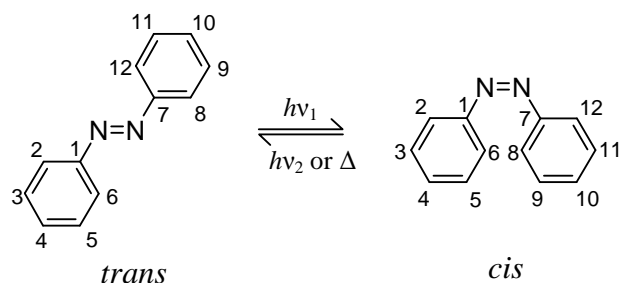


Figure 3.5 *Trans*- and *cis*-azobenzene, together with numbering system.

3.1.2.1 Structure

Azobenzene (Figure 3.5) is regarded as the simplest aromatic azo compound. In this form it is only weakly coloured, with a low intensity $n \rightarrow \pi^*$ (S_1) transition in the visible region at ca. 447 nm and a high intensity $\pi \rightarrow \pi^*$ (S_2) transition at ca. 316 nm, the positions being solvent dependent.⁵¹

Structural determination of azobenzene in solution is still ongoing. X-ray diffraction has suggested a planar structure in the crystal,⁵² but it has been thought that this is due to crystal packing forces; gas-phase electron diffraction has suggested a non-planar structure where the phenyl ring is twisted at about 30°.⁵³ Calculations on azobenzene in a polar solvent system suggest that the structure is non-planar.⁵⁴

The structure of azobenzene has also been studied by Raman spectroscopy.^{26-28,55-58} Assignments of vibrations specific to simple groups are in general not appropriate due to couplings of azo vibrations with the phenyl modes; often computational calculations are an essential aid, where normal mode coordinate analysis has shown that there is significant $\nu(\text{C-C})$, $\nu(\text{N=N})$, $\nu(\text{C-N})$, $\delta(\text{C-H})$ character in many of the modes giving bands in the region of 1000 – 1700 cm^{-1} .⁵⁹

3.1.2.2 Isomerisation

Studies on the photochemical and thermal isomerisation of azobenzene will be discussed in more detail in Chapter 5. Structurally, azobenzene type molecules can exist as a *cis* or *trans* isomer (Figure 3.5).^{51,60-62} The position of this equilibrium and hence the colour of samples can be altered by exposure to light or temperature.

NMR spectroscopy has been used to observe changes in chemical shifts between *trans* and *cis* isomers, as given in Table 3.1.⁶³ In the *trans* form, protons only experience deshielding from protons on the same aromatic ring.⁶³ However, in the *cis* form these same protons experience an additional shielding effect from the remote out-of-plane aromatic ring.⁶² Protons 2 and 6 adjacent to the N=N bond show the greatest changes (1.34 ppm), which are mirrored computationally (1.36 ppm).⁶³

Table 3.1 Experimental (in d₆-benzene) and calculated ¹H NMR chemical shifts (ppm) for *trans*- and *cis*-azobenzene.⁶³

Position	Experimental			Calculated		
	<i>trans</i>	<i>cis</i>	$\Delta(\textit{trans-cis})$	<i>trans</i>	<i>cis</i>	$\Delta(\textit{trans-cis})$
2/6	8.02	6.68	1.34	8.40	7.04	1.36
3/5	7.17	6.81	0.36	7.83	7.48	0.35
4	7.09	6.70	0.39	7.70	7.35	0.35

3.1.2.3 Substituent effect

Substitution of the aromatic ring (Figure 3.6) can change the position of the main absorption band (λ_{max}) in the UV/Visible spectrum, and Table 3.2 summarises the known values of several substituted 4,4'-azobenzenes.⁶⁴ The observation is that the addition of an electron-withdrawing group (e.g. NO₂) *para* to the azo group only produces a small shift to a longer wavelength, whereas the addition of an electron-donating group (e.g. NH₂) results in a large shift to longer wavelength. The magnitude of this change increases by having an electron-withdrawing group (NO₂) *para* to the azo group on one aromatic ring and an electron-donating group (NEt₂) *para* to the azo group on the other aromatic ring.

Substitution of azobenzene can also result in changes in the observed Raman spectrum.^{26,27} Table 3.2 summarises the known values for the most intense bands corresponding to values identified in the early literature as predominately the azo stretch and N=N-Ph symmetric bend of several substituted azobenzenes. The most notable changes between these when compared to azobenzene are of the azo stretch, with an electron-withdrawing substituent (e.g. NO₂) on the phenyl ring causing a shift to a higher wavenumber and an electron-donating substituent (e.g. NH₂) causing a shift to lower wavenumber. Interestingly, more recent DFT calculations on selected substituted azobenzene have shown coupling between motions of the azo linkage with the substituent.²⁸

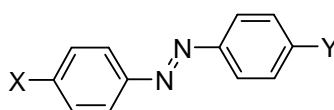


Figure 3.6 X, Y substituted 4,4'-azobenzene.

Table 3.2 Main absorption bands (λ_{\max} / nm) and (ϵ_{\max} / dm³ mol⁻¹ cm⁻¹) of substituted 4,4'-azobenzenes in ethanol,⁶⁴ and selected Raman bands (cm⁻¹) in CCl₄.^{26,27}

X	Y	λ_{\max}	ϵ_{\max}	$\nu(\text{N}=\text{N})$	$\delta(\text{N}=\text{N}-\text{Ph})$
H	H	320	21000	1440	1143
H	NO ₂	332	24000	1449	1143
H	NH ₂	385	24500	1427	1142
H	NMe ₂	407	30900	1423	1142
H	NEt ₂	415	29500	-	-
NO ₂	NEt ₂	486	33100	-	-

3.1.2.4 pH dependence

It has been long reported that azobenzene has a pK_a of -2.95 due to the protonation of the azo linkage.⁶⁵ More commonly pH dependence is observed in azobenzene-type molecules that contain -OH or -NR₂ functional groups.

Firstly, those containing an -OH functional group: 4-hydroxyazobenzene has pK_as of -0.93 and 8.2 corresponding to protonation at the azo linkage and deionisation of the -OH group, respectively.⁶⁶⁻⁶⁹ pH studies have been conducted on 4-hydroxyazobenzene-modified cyclodextrins as shown in Figure 3.7.⁶⁹

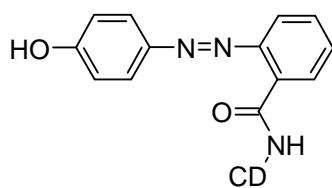


Figure 3.7 4-hydroxyazobenzene-modified cyclodextrins, where CD represents cyclodextrin.⁶⁹

The UV/Visible absorption spectrum changes with pH, at pH 4 a strong absorption band is observed at 350 nm which decreases in intensity with increasing pH as a strong absorption band at 440 nm at pH 12 grows to dominate. The observed pK_a was 8.00 and was assigned to the phenolate-phenol equilibrium as shown in Figure 3.8.⁶⁹

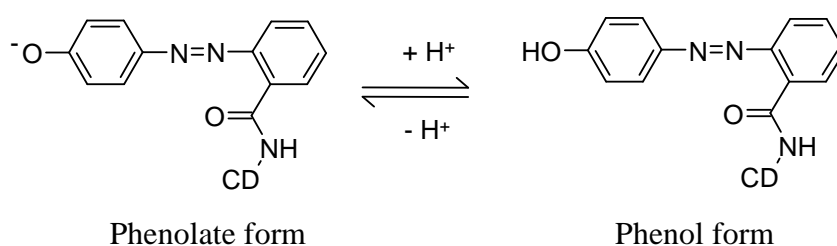


Figure 3.8 Phenolate-phenol equilibrium of 4-hydroxyazobenzene-modified cyclodextrins.⁶⁹

Although UV/visible absorption,^{66,69-79} NMR^{80,81} and Raman⁸²⁻⁸⁵ spectroscopy, and computational calculations^{41,84-86} have been used to study the site of protonation in aminoazobenzene-type molecules, evidence and conclusions often appear inconclusive.

Protonation of 4-aminoazobenzene as shown in Figure 3.9 can occur at either the azo linkage (α) or at the terminal amino group giving the azonium or ammonium tautomer, respectively. Compared to neutral 4-aminoazobenzene (λ_{max} ca. 380 nm in acetonitrile⁴¹), the ammonium tautomer (λ_{max} ca. 320 nm in acetonitrile/HCl⁴¹) now contains an electron withdrawing group resulting in absorption at shorter wavelength as opposed to the azonium tautomer (λ_{max} ca. 500 nm in acetonitrile/HCl⁴¹) that exhibits enhanced charge-transfer character (Figure 3.9) resulting in an absorption at longer wavelength.⁸⁷

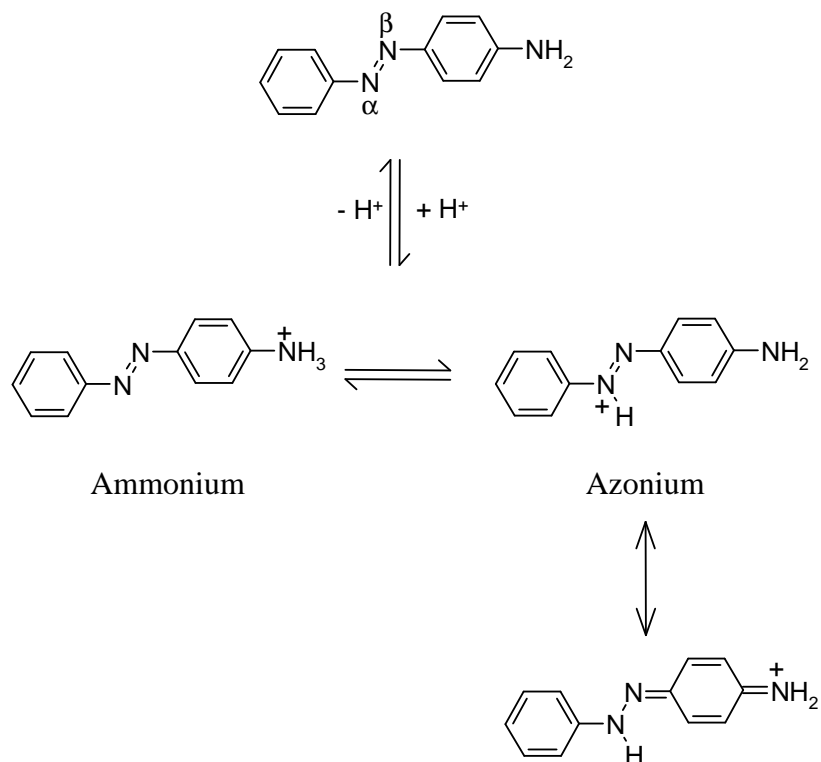


Figure 3.9 Protonation of 4-aminoazobenzene, together with the resonance structure of the azonium tautomer.⁸⁷

Methyl Orange has a pK_a of 3.39,^{64,87} upon protonation it undergoes a colour change of orange to red as a result in a shift in the band position from 465 to 507 nm,⁸⁸ as shown in Figure 3.10, where the ammonium tautomer is not observed.

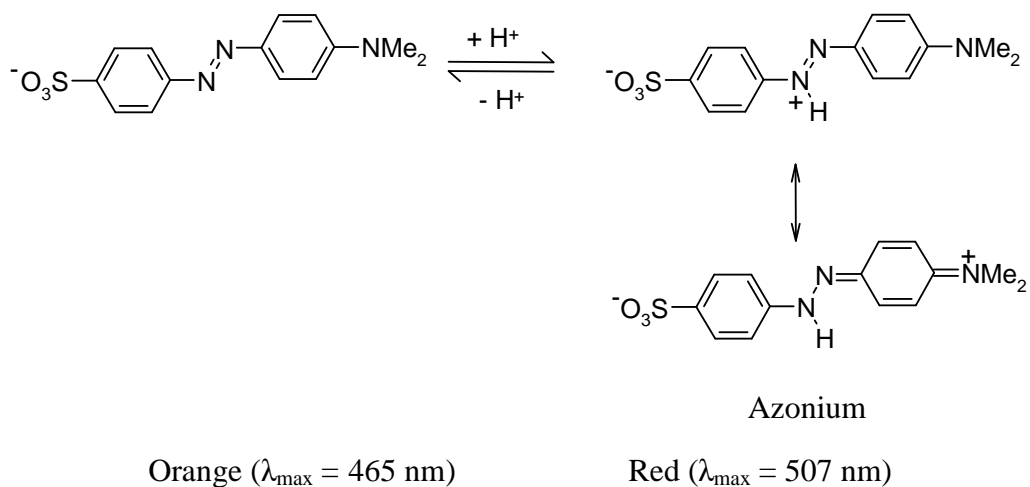


Figure 3.10 Protonation of Methyl Orange.⁶⁴

An amino substituted azobenzene such as 4-*N,N*-dimethylamino-4'-aminoazobenzene is an example of a dye that could also undergo further protonation as well azonium-ammonium tautomerisation, as shown in Figure 3.11.⁷⁷ Mono-protonation changes the π character within the dye, hence changing the spectral characteristics. The band corresponding to the neutral molecule is at 450 nm. The addition of acid results in a band appearing at 620 nm and the band at 450 nm decreasing showing that protonation results in a shift to a longer wavelength assigned to the azonium tautomer.⁷⁷ It was reported that it was not possible from the spectral data to observe the ammonium form, which may not occur or may be due to the overlap of bands with the other neutral forms and azonium form.

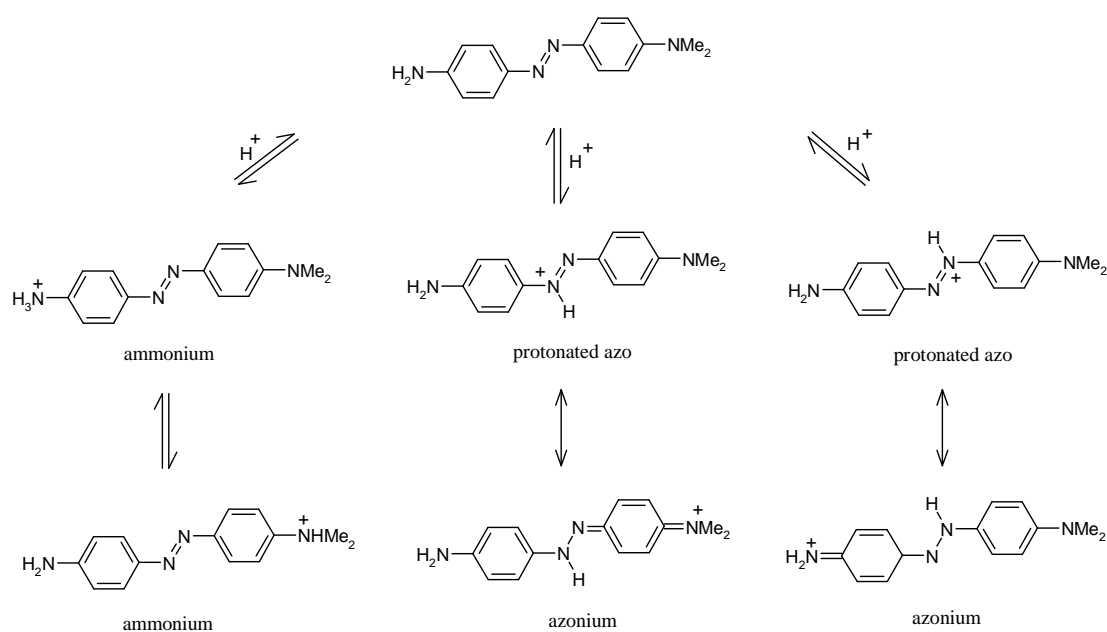


Figure 3.11 Possible protonation sites and tautomerisation of 4-*N,N*-dimethylamino-4'-aminoazobenzene.⁷⁷

3.1.3 Phenylazonaphthalenes

3.1.3.1 Structure

The structures of 1-phenylazonaphthalene (**1**) and 2-phenylazonaphthalene (**2**) are shown in Figure 3.12; as for azobenzene, when phenylazonaphthalenes are named without a prefix the *trans* form is implied in this thesis. **1** and **2** have been studied computationally⁸⁹ and have optimised as a planar *trans* form, with **1** being the more stable than **2** by ca. 7.3 kJ mol⁻¹ at the B3LYP/6-31G* level of theory. The *cis* form was found to be less stable than the *trans* form for both **1** and **2** by ca. 9.3 and 4.9 kJ mol⁻¹, respectively. In both *cis* **1** and **2** it was calculated that the benzene and naphthalene ring are rotated around the C-N bond by approximately 50°.

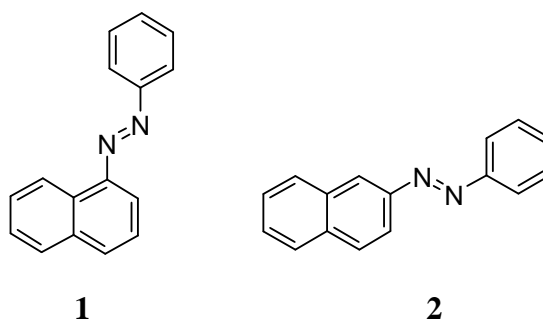


Figure 3.12 Structure of 1-phenylazonaphthalene (**1**) and 2-phenylazonaphthalene (**2**).

Spectral data obtained for a series of 4,4'-substituted 1-phenylazonaphthalenes (Figure 3.13) are shown in Table 3.3.⁹⁰ These data are consistent with those observed for 4,4'-substituted azobenzenes, where an electron-donating group on one aromatic ring and an electron-withdrawing group on a second aromatic ring as is the case where Y = OMe, X = NO₂ causes a significant shift to a longer wavelength for the $\pi \rightarrow \pi^*$ transition.⁹⁰

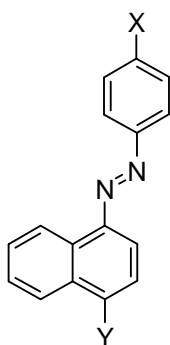


Figure 3.13 Structure of 4,4'-substituted 1-phenylazonaphthalene.

Table 3.3 Spectral data of 4,4'-substituted 1-phenylazonaphthalene.⁹⁰

X	Y	λ_{\max} / nm	ϵ_{\max} / $\text{dm}^3 \text{mol}^{-1} \text{cm}^{-1}$
H	H	375	12900
H	OMe	393	17900
Me	OMe	391	20800
OMe	OMe	393	21700
Cl	OMe	410	21500
NO ₂	OMe	435	20100

Unlike azobenzene the reported studies on the isomerisation of phenylazonaphthalenes are limited,^{63,90-94} however the photoinduced formation of the *cis* isomer and the thermal back reaction to the *trans* form have been identified and the reported studies and will be discussed in more detail in Section 5.

3.1.4 Aims

The aim of the work reported in this chapter was to use a combination of UV/Visible absorption, NMR, Raman and IR spectroscopic techniques, together with DFT calculations, to study the structural properties of the R-Span dyes (Figure 1.13) predominately in water.

The following section presents the results and analysis of these structural studies, along with a discussion in context with the established literature. The chapter concludes with a brief overview and conclusion.

3.2 Results, analysis and discussion

Spectroscopic data have been recorded for all seven R-Span dyes; there is a complete set of data from the “pure dyes” (NH₂-, OH- and NHAc-Span) and a limited set of data from the “impure dyes” (H-, Br-, and CN-Span), some data has also been recorded for OMe-Span. Where data are presented for all R-Span dyes they are given in the order of their *para* substituent Hammett σ_p constants as given in Table 3.4.⁹⁵ In general, data for all dyes are given together in the main body of the report specific to the technique, and additional data or cases where only selected data have been shown in the main body of the report, the additional or complete data sets are given in Appendix 1.

Table 3.4 *Para* substituent Hammett σ_p constants for the R-Span dye series.⁹⁵

Substituent	-NH ₂	-OH	-OMe	-NHAc	-H	-Br	-CN
σ_p	-0.66	-0.37	-0.27	0.00	0.00	+0.23	+0.66

Where possible, comparisons of values from the R-Span dyes have been made with reference to those of H-Span the “unsubstituted” structure, and the differences between them have been obtained by equation 3.2.

$$\Delta(R) = \text{Value}(R) - \text{Value}(H) \quad (3.2)$$

3.2.1 UV/Visible absorption spectroscopy

3.2.1.1 pH dependence

Initial spectroscopic work showed that spectral changes occurred within the pH range of ca. 2 to 12 for OH- and NH₂-Span but not for any of the other dyes.

Figures 3.14 and 3.15 show the UV/Visible absorption spectra of OH- and NH₂-Span over the pH range ca. 2 to 12. The spectra are plotted as $AV/n_{\text{tot}}l$, where A is the absorbance, n_{tot} (mol) is the total number of moles of dye present, V (dm³) is the total volume of solution (which changed slightly upon addition of base) and l (cm) is the pathlength of the cell. Also shown in Figures 3.14 and 3.15 are the fits to equation 3.3 where the pK_a of the dye is determined by analysis of $AV/n_{\text{tot}}l$, with ϵ_{HA} and ϵ_{A^-} the

fitted molar absorption coefficients of protonated and unprotonated dye, respectively; a full derivation of equation 3.3 is explained in Appendix A1.1.

$$\frac{AV}{n_{\text{tot}}l} = \frac{\epsilon_{\text{HA}} 10^{-\text{pH}} + \epsilon_{\text{A}^-} 10^{-\text{pK}_a}}{10^{-\text{pH}} + 10^{-\text{pK}_a}} \quad (3.3)$$

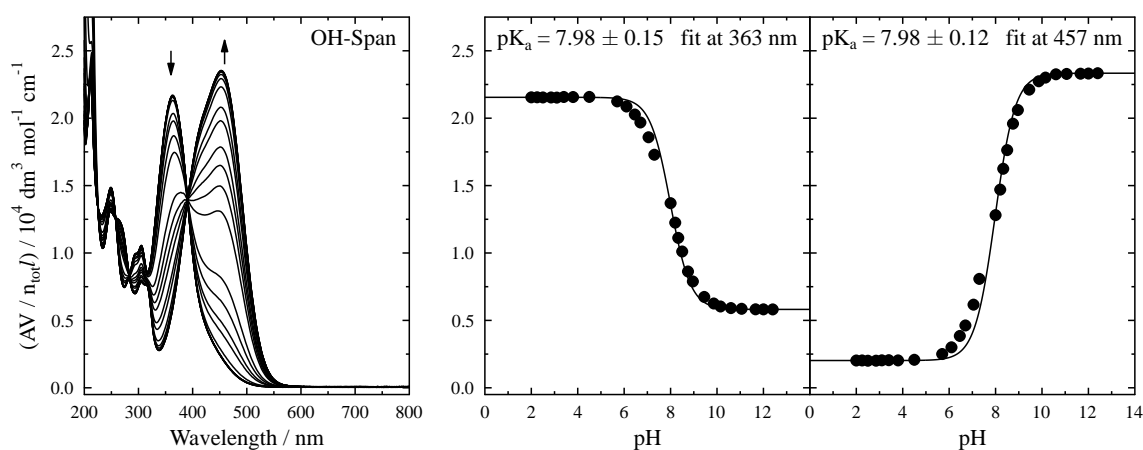


Figure 3.14 Left: UV/Visible absorption spectra of aqueous OH-Span at $5 \times 10^{-5} \text{ mol dm}^{-3}$; the arrows indicate changes with increasing pH over a range of pH ca. 2 to 12. Right: pH curves analysed using equation 3.3 at 363 and 457 nm.

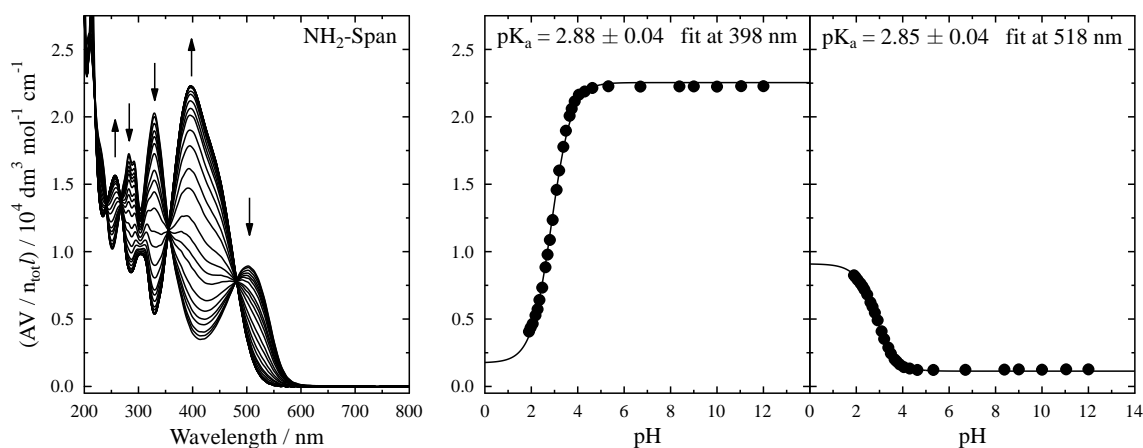


Figure 3.15 Left: UV/Visible absorption spectra of aqueous NH₂-Span at $5 \times 10^{-5} \text{ mol dm}^{-3}$; the arrows indicate changes with increasing pH over a range of pH ca. 2 to 12. Right: pH curves analysed using equation 3.3 at 398 and 518 nm.

Figure 3.16 shows a scheme for the pH dependence of OH-Span with a pK_a of 7.98 derived from the analysis (Figure 3.14) showing that upon the addition of base there is deprotonation of the OH group creating an O^- group ($\sigma_p = -0.81$),⁹⁵ which is accompanied by a colour change of yellow to orange. NH₂-Span shows a pK_a of 2.88 with a colour change of orange to pink upon the addition of acid and the interpretation will be discussed in more detail in section 3.2.5.

This pH dependence enabled OH-Span and NH₂-Span to be studied at pH 5.2 and 7.0, respectively, chosen to be away from their pK_a 's and also allowed for some limited studies to be carried out on deprotonated OH-Span (O^- -Span) and protonated NH₂-Span (P-NH₂-Span) at ca. pH 12.0 and 2.0, respectively.

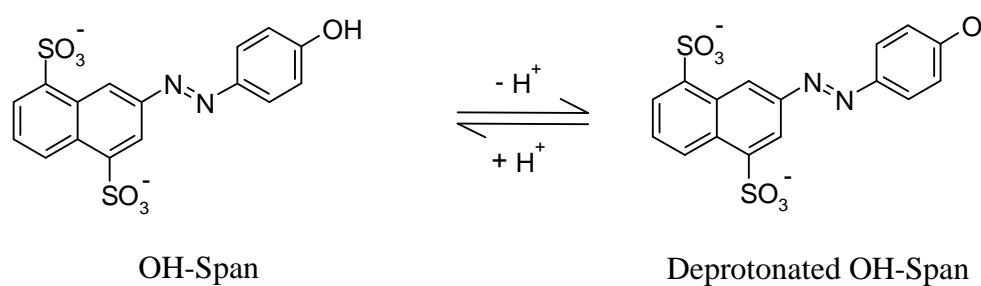


Figure 3.16 Deprotonation of OH-Span.

3.2.1.2 Spectra of all dyes at set pH values

Figure 3.17 shows the UV/Visible absorption spectra of all R-Span dyes in water at $1 \times 10^{-3} \text{ mol dm}^{-3}$ with their longest absorption band position and molar absorption coefficients shown in Table 3.5. The spectrum of OH-Span was recorded in pH 5.2 sodium acetate buffer solution, that of O⁻-Span was recorded by the addition of KOH to an aqueous solution to give pH 12 and P-NH₂-Span was recorded by the addition of H₂SO₄ to an aqueous solution to give pH 1.8.

Band positions were determined from HPLC data for all the impure dyes, where molar absorption coefficients were estimated by using the measured impurity levels in the dye. The HPLC chromatograms for all R-Span dyes are shown in Figure 3.18, with their retention times given in Table 3.6, with their corresponding spectra as pure components given in Figure 3.19 for comparison to the aqueous sample prepared as received.

Excluding H-Span and P-NH₂-Span, all of the other R-Span dyes with differing electron withdrawing and donating properties, have similar colour strengths, with peak molar absorption coefficients in the order of ca. $21000 - 24000 \text{ dm}^3 \text{ mol}^{-1} \text{ cm}^{-1}$; the colour of H-Span is weaker with a peak molar absorption coefficient of $17800 \text{ dm}^3 \text{ mol}^{-1} \text{ cm}^{-1}$; and that of P-NH₂-Span is weaker with a peak molar absorption coefficient of $9000 \text{ dm}^3 \text{ mol}^{-1} \text{ cm}^{-1}$ and will be discussed further in section 3.2.5.

H-Span has a main absorption band position in the UV region at 333 nm, and all the other dyes which have either electron withdrawing or donating groups have their main absorption band at longer wavelength

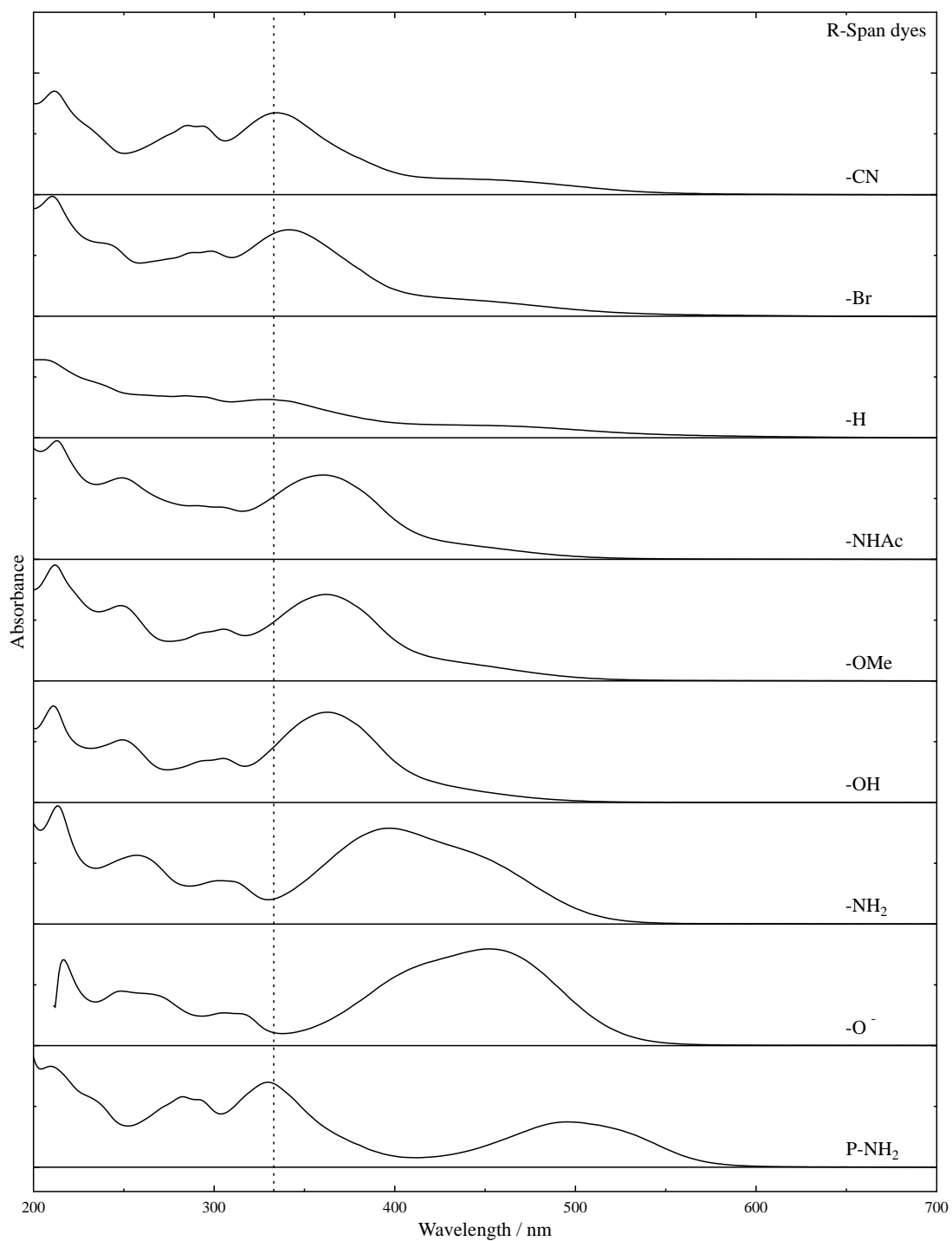


Figure 3.17 UV/Vis absorption spectra of all R-Span dyes in water (1×10^{-3} mol dm $^{-3}$); pH adjusted to 5.2, 12 and 1.2 for -OH, O $^{-}$ and p-NH $_2$, respectively; dashed line gives peak position for H-Span; O $^{-}$ -Span spectrum truncated at 210 nm due to KOH features at short wavelength.

Table 3.5 UV/Visible absorption band positions (λ_{max} / nm) and absorption coefficients ($\epsilon / 10^4 \text{ dm}^3 \text{ mol}^{-1} \text{ cm}^{-1}$) of R-Span dyes in water ($1 \times 10^{-3} \text{ mol dm}^{-3}$).

R =	λ_{max}	ϵ
-CN ¹	337	2.40
-Br ¹	341	2.31
-H ¹	333	1.78
-NHAc	362	2.43
-OMe ¹	363	2.31
-OH	364	2.16
-NH ₂	398	2.24
-O ⁻	452	2.35
-P-NH ₂	504	0.90

1. ϵ values estimated from HPLC data as shown in Figure 3.19.

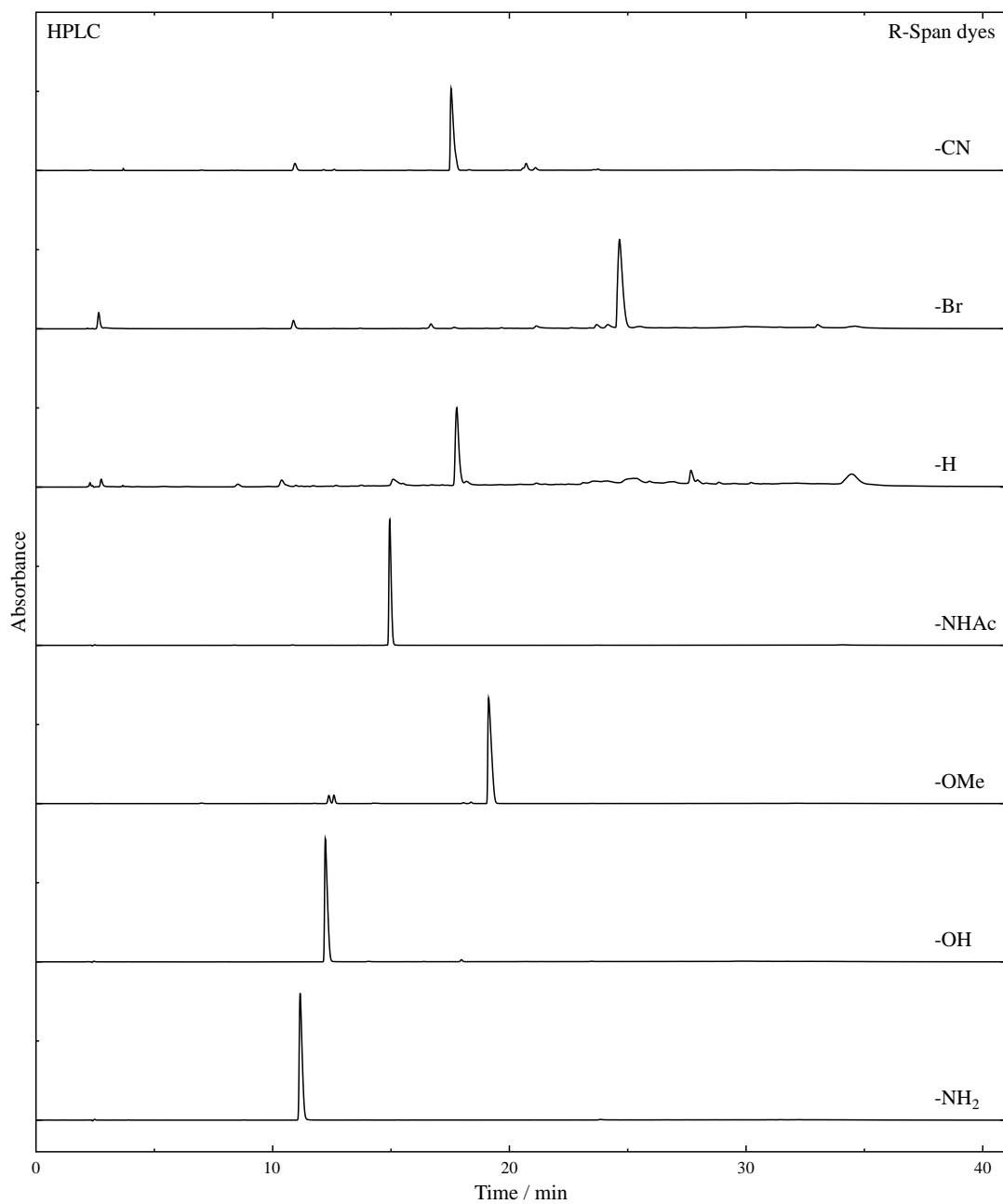


Figure 3.18 HPLC chromatograms of all R-Span dyes recorded at 254 nm.

Table 3.6 Retention times of pure R-Span dye components.

R-Span	-CN	-Br	-H	-NHAc	-OMe	-OH	-NH ₂
RT / min	17.61	24.75	17.78	14.93	17.59	12.12	10.86

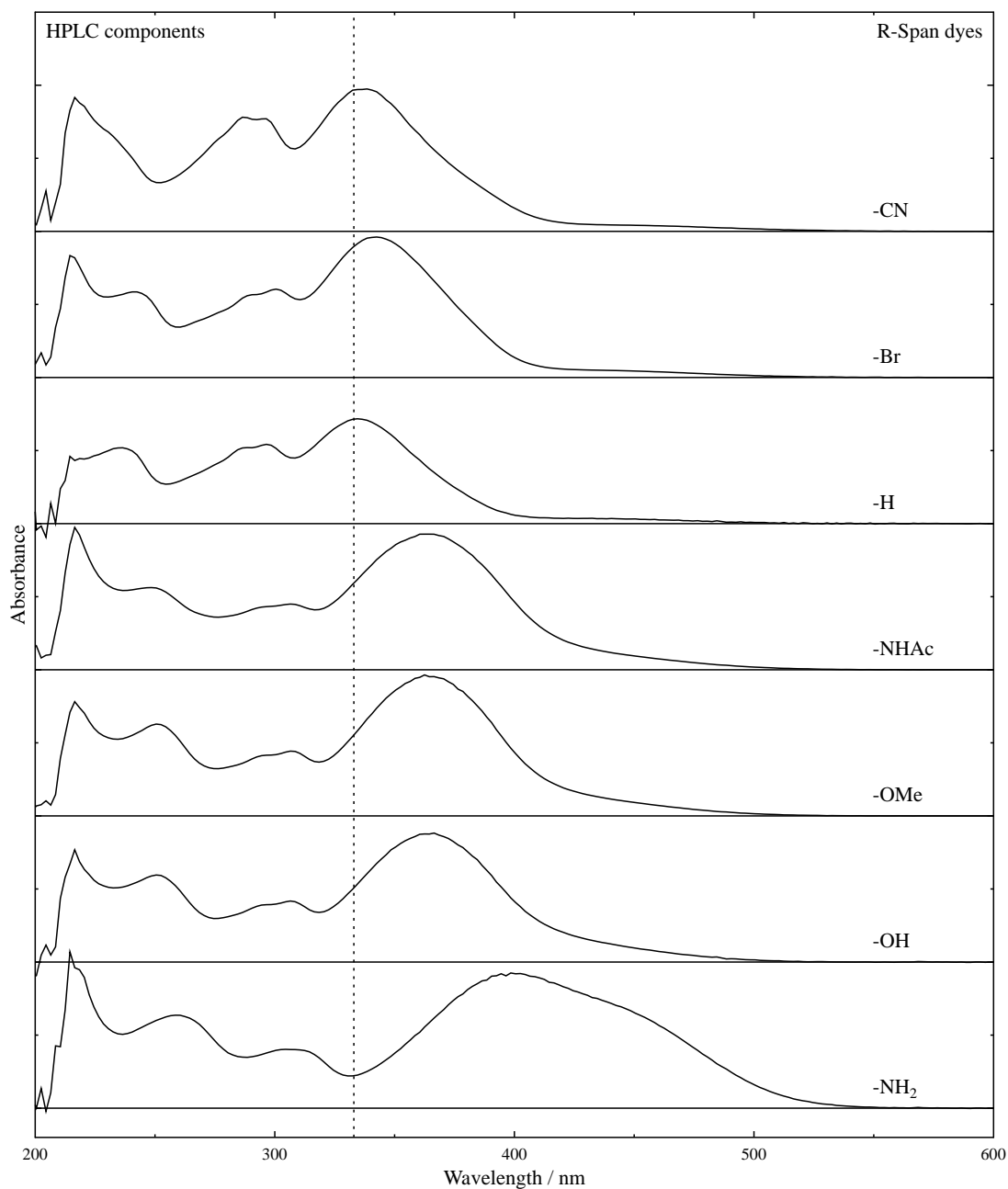


Figure 3.19 UV/Vis absorption spectra of all R-Span dyes as HPLC components in water obtained at retention times given in Table 3.6; dashed line represents peak position for H-Span.

3.2.1.3 Concentration dependence

The UV/Visible absorption spectra of OH-Span at pH 2 and pH 12 recorded in water at concentrations of 3×10^{-2} and $5 \times 10^{-5} \text{ mol dm}^{-3}$ at 298 K are shown in Figure 3.20. The profiles remain unchanged with concentration, indicating that aggregation does not occur at $\leq 3 \times 10^{-2} \text{ mol dm}^{-3}$. A similar result was observed for NH_2 -Span at pH 7 (Figure 3.19). All the other R-Span dyes showed a similar result, with no observed dependence on concentration at $\leq 3 \times 10^{-2} \text{ mol dm}^{-3}$.

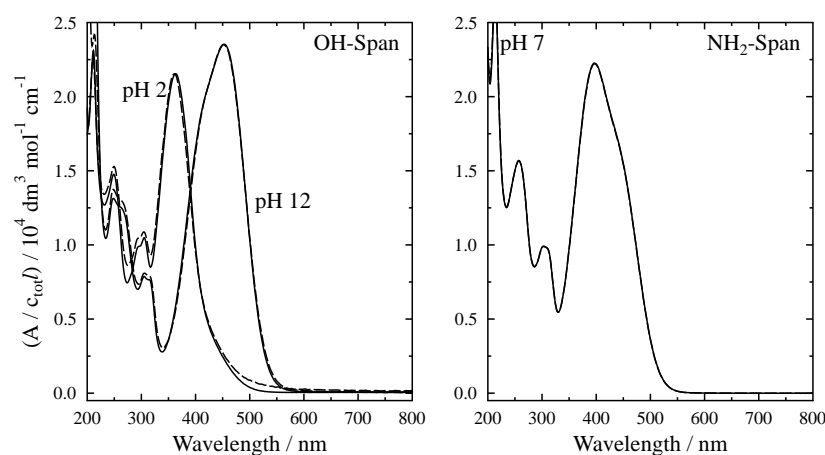


Figure 3.20 Left: UV/Vis absorption spectrum of OH-Span ($---$ 3×10^{-2} and $-$ $5 \times 10^{-5} \text{ mol dm}^{-3}$) in water at pH 2 and 12. Right: UV/Vis absorption spectrum of NH_2 -Span ($---$ 3×10^{-2} and $-$ $5 \times 10^{-5} \text{ mol dm}^{-3}$) in water at pH 7.

3.2.1.4 Solvent dependence

The UV/Visible absorption spectra of OH⁻, O⁻ and NH₂-Span recorded at 5×10^{-5} mol dm⁻³ and 298 K in DMSO, water and ethanol, which have dielectric constants of 48, 78 and 24, respectively,⁹⁶ are shown in Figure 3.21, with band positions and molar absorption coefficients shown in Table 3.7. O⁻-Span was formed in DMSO and ethanol with the addition of KOH until there were no further spectral changes. The changes in band positions are indicative of the solvent effect on each of the dyes. In general, the main band positions of the dyes are similar in water and ethanol, but in DMSO they have shifted to longer wavelength, indicating that this solvent is destabilising the ground state relative to the excited state. The peak molar absorption coefficient of NH₂-Span is larger in DMSO than water and ethanol, with O⁻-Span giving a significantly stronger but narrower band. For comparison, data for NHAc-Span are given in Appendix A1.2.

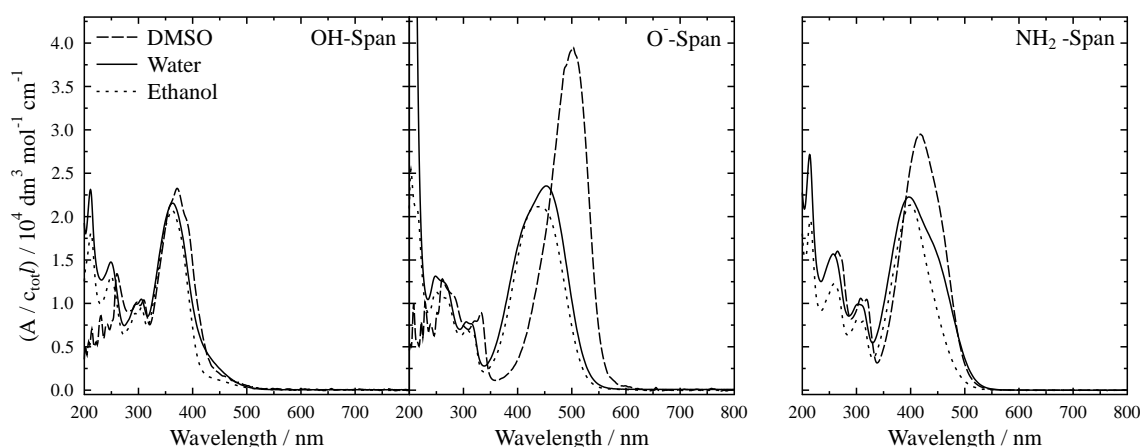


Figure 3.21 UV-visible absorption spectra of OH, O⁻ and NH₂-Span in DMSO, water and ethanol at 5×10^{-5} mol dm⁻³.

Table 3.7 UV-visible absorption band positions (λ_{\max} / nm) and absorption coefficients (ϵ / 10^4 dm³ mol⁻¹ cm⁻¹) of OH⁻, O⁻, NH₂- and NHAc-Span in DMSO, water and ethanol at 5×10^{-5} mol dm⁻³.

Solvent	OH-Span		O ⁻ -Span		NH ₂ -Span		NHAc-Span	
	λ_{\max}	ϵ	λ_{\max}	ϵ	λ_{\max}	ϵ	λ_{\max}	ϵ
DMSO	372	2.31	503	3.95	417	2.94	376	2.33
Water	364	2.16	452	2.11	398	2.24	362	2.43
Ethanol	363	2.08	441	2.35	400	2.13	363	2.54

3.2.2 DFT calculations

DFT calculations were carried out as an aid to interpretation of the experimental data, and the results are used in the following sections for comparison with NMR and vibrational data. The results also give a useful insight into geometry and electronic structure.

All DFT calculations were performed using the B3LYP DFT method with a 6-31G(d) basis set and in this chapter *trans* optimisations are reported; there is a brief consideration of *cis* optimisations in Chapter 5. Optimisations of dyes with the sulfonate groups protonated to mimic solvation in water, have been reported to give a good correlation with experimental data^{15,19,30,31} and therefore this approach was used here. Preliminary solvent field calculations were attempted, but failed to optimise the structure; hence all optimisations are given in the gas phase consistent with previous work on sulfonated dyes.^{19,30}

Excited state properties were calculated using time-dependent DFT with the same level of theory, as reported in the respective parts of this section. The optimised structures of R-Span were used as the basis for further calculations at the same level of theory for vibrational and NMR parameters as reported in sections 3.2.3 and 3.2.4, respectively.

Appendix 4 gives a full list of output files for all optimised structures, electronic structure calculations, NMR calculations and a full file of all the vibrations modes giving their positions, Raman and infrared intensities all of which are contained within a CD accompanying this thesis.

3.2.2.1 Optimised structures

Initially an AM1 semi-empirical optimisation was carried out on *trans*-H-Span from which fully optimised structures for all the R-Span dyes were calculated using DFT. As shown in Figure 3.22 all optimised structures were planar (C-N=N-C dihedral for all R-Span dyes 179.8°). Selected calculated bond lengths and angles of the R-Span dyes together with differences from H-Span (equation 3.2) are shown in Tables 3.8 and 3.9 (a full table can be viewed in Appendix A1.3).

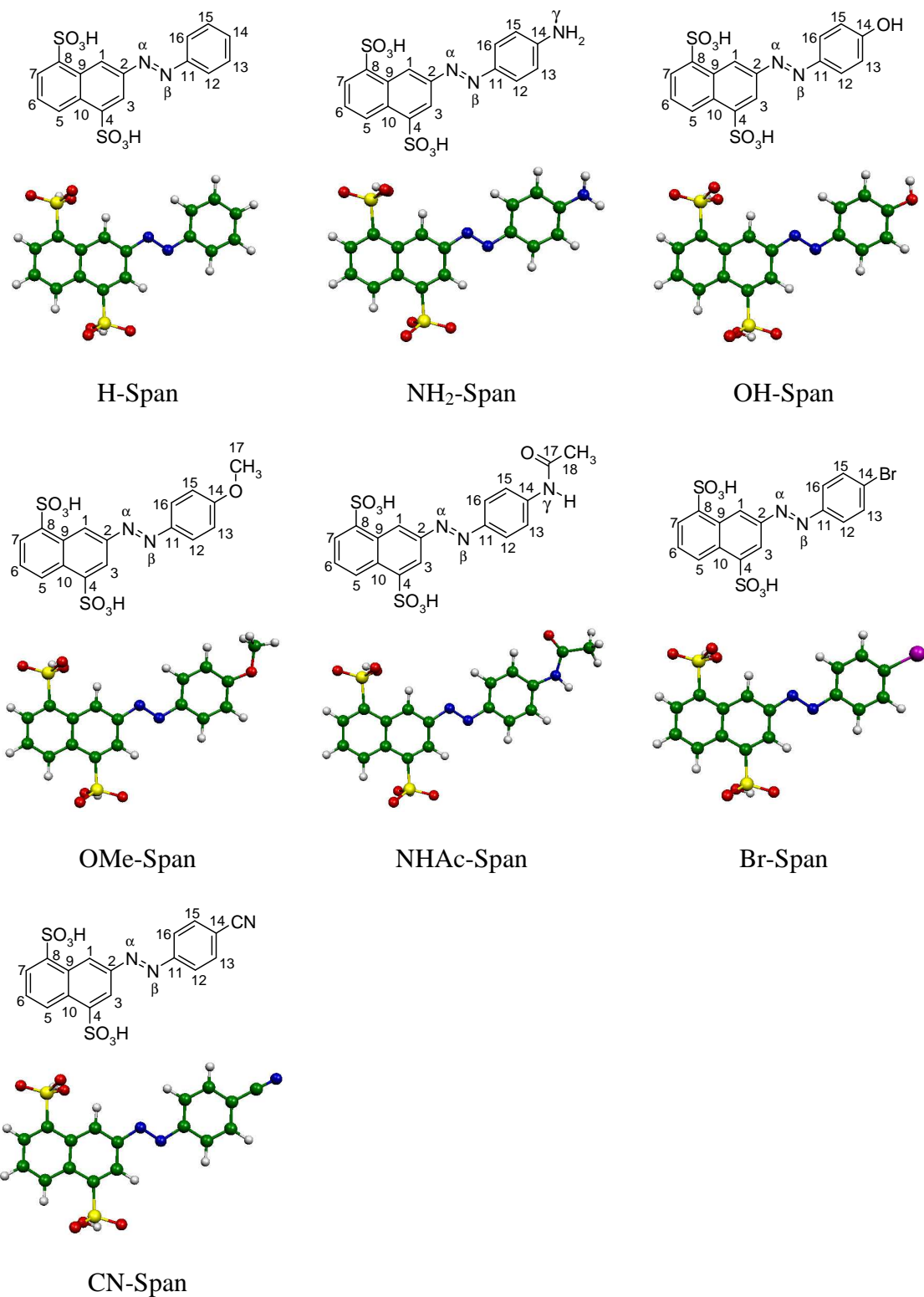


Figure 3.22 Optimised structures of R-Span dyes along with their numbering systems.
(Original in colour)

Table 3.8 Selected bond lengths (Å) of the optimised structures; differences ($\Delta / 0.001 \text{ \AA}$) given for bond lengths from the values of H-Span.

Bond	H-	NH ₂ -	$\Delta(\text{NH}_2)$	OH-	$\Delta(\text{OH})$	OMe-	$\Delta(\text{OMe})$	NHAc-	$\Delta(\text{NHAc})$	Br-	$\Delta(\text{Br})$	CN	$\Delta(\text{CN})$
C2-N α	1.416	1.413	-3	1.414	-2	1.414	-2	1.415	-1	1.415	-1	1.415	-2
N α -N β	1.261	1.268	+7	1.264	+3	1.265	+4	1.264	+3	1.262	0	1.261	0
N β -C11	1.414	1.399	-15	1.405	-9	1.405	-9	1.406	-8	1.413	-1	1.416	+2
C11-C16	1.407	1.411	+4	1.408	+1	1.406	-1	1.407	0	1.407	0	1.407	0
C16-C15	1.389	1.381	-8	1.385	-4	1.388	-1	1.386	-3	1.388	-1	1.386	-3
C15-C14	1.402	1.415	+14	1.407	+5	1.408	+6	1.411	+9	1.400	-2	1.410	+8
C14-C13	1.396	1.409	+13	1.401	+5	1.405	+9	1.407	+11	1.394	-2	1.405	+8
C13-C12	1.393	1.385	-8	1.387	-6	1.384	-9	1.386	-7	1.392	-1	1.390	-4
C12-C11	1.402	1.406	+4	1.405	+3	1.407	+5	1.403	+1	1.402	0	1.402	0
C12-H12	1.086	1.086	0	1.086	0	1.086	0	1.085	-1	1.086	0	1.085	0
C13-H13	1.086	1.087	+1	1.085	-1	1.085	-1	1.088	+2	1.084	-2	1.085	-1
C15-H15	1.087	1.088	+1	1.089	+2	1.084	-3	1.081	-6	1.084	-2	1.085	-1
C16-H16	1.084	1.084	0	1.084	0	1.084	0	1.084	0	1.084	0	1.084	0
C14-H14	1.087	-	-	-	-	-	-	-	-	-	-	-	-
C14-O14	-	-	-	1.360	-	1.356	-	-	-	-	-	-	-
C14-N γ	-	1.381	-	-	-	-	-	1.403	-	-	-	-	-
C14-Br	-	-	-	-	-	-	-	-	-	1.906	-	-	-
C14-C17	-	-	-	-	-	-	-	-	-	-	-	1.433	-

Table 3.9 Bond angles ($^\circ$) of the optimised structures; differences (Δ) given for angle from the values of H-Span.

Angle	H-	NH ₂ -	$\Delta(\text{NH}_2)$	OH-	$\Delta(\text{OH})$	OMe-	$\Delta(\text{OMe})$	NHAc-	$\Delta(\text{NHAc})$	Br-	$\Delta(\text{Br})$	CN	$\Delta(\text{CN})$
C2-N α -N β	114.1	114.0	-0.1	114.1	0.0	114.0	-0.1	113.9	-0.2	114.2	+0.1	114.4	+0.3
N α -N β -C11	115.2	115.6	+0.4	115.4	+0.2	115.5	+0.3	115.4	+0.3	115.0	-0.2	114.7	-0.5
N β -C11-C16	124.7	125.1	+0.4	124.8	+0.1	125.0	+0.3	125.3	+0.6	124.7	0.0	124.6	-0.1
C11-C16-C15	119.4	120.3	+0.9	120.0	+0.6	120.5	+1.0	120.9	+1.4	119.9	+0.5	119.7	+0.3
C16-C15-C14	120.4	120.8	+0.4	120.1	-0.3	119.8	-0.6	119.7	-0.7	119.4	-1.0	120.1	-0.3
C15-C14-C13	120.2	118.8	-1.4	120.3	+0.1	119.9	-0.2	119.5	-0.7	121.4	+1.2	120.1	-0.1
C14-C13-C12	119.8	120.2	+0.4	119.3	-0.4	119.8	+0.1	120.4	+0.6	118.8	-0.9	119.6	-0.2
C13-C12-C11	120.1	121.0	+0.9	120.9	+0.8	120.7	+0.6	120.4	+0.3	120.5	+0.4	120.3	+0.2
C12-C11-C16	120.1	118.9	-1.2	119.4	-0.8	119.2	-0.9	119.1	-1.0	118.5	-1.6	120.1	0.0
C11-C16-H16	119.0	118.8	-0.3	119.0	-0.1	118.8	-0.2	118.8	-0.2	119.1	+0.1	119.1	+0.1
H16-C16-C15	121.5	120.9	-0.6	121.0	-0.5	120.7	-0.9	120.3	-1.2	120.9	-0.6	121.1	-0.4
C16-C15-H15	119.8	120.1	+0.3	120.2	+0.4	119.4	-0.3	121.1	+1.3	120.7	+0.9	120.5	+0.7
H15-C15-C14	119.8	119.2	-0.7	119.7	-0.1	120.7	+0.9	119.2	-0.7	119.9	+0.1	119.4	-0.4
C15-C14-H14	119.8	-	-	-	-	-	-	-	-	-	-	-	-
H14-C14-C13	120.0	-	-	-	-	-	-	-	-	-	-	-	-
C14-C13-H13	120.2	119.6	-0.7	119.0	-1.2	118.6	-1.7	119.8	-0.4	120.3	+0.1	119.8	-0.5
H13-C13-C12	120.0	120.3	+0.3	121.6	+1.6	121.6	+1.6	119.9	-0.1	120.9	+0.9	120.7	+0.7
C13-C12-H12	121.6	120.8	-0.8	120.9	-0.7	121.0	-0.6	121.1	-0.5	120.9	-0.6	121.2	-0.4
H12-C12-C11	118.3	118.2	-0.2	118.2	-0.1	118.3	0.0	118.5	+0.2	118.5	+0.2	118.5	+0.2
C12-C11-N β	115.2	116.0	+0.8	115.8	+0.6	115.8	+0.6	115.6	+0.4	115.4	+0.3	115.3	+0.1
C15-C14-O14	-	-	-	122.4	-	124.4	-	-	-	-	-	-	-
O14-C14-C13	-	-	-	117.4	-	115.6	-	-	-	-	-	-	-
C14-O14-H	-	-	-	109.4	-	-	-	-	-	-	-	-	-
C14-O14-C17	-	-	-	-	-	118.9	-	-	-	-	-	-	-
C15-C14-C17	-	-	-	-	-	-	-	-	-	-	-	119.9	-
C17-C14-C15	-	-	-	-	-	-	-	-	-	-	-	120.0	-
C14-C17-N γ	-	-	-	-	-	-	-	-	-	-	-	179.9	-
C15-C14-Br	-	-	-	-	-	-	-	-	-	119.2	-	-	-
Br-C14-C13	-	-	-	-	-	-	-	-	-	119.4	-	-	-
C15-C14-N γ	-	120.3	-	-	-	-	-	123.2	-	-	-	-	-
N γ -C14-C13	-	120.8	-	-	-	-	-	117.3	-	-	-	-	-
C14-N γ -H	-	117.3	-	-	-	-	-	-	-	-	-	-	-
C14-N γ -H	-	117.3	-	-	-	-	-	-	-	-	-	-	-
H-N γ -H	-	113.6	-	-	-	-	-	-	-	-	-	-	-
C14-N γ -H	-	-	-	-	-	-	-	114.8	-	-	-	-	-
C14-N γ -C17	-	-	-	-	-	-	-	129.2	-	-	-	-	-

The most interesting changes in calculated bond lengths occur at the phenyl ring. In general, the changes are consistent with the nature of the substituent; the influence of electron donating (X) and withdrawing (Y) groups are shown as resonance forms in Figure 3.23. Upon comparison with H-Span; NH₂-, OH-, and CN-Span have longer C11–C16, C15–C14, C14–C13 and C12–C11 bonds, and shorter C16–C15 and C13–C12 bonds, indicating that the phenyl ring is more quinoidal. OMe-Span and NHAc-Span both show the same pattern except for the C11–C16 bond length which remains relatively unchanged. In the case of Br-Span, the bond lengths at the phenyl ring remain relatively unchanged except the C15–C14 and C14–C13 bond become slightly shorter. The C2–N_α and N_β–C11 bond lengths for each R-Span dye become shorter than those of H-Span (except for CN-Span for which N_β–C11 becomes longer), indicating that in each case the phenyl and naphthyl rings are closer to the azo linkage, for which there is an increase in N_α–N_β bond length (except for Br- and CN-Span). The greatest bond length changes occur for NH₂-Span. In general, the resonance model for the electron donating substituents holds across the R-Span series, where the C2–N_α shortens by 0.003 Å, the N_α–N_β lengthens by 0.007 Å C11–N_β shortens by 0.015 Å from H to NH₂-Span, showing an increase in charge transfer character and that the phenyl ring and the azo linkage becomes closer together. The electron withdrawing substituents appear to have a smaller influence on the optimised structures, which are closer to those of H-Span. In general for all R-Span dyes, the optimisation about the naphthyl ring is largely unaffected by the influence of the R substituent.

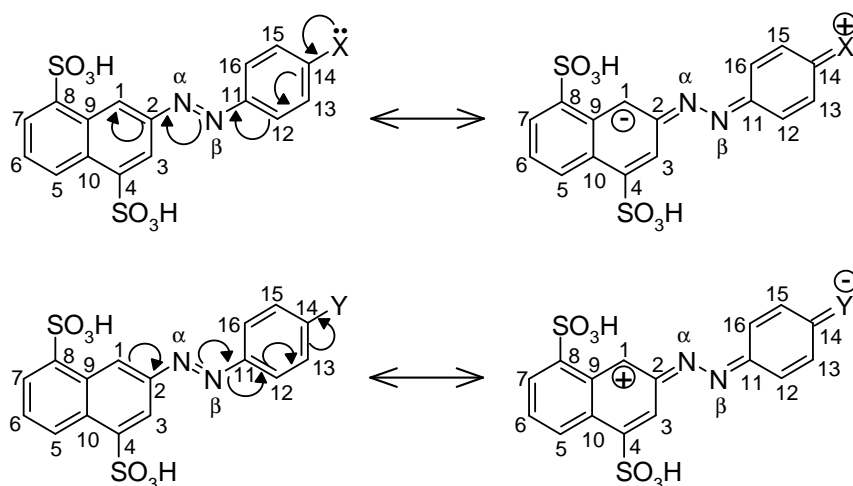


Figure 3.23 Resonance structures of R-Span dyes where X = electron donating substituent and Y = electron withdrawing substituent.

Picking out trends in bond angle changes between the dyes appears to be more difficult. However, upon comparison with H-Span; NH₂, OH, NHAc and CN-Span have smaller H15–C15–C14 and C14–C13–H13 bond angles, indicating that H15 and H13 are closer in orientation to the substituent R group than for H-Span. OMe-Span shows a larger H15–C15–C14 and a smaller C14–C13–H13 bond angle, where the H15 which is adjacent to the OMe group is further away in orientation. In the case of Br-Span, H15–C15–C14 and C14–C13–H13 have smaller bond angles, indicating that H15 and H13 are further away in orientation to Br than H14 for H-Span.

For NH₂-Span the use of the bond angles can give a further indicator as to the nature of the bonding in terms of the resonance forms (Figure 3.23). The bond angles of C14–N_γ–H and H–N_γ–H are 117.3 ° and 113.6 °, respectively, indicating that the structure is tending towards a sp² hybridised model as a result of the conjugation across the molecule. The structure of NH₂-Span is not totally planar at the NH₂ group however, the nitrogen is bent out of plane by 2.3 ° and the hydrogens are bent out of plane by 20 ° in the opposite direction as shown in an expansion about the phenyl ring in Figure 3.24.

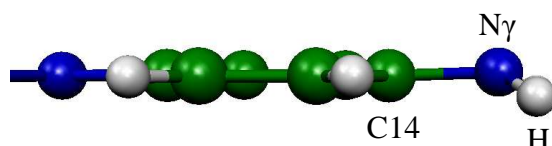


Figure 3.24 Expansion of phenyl ring of NH₂-Span. (*Original in colour*)

NHAc-Span appears capable of intramolecular hydrogen bonding between C17=O---H15, with a calculated O---H15 distance of 2.20 Å which is shorter than the sum of the van der Waals radii for O-H of 2.47 Å, and the C15-H15---O bond angle is ca. 120°, hence trigonal. There are examples of azo dyes that have strong intramolecular hydrogen bonds with their structure reported to be ca. 1.2 – 1.6 Å.⁹⁷ The bond length suggests that the intramolecular hydrogen bonding at the R substituent is relatively weak for NHAc-Span.

3.2.2.2 Electronic structure

The results of electronic structure calculations on H-Span, OH-Span and CN-Span are shown in the main body of the report so as to compare an electron withdrawing and on electron donating group to the unsubstituted dye. These results for all R-Span dyes including calculated dipole moments are given in Appendix A1.3.

The calculated HOMO-1, HOMO, LUMO and LUMO+1 for H-Span, OH-Span and CN-Span are shown in Figure 3.25, where the HOMO-1 can be described as having some non bonding character including the N atom lone pairs, the HOMO as having some π bonding including the azo linkage and the LUMO and LUMO+1 as having some π^* antibonding character.

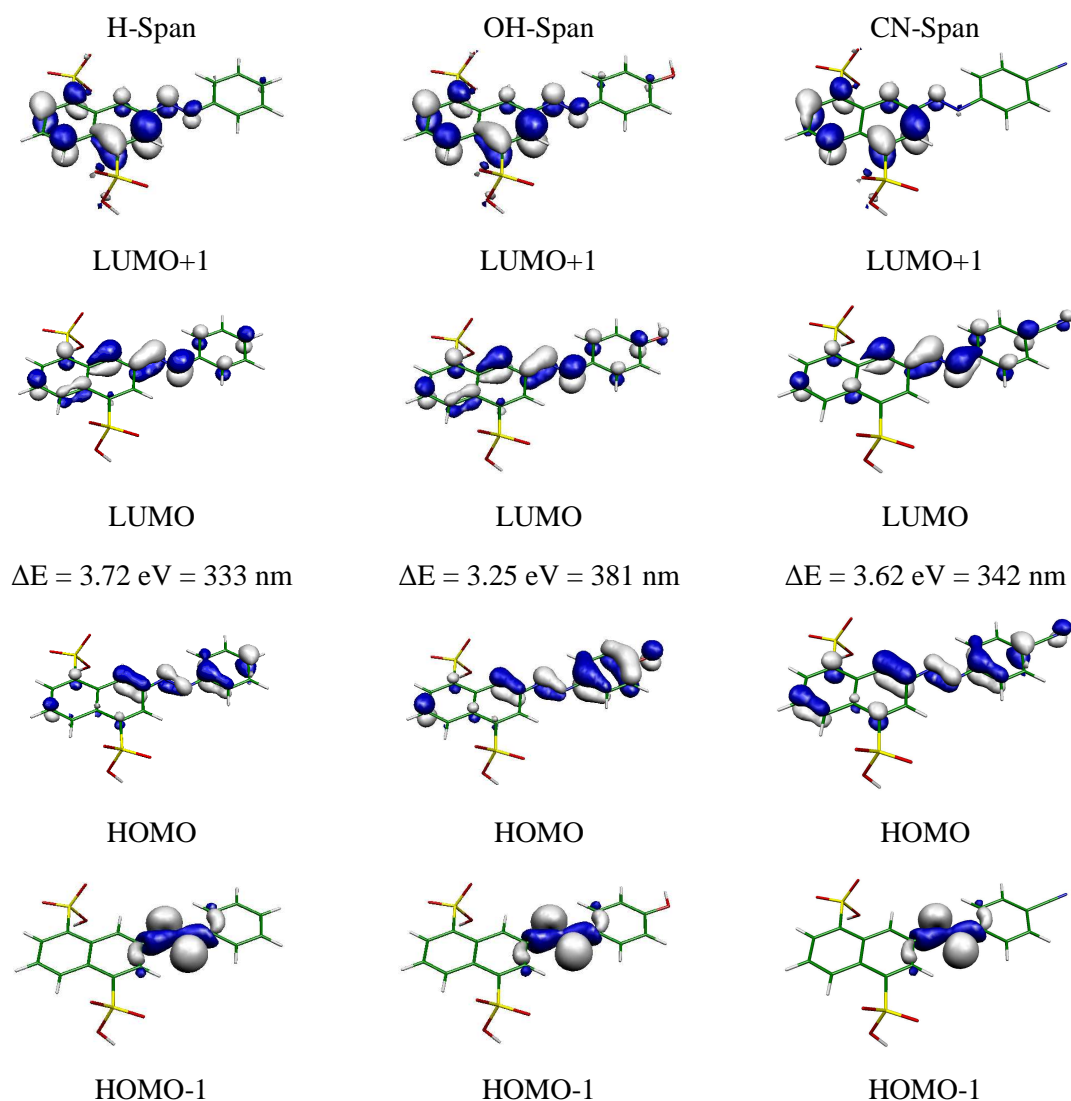


Figure 3.25 Calculated HOMO-1, HOMO, LUMO, LUMO+1 and energy difference (LUMO-HOMO) for H-Span, OH-Span and CN-Span. (*Original in colour*)

Time-dependent DFT methods also offer a way of representing changes of electron density upon excitation, which often include a combination of orbital transitions. The calculated changes in electron density on excitation to the first and second excited states of H-Span, OH-Span and CN-Span are shown in Figure 3.26. Calculated orbital contributions, transition energies, wavelengths, and oscillator strengths for the first and second excited states are given in Table 3.10 (a full table can be found in Appendix A1.3). The oscillator strengths indicate that the transition to the first excited state is disallowed and the orbitals shows it is an $n \rightarrow \pi^*$ type transition, whereas the transition to the second excited state is allowed and is a $\pi \rightarrow \pi^*$ type transition. In all cases the $n \rightarrow \pi^*$ transition is unaffected by the R substituent on the phenyl ring. For the $\pi \rightarrow \pi^*$ transition however, the changes of electron density that occur with the transition reflect the donating and withdrawing nature of the R substituent. For H-Span, there is a decrease of electron density at the phenyl and naphthyl rings and an increase in electron density at the azo group. For OH-Span, the donating nature of the -OH substituent is reflected by a decrease in electron density at the phenyl ring and increase in electron density at the azo linkage and naphthyl ring. For CN-Span, the withdrawing nature is reflected by a decrease in electron density at the naphthyl ring and an increase in electron density at the azo linkage.

Interestingly, as shown in Table 3.11, the experimental data show a comparable trend to those of the calculated UV/Visible band positions with a clearer match for the simple HOMO to LUMO transitions rather than those determined from the time-dependent DFT excited states.

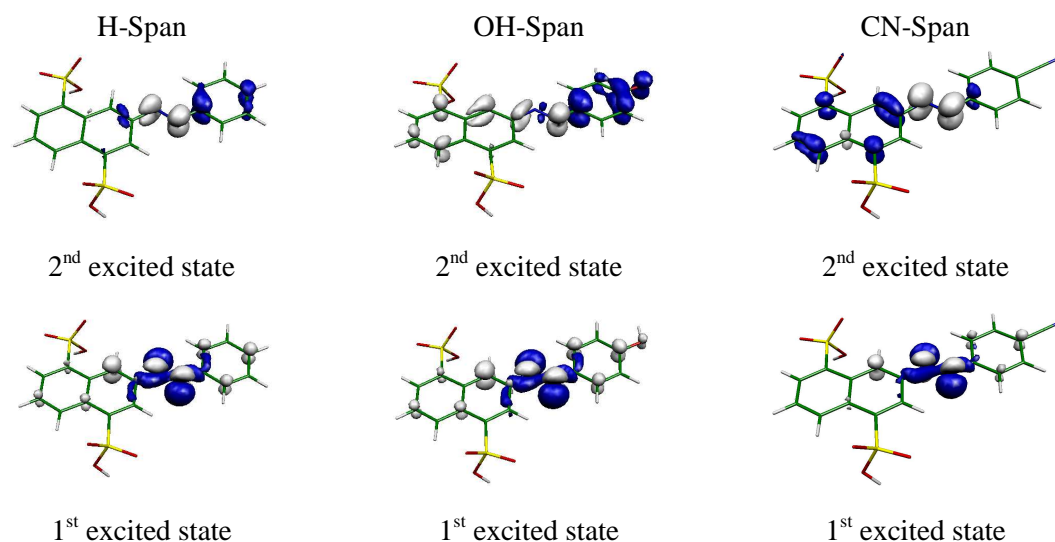


Figure 3.26 Calculated changes in electron density on excitation to the first (bottom) and second (top) excited states for H-Span (left) and OH-Span (middle) and CN-Span (right). Blue and white regions represent a decrease and increase in electron density on excitation, respectively. (*Original in colour*)

Table 3.10 Calculated orbital contributions, transition energies (E), wavelengths (λ), and oscillator strengths (f) for the first and second excited state of H-Span, OH-Span and CN-Span.

Excited state	Orbital contribution	E / eV	λ / nm	f
H-Span				
1 st	HOMO-1 \rightarrow LUMO	2.51	495	0.0001
	HOMO-1 \rightarrow LUMO+1			
	HOMO \rightarrow LUMO			
2 nd	HOMO-1 \rightarrow LUMO	3.51	353	0.8963
	HOMO \rightarrow LUMO			
OH-Span				
1 st	HOMO-1 \rightarrow LUMO+1	2.56	484	0.0001
	HOMO-1 \rightarrow LUMO			
2 nd	HOMO \rightarrow LUMO	3.27	379	0.8843
CN-Span				
1 st	HOMO-1 \rightarrow LUMO	2.45	506	0.0001
2 nd	HOMO-2 \rightarrow LUMO	3.38	366	0.9553
	HOMO \rightarrow LUMO			

Table 3.11 Comparison of experimental band positions (λ / nm) to calculated HOMO to LUMO transition wavelengths (λ / nm) and second excited state transition wavelengths (λ /nm) for all R-Span dyes.

R-Span	NH ₂ -	OH-	OMe-	NHAc-	H-	Br-	CN-
Experimental	398	364	363	362	333	341	337
HOMO to LUMO	389	382	365	355	333	347	342
2 nd Excited state	407	379	388	392	353	371	366

3.2.2.3 Atomic charges

The calculated Mulliken atomic charges (q) on each atom for the R-Span dyes are shown in Table 3.12, using the same numbering system as established in Figure 3.23. Table 3.12 also shows the differences in atomic charge on each atom from H-Span (equation 3.2), where a positive change represents a decrease in electron density.

A pictorial representation of the charge on each atom is shown in Figure 3.27, where red and blue regions represent positive and negative charge, respectively. There are significant differences between the charge distribution across the azo linkage and the phenyl ring as a result of the different substituents across the R-Span series. There is a significant charge across the protonated sulfonate groups, however these sit very much as spectators within the overall charge distribution.

The influence of electron donating (X) and electron withdrawing (Y) groups can once again be interpreted in terms of resonance forms (Figure 3.23). Upon comparison with H-Span, the most significant change of atomic charge is that of C14; for H-Span this is negatively charged, whereas for all other R-Span dyes this atom is positively charged. There is no particular trend but the magnitude of electron density on C14 is comparable at ca. 0.4 q for all the R-Span dyes with electron donating groups (NH₂, OH, OMe and NHAc), and at ca. 0.2 q for the R-Span dyes with electron withdrawing groups (Br and CN). The magnitude of change in atomic charge is smaller for all other atoms. For C13 and C15 there is an increase in electron density in all R-Span dyes when compared to H-Span. Again there is no particular trend for those containing electron donating groups, in the case of those containing electron withdrawing groups there is a smaller increase in electron density for the more electron withdrawing CN group. Interestingly CN-Span exhibits the most significant decrease in electron density on C11, possibly as a

result of the greater electron withdrawing effect of CN. For all the R-Span dyes, N_α and N_β carry negative charge. N_α shows a constant trend across the dye series, where the electron density increases with an increasingly electron donating substituent ($NH_2 > OH > OMe > NHAc$) and decreases with an increasingly electron withdrawing substituent. N_β on the other hand shows no particular trend, and there is an increase in electron density regardless of substituent.

Table 3.12 Calculated Mulliken atomic charges (q) from the optimised structures; differences ($\Delta / 0.001 q$) given from the values of H-Span.

atom	H-	NH ₂ -	$\Delta H(NH_2)$	OH-	$\Delta H(OH)$	OMe-	$\Delta H(OMe)$	NHAc-	$\Delta H(NHAc)$	Br-	$\Delta H(Br)$	CN-	$\Delta H(CN)$
C1	-0.218	-0.224	-6	-0.221	-3	-0.222	-4	-0.220	-2	-0.218	0	-0.214	+4
C2	0.289	0.294	+5	0.292	+3	0.292	+3	0.291	+2	0.289	0	0.289	0
C3	-0.160	-0.163	-3	-0.161	-1	-0.161	-1	-0.160	0	-0.160	0	-0.158	+2
C4	-0.252	-0.253	-1	-0.252	0	-0.252	0	-0.252	0	-0.252	0	-0.251	+1
C5	-0.183	-0.184	-1	-0.183	0	-0.184	-1	-0.184	-1	-0.183	0	-0.183	0
C6	-0.131	-0.134	-3	-0.133	-2	-0.133	-2	-0.133	-2	-0.131	0	-0.130	+1
C7	-0.159	-0.160	-1	-0.160	-1	-0.159	0	-0.159	0	-0.160	-1	-0.160	-1
C8	-0.241	-0.243	-3	-0.242	-1	-0.242	-2	-0.241	0	-0.240	+1	-0.238	+3
C9	0.139	0.141	+2	0.140	+1	0.140	+1	0.140	+1	0.139	0	0.138	-1
C10	0.150	0.147	-3	0.149	-1	0.149	-1	0.149	-1	0.150	0	0.151	0
C11	0.266	0.265	-1	0.266	0	0.268	+2	0.278	+12	0.272	+6	0.284	+18
C12	-0.136	-0.141	-5	-0.141	-5	-0.139	-3	-0.141	-5	-0.136	0	-0.144	-8
C13	-0.139	-0.186	-47	-0.169	-30	-0.182	-43	-0.207	-68	-0.158	-19	-0.145	-6
C14	-0.114	0.349	+463	0.369	+483	0.393	+507	0.375	+489	0.093	+207	0.142	+256
C15	-0.147	-0.189	-43	-0.209	-63	-0.209	-63	-0.177	-31	-0.164	-18	-0.153	-6
C16	-0.120	-0.126	-6	-0.123	-3	-0.128	-8	-0.138	-18	-0.117	+3	-0.125	-5
H1	0.204	0.199	-5	0.201	-3	0.201	-3	0.203	-1	0.205	+1	0.207	+3
H3	0.212	0.209	-3	0.210	-2	0.210	-2	0.210	-2	0.212	0	0.213	+1
H5	0.200	0.197	-3	0.198	-2	0.198	-2	0.198	-2	0.200	0	0.201	+1
H6	0.160	0.156	-4	0.158	-2	0.158	-2	0.158	-2	0.161	+1	0.163	+3
H7	0.195	0.193	-2	0.194	-1	0.194	-1	0.194	-1	0.196	+1	0.198	+3
H12	0.151	0.150	-1	0.154	+3	0.152	+1	0.152	+1	0.160	+9	0.164	+13
H13	0.142	0.129	-13	0.153	+11	0.150	+8	0.131	-11	0.164	+22	0.169	+27
H15	0.143	0.132	-11	0.134	-9	0.144	+1	0.199	+54	0.165	+22	0.170	+26
H16	0.165	0.166	+1	0.170	+4	0.168	+3	0.170	+5	0.174	+9	0.177	+11
N α	-0.307	-0.328	-21	-0.320	-13	-0.319	-13	-0.314	-7	-0.308	-1	-0.300	+6
N β	-0.301	-0.312	-10	-0.307	-6	-0.308	-7	-0.312	-10	-0.303	-2	-0.304	-3
S4	1.260	1.257	-2	1.258	-1	1.258	-1	1.259	-1	1.257	-2	1.258	-2
S8	1.257	1.255	-2	1.256	-1	1.256	-1	1.255	-1	1.260	+3	1.261	+4
O4	-0.519	-0.521	-3	-0.520	-1	-0.520	-2	-0.520	-2	-0.518	+1	-0.516	+3
O4	-0.503	-0.504	-1	-0.504	-1	-0.504	-1	-0.502	+1	-0.504	-1	-0.509	-6
O4	-0.653	-0.653	0	-0.654	0	-0.654	0	-0.654	0	-0.655	-1	-0.652	+2
O8	-0.505	-0.508	-2	-0.506	-1	-0.506	-1	-0.506	-1	-0.518	-13	-0.508	-3
O8	-0.513	-0.515	-2	-0.514	-1	-0.514	-1	-0.515	2	-0.503	10	-0.512	+1
O8	-0.655	-0.655	0	-0.655	0	-0.655	0	-0.655	0	-0.654	+1	-0.652	+3
H14	0.141	-	-	-	-	-	-	-	-	-	-	-	-
O14	-	-	-	-0.628	-	-0.497	-	-	-	-	-	-	-
N γ	-	-0.791	-	-	-	-	-	-0.710	-	-	-	-0.469	-
H γ a	-	0.335	-	0.415	-	-	-	0.334	-	-	-	-	-
H18a	-	-	-	-	-	-	-	0.198	-	-	-	-	-
H γ b	-	0.334	-	-	-	-	-	-	-	-	-	-	-
H18b	-	-	-	-	-	-	-	0.153	-	-	-	-	-
H18c	-	-	-	-	-	-	-	0.193	-	-	-	-	-
O17	-	-	-	-	-	-	-	-0.476	-	-	-	-	-
C18	-	-	-	-	-	-	-	-0.546	-	-	-	0.243	-
C17	-	-	-	-	-	-0.222	-	0.602	-	-	-	-	-
H17a	-	-	-	-	-	0.178	-	-	-	-	-	-	-
H17b	-	-	-	-	-	0.160	-	-	-	-	-	-	-
H17c	-	-	-	-	-	0.161	-	-	-	-	-	-	-
Br	-	-	-	-	-	-	-	-	-	-0.109	-	-	-

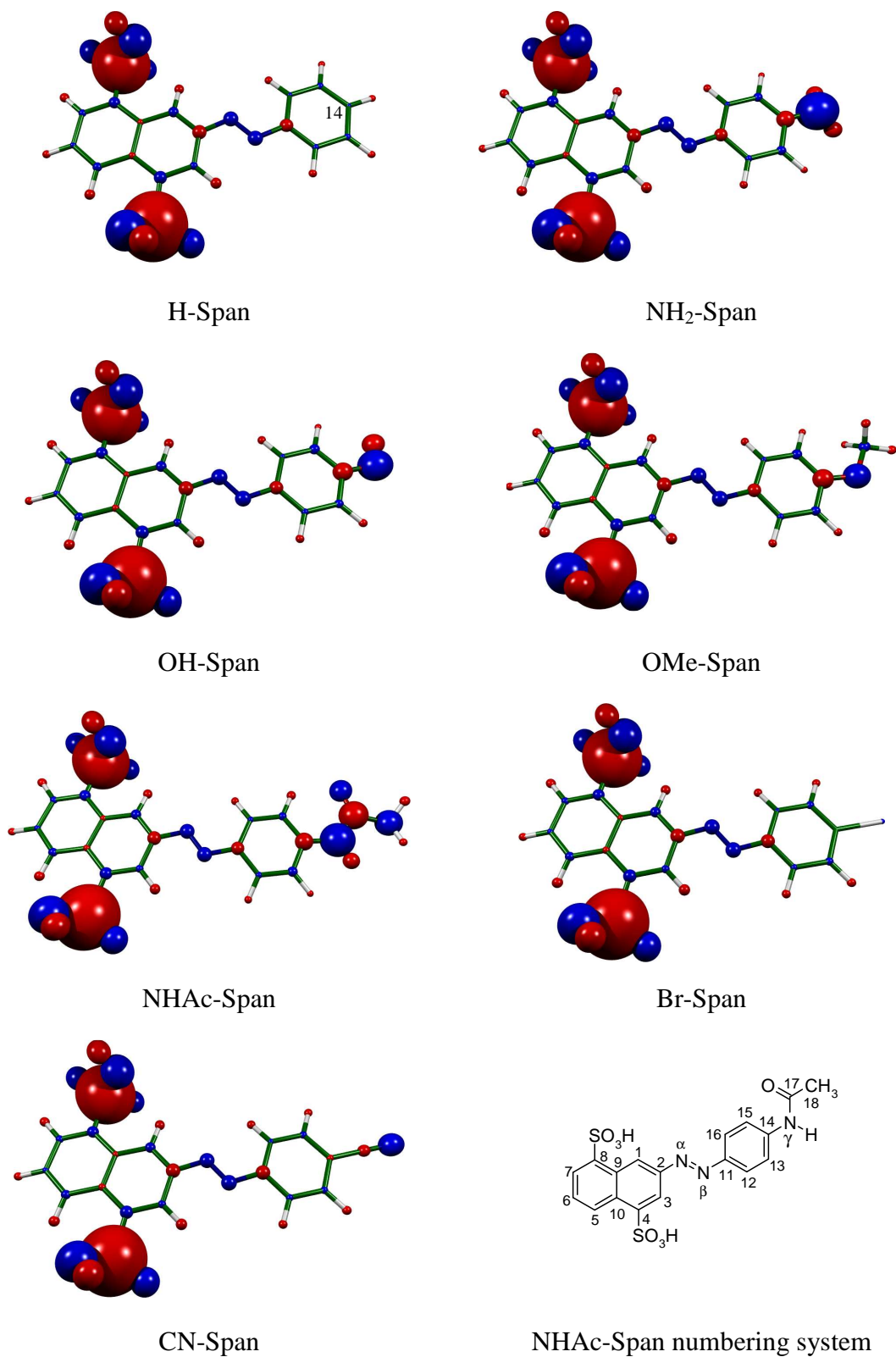


Figure 3.27 Pictorial representation of calculated Mulliken atomic charges of all R-Span dyes; red regions represent positive charge; blue regions represent negative charge; 1 Å radius per unit charge; position 14 shown for H-Span common for all dyes and NHAc-Span numbering system shown. (*Original in colour*)

3.2.3 NMR spectroscopy

1D and 2D (COSY, NOESY, HSQC and HMBC) ^1H and ^{13}C NMR spectra of the pure R-Span dyes were recorded in DMSO- d_6 and D_2O (both at ca. $3 \times 10^{-2} \text{ mol dm}^{-3}$), with spectra recorded for the impure R-Span dyes recorded in D_2O but not DMSO- d_6 due to insufficient sample quantity. ^1H NMR assignments were made using integration, multiplicity and splittings and by COSY and NOESY interactions. ^{13}C NMR assignments were made using HSQC and HMBC data and results from DFT calculations. Positions of the ^1H and ^{13}C NMR resonances are sensitive to the solvent and protons attached to oxygen and nitrogen are exchanged in D_2O .

NH_2 -Span is in one form at ca. pD 7 for D_2O , hence its NMR spectra are reported firstly in section 3.2.3.1. The NMR spectra of OH-Span and corresponding pH dependence on its structure are reported in section 3.2.3.2. Finally all the NMR spectra are reported together for comparison in section 3.2.3.3, where full spectra and assignments are shown in Appendix A1.4 for all other R-Span dyes, where assignments made are consistent with those reported for a similar dye where $\text{R} = \text{NHMe}$.³³

3.2.3.1 NH_2 -Span

^1H and ^{13}C NMR spectra of NH_2 -Span recorded in DMSO- d_6 and D_2O , numbering system and COSY and NOESY interactions are shown in Figures 3.28–3.31 with NMR assignments given in Table 3.13. ^{13}C NMR assignments were made using HSQC and HMBC data as shown in Appendix A1.4 and results from DFT calculations given in Tables 3.13. The solvent dependence in the NMR spectra, suggests that hydrogen bonding may be occurring with water molecules.

Page intentionally left blank

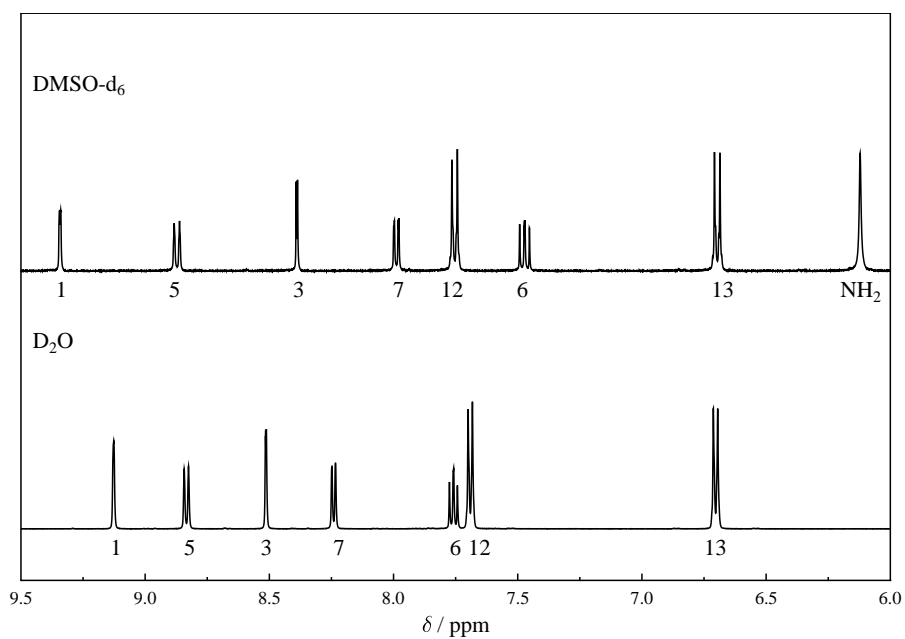


Figure 3.28 Aromatic region ¹H NMR spectrum of NH₂-Span in DMSO-d₆ (top) and D₂O (bottom).

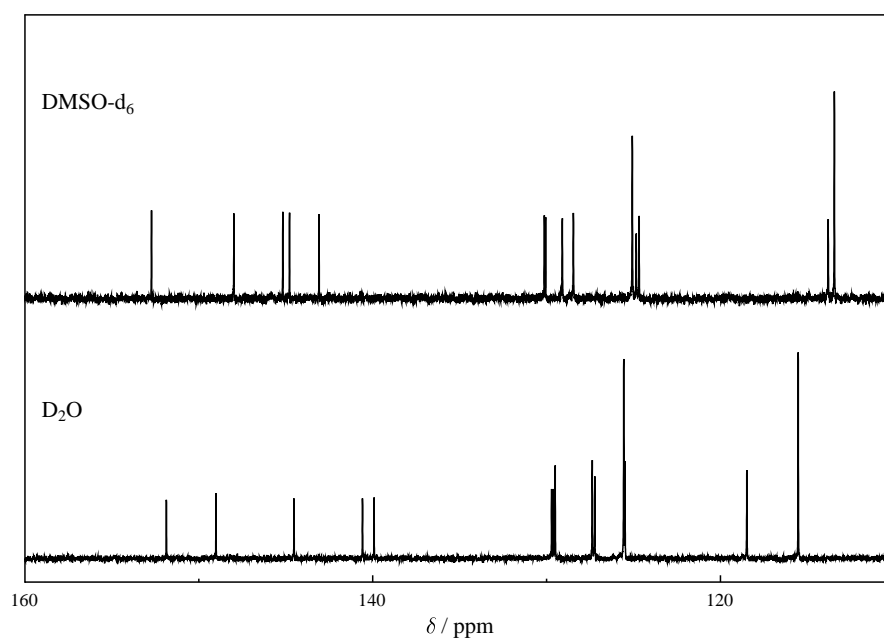


Figure 3.29 ¹³C NMR spectrum of NH₂-Span in DMSO-d₆ (top) and D₂O (bottom).

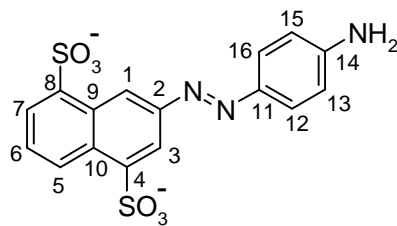


Figure 3.30 Structure of NH₂-Span with the numbering system used for NMR assignments.

Table 3.13 ¹H and ¹³C NMR chemical shifts (ppm) of NH₂-Span in DMSO-d₆ and D₂O, along with calculated values.

Atom	Experimental				Calculated			
	DMSO		D ₂ O		¹ H	¹³ C		
	¹ H ^a	¹³ C	¹ H ^a	¹³ C				
1	9.34	1 d 1.0	128.5	9.09	1 s -	125.4	9.18	128.8
2			148.0			149.0		143.4
3	8.39	1 d 2.0	119.0	8.47	1 d 2.0	118.4	8.58	112.0
4			144.8			140.6		136.6
5	8.87	1 d 9.0	129.1	8.79	1 d 9.0	129.5	8.74	126.9
6	7.47	1 t 8.0	124.8	7.72	1 t 8.0	127.2	7.52	119.2
7	7.99	1 d 7.0	124.7	8.20	1 d 8.0	127.3	7.98	122.2
8			145.2			139.9		135.8
9			130.1			129.7		124.5
10			130.1			129.6		123.3
11			152.7			151.9		138.4
12/16	7.75	2 d 9.0	125.1	7.65	2 d 9.0	125.5	8.02 ¹² , 7.92 ¹⁶	131.8 ¹² , 111.5 ¹⁶
13/15	6.69	2 d 9.0	113.4	6.66	2 d 9.0	115.5	6.42 ¹³ , 6.31 ¹⁵	106.4 ¹³ , 107.7 ¹⁵
14			152.7			144.5		142.5
NH ₂	6.09	2 s -					3.04, 3.10	

^a Integration, multiplicity (s = singlet; d = doublet; t = triplet), splitting (Hz)

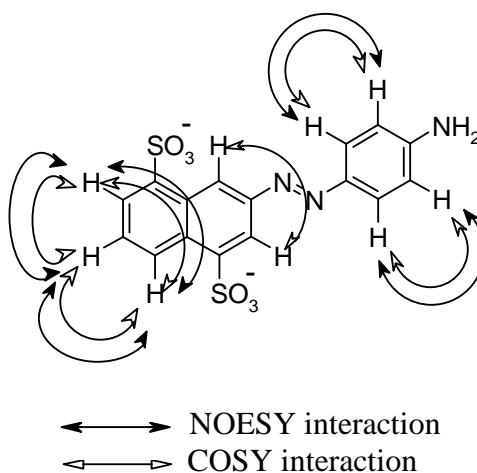


Figure 3.31 COSY and NOESY interactions for NH₂-Span in DMSO-d₆ and D₂O.

3.2.3.2 OH-Span

Due to the pH dependence of the substituent OH group in OH-Span, an NMR sample unadjusted for pD gives a solution in which there is equilibrium between OH-Span and O⁻-Span. ¹H NMR spectra were recorded from samples of OH-Span in deuterated sodium acetate buffer at pD 5.2 (assigned to OH-Span), unadjusted D₂O solution, and in deuterated sodium hydroxide adjusted to pD 12 (assigned to O⁻-Span) as shown in Figure 3.32. The numbering system is shown in Figure 3.33 with NMR peak positions and a comparison to the pure OH-Span form as calculated using equation 3.4, where a negative change represents an upfield shift given in Table 3.14. Upon going from OH-Span to O⁻-Span there is an upfield shift of the resonances from all protons in the order of 13/15 >> 1 > 12/16 = 6 > 3 > 5 = 7 indicating the influence that deprotonation has on the spectra.

$$\Delta\text{-OH}(\delta) = \delta(\text{R}) - \delta(\text{OH}) \quad (3.4)$$

NMR spectroscopy suggests that the unadjusted mixture contains ca. 60 % OH-Span form which is comparable with ca. 70 % OH-Span obtained from UV/visible spectroscopy, despite being recorded under different conditions.

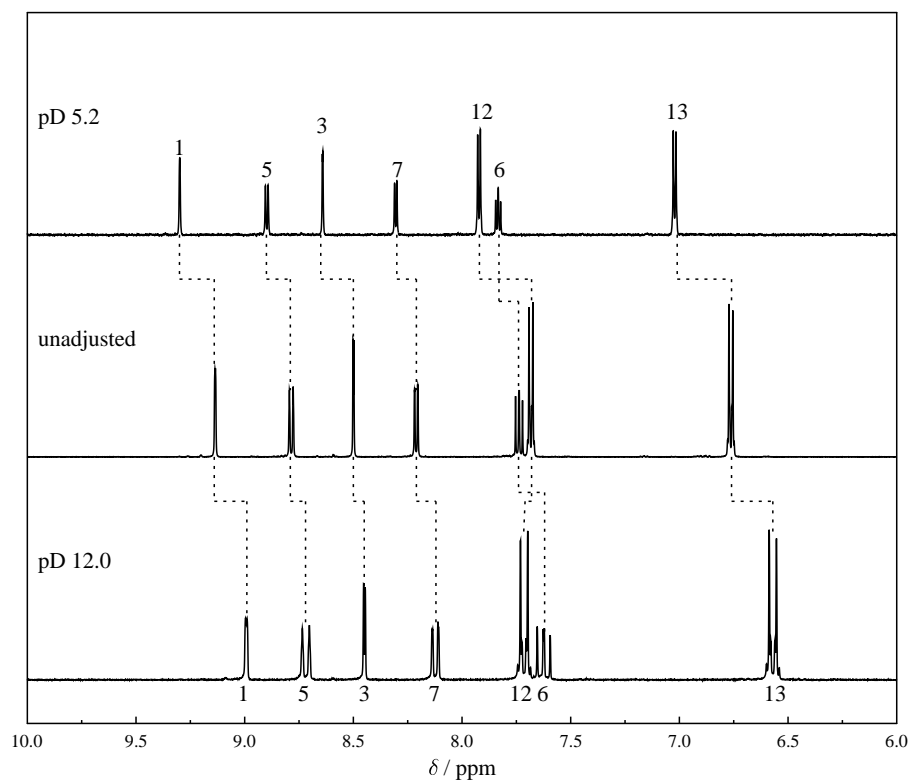


Figure 3.32 Aromatic region ^1H NMR spectrum of OH-Span in D_2O ; pD 5.2 (top, 700 MHz), unadjusted (middle, 500 MHz) and pD 12.0 (bottom, 400 MHz).

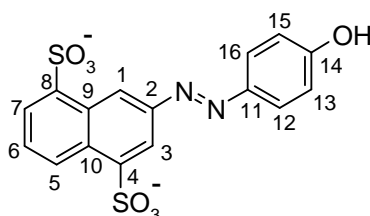


Figure 3.33 Structure of OH-Span with the numbering system used for NMR assignments.

Table 3.14 ^1H chemical shifts (ppm) of OH-Span at pD 5.2, unadjusted and pD 12.0, and an estimate of the % of OH in the unadjusted sample.

Proton	(OH-Span) pD 5.2	(O ⁻ -Span) pD 12	Unadjusted	% OH in Unadjusted
1	9.30	8.99	9.14	52
3	8.65	8.45	8.50	75
5	8.90	8.72	8.79	61
6	7.83	7.62	7.74	43
7	8.30	8.12	8.21	50
12/16	7.92	7.71	7.68	-
13/15	7.01	6.57	6.76	57

3.2.3.3 All R-Span dyes

Experimental and calculated ^1H and ^{13}C NMR spectra in the aromatic region for all the R-Span dyes (numbering system shown in Figure 3.34) recorded in D_2O are shown in Figures 3.35 and 3.36, with NMR positions given in Tables 3.15 and 3.16 along with differences from H-Span where a negative change represents an upfield shift. The general trend in shifts in NMR peak positions between all of the R-Span dyes is comparable between experimental and calculated data, with the most significant changes occurring across the phenyl ring. Despite some of the dyes being impure, assignments have been made for all atoms, although some ^{13}C signals are significantly weaker than those from the pure dyes. OMe-Span may show a small proportion of *cis* isomer which will be considered in chapter 5; for all other dyes resonances from only the *trans* isomer are observed.

In the ^1H NMR spectra, the overall trend is that upon increasing the electron donating ability of the substituent on the phenyl ring the peak positions of all protons moves upfield to lower ppm. Experimentally, the resonances of the two protons 13/15 show the greatest change, consistent with their local magnetic field being influenced most strongly by the neighbouring R group, for example on going from H-Span to NH_2 -Span there is an upfield shift of 0.88 ppm. Protons 12/16, 1 and 3 are also sensitive to the change in substituent giving an upfield shift on going from H-Span to NH_2 -Span of 0.21, 0.26 and 0.15 ppm, respectively, showing that the main changes of electron density occur across the phenyl ring and azo linkage onto the naphthyl group. In the case of an electron withdrawing group on the phenyl ring, there is also an upfield shift in peak positions. In both cases, for Br-Span and CN-Span, the largest upfield shift of 0.33 and 0.21 ppm, respectively, occurs for 12/16 accompanied by a smaller upfield shift of 0.13 and 0.06 ppm, respectively, for 13/15. Again upfield shifts in the resonances of 1 and 3 occur for both CN-Span and Br-Span indicating that the electron distribution is changing across the phenyl ring and azo linkage.

In the ^{13}C NMR spectra, there is no simple trend to follow. Experimentally, carbons 13/15 and 14 show the greatest changes. On going from H-Span to NH_2 -Span carbons 11 and 13/15 show upfield shifts of 6.3 and 15.3 ppm, respectively, and carbons 14 and 12/16 show downfield shifts of 15.7 and 2.7, ppm respectively, indicating changes in

the charge distribution across the phenyl ring. Of the electron withdrawing substituents, Br-Span shows an opposite trend where carbons 11 and 13/15 show downfield shifts of 1.0 and 5.2 ppm, respectively, and carbons 14 and 12/16 show upfield shifts of 15.7 and 2.7 ppm, respectively.

In general there is a very good match of the experimental and calculated ^1H and ^{13}C NMR data, which are showing comparable trends and with the calculated Mulliken atomic charges give a good interpretation of the electron distribution within the R-Span dye series.

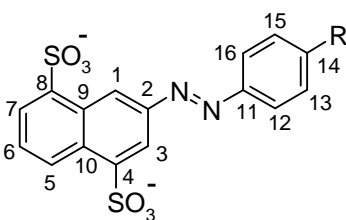


Figure 3.34 R-Span dyes numbering system used for NMR assignments.

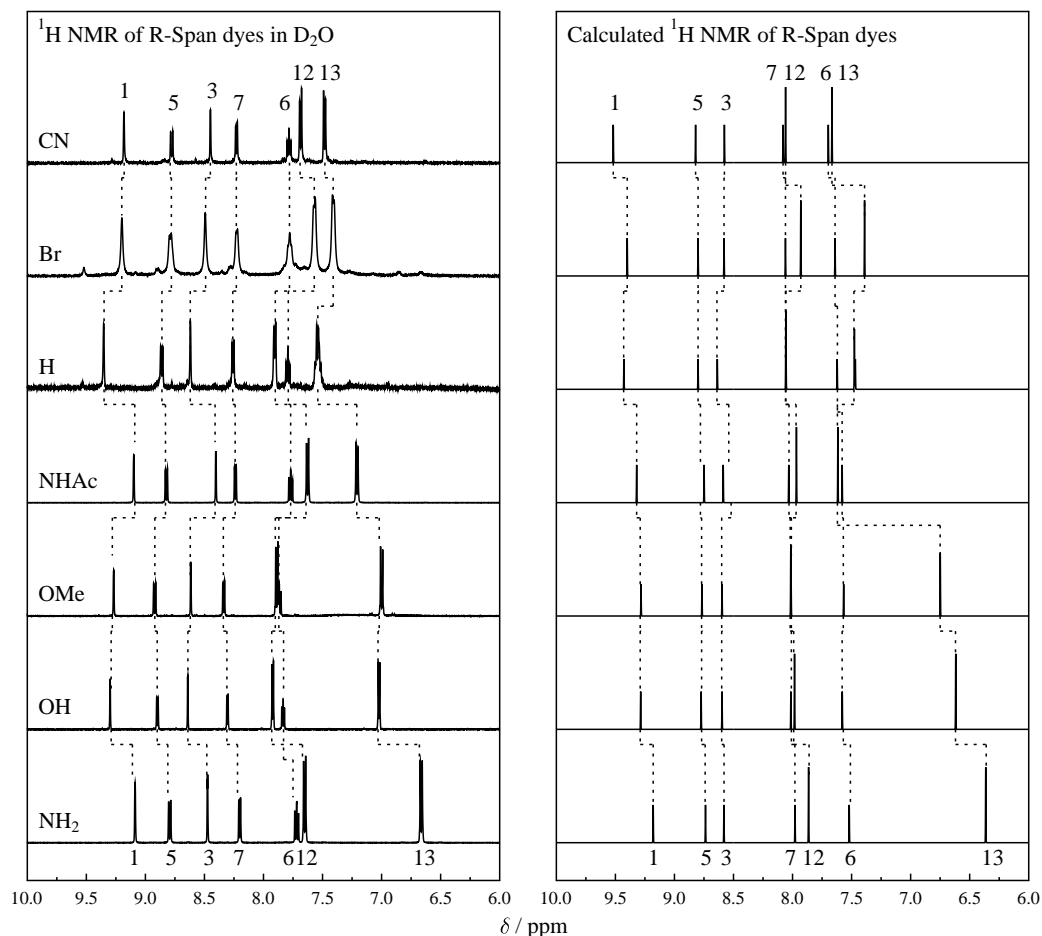


Figure 3.35 Left: Aromatic region ^1H NMR spectra for all R-Span dyes in D_2O ; Right Calculated ^1H NMR spectra for all R-Span dyes.

Table 3.15 Experimental and calculated ^1H NMR chemical shifts (δ /ppm) in the aromatic region for all R-Span dyes; differences (Δ) given for chemical shifts from the values of H-Span.

atom	Experimental												
	H-	NH ₂ -	$\Delta(\text{NH}_2)$	OH-	$\Delta(\text{OH})$	OMe-	$\Delta(\text{OMe})$	NHAc-	$\Delta(\text{NHAc})$	Br-	$\Delta(\text{Br})$	CN-	$\Delta(\text{CN})$
1	9.35	9.09	-0.26	9.03	-0.05	9.28	-0.07	9.09	-0.26	9.20	-0.15	9.18	-0.17
3	8.62	8.47	-0.15	8.65	+0.03	8.62	0.00	8.41	-0.21	8.49	-0.13	8.45	-0.17
5	8.86	8.79	-0.07	8.90	+0.04	8.92	+0.06	8.83	-0.03	8.79	-0.07	8.78	-0.08
6	7.79	7.72	-0.07	7.83	+0.04	7.87	+0.08	7.77	-0.02	7.78	-0.01	7.78	-0.01
7	8.26	8.20	-0.06	8.30	+0.04	8.34	+0.08	8.24	-0.02	8.23	-0.03	8.23	-0.03
12/16	7.90	7.69	-0.21	7.92	+0.02	7.90	0.00	7.62	-0.28	7.57	-0.33	7.69	-0.21
13/15	7.54	6.66	-0.88	7.01	-0.53	7.02	-0.52	7.21	-0.33	7.41	-0.13	7.48	-0.06
Calculated													
1	9.43	9.18	-0.25	9.29	-0.14	9.29	-0.14	9.32	-0.11	9.40	-0.03	9.52	+0.09
3	8.64	8.58	-0.06	8.60	-0.04	8.60	-0.04	8.59	-0.05	8.58	-0.06	8.58	-0.06
5	8.80	8.74	-0.06	8.77	-0.03	8.77	-0.03	8.75	-0.05	8.80	0.00	8.82	+0.02
6	7.62	7.52	-0.10	7.58	-0.04	7.57	-0.05	7.58	-0.04	7.64	+0.02	7.70	+0.08
7	8.06	7.98	-0.08	8.01	-0.05	8.01	-0.05	8.03	-0.03	8.06	0.00	8.08	+0.02
12/16	8.06	7.97	-0.09	8.06	0.00	8.02	-0.04	7.97	-0.09	7.93	-0.13	8.05	-0.01
13/15	7.48	6.37	-1.11	6.62	-0.86	6.75	-0.73	7.62	+0.14	7.39	-0.09	7.67	+0.19

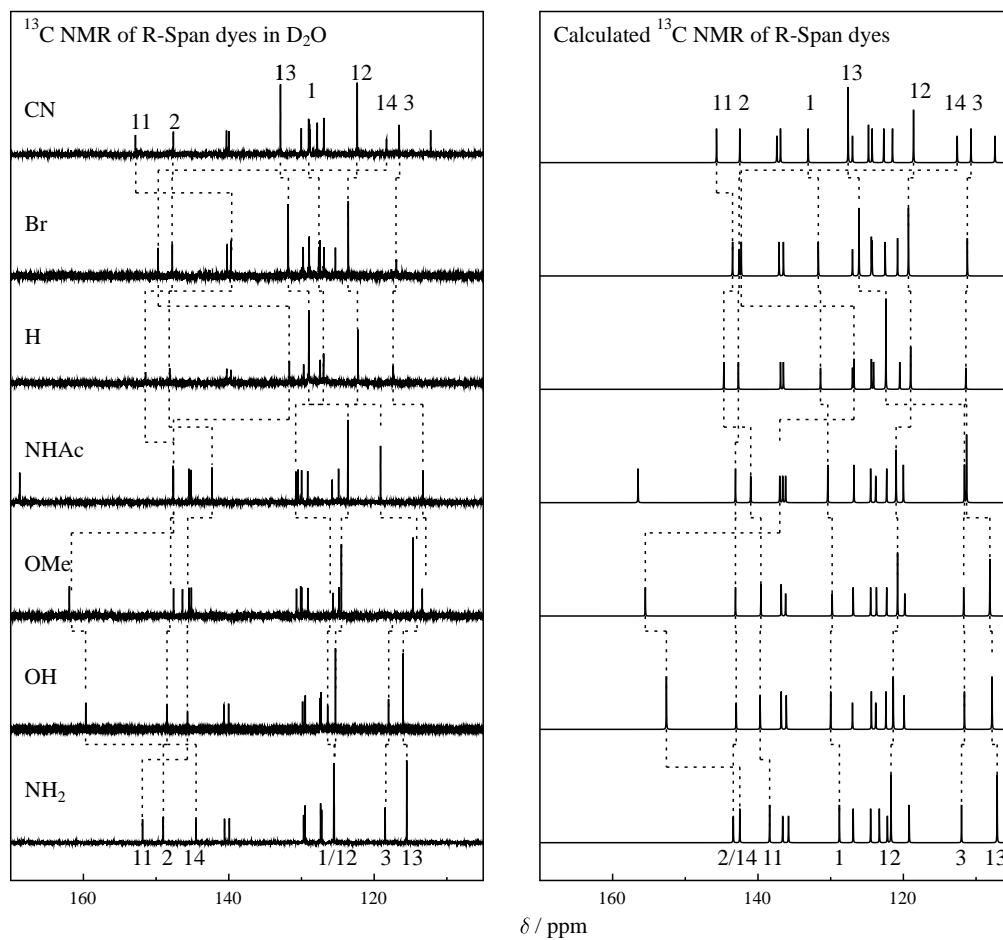


Figure 3.36 Left: Aromatic region ^{13}C NMR spectra for all R-Span dyes in D_2O ; Right Calculated ^{13}C NMR spectra for all R-Span dyes.

Table 3.16 Experimental and calculated ^{13}C NMR chemical shifts (δ /ppm) in the aromatic region for all R-Span dyes; differences (Δ) given for chemical shifts from the values of H-Span.

Experimental													
atom	H-	NH ₂ -	$\Delta(\text{NH}_2)$	OH-	$\Delta(\text{OH})$	OMe-	$\Delta(\text{OMe})$	NHAc-	$\Delta(\text{NHAc})$	Br-	$\Delta(\text{Br})$	CN-	$\Delta(\text{CN})$
1	127.0	125.4	-1.6	126.4	-0.6	126.1	-0.9	130.8	+3.8	127.6	+0.6	129.0	+2.0
2	151.5	149.0	-2.5	148.5	-3.0	148.1	-3.4	147.6	-3.9	147.8	-3.7	147.7	-3.8
3	117.4	118.4	+1.0	118.0	+0.6	112.7	-4.7	113.3	-4.1	117.0	-0.4	116.5	-0.9
4	140.3	140.6	+0.3	140.7	+0.4	140.2	-0.1	145.5	+5.2	139.7	-0.6	140.0	-0.3
5	129.0	129.5	+0.5	129.5	+0.5	129.0	0.0	129.2	+0.2	128.9	-0.1	128.9	-0.1
6	127.5	127.2	-0.3	127.4	-0.1	127.0	-0.5	125.9	-1.6	127.4	-0.1	127.8	+0.3
7	127.0	127.3	+0.3	127.3	+0.3	126.8	-0.2	124.9	-2.1	126.9	-0.1	126.9	-0.1
8	139.7	139.9	+0.2	140.0	+0.3	139.6	-0.1	145.2	+5.5	140.2	+0.5	140.3	+0.6
9	129.7	129.7	0.0	129.9	+0.2	129.4	-0.3	130.5	+0.8	129.9	+0.2	130.6	+0.9
10	129.0	129.6	+0.6	129.6	+0.6	129.0	0.0	130.0	+1.0	129.8	+0.8	128.8	-0.2
11	148.2	151.9	+3.7	145.7	-2.5	145.7	-2.5	142.3	-5.9	139.6	-8.6	152.8	+4.6
12/16	122.3	125.5	+3.2	125.3	+3.0	124.5	+2.2	123.6	+1.3	123.6	+1.3	122.4	+0.1
13/15	129.0	115.5	-13.5	116.0	-13.0	114.1	-14.9	119.1	-9.9	131.8	+2.8	132.9	+3.9
14	131.7	144.5	+12.8	159.7	+28.0	161.6	+29.9	147.6	+15.9	149.7	+18.0	118.3	-13.4
17	-	-	-	-	-	55.04	-	168.8	-	-	-	112.2	-
18	-	-	-	-	-	-	-	24.1	-	-	-	-	-
Calculated													
1	131.4	128.8	-2.6	130.0	-1.4	129.8	-1.6	130.4	-1.0	131.7	+0.3	133.1	+1.7
2	142.7	143.4	+0.7	143.0	+0.3	143.1	+0.4	143.1	+0.4	142.6	-0.1	142.5	-0.2
3	111.4	112.0	+0.6	111.6	+0.2	111.7	+0.3	111.6	+0.2	111.2	-0.2	110.7	-0.7
4	136.9	136.6	-0.3	136.8	-0.1	136.8	-0.1	136.6	-0.3	137.1	+0.2	137.4	+0.5
5	127.0	126.9	-0.1	127.0	0.0	126.9	-0.1	126.8	-0.2	127.0	0.0	127.0	0.0
6	120.5	119.2	-1.3	119.9	-0.6	119.8	-0.7	120.0	-0.5	120.8	+0.3	121.5	+1.0
7	122.4	122.2	-0.2	122.4	0.0	122.3	-0.1	122.3	-0.1	122.5	+0.1	122.7	+0.3
8	136.5	135.8	-0.7	136.1	-0.4	136.2	-0.3	136.2	-0.3	136.5	0.0	136.9	+0.4
9	124.4	124.5	+0.1	124.4	0.0	124.5	+0.1	124.5	+0.1	124.4	0.0	124.3	-0.1
10	124.1	123.3	-0.8	123.8	-0.3	123.7	-0.4	123.8	-0.3	124.3	+0.2	124.8	+0.7
11	144.7	138.4	-6.3	139.7	-5.0	139.6	-5.1	141.0	-3.7	143.5	-1.2	145.7	+1.0
12/16	119.0	121.7	+2.7	121.4	+2.4	120.8	+1.8	121.0	+2.0	119.3	+0.3	118.6	-0.4
13/15	122.4	107.1	-15.3	107.8	-14.6	108.1	-14.3	111.3	-11.1	126.1	+3.7	127.6	+5.2
14	126.8	142.5	+15.7	152.6	+25.8	155.5	+28.7	137.0	+10.2	142.3	+15.5	112.6	-14.2
17						52.7		156.5				107.4	
18								24.1					

3.2.4 Vibrational spectroscopy

Before any spectra were recorded, significant consideration was given to optimising the ideal experimental conditions and these are described in section 3.2.4.1 after which the bulk of the data collected was for OH-Span. The experimental and calculated Raman and infrared spectra together with vibrational assignments of OH-Span are reported in section 3.2.4.2. The experimental and calculated Raman spectra together with vibrational assignments of the other R-Span dyes are reported in section 3.2.4.3, with the pH dependence on OH-Span reported in section 3.2.4.4.

3.2.4.1 General experimental conditions

In terms of Raman spectroscopy, dye purity was of prime importance (see Chapter 2 for purity levels of each dye). For the pure samples, this was not so much of an issue; however for the impure samples the ideal conditions would be to record spectra with an excitation wavelength at the absorption maximum of the pure dye. Unfortunately some conditions chosen might enhance the signal from impurities if the excitation wavelength is in resonance with an impurity absorption band, which even at low concentrations may give a greater signal than from the dye. Figure 3.37 shows the UV/Vis absorption spectra of all R-Span dyes at 4×10^{-4} mol dm⁻³ in water and as pure HPLC components in water showing the positions of the chosen three laser Raman excitation wavelengths of 514.5, 413.1 and 350.6 nm. For the R-Span series the ideal excitation wavelength was in the UV region.

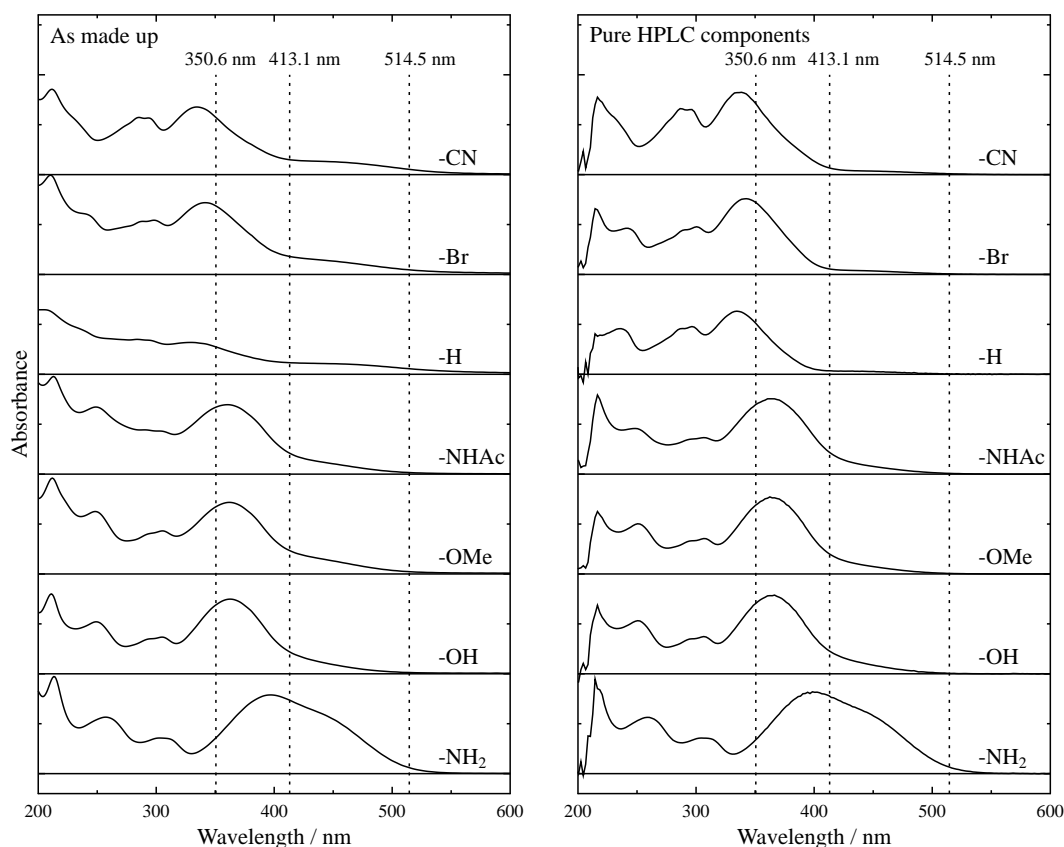


Figure 3.37 UV/Vis absorption spectra of all R-Span dyes as prepared in water (left) and as pure HPLC components (right) in water; dashed lines show Raman excitation wavelengths.

Another important consideration was the integrity of the sample through the experiment. No change in Raman profile was observed on changing the laser power, beam radius and sample flow rate during the Raman experiment, allowing short-term effects within the laser beam due to photoalteration⁹⁸ to be discounted; a more detailed description of the careful consideration of photoalteration is shown in Appendix 1.5. The observed UV/Visible absorption spectra and HPLC chromatograms of samples were the same before and after Raman experiments (with an excitation wavelength of 514.5 nm and a total collection time of 3600 s) indicating that the sample integrity remained unchanged also on a longer timescale.

Raman spectra were recorded across 300 detector pixels, and at shorter excitation wavelengths there is a lower dispersion of wavenumber per pixel and hence lower spectral resolution: The resolution was ca. 3, 5 and 7 cm^{-1} and the accuracy was ± 2 , 4 and 6 cm^{-1} (all ± 1 pixel) for 514.5, 413.1 and 350.6 nm excitation, respectively.

3.2.4.2 OH-Span

Raman spectra of OH-Span in water (pH 5) recorded with excitation wavelengths of 350.6, 413.1 and 514.5 nm, an IR spectrum of OH-Span in water (pH 5, saturated) and the calculated Raman and IR spectra are shown in Figure 3.38 with band positions given in Table 3.17. 2-naphthylamine-4,8-disulfonate (NAPDAD) and 4-aminophenol (APOL) as shown in Figures 3.39 and 3.40 are model compounds for the naphthyl and phenyl groups within OH-Span and their experimental and calculated Raman spectra are also shown in Figure 3.38 with band positions given in Table 3.17; they have been an aid in the vibrational assignments of OH-Span (Table 3.17) A selection of calculated normal mode vibrations of OH-Span and matching modes from NAPDAD and APOL are shown in Figures 3.39-3.41. Wilson mode assignments of phenyl ring vibrations have been made in accordance with those of *para*-substituted phenyl rings previously reported.⁹⁹

In general there is a good match between the experimental and calculated Raman spectra of OH-Span. Using the bands from the data recorded upon 514.5 nm excitation, the assignments of the significant bands can be made as follows; the broad band at ca. 1600 cm^{-1} can be resolved into two peaks at ca. 1614 and 1593 cm^{-1} , as supported by the IR spectrum of OH-Span in which there is a band observed at 1593 cm^{-1} (Figure 3.38). The shoulder at ca. 1593 cm^{-1} in the Raman spectrum matches the band in the IR spectrum and is assigned to the calculated mode at 1603 cm^{-1} which is both Raman and IR active (Table 3.17) predominately arising from a Wilson 8a, 9a vibration of the phenyl ring (Figure 3.41). The calculated mode at 1604 cm^{-1} predominately arises from a naphthyl vibration, is calculated to show Raman but no IR activity, and can be assigned to the experimental Raman band at ca. 1614 cm^{-1} . The Raman shoulder at ca. 1480 cm^{-1} has a matching weak IR band at 1473 cm^{-1} and is assigned to the calculated mode at 1484 cm^{-1} showing a combination of naphthyl and Wilson 18a, 19a phenyl vibrations. The Raman bands at 1464 , 1446 , 1431 , 1405 and 1379 cm^{-1} which dominate the spectrum can be tracked along with calculated vibrations at 1467 , 1430 , 1420 , 1403 and 1377 cm^{-1} , respectively, which all have significant N=N vibration in addition to naphthyl and phenyl vibrations (Figure 3.41). The mode at 1403 cm^{-1} also shows significant C-N vibration on the naphthyl side of the dye, which is not seen on the phenyl side. The weak Raman bands at 1270 , 1230 and 1216 cm^{-1} have matching

significant bands in the IR spectrum at 1270, 1230 and 1216 cm^{-1} , and are assigned to calculated modes at 1270, 1231 and 1217 cm^{-1} which all have Wilson 18a, 1 phenyl vibrations. The Raman band at 1200 cm^{-1} and shoulder at ca. 1195 cm^{-1} have matching strong bands in the IR spectrum at 1198 and 1195 cm^{-1} and are assigned to calculated modes at 1192 and 1177 cm^{-1} which both show Wilson 18a, 1 phenyl and naphthyl vibrations. A shoulder at ca. 1175 cm^{-1} and weak band at 1171 cm^{-1} have matching IR shoulder bands at ca. 1175 and 1171 cm^{-1} which can be attributed to two calculated modes at 1165 and 1162 cm^{-1} which both show OH vibration. The dominant Raman band at 1138 cm^{-1} has a shoulder at ca. 1152 cm^{-1} which matches a strong dominant IR band at 1152 cm^{-1} , this is assigned to a calculated mode that has a high IR activity at 1135 cm^{-1} , showing a strong Wilson 9a, 1 phenyl vibration. The dominant Raman 1138 cm^{-1} band can be assigned to the sulfonate group vibration matching the 1126 cm^{-1} calculated mode. The last assignment is of a Raman shoulder at ca. 1124 cm^{-1} which matches a weak band at 1124 cm^{-1} in the IR spectrum, once again showing sulfonate vibration and matching the calculated mode at 1110 cm^{-1} .

The normal mode displacement vectors (Figure 3.41) show that the calculated vibrations of OH-Span at 1604, 1588, 1551, 1336, 1321 and 1310 cm^{-1} are all predominantly localised at the naphthyl ring and the calculated vibrations at 1177, 1092, 1082 cm^{-1} are predominantly localised at the naphthyl ring and sulfonate groups which all have matching NAPDAD modes (Figure 3.40, Table 3.17). Of the other calculated vibrations of OH-Span that have matching NAPDAD modes those at 1484, 1231, 1162, 1126 cm^{-1} show coupling to vibrations on the phenyl ring. The calculated vibrations of OH-Span of 1603, 1577 and 1509 cm^{-1} are all predominantly localised at the phenyl ring and all have matching APOL modes (Figure 3.41, Table 3.17). Of the other calculated vibrations of OH-Span that have matching APOL modes those at 1501, 1345, 1291, 1231, 1165 and 1135 cm^{-1} show coupling to vibrations on the naphthyl ring. Calculated modes with significant N=N stretching in OH-Span occur at 1603, 1501, 1467 and 1420 cm^{-1} ; interestingly, only the calculated mode at 1403 cm^{-1} shows significant C2-N $_{\alpha}$ stretching motion and no modes show significant N $_{\beta}$ -C11 stretching motion. The experimental data show that the changes in the relative intensities of the Raman bands upon going from an excitation wavelength of 514.5 nm (off resonance) to 350.6 nm (in resonance) are quite small, with the overall profile largely being retained.

Page intentionally left blank

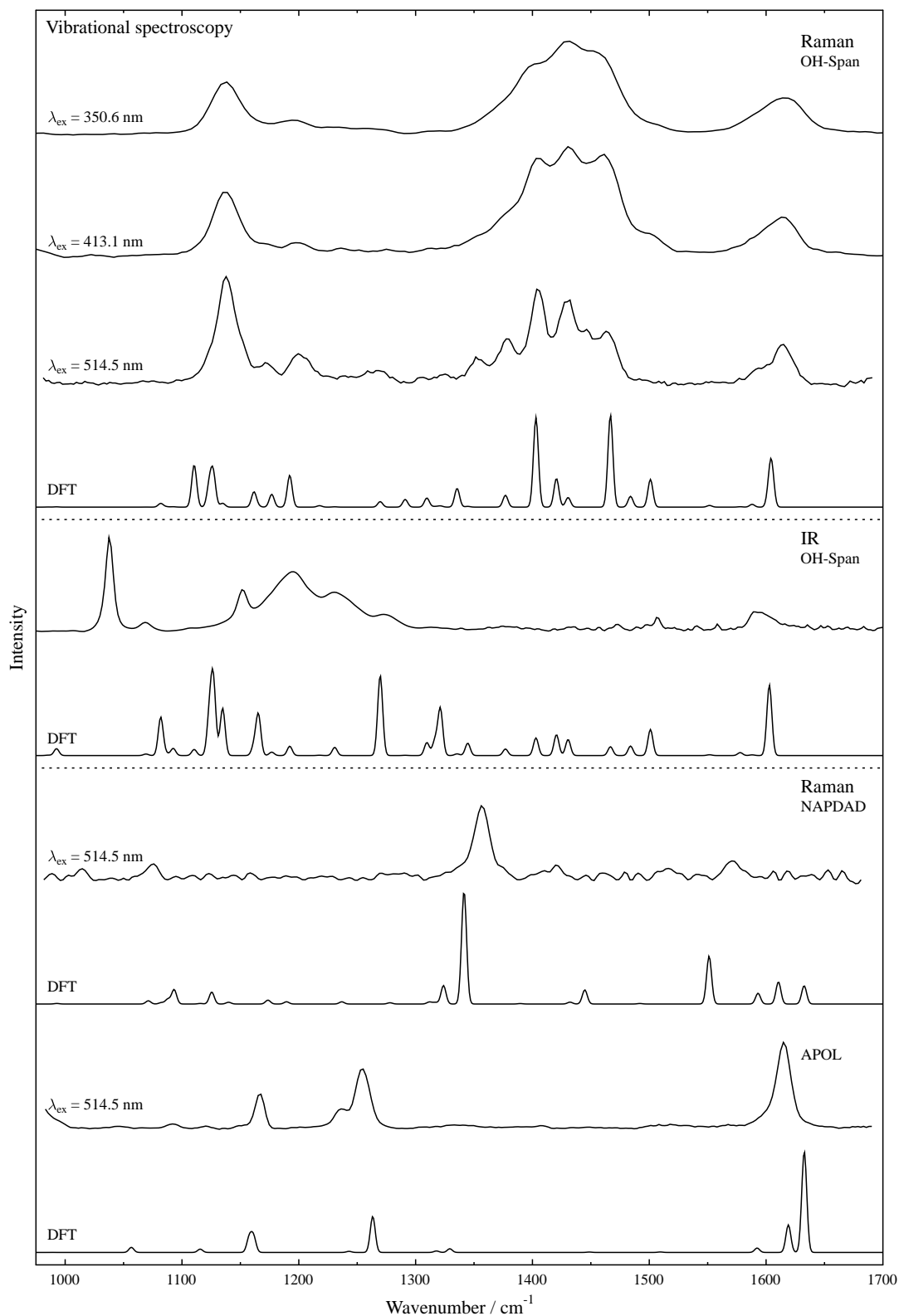


Figure 3.38 Experimental Raman spectra of OH-Span in water ($4 \times 10^{-4} \text{ mol dm}^{-3}$) with 350.6, 413.1 and 514.5 nm excitation, experimental IR spectra of OH-Span in water (saturated), experimental Raman spectra of NAPDAD (solid) and APOL in water ($1 \times 10^{-3} \text{ mol dm}^{-3}$) with 514.5 nm excitation; all with their calculated spectra.

Table 3.17 Raman and IR band positions (cm^{-1}) of OH-Span in water, calculated band positions and normal mode assignments together with matching NAPDAD and APOL assignments.

				OH-Span			NAPDAD				APOL						
Experimental ^c				Calculated			Experimental	Calculated			Experimental	Calculated					
514.5 nm	413.1 nm	350.6 nm	IR	R ^a	IR ^a	Description ^b		R ^a	IR ^a		R ^a	IR ^a					
1614m	1615m	1616m		1604	41	0	$\delta(\text{nap})$, $\nu(\text{NN})$, Ph(9a, 8a), $\delta(\text{OH})$	1581	sh	1611	18	33					
1593sh	1593sh	1590sh	1593m	1603	17	88	Ph(8a, 9a), $\nu(\text{CO})$, $\delta(\text{OH})$, $\nu(\text{NN})$, $\delta(\text{nap})$			1596	sh	1619	6	6			
1578vw	1573vw	1577sh	1578vw	1588	3	1	$\delta(\text{nap})$, $\nu(\text{NN})$	1572	m	1593	9	1					
			1559vw	1577	0	4	Ph(3, 8b), $\delta(\text{OH})$						1592	1	1		
			1541vw	1551	2	1	$\delta(\text{nap})$, $\nu(\text{NN})$, Ph(18b, 14), $\delta(\text{OH})$	1516	w	1551	38	1					
1500vw	1505w	1508w	1507w	1501	30	33	Ph(18a, 19a), $\nu(\text{NN})$, $\nu(\text{CO})$, $\delta(\text{OH})$, $\delta(\text{nap})$			1522	vw	1509	0	64			
1480sh			1473vw	1484	12	12	Ph(18a, 19a), $\delta(\text{nap})$, $\nu(\text{NN})$, $\nu(\text{CN})$, $\nu(\text{CO})$			1492	0	24					
1464m	1460s	1457s		1467	100	11	Ph(18a, 14), $\nu(\text{NN})$, $\delta(\text{nap})$, $\delta(\text{OH})$, $\nu(\text{CO})$										
1446m				1430	10	20	Ph(18b, 14), $\delta(\text{OH})$, $\nu(\text{NN})$, $\delta(\text{nap})$, $\nu(\text{CO})$										
1431s	1431s	1430s		1420	31	26	$\delta(\text{nap})$, $\nu(\text{NN})$, Ph(18b, 14), $\delta(\text{OH})$, $\nu(\text{CN})$										
1405s	1405s	1399s		1403	97	22	$\delta(\text{nap})$, $\nu(\text{NN})$, $\nu(\text{CN})$, Ph(18b, 14), $\delta(\text{OH})$										
1379m	1377sh	1380sh		1377	13	8	$\delta(\text{nap})$, $\nu(\text{NN})$, Ph(18b, 14)										
				1345	1	15	$\delta(\text{OH})$, Ph(3, 14), $\delta(\text{nap})$			1337	vw	1329	0	15			
1352w	1352sh	1356sh		1336	20	2	$\delta(\text{nap})$, Ph(3, 1), $\delta(\text{OH})$	1356	s	1341	90	12					
1323vw	1321sh			1321	1	58	$\delta(\text{nap})$, $\nu(\text{SO})$, $\delta(\text{SOH})$, $\nu(\text{CN})$, Ph(18a, 14)	1336	sh	1323	15	35					
1311vw	1312vw	1311vw		1310	10	16	$\delta(\text{nap})$, $\nu(\text{SO})$, $\delta(\text{SOH})$, $\nu(\text{NN})$, Ph(18b, 8a)			1317	1	70					
1305vw				1291	8	0	Ph(3, 14), $\delta(\text{OH})$, $\nu(\text{CN})$, $\delta(\text{nap})$						1318	0	5		
1270vw	1273vw	1272vw	1270m	1270	6	100	$\nu(\text{CO})$, Ph(18a, 1), $\delta(\text{OH})$, $\delta(\text{nap})$										
1230vw	1232vw	1232vw	1230s	1231	0	10	$\delta(\text{nap})$, $\nu(\text{CN})$, Ph(18a, 1), $\delta(\text{OH})$			1237	2	17	1236	m	1243	0	45
1216sh			1216sh	1217	2	0	Ph(18a, 1), $\delta(\text{nap})$, $\nu(\text{CN})$, $\delta(\text{OH})$										
1200m	1199m	1197m	1198sh	1192	34	12	Ph(9a, 1), $\delta(\text{nap})$, $\nu(\text{CN})$, $\delta(\text{OH})$, $\nu(\text{CN})$, $\delta(\text{SOH})$										
1195sh			1195s	1177	14	4	$\delta(\text{nap})$, Ph(9a, 1), $\delta(\text{OH})$, $\delta(\text{SOH})$, $\nu(\text{CS})$			1189	2	2					
1175sh			1175sh	1165	1	51	$\delta(\text{OH})$, $\nu(\text{CO})$, Ph(3, 8b), $\delta(\text{nap})$						1167	s	1161	4	54
1171w	1170w		1171sh	1162	16	11	$\delta(\text{nap})$, $\delta(\text{OH})$, Ph(9a, 8a),			1174	3	6					
1152sh			1152s	1135	4	59	Ph(9a, 1), $\delta(\text{nap})$, $\delta(\text{OH})$, $\nu(\text{CN})$						1151	sh	1158	30	0
1138vs	1137vs	1137vs	1138w	1126	35	91	$\delta(\text{SOH})$, $\nu(\text{CS})$, Ph(9a, 1), $\nu(\text{CN})$, $\delta(\text{OH})$			1126	10	90					
				1123	24	46	$\delta(\text{SOH})$, $\delta(\text{nap})$, Ph(9a, 1), $\nu(\text{CN})$										
1124sh			1124vw	1110	46	8	$\delta(\text{nap})$, $\delta(\text{SOH})$, $\nu(\text{CN})$, Ph(9a, 1), $\delta(\text{OH})$										
			1107vw	1092	0	9	$\delta(\text{SOH})$, $\nu(\text{SO})$, $\delta(\text{nap})$, Ph(18b), $\delta(\text{OH})$	1075	m	1093	11	0					
				1086	0	2	Ph(18b, 19b), $\delta(\text{OH})$										
			1069w	1082	0	48	Ph(18b, 14), $\delta(\text{OH})$, $\delta(\text{SOH})$, $\nu(\text{SO})$, $\delta(\text{nap})$			1083	4	6					
				1069	0	2	$\delta(\text{nap})$, $\delta(\text{SOH})$, Ph(18b, 14)										
			1038vs														

vw – very weak, w – weak, m – medium, s – strong, vs – very strong, sh - shoulder δ – bend, ν – stretch, sc – scissor, ro – rocking, ^a intensity of strongest peak scaled to 100, ^b in order of decreasing contribution.

^c alternative assignments: NH₂-Span 1463 cm^{-1} Ph(18b, 19a), $\nu(\text{NN})$, $\nu(\text{CN})$, $\delta(\text{nap})$, OMe-Span 1435 cm^{-1} $\delta(\text{nap})$, $\nu(\text{NN})$, Ph(18b, 14), $\nu(\text{CN})$, 1415 cm^{-1} Ph(18b, 14), $\delta(\text{nap})$, $\nu(\text{NN})$, NHAc-Span 1452 cm^{-1} Ph(18a, 19a), $\nu(\text{NN})$, $\nu(\text{CN})$, $\delta(\text{nap})$, 1271 cm^{-1} $\nu(\text{CN})$, $\delta(\text{nap})$, Ph(18b, 1), H-Span 1291 cm^{-1} Ph(3, 14), $\nu(\text{NN})$, $\nu(\text{CN})$, $\delta(\text{nap})$, Br-Span 1275 cm^{-1} Ph(3, 14), $\nu(\text{CN})$, $\delta(\text{nap})$, $\delta(\text{SOH})$.

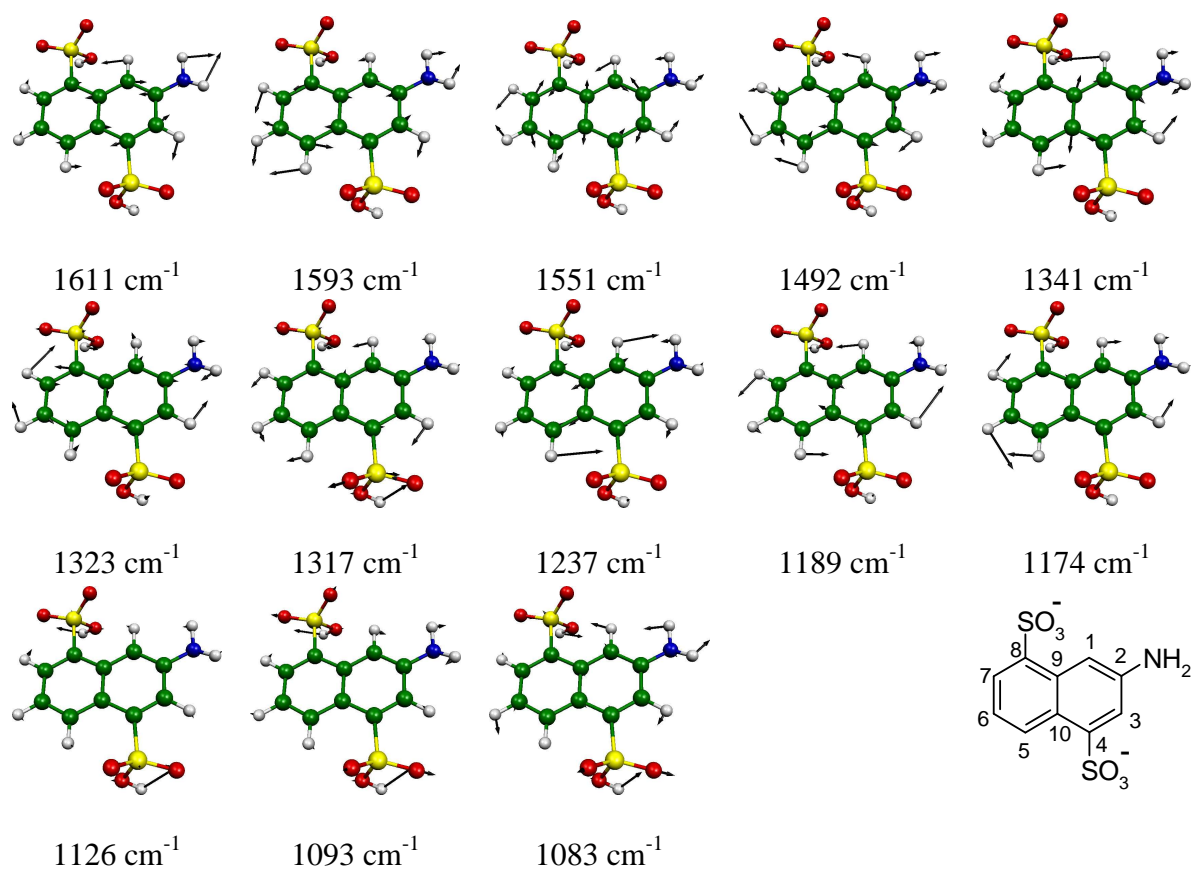


Figure 3.39 Structure of NAPDAD and selected calculated normal mode vibrations of NAPDAD that match those from OH-Span. (*Original in colour*)

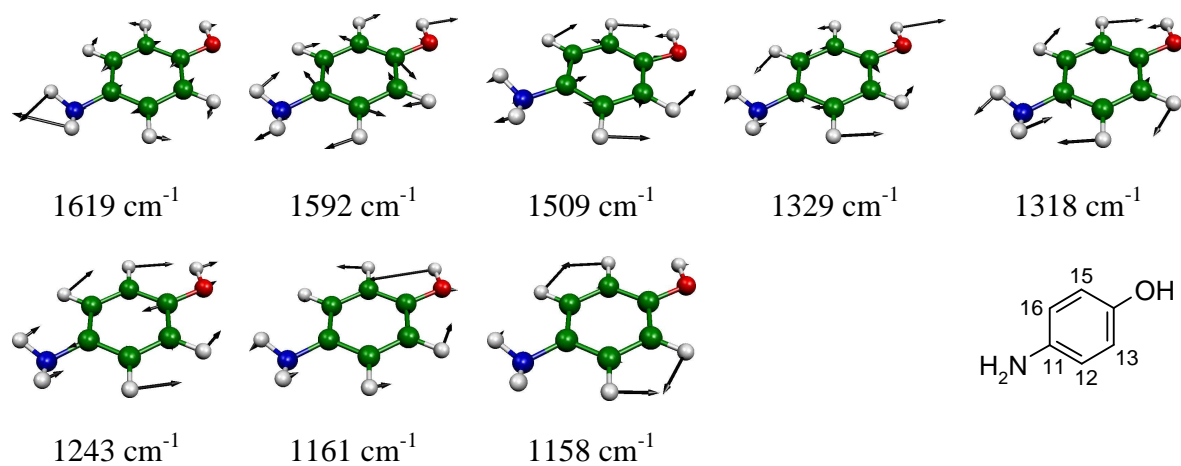


Figure 3.40 Structure of APOL and selected calculated normal mode vibrations of APOL that match those from OH-Span. (*Original in colour*)

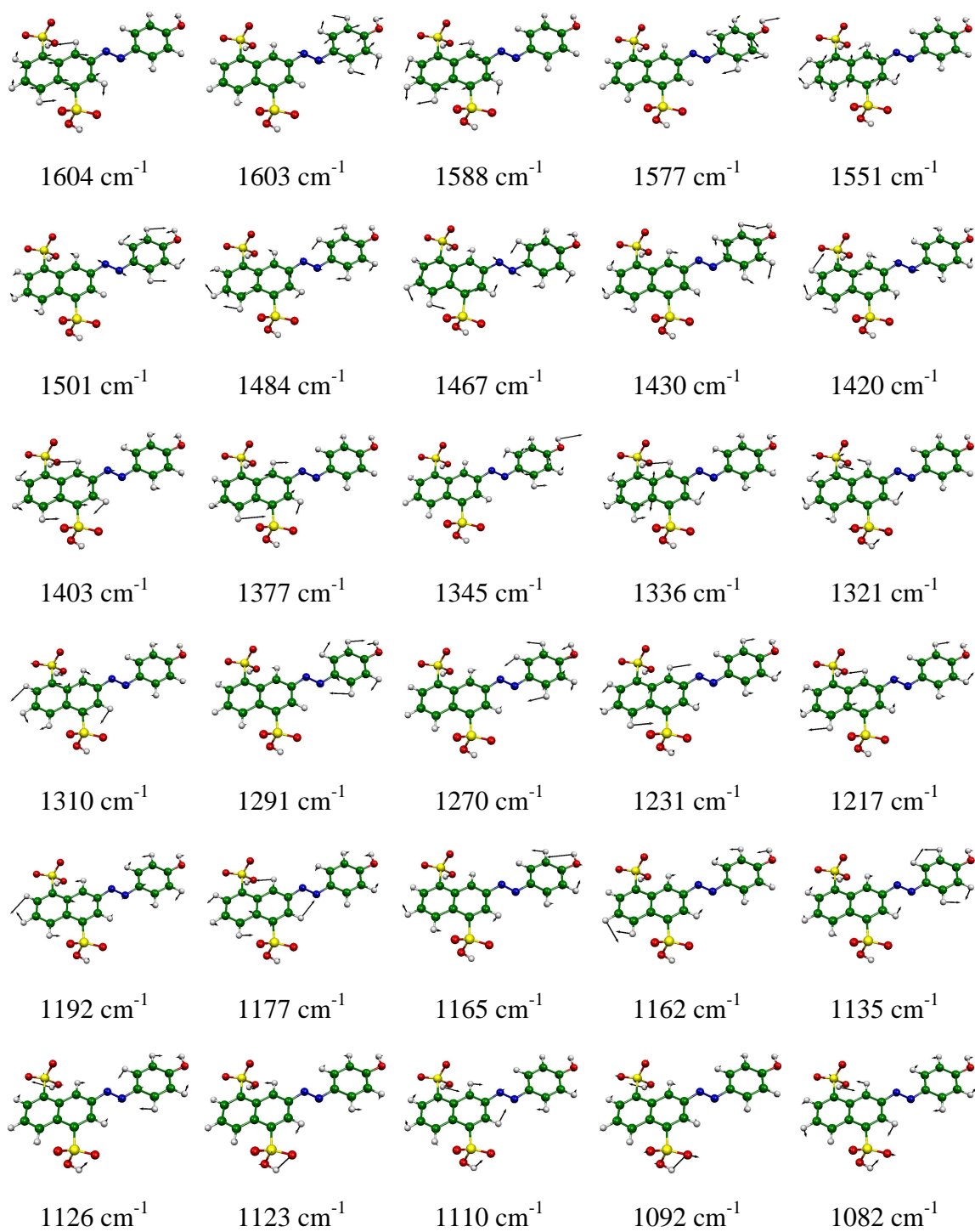


Figure 3.41 Selected calculated normal mode vibrations of OH-Span. (*Original in colour*)

3.4.2.2.3 All R-Span dyes

The Raman spectra of all the R-Span dyes in water recorded with an excitation wavelength of 514.5 nm and their calculated Raman spectra are shown in Figure 3.42, with band positions given in Table 3.18. Vibrational assignments of all the R-Span dyes are given in Table 3.18 and have been made with the aid of those already made for OH-Span (Table 3.17) along with the calculated spectra and normal mode vibrations of R-Span, all of which are shown in Appendix A1.5 where they are set out for easy comparison with those of OH-Span to show similarities and differences between modes. In general there is a very good match between the vibrational assignments of the R-Span dyes based on the comparison of experimental peaks, calculated peaks and normal mode vibrations.

Experimental and DFT calculated differences in Raman band positions between the R-Span dyes and H-Span where a positive change represents a shift to higher wavenumber on going to R-Span are given in Table 3.19. Bands assigned to vibrations which contain significant phenyl contributions appear to show the largest shifts in their positions but show no particular trend across the dye series. For those dyes containing electron donating groups, those vibrations that have shifted from that of H-Span appear to show a significant contribution from the R substituent. In the case of the electron withdrawing groups, those vibrations that have shifted show little contribution from Br and CN, which appear to act as stationary groups. Using the band positions of H-Span, the most significant changes occurs for bands at 1596, 1495, 1480, 1450, 1446, 1291, 1217, 1208 and 1155 cm^{-1} . A CN stretch was not observed experimentally.

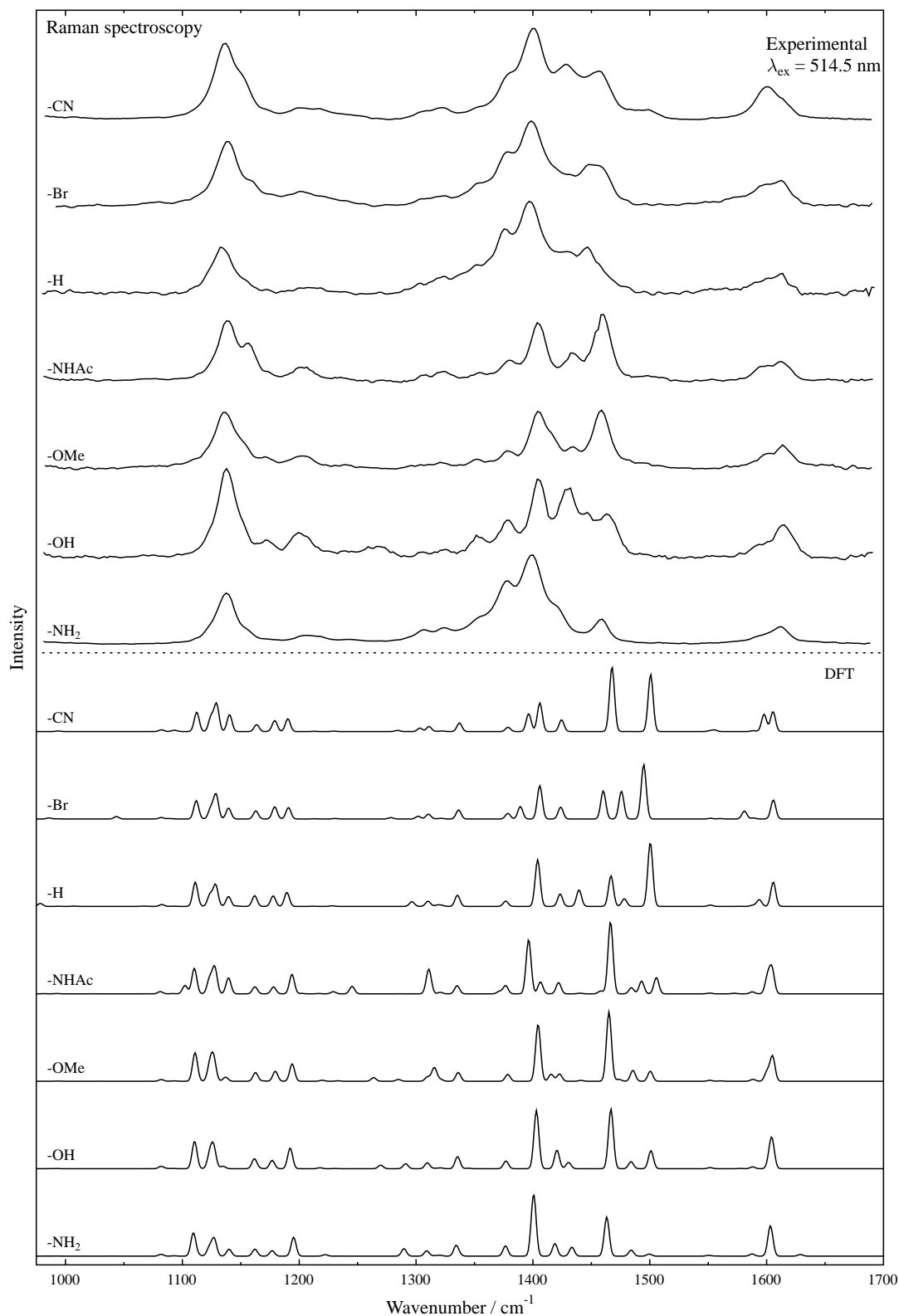


Figure 3.42 Experimental Raman spectra of R-Span ($4 \times 10^{-4} \text{ mol dm}^{-3}$) in water with 514.5 nm excitation, and their calculated spectra.

Table 3.18 Raman band positions (cm⁻¹) of R-Span dyes in water on 514.5 nm excitation and their assignments.

-NH ₂		-OH		-OMe		-NHAc		-H		-Br		-CN		Description ^a				
Exp	Calc	Exp	Calc	Exp	Calc	Exp	Calc	Exp	Calc	Exp	Calc	Exp	Calc	Backbone	-NH ₂	-OH	-OMe	-NHAc
1613m	1604	1614m	1604	1614m	1605	1614m	1604	1613m	1606	1613m	1606	1614sh	1605	δ(nap), ν(NN), Ph(9a, 8a)	δ(NH ₂ Sc)	δ(OH)		
1594m	1603	1593sh	1603	1601m	1600	1601m	1601	1596sh	1594	1599sh	1581	1601m	1598	Ph(8a, 9a), ν(NN), δ(nap)	δ(NH ₂ Sc)	ν(CO), δ(OH)	δ(Me)	δ(NH)
1571w	1587	1578vw	1588	1572vw	1588	1579vw	1587	1579sh	1588	1575sh	1588	1577sh	1588	δ(nap), ν(NN)				
	1551		1551		1551		1551	1552vw	1552	1544vw	1551	1554vw	1551	δ(nap), ν(NN), Ph(18b, 14)	δ(NH ₂ Ro)	δ(OH)	δ(Me)	δ(NH)
1500vw	1500	1500vw	1501	1507vw	1500	1504w	1505	1495vw	1500	1479sh	1495	1499w	1501	Ph(18a, 19a), ν(NN), δ(nap)	δ(NH ₂ Ro)	ν(CO), δ(OH)	δ(Me)	δ(NH), ν(CN), δ(Me)
				1495vw		1498w	1493							Ph(18a, 8b)				δ(NH)
1480vw	1484	1480sh	1484	1480w	1486	1480sh	1484	1480w	1478	1456m	1476	1484w	1482	Ph(18a, 19a), δ(nap), ν(NN), ν(CN)		ν(CO)	δ(Me), ν(CO)	ν(CN), δ(NH)
1458m	1463	1464m	1467	1459vs	1465	1460vs	1466	1455sh	1467	1448m	1460	1456s	1468	Ph(18a, 14), ν(NN), δ(nap)	δ(NH ₂ Ro)	δ(OH), ν(CO)	δ(Me)	δ(Me), ν(CN), δ(NH)
1436sh	1433	1446m	1430	1435m	1423	1452sh	1458	1446s	1439					Ph(18b, 14), ν(NN), δ(nap)	δ(NH ₂ Ro)	δ(OH), ν(CO)	δ(Me)	δ(Me), ν(CN)
1418sh	1419	1431s	1420	1415sh	1416	1435s	1422	1423sh	1423	1428sh	1424	1429s	1424	δ(nap), ν(NN), Ph(18b, 14), ν(CN)	δ(NH ₂ Ro)	δ(OH)	δ(Me), ν(OC)	δ(NH), δ(Me)
1398vs	1401	1405s	1403	1405vs	1404	1405vs	1406	1397vs	1404	1400vs	1406	1401vs	1406	δ(nap), ν(NN), ν(CN), Ph(18b, 14)	δ(NH)	δ(OH)	ν(CO)	ν(CN), ν(CO), δ(Me), δ(NH)
						1396sh	1396				1390		1396	Ph(18b, 19b), δ(nap), ν(NN), ν(CN)				δ(NH), ν(CN), δ(Me), ν(CO)
1377s	1377	1379m	1377	1379m	1378	1379m	1377	1376s	1377	1379s	1379	1378sh	1379	δ(nap), ν(NN), Ph(18b, 14)				
								1366sh										
1355sh	1334	1352w	1336	1352w	1336	1355w	1335	1355sh	1335	1351m	1336	1352sh	1337	δ(nap), Ph(3, 14)	δ(NH ₂ Ro)	δ(OH)		δ(NH), δ(Me)
						1331sh		1335sh										
1323m	1321	1323vw	1321	1321m	1321	1324w	1320	1324w	1320	1325w	1322	1332w	1323	δ(nap), ν(SO), δ(SOH), ν(CN), Ph(18a, 1)	δ(NH)		δ(Me)	δ(Me)
						1316		1316		1316		1316	1317	Ph(19b, 9a), ν(SO), ν(NN), δ(nap), δ(SOH)			δ(Me), ν(CO)	δ(NH), δ(Me)
1315m	1309	1311vw	1310	1309w	1309	1307w	1309	1305vw	1310	1305vw	1311	1305w	1311	δ(nap), ν(SO), δ(SOH), ν(NN), Ph(18b, 8a)				δ(Me)
1307m	1290	1305vw	1291	1301vw	1285			1291vw	1296	1275vw	1302		1303	Ph(3, 14), ν(CN), δ(nap)		δ(OH)		
1273vw		1270vw	1270	1271vw	1264	1271vw	1245	1269vw						Ph(18a, 1), δ(nap), ν(CN)		ν(CO), δ(OH)	ν(CO)	δ(NH)
										1253vw	1278	1251vw	1284	Ph(3, 14), ν(CN)			ν(OC), δ(Me)	
1243vw	1237	1230vw	1231	1242w	1233	1234vw	1229	1241vw	1228	1237vw	1230	1232vw	1229	δ(nap), ν(CN), Ph(18a, 1)	δ(NH ₂ Sc)	δ(OH)	δ(Me)	
1230vw	1222	1216sh	1217	1227vw	1219		1216	1217vw	1211	1217vw	1213	1217w	1212	Ph(18a, 1), δ(nap), ν(CN)	δ(NH ₂ Sc)	δ(OH)	ν(CO), δ(Me)	δ(NH)
1206w	1195	1200m	1192	1203m	1194	1203m	1194	1208vw	1189	1202w	1191	1201w	1190	Ph(9a, 1), δ(nap), ν(CN), δ(SOH)		δ(OH)	δ(Me)	δ(NH)
1196sh	1177	1195sh	1177	1197sh	1180	1194sh	1178	1194sh	1178	1195sh	1179	1195vw	1179	δ(nap), Ph(9a, 1), δ(SOH), ν(CS)		δ(OH)	δ(Me)	
		1175sh	1165											Ph(3, 8b), δ(nap)		δ(OH), ν(CO)		
1173w	1162	1171w	1162	1170m	1163	1173w	1162	1175w	1162	1175sh	1163	1173w	1164	δ(nap), Ph(9a, 8a)		δ(OH)	δ(Me)	
1151sh	1140	1152sh	1135	1151sh	1137	1155vs	1139	1155sh	1139	1158m	1140	1153sh	1140	Ph(9a, 1), δ(nap), ν(CN)	δ(NH ₂ Sc)	δ(OH)	δ(Me)	
1138vs	1127	1138vs	1126	1135vs	1126	1138vs	1127	1134s	1128	1136s	1129	1136vs	1129	δ(SOH), ν(CS), Ph(9a, 1), ν(CN)		δ(OH)		
	1123		1123		1123		1123		1123		1124		1124	δ(SOH), δ(nap), Ph(9a, 1), ν(CN)				
1121sh	1109	1124sh	1110	1110sh	1111	1115sh	1110	1111	1116sh	1112	1112sh	1112	1112	δ(nap), δ(SOH), ν(CN), Ph(9a, 1)	δ(NH ₂ Ro)	δ(OH)		
	1092		1092		1092		1091	1092	1102vw	1092		1092	1092	δ(SOH), ν(SO), δ(nap), Ph(18b)		δ(OH)		

vw – very weak, w – weak, m – medium, s – strong, vs – very strong, sh – shoulder δ – bend, ν – stretch, sc – scissor, ro – rocking ^a in order of decreasing contribution.

Table 3.19 Experimental ($\lambda_{\text{ex}} = 514.5$ nm in water) and calculated Raman band positions (cm^{-1}) of H-Span with differences from other R-Span dyes.

Experimental							Calculated						
H-Span	$\Delta(\text{NH}_2)$	$\Delta(\text{OH})$	$\Delta(\text{OMe})$	$\Delta(\text{NHAc})$	$\Delta(\text{Br})$	$\Delta(\text{CN})$	H-Span	$\Delta(\text{NH}_2)$	$\Delta(\text{OH})$	$\Delta(\text{OMe})$	$\Delta(\text{NHAc})$	$\Delta(\text{Br})$	$\Delta(\text{CN})$
1613	0	+1	+1	+1	0	+1	1606	-2	-2	-1	-2	0	-1
1596	-2	-3	+5	+5	+3	+5	1594	+9	+9	+6	+7	-13	+4
1579	-8	-1	-7	0	-4	-2	1588	-1	0	0	-1	0	0
1552	-	-	-	-	-8	+2	1552	-1	-1	-1	-1	-1	-1
1495	+5	+5	+12	+9	-16	+4	1500	0	+1	0	+5	-5	+1
1480	0	0	0	0	-24	+4	1478	+6	+6	+8	+6	-2	+4
1455	+3	+9	+4	+5	-2	+6	1467	-4	0	-2	-1	-7	+1
1446	-10	0	-11	+6	-	-	1439	-6	-9	-16	-	-	-
1423	-5	+8	-8	+12	+7	+8	1423	-4	-3	-7	-1	+1	+1
1397	+1	+8	+8	+8	+3	+4	1404	-3	-1	0	+2	+2	+2
1376	+1	+3	+3	+3	+3	+2	1377	0	0	+1	0	+2	+2
1366	-	-	-	-	-	-	-	-	-	-	-	-	-
1355	0	-3	-3	0	-4	-3	1335	-1	+1	+1	0	+1	+2
1335	-	-	-	-4	-	-	-	-	-	-	-	-	-
1324	-1	-1	-3	0	+1	+8	1320	+1	+1	+1	0	+2	+3
-	-	-	-	-	-	-	1316	-	-	0	0	0	+1
1305	+10	+6	+4	2	0	0	1310	-1	0	-1	-1	+1	+1
1291	+16	+14	+10	-	-16	-	1296	-6	-5	-11	-	+6	+7
1269	+4	+1	+2	+2	-	-	-	-	-	-	-	-	-
1241	+2	-11	+1	-7	-4	-9	1228	+9	+3	+5	+1	+2	+1
1217	+13	-1	+10	-	0	0	1211	+11	+6	+8	+5	+2	+1
1208	-2	-8	-5	-5	-6	-7	1189	+6	+3	+5	+5	+2	+1
1194	+2	+1	+3	0	+1	+1	1178	-1	-1	+2	0	+1	+1
1175	-2	-4	-5	-2	0	-2	1162	0	0	+1	0	+1	+2
1155	-4	-3	-4	0	+3	-2	1139	+1	-4	-2	0	+1	+1
1134	+4	+4	+1	+4	+2	+2	1128	-1	-2	-2	-1	+1	+1
							1123	0	0	0	0	+1	+1
							1111	-2	-1	0	-1	+1	+1
							1092	0	0	0	-1	0	0

Raman spectra for R-Span dyes in water recorded with 413.1 and 350.6 nm excitation as shown in Figures 3.43 and 3.44 with their band positions reported in Table 3.20. For all dyes 350.6 nm may have been the expected to be the ideal conditions, chosen to be in resonance with the main absorption band, however experimentally this reduced the resolution of the recorded spectra and the power was limited to ≤ 5 mW. It was not possible to observe any signal above noise for H-Span with 350.6 nm excitation, and there was low confidence in data recorded for Br-Span and CN-Span due to impurity, and these results are not presented.

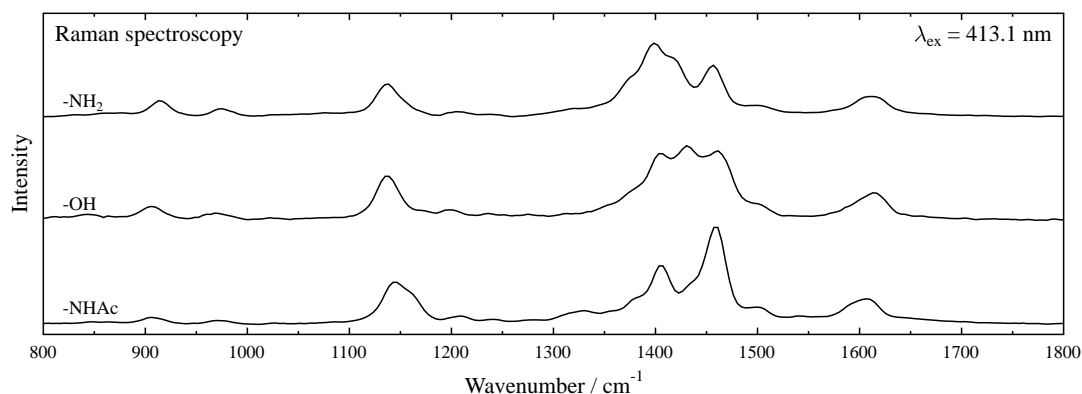


Figure 3.43 Experimental Raman spectra of NH₂-, OH- and NHAc-Span (4×10^{-4} mol dm⁻³) in water with 413.1 nm excitation.

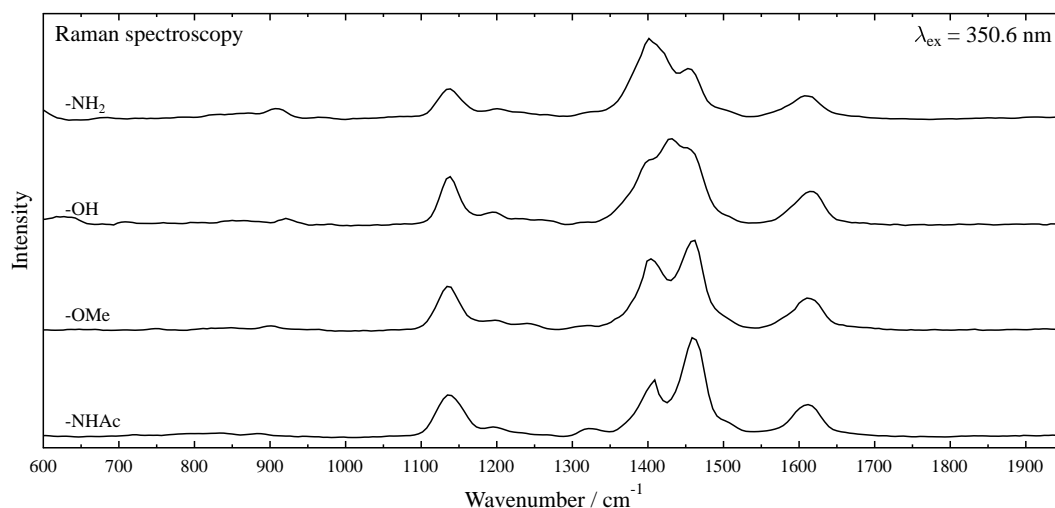


Figure 3.44 Experimental Raman spectra of NH₂-, OH-, OMe- and NHAc-Span (4×10^{-4} mol dm⁻³) in water with 350.6 nm excitation.

Table 3.20 Raman band positions (cm^{-1}) of NH_2 -, OH-, OMe-, NHAc-Span in water with 413.1 or 350.6 nm excitation.

-NH ₂		-OH		-OMe	-NHAc	
413.1 nm	350.6 nm	413.1 nm	350.6 nm	350.6 nm	413.1 nm	350.6 nm
1613m	1609m	1615m	1616m	1611m	1608m	1611m
		1593sh	1590sh		1591sh	1589sh
1573sh	1579sh	1573vw	1577sh	1574sh		
					1540vw	1546vw
1505w	1503sh	1505w	1508w	1506w	1504w	1501sh
1457s	1456s	1460s	1457s	1459vs	1460vs	1460vs
1419sh	1419sh	1431s	1430s		1440sh	
1399vs	1400vs	1405s	1399s	1403vs	1405s	1408s
1372sh	1378sh	1377sh	1380sh	1379sh	1371sh	1376sh
		1352sh	1356sh	1358sh	1355w	
					1329w	
1321w	1322w	1321sh		1320w		1317m
		1312vw	1311vw	1307vw		
1272vw	1274vw	1273vw	1272vw		1273vw	1273vw
1241w	1242vw			1247w	1242vw	1241vs
	1231vw	1232vw	1232vw			
1208w	1201m	1199m	1197m	1201w	1198m	1201m
1167sh	1167vw	1170w				
				1154sh	1155sh	
1135s	1135s	1137vs	1137vs	1136s	1138s	1139s
1077vw	1077vw					
					1015vw	
973w	976vw				972m	
	960vw					958w
914w				901w	886vw	891w

vw – very weak, w – weak, m – medium, s – strong, vs – very strong, sh – shoulder

In summary, the Raman spectra of NH_2 -, OH-, OMe- and NHAc-Span recorded with 413.1 and 350.6 nm show the same spectral features as the corresponding Raman spectrum recorded with 514.5 nm excitation, with the observable difference between them being the spectral resolution. This shows that despite the data recorded being off-resonance Raman, the spectrum recorded with 514.5 nm excitation is true of the dye and not from any impurities. The similarity of the Raman spectra recorded between these R-Span dyes and their corresponding calculated normal mode vibrations further supports the assignments made to OH-Span.

3.2.4.4 OH-Span pH dependence

As already established, there is a pH dependence for OH-Span (Section 3.2.1.1), and Raman spectra of O⁻-Span were recorded in the same way as for the R-Span dyes series. Figure 3.45 shows the UV/Vis absorption spectrum of O⁻-Span as made up at pH 12 at $4 \times 10^{-4} \text{ mol dm}^{-3}$ showing the excitation wavelengths of 514.5, 413.1 and 350.6 nm. Raman spectra of O⁻-Span are shown in Figure 3.46 with band positions given in Table 3.21 together with differences in Raman band positions from those of OH-Span as shown in equation 3.5; unfortunately DFT calculations on O⁻-Span failed to optimise to a stable structure so a calculated Raman spectrum is not available for comparison.

$$\Delta(\text{OH}) = \nu(\text{O}^-) - \nu(\text{OH}) \quad (3.5)$$

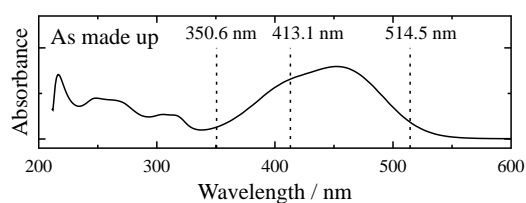


Figure 3.45 UV/Vis absorption spectrum of O⁻-Span ($4 \times 10^{-4} \text{ mol dm}^{-3}$) in water at pH 12; dashed lines show Raman excitation wavelengths.

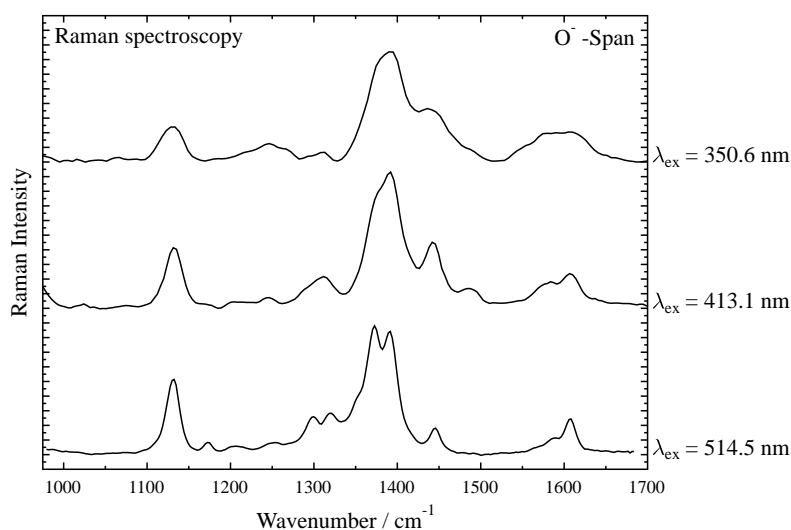


Figure 3.46 Experimental Raman spectra of O⁻-Span ($4 \times 10^{-4} \text{ mol dm}^{-3}$) in water at pH 12 with 350.6, 413.1 and 514.5 nm excitation.

Table 3.21 Experimental Raman band positions (cm^{-1}) of O^- -Span in water on 514.5, 413.1 and 350.6 nm excitation, together with differenced (Δ) from H and OH-Span at 514.5 nm.

514.5 nm		$\Delta(\text{H})$	$\Delta(\text{OH})$	413.1 nm		350.6 nm	
1607	m	-5	-7	1607	m	1607	m
1592	w	-4	-1	1588	m	1589	m
1572	sh	-7	-6	1570	sh	1577	m
1562	sh	-10	-	1560	sh	1552	sh
1525	vw	-	-	1530	vw		
1491	vw	-5	-9	1493	vw	1492	sh
				1486	w		
1479	vw	-1	-1				
				1458	sh		
1445	m	-1	-19	1443	s	1441	s
1411	sh	-11	-				
1391	vs	-8	-14	1391	vs	1392	vs
1373	vs	-3	-6	1372	sh	1372	sh
1351	sh	-4	-1	1351	sh	1351	sh
1340	sh	+5	-				
1319	m	-5	-2	1319	m	1311	w
1300	m	-5	-5	1296	sh	1291	m
1276	w	-7	+8	1280	sh	1268	sh
1254	w	-	-	1245	w	1246	w
1247	w	+6	-				
				1214	w		
1207	w	-1	+7	1206	w	1208	w
1173	w	-2	-2	1172	vw	1179	vw
1146	sh	-11	-9	1149	sh	1144	sh
1131	s	-3	-7	1133	s	1131	s
1109	sh	-	-	1110	sh		
				1071	vw	1065	vw
				967	m	966	w
				931	m		
						905	m

- either no match or low confidence in comparison

The general trend is that upon deprotonation there are small shifts of the bands to lower wavenumber (Table 3.21) suggesting that the phenyl ring has become more quinoidal and the $\text{N}=\text{N}$ bond weakens as shown in Figure 3.47. The largest downshifts are observed in the region of $1350 - 1500 \text{ cm}^{-1}$ consistent with an effect across the whole molecule.

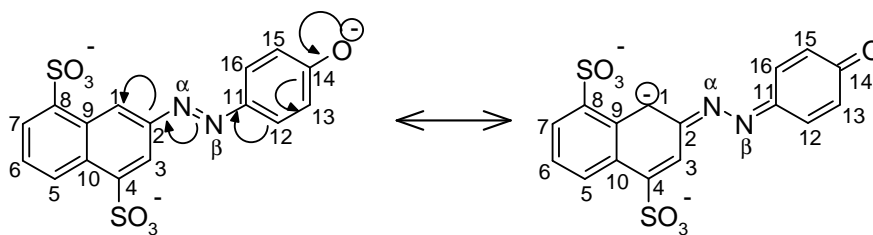


Figure 3.47 Resonance structure of the O⁻-Span.

Again there is a good comparison between the Raman spectra of O⁻-Span to those of the rest of the R-Span dyes. O⁻-Span shows larger band shifts to lower wavenumber from H-Span than any other R substituent, and O⁻ is more electron donating than any other R group studied here ($\sigma_p = -0.81$).⁹⁵

3.2.5 Protonation of NH₂-Span

It has been established that NH₂-Span has a pK_a of 2.88 (Section 3.2.1.1), and the identity of the protonated species (P-NH₂-Span) was studied due to the ambiguity of the literature on protonated aminoazobenzenes; both experimental and computational data are presented here.

3.2.5.1 UV/Visible absorption spectroscopy

Figure 3.48 shows the UV/Visible absorption spectra of NH₂-Span and P-NH₂-Span. Bands for P-NH₂-Span are observed at $\lambda = 328$ nm ($\epsilon = 20100$ dm³ mol⁻¹ cm⁻¹) and $\lambda = 504$ nm ($\epsilon = 9000$ mol⁻¹ cm⁻¹), compared to that of NH₂-Span at $\lambda = 398$ nm ($\epsilon = 22400$ dm³ mol⁻¹ cm⁻¹). Figure 3.49 shows the possible protonation of NH₂-Span, with protonation at the azo linkage to give the azonium tautomer (az) or at the terminal group to give the ammonium tautomer (am) and create the R substituent NH₃⁺ ($\sigma_p = +0.60$).⁹⁵ The band at 328 nm could be assigned to the am tautomer resembling an electron withdrawing R group and the band at 501 nm to the az tautomer, which would be consistent with assignments reported for 4-aminazobenzene, where bands at 320 and 500 nm have been attributed to the am and az forms, respectively.⁴¹

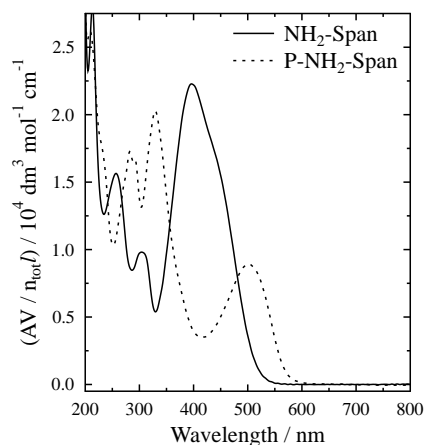


Figure 3.48 UV/Visible absorption spectra of aqueous $\text{NH}_2\text{-Span}$ and $\text{P-NH}_2\text{-Span}$ at $5 \times 10^{-5} \text{ mol dm}^{-3}$ at ca. pH 7 and pH 1.8, respectively.

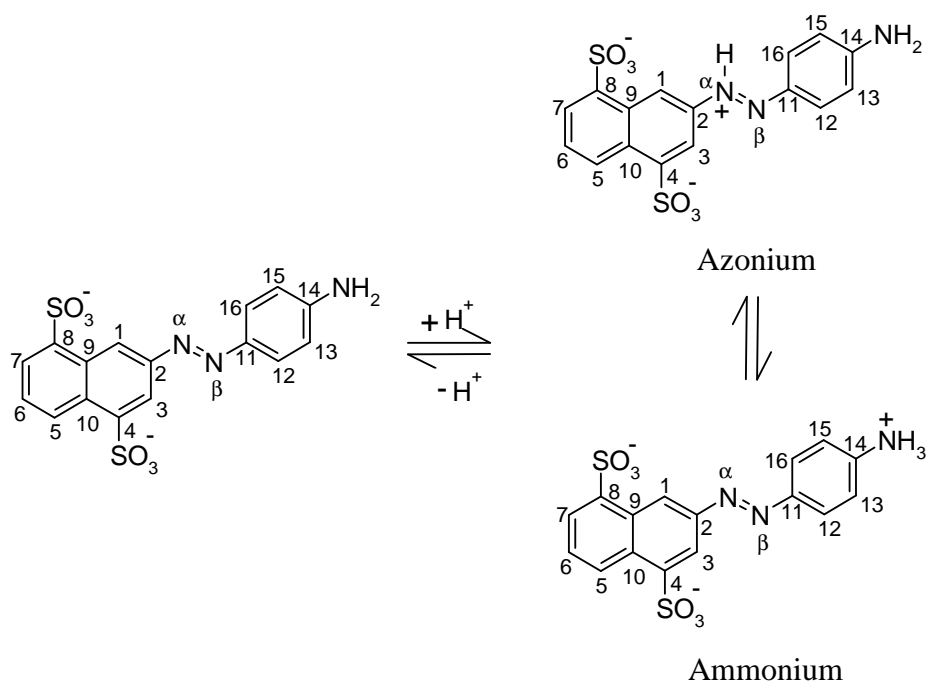


Figure 3.49 Possible protonation scheme for $\text{NH}_2\text{-Span}$.

3.2.5.2 DFT calculations

The optimised structures, a pictorial representation of the charge on each atom, the HOMO-1, HOMO, LUMO and LUMO+1 and the changes in electron density on excitation to the first three excited states for the az and am tautomers of $\text{P-NH}_2\text{-Span}$ are shown in Figures 3.50-3.53; their calculated bond lengths, angles and Mulliken atomic charges on each atom together with differences from $\text{NH}_2\text{-Span}$ calculated using

equation 3.6 are given in Table 3.22. Table 3.23 gives the calculated orbital contributions, transition energies, wavelengths, and oscillator strengths for the first, second and third excited states (a full table is given in Appendix A1.6).

$$\Delta(\text{Az or Am}) = \text{Value}(\text{Az or Am}) - \text{Value}(\text{NH}_2) \quad (3.6)$$

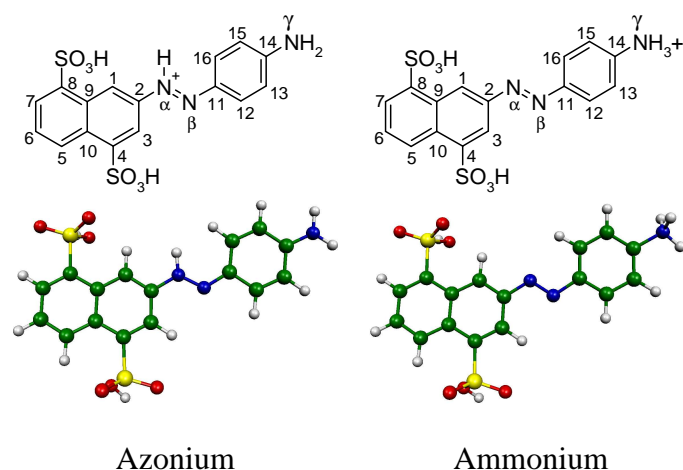


Figure 3.50 Optimised structures of the azonium and ammonium tautomer of P-NH₂-Span dyes along with the numbering system. (*Original in colour*)

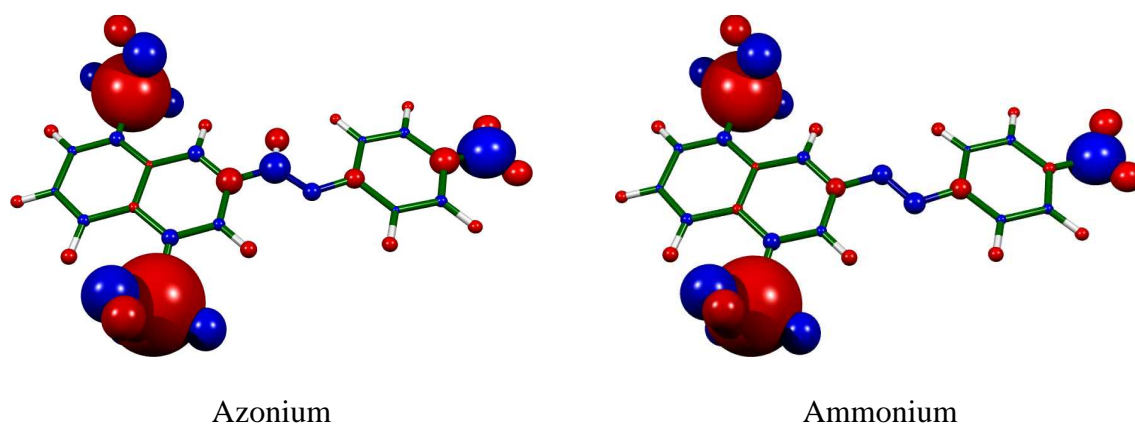


Figure 3.51 Pictorial representation of Mulliken atomic charges of the azonium and ammonium tautomers of P-NH₂-Span; red regions represent positive charge, blue regions represent negative charge; 1 Å radius per unit charge. (*Original in colour*)

Table 3.22 Calculated bond lengths (Å), bond angles (°) and Mulliken atomic charges (q) of the azonium and ammonium tautomer of P-azo NH₂-Span; differences (ΔAz and ΔAm / 0.001 Å) given for bond lengths, bond angles (°) and atomic charges (q / 0.001) from the values of NH₂-Span.

Bond	Bond length				Angle	Bond angle				Atomic charge				
	Az	ΔAz	Am	ΔAm		Az	ΔAz	Am	ΔAm	A	Az	ΔAz	Am	ΔAm
C1-C2	1.380	-1	1.380	+3	C1-C2-C3	121.8	+1.9	120.7	+0.8	C1	-0.256	-32	-0.204	+20
C2-C3	1.414	-7	1.421	0	C2-C3-C4	118.2	-1.3	119.0	-0.6	C2	0.392	+98	0.284	-10
C3-C4	1.370	0	1.368	-2	C3-C4-C10	122.9	+0.3	122.7	0.0	C3	-0.179	-16	-0.156	+7
C4-C10	1.434	-2	1.438	+2	C4-C10-C9	117.3	+0.4	117.4	+0.4	C4	-0.240	+13	-0.244	+9
C10-C5	1.419	0	1.419	0	C10-C9-C1	119.3	-0.2	119.1	-0.3	C5	-0.178	+7	-0.182	+2
C5-C6	1.377	0	1.377	0	C9-C1-C2	120.4	-1.0	121.1	-0.3	C6	-0.122	+12	-0.123	+11
C6-C7	1.411	+2	1.411	+2	C10-C5-C6	120.7	-0.3	120.8	-0.2	C7	-0.153	+7	-0.157	+3
C7-C8	1.377	-1	1.377	-1	C5-C6-C7	120.8	+0.2	120.9	+0.3	C8	-0.236	+7	-0.233	+10
C8-C9	1.431	0	1.431	0	C6-C7-C8	119.8	+0.1	119.7	0.0	C9	0.131	+10	0.134	-7
C9-C10	1.440	+1	1.439	0	C7-C8-C9	121.6	-0.5	121.7	-0.4	C10	0.157	+10	0.157	+10
C1-C9	1.416	-2	1.417	-1	C8-C9-C10	117.8	+0.6	117.8	+0.5	C11	0.291	+26	0.304	+39
C1-H1	1.084	+2	1.082	0	C9-C10-C5	119.3	-0.1	119.2	-0.2	C12	-0.121	+20	-0.146	-5
C7-H7	1.084	0	1.084	0	C1-C2-Nα	117.4	+1.2	115.2	-1.0	C13	-0.171	+15	-0.151	+35
C6-H6	1.085	0	1.085	0	Nα-C2-C3	120.7	-3.1	124.1	+0.2	C14	0.407	+58	0.183	-166
C5-H5	1.082	0	1.082	0	C2-C3-H3	120.9	+1.8	120.0	+0.9	C15	-0.170	+19	-0.158	+31
C4-S4	1.806	+8	1.802	+4	H3-C3-C4	120.9	-0.4	121.0	-0.3	C16	-0.135	-9	-0.12	+6
C3-H3	1.083	0	1.083	0	C3-C4-S4	115.0	-0.8	115.5	-0.2	H1	0.213	+14	0.212	+13
C8-S8	1.800	+5	1.800	+5	C4-C10-C5	123.5	-0.1	123.4	-0.2	H3	0.227	+18	0.214	+5
S8-O	1.457	-6	1.455	-8	C10-C5-H5	119.8	+0.2	119.9	+0.2	H5	0.215	+18	0.21	+13
S8-O	1.457	+2	1.459	+4	H5-C5-C6	119.5	+0.1	119.4	0.0	H6	0.186	+30	0.179	+23
S8-O	1.645	-4	1.656	+7	C5-C6-H6	119.9	-0.1	119.8	-0.1	H7	0.215	+22	0.209	+16
S4-O	1.641	-9	1.644	-6	H6-C6-C7	119.3	-0.1	119.3	-0.1	H12	0.203	+53	0.199	+49
S4-O	1.453	-3	1.454	-2	C6-C7-H7	120.6	-0.2	120.7	-0.1	H13	0.183	+54	0.178	+49
S4-O	1.460	-1	1.461	0	H7-C7-C8	119.6	0.0	119.7	+0.1	H15	0.183	+51	0.177	+45
C2-Nα	1.409	-4	1.404	-9	C7-C8-S8	116.6	+0.6	116.4	+0.4	H16	0.173	+7	0.208	+42
Nα-Nβ	1.284	+16	1.263	-5	S8-C8-C9	121.8	-0.1	121.9	-0.1	Nα	-0.461	-133	-0.294	+34
Nα-H	1.024	-	-	-	C8-C9-C1	122.9	-0.4	123.1	-0.3	Hα	0.369	-	-	-
Nβ-C11	1.349	-50	1.418	+19	C9-C1-H1	119.4	-1.6	120.9	-0.1	Nβ	-0.261	+51	-0.308	+4
C11-C16	1.432	+21	1.408	-3	H1-C1-C2	120.2	+2.6	118.0	+0.4	S4	1.266	+9	1.262	+5
C16-C15	1.367	-14	1.388	+7	C2-Nα-Hα	115.7	-	-	-	S8	1.271	+6	1.268	+13
C15-C14	1.433	+18	1.394	-21	Hα-Nα-Nβ	121.5	-	-	-	O4	-0.519	+2	-0.511	+10
C14-C13	1.424	+15	1.389	-20	C2-Nα-Nβ	122.8	+8.8	115.3	+1.3	O4	-0.492	+12	-0.497	+7
C13-C12	1.396	+11	1.393	+8	Nα-Nβ-C11	121.8	+6.3	113.5	-2.1	O4	-0.651	+2	-0.649	+4
C12-C11	1.428	+22	1.401	-5	Nβ-C11-C16	127.2	+2.1	124.5	-0.6	O8	-0.488	+20	-0.512	-4
C12-H12	1.085	-1	1.085	-1	C11-C16-C15	120.5	+0.1	120.1	-0.3	O8	-0.505	+10	-0.502	+13
C13-H13	1.086	-1	1.087	0	C16-C15-C14	120.7	-0.1	118.3	-2.5	O8	-0.646	+9	-0.652	+3
C15-H15	1.086	-2	1.088	0	C15-C14-C13	119.1	+0.3	123.2	+4.4	Nγ	-0.776	+15	-0.794	-3
C16-H16	1.087	+3	1.084	0	C14-C13-C12	119.9	-0.2	117.9	-2.3	Hγa	0.381	+46	0.434	+99
C14-Nγ	1.342	-39	1.498	+117	C13-C12-C11	121.4	+0.4	120.5	-0.5	Hγb	0.382	+48	0.435	+101
Nγ-Hγa	1.011	0	1.028	+17	C12-C11-C16	118.4	-0.5	120.1	+1.2	Hγc	-	-	0.438	-
Nγ-Hγb	1.011	0	1.029	+18	S4-C4-C10	122.1	+0.5	121.8	+0.1					
Nγ-Hγc	-	-	1.030	-	C11-C16-H16	117.6	-1.2	119.0	+0.2					
					H16-C16-C15	117.9	-3.0	121.0	+0.1					
					C16-C15-H15	120.2	+0.2	120.2	+0.2					
					H15-C15-C14	119.5	-0.1	121.5	+2.3					
					C14-C13-H13	119.5	0.0	121.8	+2.2					
					H13-C13-C12	120.5	+0.3	120.3	0.0					
					C13-C12-H12	120.9	+0.1	120.9	0.0					
					H12-C12-C11	117.7	-0.1	118.6	+0.5					
					C12-C11-Nβ	114.4	-1.6	115.4	-0.6					
					C15-C14-Nγ	120.0	-0.1	118.2	-2.1					
					Nγ-C14-C13	120.9	+3.6	118.6	-2.3					
					C14-Nγ-Hγa	121.7	+4.4	111.7	-5.5					
					C14-Nγ-Hγb	121.5	+7.8	111.1	-6.2					
					Hγa-Nγ-Hγb	116.9	+3.2	107.1	-6.5					
					Hγa-Nγ-Hγc	-	-	107.2	-					
					Hγb-Nγ-Hγc	-	-	107.2	-					
					C14-Nγ-Hγc	-	-	112.2	-					

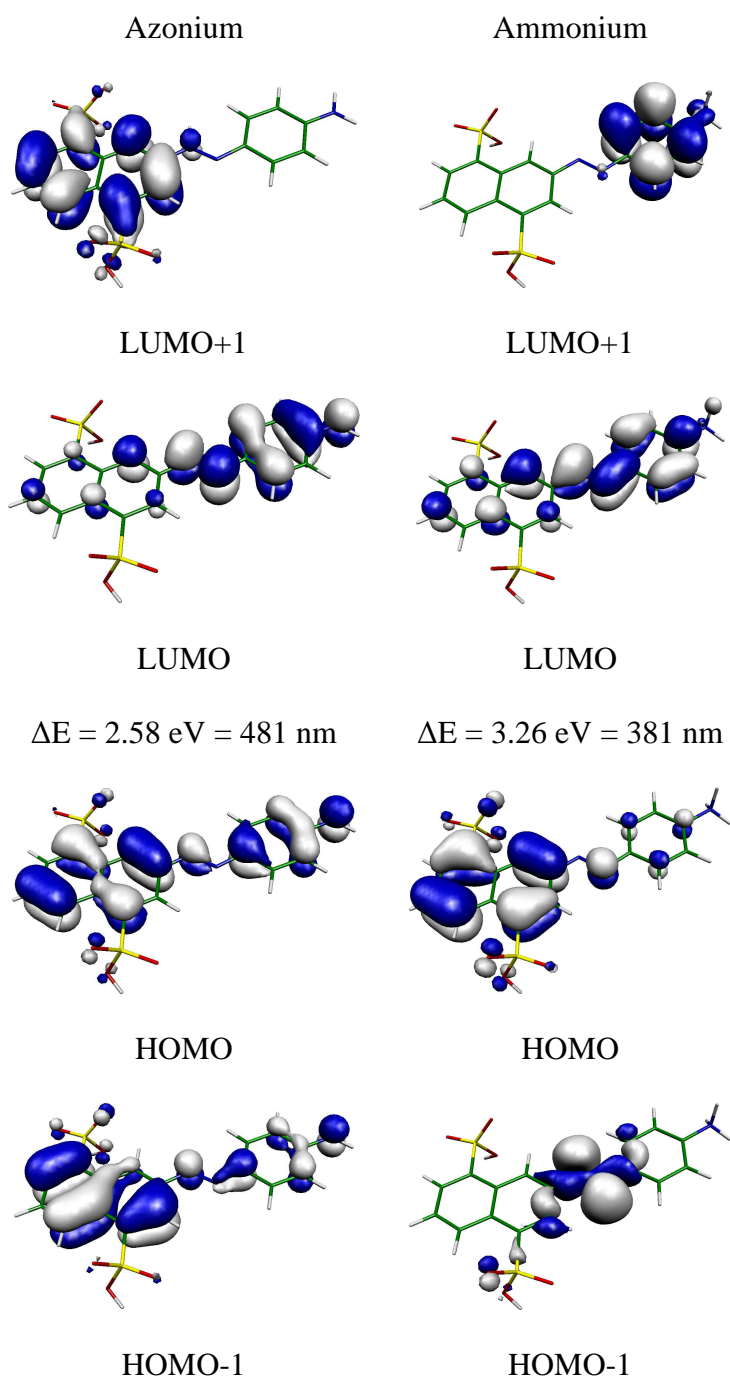


Figure 3.52 Calculated HOMO-1, HOMO, LUMO, LUMO+1 and energy differences (LUMO-HOMO) for azonium and ammonium tautomers of P-NH₂-Span. (*Original in colour*)

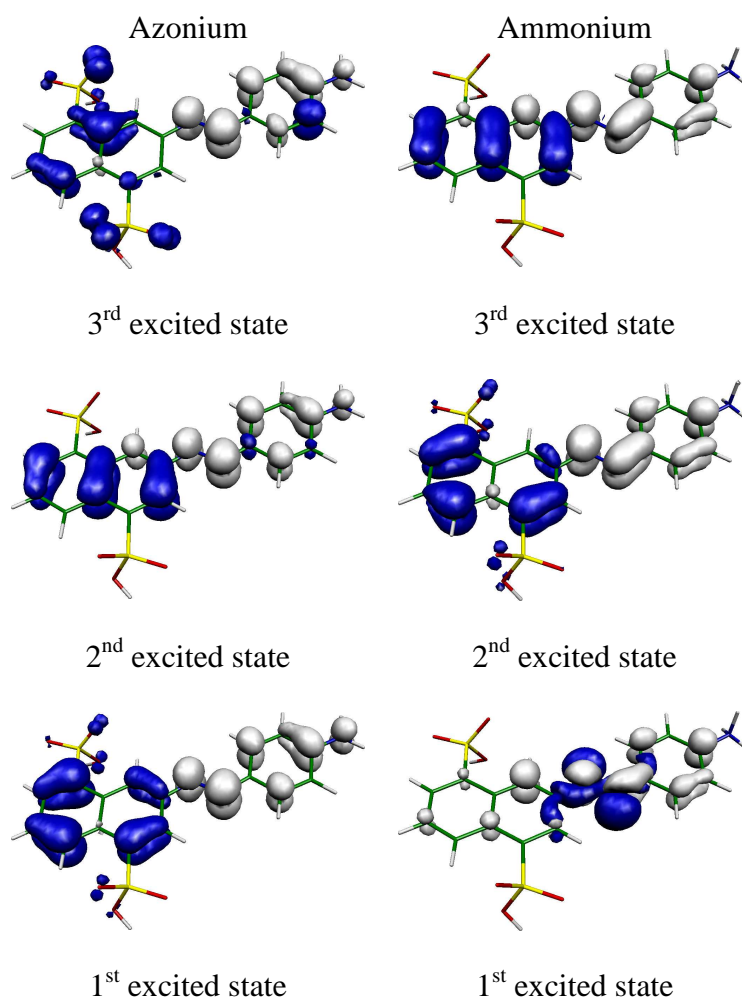


Figure 3.53 Calculated changes in electron density on excitation to the third (top), second (middle) and first (bottom) excited states for the azonium (left) and ammonium (right) tautomer of P-NH₂-Span. Blue and white regions represent a decrease and increase in electron density on excitation, respectively. (*Original in colour*)

Table 3.23 Calculated transition energies (E), wavelengths (λ), and oscillator strengths (f) for the first, second and third excited states of the azonium and ammonium tautomer of P-NH₂-Span.

Excited state	Orbital contribution	E / eV	λ / nm	f
<u>Azonium</u>				
1 st	HOMO-1 \rightarrow LUMO	2.45	506	0.4126
2 nd	HOMO \rightarrow LUMO	2.85	434	0.6552
	HOMO-2 \rightarrow LUMO			
3 rd	HOMO-1 \rightarrow LUMO	3.57	347	0.1254
	HOMO \rightarrow LUMO			
	HOMO-6 \rightarrow LUMO			
	HOMO-5 \rightarrow LUMO			
	HOMO-4 \rightarrow LUMO			
	HOMO-3 \rightarrow LUMO			
	HOMO-2 \rightarrow LUMO			
<u>Ammonium</u>				
1 st	HOMO-1 \rightarrow LUMO	2.40	517	0.0005
2 nd	HOMO-2 \rightarrow LUMO	2.91	426	0.2335
	HOMO \rightarrow LUMO			
3 rd	HOMO-2 \rightarrow LUMO	3.38	366	0.6150
	HOMO-1 \rightarrow LUMO			

The calculated structure of the az tautomer is lower in energy by ca. 100 kJ mol⁻¹ than that of the am tautomer, for isolated molecules. The bond lengths predicted are consistent with the structure of each tautomer and with calculations reported for the tautomers of protonated 4-aminoazobenzene.⁴¹ In comparison with NH₂-Span, which already has a partially quinoidal phenyl ring, calculations indicate that the az tautomer has longer C11–C16, C15–C14, C14–C13, C12–C11 and C13–C12 bonds and a shorter C16–C15 bond indicating that the phenyl ring is more quinoidal but distorted. On the other hand, in comparison with NH₂-Span the calculated am tautomer has shorter C11–C16, C15–C14, C14–C13, and C12–C11 bonds and longer C16–C15 and C13–C12 bonds, indicating that it might be less quinoidal and that the difference between the two tautomers is significant. The changes about the azo linkage are also notable; in comparison with NH₂-Span, the N–N bond is longer in the az tautomer, indicating less π character in the bond due to protonation at N α , whereas the am tautomer N–N bond length has decreased to a distance of 1.263 Å, which is comparable to that for the electron withdrawing dyes CN- and Br-Span. The C2–N α and C11–N β bonds both shorten for the az tautomer, again consistent with the positive charge being localised

across the whole dye as shown in the resonance structure in Figure 3.54. In the case of the am tautomer the C11–N β is longer but consistent with values from the electron withdrawing dyes CN- and Br-Span, whereas the C2–N α bond is significantly shorter.

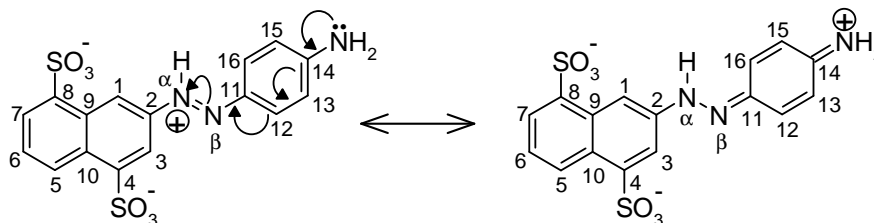


Figure 3.54 Resonance structure of the azonium tautomer of P-NH₂-Span.

As expected there are also significant changes in calculated bond angles around the azo linkage and phenyl ring upon protonation of NH₂-Span, however they offer no further insight on the site of protonation. The dihedral angles do give an indicator as to the planarity and conjugation. Both the calculated az and am structures were planar with the C-N=N-C dihedral of 179.1 ° and 178.9 °, respectively. Compared to NH₂-Span, the calculated az tautomer is highly conjugated: the C14–N γ –H and H–N γ –H bond angles are 121.4 ° and 116.9 °, respectively, indicating that the nitrogen atom is tending highly towards a sp² hybridised model as supported by an essentially planar R group in which the nitrogen is bent out of plane by only 0.1 ° and the hydrogens are bent out of plane of the plane by only 0.2 ° in the opposite direction.

Considering that calculated P-NH₂-Span has an overall charge of +1 it is unsurprising that there is a decrease in calculated electron density across the majority of atoms in both tautomeric forms. In comparison with NH₂-Span for the az tautomer there is a significant decrease in electron density at C2 and N β accompanying an increase and decrease in electron density at C11 and N α , respectively. In comparison with NH₂-Span for the am tautomer there are significant decreases and increases in electron density at H γ and C14, respectively, while that of N γ remains relatively unchanged.

Transitions between the orbitals HOMO-1, HOMO, LUMO and LUMO+1 indicate the movement of electron density (Figure 3.52), for example, transitions from HOMO to LUMO shift electron density from the naphthyl ring to the phenyl ring and azo linkage. A transition from HOMO to LUMO+1 results in a greater shift in electron density from the phenyl ring to the naphthyl ring for the az tautomer and a greater shift in electron density from the naphthyl ring to the phenyl ring for the am tautomer. What is shown nicely is that the calculated transition between HOMO to LUMO is 481 and 381 nm for the az and am tautomers, respectively.

By the time-dependent DFT method, for the am tautomer, the oscillator strengths indicate that the transition to the first excited state is disallowed and the orbitals show it is an $n \rightarrow \pi^*$ transition, whereas the transition to the second and third excited state are allowed and are $\pi \rightarrow \pi^*$ transitions (Figure 3.53). For the az tautomer, the oscillator strengths indicate that the transition to the first, second and third excited states are allowed and the orbitals indicate show that they are $\pi \rightarrow \pi^*$ transitions (Figure 3.53). The calculations may be compared with the experimental data, where the calculated wavelength for the transition to the first excited state of the az tautomer at 506 nm is similar to the experimental band for P-NH₂-Span at 504 nm, and where the calculated wavelength to the third excited state of the am tautomer giving a slightly allowed transition at 366 nm could match with the strong experimental band for P-NH₂-Span at 328 nm. These calculated transitions are also consistent with calculations performed on protonated 4-aminoazobenzene.⁴¹

3.2.5.3 NMR spectroscopy

1D and 2D (HSQC and HMBC) ^1H and ^{13}C NMR spectra of P-NH₂-Span were recorded in D₂O/DCI at pD 2.0 (both ca. 3×10^{-3} mol dm⁻³). The experimental spectra are shown in Figures 3.55 and 3.56, along with the calculated spectra of the az and am tautomers of P-NH₂-Span with NMR assignments given in Table 3.24 (using the same numbering system for NH₂-Span in Figure 3.22). Table 3.25 shows the experimental (P-NH₂-Span) and calculated (az and am) differences from NH₂-Span ^1H and ^{13}C positions as calculated using equation 3.7, where a negative change represents an upfield shift from NH₂-Span.

$$\Delta(\text{NH}_2-) = \delta(\text{P-NH}_2\text{- or az or am}) - \delta(\text{NH}_2-) \quad (3.7)$$

Any tautomerism that is occurring will result in the resonances being observed as an average of those from the tautomers due to it being fast on the NMR timescale. In comparison with NH₂-Span, the experimental ^1H NMR positions for P-NH₂-Span have shifted upfield for protons 1 > 5 > 3 > 6 > 12/16 > 7 and downfield for protons 13/15, and the experimental ^{13}C NMR positions have shifted upfield (>1 ppm) for carbons 11 > 2 >> 1 > 3 and downfield (>1 ppm) for carbons 13/15 > 12/16. The position of C14 has remained unchanged.

In comparison with NH₂-Span the calculated ^1H NMR shifts of the am tautomer of P-NH₂-Span shows that the resonances of all protons except 3 are shifted downfield, with those attached to the phenyl ring shifted significantly downfield. This can be expected due to the highly electron withdrawing substituent NH₃⁺. The same comparison for the az tautomer shows upfield shifts for protons 5, 6, 7 and 13/15 and downfield shifts for protons 1, 3 and 12/16.

Comparing the calculated ^{13}C NMR shifts of the tautomers of P-NH₂-Span shows a clearer indication as to the possible site of protonation. Significant differences between az and am forms are shown at C2 (128.9 vs 142.0 ppm), C11 (128.5 vs 149.1 ppm) and C14 (149.2 vs 115.9 ppm). The comparison with the experimental data is more difficult, firstly due to the weak signals making the assignments more speculative and secondly

with the calculation being performed in the gas phase. However the experimental data compared more clearly with those from the calculated az tautomer which can be seen when comparing the calculated az form and the experimental data at C2 (128.9 vs 128.6 ppm), C11 (128.5 vs 127.6 ppm) and C14 (149.2 vs 144.5 ppm).

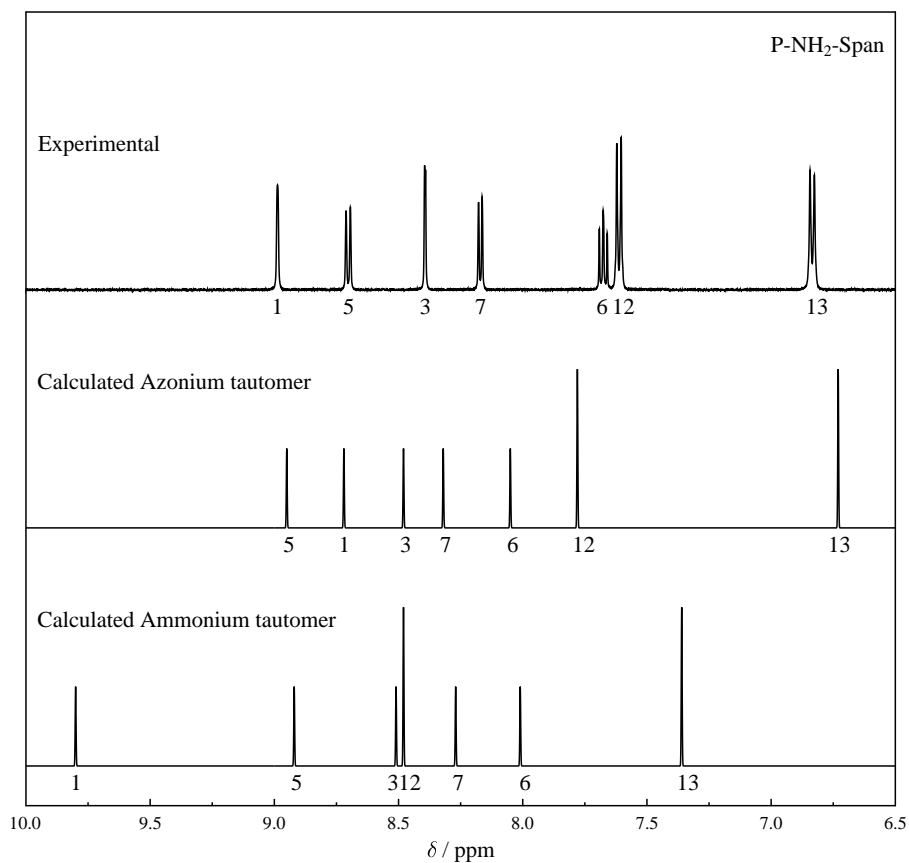


Figure 3.55 Aromatic region ¹H NMR spectra of P-NH₂-Span in D₂O/DCI at pD 2.0 (top), the calculated az tautomer (middle) and am tautomer (bottom) of P-NH₂-Span.

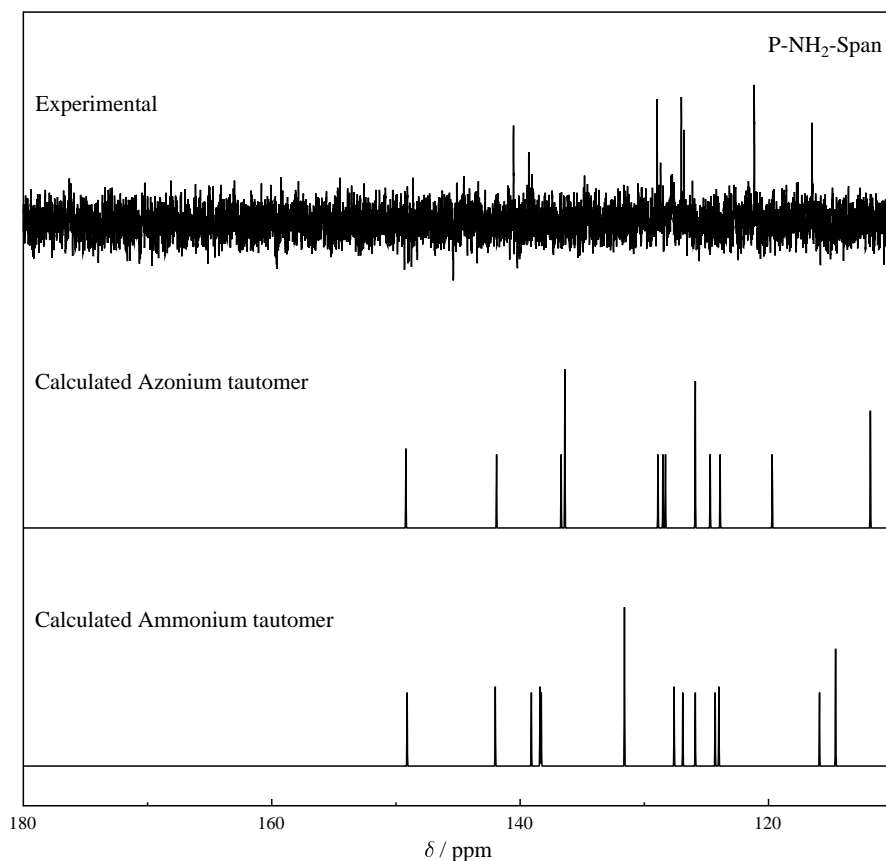


Figure 3.56 ^{13}C NMR spectra of P-NH₂-Span D₂O/DCl at pD 2.0 (top), the calculated az tautomer (middle) and am tautomer (bottom) of P-NH₂-Span.

Table 3.24 ^1H and ^{13}C NMR chemical shifts (ppm) of P-NH₂-Span in D₂O at pD 2.0 and calculated ^1H and ^{13}C NMR chemical shifts (ppm) of the az and am tautomer.

Atom	Experimental		Calculated				
	$^1\text{H}^a$	^{13}C	Azonium		Ammonium		
			^1H	^{13}C	^1H	^{13}C	
1	8.98	1 s -	122.7	8.72	119.7	9.80	138.4
2			128.6		128.9		142.0
3	8.39	1 d 2.0	116.5	8.48	108.9	8.51	108.5
4			140.5		141.9		139.1
5	8.70	1 d 9.0	128.9	8.95	128.3	8.92	127.6
6	7.68	1 t 8.0	126.8	8.05	125.9	8.01	125.9
7	8.17	1 d 8.0	127.0	8.32	125.9	8.27	124.3
8			139.1		136.7		138.3
9			128.9		123.9		124.0
10			129.0		124.7		126.9
11			127.6		128.5		149.1
12/16	7.61	2 d 9.0	127.7	7.87 ¹² , 7.69 ¹⁶	139.7 ¹² , 113.0 ¹⁶	8.52 ¹² , 8.44 ¹⁶	129.9 ¹² , 113.3 ¹⁶
13/15	6.83	2 d 9.0	121.2	6.73 ¹³ , 6.72 ¹⁵	110.5 ¹³ , 113.1 ¹⁵	7.38 ¹³ , 7.34 ¹⁵	115.3 ¹³ , 113.9 ¹⁵
14			144.5		149.2		115.9

^a Integration, multiplicity (s = singlet; d = doublet; t = triplet), splitting (Hz)

Table 3.25 Experimental and calculated ^1H and ^{13}C NMR chemical shifts (δ /ppm) in the aromatic region for NH_2 -Span (NH_2) and P- NH_2 -Span (P); with differences (Δ) given for chemical shifts from the values of NH_2 -Span.

atom	Experimental						Calculated									
	^1H			^{13}C			^1H					^{13}C				
	NH_2	P	ΔP	NH_2	P	ΔP	NH_2	Az	ΔAz	Am	ΔAm	NH_2	Az	ΔAz	Am	ΔAm
1	9.09	8.98	-0.11	125.4	122.7	-2.7	9.18	8.72	-0.46	9.80	+0.62	128.8	119.7	-9.1	138.4	+9.6
2				149.0	128.6	-20.4						143.4	128.9	-14.5	142.0	-1.4
3	8.47	8.39	-0.08	118.4	116.5	-1.9	8.58	8.48	-0.10	8.51	-0.07	112.0	108.9	-3.1	108.5	-3.5
4				140.6	140.5	-0.1						136.6	141.9	+5.3	139.1	+2.5
5	8.79	8.70	-0.09	129.5	128.9	-0.6	8.74	8.95	+0.21	8.92	+0.18	126.9	128.3	+1.4	127.6	+0.7
6	7.72	7.68	-0.04	127.2	126.8	-0.4	7.52	8.05	+0.53	8.01	+0.49	119.2	125.9	+6.7	125.9	+6.7
7	8.20	8.17	-0.03	127.3	127.0	-0.3	7.98	8.32	+0.34	8.27	+0.29	122.2	125.9	+3.7	124.3	+2.1
8				139.9	139.1	-0.8						135.8	136.7	+0.9	138.3	+2.5
9				129.7	128.9	-0.8						124.5	123.9	-0.6	124.0	-0.5
10				129.6	129.0	-0.6						123.3	124.7	+1.4	126.9	+3.6
11				151.9	127.6	-24.3						138.4	128.5	-9.9	149.1	10.7
12/16	7.65	7.61	-0.04	125.5	127.7	+2.2	7.97	7.78	-0.19	8.48	+0.51	121.7	126.4	+4.7	121.6	-0.1
13/15	6.66	6.83	+0.17	115.5	121.2	+7.6	6.37	6.73	+0.36	7.36	+0.99	107.1	111.8	+4.7	114.6	+7.5
14				144.5	144.5	0.0						142.5	149.2	+6.7	115.9	-26.6

3.2.5.4 Raman spectroscopy

Figure 3.57 shows the UV/Vis absorption spectrum of P- NH_2 -Span at pH 2.0 showing the positions of two Raman excitation wavelengths at 514.5 and 350.6 nm. The observed Raman spectra of P- NH_2 -Span presented alongside the calculated Raman spectra of the az and am tautomers are shown in Figure 3.58 with band positions given in Table 3.26. The Raman spectrum recorded with 514.5 nm excitation shows a good match to that of the calculated Raman spectrum of the az tautomer, whereas the Raman spectrum recorded upon 350.6 nm excitation shows a good match to the calculated Raman spectrum of the am tautomer (calculated vibrations are shown in Appendix A1.6). Moreover, the very different profiles observed at these wavelengths are in contrast to the similar profiles observed at the same excitation wavelengths for the R-Span dye series which are present as single species (Figures 3.42 and 3.44). Another interesting observation is that the Raman spectrum recorded upon 350.6 nm excitation has a similar profile to that from NHAc -Span (Figure 3.44), consistent with the electron withdrawing substituent of NH_3^+ being comparable of the least electron donating substituent of NHAc . The Raman spectrum recorded at 514.5 nm has a profile that shows no comparison with any other of the R-Span series, consistent with a dye with different structural features as consistent with the az tautomer of P- NH_2 -Span. Assignments made in Table 3.26 are to both tautomers, consistent with the vibrational work carried out on aminoazobenzenes.⁴¹

Page intentionally left blank

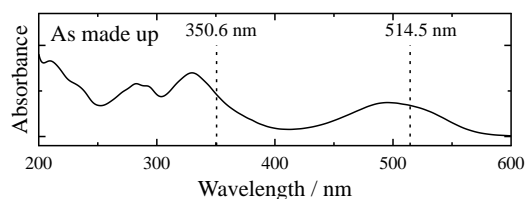


Figure 3.57 UV/Vis absorption spectrum of P-NH₂-Span in water (4×10^{-4} mol dm⁻³) at pH 2.0; dashed line represents Raman excitation wavelength.

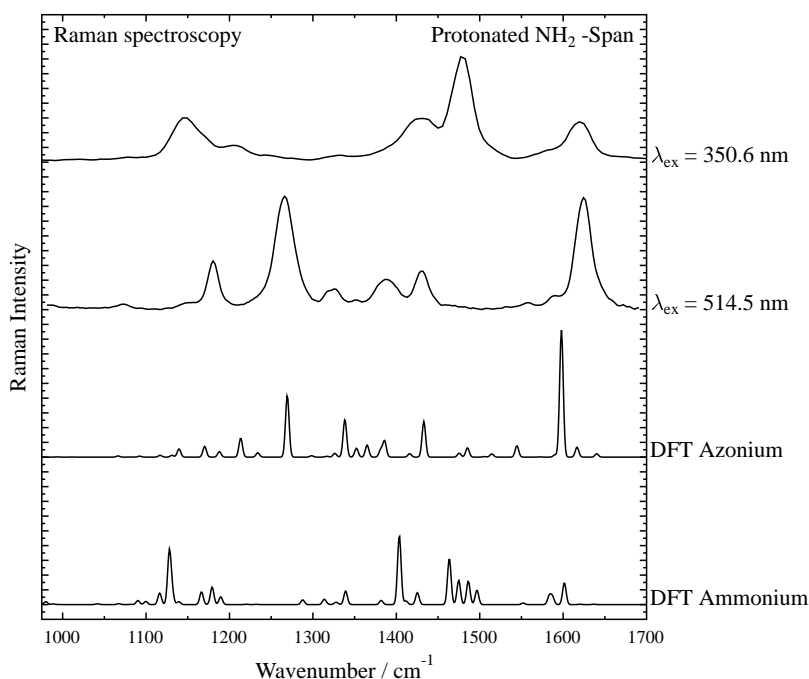


Figure 3.58 Experimental Raman spectra of P-NH₂-Span in water at pH 2.0 with 514.5 and 350.6 nm excitation and calculated Raman spectra of the azonium and ammonium tautomers of P-NH₂-Span.

The protonation of NH₂-Span observed at a pK_a of 2.88 received more attention than first envisaged at the outset, and the studies have shown that the site of protonation is difficult to determine as reported in the literature for substituted 4-aminoazobenzenes.^{70-86,88,100-103} For P-NH₂-Span, the combination of UV/Visible absorption, Raman and NMR spectroscopy along with calculations have shown that a mixture of the ammonium and azonium tautomers can be proposed.

Table 3.26 Experimental Raman band positions (cm^{-1}) of P-NH₂-Span in water, calculated band positions, intensities and matching normal mode assignments for the azonium and ammonium tautomers.

Experimental				Calculated			
514.5 nm	350.6 nm	R	IR	Azonium Description ^b	R	IR	Ammonium Description ^b
1672w	1669w	1640	3	100 $\delta(\text{NH}_2 \text{ Sc}), \nu(\text{CN}), \delta(\text{NH}), \text{Ph}(8a, 9a)$	1636	1	13 $\delta(\text{NH}_3), \text{Ph}(14, 8b)$
1651sh	1652sh	1616	8	20 $\delta(\text{NH}_2 \text{ Sc}), \delta(\text{NH}), \nu(\text{NN}), \text{Ph}(8a, 9a)$	1619	0	17 $\delta(\text{NH}_3)$
1625vs		1598	100	8 $\delta(\text{nap}), \delta(\text{NH})$			
	1618m				1601	31	12 $\delta(\text{nap}), \delta(\text{NN})$
	1598sh				1587	7	4 $\text{Ph}(8a, 9a), \delta(\text{NH}_3), \delta(\text{nap}), \delta(\text{NN})$
1589w		1590	2	14 $\delta(\text{nap}), \nu(\text{CN}), \delta(\text{NH}_2 \text{ Sc}), \text{Ph}(9a, 8a)$			
	1581sh				1583	12	7 $\delta(\text{NH}_3), \text{Ph}(8a, 9a), \delta(\text{NN}), \delta(\text{nap})$
	1565sh				1552	2	0 $\delta(\text{nap})$
1558w		1544	9	37 $\delta(\text{NH}), \delta(\text{nap}), \nu(\text{CN}), \delta(\text{NH}_2 \text{ Ro}), \text{Ph}(14, 8a)$			
1532w		1514	3	0 $\delta(\text{NH}_2), \nu(\text{CN}), \text{Ph}(14, 18a), \delta(\text{NH}), \delta(\text{nap})$			
	1515sh				1497	21	51 $\delta(\text{NH}_3), \text{Ph}(19a, 18a), \delta(\text{NN}), \delta(\text{nap})$
	1503sh				1486	34	9 $\delta(\text{NH}_3), \delta(\text{nap}), \delta(\text{NN}), \text{Ph}(14, 8a)$
	1494sh				1475	34	2 $\delta(\text{NH}_3), \text{Ph}(19a, 18a), \delta(\text{NN}), \delta(\text{nap})$
	1473vs				1464	67	100 $\delta(\text{NH}_3), \text{Ph}(18a, 14), \delta(\text{NN}), \delta(\text{nap})$
1431m	1435s	1433	28	25 $\delta(\text{nap}), \nu(\text{CN}), \nu(\text{NN}), \delta(\text{NH}), \delta(\text{NH}_2), \text{Ph}(8b, 18b)$	1425	17	3 $\delta(\text{nap}), \nu(\text{NN}), \text{Ph}(14, 18b)$
1425sh	1425sh	1416	3	41 $\delta(\text{nap}), \nu(\text{CN}), \nu(\text{NN}), \delta(\text{NH}), \delta(\text{NH}_2), \text{Ph}(1, 18a)$	1404	100	56 $\delta(\text{nap}), \nu(\text{CN}), \text{Ph}(14, 18b) \delta(\text{NH}_3)$
1400sh		1385	12	93 $\delta(\text{NH}), \nu(\text{NN}), \nu(\text{CN}), \delta(\text{nap}), \delta(\text{SOH}), \text{Ph}(1, 18a) \delta(\text{NH}_2)$			
1388m	1388sh	1381	6	44 $\delta(\text{nap}), \delta(\text{NH}), \nu(\text{NN}), \nu(\text{CN}), \text{Ph}(1, 18a), \delta(\text{NH}_2)$	1382	6	1 $\delta(\text{nap}), \nu(\text{NN})$
1374sh	1374sh	1365	9	18 $\text{Ph}(1, 18a), \nu(\text{CN}), \delta(\text{NH}_2), \nu(\text{NN})$			
1351w		1352	7	1 $\delta(\text{NH}_2), \text{Ph}(14, 3), \delta(\text{NH}), \delta(\text{nap})$			
1326w	1333w	1338	30	1 $\delta(\text{nap}), \delta(\text{NH}), \nu(\text{CN}), \text{Ph}(8b, 18a), \delta(\text{NH}_2)$	1339	20	4 $\delta(\text{nap}), \text{Ph}(14, 18b)$
1319sh	1315sh	1326	3	39 $\delta(\text{nap}), \delta(\text{SOH}), \nu(\text{SO}), \delta(\text{NH}), \text{Ph}(19a, 3), \delta(\text{NH}_2 \text{ Ro})$	1314	8	4 $\delta(\text{nap}), \delta(\text{SOH}), \nu(\text{SO}), \delta(\text{NN}), \nu(\text{CN})$
1288sh		1298	1	3			
	1272w				1288	7	2 $\text{Ph}(8b, 3), \delta(\text{NH}_3), \nu(\text{CN}), \delta(\text{nap})$
1266vs		1269	49	1 $\text{Ph}(19a, 18a), \nu(\text{NN}), \nu(\text{CN}), \delta(\text{NH}), \delta(\text{NH}_2), \delta(\text{nap})$			
1240sh	1243w	1234	4	3 $\delta(\text{nap}), \delta(\text{NH}), \text{Ph}(1, 18a), \delta(\text{NH}_2), \delta(\text{SOH})$	1232	1	17 $\delta(\text{nap}), \nu(\text{CN}), \text{Ph}(1, 18b), \nu(\text{CS})$
	1217sh				1190	11	3 $\delta(\text{nap}), \nu(\text{CN}), \text{Ph}(1, 9a), \delta(\text{SOH})$
1200sh	1206w	1213	15	2 $\delta(\text{nap}), \nu(\text{CN}), \delta(\text{NH}), \text{Ph}(1, 18b)$	1179	25	16 $\delta(\text{nap}), \nu(\text{CN}), \delta(\text{NH}), \text{Ph}(18b, 1)$
1187sh	1192sh	1187	5	1 $\delta(\text{nap}), \delta(\text{SOH}), \delta(\text{NH}), \text{Ph}(9a)$	1166	18	20 $\delta(\text{nap}), \nu(\text{CN}), \text{Ph}(1, 19a)$
1181s		1170	0	26 $\delta(\text{nap}), \delta(\text{NH}), \text{Ph}(9a, 1), \delta(\text{NH}_2), \delta(\text{NH})$			
	1169sh				1131	16	70 $\delta(\text{SOH}), \text{Ph}(1, 9a), \delta(\text{nap}), \nu(\text{CN})$
1151w		1140	6	18 $\delta(\text{nap}), \delta(\text{SOH}), \nu(\text{SO}), \nu(\text{CN}), \delta(\text{NH}_2), \delta(\text{NH}), \text{Ph}(18b)$			
	1146s				1128	75	43 $\text{Ph}(1, 9a), \nu(\text{CN}), \delta(\text{nap}), \delta(\text{SOH})$
	1127sh				1116	17	41 $\delta(\text{SOH}), \nu(\text{CS}), \nu(\text{SO}), \delta(\text{nap}), \nu(\text{CN}) \text{Ph}(19a, 18b)$
1073vw	1079vw	1092	1	11 $\delta(\text{SOH}), \nu(\text{CS}), \nu(\text{SO}), \delta(\text{nap})$	1092	6	29 $\delta(\text{SOH}), \nu(\text{CS}), \nu(\text{SO}), \delta(\text{nap}), \nu(\text{CN}) \text{Ph}(19a, 18b)$

vw – very weak, w – weak, m – medium, s – strong, vs – very strong, sh - shoulder δ – bend, ν – stretch, sc – scissor, ro – rocking, ^aintensity of peak scaled to 100, ^bin order of decreasing contribution.

3.2.6 Summary

This summary of the R-Span dyes considers the substituent's effect on their structures using Hammett σ_p substituent constants.

The easiest way to compare the dyes in the R-Span series is by considering them in terms of their substituent R by comparing their properties versus Hammett constants σ_p , as given for selected data in Table 3.27 and shown in Figures 3.60-3.62. In general, the plots highlight the discrepancies between experimental and calculated data, but also show that there are some trends with σ_p . The UV/Visible absorption wavelength and ^1H NMR shifts from H 13/15 show a clear correlation between the results and σ_p , but in the case of the ^{13}C NMR shifts and calculated Mulliken atomic charges the trends are less clear.

As is consistent with azobenzene-type molecules introduced in section 3.1.2.3, there is relatively little effect on the UV/Visible absorption upon addition of the electron-accepting groups Br and CN in the phenyl *para* position, compared to H, which is pale yellow in colour. Addition of electron donating groups results in a more significant shift in the absorption band to longer wavelength, with OMe and OH all giving rise to a more intense yellow colour whereas NH_2 gives rise to an orange colour, but duller due to a broad absorption band. The greater electron-donating effect of the NH_2 substituent stabilises its excited state compared to that of H. This is shown in its resonance form given in Figure 3.59; hence absorption occurs at a longer wavelength, as also mirrored by O⁻-Span.

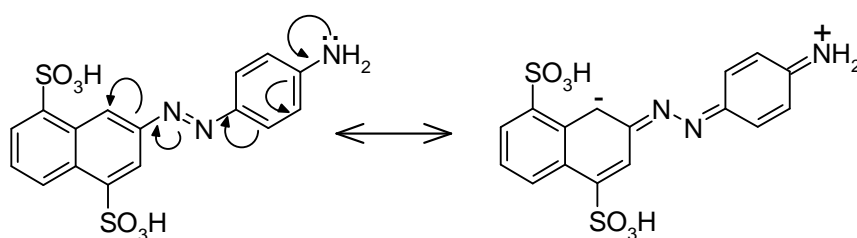


Figure 3.59 Resonance structure of NH_2 -Span.

The substituent attached to C14 has a large impact on the ^1H NMR positions for H13/15, as can be seen in Table 3.27; on going from H-Span to O⁻-Span a greater electron donor, the general trend is that the resonances move upfield due to shielding. Trends between ^{13}C NMR positions are more difficult to compare, and effects on C14 can arise from steric as well as electronic interactions. The steric effect is nicely shown by the C–R bond length; compared to H-Span (1.087 Å), all the other R-Span dyes have significantly longer bonds (>0.3 Å), with Br being at the extreme of 1.906 Å, and the calculated vibrations of Br-Span indicate that Br very much sits as an anchor group (Appendix A1.6), being a much more massive atom. From H- to NH₂-Span, the calculated C2–N α length shortens by 0.003 Å, N α –N β lengthens by 0.007 Å and C11–N β shortens by 0.015 Å, showing an increase in charge character and that the phenyl ring and the azo linkage becomes closer together. The magnitude of the calculated bond lengths are consistent with a DFT calculation reported for an R-Span dye, where R = chlorotriazine group as shown in Figure 3.63, where N=N, C2–N α and C11–N β are 1.263, 1.419 and 1.408 Å, respectively.³³

Table 3.27 Selected experimental (λ_{\max} / nm, ϵ / 10^4 dm³ mol⁻¹ cm⁻¹, δ / ppm) and calculated (λ_{\max} / nm, Charge / q, Bond length / Å) structural features of R-Span dye series related to their Hammett *para* substituent constants.

Substituent	O ⁻	-NH ₂	-OH	-OMe	-NHAc	-H	-Br	-CN
σ_p	-0.88	-0.66	-0.37	-0.27	0.00	0.00	+0.23	+0.66
<i>Absorbance</i>								
$\lambda_{\max}(\text{Exp})$	452	398	364	363	362	333	341	337
$\epsilon(\text{Exp})$	2.11	2.24	2.16	2.31	2.43	1.78	2.31	2.40
$\lambda_{\max}(\text{Calc } \pi \text{ to } \pi^*)$	-	389	382	365	355	333	347	342
$\lambda_{\max}(\text{Calc S2})$	-	407	379	388	392	353	371	366
<i>NMR (Exp)</i>								
¹ H $\delta_{\text{H13/15}}$	6.57	6.69	7.01	7.02	7.21	7.54	7.41	7.48
¹³ C $\delta_{\text{C13/15}}$	-	115.5	-	114.1	119.1	129.0	131.8	132.9
¹³ C δ_{C14}	-	152.7	-	161.0	147.4	131.7	149.7	118.3
<i>NMR (Calc)</i>								
¹ H $\delta_{\text{H13/15}}$	-	6.37	6.62	6.75	7.62	7.48	7.39	7.67
¹³ C $\delta_{\text{C13/15}}$	-	107.1	107.8	108.1	111.3	122.4	126.1	127.6
¹³ C δ_{C14}	-	142.5	152.6	155.5	137.0	126.8	142.3	112.6
<i>Charge (Calc)</i>								
C2	-	0.294	0.292	0.292	0.291	0.289	0.289	0.289
C11	-	0.265	0.266	0.268	0.278	0.266	0.272	0.284
C14	-	0.349	0.369	0.393	0.375	-0.114	0.093	0.142
<i>Bond length (Calc)</i>								
C14-R ^a	-	1.381	1.360	1.356	1.403	1.087	1.906	1.433
N α -N β	-	1.268	1.264	1.265	1.264	1.261	1.262	1.261
C2-N α	-	1.413	1.414	1.414	1.415	1.416	1.415	1.415
C11-N β	-	1.399	1.405	1.405	1.406	1.414	1.413	1.416

^a substituent of the phenyl ring

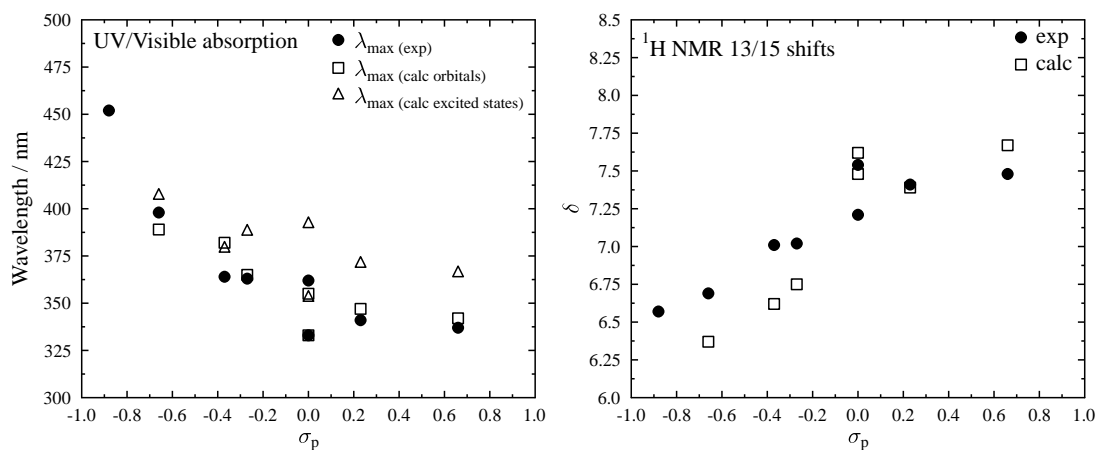


Figure 3.60 Left: Experimental and calculated wavelength (λ_{\max}) vs *para* Hammett constant σ_p for the R-Span dye series, Right: Experimental and calculated ^1H NMR position of H13/15 vs *para* Hammett constant σ_p for the R-Span dye series.

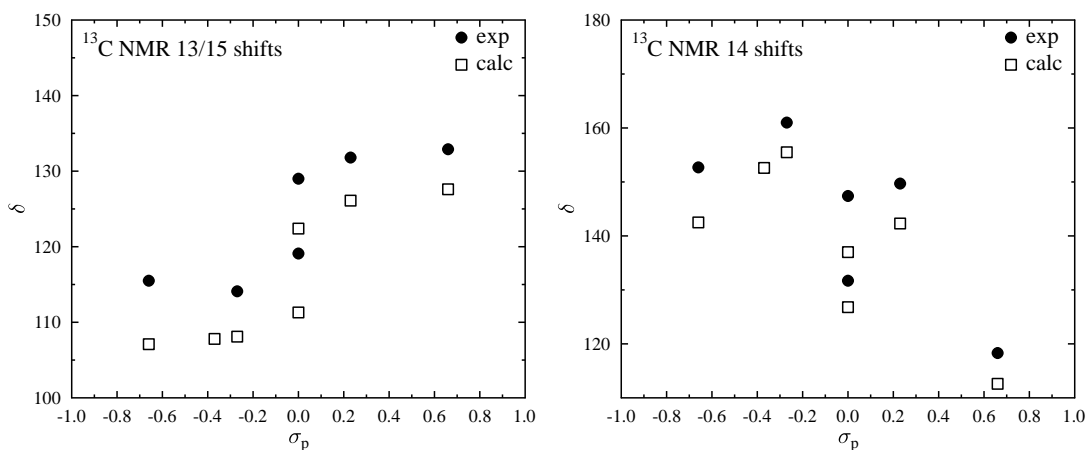


Figure 3.61 Experimental and calculated ^{13}C NMR position of C13/15 (left) and C14 (right) vs *para* Hammett constant σ_p for the R-Span dye series.

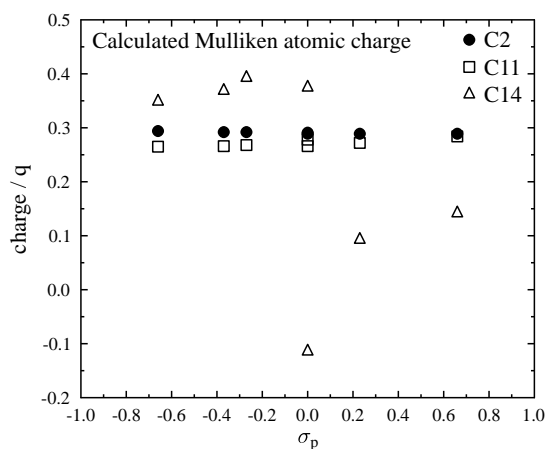


Figure 3.62 Calculated Mulliken atomic charge of C2, C11 and C14 vs *para* Hammett constant σ_p for the R-Span dye series.

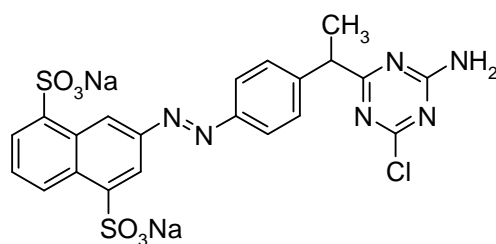


Figure 3.63 Structure of chlorotriazine-Span dye.

Picking out any trends in the Raman band positions appears difficult because there are no easily identifiable bands which track across the R-Span dye series, although small shifts are observable as well as intensity changes. However, there are three distinct spectral regions in their Raman spectra as shown in Figure 3.64. The calculations indicate that there are significant contributions to the vibrational modes across a significant number of atoms and the assignments lead to the interpretation that region 1 ($1100 - 1175 \text{ cm}^{-1}$) can be assigned to predominantly sulfonate motion as seen in other sulfonated dyes,^{104,105} region 2 ($1300 - 1500 \text{ cm}^{-1}$) to predominantly N=N motion in addition to phenyl and naphthyl motion and region 3 ($1550 - 1650 \text{ cm}^{-1}$) to mainly phenyl and naphthyl motion.^{31,38,41,59,106-108}

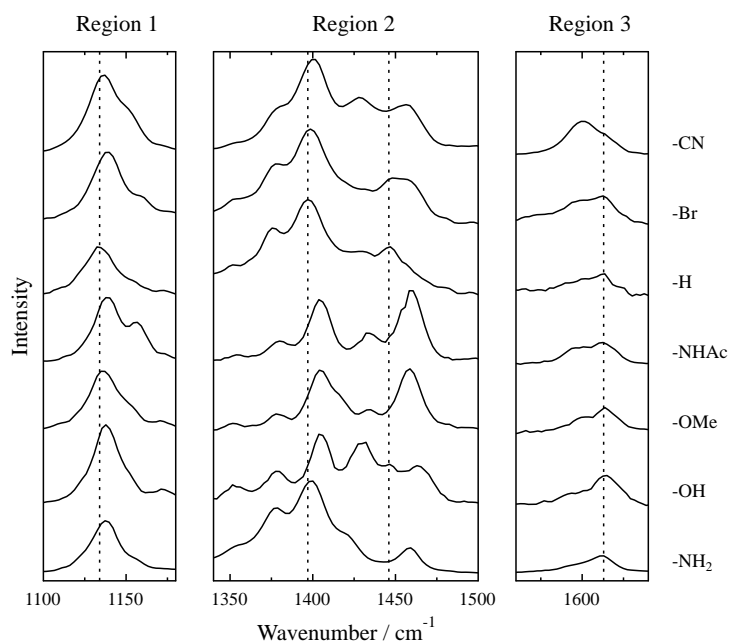


Figure 3.64 Experimental Raman spectra of R-Span ($4 \times 10^{-4} \text{ mol dm}^{-3}$) in water with 514.5 nm excitation focused on the three main regions of interest, dashed lines indicate the position of H-Span.

3.3 Conclusions

A combination of UV/Visible absorption, NMR, Raman and IR spectroscopic techniques, together with DFT calculations were used to study the structural properties of a set of true azo R-Span dyes predominately in water in which the R substituent is the only difference between them.

The combination of techniques used has shown that the R-Span dyes are planar, exist as the *trans* form and as monomers, consistent with the sulfonate groups in these small dyes preventing aggregation. All the R-Span dyes will exhibit protonation at the azo linkage; the pK_a values were < 2 apart from NH₂-Span which was found to have a pK_a of 2.88. A combination of UV/Visible, NMR and Raman spectroscopy together with DFT calculations suggests that protonation in NH₂-Span occurs as a fast equilibrium at both the azo linkage and the terminal amine. OH-Span was observed to have a pK_a of 7.98 due to deprotonation of the OH substituent on the phenyl ring, introducing another substituent into the dyes series, O⁻-Span.

The electron donating and withdrawing capacity of the R substituent influences the electronic properties of the dye affecting the nature of the bonding within the dyes, although this is not a large effect as the vibrational Raman spectra for all the R-Span dyes are comparable. Changing the substituent on the phenyl ring to either electron donating or withdrawing shifts the main absorption band to a longer wavelength than that of H-Span at 333 nm indicating stabilisation of the excited state relative to the ground state.

In general there are good matching trends between the experimental data and those calculated from the DFT optimised structures for the R-Span dyes, particularly in making vibrational assignments. The resonance model provided by the Hammett σ_p substituent constants has provided a useful way of considering the data reported in this chapter, where structural properties have generally followed the electronic properties of the R substituent.

3.4 References

1. Olivieri, A. C.; Wilson, R. B.; Paul, I. C.; Curtin, D. Y. *J. Am. Chem. Soc.* **1989**, *111*, 5525-5532.
2. Jala, W. H.; Lu, L. K.; Albers, K. E.; Gleason, W. B.; Richardson, T. I.; Lovrien, R. E.; Sudbeck, E. A. *Acta Crystallogr., Sect. B* **1994**, *50*, 684-694.
3. Ojala, W. H.; Sudbeck, E. A.; Lu, L. K.; Richardson, T. I.; Lovrien, R. E.; Gleason, W. B. *J. Am. Chem. Soc.* **1996**, *118*, 2131-2142.
4. Malone, J. F.; Andrews, S. J.; Bullock, J. F.; Docherty, R. *Dyes Pigm.* **1996**, *30*, 183-200.
5. Park, K. M.; Yoon, I.; Lee, S. S.; Choi, G.; Lee, J. S. *Dyes Pigm.* **2002**, *54*, 155-161.
6. Kocaokutgen, H.; Gur, M.; Soylu, M. S.; Lonneck, P. *Dyes Pigm.* **2005**, *67*, 99-103.
7. Maciejewska, D.; Wolska, I.; Kowalska, V. *J. Mol. Struct.* **2004**, *693*, 27-34.
8. Michalski, J.; Kucharska, E.; Wandas, M.; Hanuza, J.; Waskowska, A.; Maczka, M.; Talik, Z.; Olejniczak, S.; Potrzebowski, M. *J. Mol. Struct.* **2005**, *744*, 377-392.
9. Yang, W.; You, X. L.; Zhong, Y.; Zhang, D. C. *Dyes Pigm.* **2007**, *73*, 317-321.
10. Kennedy, A. R.; Kirkhouse, J. B. A.; McCarney, K. M.; Puissegur, O.; Smith, W. E.; Staunton, E.; Teat, S. J.; Cherryman, J. C.; James, R. *Chem. Eur. J.* **2004**, *10*, 4606-4615.
11. Kennedy, A. R.; Hughes, M. P.; Monaghan, M. L.; Staunton, E.; Teat, S. J.; Smith, W. E. *J. Chem. Soc., Dalton Trans.* **2001**, *14*, 2199-2205.
12. McGeorge, G.; Harris, R. K.; Batsanov, A. S.; Churakov, A. V.; Chippendale, A. M.; Bullock, J. F.; Gan, Z. H. *J. Phys. Chem. A* **1998**, *102*, 3505-3513.
13. Kennedy, A. R.; Kirkhouse, J. B. A.; Whyte, L. *Inorg. Chem.* **2006**, *45*, 2965-2971.
14. Abbott, L. C.; Batchelor, S. N.; Jansen, L.; Oakes, J.; Lindsay Smith, J. R.; Moore, J. N. *New J. Chem.* **2004**, *28*, 815-821.
15. Abbott, L. C.; Batchelor, S. N.; Oakes, J.; Lindsay Smith, J. R.; Moore, J. N. *J. Phys. Chem. B* **2004**, *108*, 13726-13735.
16. Abbott, L. C.; MacFaul, P.; Jansen, L.; Oakes, J.; Lindsay Smith, J. R.; Moore, J. N. *Dyes Pigm.* **2001**, *48*, 49-56.
17. Hamada, K.; Mitshishi, M.; Ohira, M.; Miyazaki, K. *J. Phys. Chem.* **1993**, *97*, 4926-4929.
18. Neumann, B.; Huber, K.; Pollmann, P. *Phys. Chem. Chem. Phys.* **2000**, *2*, 3687-3695.

19. Kunanandam, S. PhD Thesis, University of York, 2004.
20. Hamada, K.; Fujita, M.; Mitsuishi, M. *J. Chem. Soc., Faraday Trans.* **1990**, *86*, 4031-4035.
21. Monahan, A. R.; Germano, N. J.; Blossey, D. F. *J. Phys. Chem.* **1971**, *75*, 1227-1233.
22. Monahan, A.R.; Blossey, D. F. *J. Phys. Chem.* **1970**, *74*, 4014-4021.
23. Hamada, K.; Take, S.; Iijima, T.; Amiya, S. *J. Chem. Soc., Faraday Trans. 1.* **1986**, *82*, 3141-3148.
24. Lyčka, A. *Dyes Pigm.* **1999**, *43*, 27-32.
25. Lyčka, A.; Vrba, Z.; Vrba, M. *Dyes Pigm.* **2000**, *47*, 45-51.
26. Cataliotti, R. S.; Murgia, S. M.; Paliani, G.; Poletti, A.; Zgierski, M. Z. *J. Raman Spectrosc.* **1985**, *16*, 251-257.
27. Barker, I. K.; Fawcett, V.; Long, D. A. *J. Raman Spectrosc.* **1987**, *18*, 71-75.
28. Biswas, N.; Umaphathy, S. *J. Phys. Chem. A.* **2000**, *104*, 2734-2745.
29. Biancalana, A.; Campani, E.; Gorini, G.; Masetti, G.; Quaglia, M. *J. Raman Spectrosc.* **1992**, *23*, 155-160.
30. Atkinson, D. PhD Thesis, University of York, 2007.
31. Abbott, L. C.; Batchelor, S. N.; Oakes, J.; Gilbert, B. C.; Whitwood, A. C.; Lindsay Smith, J. R.; Moore, J. N. *J. Phys. Chem. A.* **2005**, *109*, 2894-2905.
32. Rau, H. *Angew. Chem. Int. Edit. Engl.* **1973**, *12*, 224-235.
33. Tait, K. M.; Parkinson, J. A.; Gibson, D. I.; Richardson, P. R.; Ebenzer, W. J.; Hutchings, G. H.; Jones, A. C. *Photochem. Photobiol. Sci.*, **2007**, *6*, 1010-1018.
34. Kojima, M.; Nebashi, S.; Ogawa, K.; Kurita, N. *J. Phys. Org. Chem.* **2005**, *18*, 994-1000.
35. Tecklenburg, M. M. J.; Kosnak, D.J.; Bhatnager, A.; Mohanty, D. K. *J. Raman Spectrosc.* **1997**, *28*, 755-763.
36. Armstrong, D. R.; Clarkson, J.; Smith, W. E. *J. Phys. Chem.* **1995**, *99*, 17825-17831.
37. Bredereck, K.; Schumacher, C. *Dyes Pigm.* **1993**, *21*, 23-43.
38. Dines, T. J.; MacGregor, L. S.; Rochester, C. H.; *J. Raman Spectrosc.* **2007**, *38*, 832-840.
39. Morley, J. O.; Guy, O. J.; Charlton, M. H. *J. Phys. Chem. A.* **2004**, *108*, 2894-2905.
40. Jacquemin, D.; Perpéte, E. A.; Scuseria, G. E.; Ciofini, I.; Adamo, C. *Chem. Phys. Lett.* **2008**, *465*, 226-229.

41. Matazo, D. R. C.; Ando, R. A.; Borin, A. C.; Santos, P. S. *J. Phys. Chem. A* **2008**, *112*, 4437-4443.
42. Reeves, R. L.; Kaiser, R. S. *J. Phys. Chem.* **1969**, *73*, 2279-2286.
43. Kishimoto, S.; Kitahara, S.; Manabe, O.; Hiyama, H. *J. Org. Chem.* **1978**, *43*, 3882-3886.
44. Cheon, K.; Park, Y. S.; Kazmaier, P. M.; Buncel, E. *Dyes Pigm.* **2002**, *53*, 3-14.
45. Iijima, T.; Jojima, E.; Antonov, L.; Stoyanov, S. T.; Stoyanova, T. *Dyes Pigm.* **1998**, *37*, 81-92.
46. Murakami, K. *Dyes Pigm.* **2002**, *53*, 31-43.
47. Ball, P.; Nicholls, C. H. *Dyes Pigm.* **1982**, *3*, 5-26.
48. Kasha, M. *Rev. Mod. Phys.* **1959**, *31*, 162-169.
49. Kasha, M. *Radiat. Res.* **1963**, *20*, 55-68.
50. Kasha, M. *Molecular Excitons in Small Aggregates in 'Spectroscopy of the Excited State'*. Plenum Press: New York, 1976, 337-361.
51. Rau, H. *Photoisomerization of azobenzenes in 'Photochemistry and photophysics'*. Rabek . J. F. Ed. Volume 2; CRC Press: Boca Raton, 1990, Chapter 4, 119-140.
52. Bouwstra, J. A.; Schouten, A.; Kroon, J. *Acta Crystallogr.* **1983**, *C39*, 1121-1123.
53. Traetteberg, M.; Hilmo, I.; Hagen, K. *J. Mol. Struct.* **1977**, *39*, 231-239.
54. Briquet, L.; Vercauteren, D. P.; Perpete, E. A.; Jacquemin, D. *Chem. Phys. Lett.* **2006**, *417*, 190-195.
55. Kellerer, B.; Brandmul, J.; Hacker, H. H. *J. Indian J. Pure Appl. Phys.* **1971**, *9*, 903-909.
56. Koide, S.; Udagawa, Y.; Mikami, N.; Kaya, K.; Ito, M. *Bull. Chem. Soc. Jpn.* **1972**, *45*, 3542-3543.
57. Biswas, N.; Umapathy, S. *Chem. Phys. Lett.* **1995**, *236*, 24-29.
58. Armstrong, D. R.; Clarkson, J.; Smith, W. E. *J. Phys. Chem.* **1995**, *99*, 17825-17831.
59. Umapathy, S. *J. Phys. Chem. A* **1997**, *101*, 5555-5566.
60. Lednev, I. K.; Ye, T.-Q.; Hester, R. E.; Moore, J. N. *J. Phys. Chem.* **1996**, *100*, 13338-13341.
61. Lednev, I. K.; Ye, T.-Q.; Abbott, L. C.; Hester, R. E.; Moore, J. N. *J. Phys. Chem A* **1998**, *102*, 9161-9166.
62. Wildes, P. D.; Pacifici, J. G.; Irick, G.; Whitten, D. G. *J. Am. Chem. Soc.* **1971**, *93*, 2004-2008.

63. Tait, K. M.; Parkinson, J. A.; Bates, S. P.; Ebenezer, W. J.; Jones, A. C. *J. Photochem. Photobiol., A* **2003**, *154*, 179-188.
64. Christie, R. M. *Colour Chemistry*. RSC Paperbacks: Cambridge, 2001.
65. Krueger, P. J. *Basicity, Hydrogen Bonding and Complex Formation*. John Wiley and Sons: New York, 2003; Volume 1.
66. Klotz, I. M.; Fiess, H. A.; Ho, J. Y. C.; Mellody, M. *J. Am. Chem. Soc.* **1954**, *76*, 5136-5140.
67. Shamsipur, M.; Maddah, B.; Hemmeteenejad, B.; Rouhani, S.; Haghbeen, K.; Alizadeh, K. *Spectrochim. Acta, Part A* **2008**, *70*, 1-6.
68. Dunn, N. J.; Humpries IV, W. H.; Offenbacher, A. R.; King, T. L.; Gray, J. A. *J. Phys. Chem.* **2009**, *113*, 13144-13151.
69. Kuwabara, T.; Shiba, K.; Nakajima, H.; Ozawa, M.; Miyajima, N.; Hosoda, M.; Kuramoto, N.; Suzuki, Y. *J. Phys. Chem. A* **2006**, *110*, 13521-13529.
70. Jaffé, H. H.; Yeh, S. J. *J. Org. Chem.* **1957**, *22*, 1281-1282.
71. Jaffé, H. H.; Gardner, R. W. *J. Am. Chem. Soc.* **1958**, *80*, 319-323.
72. Yeh, S. J.; Jaffé, H. H. *J. Am. Chem. Soc.* **1959**, *81*, 3279-3283.
73. Yeh, S. J.; Jaffé, H. H. *J. Am. Chem. Soc.* **1959**, *81*, 3283-3287.
74. Isaks, M.; Jaffé, H. H. *J. Am. Chem. Soc.* **1964**, *86*, 2209-2213.
75. Jaffé, H. H.; Yeh, S. J.; Gardner, R. W. *J. Mol Spectrosc.* **1958**, *2*, 120-136.
76. Cilento, G.; Miller, E. C.; Miller, J. A. *J. Am. Chem. Soc.* **1956**, *78*, 1718-1722
77. Antonov, L.; Kamada, K.; Nedeltcheva, D.; Ohta, K.; Kamounah, F. S. *J. Photochem. Photobiol., A* **2006**, *181*, 274-282.
78. Stoyanova, S.; Stoyanoz, S.; Antonov, L.; Petrova, V. *Dyes Pigm.* **1996**, *31*, 1-12.
79. Stoyanova, S.; Stoyanoz, S.; Antonov, L.; Petrova, V. *Dyes Pigm.* **1996**, *32*, 171-185.
80. Kuroda, Y.; Lee, H.; Kuwae, A. *J. Phys. Chem.* **1980**, *84*, 3417-3423.
81. Chippendale, A. M.; McGeorge, G.; Harris, R. K.; Brennan, C. M. *Magn. Reson. Chem.* **1999**, *37*, 232-238
82. Machida, K.; Kim, B. K.; Saito, Y.; Igarashi, K.; Uno, T. *Bull. Chem. Soc. Jpn.* **1974**, *47*, 78-83.
83. Uno, T.; Kim, B. K.; Saito, Y.; Machida K. *Spectrochim. Acta Pt. A-Mol. Biomol. Spectrosc.* **1976**, *32*, 1179-1183.
84. Bell, S.; Bisset, A.; Dines, T. J. *J. Raman Spectrosc.* **1998**, *29*, 447-462.
85. Dines, T. J.; MacGregor, L. D.; Rochester, C. H. *Chem. Phys.* **2006**, *322*, 445-458.

86. Liwo, A.; Tempczyk, A.; Widernik, T.; Klentak, T.; Czerminski, J. *J. Chem. Soc., Perkin Trans. 2* **1994**, 2, 3471-3423.
87. Gordon, P. F.; Gregory, P. *Organic Chemistry in Colour*. Springer-Verlag: New York, 1983.
88. Reeves, R. L. *J. Am. Chem. Soc.* **1966**, 88, 2240-2247.
89. Gong, X. D.; Lu, Y. L.; Xiao, H. M.; Chen, K. C.; Titan, H. *Int. J. Quantum Chem.* **2000**, 79, 25-33.
90. Yoshida, K.; Koujiri, T.; Horii, T.; Kubo, Y. *Bull. Chem. Soc. Jpn.* **1990**, 63, 1658-1664.
91. Zhang, A. D.; Qin, J. G. *Supramol. Sci.* **1998**, 5, 573-576.
92. Sanchez, A. M.; deRossi, R. H. *J. Org. Chem.* **1995**, 60, 2974-2976
93. Tait, K. M.; Parkinson, J. A.; Jones, A. C.; Ebenezer, W. J.; Bates, S. P. *Chem. Phys. Lett.* **2003**, 374, 372-380.
94. Magennis, S. W.; Mackay, F. S.; Jones, A. C.; Tait, K. M.; Sadler, P. J. *Chem. Mater.* **2005**, 17, 2059-2062.
95. Hansch, C.; Leo, A.; Taft, R. W. *Chem. Rev.* **1991**, 91, 165-195.
96. CRC Handbook of Chemistry and Physics. 49th ed.; Weast, R. C.; Ed.; The Chemical Rubber Co: Cleveland, 1968.
97. Özen, A. S.; Doruker, P.; Aviyente, V. *J. Phys. Chem. A.* **2007**, 111, 13506-13514.
98. Abbott, L. C.; Feilden, C. J.; Anderton, C. L.; Moore, J. N. *Appl. Spectrosc.* **2003**, 57, 960-969.
99. Okamoto, H.; Inishi, H.; Nakamura, Y.; Kohtani, S.; Nakagaki, R. *Chem. Phys.* **2000**, 260, 193-214.
100. Sawicki, E. *J. Org. Chem.* **1957**, 23, 532-535.
101. Sawicki, E. *J. Org. Chem.* **1957**, 22, 915-919.
102. Sawicki, E. *J. Org. Chem.* **1957**, 22, 621-625.
103. Sawicki, E. *J. Org. Chem.* **1957**, 22, 365-367.
104. Sperline, R. P.; Song, Y.; Freiser, H. *Langmuir* **1994**, 10, 37-44.
105. Bauer, C.; Jacques, P.; Kalt, A. *Chem. Phys. Lett.* **1999**, 307, 397-406.
106. Machida, K.; Lee, H.; Saito, Y.; Uno, T. *J. Raman Spectrosc.* **1978**, 7, 184-187.
107. Armstrong, D. R.; Clarkson, J.; Smith, W. E. *J. Phys. Chem.* **1995**, 99, 17825-17831.
108. Cataliotti, R. S.; Murgia, S. M.; Paliana, G.; Poletti, A. *J. Raman Spectrosc.* **1985**, 16, 251-257.

Chapter 4 Electrochemistry

4.1 Introduction

The introduction to this chapter gives a general literature overview of the electrochemical techniques that have been used to study electron transfer reactions of azo dyes and reported substituent effects. The specific aims of the electrochemical studies of the R-Span dye series conclude this section.

4.1.1 Electrochemical techniques

Cyclic voltammetry (CV),¹⁻¹⁴ spectroelectrochemistry,^{4,9,15} and controlled potential electrolysis (CPE)^{1,6,9,10,16-18} have been used to study electron transfer processes in azo dyes in aqueous solution. CV is used to determine redox potentials, spectroelectrochemistry to observe the spectral changes that accompanying electron transfer processes and CPE to determine the number of electrons transferred during the electron transfer process. Their success has been limited due to solvent windows for measurement of aqueous solutions being restricting. In the case of CV, the main problem with studying aqueous dye solutions is the irreversibility of the electron transfer processes that has meant that signals from the sample are often not observed.

Historically polarography was employed to study electron transfer processes where mercury was used for the working electrode.^{2,14,16-22} In modern electrochemistry, the use of mercury has declined as has this technique. It is now standard to have a three electrode set up, where the working electrode is made of carbon or platinum with the counter electrode made of platinum.^{23,24} The reference electrode against which the potential is measured often consists of a standard hydrogen electrode (SHE)^{1,4,19,25} or Ag/AgCl^{16,20} electrode defined as having potentials of 0.0 V and 0.20 V at 25 °C, respectively. Often electrochemical processes are carried out in buffer solutions to counteract the changes in pH in the solution as a result of proton transfer that occur at the electrodes.²⁶ Without a buffer, the reduction potential shifts to more negative values with increasing pH.²⁶

Where possible, for non-reversible electron transfer processes, various analytical techniques are used to characterise products. These include HPLC,^{9,27} GC,^{1,6} LC-MS,^{9,28} EPR spectroscopy,²⁹ NMR spectroscopy^{4,9,10} and vibrational spectroscopy.^{4,28,30} These analytical techniques have not been commonly used in identifying products from azo dyes, where a lack of using a combination of techniques means that mechanisms may not have been elucidated.

4.1.2 Electron transfer processes

Several electrochemical studies have been carried out on the azo dye, Orange II as shown in Figure 4.1.^{27-29,31}

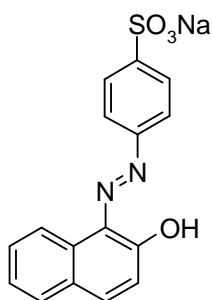


Figure 4.1 Structure of Orange II.

CV has revealed that there is a non-reversible reduction for a sample of Orange II at ca. -0.56 V (vs Ag/AgCl) in pH 4.7 sodium acetate buffer solution;²⁹ oxidation was not observed within the usable solvent window. The chemical reduction of Orange II using zerovalent iron gave a four electron reduction process as shown in Figure 4.2, from which the reduction products, sulfanilic acid and 1-amino-2-naphthol were characterised by mass spectrometry and infrared spectroscopy.²⁸

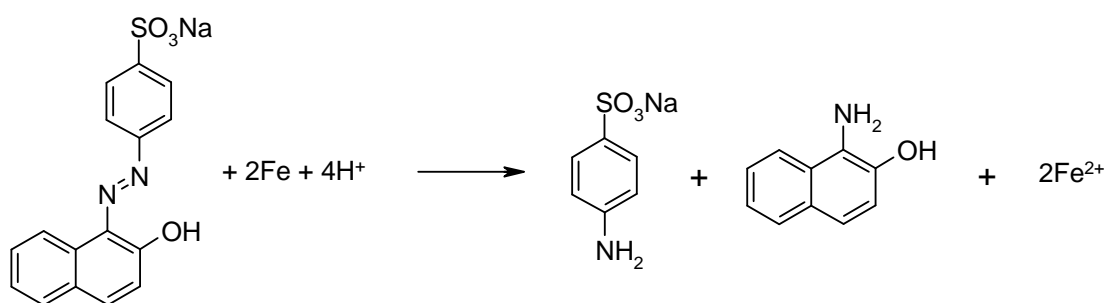


Figure 4.2 Four electron reduction of Orange II by zerovalent Iron.

The mechanism proposed for the electron transfer reduction of azo dyes involves a two-step process involving four electrons. Using Figure 4.3 as an example, in which Orange I¹⁸ was found to have a reduction potential of ca. -0.43 V (vs Ag/AgCl) in pH 5.5 Britton-Robinson buffer solution, the first step has been described as a reversible protonation of the azo linkage accompanied by electron transfer producing an unstable hydrazine intermediate species. The second step is a non-reversible disproportionation, in which spectroscopy shows that the parent dye reforms.

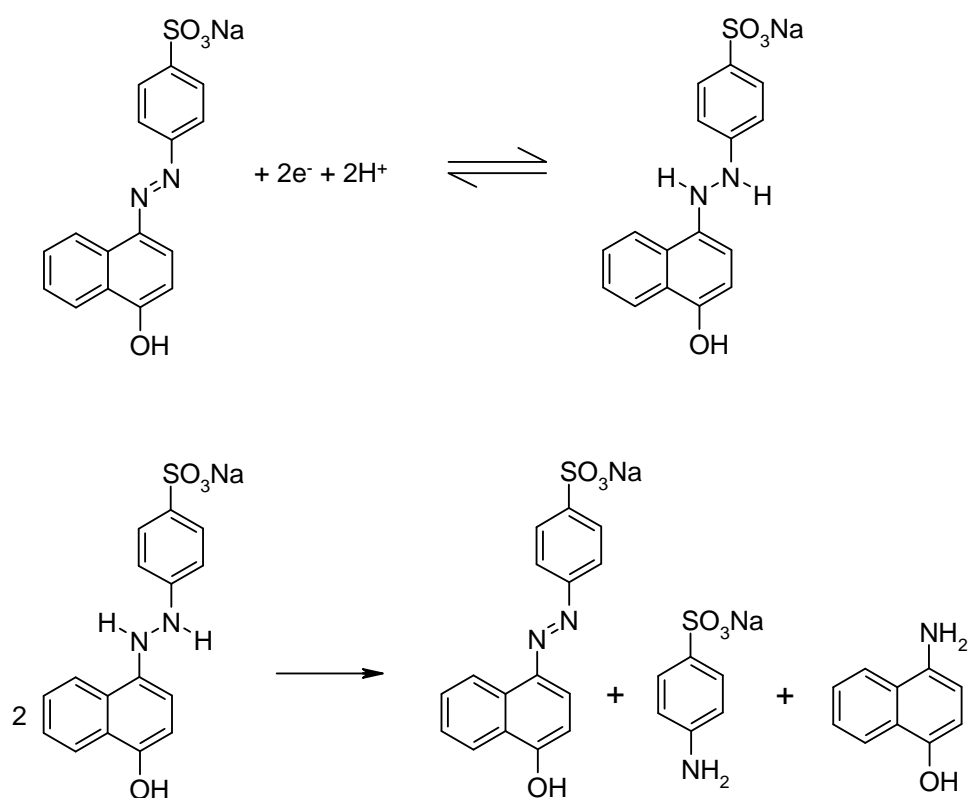


Figure 4.3 Two-step four-electron reduction of Orange I via disproportionation.

In the case of Methyl Red³ which has a reduction potential at ca. -0.25 V (vs SCE) in pH 4.6 sodium acetate buffer solution, CPE has shown that the number of electrons transferred per mole is four. Figure 4.4 gives the proposed two-step four-electron reduction of Methyl Red showing the reversible protonation and reduction producing the hydrazine intermediate. Compared to azobenzene, the dimethylamino substituent enhances the azo group basicity for further protonation at the azo linkage, hence there is a rapid second irreversible formation of 2-aminobenzoic acid and N,N-dimethyl-1,4-phenylenediamine.

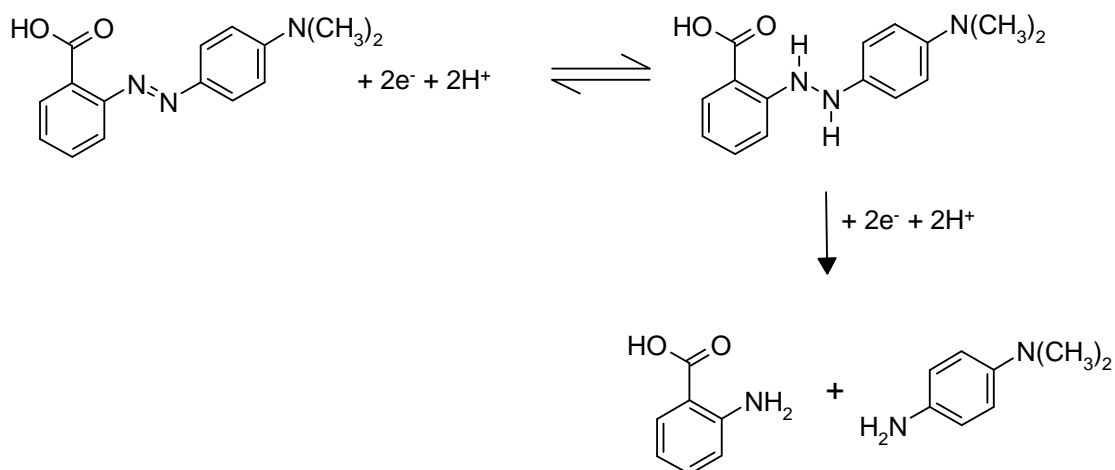


Figure 4.4 Proposed two-step four-electron reduction of Methyl Red.

In the case of 4-hydroxyazobenzene,²² it gives a reduction potential at ca. -0.35 V (vs SCE) in pH 4.7 sodium acetate buffer solution. Figure 4.5 shows the same first reversible protonation of the azo linkage accompanied by electron transfer, followed by two further steps involving further protonation and N-N bond scission accompanied by electron transfer forming aminobenzene and 4-aminophenol.

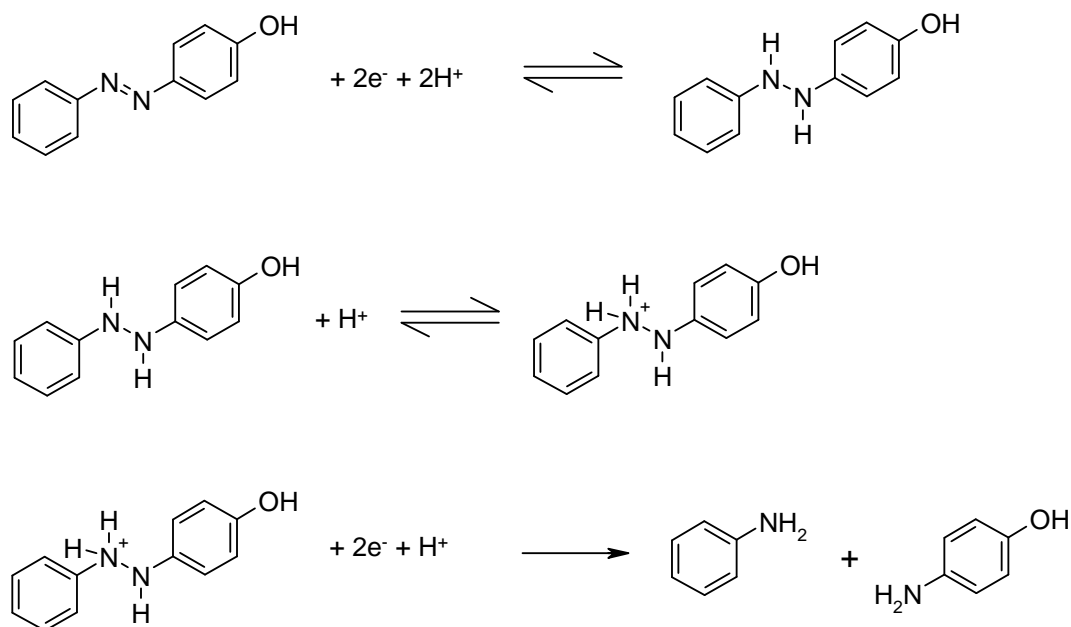


Figure 4.5 Proposed four-electron reduction of 4-hydroxyazobenzene via N-N bond scission.

4.1.3 Substituent effect

In two studies of azobenzenes the potential at which the first step occurs, the formation of the hydrazine, was studied. In the first,³² the potential of the one-step two electron reduction of azobenzene in pH 4.7 sodium acetate buffer solution was found to be -0.25 V (vs SCE) by CV with a rate constant of 200 s^{-1} forming hydroazobenzene³³ as shown in Figure 4.6.

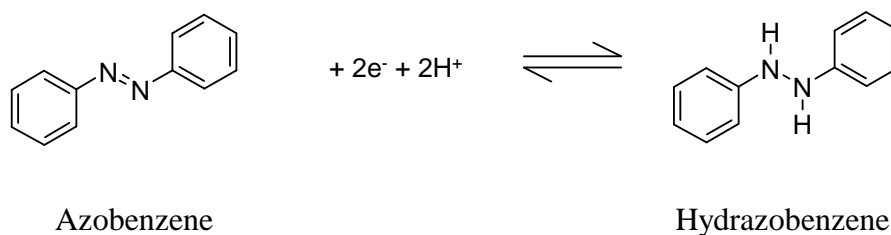


Figure 4.6 One-Step two-electron reduction of azobenzene.

Other *para* substituted azobenzenes have been investigated by CV and their structures are shown in Figure 4.7,³ and the potentials for hydrazine formation for 4-dimethylaminoazobenzene and 4-aminoazobenzene are -0.30 and -0.31 V (vs SCE) in pH 4.6 sodium acetate buffer solution, respectively, which are quite comparable. For 4-dimethylaminoazobenzene versus 4-aminoazobenzene the rate constants for formation of the hydrazine are 259 vs 199 s^{-1} and for N-N bond scission 49.1 vs 20.9 s^{-1} , respectively.³

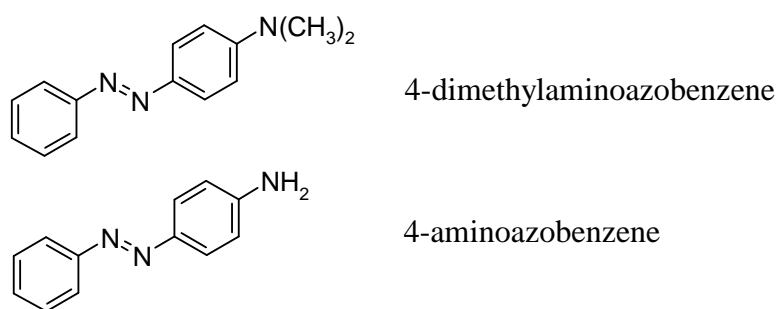


Figure 4.7 Structures of 4-dimethylaminoazobenzene and 4-aminoazobenzene.

In another study,³⁴ the potential for hydrazine formation was recorded by CV on substituted azobenzenes (Figure 4.8) in aqueous dioxane solutions, and showed a good correlation with their Hammett substituent constants σ_p as shown in Table 4.1 and

Figure 4.9. There is a larger negative potential for the reversible formation of hydrazine with increasing electron-donating capacity of the R substituent.

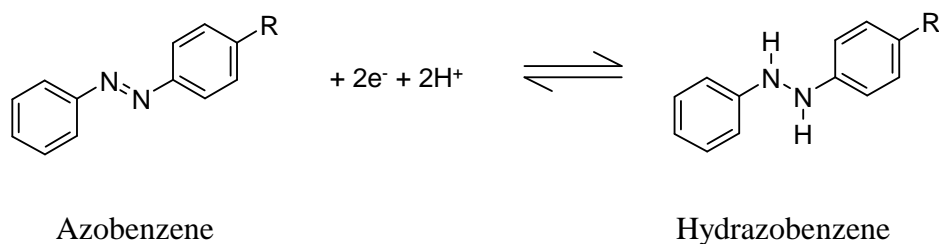


Figure 4.8 One-Step two-electron reduction of substituted azobenzenes, where R= NH₂, OH, OMe, H and Br.

Table 4.1 Hammett constants σ_p and Half-wave potential $E_{1/2}$ for hydrazine formation for substituted azobenzenes where R= NH₂, OH, OMe, H and Br in aqueous dioxane.³⁴

R	σ_p	$E_{1/2} / \text{V (vs SCE)}$
NH ₂	-0.66	-1.126
OH	-0.37	-1.050
OMe	-0.27	-1.050
H	0.00	-0.986
Br	+0.23	-0.929

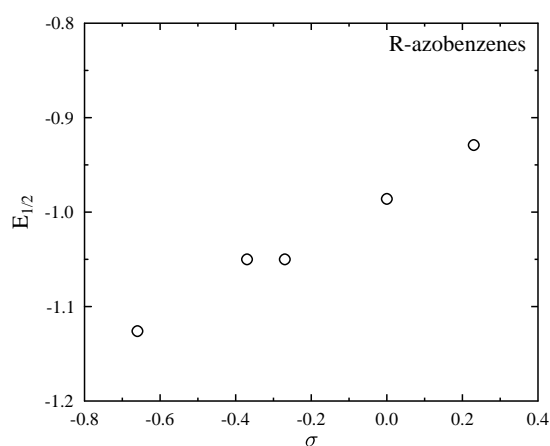


Figure 4.9 Half wave potential for the reduction of substituted azobenzenes where R= NH₂, OH, OMe, H and Br in aqueous dioxane vs their Hammett substituent constants σ_p .

1-(4-Nitrophenylazo)-2-naphthol undergoes a one-step two-electron reduction in which a stable hydrazine product forms as shown in Figure 4.10.²² The reduction potential of this process is -0.298 V (vs SCE) in pH 4.48 sodium acetate buffer ethanol solution, which is significantly lower than that for the corresponding process in the unsubstituted dye, 1-phenylazo-2-naphthol which has a reduction potential of -0.425 V (vs SCE) in pH 4.48 sodium acetate buffer ethanol solution. The lower potential can be attributed to the electron withdrawing NO₂ substituent allowing reduction to occur more easily.

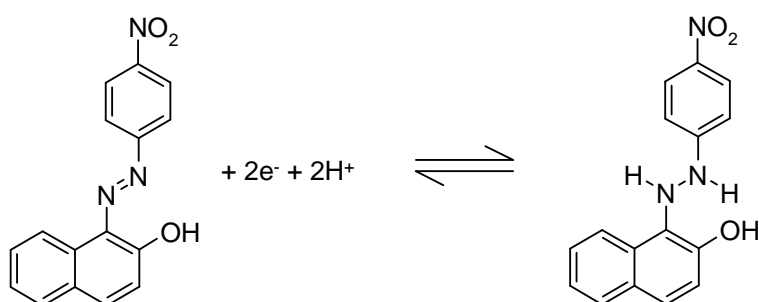


Figure 4.10 One-Step two-electron reduction of 1-(4-Nitrophenylazo)-2-naphthol.

4.1.4 Aims

The main aim of exploring electrochemically induced reactions of the R-Span dyes was to study reduction using a range of analytical techniques to identify products and mechanisms as well as assessing the substituent effect on the reactivity.

More specifically, the aim was to use a combination of CV, spectroelectrochemistry and CPE allied with UV/Visible absorption, HPLC, LC-MS, 1D and 2D NMR techniques to identify products and elucidate mechanisms. Among the NMR techniques, DOSY NMR was identified as a relatively new method of analysing components as part of a mixture and one aim was to explore its application for analysing mixtures of azo dye products.

Another aim of the studies presented in this chapter was to examine electrochemically induced reactions that would enable comparisons to be made with photochemically induced reduction reactions reported in Chapter 5.

4.2 Results, analysis and discussion

The R-Span dye series has been studied through a combination of electrochemical techniques to understand electron transfer processes, where the main focus of the work reported in this section was on reduction processes; however there are some limited results from oxidation studies also included. All the electrochemical reduction studies have been carried out on solutions that were purged and were under nitrogen.

A large amount of work has been carried out on OH-Span due to the availability of relatively large quantities of high purity material, hence CV, spectroelectrochemistry, CPE have been used on this dye. A combination of HPLC, LC-MS, 1D and 2D NMR spectroscopy has been used to identify the products of electron transfer reactions of OH-Span, the results are reported in section 4.2.1 For two of the other “pure dyes”, NH₂-Span and NHAc-Span, spectroelectrochemistry and CPE have been performed along with product analysis by HPLC, the results are reported in section 4.2.2 For OMe-Span and the “impure dyes” H-Span, Br-Span and CN-Span spectroelectrochemistry alone has been performed, the results are also reported in section 4.2.2 The results reported here are summarised in section 4.2.3.

Two aspects of the work reported are particularly notable. Firstly, DOSY NMR is one analytical technique that has been applied to mixtures, as reported in this section, to separate components based on their size and mass. Secondly, where possible, HPLC and NMR analyses have been used to give a quantitative approach to product analysis, where for HPLC analysis extensive concentration calibrations have been used to determine the concentration of species formed as a result of electron transfer processes.

4.2.1 OH-Span

Section 4.2.1.1 outlines the results from the CV studies, section 4.2.1.2 reports on the spectroelectrochemical studies, section 4.2.1.3 reports on the CPE reduction studies and section 4.2.2.4 reports on the product analysis of OH-Span.

4.2.1.1 Cyclic voltammetry

The usable solvent window for CV in pH 5.2 sodium acetate buffer solution was up to ca. -0.55 V (vs Ag/AgCl) for reduction and was up to ca. +1.3 V (vs Ag/AgCl) for oxidation (Appendix 2.1).

Cyclic voltammetry was performed on OH-Span at 1×10^{-3} mol dm⁻³ in pH 5.2 sodium acetate buffer solution and recorded at a scan rate of 10 mV s⁻¹. No signal attributed to the dye was observed within the usable window for the reduction of OH-Span. Figure 4.11 shows the cyclic voltammogram for the oxidation of OH-Span, where a weak poorly defined peak can be observed at ca. +0.55 V (vs Ag/AgCl) within the usable window.

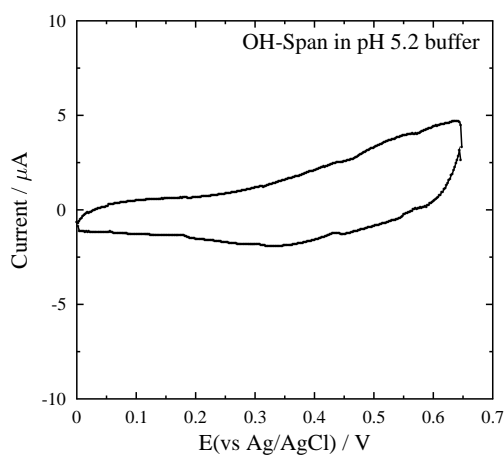


Figure 4.11 Cyclic voltammogram of OH-Span (1×10^{-3} mol dm⁻³) in pH 5.2 sodium acetate buffer solution recorded with a sweep rate of 10 mV s⁻¹.

4.2.1.2 Spectroelectrochemistry

Figures 4.12 and 4.13 show the UV/Visible absorption spectra of OH-Span recorded over the potential range of 0 to -1.2 V and 0 to +1.0 V (vs Ag wire); the changes were found to be irreversible (the spectrum of OH-Span did not reform when the potential was reversed). Also shown in Figures 4.12 and 4.13 are the fits to equation 4.1 (as derived for a reversible system in Appendix 2.2) where E^\ominus , the reduction or oxidation potential of the dye, is determined by analysis of the absorbance A and the applied potential E , where R ($8.314 \text{ J K}^{-1} \text{ mol}^{-1}$) is the molar gas constant, T (K) is the temperature, n is the number of electrons transferred in the electrochemical process, F (96485 C mol^{-1}) is the Faraday constant and where A_0 and A_∞ are the limiting absorbances at low and high potential.

$$A = \frac{A_0 + A_\infty e^{\left(\frac{nF(E^\ominus - E)}{RT}\right)}}{1 + e^{\left(\frac{nF(E^\ominus - E)}{RT}\right)}} \quad (4.1)$$

Equation 4.1 applies to a reversible redox equilibrium, but it can be used to fit the data for the non-reversible redox processes of OH-Span to give an estimate of the reduction and oxidation potentials. Equation 4.1 provides a quantitative fit of the data, where the start and end points given by the absorbance are well defined, where E^\ominus is determined from the inflection point of the curve to give an estimate of the reduction and oxidation potential, and the value of n determines the slope of the curve. The fitted values of n were 0.45 and 0.39 for reduction and oxidation of OH-Span, respectively reflecting the irreversibility rather than the actual number of electrons transferred, which were obtained by CPE (see section 4.2.1.3); the effect of the arbitrary value of n for this system can be seen in Appendix A.2.2 Figure A2.2, where an increase in n increases the sharpness of the curve.

Using this analysis for OH-Span in pH 5.2 buffer solution the estimated reduction and oxidation potentials were -0.75 V and +0.51 V (vs Ag wire), respectively.

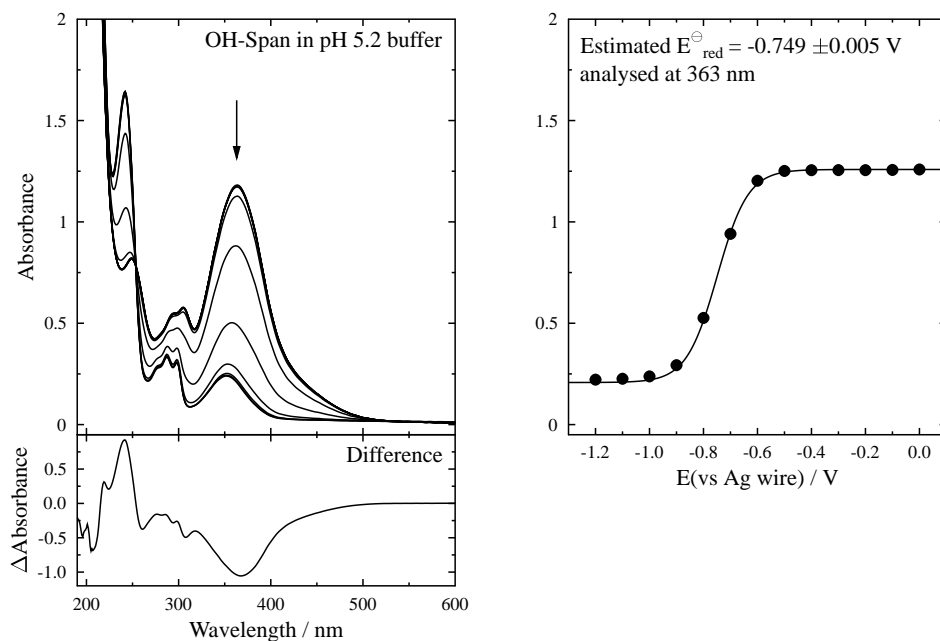


Figure 4.12 Left: UV/Visible absorption spectra of OH-Span ($5 \times 10^{-4} \text{ mol dm}^{-3}$) in pH 5.2 sodium acetate buffer solution; the arrow indicates the change with decreasing potential over a range of 0 to -1.2 V (vs Ag wire) and with the overall difference spectrum (final – initial) shown. Right: Potential curve analysed using equation 4.1 at 363 nm, where $n = 0.45$.

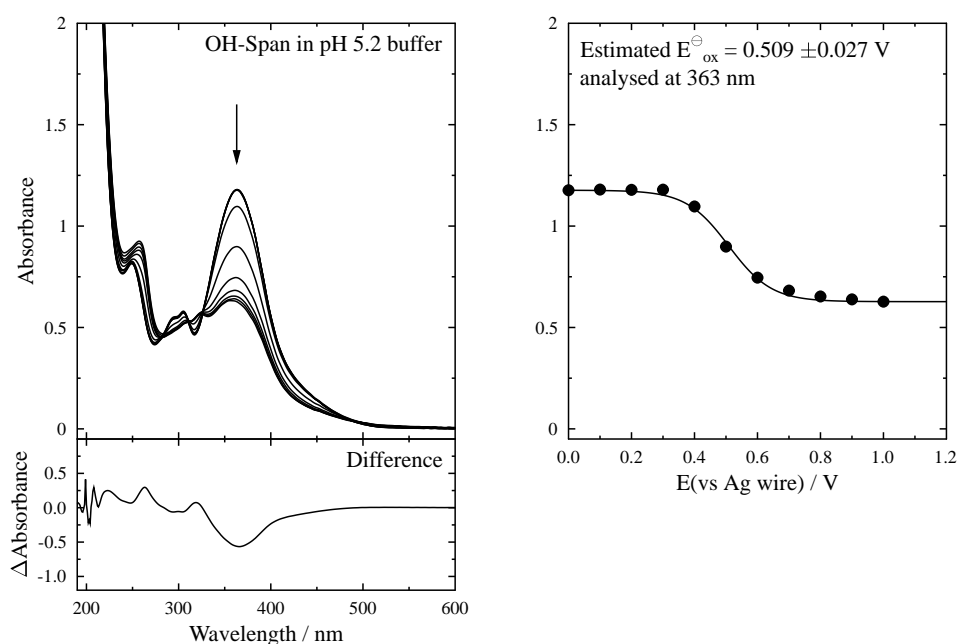


Figure 4.13 Left: UV/Visible absorption spectra of OH-Span ($5 \times 10^{-4} \text{ mol dm}^{-3}$) in pH 5.2 sodium acetate buffer solution; the arrow indicates the change with increasing potential over a range of 0 to +1.0 V (vs Ag wire) and with the overall difference spectrum (final – initial) shown. Right: Potential curve analysed using equation 4.1 at 363 nm where $n = 0.39$.

4.2.1.3 Controlled potential electrolysis reduction

Controlled potential electrolysis (CPE) was used to determine the number of electrons involved in the reduction of OH-Span. A potential of -1.2 V (vs Ag/AgCl) was applied to 50 cm^3 of OH-Span in 0.5 mol dm^{-3} sodium acetate buffer solution with the current monitored over a period of 30 min as shown in Figure 4.14: the total charge (Q) from OH-Span was calculated by the integration of the current-time plot, to give a charge-time plot.

The number of electrons was calculated using $Q = nFz$, where n is the number of moles of sample F is the Faraday constant (96485 C mol^{-1}) and z is the number of electrons transferred per molecule in the electrochemical process. Hence, after taking into account the current from the solvent background (Appendix 2.3 Figure A2.3), the total charge from OH-Span was 14.4 C ($21.63 - 7.24\text{ C}$) giving $3.85 \approx 4$ electrons transferred during the reduction process.

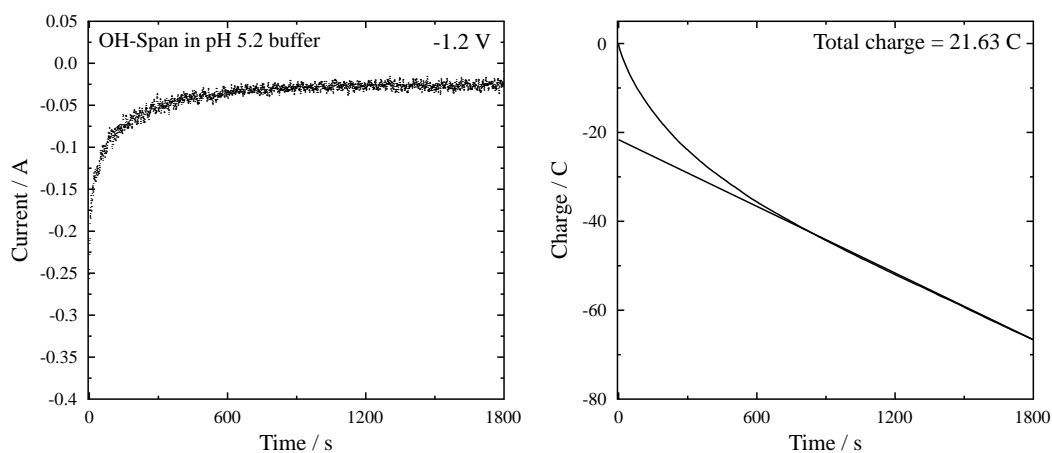


Figure 4.14 CPE reduction on OH-Span ($8 \times 10^{-4}\text{ mol dm}^{-3}$) in pH 5.2 sodium acetate buffer solution over 30 min at a potential of -1.2 V (vs Ag/AgCl) Left: Current-time profile, Right: Charge-time profile.

4.2.1.4 Product analysis

The UV/Visible absorption spectrum of OH-Span recorded after CPE reduction gave a match to that after spectroelectrochemical reduction showing that the same process has occurred in each technique. To identify the products of the electrochemical reduction, OH-Span samples were analysed by HPLC, LC-MS and NMR before and after the CPE reduction process. HPLC was used to give the retention times, spectral information and peak integration allowing for quantitative analysis for each component, and where LC-MS was used to give masses and fragmentation for each component where possible. DOSY NMR was used to separate the signals from components in these complicated mixtures based on their diffusion coefficients, which used in combination to 1D ^1H NMR allowed for the quantitative determination of components. Firstly all the results before and after CPE reduction are presented before making assignments of the components towards the end of this section, where all the data is collated together in Tables 4.3 and 4.4 for LC and NMR data, respectively.

HPLC analysis

The HPLC chromatograms before and after CPE of OH-Span and the UV/Visible absorption spectra for each significant component are shown in Figures 4.15 and 4.16. The retention times, peak integrations and UV/Visible absorption band positions are given in Table 4.3, which is presented at the end of this section and includes additional data reported below. The peak corresponding to OH-Span at a retention time of 12.22 min disappears after CPE giving components labelled A, B and C which are observed at 2.43, 3.87 and 4.26 min, respectively, in the HPLC chromatogram. Component A shows a split peak due to a concentration effect, overloading the column, as careful test studies showed (as discussed below).

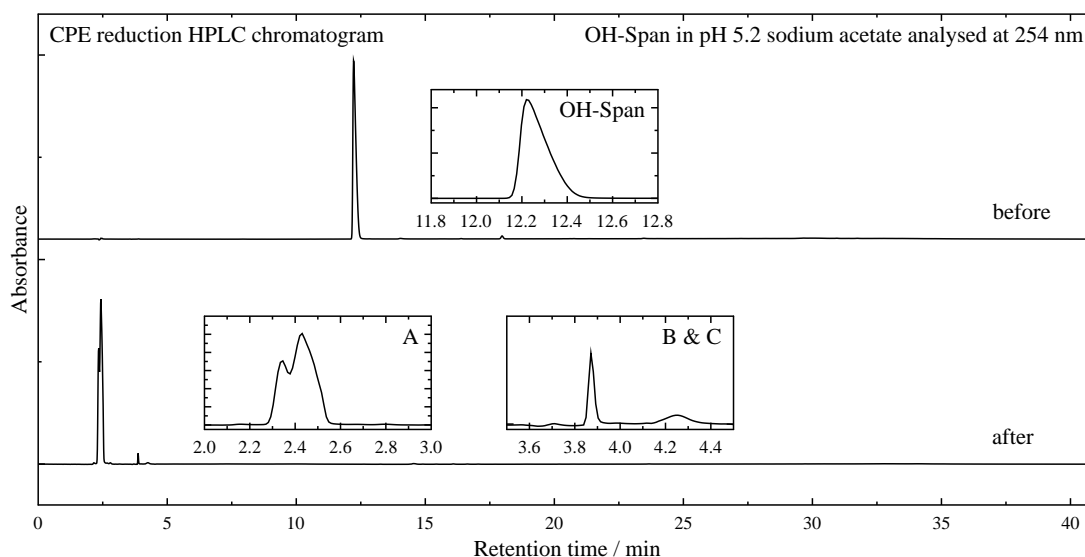


Figure 4.15 HPLC chromatograms of OH-Span ($8 \times 10^{-4} \text{ mol dm}^{-3}$) before (top) and after (bottom) CPE reduction. Inserts show the expansions of the HPLC chromatogram of each component.

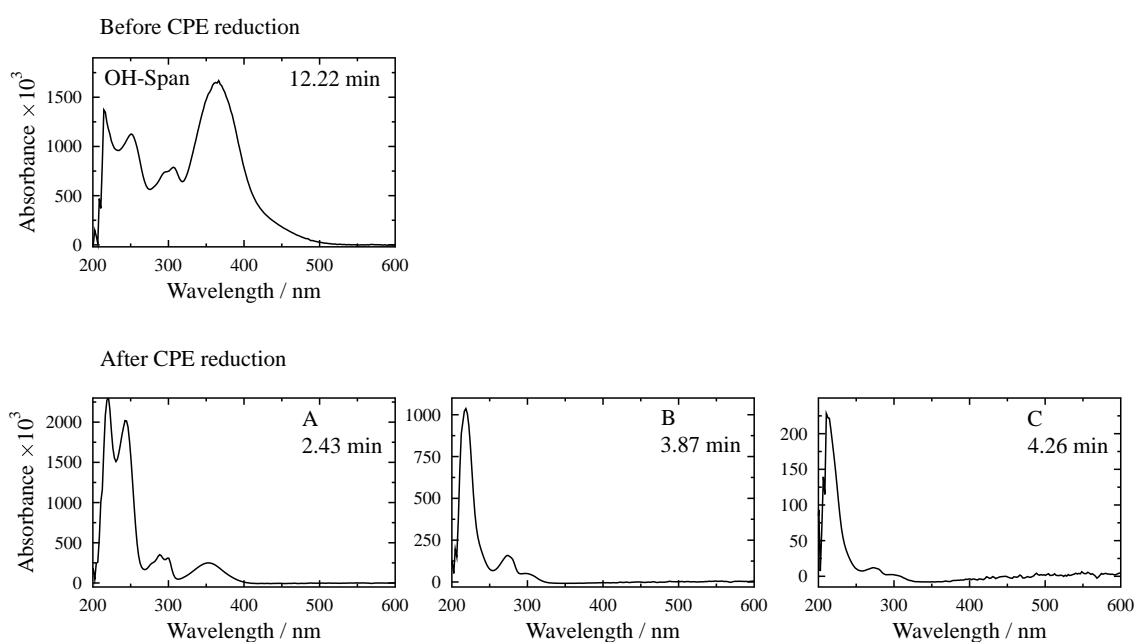


Figure 4.16 Top: UV/Visible absorption spectrum of OH-Span ($8 \times 10^{-4} \text{ mol dm}^{-3}$) before CPE reduction at an elution time of 12.22 min. Bottom: UV/Visible absorption spectra of Components A, B and C after CPE reduction at retention times of 2.43, 3.87 and 4.26 min.

LC-MS analysis

The negative ion ESI, first fragmentation (MS/MS-1) and second fragmentation (MS/MS-2) mass spectra of OH-Span alone with a retention time of 12.12 min are shown in Figure 4.17 with the results summarised in Table 4.3 at the end of this section.

Figure 4.18 shows the structure that gives rise to the observed base peak with an m/z value of 407.0 corresponding to OH-Span with one sulfonate protonated. In the first fragmentation, MS/MS-1 a fragment with an m/z value of 327.0 has formed corresponding to a mass loss of 80 which may be assigned to the loss of a SO_3 from OH-Span as will be seen below; this alone is a useful piece of evidence for any component that may contain the sulfonated naphthalene group from the dye. In the second fragmentation, MS-MS-2 a fragment with an m/z value of 206.0 has formed corresponding to a loss of $\text{N}_2\text{C}_6\text{H}_4\text{OH}$.

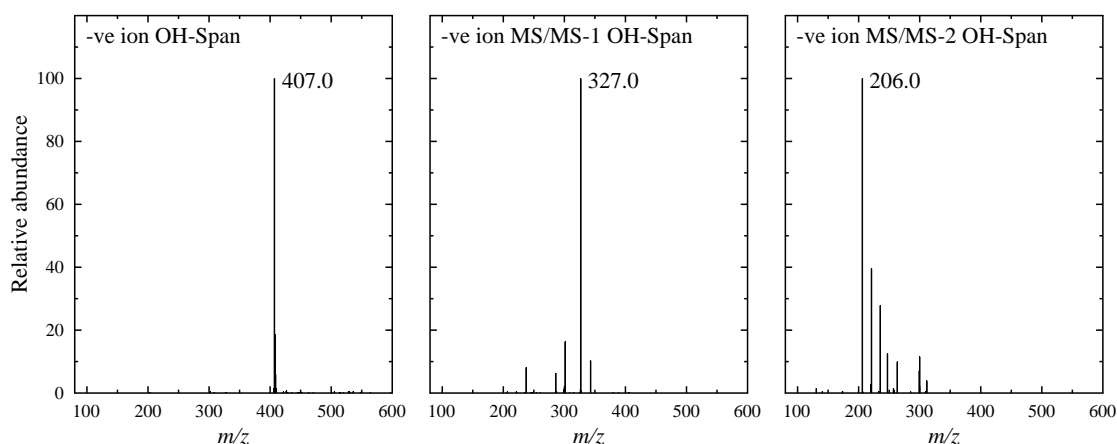


Figure 4.17 Left: Negative ion ESI mass spectrum of OH-Span with a retention time of 12.12 min. Middle: Negative ion MS/MS-1 mass spectrum of the ion with 407.0 m/z . Right: Negative ion MS/MS-2 mass spectrum on the ion with 327.0 m/z .

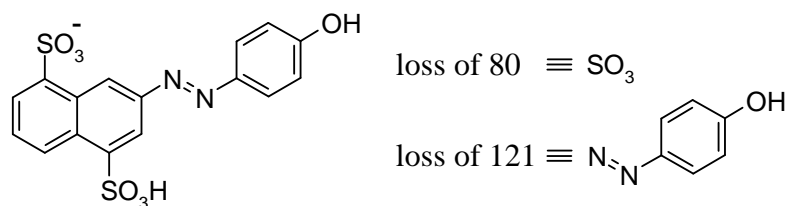


Figure 4.18 Structure of $[\text{OH-Span} + \text{H}^+]^-$ corresponding to base peak at 407.0 m/z and its observed fragmentations.

The negative ion ESI, MS/MS-1 mass spectra of component A formed from a sample of OH-Span after CPE, with a retention time of 2.28 min, are shown in Figure 4.19 with the results summarised in Table 4.3 at the end of this section. In the first fragmentation, MS/MS-1 a fragment with an m/z value of 222.1 has formed corresponding to a mass loss of 80. No MS/MS-2 was observed for this component. Components B and C were not observed by mass spectrometry after CPE on OH-Span, although observation was attempted.

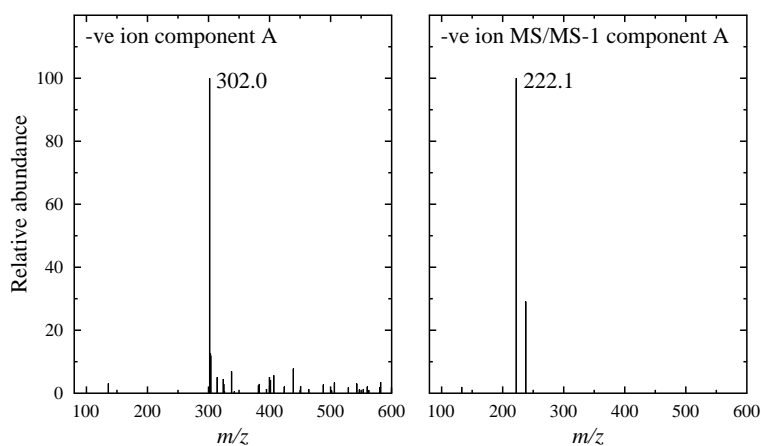


Figure 4.19 Left: Negative ion ESI mass spectrum of component A formed after CPE of OH-Span with a retention time of 2.32 min. Right: Negative ion MS/MS-1 mass spectrum on the ion with 302.0 m/z .

NMR analysis

1D and 2D (COSY, NOESY, DOSY) ^1H spectra were recorded from samples in deuterated 0.05 mol dm^{-3} sodium acetate buffer at pD 5.2 using a Bruker 700 MHz spectrometer.

In a DOSY experiment, spectra are recorded as a function of pulsed field gradient (PFG), these 1D spectra are then converted to a 2D spectrum by fitting the decay of the signal as a function of the square of the PFG amplitude. The Stejskal-Tanner equation,³⁵ as shown in equation 4.2, describes the decay of the signal in a ideal pulsed field gradient, where S (arbitrary units) is the signal amplitude, S_0 (arbitrary units) is the signal amplitude had there been no diffusion, D ($\text{m}^2 \text{ s}^{-1}$) is the diffusion coefficient, δ (s) is the gradient pulse width, γ ($\text{s}^{-1} \text{ T}^{-1}$) is the magnetogyric ratio, g (T m^{-1}) is the gradient amplitude and Δ (s) is the diffusion time.

$$S = S_0 e^{-D\gamma^2\delta^2g^2\Delta} \quad (4.2)$$

All the NMR figures here are set out to show the 1D ^1H NMR spectrum recorded, with the 2D DOSY data shown as a series of data points relating the chemical shift of each peak with the corresponding apparent diffusion coefficient. A histogram of apparent diffusion coefficients is shown to give an indication of the spread of diffusion coefficient data. ^1H NMR assignments were made using integration, multiplicity and splitting values and by COSY interactions and apparent diffusion coefficients (experimental data) obtained from the DOSY data.

The data from an OH-Span sample before and after CPE reduction are shown in Figures 4.20 and 4.21 with NMR assignments shown in Table 4.4 at the end of this section. OH-Span has an apparent diffusion coefficient of $4.16 \times 10^{-10} \text{ m}^2 \text{ s}^{-1}$, and components labelled E, F and G have coefficients of 5.08×10^{-10} , 6.53×10^{-10} and $6.57 \times 10^{-10} \text{ m}^2 \text{ s}^{-1}$, respectively. The higher diffusion coefficient values indicate that the products that have formed are all smaller than the parent dye.

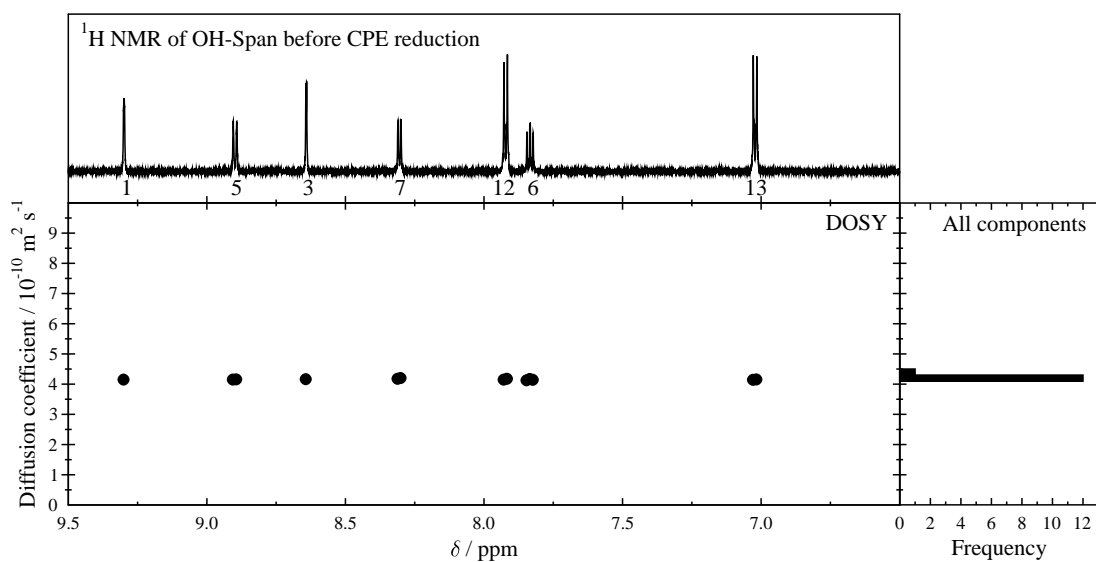


Figure 4.20 Left: Aromatic region ^1H NMR (700 MHz) DOSY display OH-Span at $5 \times 10^{-3} \text{ mol dm}^{-3}$ and pD 5.2. Right: Histogram of all components in DOSY display.

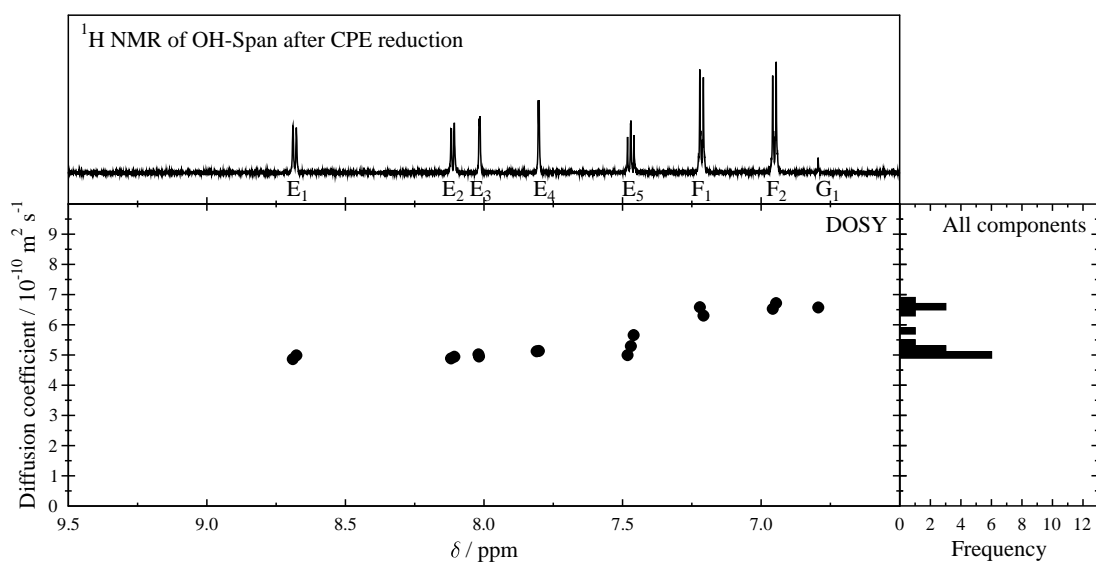


Figure 4.21 Left: Aromatic region ^1H NMR (700 MHz) DOSY display of components E, F and G formed after CPE reduction of OH-Span at $5 \times 10^{-3} \text{ mol dm}^{-3}$ and pD 5.2. Right: Histogram of all components in DOSY display.

OH-Span reduction product assignment

The proposal for the electrochemical reduction of OH-Span is a two-step four-electron reduction, as shown in Figure 4.22, resulting in the formation of 2-naphthylamine-4,8-disulfonate (NAPDAD) and 4-aminophenol (APOL).

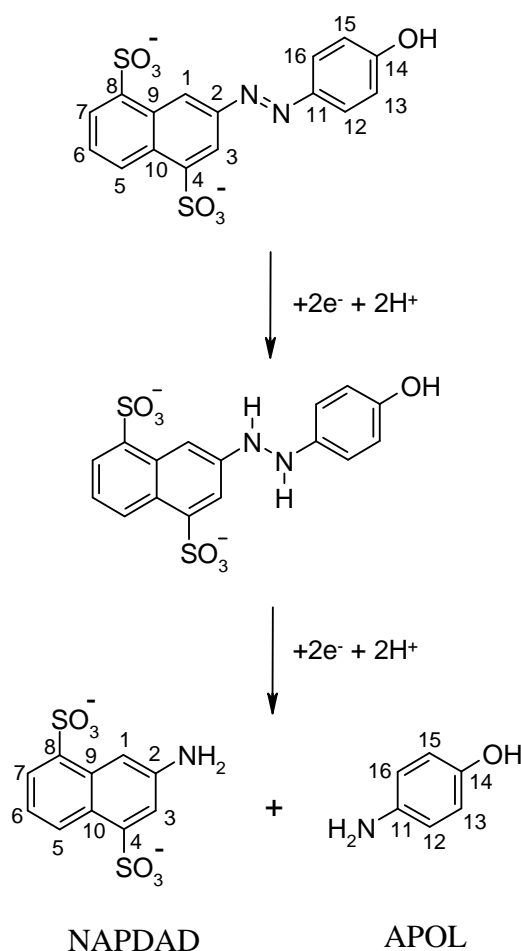


Figure 4.22 Proposed two-step four-electron reduction of OH-Span producing NAPDAD and APOL (numbering system shown).

There is a pH dependence on the structure of OH-Span and experimental conditions at pH 5.2 were chosen to study OH-Span in that form. It was discovered that the structure of NAPDAD and APOL were also pH dependent, important for interpretation of results aimed at product determination. The UV/Visible absorption spectra of NAPDAD over the pH range ca. 2 to 12 are shown in Figure 4.23, and this spectrophotometric pH titration (analysis method as reported in section 3.2.1.1) gave a pK_a of 3.03 assigned to

protonation of the NH_2 group. It has been reported that APOL has pK_a values of 5.29 and 10.46 due to protonation / deprotonation at the NH_2 and OH group, respectively.^{36,37} The UV/Visible absorption spectrum of NAPDAD and APOL in water and in pH 5.2 sodium acetate buffer solution, both at $5 \times 10^{-5} \text{ mol dm}^{-3}$, are shown in Figure 4.24 with the band positions given in Table 4.2. HPLC, LC-MS and NMR data were obtained for NAPDAD and APOL alone as described below, enabling assignments made to components formed after CPE reduction of OH-Span performed at pH 5.2.

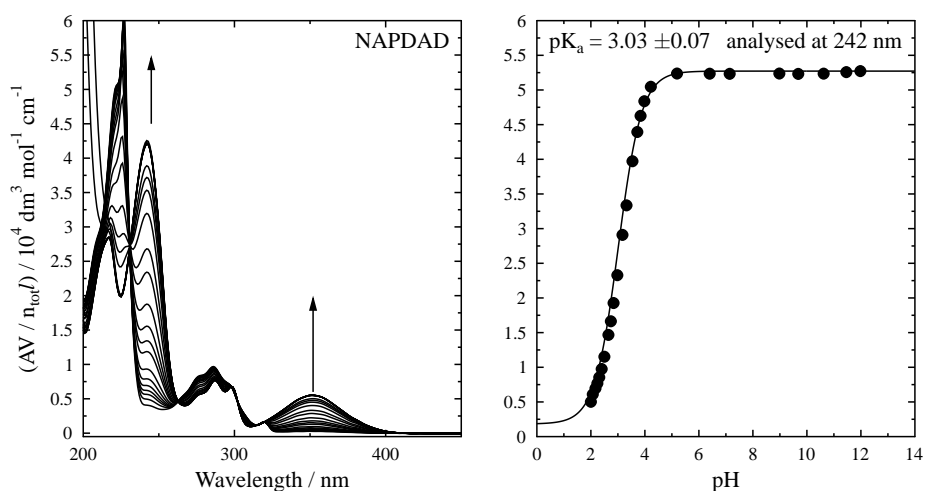


Figure 4.23 Left: UV/Visible absorption spectra of aqueous NAPDAD at $5 \times 10^{-5} \text{ mol dm}^{-3}$; the arrows indicate changes with increasing pH over a range of pH 2 to 12. Right: pH curve analysed using equation 3.3 (Chapter 3) at 242 nm.

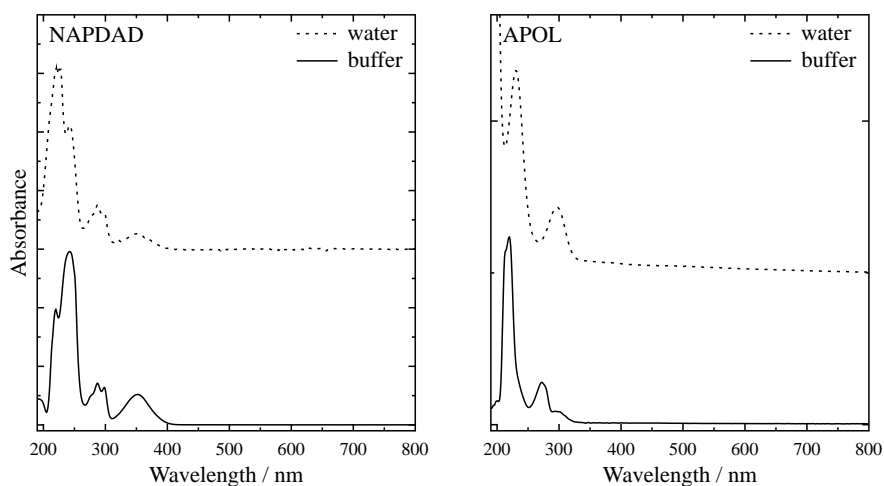


Figure 4.24 UV/Visible absorption spectrum of NAPDAD (left) and APOL (right) in water and in pH 5.2 sodium acetate buffer solution, both at $5 \times 10^{-5} \text{ mol dm}^{-3}$.

Table 4.2 UV/Visible absorption band positions of NAPDAD and APOL in water and in pH 5.2 sodium acetate buffer solution, both at 5×10^{-5} mol dm⁻³.

Compound	λ / nm	
	Water	pH 5.2 sodium acetate buffer
NAPDAD	219, 241, 289, 299, 353	219, 241, 289, 299, 353
APOL	232, 296	219, 274, 300

Figures 4.25 and 4.26 show the HPLC chromatograms and the UV/Visible absorption spectra of NAPDAD and APOL alone (both at 1×10^{-3} mol dm⁻³ in pH 5.2 sodium acetate buffer solution). The retention times, peak integrations and UV/Visible absorption band positions are given in Table 4.3. Figure 4.27 shows the negative ion ESI and MS/MS-1 mass spectra of NAPDAD with a retention time of 2.41 min with the results summarised in Table 4.3. Figure 4.27 also shows the structure that gives rise to the observed base peak ion with an m/z value of 302.0, corresponding to [NAPDAD + H]⁻ with one sulfonate protonated. A fragment with m/z 222.1, a mass loss of 80 can be assigned to the loss of SO₃ from NAPDAD, consistent with the loss observed from OH-Span (Figure 4.17). Figure 4.28 shows the positive ion ESI mass spectrum of APOL with a retention time of 3.71 min with the results summarised in Table 4.3. Figure 4.28 also shows the structure that gives rise to the observed base peak ion with an m/z value of 110.1, corresponds to [APOL + H]⁺, with the NH₂ group protonated.

The HPLC chromatogram of NAPDAD (Figure 4.25) shows a split peak at ca. 2.4 min that arises from overloading of the column (injection volume dependent HPLC chromatograms of NAPDAD are shown in Appendix A2.4 Figure A2.4) rather than two components. The HPLC chromatogram of APOL (Figure 4.25) also shows two peaks at 3.87 and 4.26 min, and this arises from the sample containing both neutral and protonated APOL due to the amino group $pK_a = 5.29$;³⁶ the pH dependent HPLC chromatograms of APOL at pH 4.6 and 5.2 shown in Appendix 2.4 support this conclusion.

Together, the HPLC and LC-MS analyses indicate that NAPDAD corresponds to component A and that APOL corresponds to components B and C formed on reduction of OH-Span (Table 4.3).

Calibration curves were produced for NAPDAD and APOL; as reported in Appendix A2.4, where HPLC peak integrations were determined as a function of concentration. These were generated in order to determine the concentration of NAPDAD and APOL produced after CPE reduction of OH-Span. Quantitative analysis, using the peak integration of A (NAPDAD) and B & C (APOL), as shown in Table 4.3, and the calibration curves showed that a starting OH-Span concentration of $8.0 \times 10^{-4} \text{ mol dm}^{-3}$ gave concentrations of NAPDAD and APOL of $7.0 \times 10^{-4} \text{ mol dm}^{-3}$ and $7.4 \times 10^{-4} \text{ mol dm}^{-3}$, respectively. Therefore, within experimental error, the HPLC analysis (Table 4.3) showed that all the OH-Span had disappeared after CPE reduction and showed that 1 mole of OH-Span electrochemically reduces to ca. 0.9 mole of NAPDAD and ca. 0.9 mole of APOL, consistent with the proposed two-step four-electron reduction of OH-Span (Figure 4.22).

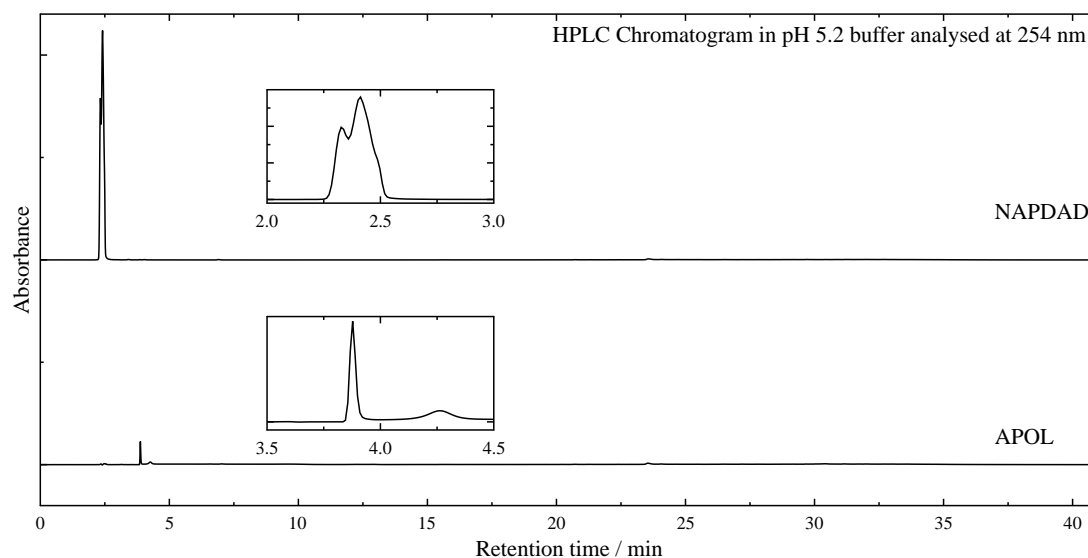


Figure 4.25 HPLC chromatogram of NAPDAD (top) and APOL (bottom) both at $1 \times 10^{-3} \text{ mol dm}^{-3}$. Inserts show expansions of the regions of the HPLC chromatogram of each component.

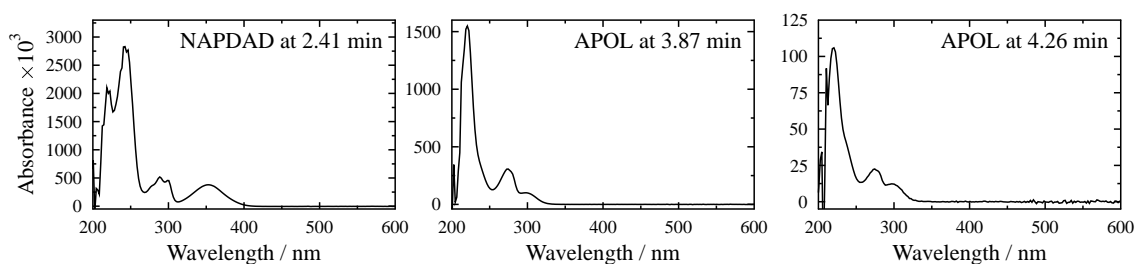


Figure 4.26 UV/Visible absorption spectra of NAPDAD (left) and APOL (right) both at $1 \times 10^{-3} \text{ mol dm}^{-3}$ at retention times of 2.41, 3.87 and 4.26 min, respectively.

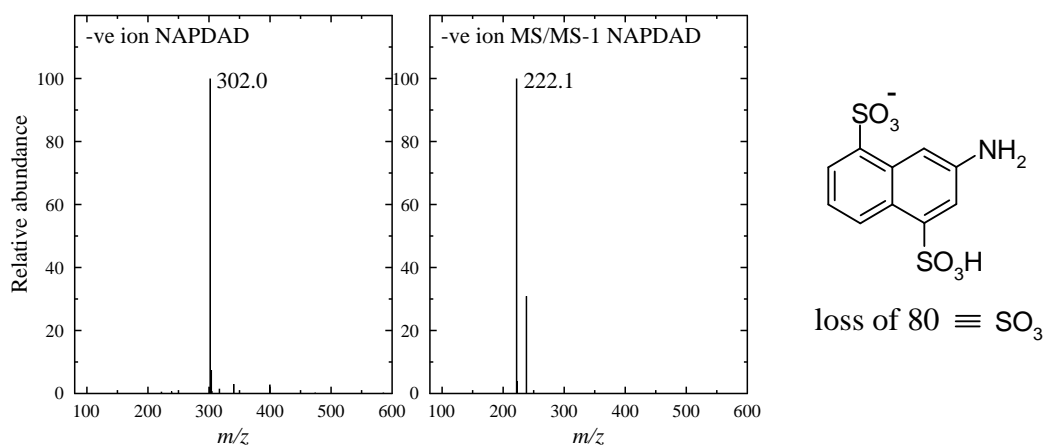


Figure 4.27 Left: Negative ion ESI mass spectrum of NAPDAD with a retention time of 2.41 min. middle: Negative ion MS/MS-1 mass spectrum on the ion with 302.0 m/z. Right: Structure of $[\text{NAPDAD} + \text{H}^+]^-$ corresponding to base peak at 302.0 m/z and its observed fragmentation.

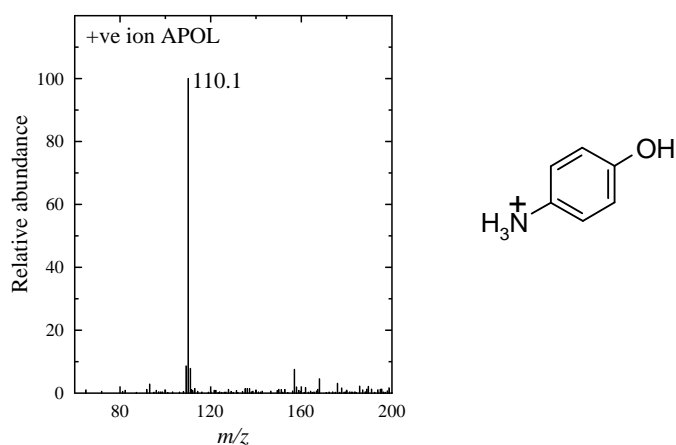


Figure 4.28 Left: Positive ion ESI mass spectrum of APOL with a retention time of 3.71 min. Right: Structure of $[\text{APOL} + \text{H}^+]^+$ corresponding to base peak at 110.1 m/z.

The DOSY NMR spectra of APOL and NAPDAD (both at $1 \times 10^{-3} \text{ mol dm}^{-3}$) are shown in Figure 4.29 with NMR assignments given in Table 4.4. Individually, APOL and NAPDAD have different apparent diffusion coefficients of 7.25×10^{-10} and $5.36 \times 10^{-10} \text{ m}^2 \text{ s}^{-1}$, respectively.

The DOSY NMR spectrum of a control mixture of APOL, NAPDAD and the dye OH-Span (prepared with all at $1 \times 10^{-3} \text{ mol dm}^{-3}$) is shown in Figure 4.30 with the assignments given in Table 4.4. The components of the mixture of APOL, NAPDAD and OH-Span have different apparent diffusion coefficients of 6.66×10^{-10} , 5.17×10^{-10} and $4.16 \times 10^{-10} \text{ m}^2 \text{ s}^{-1}$, respectively.

The apparent diffusion coefficients of components E ($6.53 \times 10^{-10} \text{ m}^2 \text{ s}^{-1}$) and F ($5.08 \times 10^{-10} \text{ m}^2 \text{ s}^{-1}$) from the OH-Span sample after CPE reduction gives a good match to those of NAPDAD and APOL as do the positions of the resonances (Tables 4.4). A quantitative analysis of the 1D NMR peak integration shows that from a starting concentration of OH-Span of $5.00 \times 10^{-3} \text{ mol dm}^{-3}$ the resulting concentration of NAPDAD and APOL after CPE reduction are 4.61×10^{-3} and $4.60 \times 10^{-3} \text{ mol dm}^{-3}$, respectively, supporting the HPLC analysis, with ca. 0.9 moles of NAPDAD and APOL produced from 1 mole of OH-Span.

The use of DOSY NMR has shown that there is a third possible component, G that has formed after CPE reduction of OH-Span that has not been observed by any of the other analytical techniques (Figure 4.21). Component G has a ^1H chemical shift of 6.81 ppm and an apparent diffusion coefficient of $6.57 \times 10^{-10} \text{ m}^2 \text{ s}^{-1}$, as given in Table 4.3. 1,4-Hydroquinone (HQ), formed by the hydrolysis³⁸ of the hydrazine dye intermediate as shown in Figure 4.31, could account for component G because HQ has a ^1H chemical shift of 6.79 ppm and an apparent diffusion coefficient of $7.63 \times 10^{-10} \text{ m}^2 \text{ s}^{-1}$, as shown in Figure 4.32 and given in Table 4.4. The ^1H shift of the protons in HQ is very comparable and the diffusion coefficient is similar to that of G. The yield of this component is very low at ca. 2 % of APOL and NAPDAD.

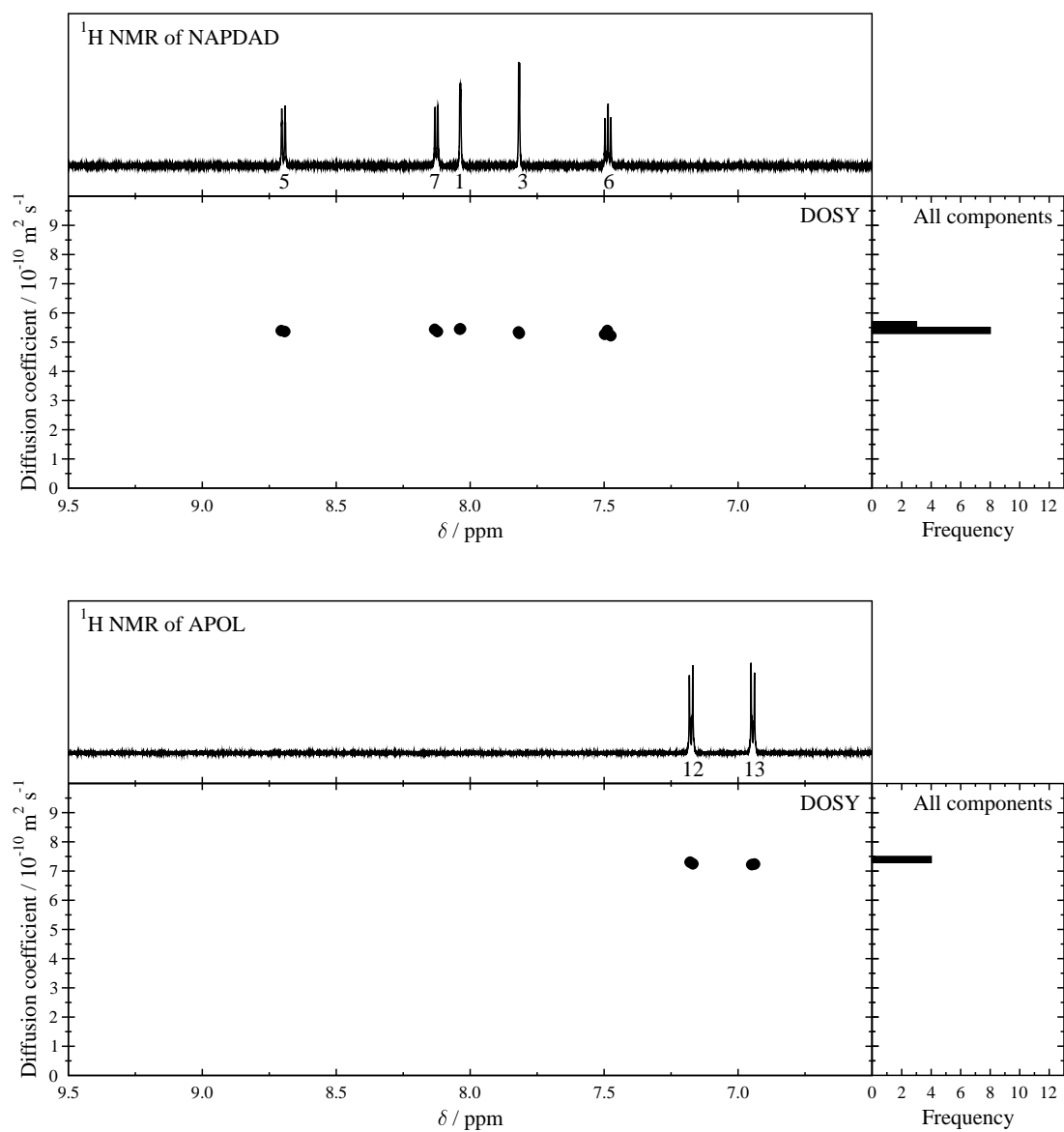


Figure 4.29 Left: Aromatic region ^1H NMR (700 MHz) DOSY display of NAPDAD (top), APOL (bottom) at $5 \times 10^{-3} \text{ mol dm}^{-3}$ and pD 5.2. Right: Histogram of all components in DOSY display.

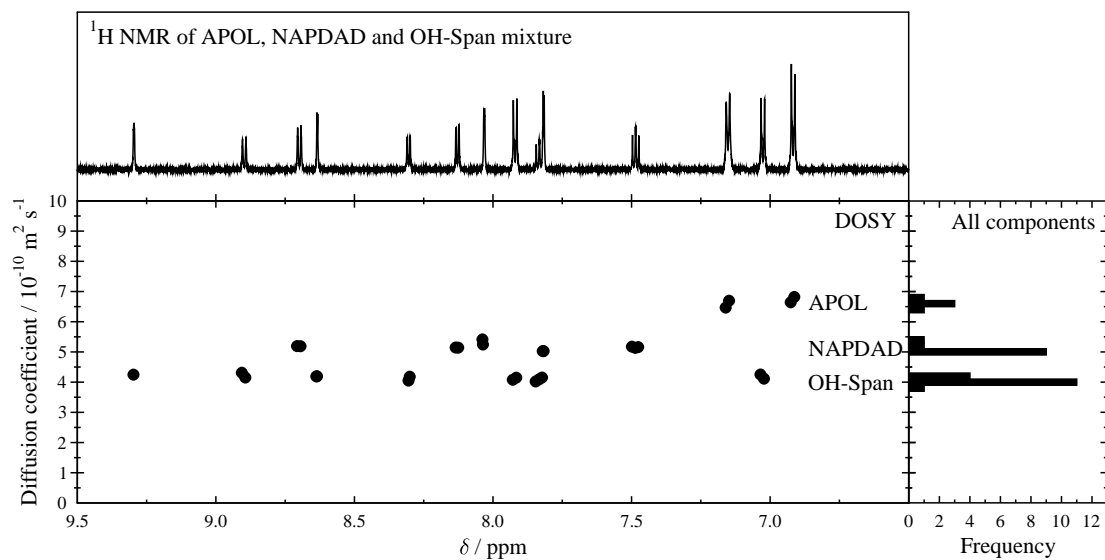


Figure 4.30 Left: Aromatic region ^1H NMR (700 MHz) DOSY display of a mixture of APOL, NAPDAD and OH-Span mixture at $5 \times 10^{-3} \text{ mol dm}^{-3}$ and pD 5.2. Right: Histogram of all components in DOSY display.

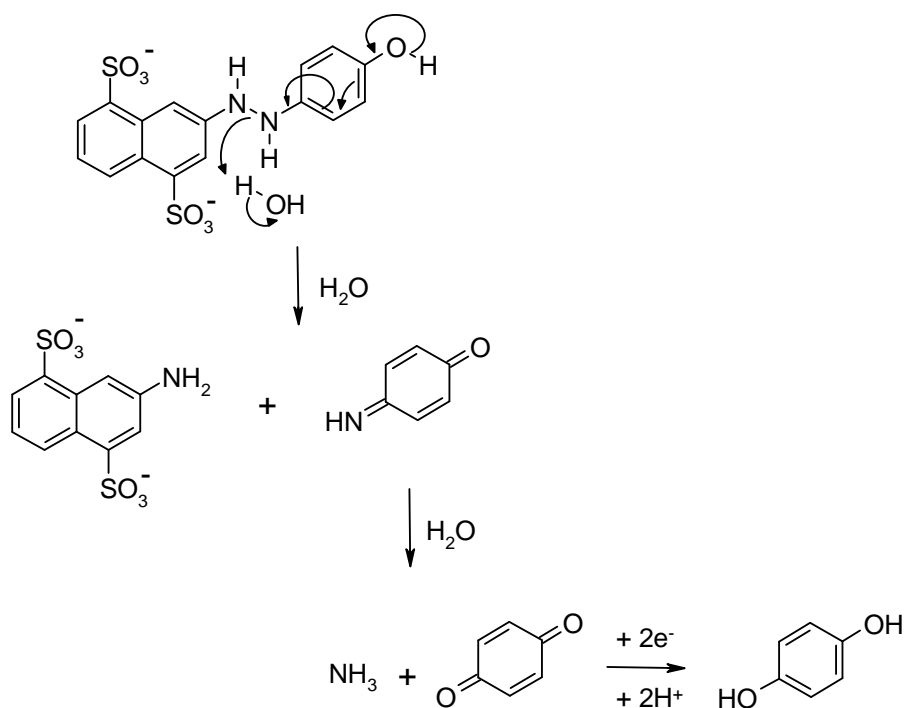


Figure 4.31 Hydrolysis of hydrazine-dye-intermediate to produce hydroquinone.

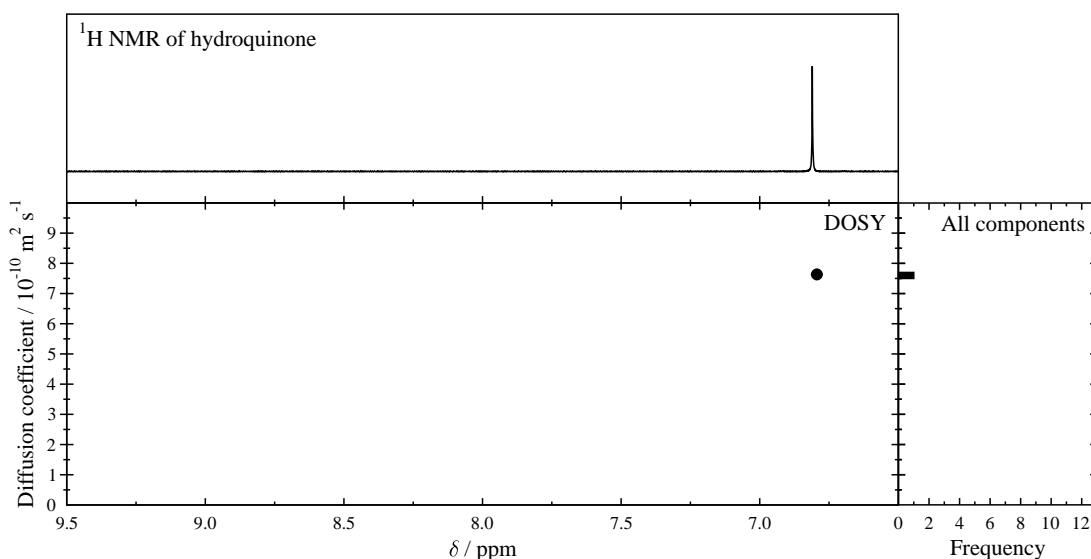


Figure 4.32 Left: Aromatic region ^1H NMR (700 MHz) DOSY display of 1,4-hydroquinone at $1 \times 10^{-3} \text{ mol dm}^{-3}$ and pD 5.2. Right: Histogram of all components in DOSY display.

Using the DFT optimised structures to provide radii from across the shortest and longest parts of APOL, NAPDAD and OH-Span, diffusion coefficients were calculated using the Stokes-Einstein equation as shown in equation 4.2 where R_{H} (m), is the hydrodynamic radius, k ($\text{m}^2 \text{ kg s}^{-2} \text{ K}^{-1}$) is the Boltzmann constant, T (K) is the temperature and η ($\text{kg m}^{-1} \text{ s}^{-1}$) is the solvent viscosity with the results given in Table 4.5 which are shown comparatively in Table 4.4. Taking the experimentally determined diffusion coefficients of NAPDAD, APOL and OH-Span alone of 4.16, 5.36 and $7.25 \times 10^{-10} \text{ m}^2 \text{ s}^{-1}$, respectively, with those calculated from the longest axis of 4.26, 4.73 and $7.71 \times 10^{-10} \text{ m}^2 \text{ s}^{-1}$, respectively, it can be seen that there is a comparable match, showing that the optimised structure can be used to predict the diffusion coefficients likely to be observed by experimental methods.

$$D = \frac{kT}{6\pi\eta R_{\text{H}}} \quad (4.2)$$

Table 4.3 Retention times (RT / min), peaks integrations (PI) and UV/Visible absorption band positions (λ / nm) from HPLC and Retention times (RT / min), base peak ions (BP / m/z) and fragment ions (F / m/z) of components before and after CPE of OH-Span (8×10^{-4} mol dm⁻³) and the model compounds NAPDAD (1×10^{-3} mol dm⁻³) and APOL (1×10^{-3} mol dm⁻³).

Component	HPLC			LC-MS				
	RT	PI	λ	RT	BP	Assignment	F	Assignment
<i>Before CPE</i>								
OH-Span	12.22	151.81	215, 251, 294, 308, 363	12.12	407.0	[OH-Span + H] ⁺	327.0 206.0	Loss of SO ₃ Loss of N ₂ C ₆ H ₄ OH
<i>After CPE</i>								
A	2.43	175.18	217, 244, 288, 299, 353	2.32	302.0	[NAPDAD + H] ⁺	222.1	Loss of SO ₃
B	3.87	2.74	215, 274, 300	*	-	-	-	-
C	4.26	1.64	215, 274, 300	*	-	-	-	-
<i>Models</i>								
NAPDAD	2.41	252.17	219, 244, 289, 299, 353	2.8	302.0	[NAPDAD + H] ⁺	222.1	Loss of SO ₃
APOL	3.87 4.26	6.27 ^a	219, 274, 300	3.71	110.1	[APOL + H] ⁺	-	-

* Not observed

^a Integration across both peaks.

Table 4.4 ^1H chemical shifts (ppm), apparent diffusion coefficient per splitting ($D_{\text{All}} / 10^{-10} \text{ m}^2 \text{ s}^{-1}$), mean apparent diffusion coefficient per component ($D_{\text{mean}} / 10^{-10} \text{ m}^2 \text{ s}^{-1}$) and calculated diffusion coefficient ($D_{\text{Calculated}} / 10^{-10} \text{ m}^2 \text{ s}^{-1}$) for OH-Span, NAPDAD, APOL and HQ and ^1H chemical shifts (ppm), apparent diffusion coefficient per splitting ($D_{\text{All}} / 10^{-10} \text{ m}^2 \text{ s}^{-1}$), mean apparent diffusion coefficient per component ($D_{\text{mean}} / 10^{-10} \text{ m}^2 \text{ s}^{-1}$) and concentrations (Concn / $10^{-4} \text{ mol dm}^{-3}$) for each component (Comp) formed after CPE reduction.

Atom	Models						After CPE								
	$^1\text{H}^{\text{a}}$	Individual DOSY			Mixture DOSY		$D_{\text{calculated}}^{\text{b}}$	Comp	$^1\text{H}^{\text{a}}$	Individual DOSY		Concn ^c			
		D_{All}	D_{Mean}	D_{All}	D_{Mean}	D_{All}				D_{Mean}					
<i>OH-Span</i>															
1	9.30	1.00	s -	4.15		4.25									
3	8.65	1.00	s -	4.16		4.19, 4.19									
5	8.90	1.00	d 8.0	4.16, 4.15		4.15, 4.31									
6	7.83	1.00	t 8.0	4.14, 4.17, 4.12	4.16 ± 0.04	4.15, 4.09, 4.02	4.16 ± 0.08	2.74, 4.26							
7	8.30	1.00	d 8.0	4.20, 4.18		4.18, 4.05									
12/16	7.92	2.00	d 9.5	4.17, 4.15		4.18, 4.08									
13/15	7.01	2.00	d 9.5	4.16, 4.14		4.11, 4.25									
<i>NAPDAD</i>															
1	8.03	1.00	d 1.0	5.45, 5.45		5.24, 5.41		E ₃	8.03	1.00	d 1	4.95, 5.02			
3	7.81	1.00	d 1.0	5.30, 5.34		5.03, 5.03		E ₄	7.81	1.00	d 1	5.13, 5.12			
5	8.70	1.00	d 8.0	5.36, 5.39	5.36 ± 0.11	5.19, 5.19	5.17 ± 0.19	4.27, 4.73	E ₁	8.70	1.00	d 8	4.99, 4.87	5.08 ± 0.21	4.61
5	7.48	1.00	t 8.0	5.22, 5.40, 5.27		5.16, 5.14, 5.18			E ₅	7.48	1.00	t 8	5.66, 5.30, 5.00		
7	8.13	1.00	d 8.0	5.37, 5.44		5.14, 5.15			E ₂	8.13	1.00	d 8	4.94, 4.89		
<i>APOL</i>															
12/16	7.16	2.00	d 9.5	7.25, 7.30		6.82, 6.64			F ₁	7.20	2.00	d 9.5	6.72, 6.53		
13/15	6.93	2.00	d 9.5	7.22, 7.23	7.25 ± 0.04	6.70, 6.47	6.66 ± 0.18	5.82, 7.71	F ₂	6.94	2.00	d 9.5	6.30, 6.58	6.53 ± 0.21	4.60
<i>HQ</i>															
1	6.79	1.00	s -	7.63	7.63	-	-	-	G ₁	6.81	0.08	- -	6.57	6.57	0.09

^a Integration, multiplicity (s = singlet; d = doublet; t = triplet), splitting (Hz)

^b Diffusion coefficients calculated using Stokes-Einstein equation

^c Based on known sodium acetate concentration

Table 4.5 Estimated radius (R_H) from DFT structures and diffusion coefficients (D) for APOL, NAPDAD and OH-Span.

Compound	$R_H / 10^{-10} \text{ m}$	$D / 10^{-10} \text{ m}^2 \text{ s}^{-1}$
NAPDAD	4.51	4.27
	4.08	4.73
APOL	3.31	5.82
	2.50	7.71
OH-Span	7.03	2.74
	4.52	4.26

The DOSY aspect of the NMR technique was used here as a test case for analysis of a mixture of initially unknown products. So far reports in the literature indicate that the technique has been predominantly used for a mixture of components as made up.³⁹ The DOSY spectra of the NAPDAD, APOL and OH-Span alone showed slightly different diffusion coefficients compared to when they were studied as a mixture (Table 4.4). This can be attributed to either a genuine difference for example differences in viscosity, ionic strength, temperature as a mixture or to the processing of the data which is a fit to an exponential decay, where errors become greater when the signal-to-noise ratio decreases. There is certainly less spread of data when DOSY is recorded on individual components (Figures 4.20 and 4.29) compared to a mixture (Figure 4.30). The DOSY technique becomes very useful when it can resolve components of different diffusion coefficients which have overlapping peaks in the 1D ^1H spectra. This can be seen for the triplet peak of proton 6 on OH-Span and the doublet from proton 3 on NAPDAD (Figure 4.30), where there is a clear resolution of the diffusion coefficients of 4.16 and $5.32 \times 10^{-10} \text{ m}^2 \text{ s}^{-1}$, respectively. This may be a very useful feature when considering more complex systems.

In this work DOSY has also been used to study a mixture of components that have been produced by reactive chemical processes (Figure 4.21) and in summary the diffusion coefficients for the components produced after the CPE of OH-Span are comparable to those recorded from a mixture of NAPDAD and APOL, allowing their easy identification (Table 4.4). The DOSY spectrum of NAPDAD for proton 6 shows a spread of diffusion coefficients from 5.00 to $5.66 \times 10^{-10} \text{ m}^2 \text{ s}^{-1}$ possibly showing the increased level of inaccuracy in processing peaks with high order splitting.^{40,41}

4.2.2 Other R-Span dyes

Section 4.2.2.1 outlines the results from the spectroelectrochemical studies on all the other R-Span for comparison with OH-Span. Section 4.2.2.2 reports on the CPE reduction and section 4.2.2.3 reports on the HPLC analyses of NH₂-Span and NHAc-Span samples after CPE reduction; as with OH-Span, evidence for the formation of NAPDAD and the corresponding phenyl half of the dye (i.e APOL analogue) for NH₂-Span and NHAc-Span is reported.

4.2.2.1 Spectroelectrochemistry

Figures 4.33, 4.35 and 4.37 – 4.40 show the UV/Visible absorption spectra following the reduction of the NH₂-, NHAc-, OMe-, H-, Br and CN-Span dyes under nitrogen. Figures 4.34 and 4.36 show the UV/Visible absorption spectra following the oxidation of NH₂- and NHAc-Span dyes under nitrogen; none of the other R-Span dyes showed any evidence of oxidation in the range of 0 to +1.5 V. As for OH-Span, equation 4.1 was used to estimate the reduction and oxidation potentials of the dyes, which are given in Table 4.6 at the end of this section. In all cases the electrochemical process was found to be irreversible (the dye did not reform when the potential was reversed).

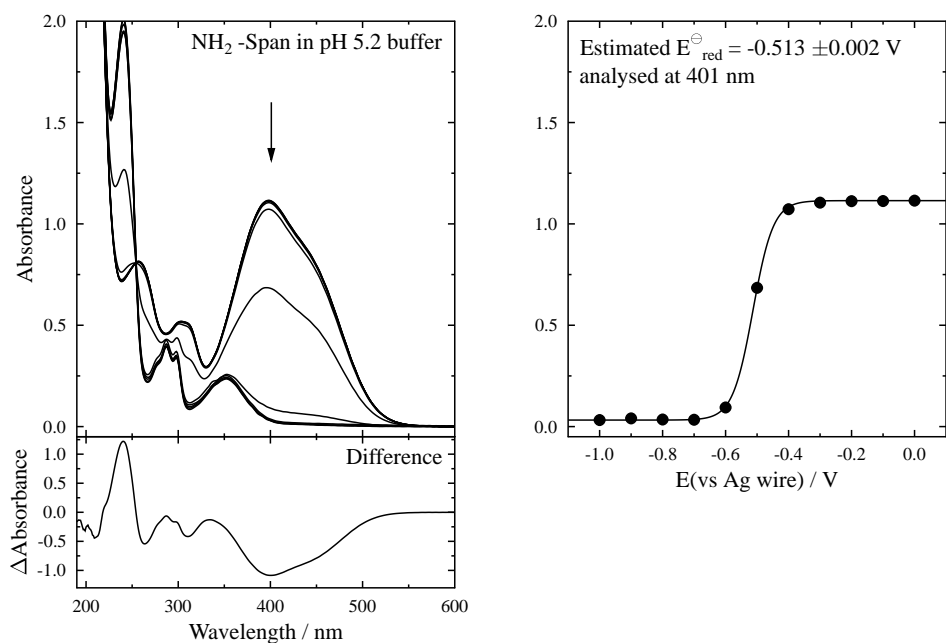


Figure 4.33 Left: UV/Visible absorption spectra of NH₂-Span (5×10^{-4} mol dm⁻³) in pH 5.2 sodium acetate buffer solution; the arrow indicates the change with decreasing potential over a range of 0 to -1.0 V (vs Ag wire) and with the overall difference spectrum (final – initial) shown. Right: Potential curve analysed using equation 4.1 at 401 nm where $n = 0.79$.

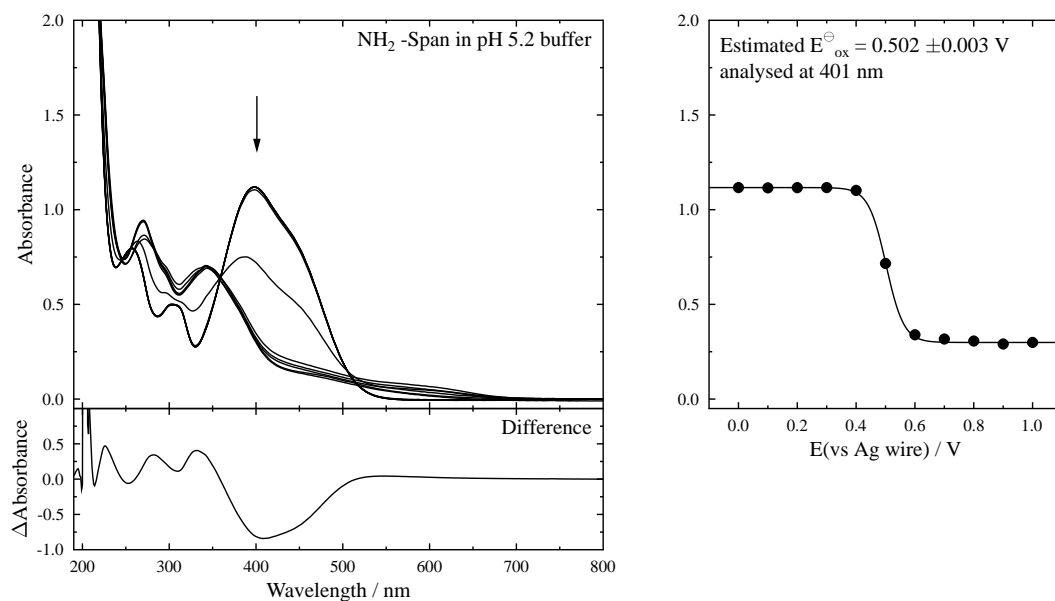


Figure 4.34 Left: UV/Visible absorption spectra of NH₂-Span (5×10^{-4} mol dm⁻³) in pH 5.2 sodium acetate buffer solution; the arrow indicates the change with increasing potential over a range of 0 to +1.0 V (vs Ag wire) and with the overall difference spectrum (final – initial) shown. Right: Potential curve analysed using equation 4.1 at 401 nm where $n = 0.85$.

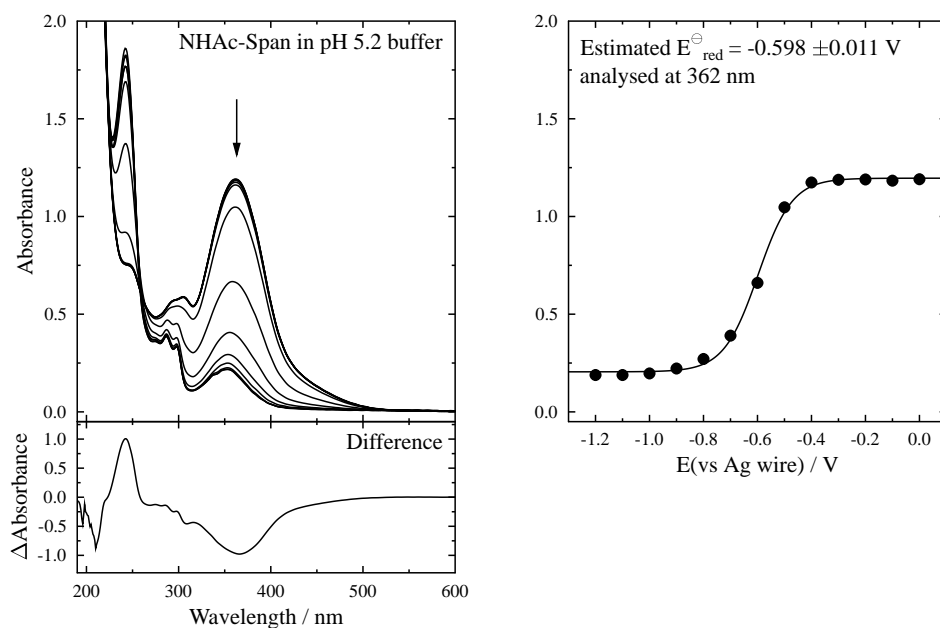


Figure 4.35 Left: UV/Visible absorption spectra of NHAc-Span ($5 \times 10^{-4} \text{ mol dm}^{-3}$) in pH 5.2 sodium acetate buffer solution; the arrow indicates the change with decreasing potential over a range of 0 to -1.2 V (vs Ag wire) and with the overall difference spectrum (final – initial) shown. Right: Potential curve analysed using equation 4.1 at 362 nm where $n = 0.40$.

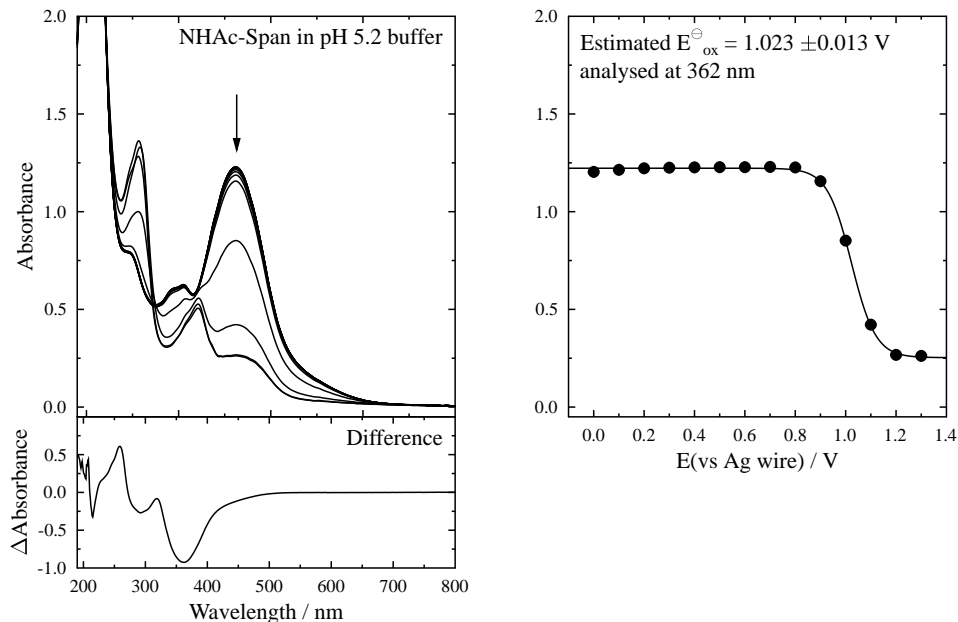


Figure 4.36 Left: UV/Visible absorption spectra of NHAc-Span ($5 \times 10^{-4} \text{ mol dm}^{-3}$) in pH 5.2 sodium acetate buffer solution; arrow indicates the change with increasing potential over a range of 0 to +1.0 V (vs Ag wire) and with the overall difference spectrum (final – initial) shown. Right: Potential curve analysed using equation 4.1 at 362 nm where $n = 0.53$.

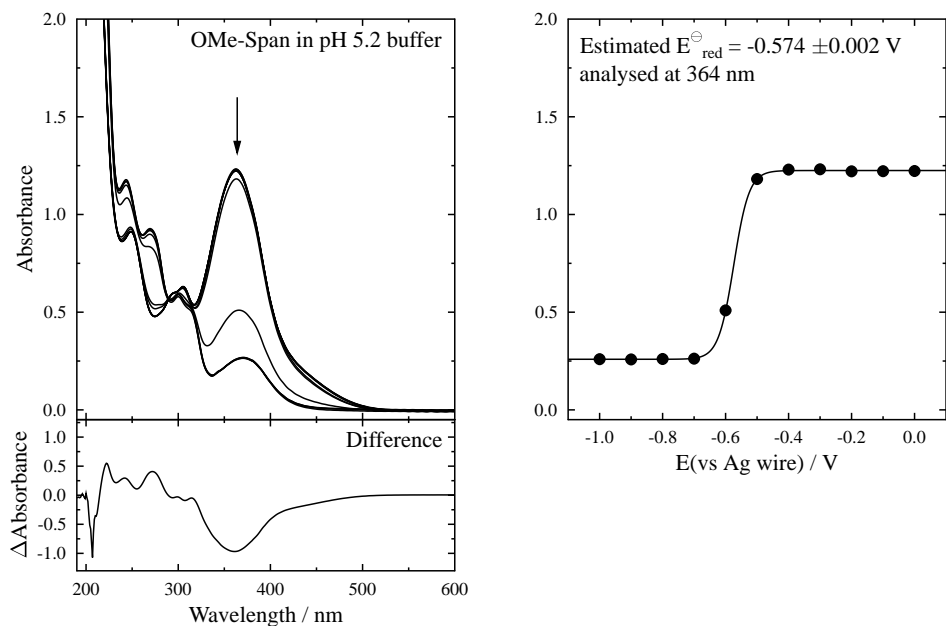


Figure 4.37 Left: UV/Visible absorption spectra of OMe-Span (5×10^{-4} mol dm $^{-3}$) in pH 5.2 sodium acetate buffer solution; the arrow indicates the change with decreasing potential over a range of 0 to -1.0 V (vs Ag wire) and with the overall difference spectrum (final – initial) shown. Right: Potential curve analysed using equation 4.1 at 364 nm where $n = 1.05$.

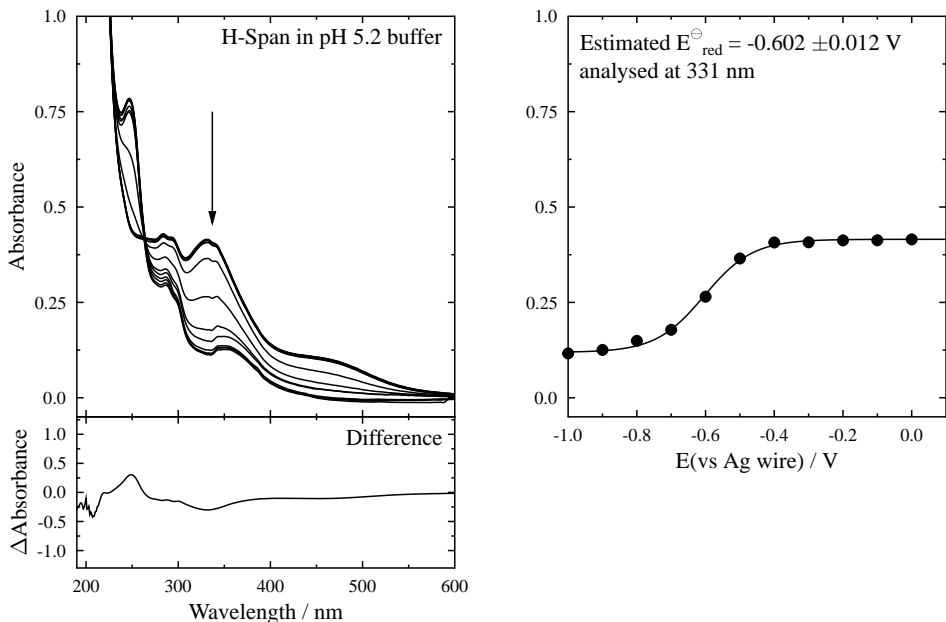


Figure 4.38 Left: UV/Visible absorption spectra of H-Span (5×10^{-4} mol dm $^{-3}$) in pH 5.2 sodium acetate buffer solution; the arrow indicates the change with decreasing potential over a range of 0 to -1.0 V (vs Ag wire) and with the overall difference spectrum (final – initial) shown. Right: Potential curve analysed using equation 4.1 at 331 nm where $n = 0.36$.

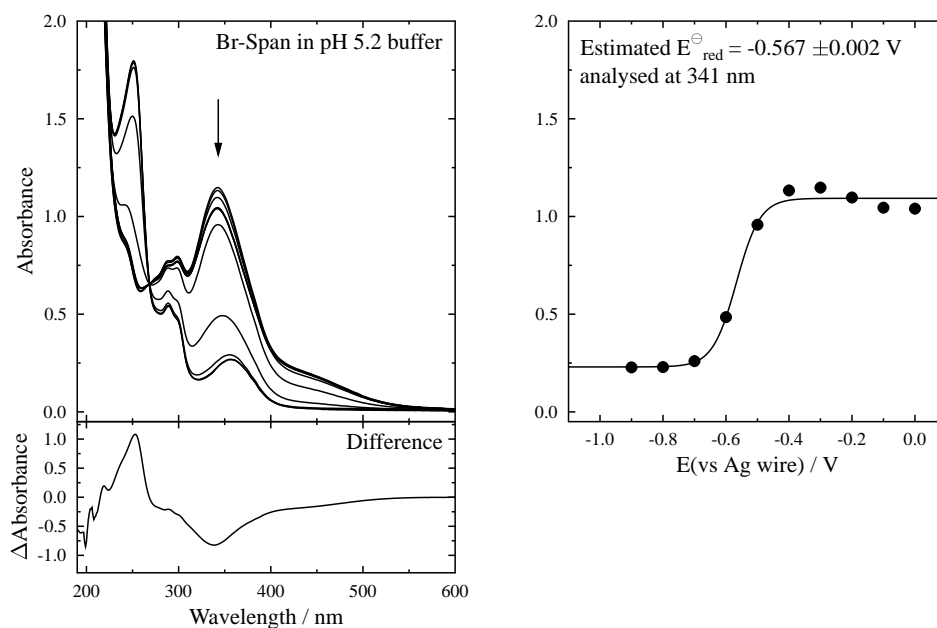


Figure 4.39 Left: UV/Visible absorption spectra of Br-Span ($5 \times 10^{-4} \text{ mol dm}^{-3}$) in pH 5.2 sodium acetate buffer solution; the arrow indicates the change with decreasing potential over a range of 0 to -0.9 V (vs Ag wire) and with the overall difference spectrum (final – initial) shown. Right: Potential curve analysed using equation 4.1 at 341 nm where $n = 0.68$.

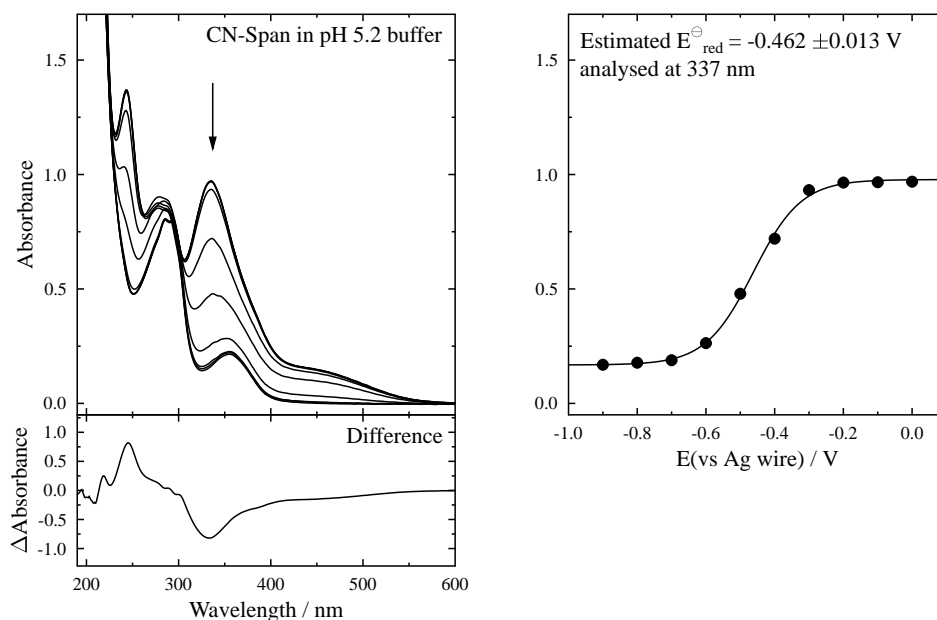


Figure 4.40 Left: UV/Visible absorption spectra of CN-Span ($5 \times 10^{-4} \text{ mol dm}^{-3}$) in pH 5.2 sodium acetate buffer solution; the arrow indicates the change with decreasing potential over a range of 0 to -0.9 V (vs Ag wire) and with the overall difference spectrum (final – initial) shown. Right: Potential curve analysed using equation 4.1 at 337 nm where $n = 0.37$.

Table 4.6 The estimated reduction and oxidation potentials for R-Span dyes in pH 5.2 sodium acetate buffer solution.

R-Span	-NH ₂	-OH	-OMe	-NHAc	-H	-Br	-CN
$E_{\text{red}}^{\ominus} / \text{V}$	-0.513	-0.749	-0.574	-0.598	-0.602	-0.567	-0.462
$E_{\text{ox}}^{\ominus} / \text{V}$	+0.502	+0.509	> 1.5	+1.023	> 1.5	> 1.5	> 1.5

4.2.2.2 Controlled potential electrolysis reduction

CPE was used to determine the number of electrons involved in the reduction of NH₂- and NHAc-Span. A potential of -1.2 V (vs Ag/AgCl) was applied to each dye sample and the current monitored over a period of 30 min as shown in Figures 4.41 and 4.42. The total charge (Q) was calculated by the integration of the current-time plot to give a charge-time plot and the number of electrons transferred was calculated as for OH-Span. After taking into account the current from the solvent background, the total charge from NH₂-Span was 17.3 C giving $4.49 \approx 4$ electrons transferred for the reduction process and the total charge from NHAc-Span was 19.45 C giving $5.00 \approx 5$ electrons transferred for the reduction process.

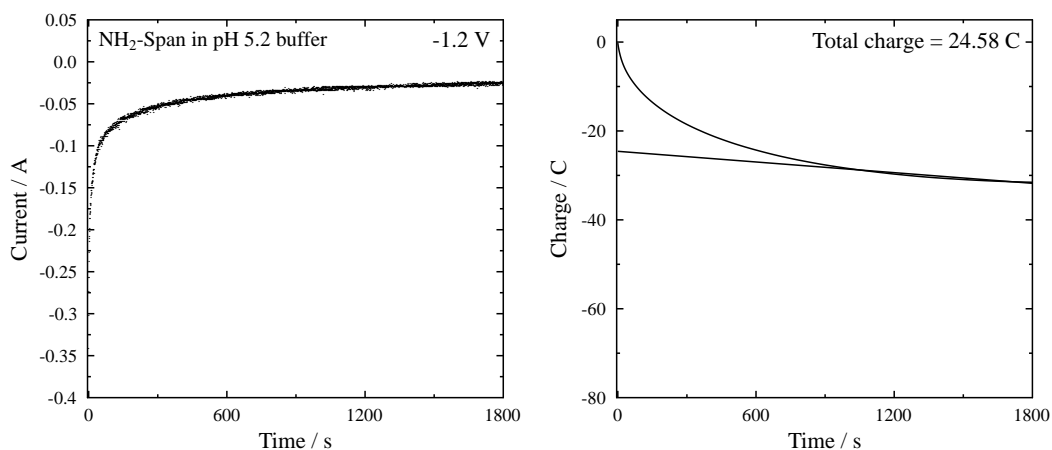


Figure 4.41 CPE reduction on $\text{NH}_2\text{-Span}$ ($8 \times 10^{-4} \text{ mol dm}^{-3}$) in pH 5.2 sodium acetate buffer solution over 30 min at a potential of -1.2 V (vs Ag/AgCl) Left: Current-time profile, Right: Charge-time profile.

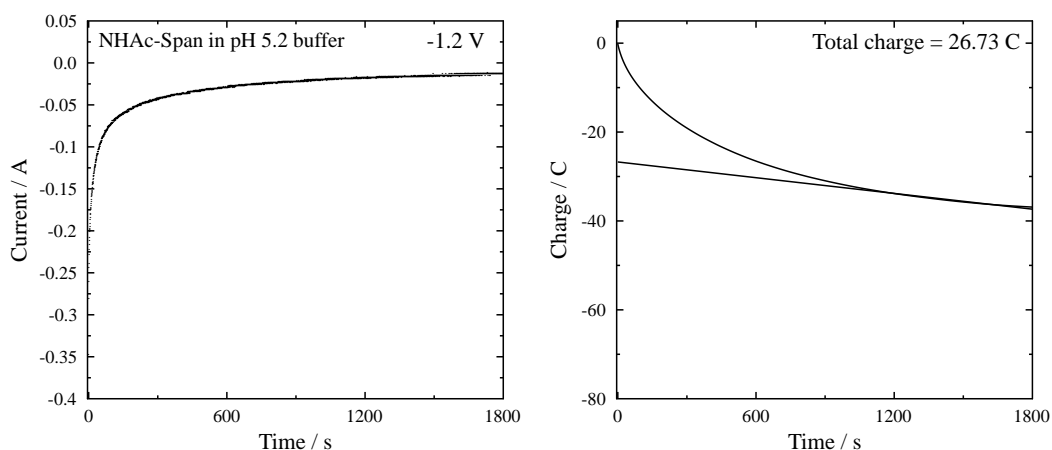


Figure 4.42 CPE on NHAc-Span ($8 \times 10^{-4} \text{ mol dm}^{-3}$) in pH 5.2 sodium acetate buffer solution over 30 min at a potential of -1.2 V (vs Ag/AgCl) Left: Current-time profile, Right: Charge-time profile.

4.2.2.3 Product analysis

The UV/Visible absorption spectrum of $\text{NH}_2\text{-}$ and NHAc-Span after CPE reduction gave a match to that after spectroelectrochemistry showing that the same process had occurred in each technique. Unlike OH-Span , samples were analysed only by HPLC before and after the CPE reduction process and are reported below.

NH₂-Span

The HPLC chromatograms before and after CPE reduction of NH₂-Span along with their UV/Visible absorption spectra for each component are shown in Figures 4.43 and 4.44. The retention times, peak integrations and UV/Visible absorption band positions are given in Table 4.7.

NH₂-Span alone has a peak with a retention time of 10.72 min in the HPLC chromatogram which disappears after CPE reduction giving products A' and B' with peaks at 2.41 and 3.65 min, respectively. Component A' can be assigned to NAPDAD by comparison with the analysis reported for OH-Span in section 4.2.1 (Table 4.3). The HPLC chromatogram (RT = 3.64 min) and UV/Visible absorption spectrum of an authentic sample of 1,4-diaminobenzene (DAB, Figure 4.45) shown in Figure 4.46 matches those of component B'. The retention times, peak integrations and UV/Visible absorption band positions of DAB are given in Table 4.8. The UV/Visible absorption spectra of DAB over the pH range ca. 2 to 12 are shown in Figure 4.47; this spectrophotometric pH titration gave pK_a values of 2.72 and 5.35 attributed to the protonation of the NH₂ group shown in Figure 4.48 (method like the one used in section 3.2.1.1). Therefore reduction studies carried out here at pH 5.2 are in the region of the pK_a for the equilibrium between DAB and protonated DAB. A third pK_a was observed at 10.76, however this was found to be a irreversible chemical effect.

Quantitative analysis of the HPLC traces (where concentration calibration curves for DAB are shown in Appendix A2.4) shows that a NH₂-Span starting concentration of $8.0 \times 10^{-4} \text{ mol dm}^{-3}$ gives NAPDAD and DAB concentrations of $6.9 \times 10^{-4} \text{ mol dm}^{-3}$ and $7.0 \times 10^{-4} \text{ mol dm}^{-3}$, respectively at the end of the reduction. Therefore within experimental error, 1 mole of NH₂-Span electrochemically reduces to ca. 0.9 mole of NAPDAD and ca. 0.9 mole of DAB, consistent with a two-step four-electron transfer reduction process.

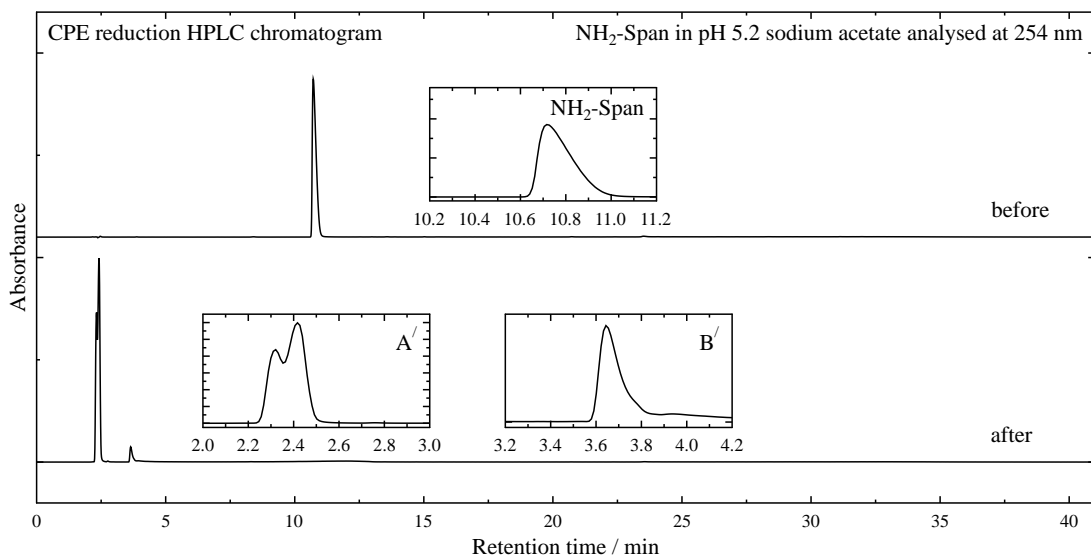


Figure 4.43 HPLC chromatograms of NH₂-Span (8×10^{-4} mol dm⁻³) before (top) and after (bottom) CPE reduction. Inserts show the expansions of the HPLC chromatogram of each component.

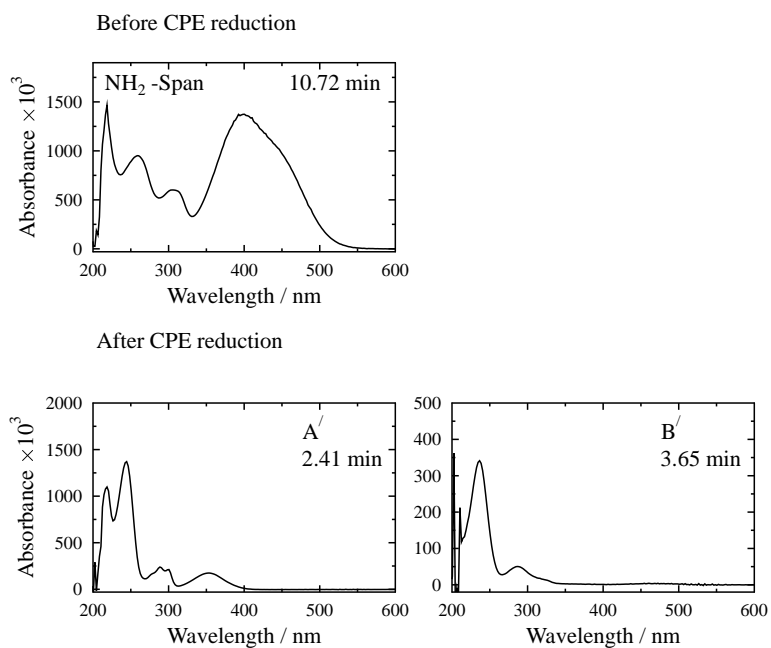


Figure 4.44 Top: UV/Visible absorption spectrum of NH₂-Span (8×10^{-4} mol dm⁻³) before CPE reduction at an elution time of 10.72 min. Bottom: UV/Visible absorption spectra of Components A' and B' after CPE reduction at retention times of 2.41, 3.65 min.

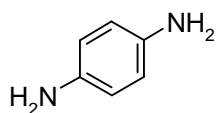


Figure 4.45 Structure of DAB.

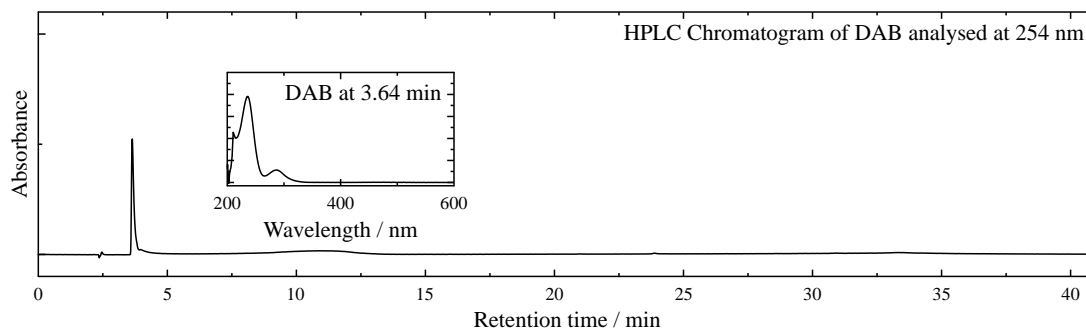


Figure 4.46 HPLC chromatogram DAB at $1 \times 10^{-3} \text{ mol dm}^{-3}$ and pH 5.2. Insert: UV/Visible absorption spectra of DAB at retention time of 3.64 min.

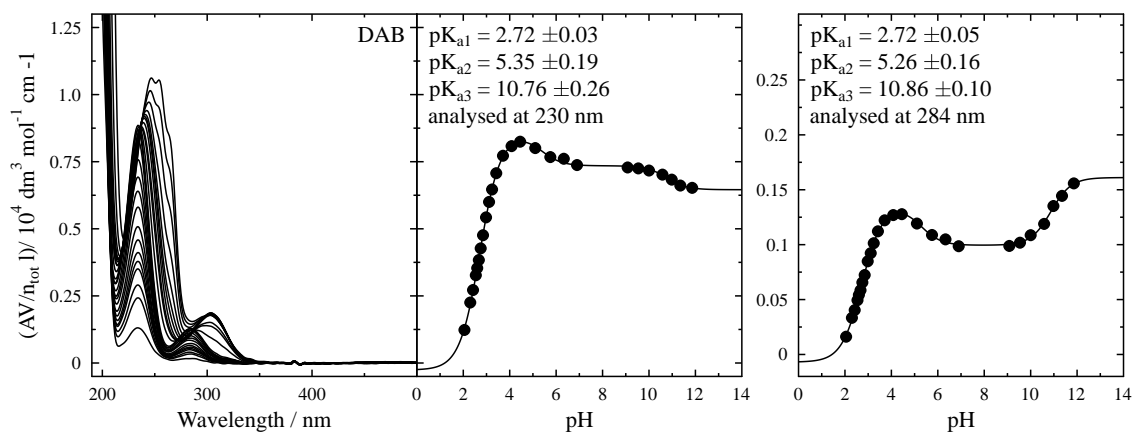
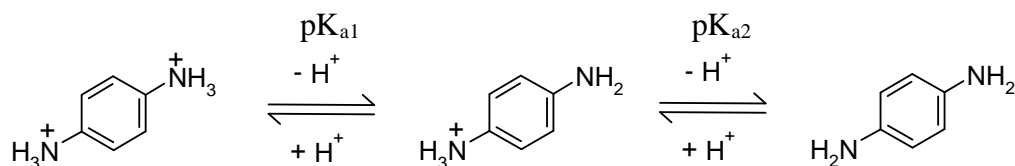


Figure 4.47 Left: UV/Visible absorption spectra of aqueous DAB at $5 \times 10^{-5} \text{ mol dm}^{-3}$ over a pH range of pH 2 to 12. Right: pH curve analysed using a multi pK_a equation (Appendix 1 equation A1.42) at 230 and 284 nm.



Di-protonated DAB

Protonated DAB

DAB

Figure 4.48 Protonation of DAB; pK_a of 2.72 and 5.35 in water, pK_{a3} is non-reversible, hence a chemical effect.

Table 4.7 Retention times (RT / min), peak integrations (PI) and UV/Visible absorption band positions (λ / nm) from HPLC and Retention times (RT / min) components before and after CPE reduction of NH₂-Span (8×10^{-4} mol dm⁻³) and DAB (1×10^{-3} mol dm⁻³).

Component	RT	PI	λ
<i>Before CPE reduction</i>			
NH ₂ -Span	10.72	164.50	218, 260, 307, 401
<i>After CPE reduction</i>			
A'	2.41	175.38	217, 244, 288, 299, 353
B'	3.65	14.35	237, 288, 322, 470
DAB	3.64	20.51	213, 288, 322, 470

NHAc-Span

The HPLC chromatograms before and after CPE of NHAc-Span along with their UV/Visible absorption spectra for each component are shown in Figures 4.49 and 4.50. The retention times, peak integrations and UV/Visible absorption band positions are given in Table 4.8.

NHAc-Span alone has a peak with retention time of 14.89 min in the HPLC chromatogram which disappears after CPE reduction giving products A^{//}, B^{//}, C^{//}, D^{//} and E^{//} with retention times of 2.37, 3.10, 3.79, 6.28 and 10.36 min, respectively. Component A^{//} can be assigned to NAPDAD by comparison with the analysis reported for OH-Span in section 4.2.1 (Table 4.3). The HPLC chromatogram (RT = 10.36 min) and UV/Visible absorption spectrum of an authentic sample of N-(4-aminophenyl)acetamide (APA) shown in Figure 4.52 match those of component E^{//}. The retention times, peak integrations and UV/Visible absorption band positions of APA are given in Table 4.8. The UV/Visible absorption spectra of APA over the pH range ca. 2 to 12 are shown in Figure 4.53; this spectrophotometric pH titration gave a pK_a of 4.39 due to the protonation of the NH₂ group shown in Figure 4.54. Therefore reduction studies carried out here at pH 5.2 are on the edge of the pK_a for the equilibrium between APA and protonated APA.

Quantitative analysis of the HPLC traces (where concentration calibration curves for APA are shown in Appendix A2.4) shows that a NHAc-Span starting concentration of $8.0 \times 10^{-4} \text{ mol dm}^{-3}$ gives NAPDAD and APA concentrations of $6.3 \times 10^{-4} \text{ mol dm}^{-3}$ and $5.6 \times 10^{-4} \text{ mol dm}^{-3}$, respectively at the end of the reduction. Therefore within experimental error, 1 mole of NHAc-Span electrochemically reduces to ca. 0.8 mole of NAPDAD and ca. 0.7 mole of APA. In contrast to OH-Span and NH₂-Span reductions, it is clear that other electron transfer processes are occurring with NHAc-Span in addition to the two-step four-electron transfer reactions. This is supported by CPE reduction which shows a 5 electron process and the additional products B^{//}, C^{//} and D^{//} observed by HPLC.

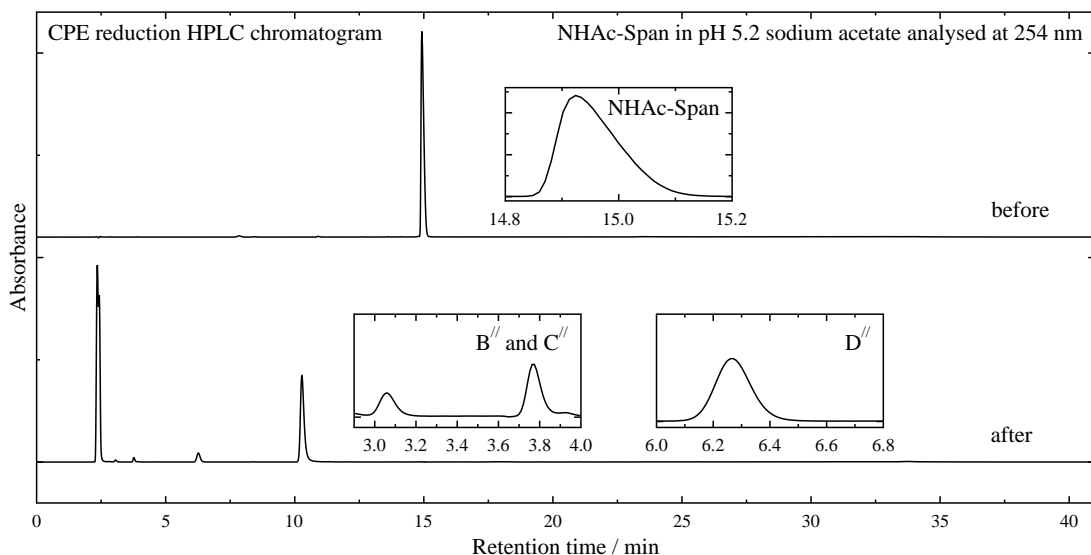


Figure 4.49 HPLC chromatograms of NHAc-Span ($8 \times 10^{-4} \text{ mol dm}^{-3}$) before (top) and after (bottom) CPE reduction. Inserts show expansion of selected regions of the HPLC chromatogram of components at ca. 3 and 6 min.

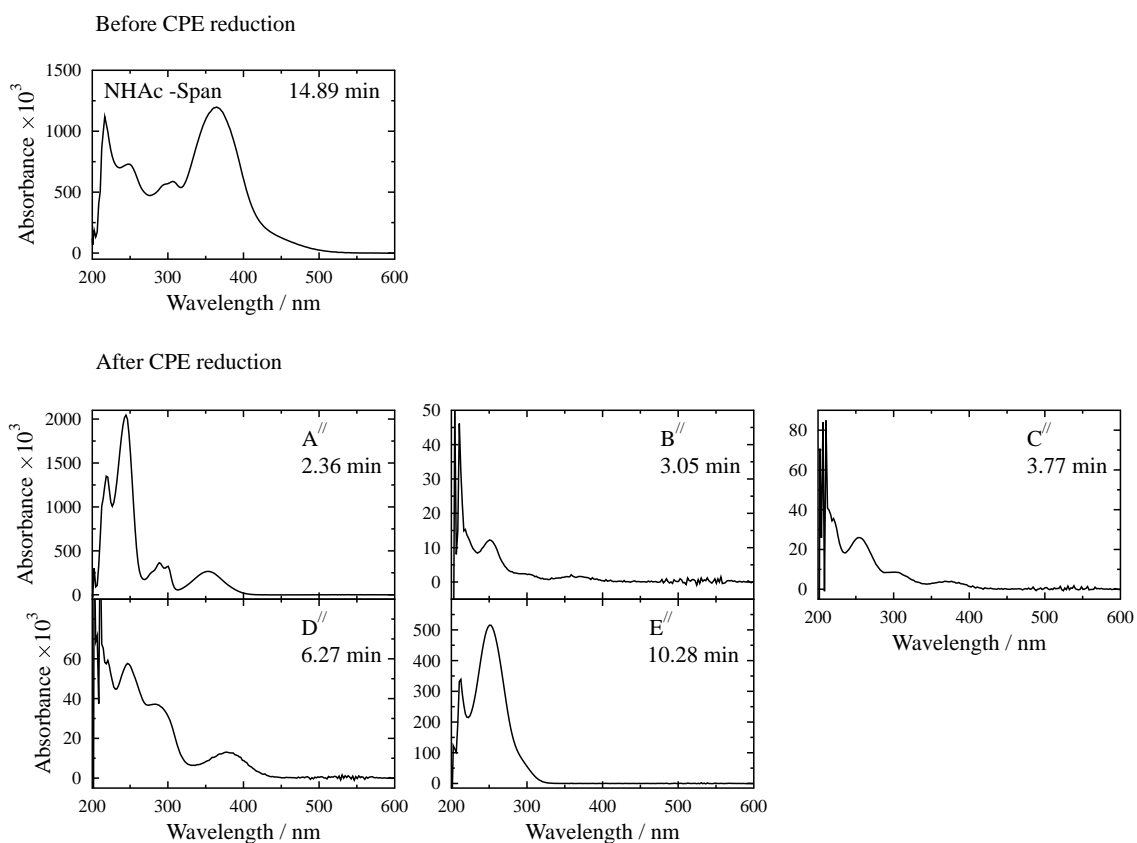


Figure 4.50 Top: UV/Visible absorption spectrum of NHAc-Span ($8 \times 10^{-4} \text{ mol dm}^{-3}$) before CPE at an elution time of 14.89 min. Bottom: UV/Visible absorption spectra of Components A'', B'', C'', D'' and E'' after CPE at retention times of 2.36, 3.05, 3.77, 6.27, 10.28 min.

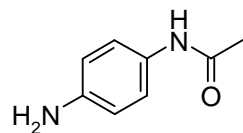


Figure 4.51 Structure of APA.

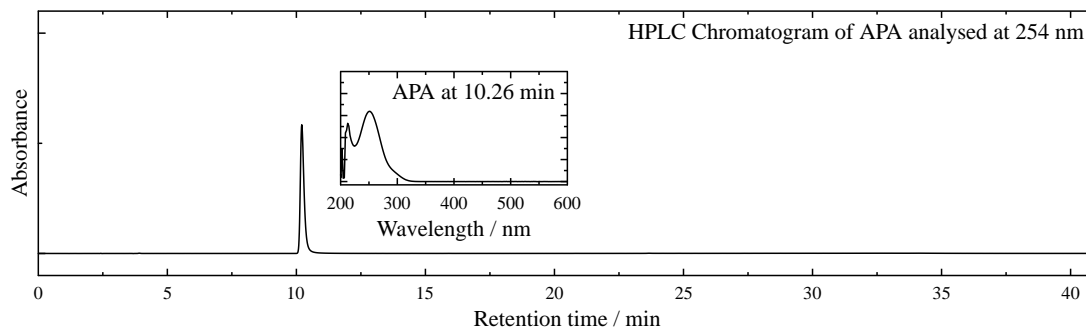


Figure 4.52 HPLC chromatogram APA at $1 \times 10^{-3} \text{ mol dm}^{-3}$ and pH 5.2. Insert: UV/Visible absorption spectra of APA at retention time of 10.26 min.

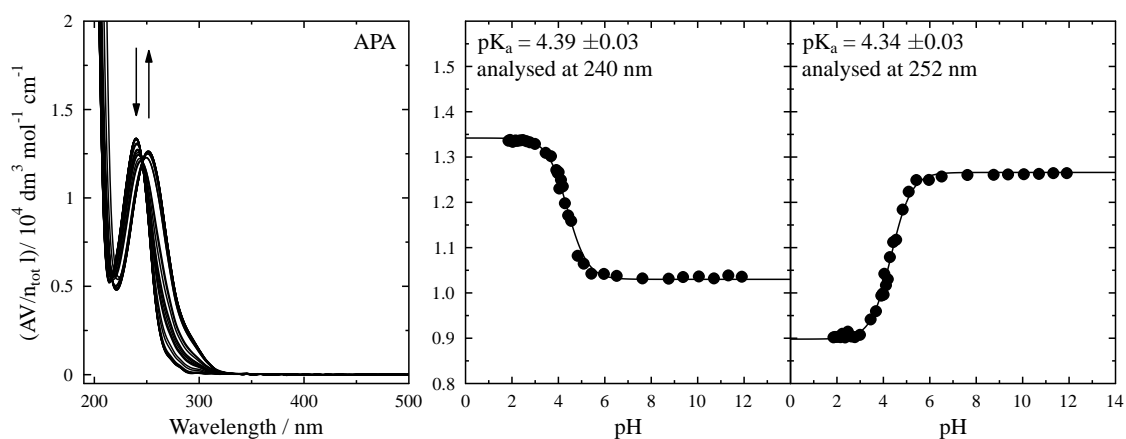


Figure 4.53 Left: UV/Visible absorption spectra of aqueous APA at $5 \times 10^{-5} \text{ mol dm}^{-3}$; the arrows indicate changes with increasing pH over a range of pH 2 to 12. Right: pH curve analysed using equation 3.3 (Chapter 3) at 240 and 252 nm.

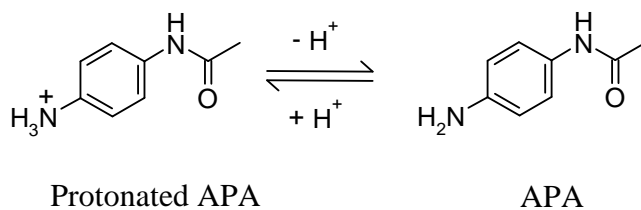


Figure 4.54 Protonation of APA; pK_a of 4.39 in water.

Table 4.8 Retention times (RT / min), peak integrations (PI) and UV/Visible absorption band positions (λ / nm) from HPLC and Retention times (RT / min) components before and after CPE of NHAc-Span (8×10^{-4} mol dm⁻³) and compound APA (1×10^{-3} mol dm⁻³).

Component	RT	PI	λ
<i>Before CPE</i>			
NHAc-Span	14.94	152.59	218, 250, 295, 307, 365
<i>After CPE</i>			
A ^{//}	2.37	159.26	217, 244, 288, 299, 353
B ^{//}	3.10	1.04	220, 252, 297, 356
C ^{//}	3.79	2.21	218, 254, 304, 372
D ^{//}	6.28	8.74	214, 221, 248, 291, 382
E ^{//}	10.36	86.00	213, 251
APA	10.27	151.45	213, 251

4.2.3 Summary

This summary firstly considers electrochemical reduction studies of the R-Span dye series, before considering the effect of the R substituent; finally there is a brief consideration of the limited electrochemical oxidation studies.

4.2.3.1 Reduction

Spectroelectrochemistry on all R-Span dyes has shown a bleach of the main dye absorption band which is irreversible, occurring at potentials of ca -0.4 to -0.8 V. CPE reduction studies of NH₂- and OH-Span have shown that four electrons are consumed per mole of dye, consistent with a four-electron four-proton reduction process.^{3,14} The proposed mechanism is a two-step four-electron reduction process (Figure 4.20),^{3,9,18,22,34} which has been reported in other studies, however, the CV and spectroelectrochemistry reported here have not resolved the individual steps in the mechanism. The careful quantitative product analysis on the components formed after CPE reduction of NH₂- and OH-Span has shown that the near equimolar formation of two main products; the naphthyl half of the dye NAPDAD and the phenyl half of the dye, DAB and APOL, respectively. The formation of these products is consistent with reduction taking place across the azo linkage by a process of N-N bond scission. It has been observed through the more detailed product analysis on the components formed after CPE reduction of OH-Span that there is at least one additional side reaction occurring, which is proposed here to be the formation of 1,4-hydroquinone at very low yield.²⁷

Studies on NHAc-Span have shown that reduction is more complicated, where CPE studies have shown that a five electron reduction process is occurring, and where product analysis by HPLC alone has shown that additional products have formed. However, the quantitative analysis of these products has shown that the main products are NAPDAD and the phenyl half of the dye APA, again consistent with the proposed reduction process occurring across the azo linkage. The additional electron transfer processes observed could be from the acetamide group, being activated by the benzene ring towards reduction.⁴²

CPE reduction and the associated product studies were not performed on OMe-, H-, Br and CN-Span due to limiting quantities and purity. The UV/Visible absorption spectra recorded after the spectroelectrochemical reduction of all the R-Span dyes are shown in Figure 4.55 from which the following observations can be made. Firstly, the product spectra for H-, Br- and CN-Span after spectroelectrochemical reduction all have band features at 353 nm, the same band that is observed in the product spectra of NH₂-, OH- and NHAc-Span, which has been assigned to NAPDAD (also shown in Figure 4.55). The formation of NAPDAD from H-, Br- and CN-Span is consistent with reduction occurring at the azo linkage. Secondly the product spectrum from OMe-Span shows a band at a longer wavelength of 372 nm; from this, one can conclude that, as for NHAc-Span, there are additional products being formed due to other electron transfer processes.

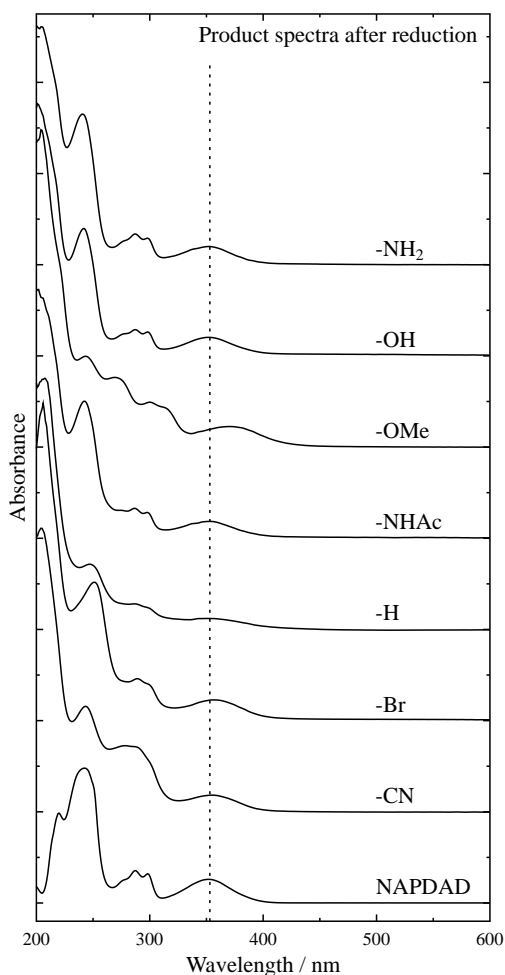


Figure 4.55 UV/Visible absorption product spectra formed after the spectroelectrochemical reduction of the R-Span dyes; dashed line represents the absorption band of NAPDAD at 353 nm.

4.2.3.2 Substituent effect

Spectroelectrochemistry on all R-Span dyes has allowed for the estimation of their reduction potentials, allowing some insight to be gained into the R substituent effect. However, interpreting the experimental data in this way is complicated by what the estimated reduction potentials represent; the individual steps in the reduction mechanism are not identified and the analysis of the spectral changes using equation 4.1 (section 4.2.1.2) is simply a functional fit to the data because this equation applies to a reversible electrochemical process. The reported two step reduction of azo dyes attributes the first step to a reversible formation of the hydrazine followed by the second step, an irreversible N-N scission (Figure 4.20).^{3,4,9,18,22,34} In the case of the R-Span dyes studied here, the potential at which the second step occurs is unknown. It is possible that the two steps could be occurring at overlapping potentials for R-Span, which contrasts the reduction of a set of substituted azobenzenes in which the potential for the formation of the hydrazine was clearly observed, as described in section 4.1.3.^{18,34}

An overlay plot of the fitted curves for the spectroelectrochemical reduction of the R-Span dyes using equation 4.1 (section 4.2.1.2) is shown in Figure 4.56, in which the estimated potential for the start (E_1) and end (E_2) of the reduction process and potential range (Δ) in which reduction is occurring is given in Table 4.9. The observation from this is that the start of the reduction process (E_1) for R-Span is in the order CN-, H-, NHAc-, NH₂-, Br-, OMe-, OH-Span and the end of the reduction process (E_2) is in the order NH₂-, OMe-, Br-, CN-, NHAc-, H-, OH-Span, on going from low to high potential. There appears to be no clear trend to the substituent effect, but evidently the potential range in which the dye undergoes reduction is dependent on the substituent, which at the two extremes is ca. 0.30 V and 0.77 V for OMe-Span containing an electron-donating substituent and CN-Span containing an electron-withdrawing substituent, respectively; the fitted values of n relate inversely to the value of the range (Table 4.9). The onset of the reduction for the dye containing the most electron-withdrawing substituent CN occurs at ca. -0.08 V, a lower potential than any of the other R-Span dyes. The onset of the reduction for the dye containing the second most electron-donating substituent OH, occurs at ca. -0.49 V, a higher potential than any of the other R-Span dyes.

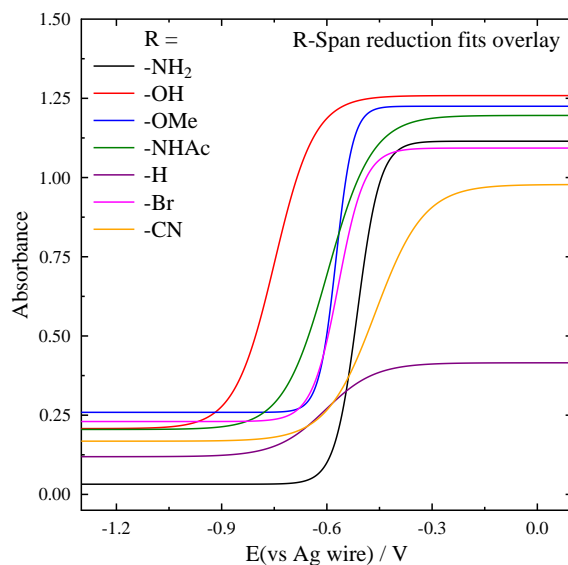


Figure 4.56 Fitted curves of the spectroelectrochemical reduction of the R-Span dyes analysed by equation 4.1. (*Original in colour*)

Table 4.9 Estimated reduction potentials (vs Ag wire) for the start (E_1), (E_2), potential range (Δ) and a measure of the slope (n) in which reduction is occurring for R-Span dyes in pH 5.2 sodium acetate buffer solution.

R-Span	-NH ₂	-OH	-OMe	-NHAc	-H	-Br	-CN
E_1 / V	-0.36	-0.49	-0.45	-0.30	-0.24	-0.40	-0.08
E_2 / V	-0.73	-1.06	-0.75	-0.93	-0.97	-0.80	-0.85
$\Delta (E_1 - E_2) / V$	0.37	0.57	0.30	0.63	0.73	0.40	0.77
n	0.79	0.45	1.05	0.40	0.36	0.68	0.37

The fits to equation 4.1 give an estimate of the reduction potential of each R-Span dye, which despite being an estimate give a set of values which can be compared using the R substituent Hammett constants σ_p and σ_p^- as given in Table 4.10 and plotted in Figure 4.57. σ_p^- constants are an alternative set of values to σ_p that can be considered where the substituent interacts directly with a developing negative charge at the reaction centre, as is occurring in a reduction process. In general, reduction occurs at less negative voltages upon the increasing electron withdrawing capacity of substituents, which may be due to the stabilisation of negative charge after the addition of an electron. Using σ_p , there is a clear trend upon going across the dye series from CN-Span to OH-Span, where the exception appears to be NH₂-Span, in which reduction is occurring at a lower potential than predicted by σ_p . σ_p^- shows a similar trend to σ_p , in which fitting to a straight line gives a better fit as indicated by R^2 values of 0.4521 and 0.1776, respectively. The use

of σ_p showed a good fit to the reduction potentials in the study of substituted azobenzenes as reported in the literature (Figure 4.9).³⁴

The observation of a lower estimated potential than expected for NH_2 -Span could occur if NH_3^+ -Span were present ($\sigma_p = +0.60$), although these studies at pH 5.2 were well removed from the pK_a of 2.88 indicating that the unprotonated form was dominant at ca. 99.6 % (Chapter 3 Figure 3.15); further studies would be required to explore any possible effect further.

Table 4.10 *Para* substituent Hammett σ_p and σ_p^- constants⁴³ and the estimated reduction potentials for R-Span dyes in pH 5.2 sodium acetate buffer solution.

R-Span	-NH ₂	-OH	-OMe	-NHAc	-H	-Br	-CN
σ_p	-0.66	-0.37	-0.27	0.00	0.00	+0.23	+0.66
σ_p^-	-0.15	-0.37	-0.26	-0.46	0.00	+0.25	+1.00
$E_{\text{red}}^\ominus / \text{V}$	-0.513	-0.749	-0.574	-0.598	-0.602	-0.567	-0.462

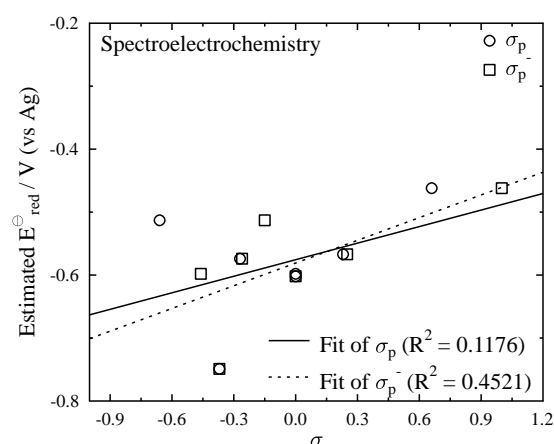


Figure 4.57 Estimated reduction potentials for R-Span dyes in pH 5.2 sodium acetate buffer solution vs *para* substituent Hammett constants, σ_p and σ_p^- and their fits to a straight line.

The site of electron transfer on reduction of the azo dyes can be considered using the calculated Mulliken atomic charges (section 3.2.2.3). Figure 4.58 shows a plot of the Mulliken atomic charges given in Table 4.11 for the R-Span dyes at $\text{N}\alpha$ and $\text{N}\beta$ against the *para* substituent Hammett constants σ_p and σ_p^- . In the case of $\text{N}\alpha$ there is a very clear trend with R substituent constant σ_p in which upon increasing electron withdrawing capacity the calculated charge decreases linearly, showing a decrease in

electron density. For N β there is a similar trend, but it is less distinct. The comparison to σ_p^- shows less distinct trends. The calculations show that for all the R-Span dyes except CN-Span the calculated Mulliken atomic charge for N β is lower than N α , suggesting that the initial site of reduction may be N β . However, Figure 4.59 shows that there is little correlation with the estimated reduction potential obtained experimentally for the R-Span series and further work would need to be considered to test this interpretation, for example calculations on the reduced forms; it is therefore unknown at this stage whether the use of the calculated Mulliken atomic charges can be used to give a good indicator as to the initial site of reduction.

Table 4.11 *Para* substituent Hammett σ_p and σ_p^- constants⁴³ and the calculated Mulliken atomic charges (*q*) for the R-Span dyes.

R-Span	-NH ₂	-OH	-OMe	-NHAc	-H	-Br	-CN
σ_p	-0.66	-0.37	-0.27	0.00	0.00	+0.23	+0.66
σ_p^-	-0.15	-0.37	-0.26	-0.46	0.00	+0.25	+1.00
N α	-0.328	-0.320	-0.319	-0.314	-0.307	-0.308	-0.300
N β	-0.312	-0.307	-0.308	-0.312	-0.301	-0.303	-0.304

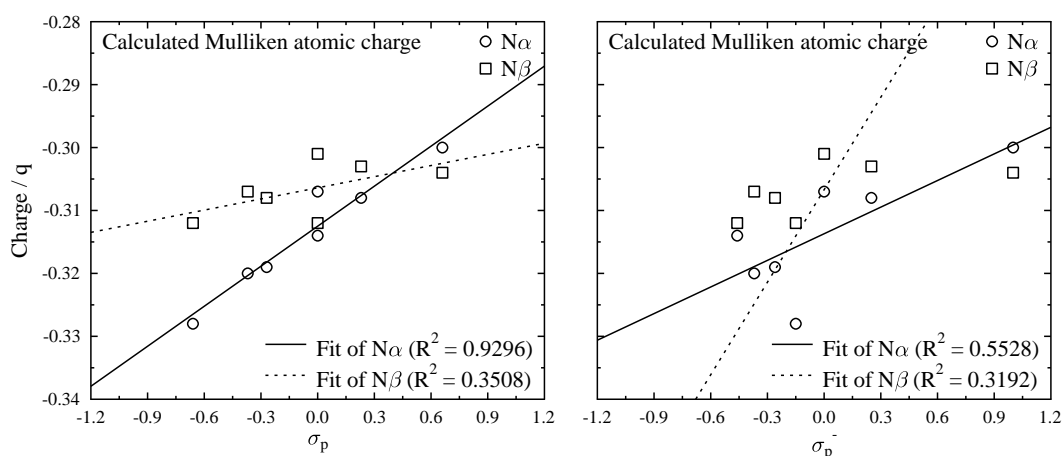


Figure 4.58 Calculated Mulliken atomic charges for N α and N β for the R-Span dyes vs; Left: *Para* substituent Hammett σ_p constants and Right: *Para* substituent Hammett σ_p^- constants and their fits to a straight line.

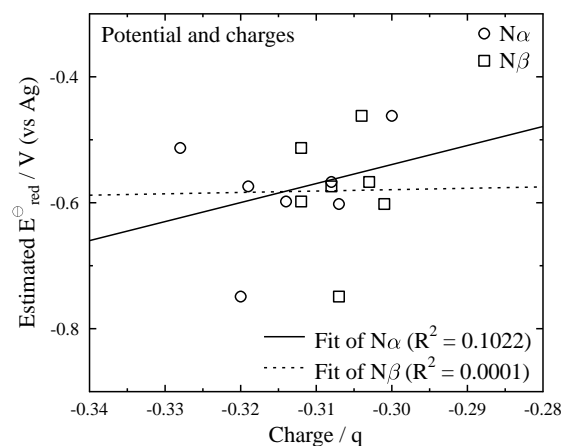


Figure 4.59 Estimated reduction potentials for R-Span dyes in pH 5.2 sodium acetate buffer solution vs calculated Mulliken atomic charges for N_{α} and N_{β} for the R-Span dyes and their fits to a straight line.

4.2.3.3 Oxidation

Spectroelectrochemistry allowed the irreversible oxidation of solutions of NH_2^- , OH^- and $NHAc$ -Span dyes in pH 5.2 sodium acetate buffer solution to be observed. No oxidation was detected for any of the other R-Span dyes up to a potential of +1.5 V. The oxidation at lower potentials for increasing electron-donating substituents may be attributed to the resulting increase in electron density across the azo linkage. The absence of an observed oxidation for those dyes containing electron-withdrawing substituents indicates that these derivatives are well suited for oxidation resistance.

4.3 Conclusions

Predominately, the electrochemical techniques spectroelectrochemistry and CPE have been used to study the electron transfer reactions that occur in aqueous samples of R-Span dyes. CV has not proved useful for these dyes due to the irreversibility of the electron transfer process.

The combination of HPLC, LC-MS and NMR analysis has proved useful in analysing products formed after CPE reduction of OH-Span which showed an irreversible four-electron process, proposed to occur in two steps as shown in Figure 4.60. More limited studies on other R-Span dyes have shown that, like OH-Span, they are reduced in a reductive cleavage giving NAPDAD along with the corresponding *para* substituted aminobenzene. The extensive use and combination of methods for quantitative product analysis after reduction has shown there are also other side reactions occurring for some substituents.

DOSY NMR was investigated here to assess how it can be used to study a mixture of products formed after CPE reduction of OH-Span. The techniques have proved useful in being able to resolve the components formed based on their size, and the study has opened up the possibility of being able to apply this approach to more complicated systems, for example photochemical studies of azo dyes as reported in Chapter 5.

In general those R-Span dyes containing electron withdrawing groups are more easily reduced and less easily oxidised. The use of the *para* substituent Hammett constants σ_p and σ_p^- provide comparable trends to the experimental data. The use of the calculated Mulliken atomic charges, predicting the site of reduction has shown that there is a direct correlation between the calculated charge across the azo linkage, but does not correlate well with the estimated reduction potentials found experimentally by spectroelectrochemistry. The study has shown that without being able to determine the potential at which the hydrazine forms from these dyes, it is hard to compare the results directly with Hammett constants.

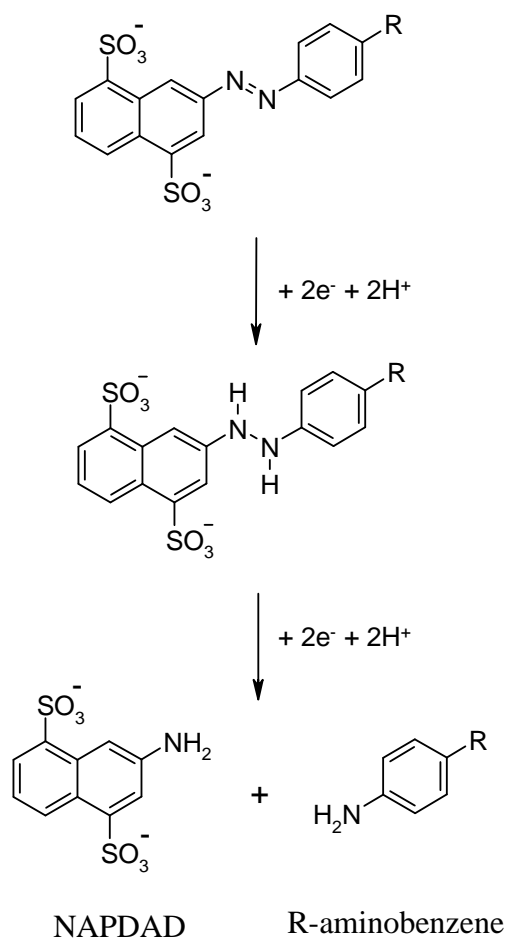


Figure 4.60 Generic two-step four-electron reduction of R-Span producing NAPDAD and R-aminobenzene.

4.4 References

1. Goyal, R. N.; Minocah, A. *J. Electroanal. Chem.*, **1985**, *193*, 231-240.
2. Peng, X.; Yang, Jinzong. *Dyes Pigm.* **1992**, *20*, 73-81.
3. Xu, G.; O'Dea, J. J.; Osteryoung, J. G. *Dyes Pigm.* **1996**, *30*, 201-223.
4. Goyal, R. N.; Verma, M. S.; Singhal, N. K. *Croat. Chem. Acta*, **1998**, *71*, 715-726.
5. Yasin, S. A. *Port. Electrochimica Acta*, **2006**, *24*, 23-36.
6. Jain, R.; Vershney, S.; Sikarwar, S. *J. Colloid Interface Sci.* **2007**, *313*, 248-253.
7. Jain, R.; Bhargava, M.; Sharma, N. *Ind. Eng. Chem. Res.* **2003**, *42*, 243-247.
8. Bicer, E.; Arat, C. *Croat. Chem. Acta*, **2009**, *82*, 583-593.
9. Atkinson, D. PhD Thesis, University of York, 2007.
10. Zanon, M. V. B.; Carneiro, P. A.; Furlan, M.; Duarte, E. S.; Guaratini, C. C. I.; Fogg, A. G. *Anal. Chim. Acta.* **1999**, *385*, 385-392.
11. Cakir, S.; Bicer, E.; Odabasoglu, M.; Albayrak, C. *J. Braz. Chem.* **2005**, *16*, 711-717.
12. Ilyasov, A. V.; Vafina, A. A.; Morozov, V. I.; Zaripova, R. M.; Gruzdnova, V. N.; Kazitsyna, L. A. *Russ. Chem Bull.* **1979**, *28*, 311-315.
13. Ucar, M.; Polat, K.; Solak, A. O.; Toy, M.; Aksu, M. L. *Dyes Pigm.* **2010**, *87*, 55-61.
14. Hart, J. P.; Smyth, W. F. *The Analyst* **1980**, *105*, 929-938.
15. Salbeck, J. *Anal. Chem.* **1993**, *65*, 2189-2173.
16. Guaratini, C. C. I.; Fogg, A. G.; Zanon, M. V. B. *Electroanalysis* **2001**, *13*, 1535-1543.
17. Florence, T. M. *Aust. J. Chem.*, **1965**, *18*, 619-626.
18. Florence, T. M. *Aust. J. Chem.*, **1965**, *18*, 609-618.
19. Capitan, F.; Guiraum, A.; Vilchez, J. L.; Bosque, J. M. *Proc. Indian Acad. Sci (Chem Sci)* **1984**, *93*, 1273-1279.
20. Menek, N.; Basaran, S.; Odabasoglu, M. *Dyes Pigm.* **2004**, *61*, 85-91.
21. Florence, T. M.; Belew, W. L. *J. Electroanal. Chem.*, **1969**, *21*, 157-167.
22. Florence, T. M. *J. Electroanal. Chem.*, **1974**, *52*, 115-132.
23. Goyal, R. N.; Srivastava, S. K.; Nautiyal, A. P. *Indian J. Chem.* **1987**, *26A*, 871-877.
24. Ma, M. H.; Johnson, K. E. *J. Electroanal. Chem.* **1993**, *355*, 97-99.
25. Gooding, J. J.; Compton, R. G.; Brennan, C. M.; Atherton, J. *Electroanalysis* **1996**, *8*, 519-523.

26. Gupta, P. N.; Kachru, C. N.; Bhat, S. A. *Denki Kagaku*, **1978**, *46*, 96-101.
27. Abbott, L. C.; Batchelor, S. N.; Lindsay Smith, J. R.; Moore, J. N. *J. Phys. Chem.* **2009**, *113*, 6091-6103.
28. Hou, M.; Li, F.; Liu, X.; Wang, X.; Wan, H. *J. Hazard. Mater.* **2007**, *145*, 305-314.
29. Stanoeva, T.; Neshchadin, D.; Gescheidt, G.; Ludvik, J.; Lajoie, B.; Batchelor, S. N. *J. Phys. Chem. A* **2005**, *109*, 11103-11109.
30. Itoh, T.; McCreery, R. L. *J. Am. Chem. Soc.* **2002**, *124*, 10894-10902.
31. Hastie, J.; Bejan, D.; Teutli-Leon, M.; Bumce, N. J. *Ind. Eng. Chem. Res.* **2006**, *45*, 4898-4904.
32. Xu, G.; O'Dea, J. J.; Mahoney, L. A.; Osteryoung, J. G. *Anal. Chem.* **1994**, *66* 808-812.
33. O'Dea, J. J.; Osteryoung, J. G.; Lane, T. *J. Phys. Chem.* **1986**, *90*, 2761-2764.
34. Klopman, G.; Doddapaneni, N. *J. Phys. Chem.* **1974**, *78*, 1825-1828.
35. Tanner, J. E.; Stejskal, E. O. *J. Phys. Chem.* **1965**, *42*, 288-292.
36. Schwarz, J. Oelbner, W.; Kaden, H.; Schumer, F.; Henning, H. *Electrochim. Acta.* **2003**, *48*, 2479-2486.
37. Vieira, S. N.; Ferreira, L. C.; Franco, D. L.; Afonso, A. S.; Madurro, J. M. *Macro. Symp.* **2006**, 236-242.
38. Irving, C. *J. Org. Chem.* **1960**, *25*, 464-465.
39. Johnson, C. S. *Prog. Nucl. Mag. Reson. Spectrosc.* **1999**, *34*, 203-256.
40. Nilsson, N. *J. Magn. Reson.* **2009**, *200*, 296-302.
41. Huo, R.; Wehrens, R.; Duynhoven, J. V.; Buydens, L. M. C. *Anal. Chim. Acta.* **2003**, 231-251.
42. Avaca, L. A.; Bewick, A. *J. Chem. Soc., Perkin Trans. 2*, **1972**, 1712-1715.
43. Hansch, C.; Leo, A.; Taft, R. W. *Chem. Rev.* **1991**, *91*, 165-195.

Chapter 5 Photochemistry

5.1 Introduction

The introduction to this chapter begins with a general overview of photochemical reactions that occur in azo dyes and how azo dye reactivity may be studied by the use of photoinitiators. The specific aims of the photochemical studies of the R-Span dyes reported in this chapter conclude the section.

In general, when a molecule in its S_0 ground state absorbs light it then exists in its S_1 excited state with the transitions that can occur shown in a Jablonski diagram in Figure 5.1. The excited states are short lived and they decay to the ground state through radiationless transitions or emission of radiation, or they undergo photochemical reactions often involving T_1 triplet states which have a longer lifetime (ca. 100 ns – 10 s) than singlet states (ca. 1 ps – 1000 ns).¹

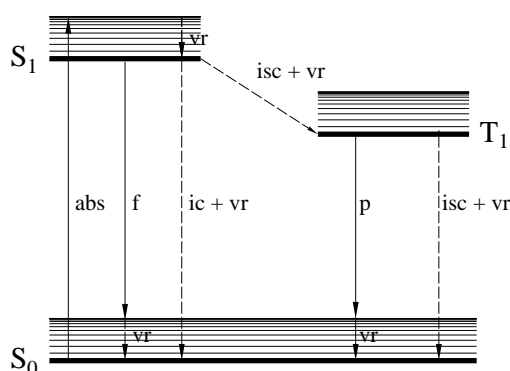


Figure 5.1 Jablonski diagram of the routes of excitation and decay of electronic states; abs = absorption, ic = internal conversion, isc = intersystem crossing, f = fluorescence, p = phosphorescence, vr = vibrational relaxation.

5.1.1 Isomerisation

The isomerisation of azobenzene and phenylazonaphthalene are considered here, and as is consistent with the rest of this thesis, their structures are considered to be in the *trans* form when named without a prefix, however, the *trans* prefix is used where necessary for clarity.

5.1.1.1 Azobenzene

Studies on the isomerisation of azobenzene, as introduced in section 3.1.2.2, have included steady-state and time-resolved UV/Visible absorption spectroscopy, NMR and theoretical calculations.²⁻¹⁴ Unsubstituted azobenzene can exist as the *cis* or *trans* isomer as shown in Figure 5.2. The more thermodynamically stable *trans*-azobenzene can be converted to *cis*-azobenzene upon irradiation at 447 or 316 nm.^{2,4,5} Exposure with a different wavelength can change the *cis* isomer back to the *trans* isomer or it can go back thermally to the *trans* form. The interconversion between the *trans* and *cis* isomers can be identified by a colour change, as utilised in applications such as energy storage systems and photochemical devices.⁸

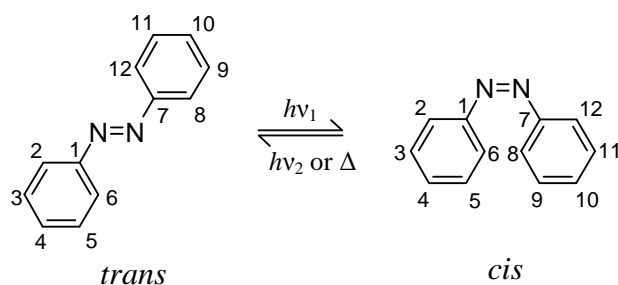


Figure 5.2 *Trans*- and *cis*-azobenzene, together with numbering system.

The mechanism of azobenzene *trans* to *cis* photoisomerisation has been widely debated for a long time.^{3,5-7} The two proposed mechanisms of photoisomerisation as shown in Figure 5.3 are rotation, a twisting of the phenyl ring about the N=N linkage proposed to occur via excitation to S_2 ($\pi\pi^*$), and inversion, an in-plane motion of the phenyl ring thought to occur via excitation to S_1 ($n\pi^*$). The thermal back reaction of the *cis* to *trans* form could also occur via an inversion or rotation mechanism. The mechanisms and

rates depend generally on the energy gap between the energy levels, S_0 , S_1 and S_2 and the energy barriers between the isomers.

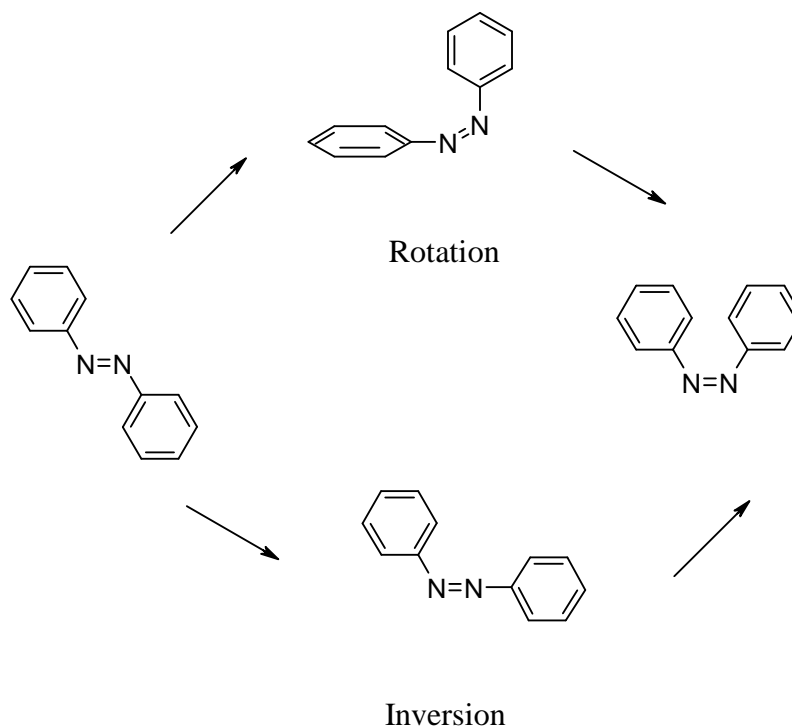


Figure 5.3 Mechanism of azobenzene isomerisation.³

5.1.1.2 Phenylazonaphthalene

In comparison with azobenzene the studies on the isomerisation of phenylazonaphthalenes are limited. Upon irradiation of a series of phenylazonaphthalene dyes (Figure 5.4) at 366 nm, photostationary *cis-trans* mixtures were reported to be obtained within five minutes, where the *cis* isomers formed were stable enough to allow for chromatographic separation.¹⁵ The composition of the isomers in the photostationary state and the rate constant for the thermal back reaction were reported to be dependent on the type of substituent as shown in Table 5.1¹⁵ and the *cis* to *trans* thermal back reactions occurred by first order kinetics.

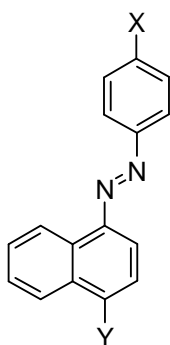


Figure 5.4 Structure of 4,4'-substituted 1-phenylazonaphthalene.

Table 5.1 Isomeric composition in the photostationary state at 366 nm (determined by HPLC analysis) and first-order rate constant (k) of the thermal *cis* to *trans* isomerisation of substituted 1-phenylazonaphthalenes in benzene at 30 °C.¹⁵

X	Y	Isomers in photostationary state		$k / 10^{-3} \text{ min}^{-1}$	k / s^{-1}
		<i>cis</i> / %	<i>trans</i> / %		
H	H	72	28	5.22	0.31
H	OMe	39	61	21.4	1.28
Me	OMe	55	46	34.9	2.09
OMe	OMe	61	40	62.6	3.76
Cl	OMe	45	55	39.8	2.39
NO ₂	OMe	22	78	57.8	3.47

In general the percentage of *cis* isomer of substituted 1-phenylazonaphthalene formed in the photostationary state was reported to decrease with increased electron-withdrawing character of the substituent on the phenyl ring.^{15,16} The rate constant of the thermal back reaction was reported to be greater for those substituents where X = OMe and NO₂. Viscosity and temperature can also influence the kinetics of the *cis* to *trans* thermal back reaction, the rate of which was reported to increase with increasing temperature and decrease with increasing viscosity of the solvent.¹⁶

The photoisomerisation of a series of sulfonated phenylazonaphthalene dyes has been observed by NMR spectroscopy;¹⁷ the structure of one of these is very similar to those of the R-Span dyes reported in this thesis and is shown in Figure 5.5 and named here as NHMe-Span. A photostationary state of NHMe-Span in DMSO-d₆ was created upon 514 nm irradiation, and the *cis* isomer was found to revert completely to the *trans* forms thermally. The ¹H NMR positions of *trans* and *cis* NHMe-Span are shown in Table 5.2.¹⁷

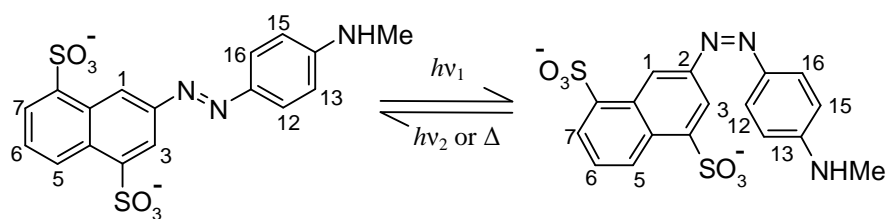


Figure 5.5 *Trans*- and *cis*-NHMe-Span, together with numbering system.

Table 5.2 ^1H NMR chemical shifts (ppm) of the *cis* and *trans* forms of NHMe-Span in DMSO- d_6 and differences (Δ) between them.¹⁷

Atom	<i>trans</i>	<i>cis</i>	$\Delta(\textit{trans-cis})$
1	9.33	8.58	0.75
3	8.40	7.17	1.23
5	8.87	8.78	0.09
6	7.48	7.41	0.07
7	7.99	7.95	0.04
12/16	7.82	6.92	0.90
13/15	6.70	6.36	0.34

5.1.2 Reactivity

Azo dyes may undergo fading due to either photo-oxidation or photo-reduction; the favoured route through which this occurs is dependent on environment.^{18,19} Often the presence of oxygen favours photo-oxidation which is usually irreversible,²⁰ whereas the presence of an electron or H-atom donor allows photo-reduction to occur and may be reversible.^{18,20,21} These fading processes generally occur with low quantum yields and therefore take long time periods under typical conditions, hence photoinitiators²¹⁻²⁹ are commonly used in experimental methods to help mimic fading and enable its study over practicable time periods. In this type of study, the photoinitiator is photolysed to create radicals which can then rapidly react with the dye under oxidative or reductive conditions, allowing fading to be studied experimentally.²¹⁻²⁹ Examples of photo-reduction, photo-oxidation and the use of photoinitiators are given below.

5.1.2.1 Photo-oxidation

Photo-oxidation is reported generally to proceed by one of two methods, the first involving singlet oxygen^{20,30-37} and the second involving oxygen radicals.^{34,35}

In many cases the photo-oxidation pathway via singlet oxygen has been proposed when there is a hydrazone tautomer of an azo dye present. Firstly, absorption of light creates a dye singlet excited state which then undergoes intersystem crossing forming an excited triplet state as shown in equation 5.1.¹ The energy in the excited state can then be transferred to an oxygen molecule in its triplet ground state forming singlet oxygen as shown in equation 5.2.¹ The presence of the singlet oxygen in its excited state triggers the degradation of the dye as shown in Figure 5.6 for 1-arylazo-4-naphthol.³⁰

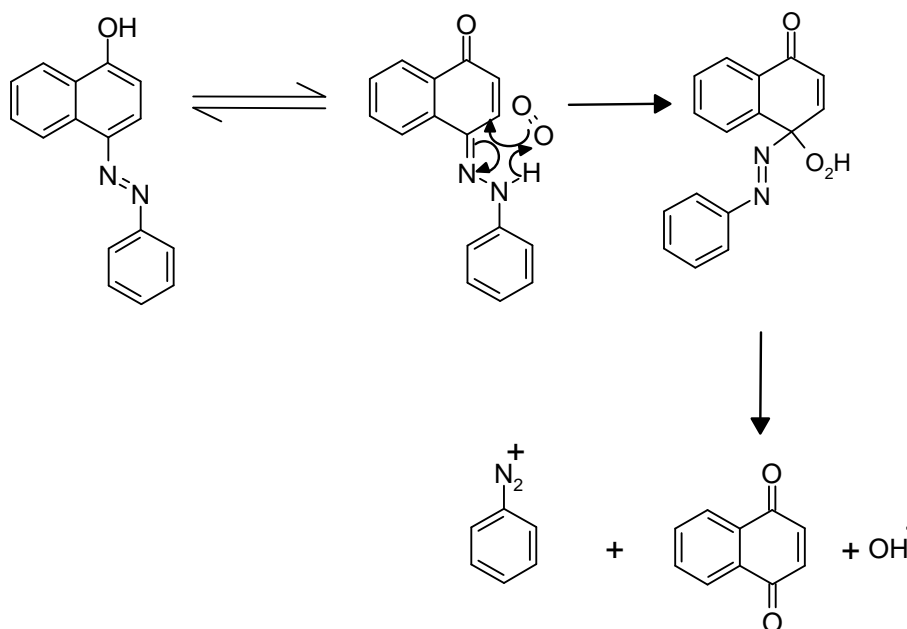
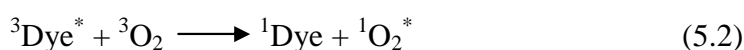
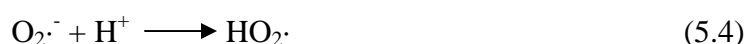
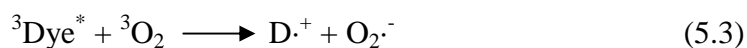


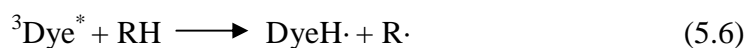
Figure 5.6 Reaction mechanism, of singlet oxygen with 4-aryl azo-1-naphthol.³⁰

In the second photo-oxidation mechanism, oxygen radicals are produced when the excited triplet state of the dye reacts with the triplet ground state of oxygen through electron transfer forming superoxide³⁴ or hydroperoxyl³⁵ radicals as shown in equation 5.3 and 5.4, respectively, these radicals can then trigger the degradation of the dye. It has been reported for Orange II that oxidation only occurs via radical mechanisms.³⁵



5.1.2.2 Photo-reduction

Photo-reduction is reported to involve reductive radical formation with light leading to the degradation of the dye via N=N bond cleavage.^{1,34,38-40} Upon excitation, the dye can react with another molecule (RH) capable of hydrogen atom transfer, leading to the formation of radicals including a dye hydrazyl radical (DyeH·) as shown in equations 5.5 and 5.6.¹ In the case of azobenzene as shown in Figure 5.7 the hydrazyl radical quickly accepts a further hydrogen atom leading to the formation of a hydroazo intermediate which then undergoes disproportionation to reform azobenzene and the reduction product phenylamine. Cellulose, the main constituent of paper and to which dyes are often applied, appears to offer a reducing environment from which the excited dye is capable of removing a hydrogen atom or electron.¹



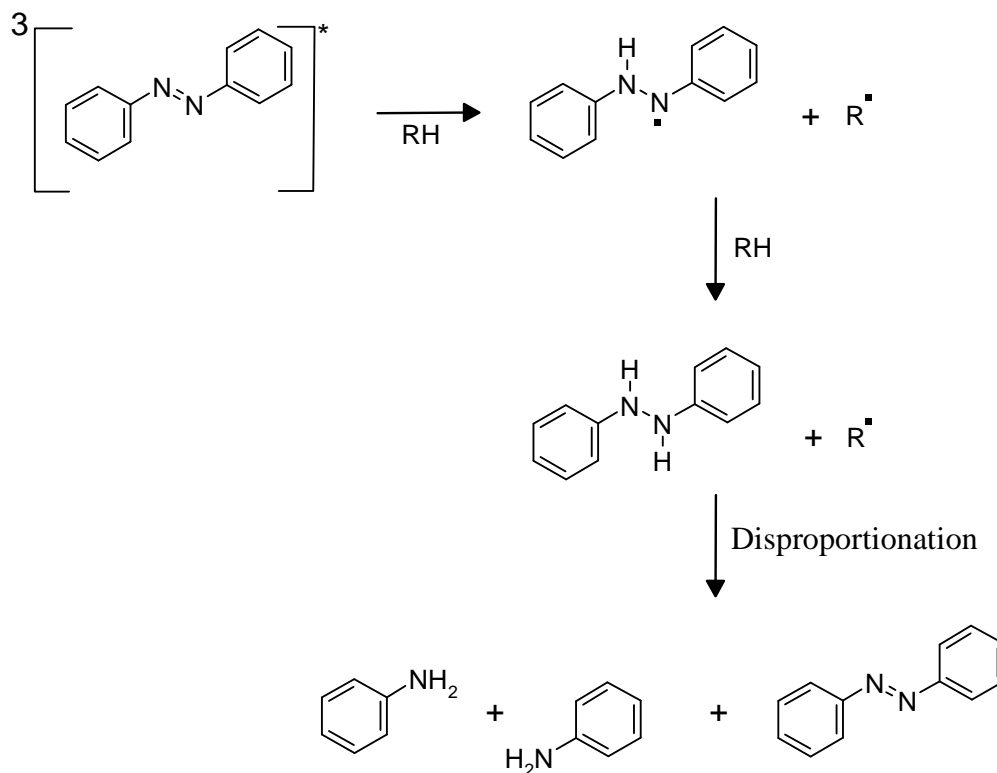


Figure 5.7 Photo-reduction of azobenzene.¹

5.1.2.3 Photoinitiators

Photoinitiators may be used to mimic photo-oxidation and photo-reduction to study in the laboratory. 2-Hydroxy-2-methylphenylpropanone derivatives⁴¹ are a class of photoinitiators that have been used to initiate free radical polymerisation.⁴²⁻⁴⁷ For example 2-hydroxy-4'-(2-hydroxyethoxy)-2-methylpropiophenone, shown in Figure 5.8 is a water soluble photoinitiator that has been used to create radicals which can then react with dyes in aqueous solution.^{43,48-53}

It has been reported that irradiation of the photoinitiator leads to α -cleavage and the formation of benzoyl and 2-hydroxy-2-propyl radicals as shown in Figure 5.8.^{53,54} Thereafter hydrogen atom transfer between benzoyl and 2-hydroxy-2-propyl radicals produces 4-(2-hydroxy-ethoxy)-benzaldehyde (H-benzaldehyde), where H represents the alkyl chain of the photoinitiator and acetone (Figure 5.8). Under air the benzoyl radicals can be quenched by oxygen to produce 4-(2-hydroxyethoxy)benzoic acid (H-benzoic acid) (Figure 5.8).⁵⁴

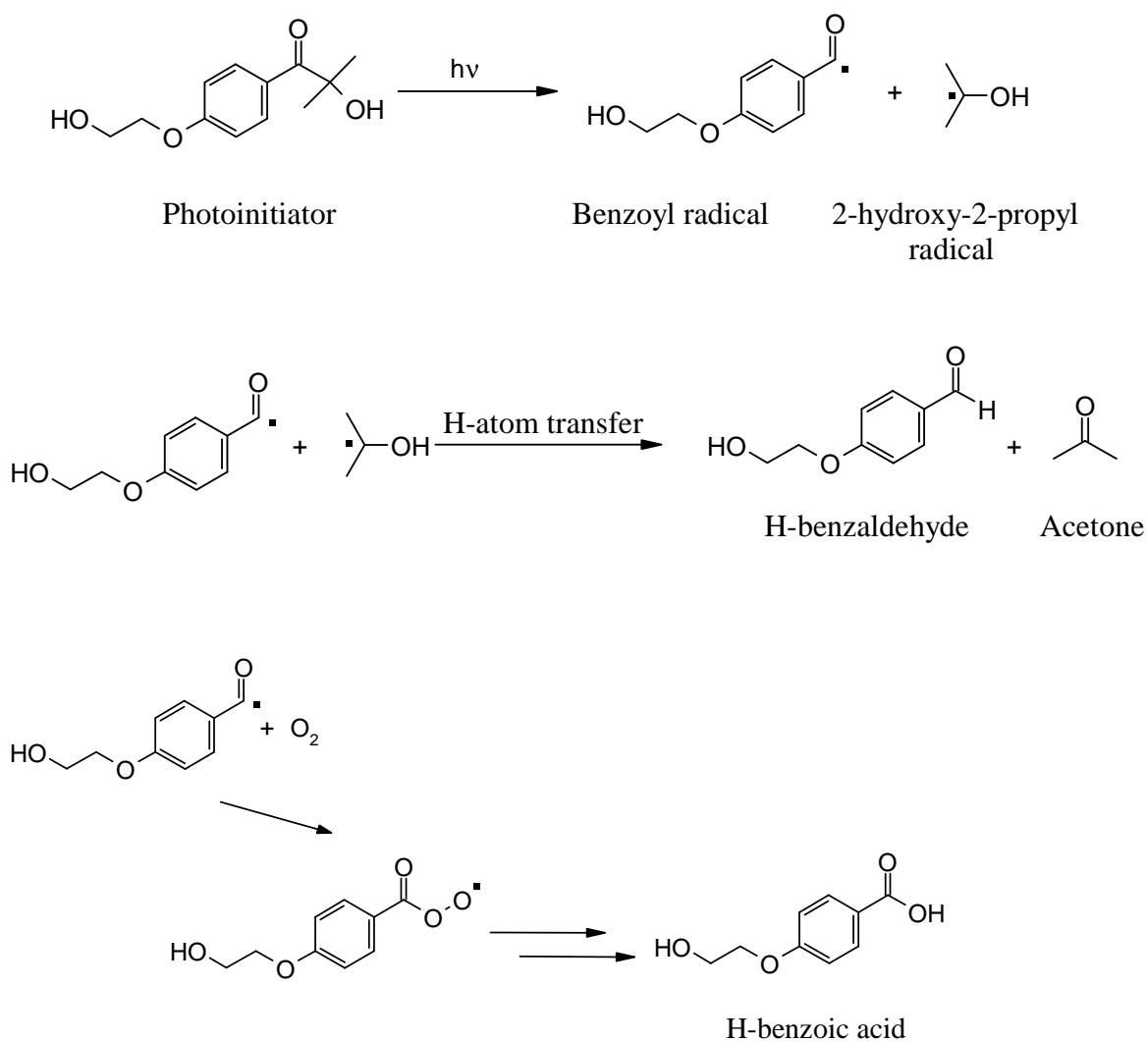


Figure 5.8 Top: Irradiation of the photoinitiator (2-hydroxy-4-(2-hydroxyethoxy)-2-methylpropiophenone) resulting in the formation of benzoyl and 2-hydroxy-2-propyl radicals. Middle: Hydrogen atom transfer between benzoyl and 2-hydroxy-2-propyl radicals to produce H-benzaldehyde (4-(2-hydroxyethoxy)-benzaldehyde) and acetone. Bottom: Reaction of benzoyl radicals with oxygen to produce H-benzoic acid (4-(2-hydroxyethoxy)benzoic acid).⁵²⁻⁵⁴

Under anaerobic conditions 2-hydroxy-2-propyl radicals react efficiently with dyes, as for example the one electron reduction of Orange II shown in Figure 5.9.⁵⁵

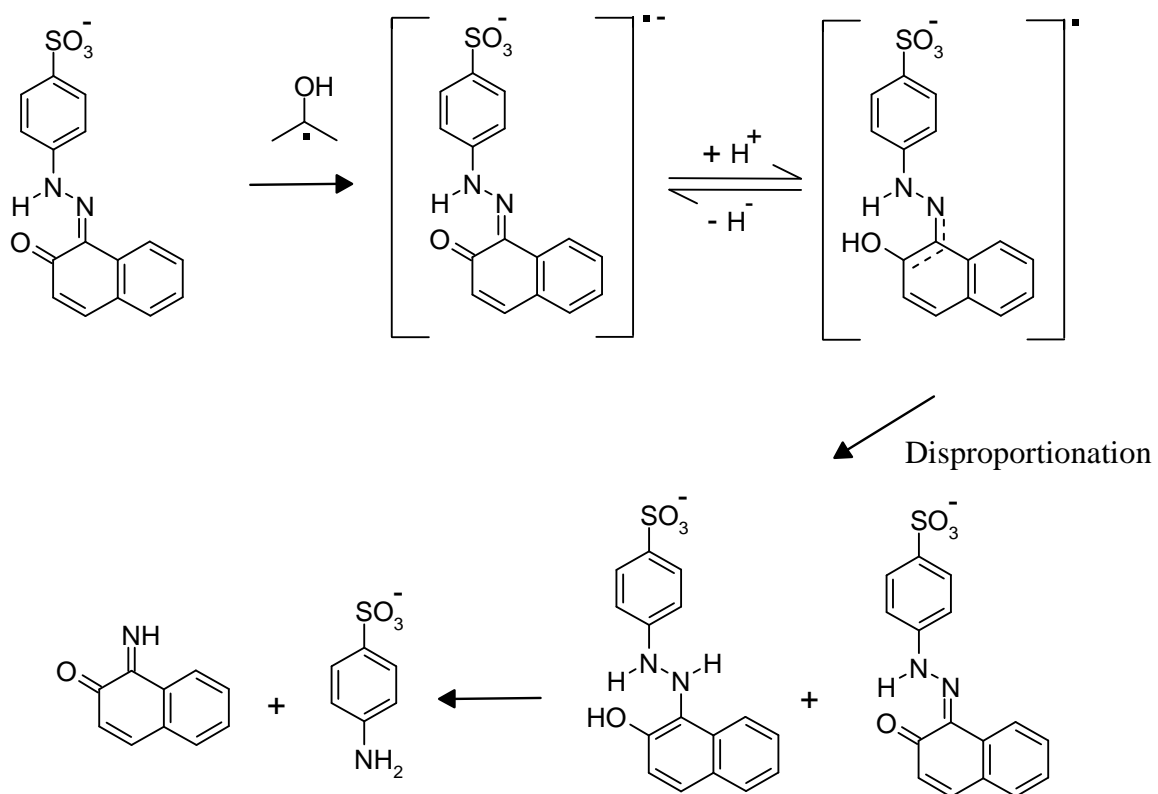


Figure 5.9 Proposed one-electron reduction mechanism of Orange II by 2-hydroxy-2-propyl radicals.⁵⁵

Under aerobic conditions, the dye can also react with the benzoyl radicals as shown in Figure 5.10, leading to different products.⁵⁴

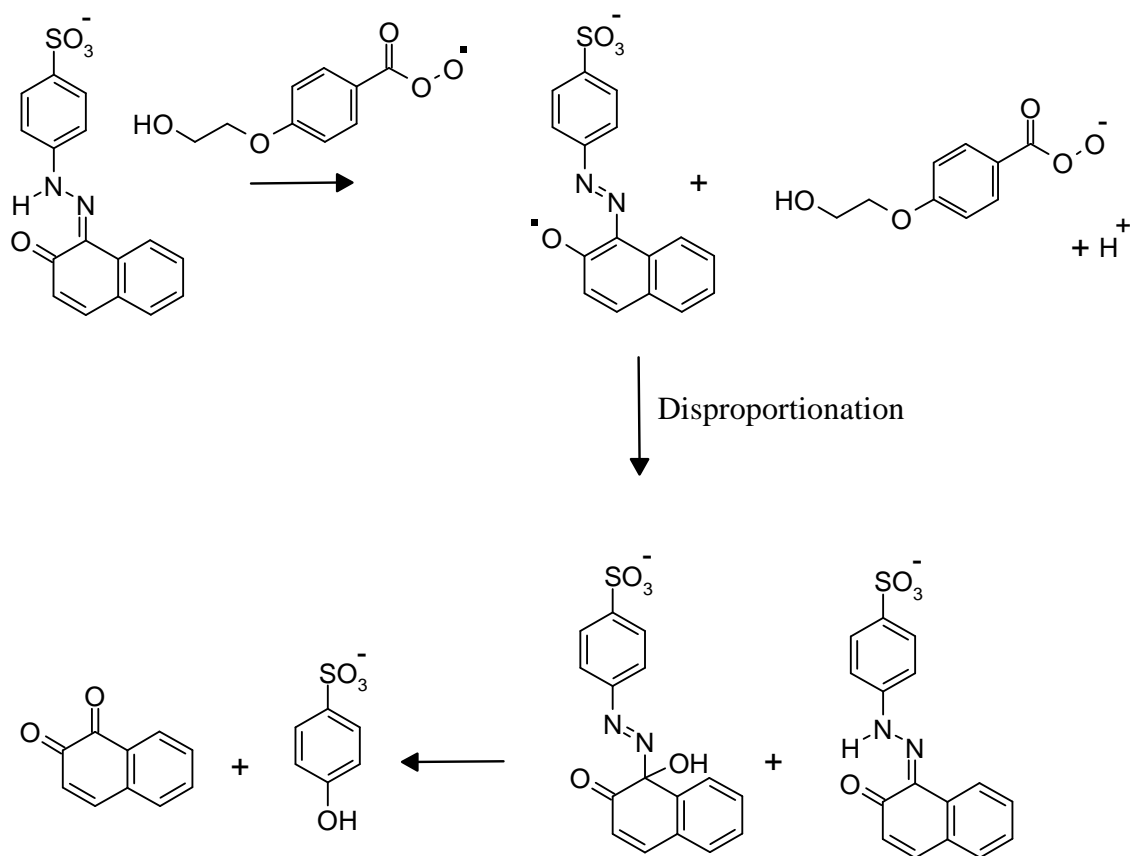


Figure 5.10 Proposed one-electron oxidation mechanism of Orange II.⁵⁴

5.1.3 Aims

The main aim was to explore the photochemically induced reactions of the R-Span dyes to study their stability and understand mechanisms using a range of techniques. In particular, the main aim was to study fading of the dyes induced by direct photochemical reactions and by photoinitiator-generated radicals, linking to the electrochemically induced electron transfer reactions reported in Chapter 4, and again focusing on reduction; a secondary aim was to explore whether the dyes undergo photoisomerisation.

More specifically, the aim was to use steady-state and time-resolved irradiation techniques to initiate reactions and a combination of UV/Visible absorption, HPLC, LC-MS, 1D and 2D NMR techniques to identify products, quantitatively where possible, and elucidate mechanisms. Another aim of the work presented in this chapter was to assess the DOSY NMR technique used in the Chapter 4 by applying it to a more complicated system.

5.2 Results, analysis and discussion

The R-Span dye series has been studied through a combination of techniques to investigate their fading by photoinitiator-generated radical reactions and also by direct photolysis. The main focus of the work reported in this section was on OH-Span; however there are also some limited results from the other R-Span dyes.

Section 5.2.1 reports a full set of studies on OH-Span alone and also in the presence of photoinitiator, including steady-state studies using flash gun irradiation (section 5.2.1.1) and time-resolved studies using laser irradiation (section 5.2.1.2) The photoinitiator used in this study was the same as that introduced in section 5.1.2.3 (Figure 5.8). The products from the steady-state studies on solutions of photoinitiator alone and OH-Span:photoinitiator have been identified through a combination of HPLC, LC-MS, 1D and 2D NMR spectroscopy. The time-resolved UV/Visible studies were carried out with nanosecond apparatus and have focused on reactions with the photoinitiator-generated radicals with some preliminary studies on the dyes alone.

Section 5.2.2 reports a limited set of studies on the other R-Span dyes. Section 5.2.2.1 reports firstly on simple steady-state and time-resolved irradiation studies on solutions of NH₂⁻, CN⁻ and O⁻-Span alone, and then on more complicated steady-state and time-resolved studies on solutions of OMe⁻ and NHAc-Span alone. Section 5.2.2.2 reports on steady-state irradiation studies on solutions of NH₂⁻, NHAc⁻ and O⁻-Span in the presence of photoinitiator, with products identified by HPLC.

Photophysics

Preliminary studies showed that no UV/Visible emission signal above noise was observed for the pure R-Span dyes in water indicating that their excited states decay predominately by non-radiative processes, which may include internal conversion and intersystem crossing and where the energy is lost ultimately to the surrounding environment. It has been reported for other azo dyes that fluorescence is weak and that the main decay route of the excited states is through internal conversion.⁵⁶⁻⁶¹

5.2.1 OH-Span

5.2.1.1 Steady-state studies

The following section reports on the steady-state studies using a flash gun on OH-Span alone, photoinitiator alone and OH-Span:photoinitiator solutions.

OH-Span alone

Irradiation of OH-Span alone showed no significant change in the UV/Visible absorption spectrum (Figure 5.11) after 30 flash gun light pulses where $\sim 1\%$ absorbance loss occurs, indicating that the dye does not fade readily on direct photolysis in solution.

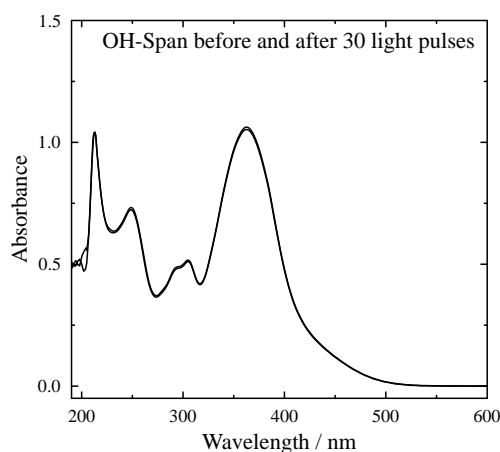


Figure 5.11 UV/Visible absorption spectra of OH-Span alone in pH 5.2 sodium acetate buffer solution at $5 \times 10^{-5} \text{ mol dm}^{-3}$ before and after 30 light pulses.

Photoinitiator alone

Irradiation of photoinitiator alone in pH 5.2 sodium acetate buffer solution was monitored by steady-state UV/Visible spectroscopy. Irradiation was performed on samples under nitrogen and under air in a 1 cm pathlength cell using a flash gun and the UV/Visible absorption spectra recorded as a function of light pulse are shown in Figure 5.12. The spectra show clearly that different processes occur under nitrogen and air.

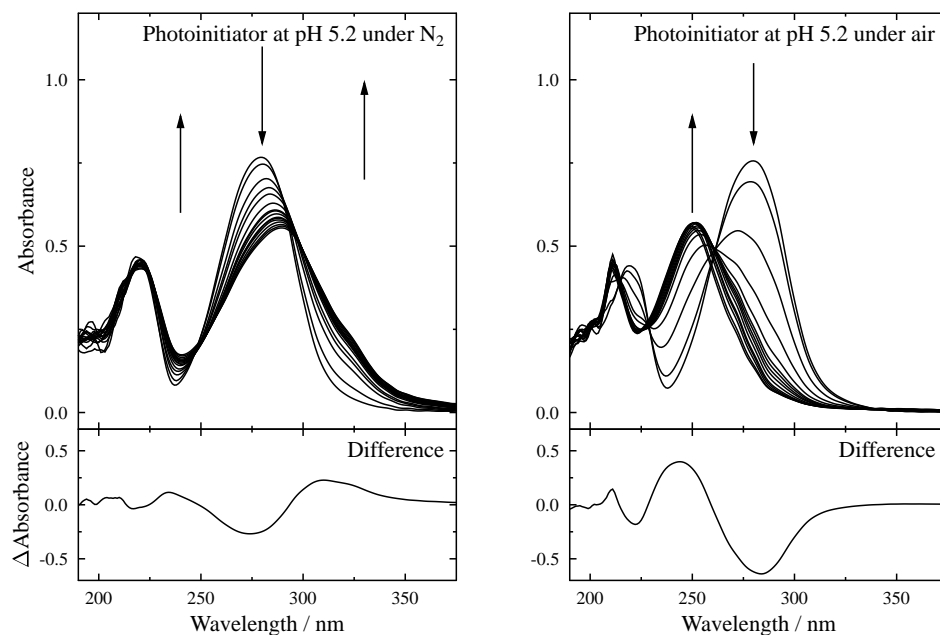


Figure 5.12 UV/Visible absorption spectra obtained on irradiation of photoinitiator in pH 5.2 sodium acetate buffer solution at $5 \times 10^{-5} \text{ mol dm}^{-3}$ under nitrogen (left) and air (right) over 30 light pulses, with arrows indicating changes and with the overall difference spectrum (final – initial) shown.

A detailed product analysis using several techniques was carried out on samples under nitrogen and is described below; a simple analysis using HPLC alone was carried out first on the samples under air, as shown in Figures 5.13 and 5.14 with retention times, peak integrations and UV/Visible absorption band positions given in Table 5.3. One main product is formed, and it elutes at a shorter time than the parent photoinitiator, and may be assigned to H-benzoic acid (Figure 5.8).^{54,55} More conclusive evidence is given below, when considering the products formed under nitrogen, including that of the species labelled simply photoinitiator product (PI product) in Figure 5.14 and Table 5.3.

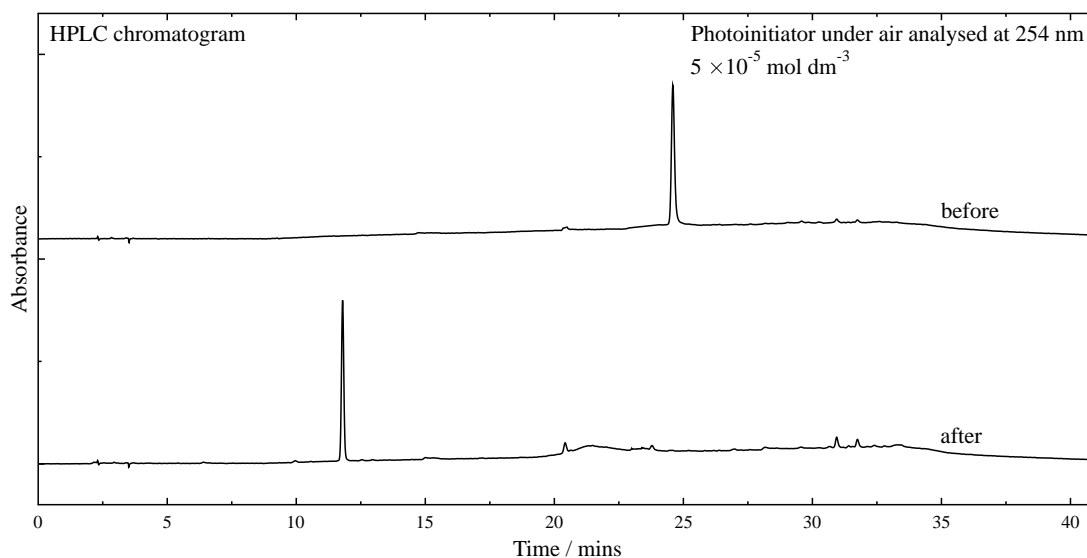


Figure 5.13 HPLC chromatogram of photoinitiator alone ($5 \times 10^{-5} \text{ mol dm}^{-3}$) under air before (top) and after (bottom) 30 light pulses.

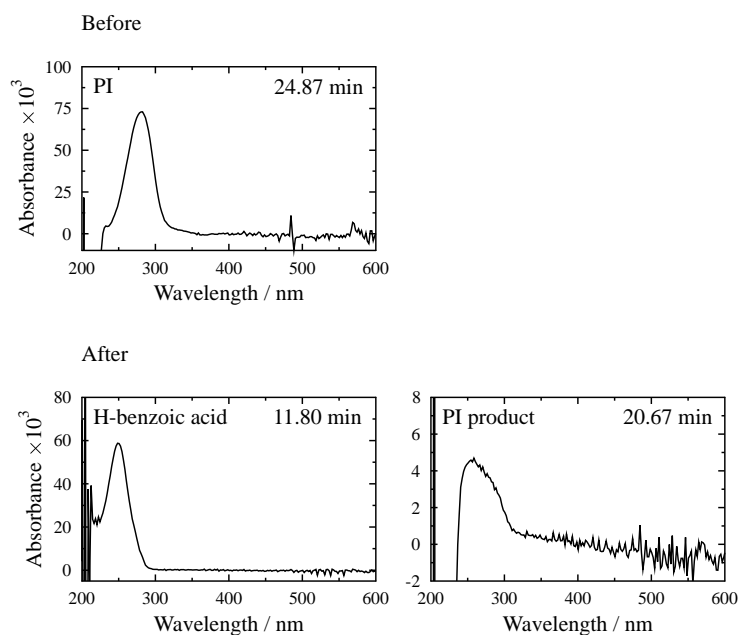


Figure 5.14 Top: UV/Visible absorption spectra of photoinitiator ($5 \times 10^{-5} \text{ mol dm}^{-3}$) before irradiation. Bottom: UV/Visible absorption spectra of H-benzoic acid (left), photoinitiator (PI) product (right) formed after 30 light pulses.

Table 5.3 Retention times (RT / min), peak integrations (PI) and UV/Visible absorption band positions (λ \ nm) of each component before and after 30 light pulses for photoinitiator under air.

Component	RT	PI	λ
<i>Before</i>			
Photoinitiator	24.87	3.35	279
<i>After</i>			
H-benzoic acid	11.80	5.95	249
Photoinitiator product	20.67	0.40	283

A more detailed product analysis was carried out on the sample irradiated under nitrogen in which HPLC, LC-MS and NMR spectroscopy were used. The HPLC chromatograms of the photoinitiator before and after irradiation along with UV/Visible absorption spectra of identified components are shown in Figures 5.15 and 5.16 with retention times, peak integration and UV/Visible absorption band positions given in Table 5.14. In addition to H-benzoic acid and the species labelled PI product, a third component is observed which elutes at a longer time than the parent photoinitiator, and it is assigned to H-benzaldehyde (Figure 5.8).^{54,55} LC-MS provides more conclusive evidence as to the products: ESI mass spectra obtained for the photoinitiator before irradiation and for H-benzoic acid formed after irradiation are shown in Figures 5.17 and 5.18, respectively, with their base peak ions given in Table 5.4. The positive ion ESI mass spectra of photoinitiator alone, with a retention time of 24.83 min, shows a base peak ion with an m/z value of 225.0 that corresponds to protonated photoinitiator (Figure 5.17). Upon fragmentation it is observed that there is a mass loss of 46 corresponding to loss of C₂H₆O from the alkyl chain of the photoinitiator, which is a useful piece of information when considering solutions containing dye as well as photoinitiator (see below). The peak in the HPLC chromatogram with a retention time of 11.80 min gives a negative ion ESI mass spectrum with a base peak of 181.2 m/z which can be assigned to [H-Benzoic acid - H⁺] (Figure 5.18).

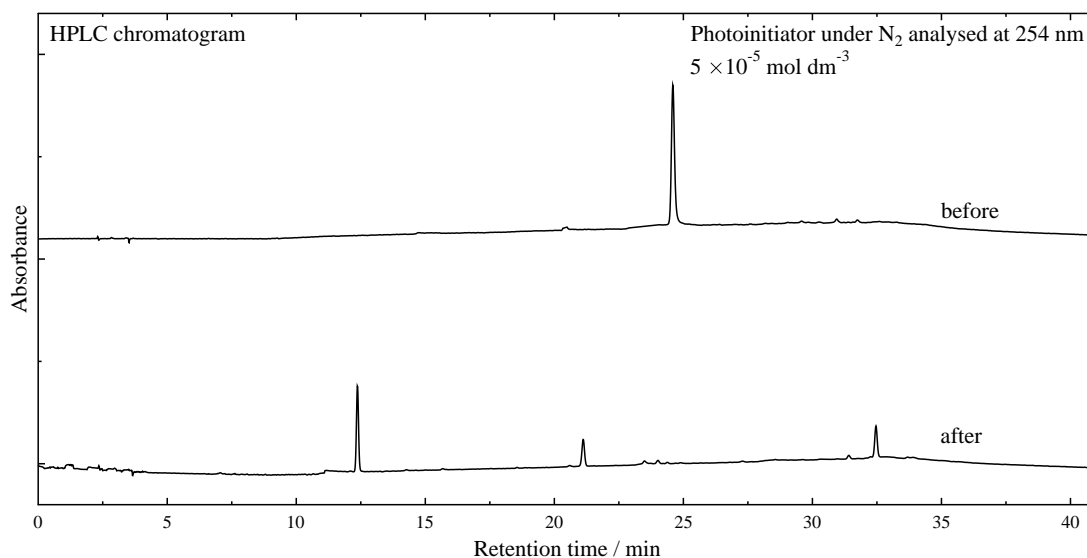


Figure 5.15 HPLC chromatogram of photoinitiator alone ($5 \times 10^{-5} \text{ mol dm}^{-3}$) under nitrogen before (top) and after (bottom) 30 light pulses.

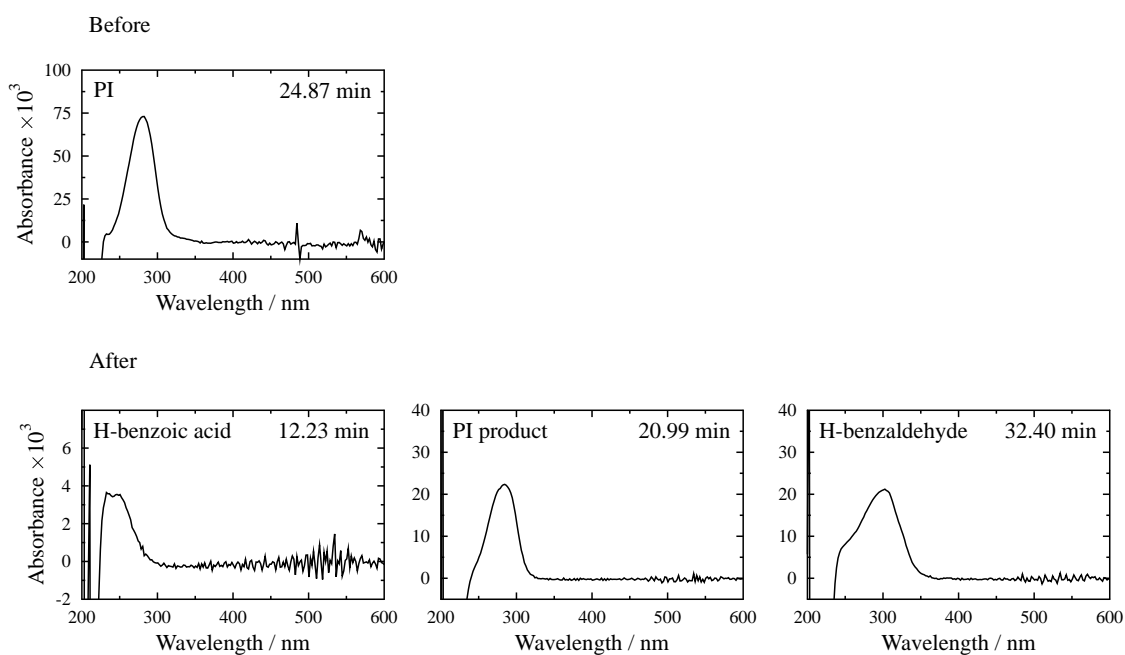


Figure 5.16 Top: UV/Visible absorption spectra of photoinitiator ($5 \times 10^{-5} \text{ mol dm}^{-3}$) before irradiation. Bottom: UV/Visible absorption spectra of H-benzoic acid (left), photoinitiator product (middle) and H-benzaldehyde (right) formed after 30 light pulses.

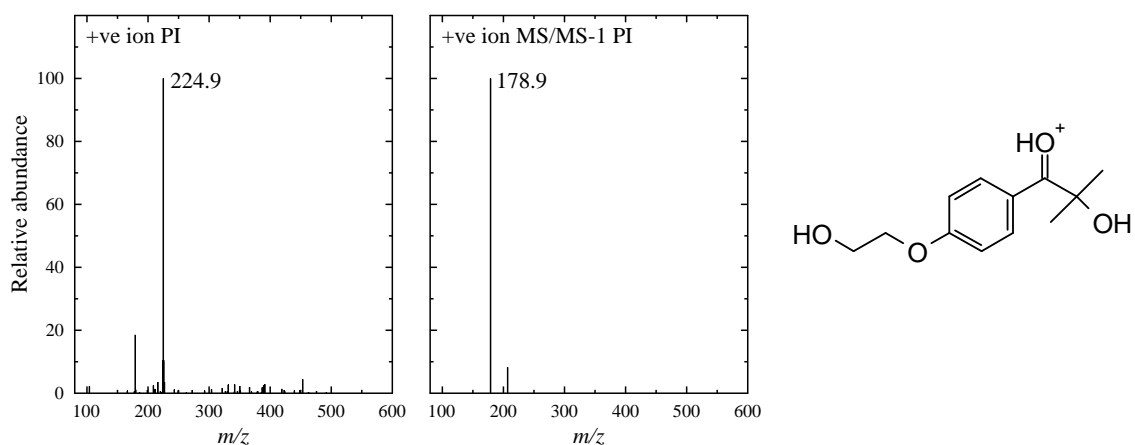


Figure 5.17 Left: Positive ion ESI mass spectrum of photoinitiator with a retention time of 24.83 min. Middle: Positive ion MS/MS-1 mass spectrum of the ion with 224.9 m/z. Right: Structure of [PI + H⁺]⁺ corresponding to base peak at 224.9 m/z

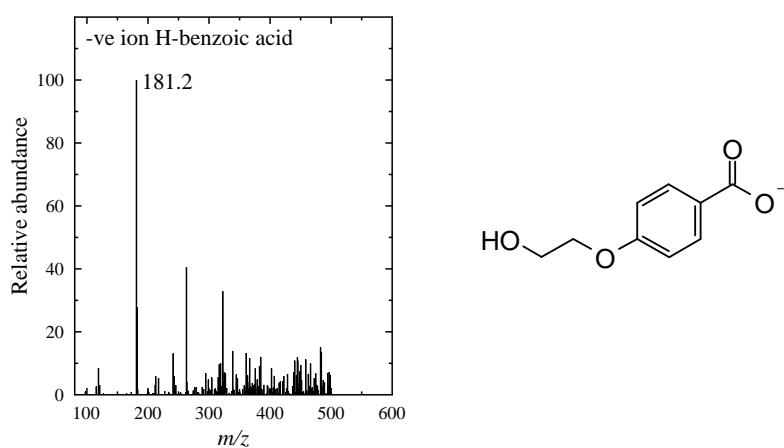


Figure 5.18 Left: Negative ion ESI mass spectrum of component H-benzoic acid formed after irradiation of photoinitiator alone with a retention time of 12.17 min. Right: Structure of [H-Benzoic acid - H⁺]⁻ corresponding to base peak at 181.2 m/z.

Table 5.4 Retention times (RT / min), peaks integrations (PI) and UV/Visible absorption band positions (λ / nm) from HPLC and Retention times (RT / min), base peak ions (BP / m/z) and fragment ions (F / m/z) of components before and after 30 light pulses on photoinitiator alone (5×10^{-5} mol dm⁻³).

Component	HPLC			LC-MS				
	RT	PI	λ	RT	BP	Assignment	F	Assignment
<i>Before</i>								
Photoinitiator	24.87	3.35	279	24.83	224.9	[PI + H ⁺] ⁺	178.9	Loss of C ₂ H ₆ O
<i>After</i>								
H-benzoic acid	12.23	0.57	249	12.17	181.2	[H-Benzoic acid - H ⁺] ⁻	-	-
Photoinitiator product	20.99	0.74	283	*	-	-	-	-
H-benzaldehyde	32.40	0.91	300	*	-	-	-	-

* Not observed

NMR spectroscopy provides more conclusive evidence as to the nature of the products and also gives a quantitative measure of the species formed. 1D and 2D (COSY, NOESY, DOSY) ¹H spectra were recorded from photoinitiator samples at 5×10^{-4} mol dm⁻³ in deuterated 0.05 mol dm⁻³ sodium acetate buffer at pD 5.2 on a Bruker 700 MHz spectrometer. As in chapter 4 all the NMR figures here are set out to show the 1D ¹H NMR spectrum recorded, with the 2D DOSY data shown as a series of data points relating the chemical shift of each peak with the corresponding apparent diffusion coefficient. A histogram of apparent diffusion coefficients is shown to give an indication of the spread of diffusion coefficient data. ¹H NMR assignments were made using integration, multiplicity and splitting values and by COSY interactions and apparent diffusion coefficients (experimental data) obtained from the DOSY data. Concentrations of products formed were estimated by comparing the integration of the peaks to that of the integration of the sodium acetate peak (2.24 ppm) at a known concentration.

The spectra of photoinitiator alone before and after 50 light pulses are shown in Figure 5.19. Figure 5.20 shows possible components that have formed with NMR assignments given in Table 5.5. Photoinitiator alone has an apparent diffusion coefficient of 5.48×10^{-10} m² s⁻¹. Upon irradiation products have formed that have both higher and lower apparent diffusion coefficients, hence have lower and higher masses than the photoinitiator. ¹H NMR gives further evidence for the benzaldehyde derivative labelled HEB for NMR (Figure 5.20) with its distinctive aldehyde proton with a chemical shift of 9.82 ppm and it has an apparent diffusion coefficient of 5.50×10^{-10} m² s⁻¹, consistent

with it being slightly smaller than the photoinitiator and it is formed in ca. 16 % yield. The usefulness of the DOSY technique is clearly seen in that there are many photoinitiator products (PIP) that can be separated (Table 5.5). For example, PIP B has an apparent diffusion coefficient of $5.33 \times 10^{-10} \text{ m}^2 \text{ s}^{-1}$, consistent with it being similar in size to photoinitiator and the fact that it contains both aromatic and aliphatic protons would be consistent with it being assigned to H-benzoic acid, and it is formed in ca. 9 % yield. PIP A which is formed in ca. 18 % yield has an apparent diffusion coefficient of $4.63 \times 10^{-10} \text{ m}^2 \text{ s}^{-1}$, consistent with it being larger than the photoinitiator, and with it containing aliphatic and aromatic protons it could be assigned to the formation of a photoinitiator dimer (Figure 5.20). This however is a very tentative proposal and unfortunately LC-MS provides no insight into this component or the other possible PIP components identified by NMR. As well as the diffusion coefficients showing the separation of peaks, there are COSY interactions between protons 3 & 4 and 1 & 2 in all the products proposed in Figure 5.20. What the DOSY technique has shown is that it can provide extra insight into interpreting the 1D NMR of a complex mixture which may have not been forthcoming otherwise. It should be noted that the PIP products proposed account for a 61 % yield, and that there are unassigned peaks in the aromatic region. Acetone, 2-propanol and ethylene glycol (EG) have been assigned previously^{50,62} and give matching assignments in this study (Table 5.5), and may be assigned as products coming from the non-aromatic segments of the photoinitiator.

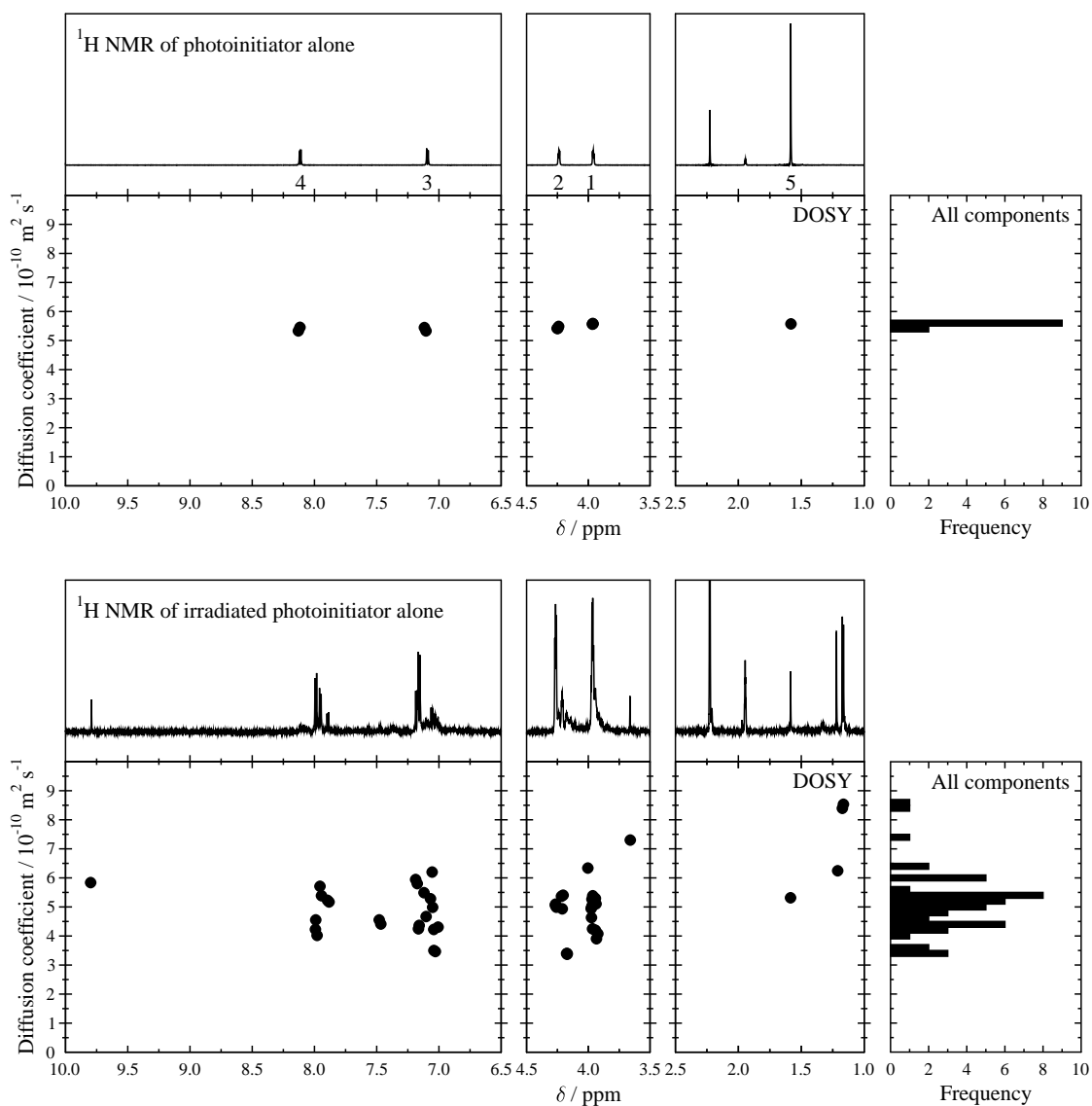


Figure 5.19 Left ^1H NMR (700 MHz) DOSY display of photoinitiator alone before (top) and after 50 light pulses (bottom) at $5 \times 10^{-4} \text{ mol dm}^{-3}$ at pD 5.2 under nitrogen. Right: Histogram of all components in DOSY display.

Table 5.5 ^1H chemical shifts (ppm), apparent diffusion coefficient per splitting ($D_{\text{All}} / 10^{-10} \text{ m}^2 \text{ s}^{-1}$), mean apparent diffusion coefficient per component ($D_{\text{Mean}} / 10^{-10} \text{ m}^2 \text{ s}^{-1}$) and concentration (Concn / $10^{-4} \text{ mol dm}^{-3}$) of each component of photoinitiator alone before and after irradiation under nitrogen.

atom	Before Irradiation				After Irradiation			
	$^1\text{H}^a$	Concn	DOSY		$^1\text{H}^a$	Concn	DOSY	
Photoinitiator			D_{All}	D_{Mean}			D_{All}	D_{Mean}
1	3.96 2.0 t 4.5	5.00	5.57, 5.56, 5.59		3.93 0.10 t 4.5	0.24	-	
2	4.24 2.0 t 4.5	5.00	5.49, 5.41, 5.41		4.24 0.10 t 4.5	0.24	-	
3	7.09 2.0 d 9.0	5.00	5.33, 5.45	5.48±0.13	7.09 0.10 d 9.0	0.24	5.49	5.40±0.09
4	8.11 2.0 d 9.0	5.00	5.46, 5.33		8.11 0.10 d 9.0	0.24	-	
5	1.58 6.0 s -	5.00	5.73		1.58 0.29 s -	0.24	5.31	
<i>Products</i>								
2-propanol					1.17 0.66 d 6.5	0.55	8.54, 8.39	8.47±0.08
Acetone					2.24 0.42 s -	0.35	16.43	16.43
EG					3.59 0.13 s -	0.17	7.30	7.30
HEB 1					3.94 0.31 t 4.5	0.77	5.11, 5.29, 5.29	
HEB 2					4.21 0.26 t 4.5	0.77	5.40, 4.93, 5.37	
HEB 3					7.21 0.27 d 9.0	0.77	5.80, 5.94	5.50±0.51
HEB 4					7.98 0.48 d 9.0	0.77	5.88, 5.71	
HEB α					9.82 0.33 s -	0.77	5.83	
PIP A 1					3.99 - t 4.5	0.88	4.25, 4.63, 4.90	
PIP A 2					4.26 - t 4.5	0.88	4.99, 5.10, 5.06	4.63±0.44
PIP A 3					7.18 0.47 d 9.0	0.88	4.36, 4.24	
PIP A 4					8.01 0.41 d 9.0	0.88	4.56, 4.22	
PIP B 1					3.98 - t 4.5	0.40	5.38, 5.26, 4.99	
PIP B 2					4.26 - -	0.40	4.99	5.33±0.60
PIP B 3					7.06 0.16 d 9.0	0.40	6.20, 5.28	
PIP B 4					7.92 0.10 d 9.0	0.40	5.39, 5.22	
PIP C 3					7.00 0.10 d 9.0	0.26	4.22	4.44±0.23
PIP C 4					7.10 0.10 d 9.0	0.26	4.67	
PIP D 3					7.09 0.05 d 9.0	0.13	4.22, 4.98	4.52±0.38
PIP D 4					7.47 0.05 d 9.0	0.13	4.41, 4.47	
PIP E 1					3.93 0.14 t 4.5	0.27	3.90, 4.08, 4.19	
PIP E 2					4.17 0.14 t 4.5	0.27	3.37, 3.40, 3.40	3.92±0.44
PIP E 3					7.05 0.11 d 9.0	0.27	4.28, 4.31	
PIP E 4					7.98 0.09 d 9.0	0.27	4.07, 4.19	
PIP F 3					7.00 0.05 t 9.0	0.19	-	-
PIP F 4					7.37 0.07 dd8.5	0.19	-	-
PIP F 0					7.56 0.02 d 8.5	0.19	-	-
Unassigned					1.22 0.38 s -	-	6.24	6.24
Unassigned					1.33 0.04 d 9.0	-	-	-
Unassigned					1.45 0.04 s -	-	-	-
Unassigned					3.81 0.09 t 4.5	-	4.24	4.24
Unassigned					3.88 0.07 t 4.5	-	4.22	4.22
Unassigned					4.01 0.07 t 4.5	-	6.34	6.34
Unassigned					4.11 0.10 t 4.5	-	-	-
Unassigned					7.24 0.02 d 9.0	-	-	-
Unassigned					7.34 0.03 d 9.0	-	-	-
Unassigned					8.08 0.07 d 9.0	-	-	-
Unassigned					8.11 0.07 d 9.0	-	-	-

^a Integration, multiplicity (s = singlet; d = doublet; t = triplet), splitting (Hz).

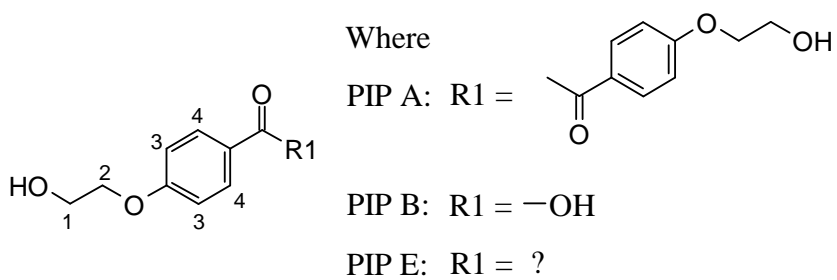
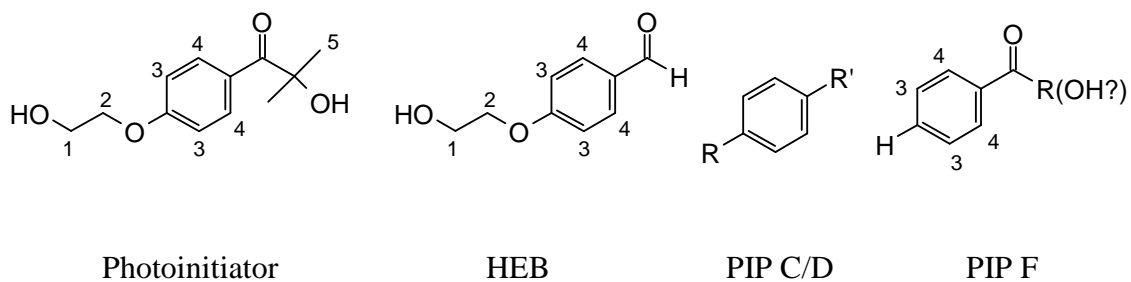


Figure 5.20 Possible components present after the irradiation of photoinitiator alone under nitrogen after 50 light pulses, where PIP = photoinitiator product, HEB = H-benzaldehyde and R and R' are unknown.

OH-Span:photoinitiator solutions

The main focus of this work was reduction, and irradiation of 1:1 and 1:10 OH-Span:photoinitiator samples in pH 5.2 sodium acetate buffer solution under nitrogen was monitored by steady-state UV/Visible absorption spectroscopy, HPLC, LC-MS and NMR spectroscopy. Some preliminary studies of samples under air were also carried out and monitored by UV/Visible absorption spectroscopy. The UV/Visible absorption spectra recorded in a 1 cm pathlength cell on irradiation under nitrogen and air are shown in Figures 5.21 and 5.22. For both 1:1 and 1:10 OH-Span:photoinitiator solutions the largest change in absorbance with irradiation was observed at 363 nm, attributed to loss of dye absorbance and this change is plotted as normalised absorbance versus light pulse in Figure 5.23. Qualitatively, the rate of decay of the main absorption band of the dye with number of light pulses was faster for reduction than oxidation. There was a total dye bleach observed for 1:10 OH-Span:photoinitiator solutions and a partial dye bleach for 1:1 OH-Span:photoinitiator solutions. This observation is in contrast to the very small spectral changes observed in the absence of photoinitiator under comparable conditions after 30 light pulses (Figure 5.11), and therefore the dye bleach can be attributed to the effect of the photoinitiator rather than direct photochemistry of the dye.

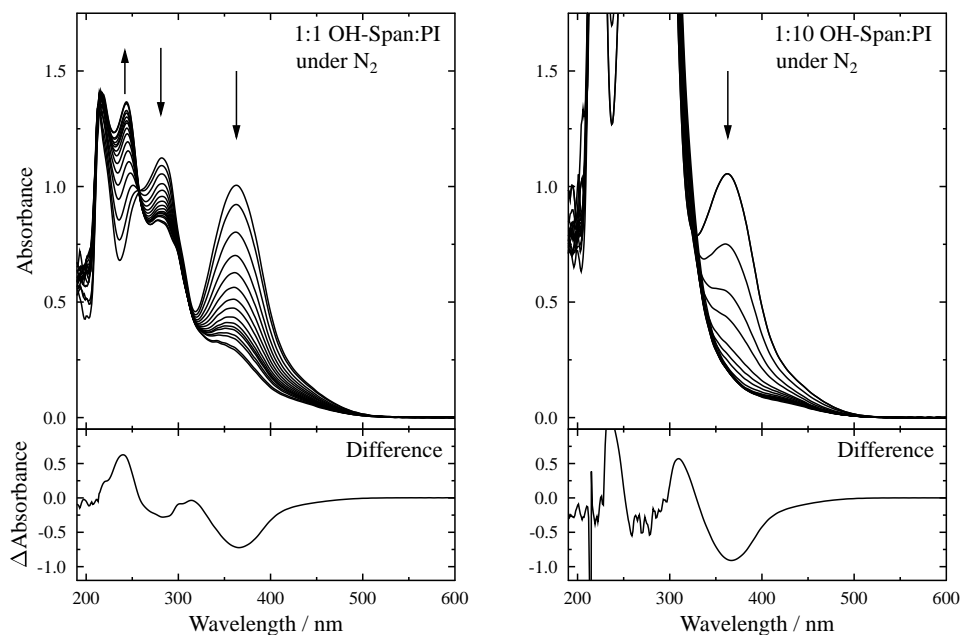


Figure 5.21 Irradiation of 1:1 (left) and 1:10 (right) OH-Span:photoinitiator (5×10^{-4} mol dm⁻³ dye concentration) in pH 5.2 sodium acetate buffer solution under nitrogen over 30 light pulses; arrows indicate changes with increasing light pulse, with the overall difference spectrum (final – initial) shown.

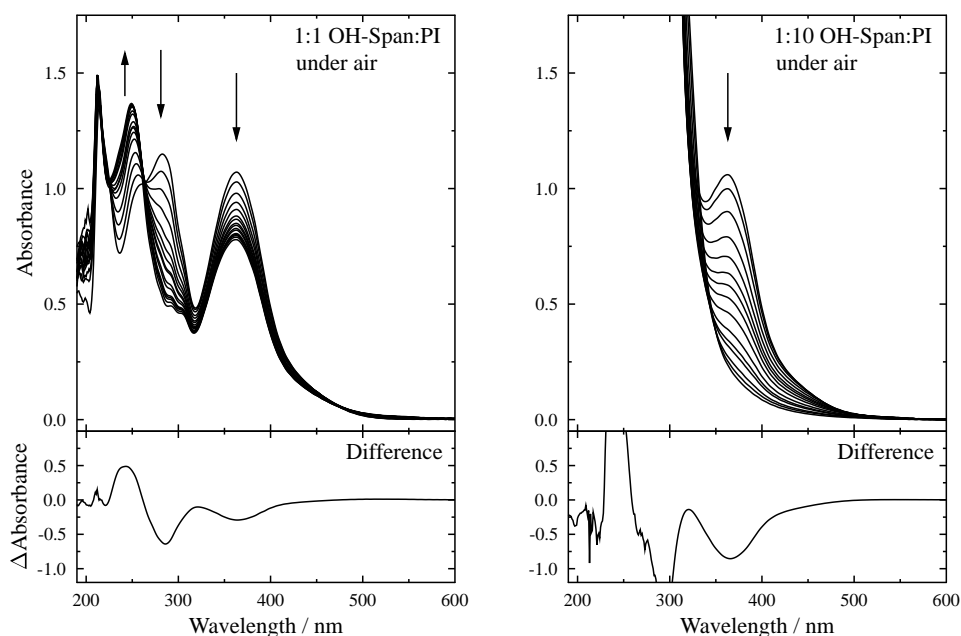


Figure 5.22 Irradiation of 1:1 (left) and 1:10 (right) OH-Span:photoinitiator (5×10^{-4} mol dm⁻³ dye concentration) in pH 5.2 sodium acetate buffer solution under air over 30 light pulses; arrows indicate changes with increasing light pulse, with the overall difference spectrum (final – initial) shown.

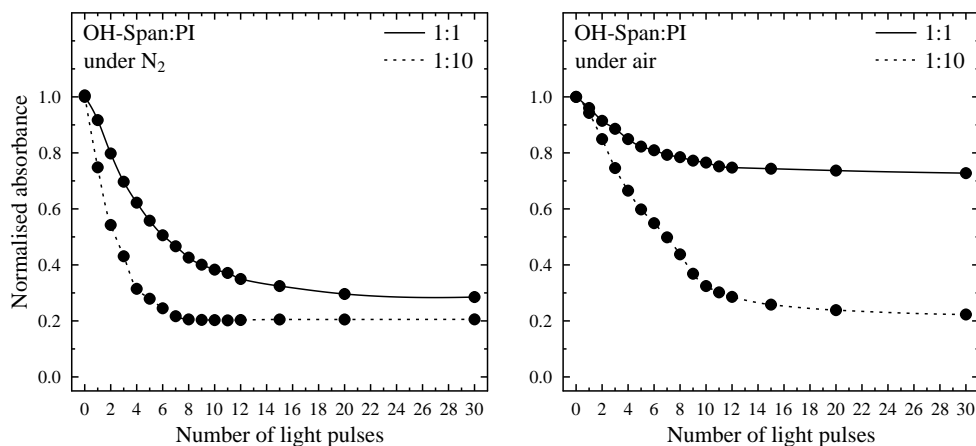


Figure 5.23 Normalised absorbance at 363 nm as a function of light pulse for 1:1 and 1:10 H-Span:photoinitiator in pH 5.2 sodium acetate buffer solution under nitrogen (left) and air (right).

Detailed product analysis was carried out on samples irradiated under nitrogen to study reduction, where 1:1 and 1:10 OH-Span:photoinitiator solutions were analysed by HPLC before and after 50 light pulses using a dye concentration of $5 \times 10^{-4} \text{ mol dm}^{-3}$, ten times the concentrations previously studied by UV/Visible absorption spectroscopy (Figure 5.21), so as to more easily identify the products. Figures 5.24 and 5.25 show the HPLC chromatograms before and after irradiation of a 1:1 and 1:10 OH-Span:photoinitiator sample under nitrogen, with the UV/Visible absorption spectra recorded from each of the 23 components (labelled A to W) observed from the 1:10 solution shown in Figure 5.26. The retention times, peak integrations and UV/Visible absorption band positions are given in Table 5.6 for both the 1:1 and 1:10 solutions. LC-MS was used to help identify the products and the mass spectra of components observed are shown in Figures 5.27 and 5.28 with assignments in Table 5.6.

The assignments of the products observed by HPLC and LC-MS can be made by drawing on those already made from samples after electrochemical reduction (Chapter 4) and from the irradiation of the photoinitiator alone (above): Component A has a retention time of 2.34 min, and it gives a negative ion base peak ion with an m/z value of 302.0 and a fragment ion with an m/z value of 222.1, a mass loss of 80 corresponding to a loss of SO_3 which matches the observed pattern, retention time and spectral features for NAPDAD produced after CPE reduction of OH-Span (Chapter 4

Figures 4.15 and 4.19). Component B has a retention time of 4.21 min and spectral features which match that of APOL produced after CPE reduction of OH-Span (Chapter 4 Figure 4.15). Component D has a retention time of 10.71 min, and it gives a negative ion base peak ion with an m/z value of 573.0 and fragment ions with m/z values of 302.0 and 222.1. The structure of component D is not yet known; but fragmentation of a component with an m/z value of 302.0 to 222.1 results from a mass loss of 80, which is the same ion pattern observed for NAPDAD (Chapter 4 Figure 4.28) indicating that component D contains the NAPDAD moiety. Component E has a retention time of 10.88 min, and it gives a positive ion base peak ion with an m/z value of 274.2 and a fragment ion with an m/z value of 165.1; this mass loss of 109 corresponds to loss of APOL, which indicates that this is part of the structure of component E. Component F has a retention time of 11.16 min and it gives a negative ion base peak ion with an m/z value of 466.0 which is a higher m/z than either OH-Span or photoinitiator, and fragment ions with m/z values of 386.1 and 342.0. The first fragmentation results from a mass loss of 80, consistent with a loss of SO_3 indicating the NAPDAD moiety is present. The second fragmentation results from a mass loss of 44 which may result from the loss of $\text{C}_2\text{H}_4\text{O}$, an alkyl chain which may come from the photoinitiator, indicating a parent structure containing both dye and photoinitiator components as a stable product. Component G with a retention time of 12.15 min matches the retention time and spectral features of H-benzoic acid assigned as a product of photoinitiator irradiation (Figures 5.16 and 5.18). Component K has a retention time of 14.68 min and it gives base peak ions with m/z values of 577.1 and 557.1 in negative and positive ion mode, respectively. Component Q has a retention time of 21.05 min and it gives a base peak ion with an m/z value of 577.1. Mass spectrometry therefore shows that components K and Q have structures with relatively high mass, both being higher than either OH-Span or photoinitiator alone. Component W has a retention time of 32.61 min that matches the retention time and spectral features of H-benzaldehyde assigned as a product of photoinitiator irradiation (Figures 5.13 and 5.14). Components C, I, J, L, M, N, O, P, R, S, T and V are unknown products, and H and U are residual OH-Span and photoinitiator, respectively.

Quantitatively, the peak integration and calibration from HPLC indicate that NAPDAD is produced in 11% and 22% yield for 1:1 and 1:10 solutions, respectively, and APOL is produced in 30% and 40% yield for 1:1 and 1:10 solutions, respectively.

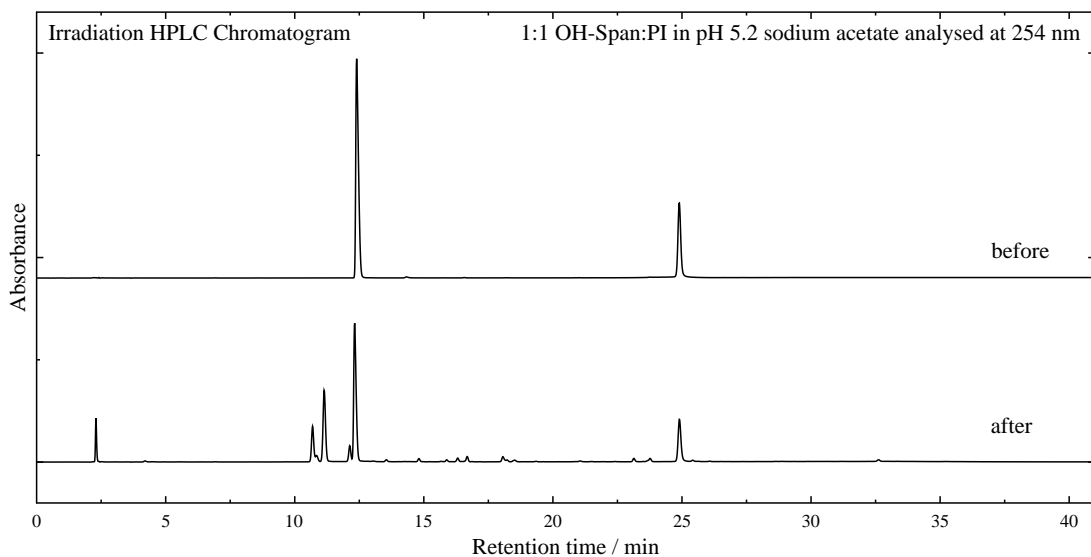


Figure 5.24 HPLC chromatogram of 1:1 OH-Span:photoinitiator ($5 \times 10^{-4} \text{ mol dm}^{-3}$ dye concentration) under nitrogen before (top) and after (bottom) 50 light pulses.

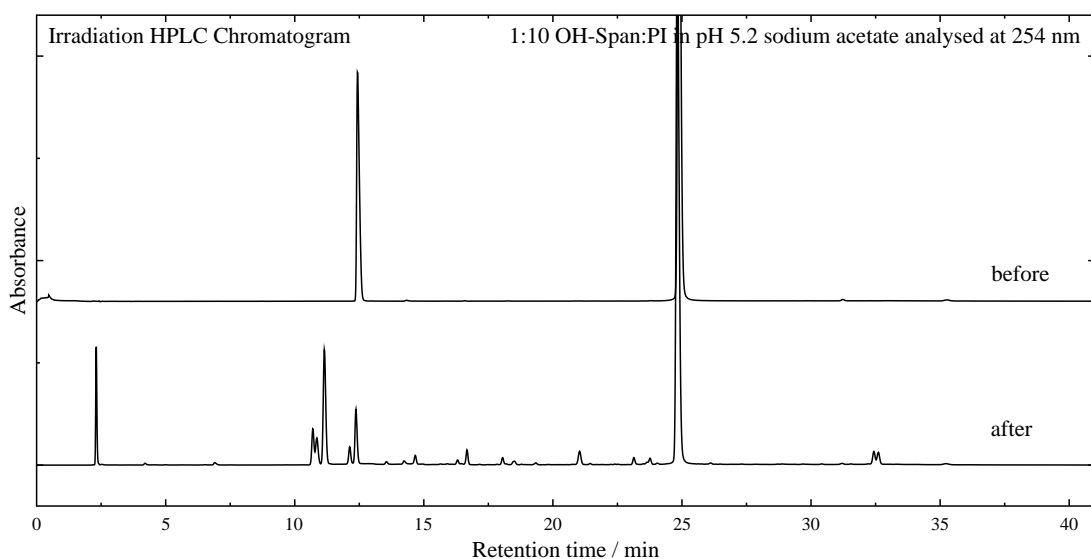


Figure 5.25 HPLC chromatogram of 1:10 OH-Span:photoinitiator ($5 \times 10^{-4} \text{ mol dm}^{-3}$ dye concentration) under nitrogen before (top) and after (bottom) 50 light pulses.

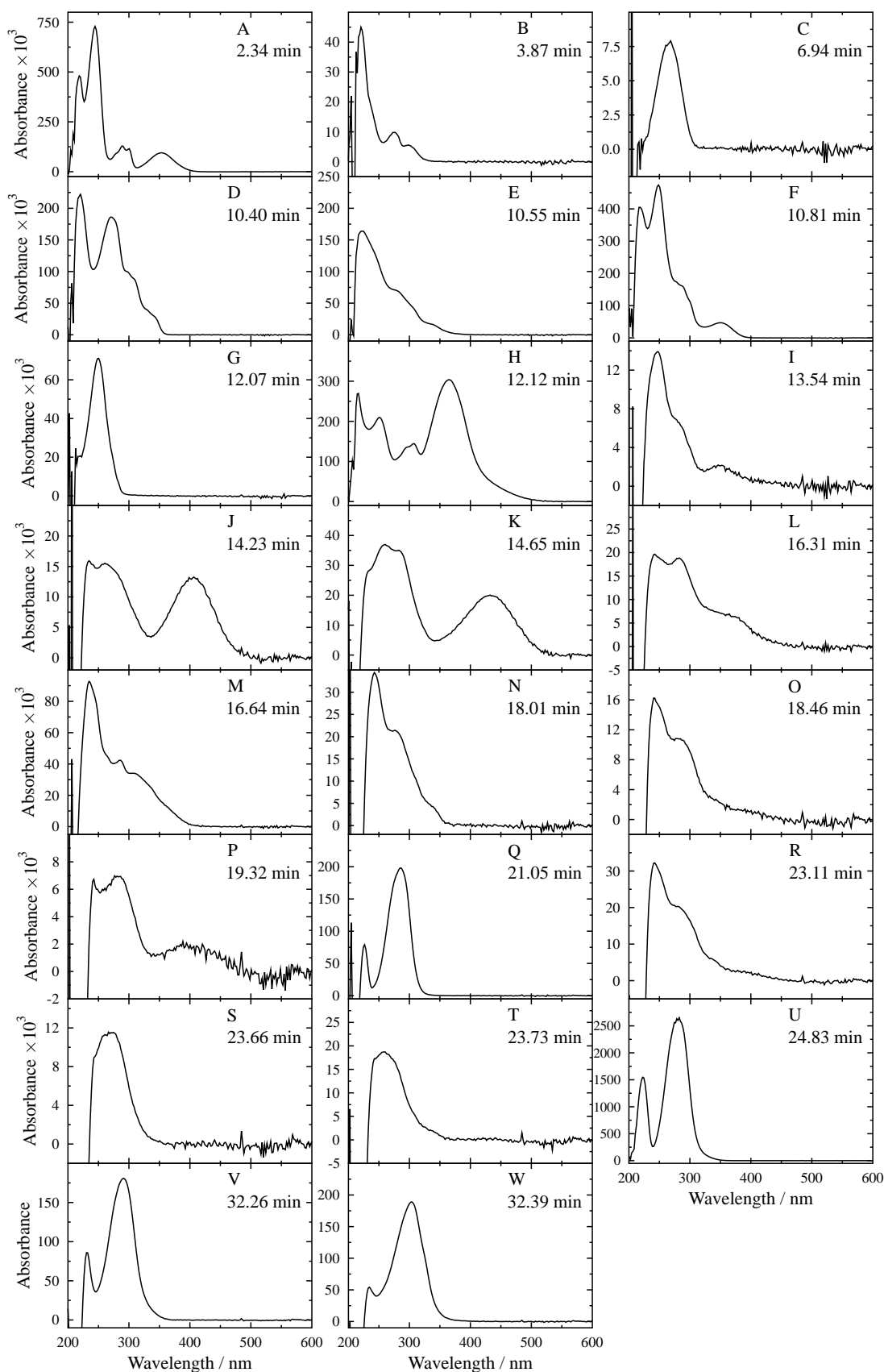


Figure 5.26 UV/Visible absorption spectra of components identified from 1:10 OH-Span:photoinitiator (5×10^{-4} mol dm $^{-3}$ dye concentration) under nitrogen after 50 light pulses.

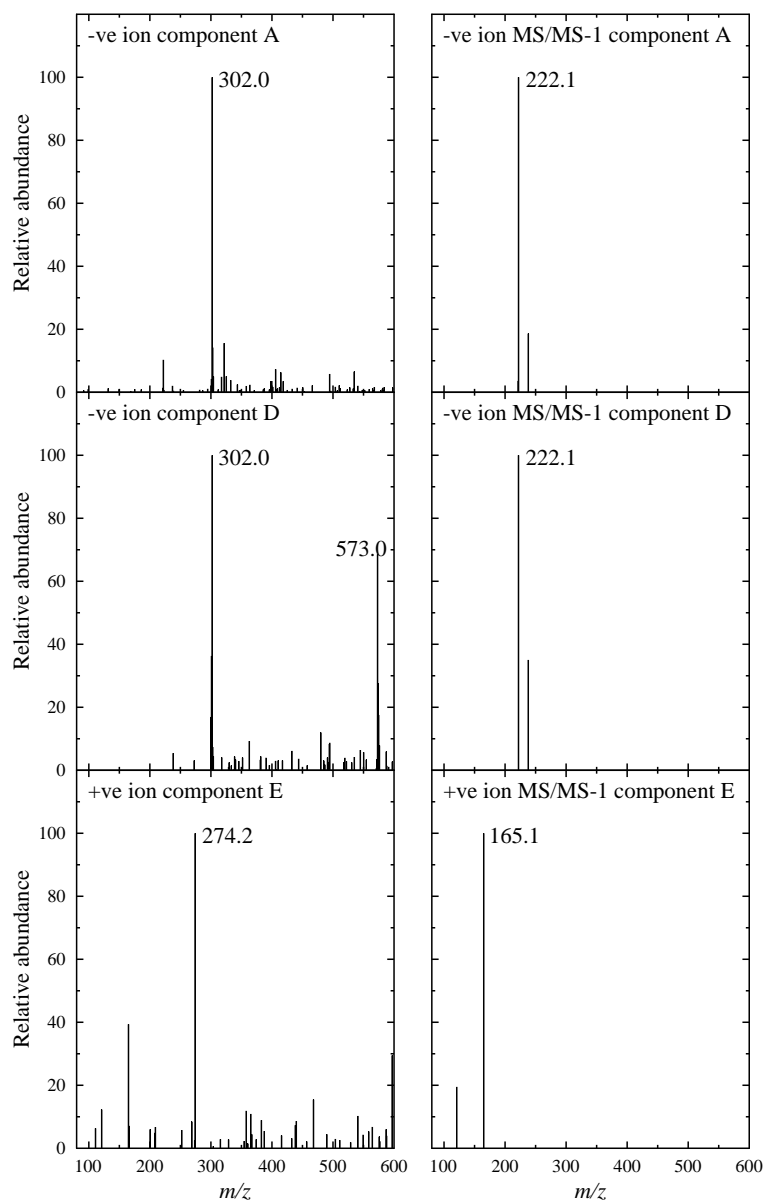


Figure 5.27 Left: ESI mass spectrum of component A, D and E with a retention times of 2.32, 10.40 and 10.55 min, respectively, formed after irradiation of 1:10 OH-Span:photoinitiator. Right: MS/MS-1 mass spectrum on the base peak ion of each component.

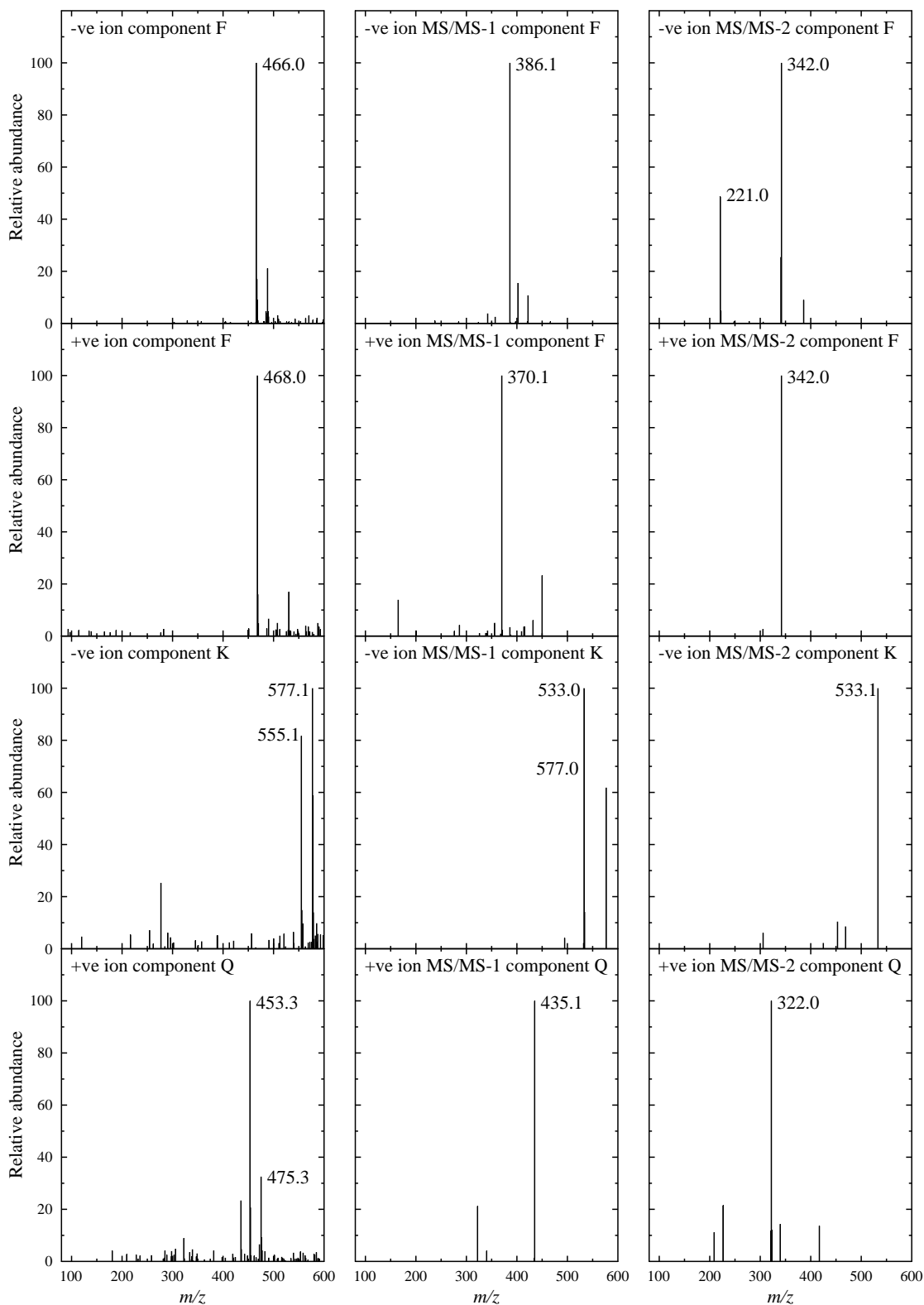


Figure 5.28 Left: ESI mass spectrum of component F, K and Q with a retention time of 10.81, 14.65 and 21.05 min, respectively, formed after irradiation of 1:10 OH-Span:photoinitiator. Middle: MS/MS-1 mass spectrum on the base peak ion of each component. Right: MS/MS-2 mass spectrum of each component.

Table 5.6 Retention times (RT / min), peaks integrations (P), concentrations (Concn / 10^{-4} mol dm⁻³) and UV/Visible absorption band positions (λ / nm) from HPLC and Retention times (RT / min), base peak ions (BP / m/z) and fragment ions (F / m/z) of components before and after 50 light pulses on 1:1 and 1:10 OH-Span:photoinitiator in pH 5.2 sodium acetate buffer solution under nitrogen.

Component	HPLC						λ	LC-MS						
	1:1			1:10				RT	BP	Assignment	F ₁	Assignment	F ₂	Assignment
<i>Before</i>														
OH-Span	12.45	97.15	5.00	12.40	97.61	5.00	215, 251, 294, 308, 363	12.12	407.0	[OH-Span + H] ⁺	327.0	Loss of SO ₃	206.0	Loss of azo
PI	24.88	36.34	5.00	24.88	361.15	50.00	217, 279	24.83	224.9	[PI + H] ⁺	178.9	Loss of C ₂ H ₆ O		
<i>After</i>														
A	2.34	9.91	0.36	2.34	22.81	0.83	217, 244, 288, 299, 353	2.32	302.0	[NAPDAD + H] ⁺	222.1	Loss of SO ₃		
B	4.21	0.59	0.94	3.87	1.00	1.59	219, 274, 300							
C	6.96	0.12	-	6.94	0.98	-	266							
D	10.71	12.44	-	10.40	13.95	-	213, 271, 306, 342	10.40	573.0	[M - Na] ⁺	302.0	[NAPDAD + H] ⁺	222.1	Loss of SO ₃
E	10.88	8.88	-	10.55	11.23	-	213, 271, 306, 342	10.55	274.2	[M + H] ⁺	165.1	Loss of APOL		
F	11.16	41.64	-	10.81	47.74	-	211, 248, 287, 352	10.81	466.0	[M - Na] ⁺	386.1	Loss of SO ₃	342.0	Loss of C ₂ H ₄ O
									468.0	[M + 3H ⁺ - 2Na] ⁺	450.0	Loss of H ₂ O	221.0	Unknown
									370.1		370.1	Loss of SO ₃	342.0	Unknown
G	12.15	15.55	-	12.07	5.89	-	217, 250	12.17	181.2	[H-benzoic acid - H] ⁺				
H	12.37	31.77	1.64	12.12	19.57	1.00	215, 251, 294, 308, 363							
I	13.55	10.05	-	13.54	0.97	-	248, 282, 253							
J	14.28	0.38	-	14.23	1.37	-	265, 404							
K	14.68	0.62	-	14.65	2.96	-	258, 248, 433	14.65	577.1	[M] ⁺	533.0	Loss of CO ₂	533.1	No change
											577.0	Base peak ion		
L	16.31	2.05	-	16.31	1.59	-	243, 285, 373							
M	16.64	2.17	-	16.64	4.67	-	236, 286, 311							
N	18.07	2.46	-	18.01	2.30	-	242, 280, 399							
O	18.46	1.91	-	18.46	1.83	-	240, 289, 393							
P	19.38	0.58	-	19.32	0.74	-	281, 394							
Q	21.05	0.55	-	21.05	6.21	-	217, 283	21.05	453.3	[M] ⁺	435.1	Loss of H ₂ O	322.0	Unknown
R	23.11	3.13	-	23.11	2.54	-	243, 283, 390							
S	-	-	-	23.66	1.04	-	260							
T	23.76	2.20	-	23.73	2.55	-	258, 334							
U	24.71	6.84	0.94	24.83	275.42	38.13	217, 279							
V	-	-	-	32.26	4.96	-	217, 280							
W	32.61	0.80	-	32.39	5.33	-	217, 300							

^a Concentration of NAPDAD (A) and APOL (B) calculated using the calibration curve (Appendix A2.4), ¹ concentration of residual OH-Span (H) and photoinitiator (U) calculated from peak integration.

In summary, HPLC and LC-MS product analysis has shown the large number of products that are formed after the irradiation of OH-Span in the presence of photoinitiator; importantly, NAPDAD and APOL are both observed. The results also indicate that components have formed with a higher mass than either OH-Span or photoinitiator, indicating that parts of OH-Span and/or photoinitiator have reacted together, which would be consistent with the relatively low yields of NAPDAD and APOL in comparison with those obtained from electrochemical reduction (ca. 90% yield).

It was important to know if NAPDAD and APOL reacted photoinitiator induced radicals, hence solutions of NAPDAD and APOL were irradiated in the presence of photoinitiator under nitrogen using the same conditions used for OH-Span. 1:1 NAPDAD:photoinitiator and 1:1 APOL:photoinitiator solutions were analysed by HPLC analysis before and after 50 light pulses as shown in Figures 5.29 and 5.31, respectively, with the UV/Visible absorption spectra recorded from each component shown in Figures 5.30 and 5.32, respectively. The retention times, peak integrations and UV/Visible absorption band positions are given in Table 5.7. The results indicate a ca. 12 % decrease in APOL and a ca. 2 % decrease in NAPDAD concentrations during irradiation in the presence of photoinitiator. Excluding those components thought to result from the photoinitiator breakdown, the irradiation of NAPDAD in the presence of photoinitiator (Figure 5.30) shows the same component E observed at a retention time of 10.55 min in the irradiation of OH-Span in the presence of photoinitiator (Figure 5.26); by contrast, irradiation of APOL in the presence of photoinitiator does not show any of the same components observed in the irradiation of OH-Span in the presence of photoinitiator. Therefore the low yield of NAPDAD and APOL observed in the OH-Span:photoinitiator solutions cannot be attributed to their loss by direct reactions with photoinitiator radicals.

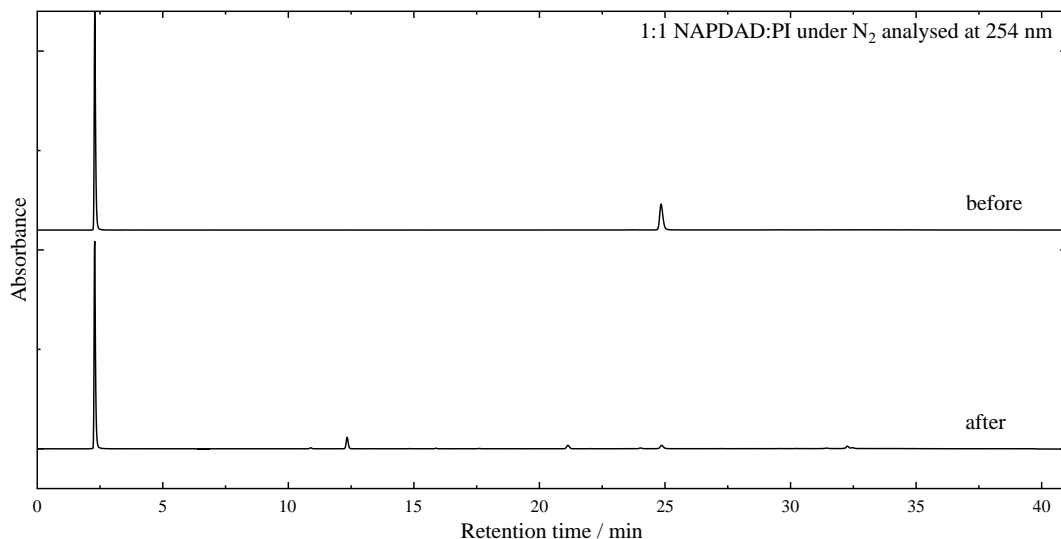


Figure 5.29 HPLC chromatogram of 1:1 NAPDAD:photoinitiator (both at 5×10^{-4} mol dm^{-3}) at pH 5.2 under nitrogen before (top) and after (bottom) 50 light pulses.

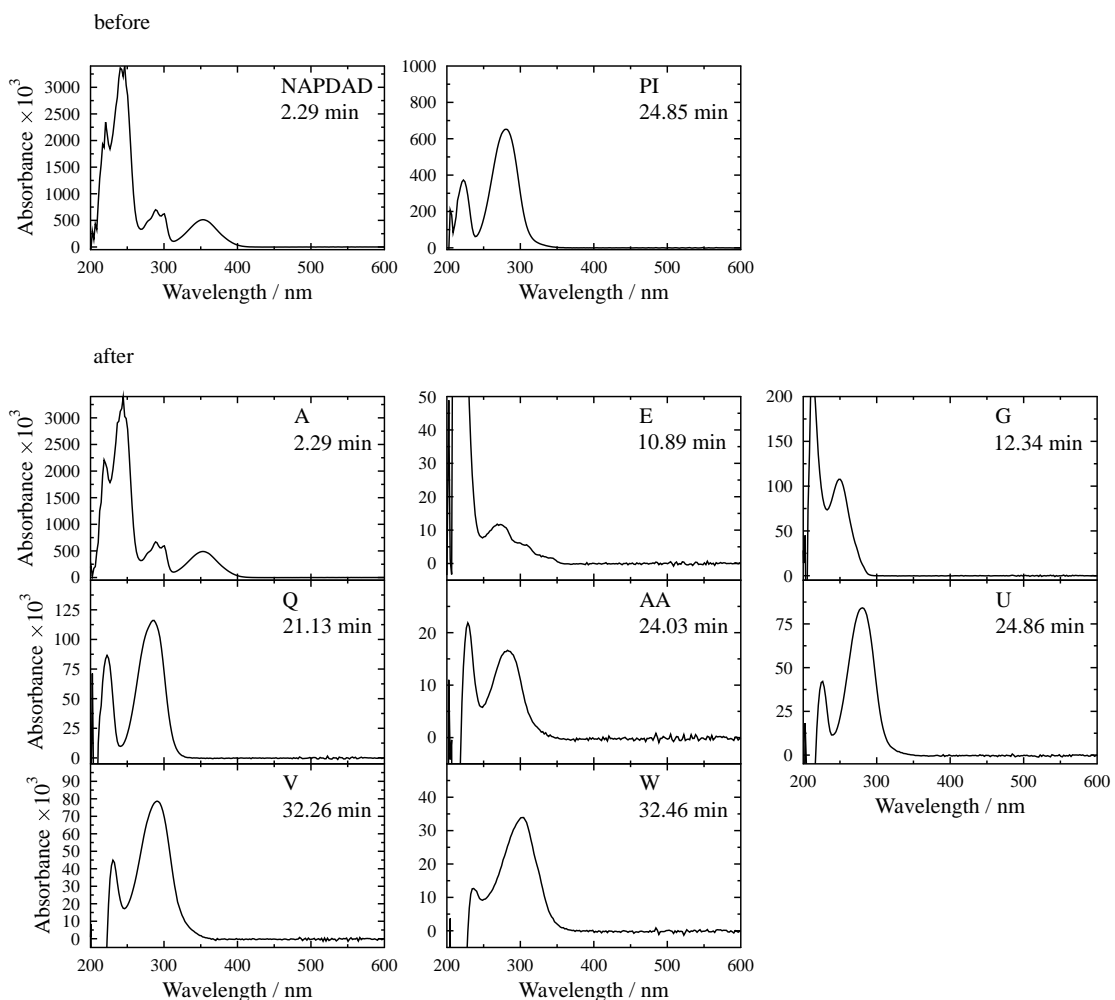


Figure 5.30 Top: UV/Visible absorption spectra of 1:1 NAPDAD:photoinitiator before irradiation. Bottom: UV/Visible absorption spectra of components formed after 50 light pulses.

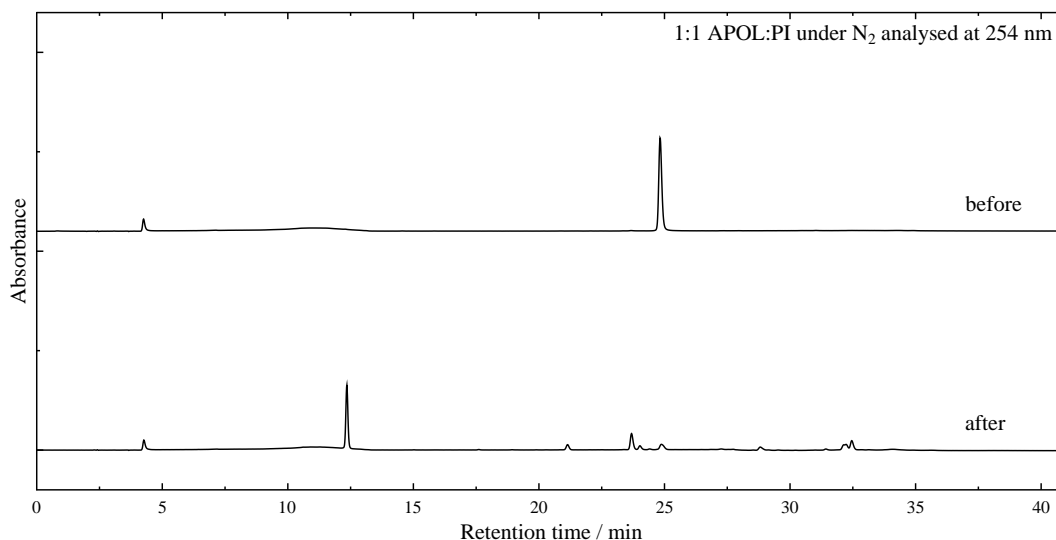


Figure 5.31 HPLC chromatogram of 1:1 APOL:photoinitiator (both at 5×10^{-4} mol dm^{-3}) at pH 5.2 under nitrogen before (top) and after (bottom) 50 light pulses.

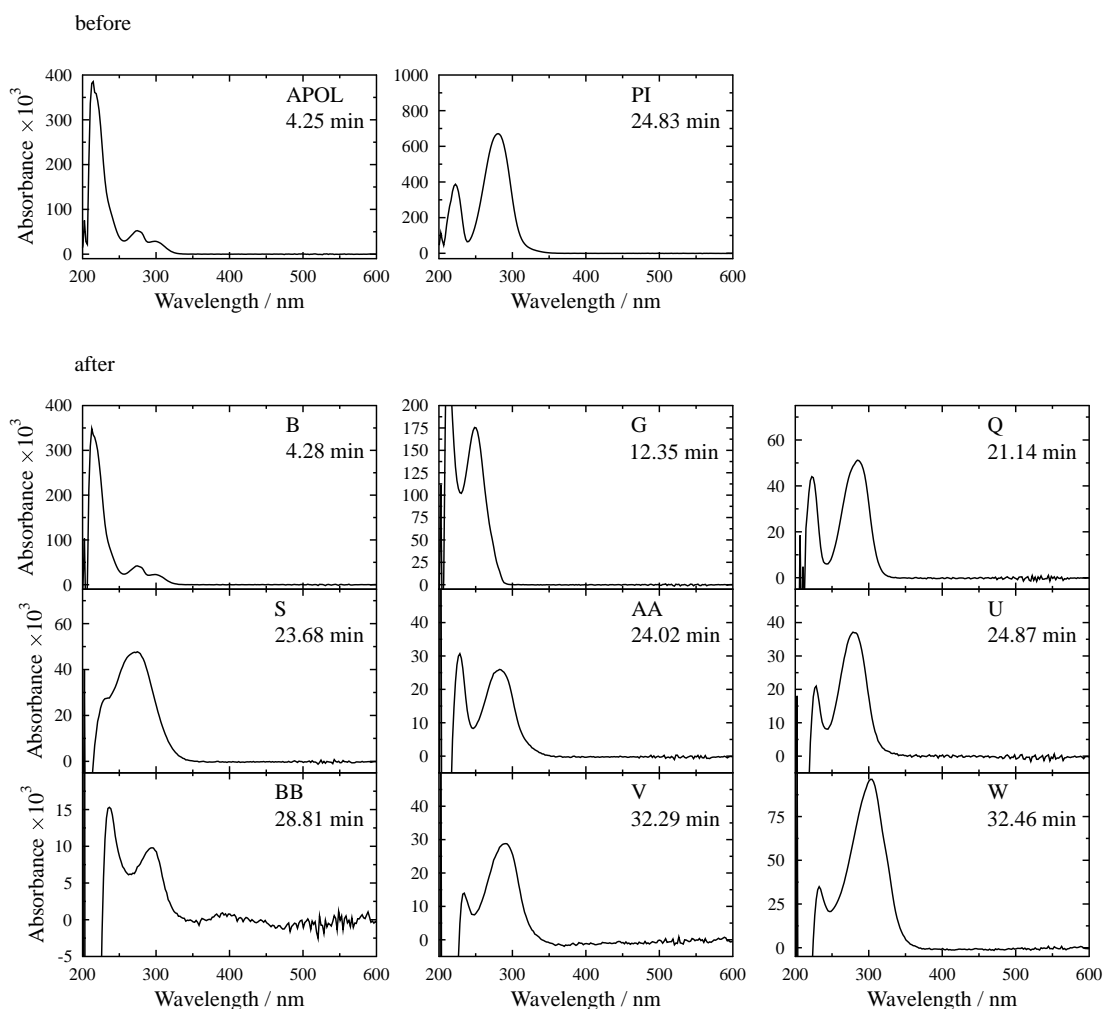


Figure 5.32 Top: UV/Visible absorption spectra of 1:1 APOL:photoinitiator before irradiation. Bottom: UV/Visible absorption spectra of components formed after 50 light pulses.

Table 5.7 Retention times (RT / min), peak integrations (PI), concentrations (Concn / 10^{-4} mol dm^{-3}) and UV/Visible absorption band positions (λ / nm) of each component before and after 50 light pulses for 1:1 APOL:photoinitiator and 1:1 NAPDAD:photoinitiator under nitrogen.

Component	APOL			NAPDAD			λ
	RT	PI	Concn ^a	RT	PI	Concn ^a	
<i>Before</i>							
NAPDAD	-	-	-	2.29	120.83	5.00	217, 244, 288, 299, 353
APOL	4.27	3.42	5.00	-	-	-	219, 274, 300
Photoinitiator	24.85	34.91	5.00	24.83	34.56	5.00	217, 279
<i>After</i>							
A (NAPDAD)	-	-	-	2.29	118.83	4.91	217, 244, 288, 299, 353
B (APOL)	4.27	3.02	4.41	-	-	-	219, 274, 300
E	-	-	-	10.89	0.90	-	271, 304, 342
S	23.68	5.15	-	-	-	-	260
AA	24.03	1.23	-	24.03	0.75	-	222, 283
BB	28.81	1.41	-	-	-	-	237, 295, 400
V	32.29	2.94	-	32.26	2.76	-	217, 280
U (Photoinitiator)	24.87	2.68	0.38	24.86	4.51	0.65	217, 279
Q (Photoinitiator prod)	21.14	1.71	-	21.13	3.91	-	217, 283
G (H-benzoic acid)	12.35	16.07	-	12.34	1.78	-	217, 249
W (H-benzaldehyde)	32.46	3.19	-	32.46	1.02	-	217, 300

^a Concentration of NAPDAD and APOL calculated using the calibration curve (Appendix A2.4),¹ concentration of residual photoinitiator calculated from peak integration.

Once again NMR spectroscopy was used to provide further evidence as to the nature of the products and also to give a quantitative measure of the species formed. 1D and 2D (COSY, NOESY, DOSY) ^1H spectra were recorded from 1:1 OH-Span:photoinitiator ($5 \times 10^{-4} \text{ mol dm}^{-3}$ dye concentration) samples in deuterated 0.05 mol dm^{-3} sodium acetate buffer at pD 5.2 under nitrogen using a Bruker 700 MHz spectrometer, and the spectra before and after 50 light pulses are shown in Figure 5.33. The DOSY dimension after irradiation shows the complexity of this study by highlighting further the large number of products formed with various diffusion coefficients indicating various sizes and masses. Figure 5.34 shows possible products that have formed with NMR assignments given in Table 5.8.

Before irradiation, photoinitiator and OH-Span have apparent diffusion coefficients of 5.48×10^{-10} and $4.73 \times 10^{-10} \text{ m}^2 \text{ s}^{-1}$, respectively. Upon irradiation products form with higher and lower apparent diffusion coefficients, hence have lower and higher masses than photoinitiator or OH-Span. Compounds from both photoinitiator and OH-Span have formed, for example: HEB with its distinctive aldehyde proton at a chemical shift of 9.82 ppm, NAPDAD and APOL by their apparent diffusion coefficients of 5.58×10^{-10} and $6.63 \times 10^{-10} \text{ m}^2 \text{ s}^{-1}$, respectively, comparable to those observed after CPE reduction of OH-Span (Chapter 4 Figure 4.21). Products labelled * and *P in Table 5.8 show NAPDAD and photoinitiator ^1H NMR chemical shift patterns, respectively, and have diffusion coefficients of ca. 4.3 to $4.4 \times 10^{-10} \text{ m}^2 \text{ s}^{-1}$ that are lower than those of OH-Span or photoinitiator; products of high mass containing NAPDAD and photoinitiator moieties are comparable with the LC-MS data. 1,4-hydroquinone is observed at a chemical shift of 6.81 ppm with an apparent diffusion coefficient of $6.72 \times 10^{-10} \text{ m}^2 \text{ s}^{-1}$ which is consistent with that observed upon CPE reduction of OH-Span.

In addition, COSY interactions are observed for components proposed in Figure 5.34: for OH-Span between protons 5 & 6, 6 & 7, 12 & 13 and 15 & 16; for NAPDAD between protons 5 & 6, 6 & 7; for APOL between protons 12 & 13 and 15 & 16; for species labelled * between 5 & 6, 6 & 7 in NAPDAD and for species labelled *P there are COSY interactions in both the aliphatic and aromatic protons, consistent with assignments made to photoinitiator components.

Quantitatively NMR has shown that NAPDAD is produced in 14% yield and APOL in 30% yield, which is comparable to the quantitative HPLC analysis for a 1:1 solution of 11% and 30%, respectively. Thereafter, NMR shows that HEB, PIP A, PIP B (assigned to H-benzoic acid), species labelled *, and hydroquinone are produced in yields of 42%, 10%, 25%, 27% and 4%, respectively, therefore by yield only ca. 41% of the naphthyl half (NAPDAD and *), and only ca. 34 % of the phenyl half (APOL and HQ) of OH-Span can be accounted for. There are however several aromatic protons unassigned.

In summary, quantitative 1D ^1H NMR, 2D COSY and DOSY NMR have been used in the elucidation of products. ^1H chemical shifts and apparent diffusion coefficients have shown that NAPDAD and APOL are produced by the reaction of OH-Span with radical species formed on irradiation of the photoinitiator under nitrogen. NMR analysis has also shown that products form with higher and lower apparent diffusion coefficients than OH-Span and photoinitiator, indicative of low and high mass components. Importantly, the results suggest that the products have structural elements of both OH-Span and photoinitiator, consistent with LC-MS analysis. The product analysis, in general, has shown that in addition to the simple reduction observed electrochemically, the reduction of OH-Span in the presence of photoinitiator-generated radicals gives side reactions, and these products require a combination of different analytical techniques for their identification.

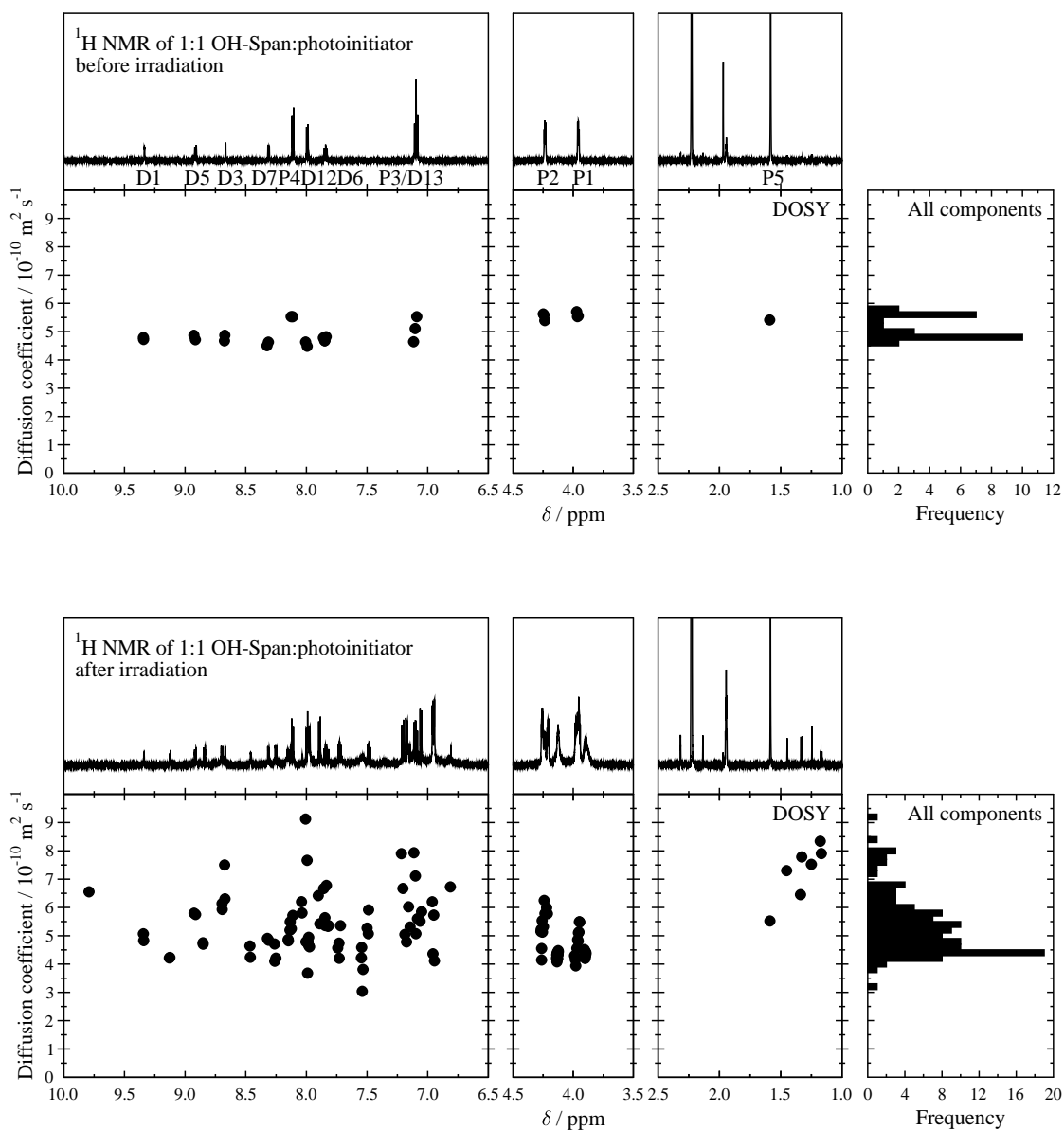
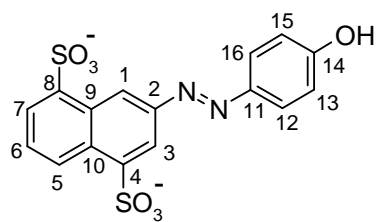


Figure 5.33 Left: ^1H NMR (700 MHz) DOSY display of 1:1 OH-Span:photoinitiator before (top) and after 50 light pulses (bottom) at $5 \times 10^{-4} \text{ mol dm}^{-3}$ at pD 5.2 under nitrogen (D = Dye P = Photoinitiator). Right: Histogram of all components in DOSY display.

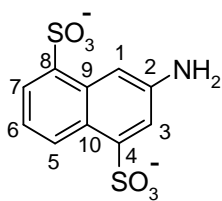
Table 5.8 ^1H chemical shifts (ppm), apparent diffusion coefficient per splitting ($D_{\text{All}} / 10^{-10} \text{ m}^2 \text{ s}^{-1}$), mean apparent diffusion coefficient per component ($D_{\text{mean}} / 10^{-10} \text{ m}^2 \text{ s}^{-1}$) and concentration (Concn / $10^{-4} \text{ mol dm}^{-3}$) of each component of OH-Span:photoinitiator alone before and after irradiation under nitrogen.

Atom	Before Irradiation				After Irradiation			
	$^1\text{H}^a$	Concn	DOSY		$^1\text{H}^a$	Concn	DOSY	
			D_{All}	D_{Mean}			D_{All}	D_{Mean}
Photoinitiator								
1	3.96 2.0 t	4.5 5.00	5.55, 5.53, 5.70		3.93 0.41 t	4.5 1.03	5.10, 4.86, 4.80	
2	4.24 2.0 t	4.5 5.00	5.39, 5.58, 5.62		4.24 0.41 t	4.5 1.03	5.32, 5.12, 5.53	
3	7.09 2.0 d	9.0 5.00	5.53, 5.10		7.09 0.38 d	9.0 0.95	5.60, 5.07	
4	8.11 2.0 d	9.0 5.00	5.53, 5.33		8.11 0.38 d	9.0 0.95	5.72, 5.25	
5	1.59 6.0 s	- 5.00	5.41		1.58 1.23 s	- 1.03	5.52	
OH-Span								
1	9.34 1.0 d	1.0 5.00	4.72, 4.79		9.34 0.30 d	1.0 1.50	4.83, 5.07	
3	8.67 1.0 d	2.0 5.00	4.87, 4.67		8.67 0.32 d	2.0 1.60	6.30, 7.50	
5	8.92 1.0 d	9.0 5.00	4.71, 4.87		8.92 0.32 d	9.0 1.60	5.76, 5.80	
6	7.84 1.0 t	9.0 5.00	4.82, 4.68, 4.78		7.84 0.28 t	9.0 1.40	6.77, 5.36, 5.63	
7	8.32 1.0 d	9.0 5.00	4.63, 4.50		8.32 0.34 d	9.0 1.70	4.84, 4.91	
12/16	8.00 2.0 d	9.0 5.00	4.48, 4.63		8.00 0.60 d	9.0 1.50	4.78, 4.78	
13/15	7.09 2.0 d	9.0 5.00	5.10, 4.64		7.10 0.60 d	9.0 1.50	7.11, 7.93	
Products								
2-propanol					1.17 0.04 d	6.5 0.01	7.90, 8.33	
EG					3.35 0.02 s	- 0.02	-	
HEB 1					3.94 0.37 t	4.5 1.85	5.48, 5.49, 5.13	
HEB 2					4.21 0.37 t	4.5 1.85	5.99, 5.78, 6.25	
HEB 3					7.17 0.32 d	9.0 1.60	4.78, 5.04	
HEB 4					7.98 0.33 d	9.0 1.65	7.66, 9.12	
HEB α					9.82 0.02 s	- 0.10	6.55	
PIP A 1					3.99 0.08 t	4.5 0.20	4.56, 4.21, 3.94	
PIP A 2					4.25 0.08 t	4.5 0.20	4.26, 4.26, 5.26	
PIP A 3					7.15 0.07 d	9.0 0.18	5.30, 6.02	
PIP A 4					8.01 0.08 d	9.0 0.20	4.94, 3.68	
PIP B 1					3.98 0.41 t	4.5 1.02	4.20, 4.15, 4.33	
PIP B 2					4.26 0.41 t	4.5 1.02	5.15, 5.22, 5.30	
PIP B 3					7.05 0.38 d	9.0 0.95	5.85, 5.51	
PIP B 4					7.98 0.39 d	9.0 0.98	5.42, 6.41	
NAPDAD 1					8.03 0.08 d	1.0 0.40	5.81, 6.20	
NAPDAD 3					7.81 0.08 d	1.0 0.40	5.36, 5.35	
NAPDAD 5					8.70 0.11 d	9.0 0.55	5.59, 6.14	
NAPDAD 6					7.48 0.10 t	9.0 0.50	5.91, 5.07, 5.27	
NAPDAD 7					8.13 0.11 d	9.0 0.55	5.49, 5.19	
APOL 12/16					6.93 0.42 d	9.0 1.05	5.73, 6.19	
APOL 13/15					7.20 0.40 d	9.0 1.00	6.68, 7.90	
*1					9.12 0.16 d	1.0 0.80	4.23, 4.21	
*3					8.46 0.18 d	2.0 0.90	4.23, 4.63	
*5					8.85 0.20 d	9.0 1.00	4.70, 4.75	
*6					7.73 0.21 t	9.0 1.05	4.20, 4.75, 4.56	
*7					8.25 0.21 d	9.0 1.05	4.10, 4.71	
*P					6.91 0.22 d	9.0 1.10	4.11, 4.36	
*P					8.14 0.22 d	9.0 1.10	4.83, 4.87	
*P					7.54 0.41 br	- -	3.81, 3.03, 4.59	
*P					4.13 0.41 br	- -	4.12-4.13	
*P					3.90 0.42 br	- -	4.19-4.43	
Hydroquinone					6.81 0.12 s	- -	6.72	
unassigned					1.25 0.02 s	- -	7.79	
unassigned					1.32 0.08 d	7.0 -	6.45	
unassigned					1.45 0.04 d	7.0 -	7.30	
unassigned					7.00 0.08 dd	8.5 -	7.32	
unassigned					7.37 0.08 dd	8.5 -	-	
unassigned					7.94 0.02 d	9.0 -	-	

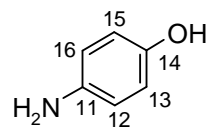
^a Integration, multiplicity (s = singlet; d = doublet; t = triplet), splitting (Hz)



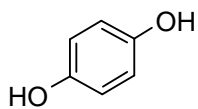
OH-Span



NAPDAD



APOL



Hydroquinone

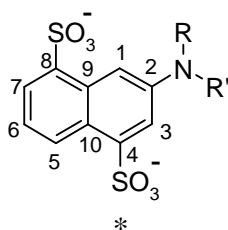


Figure 5.34 Possible components from the irradiation of 1:1 OH-Span:photoinitiator after 50 light pulses under nitrogen. For component *, R' contains *P.

5.2.1.2 Time-resolved studies

The following section reports on the pulsed laser, time-resolved UV/Visible absorption (TRVIS) studies on OH-Span alone, photoinitiator alone and OH-Span:photoinitiator solutions.

OH-Span alone

The TRVIS spectra of OH-Span (4×10^{-4} mol dm⁻³) in pH 5.2 sodium acetate buffer solution obtained 150, 300, 650, 1250 and 3500 ns after 308 nm excitation in a 1 cm pathlength cell at 20.5 °C are shown in Figure 5.35. The TRVIS spectra are dominated by a bleaching band at ca. 360 nm that can be assigned to loss of *trans*-OH-Span reactant, and a new absorption band occurs at ca. 460 nm which decays as the bleaching band at ca. 360 nm recovers. Both features develop within the instrument response time and then decay on a similar microsecond timescale. Figure 5.36 shows the kinetic traces at 360 and 460 nm as a function of time (t) analysed by fitting to a single exponential decay as shown in equation 5.7 to determine the first order rate constant (k_{obs}), where ΔA , A_1 and A_∞ are the change in absorbance, absorbance arising from the transient signal, and the absorbance at $t = \infty$, respectively. The analysis gave a rate constant of ca. 1.5×10^6 s⁻¹ across the probe wavelength range of 350 – 420 and 450 – 510 nm.

$$\Delta A = A_1 e^{-kt} + A_\infty \quad (5.7)$$

The results are consistent with the sub-nanosecond formation of the *cis* form of OH-Span, as observed for azobenzene,⁵ the formation of which is beyond the instrument response, followed by the thermal back reaction back to the *trans* form as shown in Figure 5.37. The rate constant for the thermal back reaction gave a lifetime ($\tau = 1/k$) of ca 666 ns for the *cis* isomer.

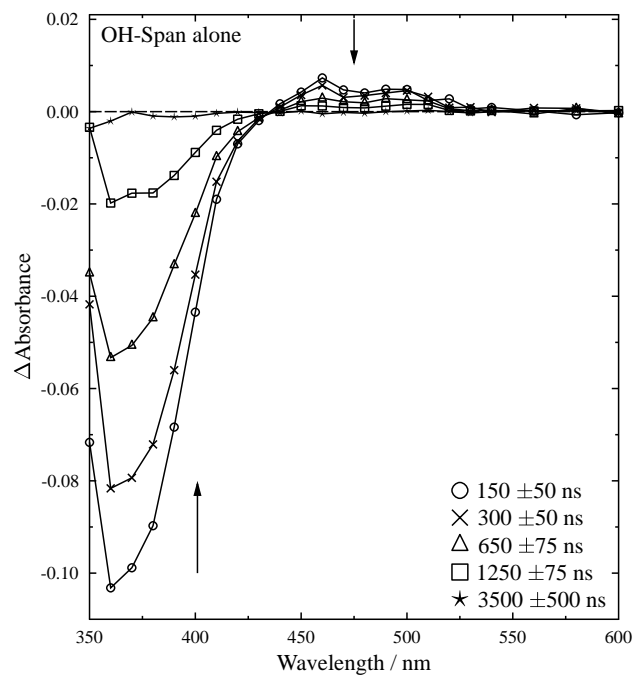


Figure 5.35 TRVIS spectra of OH-Span alone (4×10^{-4} mol dm $^{-3}$) in pH 5.2 sodium acetate buffer solution, 150, 300, 600 1250 and 3500 ns after excitation; arrows indicate changes with time.

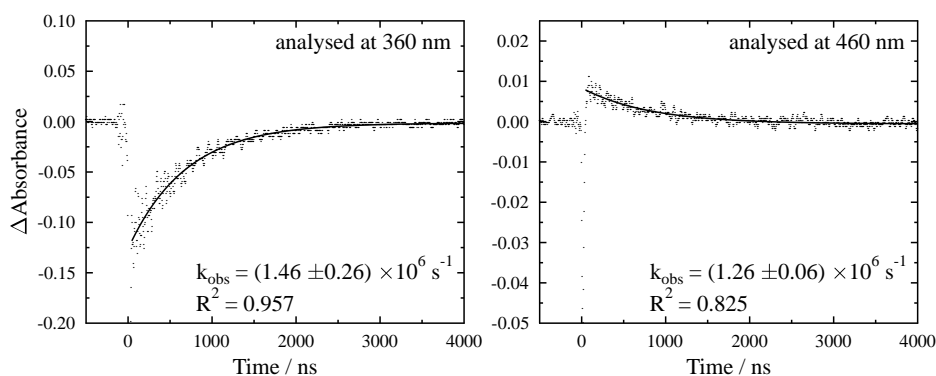


Figure 5.36 TRVIS kinetic traces of OH-Span alone (4×10^{-4} mol dm $^{-3}$) in pH 5.2 sodium acetate buffer solution at 360 and 460 nm, fitted using equation 5.7.

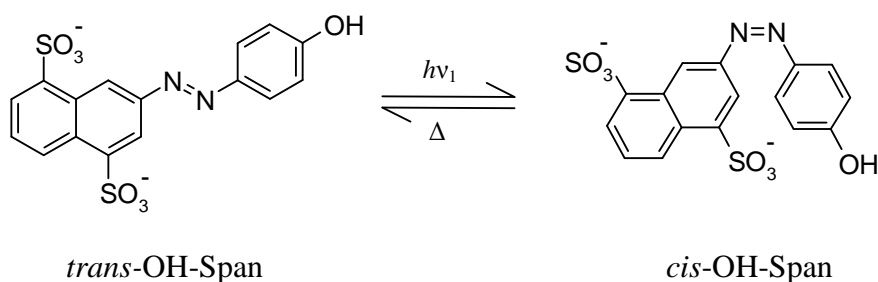


Figure 5.37 Isomerisation of OH-Span.

Photoinitiator alone

TRVIS data have been reported previously for the photoinitiator alone in water,⁵⁰ and Figure 5.38 shows a kinetic trace obtained at 410 nm for photoinitiator in pH 5.2 sodium acetate buffer solution under nitrogen after 308 nm excitation in a 1 mm pathlength cell at 20 °C, which when analysed using equation 5.7 gave a rate constant of $9.05 \times 10^6 \text{ s}^{-1}$, corresponding to $\tau = 110 \text{ ns}$, which is consistent with the reported decay of the triplet state of the photoinitiator to give the radical fragments shown in Figure 5.8.^{41,50}

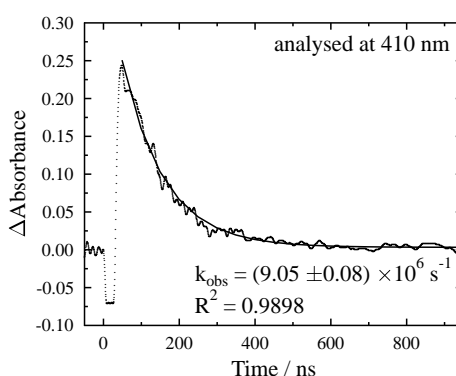


Figure 5.38 TRVIS kinetic traces of photoinitiator alone ($1 \times 10^{-3} \text{ mol dm}^{-3}$) in pH 5.2 sodium acetate buffer solution under nitrogen analysed at 410 nm, fitted using equation 5.7.

OH-Span:photoinitiator solutions

The TRVIS spectra of 1:10 OH-Span:photoinitiator ($1 \times 10^{-4} \text{ mol dm}^{-3}$ dye concentration) in pH 5.2 sodium acetate buffer solution under nitrogen obtained 325 ns after 308 nm excitation in a 1 mm pathlength cell at 21 °C is shown in Figure 5.39 and can be attributed to the photoinitiator triplet state. The TRVIS spectra obtained at 1.3, 3.5, 6.5, 15.0, 45.0 and 85.0 μs after excitation are shown in Figure 5.40, and the kinetic traces at 360 and 490 nm are shown in Figure 5.41. Similar TRVIS data were also obtained for a of 1:30 OH-Span:photoinitiator ($1 \times 10^{-4} \text{ mol dm}^{-3}$ dye concentration) solution and are given in Appendix 3.

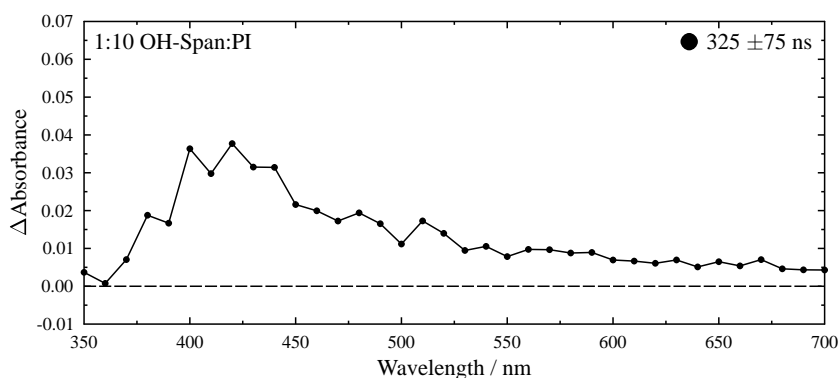


Figure 5.39 TRVIS spectra of 1:10 OH-Span:photoinitiator (1×10^{-4} mol dm⁻³ dye concentration) in pH 5.2 sodium acetate buffer solution under nitrogen, 325 ns after excitation.

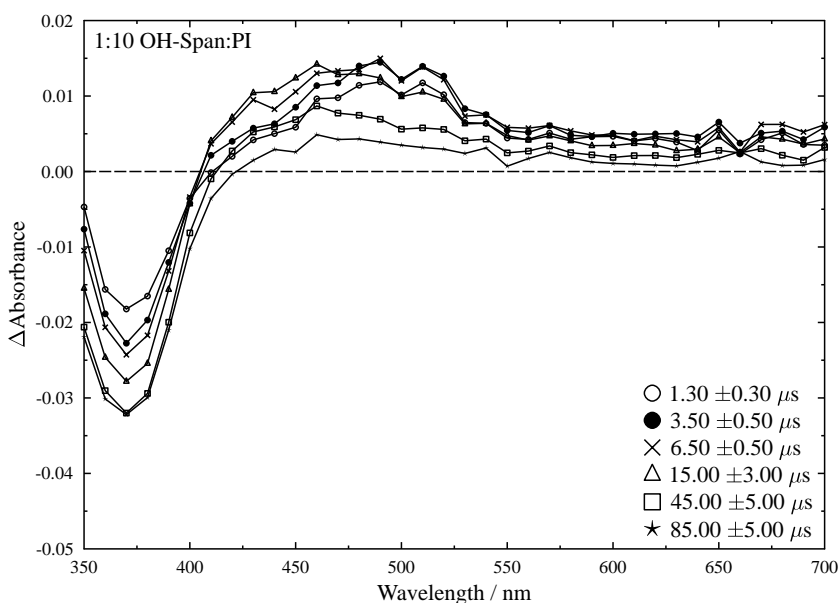


Figure 5.40 TRVIS spectra of 1:10 OH-Span:photoinitiator (1×10^{-4} mol dm⁻³ dye concentration) in pH 5.2 sodium acetate buffer solution under nitrogen, 1.30, 3.50, 6.50, 15.00, 45.00 and 85.00 μ s after excitation.

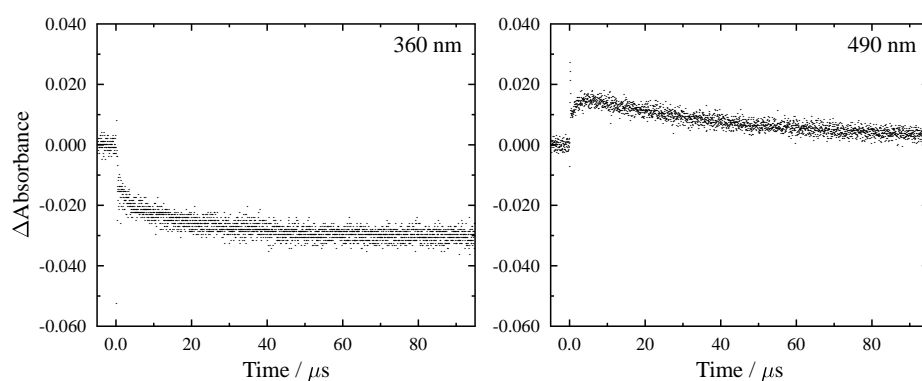


Figure 5.41 TRVIS kinetic traces of 1:10 OH-Span:photoinitiator (1×10^{-4} mol dm⁻³ dye concentration) in pH 5.2 sodium acetate buffer solution under nitrogen at 360 and 490 nm.

Figure 5.42 gives an overlay of the kinetic traces at 360 nm for OH-Span alone and 1:10 OH-Span:photoinitiator, recorded under the same conditions and with the same dye concentration of $1 \times 10^{-4} \text{ mol dm}^{-3}$ in a 1 mm pathlength cell (as opposed to a dye concentration of $4 \times 10^{-4} \text{ mol dm}^{-3}$ in a 1 cm cell as recorded for OH-Span alone previously in Figures 5.35 and 5.36). Any signal from OH-Span alone, due to isomerisation, was very small under these conditions. This indicates that the *trans* isomer was dominant and hence that the radical reactions being observed can be attributed to the *trans* form of OH-Span, even though the *cis-trans* thermal back reaction occurs on a similar timescale to that of the decay of the photoinitiator triplet state.

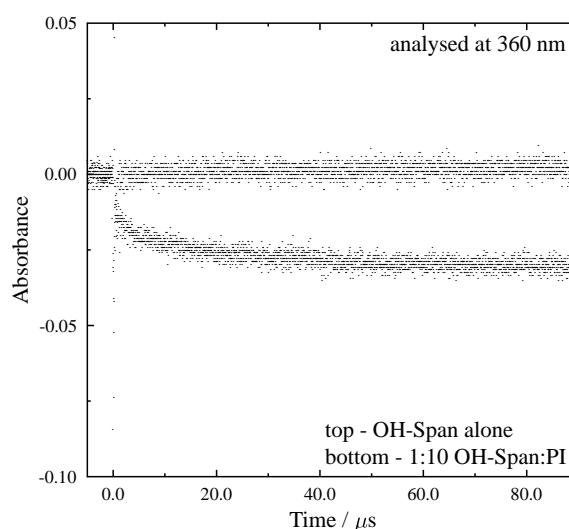


Figure 5.42 TRVIS kinetic traces of OH-Span alone and 1:10 OH-Span:photoinitiator (all $1 \times 10^{-4} \text{ mol dm}^{-3}$ dye concentration) in pH 5.2 sodium acetate buffer solution under nitrogen at 360 nm.

The negative ΔA values between ca. 340 and 400 nm ($\lambda_{\text{max}} = 360 \text{ nm}$) may be assigned to the bleach of the main absorption band of OH-Span which appears to be complete within ca. 45 μs , and which may be attributed to its reaction with 2-hydroxy-2-propyl radicals (Figure 5.8) as reported for other dyes.⁵⁴ Within ca. 3.5 μs a species has formed with a positive ΔA between ca. 420 and 540 nm ($\lambda_{\text{max}} = 490 \text{ nm}$), which itself has decayed after ca. 85 μs . The formation of a species with a long wavelength absorption band is consistent with the formation of a dye radical anion, which has been observed for Naphthol Blue Black²⁸ and Orange II⁵⁵ which showed bands forming at longer

wavelength than the dye bleach after ca. 3 and 10 μs , respectively. The TRVIS spectra at long times was found to be similar to that obtained from the steady-state studies of OH-Span:photoinitiator under nitrogen (Figure 5.21).

A general mechanism for dye reduction by photoinitiator radicals has been proposed in the literature⁵⁵ and it has been used to provide a model for the reaction of OH-Span. Equations A.1 to A.8 describe the reduction of the dye, disproportionation, several radical side reactions and the formation of several non-radical products (NRP) which are thought not to undergo any further reactions, at least of the timescale of these studies, and where $\text{ArCO}\cdot$, $\cdot\text{C}(\text{CH}_3)_2\text{OH}$, $\text{Dye}\cdot^-$ and Dye^{2-} are the benzoyl and 2-hydroxy-2-propyl radicals, dye radical anion and hydrazine respectively. A full kinetic analysis on Orange II has been reported⁵⁵ that can be used to model initially the rate constants for OH-Span to analyses the TRVIS data. Despite the product analysis reported here showing that a wide array of products form, this model provides a method of understanding the initial stages of the mechanism of dye reduction. The software used for the modelling was written in-house and has been used as reported,⁵⁵ and the corresponding rate laws are given in Appendix 3 for equations A.1 to A.8.



In this model, equation A.1, the decay of the triplet photoinitiator is considered to be instantaneous ($\tau = 0.11 \mu\text{s}$) on the timescale of observation of the dye signals (ca. $\geq 1 \mu\text{s}$) and hence the model considers the other reactions after $\text{ArCO}\cdot$ and $\cdot\text{C}(\text{CH}_3)_2\text{OH}$ have formed. Equation 5.8⁵⁰ has been reported to estimate the initial concentration of $\text{ArCO}\cdot$ and $\cdot\text{C}(\text{CH}_3)_2\text{OH}$, where E is the laser pulse energy at the sample (3 mJ), λ is the laser excitation wavelength (308 nm), Φ is the photoinitiator quantum yield (reported to be 0.29)⁴¹, ε is the molar absorption coefficient at 308 nm ($2800 \text{ dm}^3 \text{ mol}^{-1} \text{ cm}^{-1}$), c is the photoinitiator concentration ($1 \times 10^{-3} \text{ mol dm}^{-3}$), l is cell pathlength (1 mm) and a is the laser beam area (0.4 cm^2).

$$[\text{ArCO}\cdot]_0 = [\cdot\text{C}(\text{CH}_3)_2\text{OH}]_0 = \frac{E\lambda\Phi(1-10^{-\varepsilon cl})}{la} \times 8.35 \times 10^{-9} \text{ mol dm}^{-3} \quad (\text{5.8})$$

Equation 5.8 calculates the initial concentration of $\cdot\text{C}(\text{CH}_3)_2\text{OH}$ as an upper limit because it assumes that the dye does not absorb any of the laser light at 308 nm, and this value and the modelled rate constants for each reaction step A2 – A8 are given in Table 5.9. The rate constants k_4 ,⁶³ k_5 ,⁵⁵ k_6 ,⁵⁵ k_7 ⁵⁵ and k_8 ⁵⁷ were obtained from the literature, and are the same as those reported to model the reduction of Orange II and

were fixed in the modelling used for OH-Span. k_2 and k_3 values of 2.23×10^9 and $2.61 \times 10^9 \text{ dm}^3 \text{ mol}^{-1} \text{ s}^{-1}$, respectively, from the literature on the reduction of Orange II were used as initial estimates and thereafter changed by inspection to fit the experimental data at 360 and 490 nm, allowing rate constants for the formation and decay of $\text{Dye}\cdot^-$ to be obtained. Figure 5.43 shows the result of this modelling where a value of $k_2 = 6.00 \times 10^9 \text{ dm}^3 \text{ mol}^{-1} \text{ s}^{-1}$ was obtained for $\cdot\text{C}(\text{CH}_3)_2\text{OH}$ reducing the dye to give $\text{Dye}\cdot^-$, and a value of $k_3 = 5.00 \times 10^8 \text{ dm}^3 \text{ mol}^{-1} \text{ s}^{-1}$ was obtained for $\text{Dye}\cdot^-$ disproportionating to reform OH-Span and a hydrazine intermediate, where $\epsilon_{360}(\text{Dye}\cdot^-)$ and $\epsilon_{490}(\text{Dye}\cdot^-)$ were also estimated from the modelling. Compared to the starting values of k_2 and k_3 this indicates that $\text{Dye}\cdot^-$ for OH-Span has higher rate constants for formation and decay than Orange II, and that k_2 is close to a diffusion-controlled rate constant. It is also interesting that the rate constant for reaction of 2-hydroxy-2-propyl radicals with azobenzene in 2-propanol is much lower at $3 \times 10^7 \text{ dm}^3 \text{ mol}^{-1} \text{ s}^{-1}$.⁶⁴ In other studies, k_2 was found to be $2.00 \times 10^9 \text{ dm}^3 \text{ mol}^{-1} \text{ s}^{-1}$ for aqueous 2-(aryloxy)-1-naphthols and $1.5 \times 10^9 \text{ dm}^3 \text{ mol}^{-1} \text{ s}^{-1}$ for aqueous Orange I at 20 °C;⁶⁵ in another study of a series of aqueous 2-(aryloxy)-1-naphthol k_2 and k_3 was found to be ca. $2 - 4 \times 10^9 \text{ dm}^3 \text{ mol}^{-1} \text{ s}^{-1}$ and ca. $2 - 5 \times 10^7 \text{ dm}^3 \text{ mol}^{-1} \text{ s}^{-1}$, respectively at 20 °C;⁵⁰ in general, rate constants for the other steps have not been reported other than for Orange II.⁵⁵

Table 5.9 Calculated concentration of initial $\cdot\text{C}(\text{CH}_3)_2\text{OH}$ (mol dm^{-3}) and estimated molar absorption coefficient ($\epsilon / \text{dm}^3 \text{ mol}^{-1} \text{ cm}^{-1}$) the modelled values of rate constants ($k / \text{dm}^3 \text{ mol}^{-1} \text{ s}^{-1}$) at 21 °C, from equations A1-A8.

$[\cdot\text{C}(\text{CH}_3)_2\text{OH}]_0$	2.70×10^{-5}
k_2	6.00×10^9
k_3	5.00×10^8
k_4	6.50×10^8
k_5	2.33×10^8
k_6	3.18×10^8
k_7	1.74×10^8
k_8	5.00×10^8
$\epsilon_{360}(\text{Dye}\cdot^-)$	14000
$\epsilon_{490}(\text{Dye}\cdot^-)$	7000

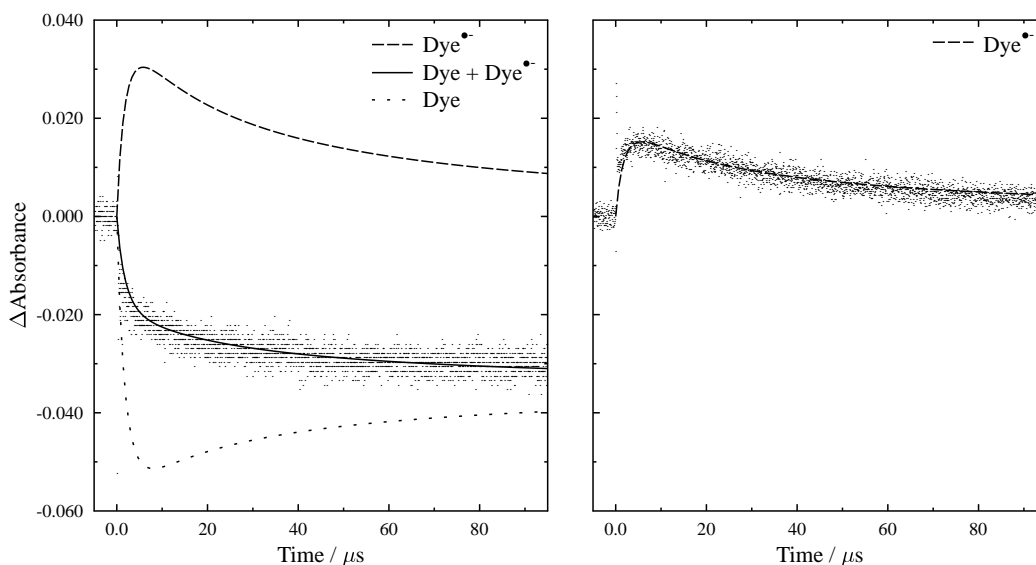


Figure 5.43 TRVIS kinetics of 1:10 OH-Span:photoinitiator ($1 \times 10^{-4} \text{ mol dm}^{-3}$ dye concentration) in pH 5.2 sodium acetate buffer solution at 360 nm (left) and 490 nm (right) together with modelled overall contribution (solid line) alongside $\text{Dye}^{\bullet-}$ (dashed line) and Dye (dotted line) contributions.

Figure 5.44 attempts to model the spectrum of the OH-Span dye radical anion, using the kinetic model to give an estimate of species concentrations as a function of time. The assumption here is that only the Dye and $\text{Dye}^{\bullet-}$ absorb in the visible region, hence the TRVIS spectrum is a composite of these two species. The concentration of OH-Span from the modelling was $2.01 \times 10^{-5} \text{ mol dm}^{-3}$ at $45 \mu\text{s}$, from which the spectrum of OH-Span ($\epsilon \approx 21500 \text{ dm}^3 \text{ mol}^{-1} \text{ cm}^{-1}$) was scaled and is shown as a dashed line in Figure 5.44. The estimated $\text{Dye}^{\bullet-}$ spectrum was then created by adding the scaled OH-Span spectrum to the observed TRVIS spectrum at $45 \mu\text{s}$, and is shown as a solid line (Figure 5.44).

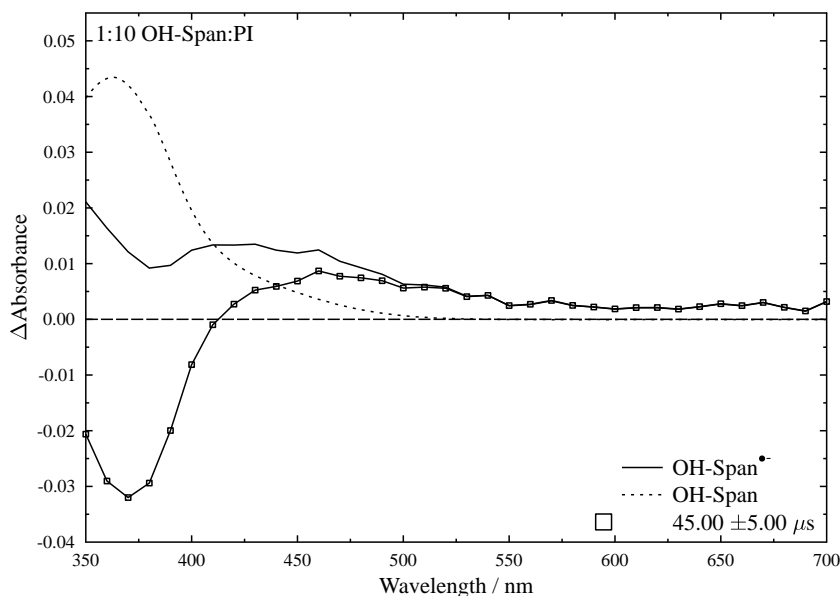


Figure 5.44 OH-Span radical anion spectrum (solid line), produced by addition of OH-Span bleach (dashed line) at a concentration of ca. $2.01 \times 10^{-5} \text{ mol dm}^{-3}$ to the TRVIS spectra at $45 \mu\text{s}$.

In summary, initial kinetic modelling has shown a good fit to the experimental data, in which the k_2 and k_3 rate constants obtained are comparable to those reported for other dyes. The modelling therefore is consistent with OH-Span undergoing reduction by disproportionation as proposed in Figure 5.45. In order to do a more rigorous and full kinetic analysis, different experimental conditions could be used by changing pump energy and concentration in order to fully quantify the rate constants accurately.^{50,55} The detailed product analysis (section 5.2.2.1) shows that there is a complex array of compounds formed, however the good fit to the kinetic model indicates that these products are not observed by TRVIS and may form on a longer timescale than this experiment ($> 85 \mu\text{s}$). The results also show that the photoinitiator photolysis results in the formation of the $\text{Dye}^{\bullet-}$ efficiently and therefore is effective at producing radicals that can be used to study reactions with the R-Span dyes. Figure 5.45 also shows two possible routes by which the hydrazine may decay, directly or indirectly, to the NAPDAD and APOL products.

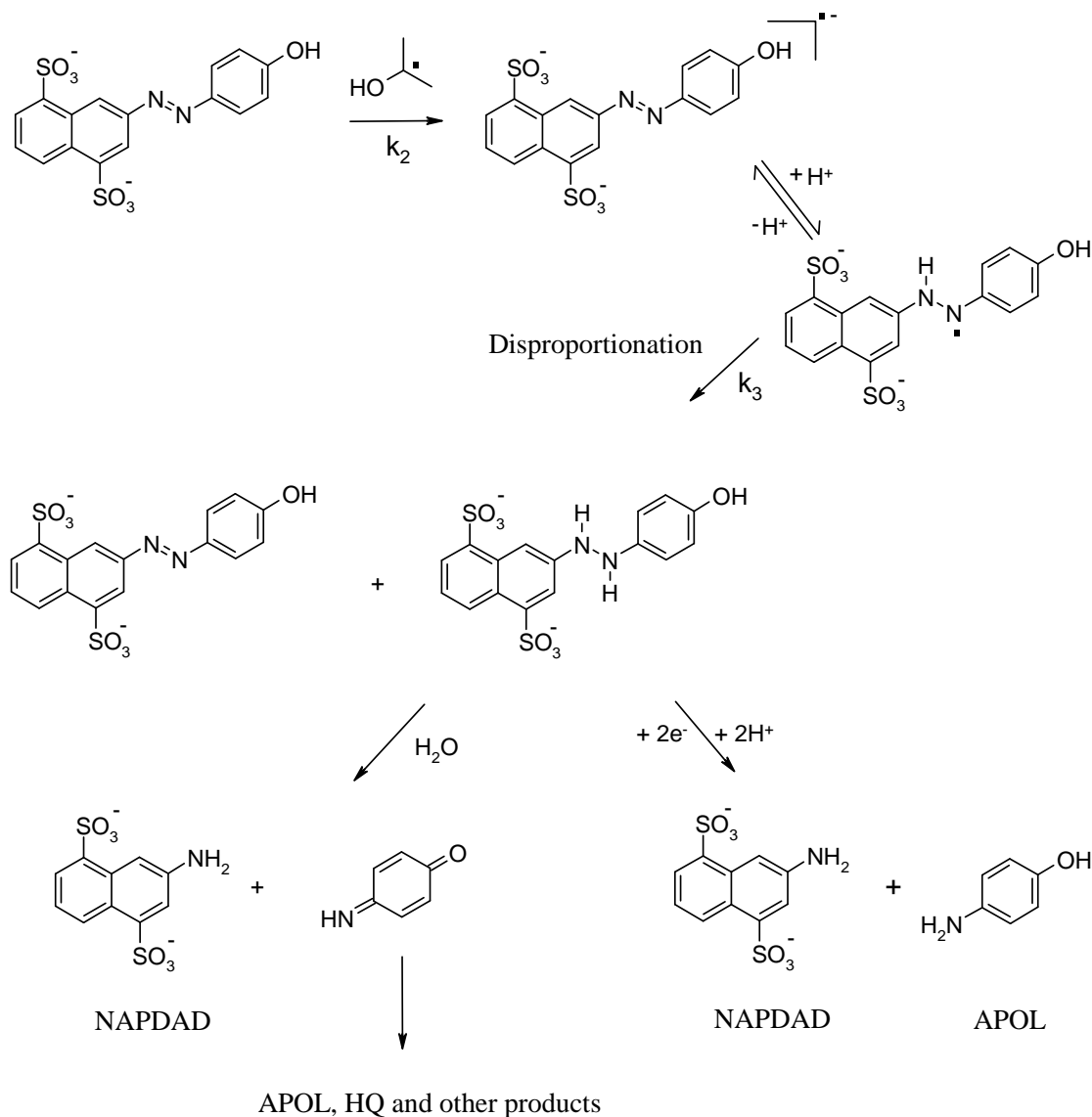


Figure 5.45 Proposed reduction of OH-Span in the presence of 2-hydroxy-2-propyl radicals.

5.2.2 Other R-Span dyes

Section 5.2.2.1 reports the simple steady-state studies on NH_2^- , O^- , and CN-Span alone and time-resolved studies on NH_2^- , and CN-Span alone before considering the more complicated steady-state studies on OMe- and NHAc-Span alone and time-resolved studies on OMe- and NHAc-Span alone. Section 5.2.2.2 briefly reports on the steady-state studies on O^- -Span, NH_2^- -Span and NHAc-Span with photoinitiator; such studies were not carried out on OMe-Span or the impure dyes.

5.2.2.1 Dyes alone

Steady-state studies on NH₂⁻, CN⁻, and O⁻-Span.

The irradiation using a flash gun of NH₂⁻, O⁻, and CN-Span alone showed no significant change in the steady-state UV/Visible absorption spectra (Figure 5.46 and 5.47) after 30 light pulses, indicating that the dyes do not fade readily upon direct photolysis in solution.

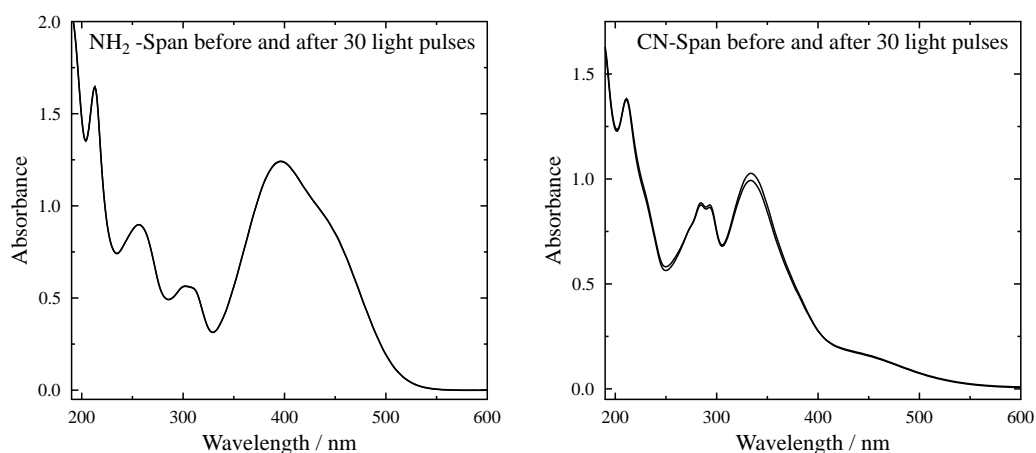


Figure 5.46 UV/Visible absorption spectra of NH₂-Span (left) and CN-Span (Right) alone in water at $5 \times 10^{-5} \text{ mol dm}^{-3}$ before and after 30 light pulses.

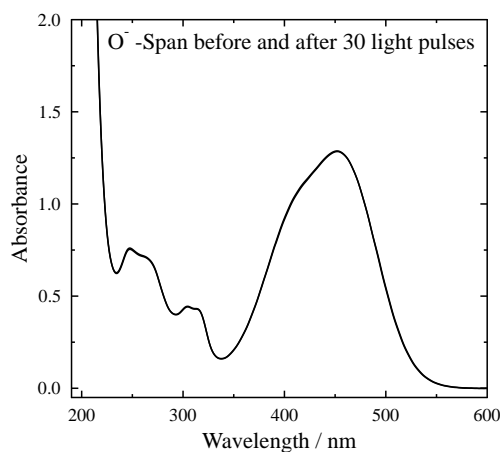


Figure 5.47 UV/Visible absorption spectra of O⁻-Span alone in pH 11 phosphate buffer solution at $5 \times 10^{-5} \text{ mol dm}^{-3}$ before and after 30 light pulses.

Time-resolved studies on NH₂- and CN-Span

The TRVIS spectra of NH₂-Span (4×10^{-4} mol dm⁻³) in water at 21 °C obtained 1.0, 2.5, 4.5, 14.5 and 30.0 ms after 308 nm excitation in a 1 cm pathlength cell are shown in Figure 5.48. Upon irradiation a band at ca. 400 nm attributed to the *trans*-NH₂-Span reactant bleaches and then recovers, consistent with *trans-cis* photoisomerisation and recovery. Figure 5.49 shows a kinetic trace at 400 nm analysed by fitting to a single exponential decay to determine the first order rate constant (k_{obs}). The analysis gave a rate constant of ca. 1.4×10^2 s⁻¹ across the range of 370 – 440 nm, corresponding to the thermal back reaction of *cis* to *trans* NH₂-Span, and giving a lifetime of ca. 7 ms for the *cis* isomer.

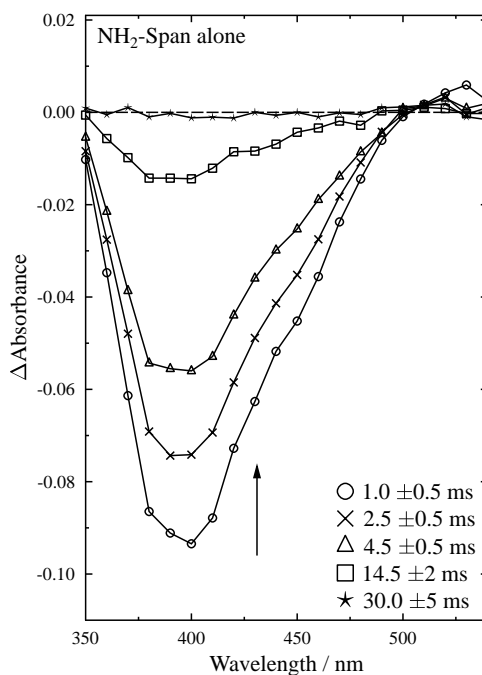


Figure 5.48 TRVIS spectra of NH₂-Span alone (4×10^{-4} mol dm⁻³) in water, 1.0, 2.5, 4.5, 14.5 and 30.0 ms after excitation.

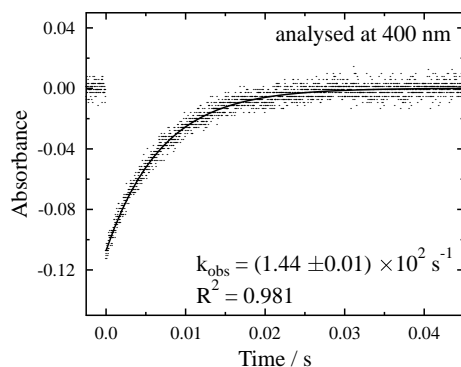


Figure 5.49 TRVIS Kinetic traces of $\text{NH}_2\text{-Span}$ alone ($4 \times 10^{-4} \text{ mol dm}^{-3}$) in water at 400 nm.

The TRVIS spectra of CN-Span ($4 \times 10^{-4} \text{ mol dm}^{-3}$) in water at 21 °C obtained 0.1, 0.5, 1.0, 2.0 and 4.0 ms after 308 nm excitation in a 1 cm pathlength cell, as given in Figure 5.50, showed no appreciable effect. The kinetic trace at 400 nm as shown in Figure 5.51 may be an impurity in the sample because the data did not fit to a single exponential decay.

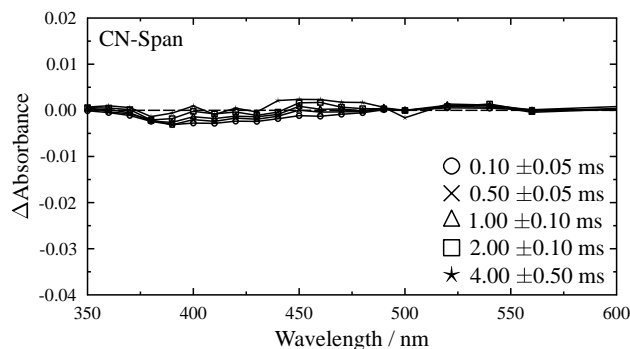


Figure 5.50 TRVIS spectra of CN-Span alone ($4 \times 10^{-4} \text{ mol dm}^{-3}$) in water, 0.1, 0.5, 1.0, 2.0 and 4.0 ms after excitation.

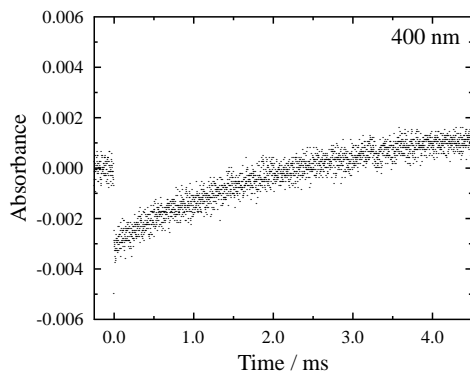


Figure 5.51 TRVIS Kinetic traces of CN-Span alone ($4 \times 10^{-4} \text{ mol dm}^{-3}$) in water at 400 nm.

Studies on OMe- and NHAc-Span

The irradiation of OMe- and NHAc-Span alone showed significant changes in the steady-state UV/Visible absorption spectra after just one light pulse, and little further difference after 30 light pulses, as shown in Figure 5.52. It is proposed that this is due to *trans-cis* photoisomerisation which does not recover rapidly.

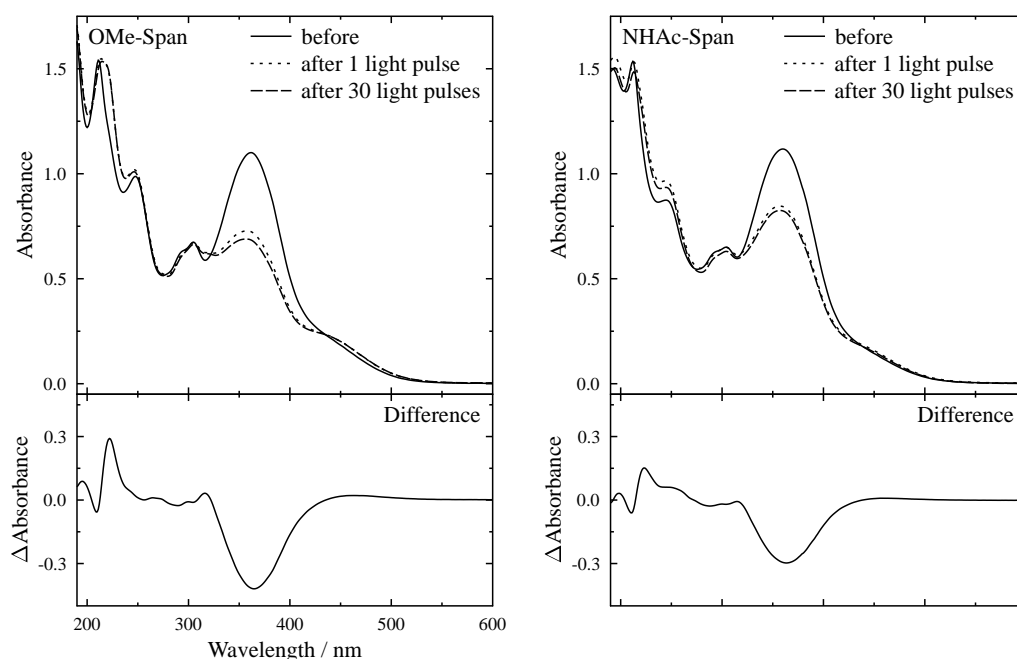


Figure 5.52 UV/Visible absorption spectra of OMe-Span (left) and NHAc-Span (Right) alone in water at 1×10^{-4} mol dm⁻³ before and after 1 and 30 light pulses, with the overall difference spectrum (final – initial) shown.

Further evidence for this proposal came from analysing the HPLC and LC-MS data from a sample of OMe-Span that had been exposed to roomlight, in which two peaks were observed in the HPLC chromatogram at 12.41 and 19.29 min (Figure 5.53). The components giving rise to these peaks showed the same negative ion ESI mass spectra (Figure 5.54) with a base peak ion at 420.9 m/z corresponding to [OMe-Span + H⁺]. The peak at 19.29 min is clearly consistent with the *trans* form with a band at 364 nm in the UV/Visible absorption spectrum, whereas the corresponding spectrum at 12.41 min shows a longer wavelength band at 443 nm, consistent with an n to π^* transition from the *cis* form of OMe-Span.

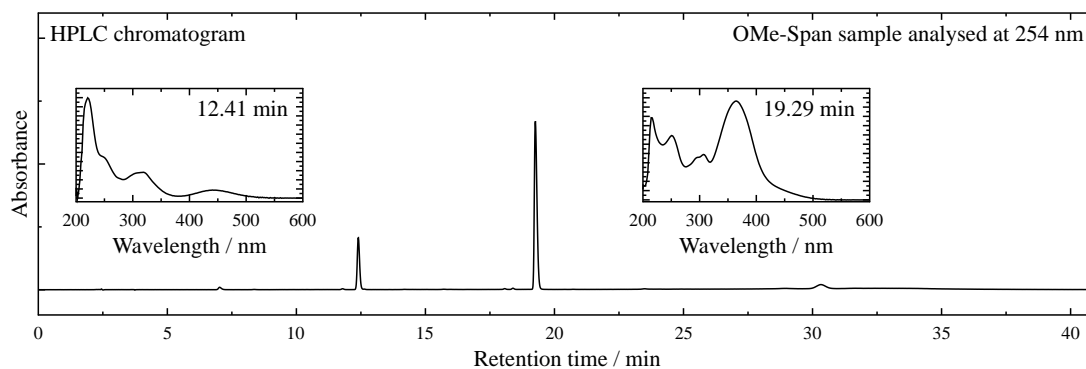


Figure 5.53 HPLC chromatogram of a OMe-Span sample (40% dye, 60 % NaCl).

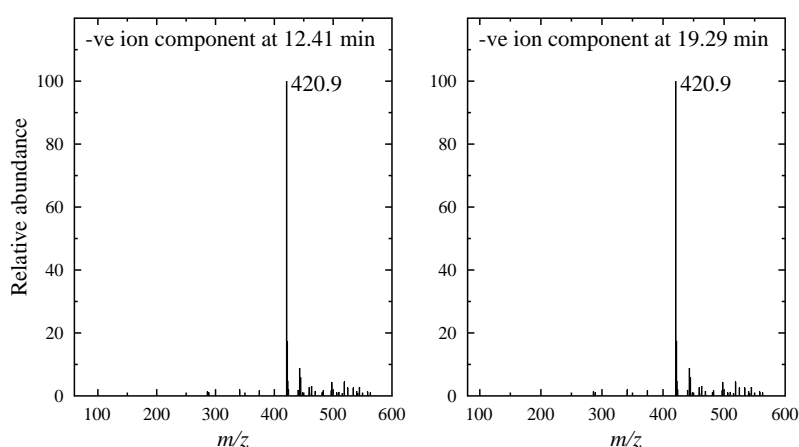


Figure 5.54 Left: Negative ion ESI mass spectrum of *cis*-OMe-Span with a retention time of 12.41 min. Right: Negative ion ESI mass spectrum of *trans*-OMe-Span with a retention time of 19.29 min.

NMR spectroscopy probably provides the most convincing evidence that relatively stable *cis* isomers of OMe- and NHAc-Span formed. Figure 5.55 shows the numbering system and DFT optimised structures of *cis*-OMe- and *cis*-NHAc-Span used to give calculated NMR positions for comparison with experimental data. Figure 5.56 shows the ^1H NMR spectrum recorded within a few minutes after 30 flash gun pulses of OMe- and NHAc-Span in D_2O under nitrogen with assignments given in Table 5.10 The assignments given for the *trans* form are consistent with those made in Chapter 3 while those made for the *cis* form are consistent with *cis*-NHMe-Span reported in the literature (section 5.1.1.2).¹⁷ As is noted in the literature, the greatest shifts between the two forms are for protons 1, 3, 12/16, and 13/15, with protons 5, 6 and 7 remaining relatively unchanged,¹⁷ although the resonances from protons 13/15 shows relatively

little change for OMe-Span. In general the changes predicted computationally are similar but of greater magnitude.

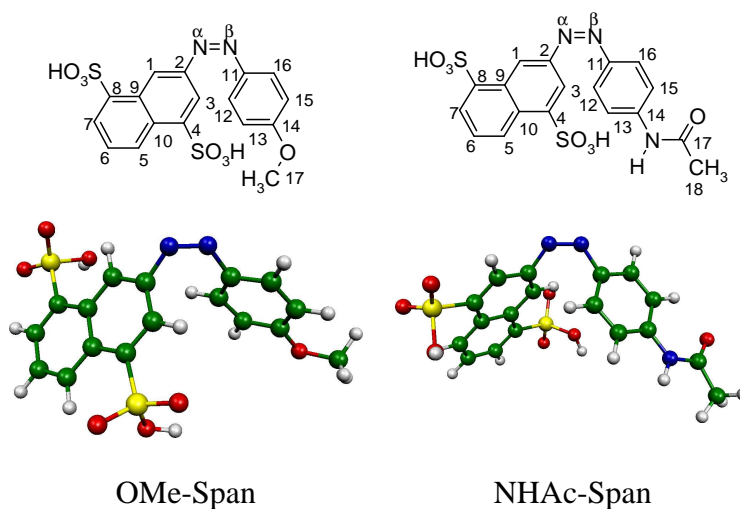


Figure 5.55 Optimised structures of *cis*-OMe-Span (left) and *cis*-NHAc-Span (right) along with the numbering system. (Original in colour)

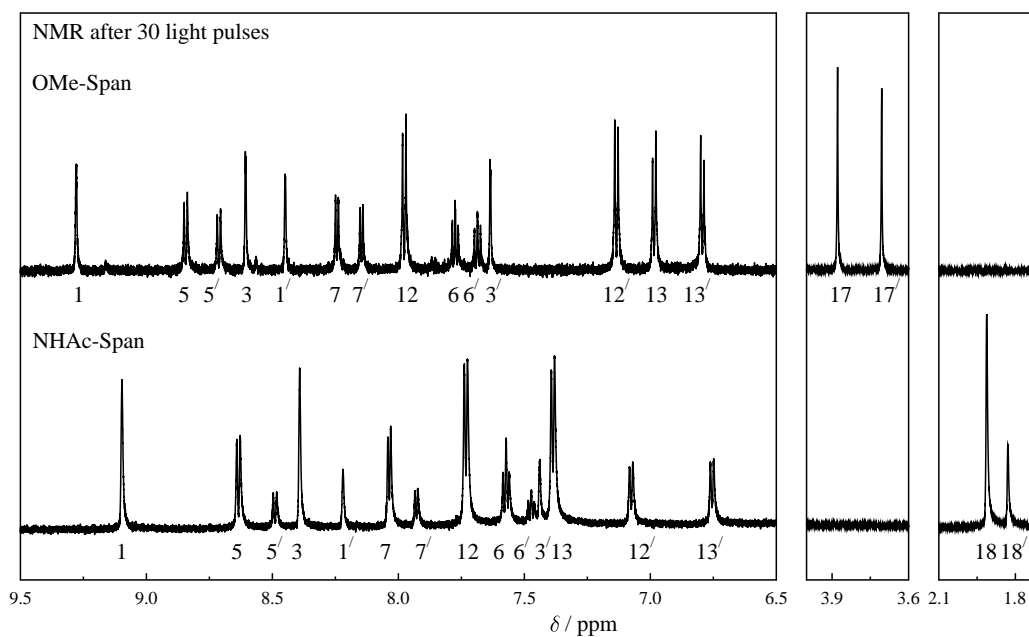


Figure 5.56 Aromatic and non-aromatic region ¹H NMR spectrum of OMe-Span (top) and NHAc-Span (bottom) both at 1×10^{-4} mol dm⁻³ after 30 light pulses.

Table 5.10 ^1H NMR chemical shifts (ppm) of OMe-Span and NHAc-Span after 30 light pulses in D_2O , together with their calculated *cis* positions and differences between the *cis* and *trans* forms.

Atom	Experimental							Calculated			
	<i>trans</i> $^1\text{H}^a$			<i>cis</i> $^1\text{H}^a$			$\Delta(\text{trans} - \text{cis})$	<i>cis</i> ^1H	$\Delta(\text{trans} - \text{cis})$		
OMe-Span											
1	9.28	1.00	d	1.0	8.61	0.95	d	1.0	0.67	8.86	0.43
3	8.45	1.00	d	1.0	7.63	0.95	d	1.0	0.82	6.87	1.73
5	8.85	1.00	d	8.0	8.72	0.95	d	9.0	0.13	8.64	0.13
6	7.78	1.00	t	7.0	7.52	0.95	t	7.0	0.26	7.53	0.04
7	8.25	1.00	d	8.0	8.15	0.95	d	8.0	0.10	8.01	0.00
12/16	7.98	2.00	d	8.0	7.13	1.96	d	8.0	0.85	6.02 ¹² , 7.91 ¹⁶	1.06
13/15	6.98	2.00	d	8.0	6.79	1.96	d	8.0	0.19	6.18 ¹³ , 6.70 ¹⁵	0.31
17	3.88	3.00	s	-	3.71	2.94	s	-	0.17	3.73	-0.06
NHAc-Span											
1	9.09	1.00	s	-	8.21	0.47	s	-	0.88	7.29	2.03
3	8.39	1.00	s	-	7.44	0.47	s	-	0.95	8.25	0.34
5	8.63	1.00	d	8.0	8.49	0.47	d	8.0	0.14	8.70	0.05
6	7.56	1.00	t	8.0	7.47	0.47	t	8.0	0.09	7.47	0.11
7	8.04	1.00	d	8.0	7.93	0.47	d	8.0	0.11	7.86	0.15
12/16	7.73	2.00	d	8.5	7.08	0.94	d	8.5	0.65	8.00 ¹² , 8.03 ¹⁶	-0.05
13/15	7.38	2.00	d	8.5	6.75	0.94	d	8.5	0.63	6.95 ¹³ , 6.55 ¹⁵	0.87
18	1.91	3.00	s	-	1.83	1.84	s	-	0.05	1.81	-0.13

^a Integration, multiplicity (s = singlet; d = doublet; t = triplet), splitting (Hz)

Quantitatively, NMR spectroscopy allows for the percentage of the two forms to be determined using peak integrations. After irradiation, the OMe-Span sample consisted of 51 % *trans* and 49 % *cis* form, whereas NHAc-Span sample consisted of 68 % *trans* and 32 % *cis* form. Using this information, a *cis* UV/Visible absorption spectrum for each dye can be calculated using the UV/Visible absorption spectrum recorded after irradiation, and subtracting the *trans* spectrum corresponding to the percentage determined from the NMR data as shown in Figure 5.57. The calculated *cis* spectra show the expected longer wavelength band at 443 and 438 nm for *cis*-OMe-Span and *cis*-NHAc-Span, respectively, and the spectrum of *cis*-OMe-Span matches that recorded for the OMe-Span sample exposed to light observed on HPLC analysis (Figure 5.57).

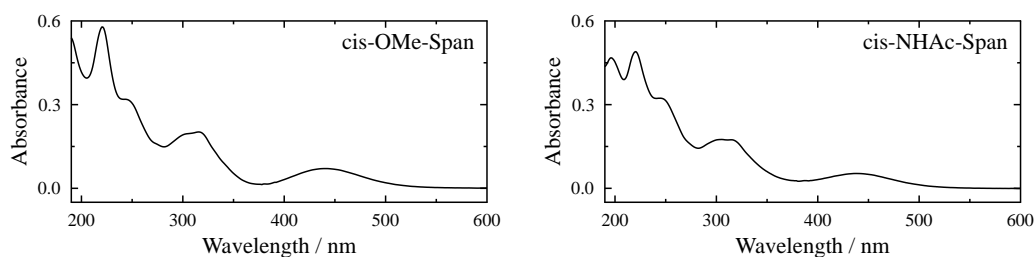


Figure 5.57 Calculated UV/Visible absorption spectrum of *cis*-OMe-Span (left) and *cis*-NHAc-Span (right).

The rate constant of the *trans-cis* thermal back reaction was measured by recording the UV/Visible absorption spectrum of irradiated samples of OMe-Span and NHAc-Span after 30 flash gun light pulses which were then left in the dark with spectra recorded as a function of time shown in Figures 5.58 and 5.59. Also shown in Figures 5.58 and 5.59 are fits to single exponential decays giving rate constants for the *cis-trans* thermal back reactions. The spectra of OMe-Span were recorded over 28 days at 21 °C and the observed rate constant for the *cis-trans* thermal back reaction was $4.20 \times 10^{-6} \text{ s}^{-1}$ giving a lifetime of $2.4 \times 10^5 \text{ s}$ or 2.8 days. The spectra of NHAc-Span were recorded over 32 hours at 21 °C and the observed rate constant for the *cis-trans* thermal back reaction was $3.70 \times 10^{-5} \text{ s}^{-1}$ giving a lifetime of $2.7 \times 10^4 \text{ s}$ or 7.5 hours. OMe-Span and NHAc-Span clearly display different properties than the other R-Span dyes, in that their thermal *cis-trans* isomerisation reactions occur on much longer timescales.

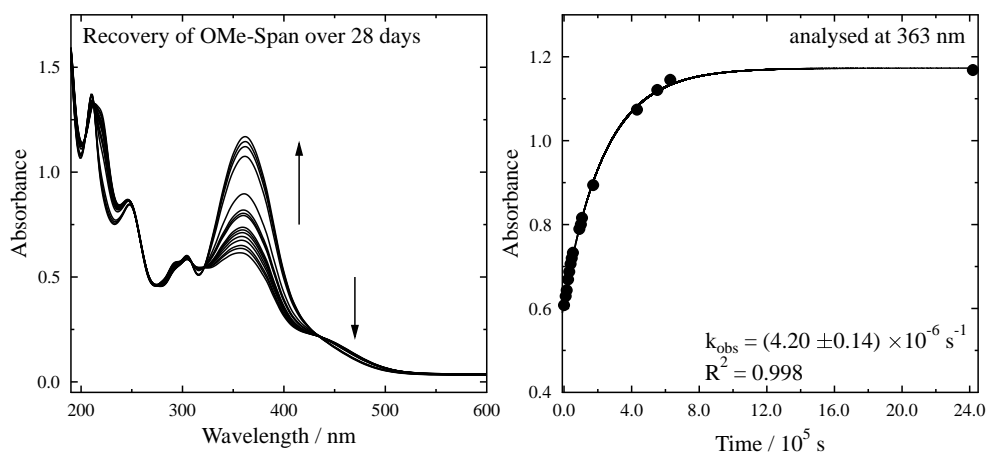


Figure 5.58 Left: UV/Visible absorption spectra of OMe-Span (1×10^{-4} mol dm $^{-3}$) in water recorded for 28 days after 30 light pulses at 21 °C, Right: Single exponential fit at 363 nm.

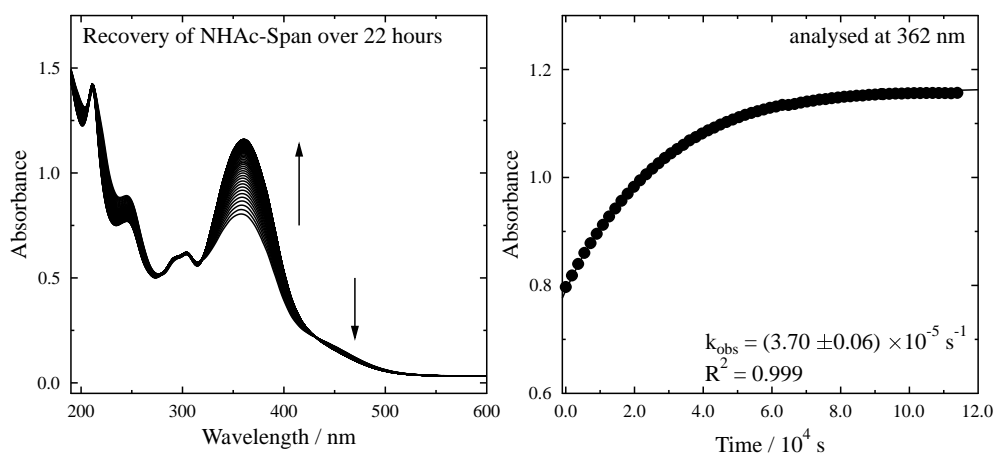


Figure 5.59 Left: UV/Visible absorption spectra of NHAc-Span (1×10^{-4} mol dm $^{-3}$) in water recorded for 32 hr after 30 light pulses at 21 °C Right: Single exponential fit at 363 nm.

TRVIS was used to explore whether there were any processes occurring on a short timescale, and the TRVIS spectra of OMe- and NHAc-Span alone (4×10^{-4} mol dm $^{-3}$) in water at 20, 40, 120, 250 and 600 ms after excitation are shown in Figure 5.60. The TRVIS spectra observed are opposite in phase to those observed from OH- and NH $_2$ -Span (Figures 5.34 and 5.48), with positive bands observed at ca. 360 nm for both OMe- and NHAc-Span. This observation can be attributed to changes that occur in the system due to *trans-cis* processes, but the situation is complicated by photoalteration by the probe beam from the arc lamp. Experimentally, the probe beam shutter was under

manual control; hence the sample was exposed to the probe light from the arc lamp, generating a photostationary state with significant *cis* isomer present before the laser pulse was fired. Thereafter it is proposed that upon 308 nm excitation *cis-trans* photoisomerisation occurred, with the TRVIS data showing an increase in *trans* isomer concentration and then decay to the starting photo equilibrium as the sample returns to the photostationary state due to the effect of the arc lamp. Therefore, due to the effect of the arc lamp, no comparative TRVIS studies could be carried out on OMe- and NHAc-Span with the present experimental conditions.

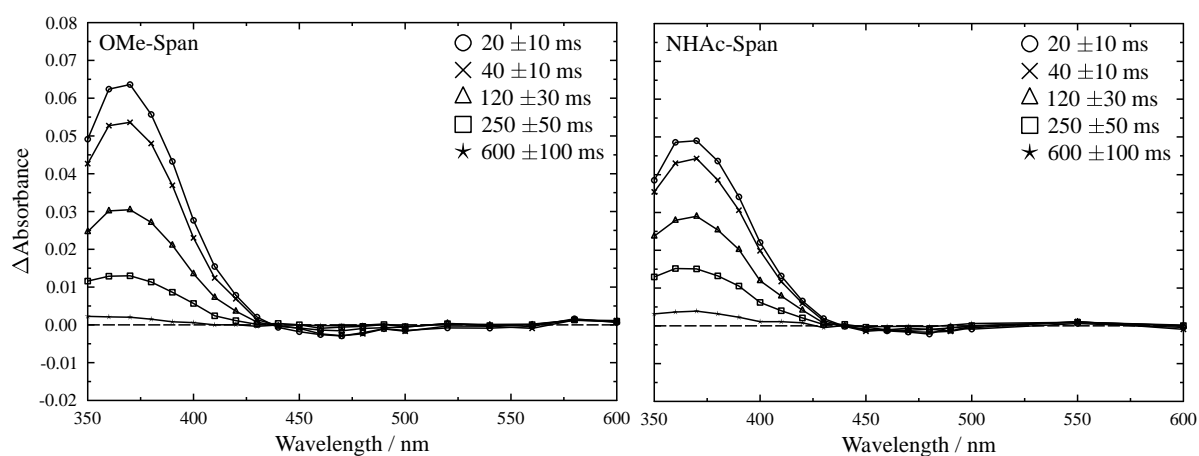


Figure 5.60 TRVIS spectra from OMe-Span (left) and NHAc-Span (right) alone (4×10^{-4} mol dm $^{-3}$) in water, 20, 40, 120, 250 and 600 ms after excitation.

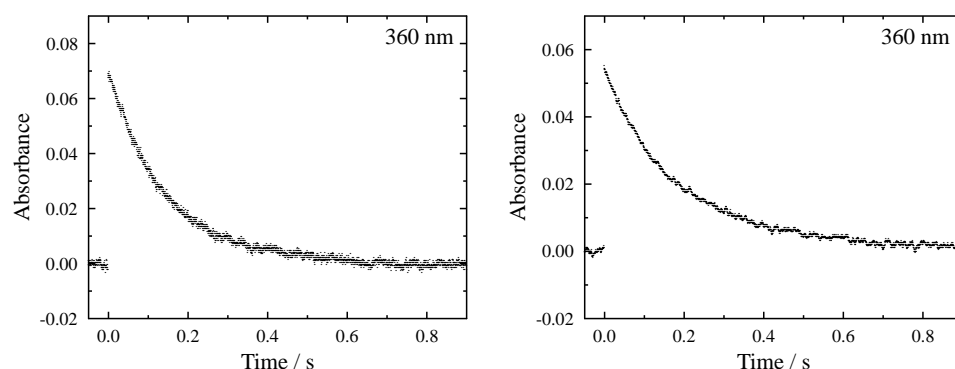


Figure 5.61 TRVIS Kinetic traces for OMe-Span alone (left) and NHAc-Span (right) alone (4×10^{-4} mol dm $^{-3}$) in water at 360 nm.

The long-lived nature of the *cis* form observed here for OMe- and NHAc-Span has been reported for other azo dyes.⁶⁶⁻⁷¹ The observed rate constant for the *cis-trans* thermal back reaction for azobenzene in benzene at 21 °C is 1.6×10^{-6} s $^{-1}$.⁶⁶ In one study a

comparison as to the thermostability of the *cis* forms of a set of substituted azobenzenes was made in which it was found that electron-withdrawing substituents stabilise the *cis* isomer, whereas an electron donating substituent *para* to the azo linkage destabilised the *cis* isomer.⁷¹ This is an useful piece of information because of those dyes for which isomerisation was observed (NH₂-, OH-, OMe- and NHAc-Span), OMe-Span and NHAc-Span can be considered to be those dyes containing the least donating R substituents, which would correlate with this proposal. The timescale of the *cis-trans* back reaction will depend on the energy barriers that exist between the isomers, which may arise along two different pathways, inversion and rotation, which are competitive depending on the electronic effects of the substituent and the polarity of the solvent.⁷⁰ In a comparison of macrocyclic and non-cyclic azobenzene, it was reported that the *cis-trans* thermal back reaction occurred on longer timescales due to higher energy barriers for the macrocyclic form.⁶⁹ This is indicative of steric effects influencing the stability of the isomers, which when considering OMe- and NHAc-Span offer larger R substituent groups than NH₂- and OH-Span. A study on a reactive dye shown in Figure 5.62 gave a thermal *cis-trans* isomerisation rate constant of $2.4 \times 10^{-6} \text{ s}^{-1}$ in DMSO at 25 °C resulting in a lifetime of ca. 4.8 days,⁷² which is longer than for OMe- and NHAc-Span; although not discussed in the literature, this could be postulated to be due to further electronic or steric influence of the large reactive group R.

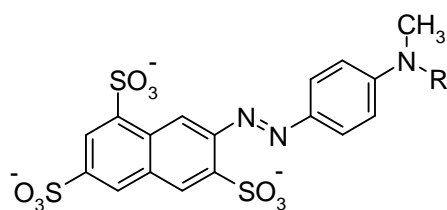


Figure 5.62 Structure of a reactive dye where R is a reactive group.

5.2.2.2 Dyes with photoinitiator

R-Span:photoinitiator studies were followed by UV/Visible absorption spectroscopy and some preliminary product analysis was carried out by HPLC.

UV/Visible absorption spectroscopy

Steady-state studies of photochemical reactions using a flash gun on samples of 1:1 and 1:10 O⁻-Span:photoinitiator in pH 11 phosphate buffer, 1:1 and 1:10 NH₂-Span:photoinitiator in water and 1:1 and 1:10 NHAc-Span:photoinitiator in water, all in a 1 cm pathlength cell under nitrogen and under air were studied by UV/Visible absorption spectroscopy as shown in Figures 5.63 – 5.68. Figures 5.69 – 5.71 show the normalised absorbance of the main dye band as a function of light pulse. It has already been established that there is a direct photolysis effect on the structure of NHAc-Span, and hence the more complicated nature of the decay of the main absorption band may arise in part from the *cis* isomer forming. It can be seen that one flash pulse generally has a greater effect on the spectra of NHAc-Span than the other R-Span dyes (Figure 5.67). In all cases, however, the bleaches of the main absorption bands in each of these dyes are broadly comparable to that of OH-Span under comparable conditions (Figure 5.21) showing that photoinitiator-generated radicals result in fading of the dyes.

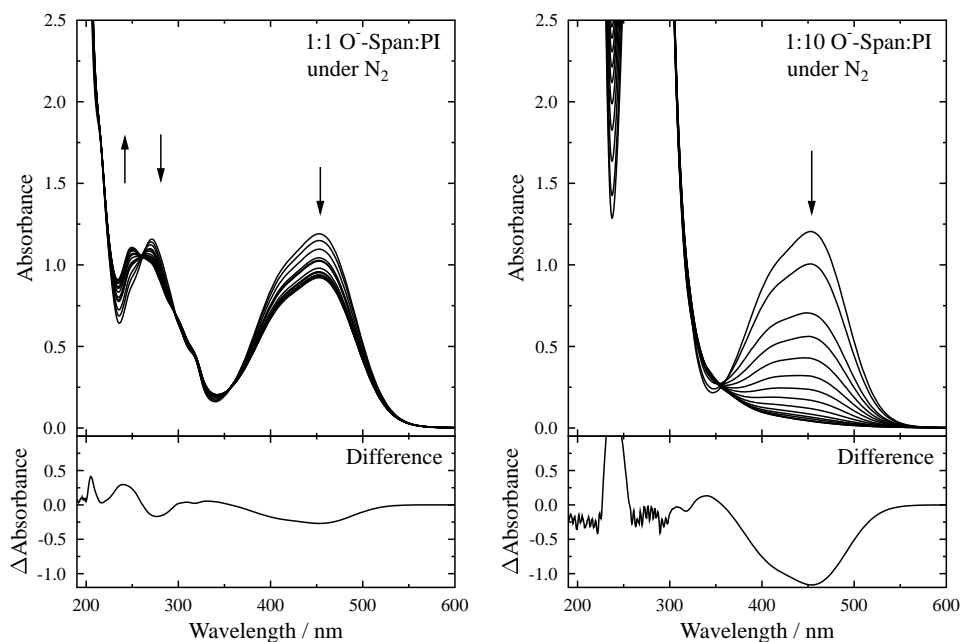


Figure 5.63 Irradiation of 1:1 (left) and 1:10 (right) O⁻-Span:photoinitiator in pH 11 phosphate buffer solution under nitrogen over 30 light pulses; arrows indicate changes with increasing light pulse, with the overall difference spectrum (final – initial) shown.

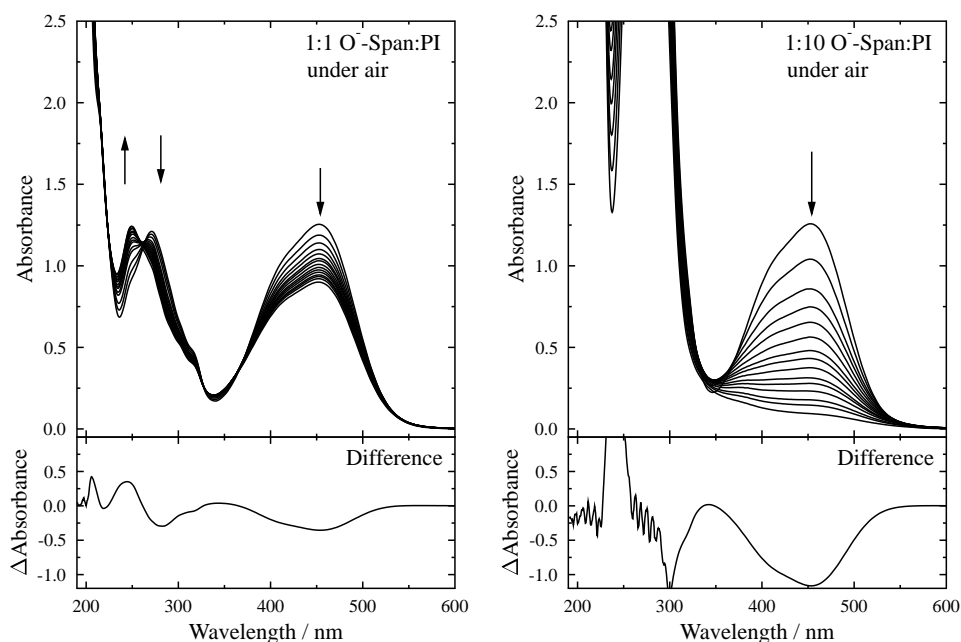


Figure 5.64 Irradiation of 1:1 (left) and 1:10 (right) O⁻-Span:photoinitiator in pH 11 phosphate buffer solution under air over 30 light pulses; arrows indicate changes with increasing light pulse, with the overall difference spectrum (final – initial) shown.

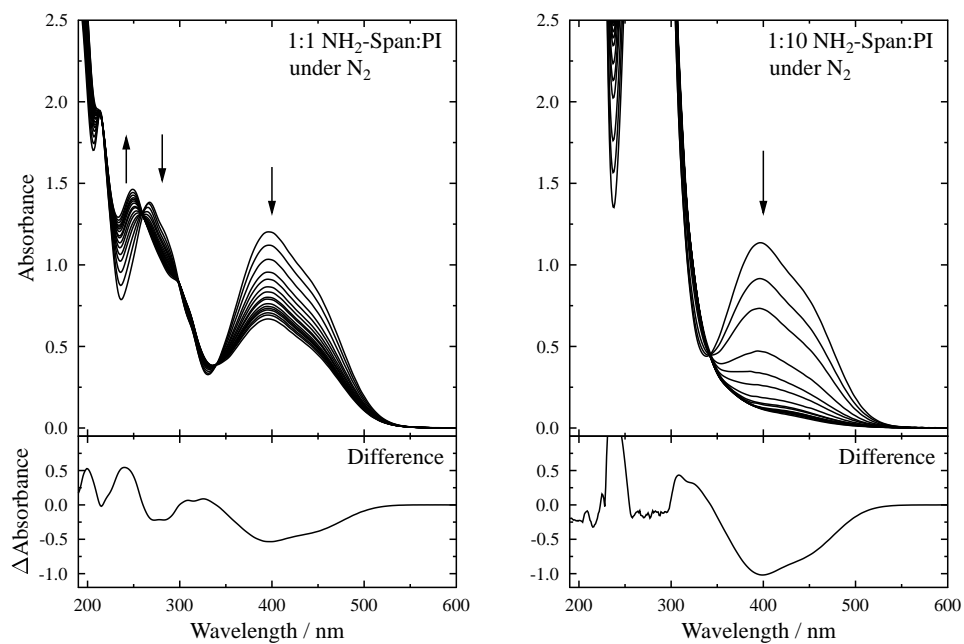


Figure 5.65 Irradiation of 1:1 (left) and 1:10 (right) NH_2 -Span:photoinitiator in water under nitrogen over 30 light pulses; arrows indicate changes with increasing light pulse, with the overall difference spectrum (final – initial) shown.

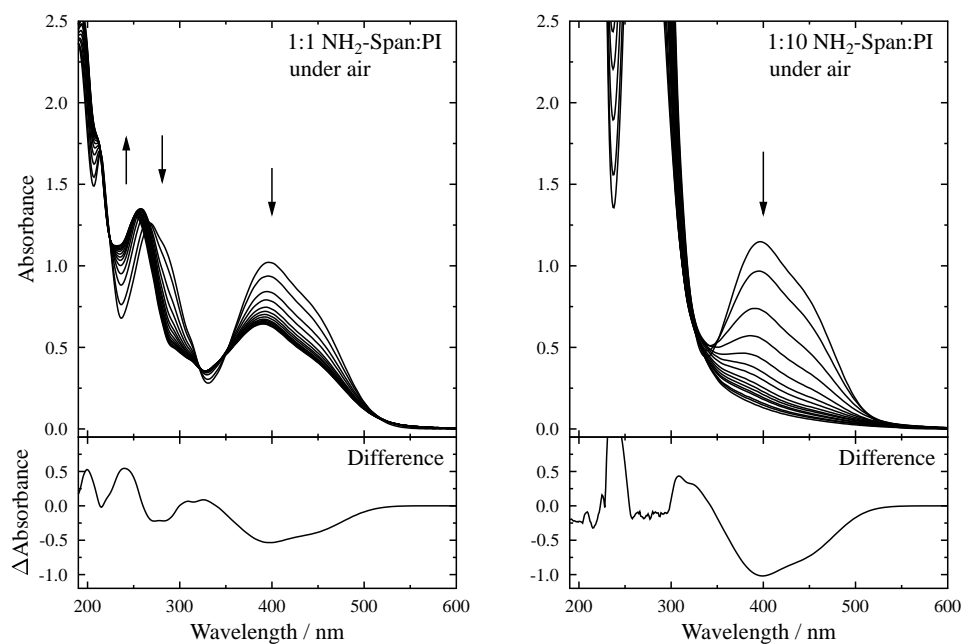


Figure 5.66 Irradiation of 1:1 (left) and 1:10 (right) NH_2 -Span:photoinitiator in water under air over 30 light pulses; arrows indicate changes with flash, with the overall difference spectrum (final – initial) shown.

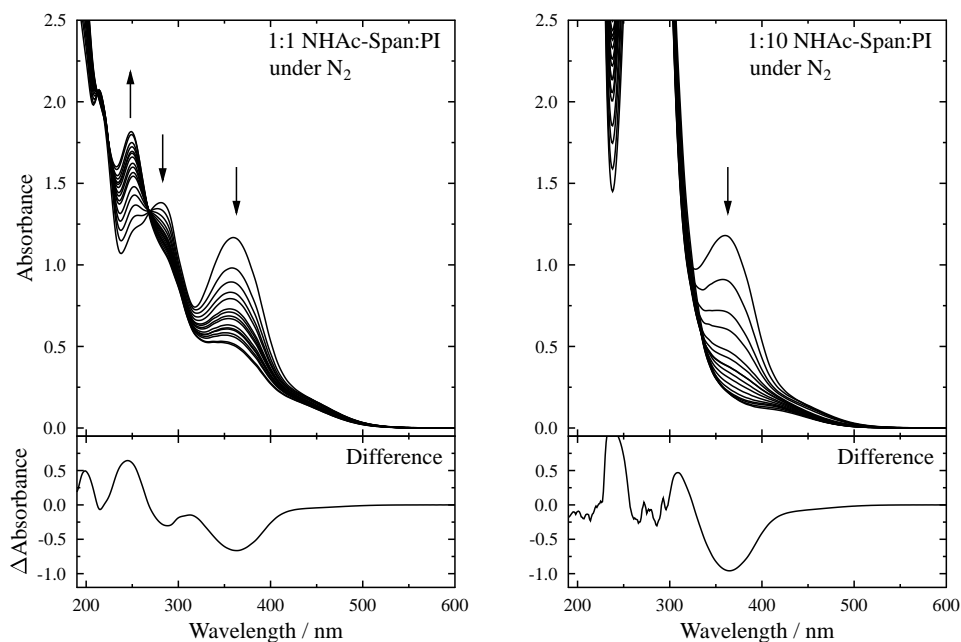


Figure 5.67 Irradiation of 1:1 (left) and 1:10 (right) NHAc-Span:photoinitiator in water under nitrogen over 30 light pulses; arrows indicate changes with increasing light pulse, with the overall difference spectrum (final – initial) shown.

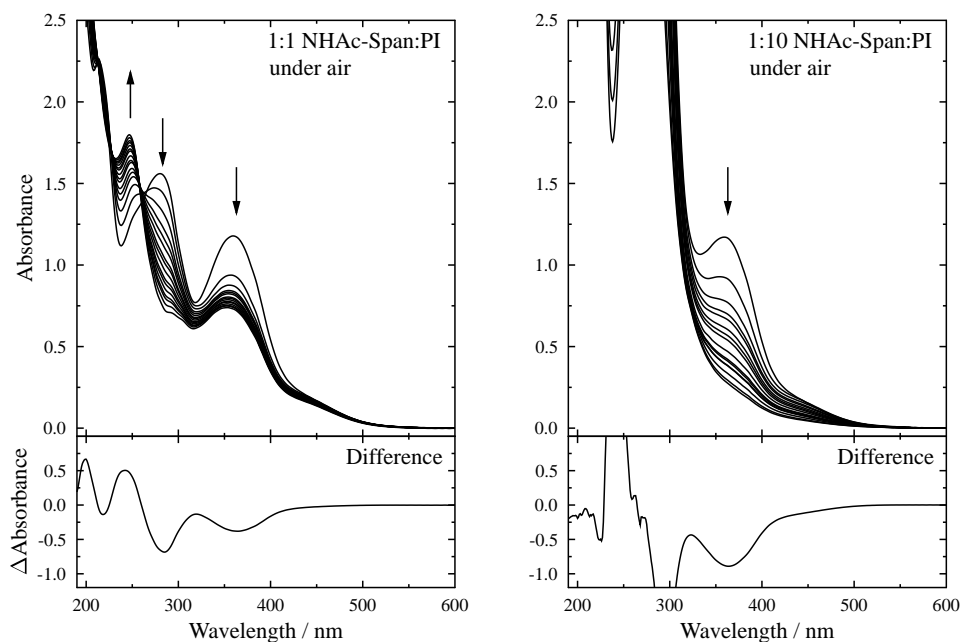


Figure 5.68 Irradiation of 1:1 (left) and 1:10 (right) NHAc-Span:photoinitiator under air over 30 light pulses; arrows indicate changes with increasing light pulse, with the overall difference spectrum (final – initial) shown.

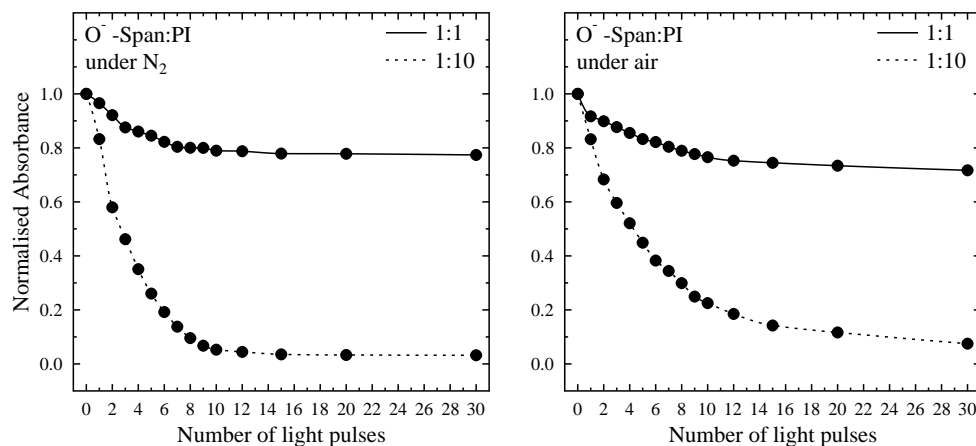


Figure 5.69 Normalised absorbance at 457 nm as a function of light pulse for 1:1 and 1:10 H-Span:photoinitiator in pH 11 phosphate buffer solution under nitrogen (left) and air (right).

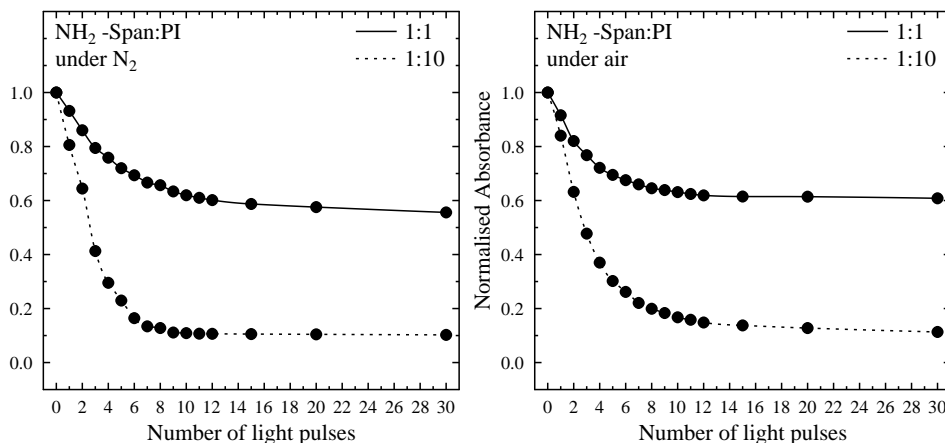


Figure 5.70 Normalised absorbance at 401 nm as a function of light pulse for 1:1 and 1:10 NH₂-Span:photoinitiator under nitrogen (left) and air (right).

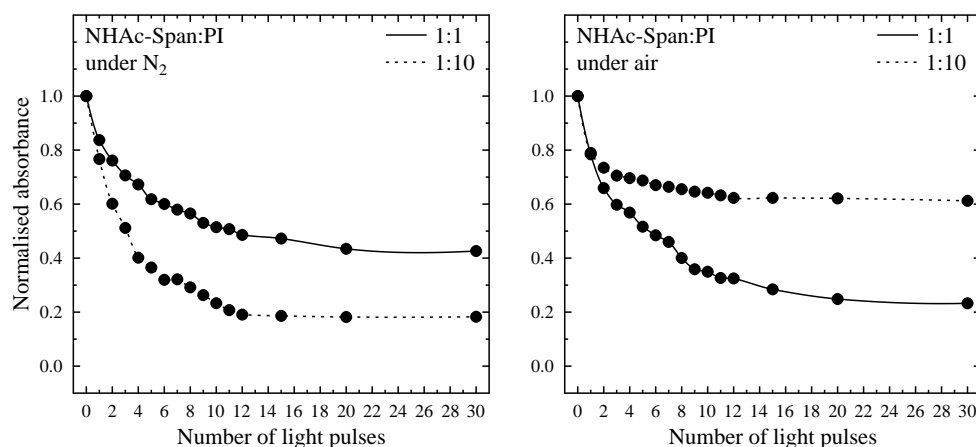


Figure 5.71 Normalised absorbance at 364 nm as a function of light pulse for 1:1 and 1:10 NHAc-Span:photoinitiator under nitrogen (left) and air (right).

Product analysis

Preliminary product analysis was carried out by HPLC on 1:1 and 1:10 O⁻-Span:photoinitiator, NH₂-Span:photoinitiator and NHAc-Span:photoinitiator solutions under nitrogen analysed before and after 30 light pulses, and where the dye concentration was 5×10^{-5} mol dm⁻³. The HPLC chromatograms and UV/Visible spectra of components identified are shown in Figures 5.72 – 5.80, with the retention times, peak integrations and UV/Visible absorption band positions given in Tables 5.11 – 5.13. It should be noted that a relatively small number of products have been identified for each of these dyes, which can be attributed to the lower dye concentrations than used for OH-Span studies reported earlier (section 5.2.1.1).

The important observation is that for each dye, NAPDAD is produced showing that cleavage has occurred across the azo linkage; although the phenyl half products were not observed, further studies may show their presence as in the case of OH-Span. Interestingly, the yield of NAPDAD produced after irradiation of the 1:10 O⁻-, NH₂- and NHAc-Span:photoinitiator solutions was 18%, 19%, and 9%, respectively. Therefore O⁻ and NH₂-Span show comparative NAPDAD yields to that from OH-Span (22% yield). The lower yield of NAPDAD from NHAc-Span shows that other processes are occurring, similar to the observation of further electron transfer processes for NHAc-Span observed by electrochemistry (Chapter 4).

Another observation is that components A' and B' for O⁻-Span, A'' for NH₂-Span and A''' for NHAc-Span show comparable retention times and spectra to the unknown components of D and F for OH-Span (Figures 5.25 and 5.26), which would warrant further investigation of these products.

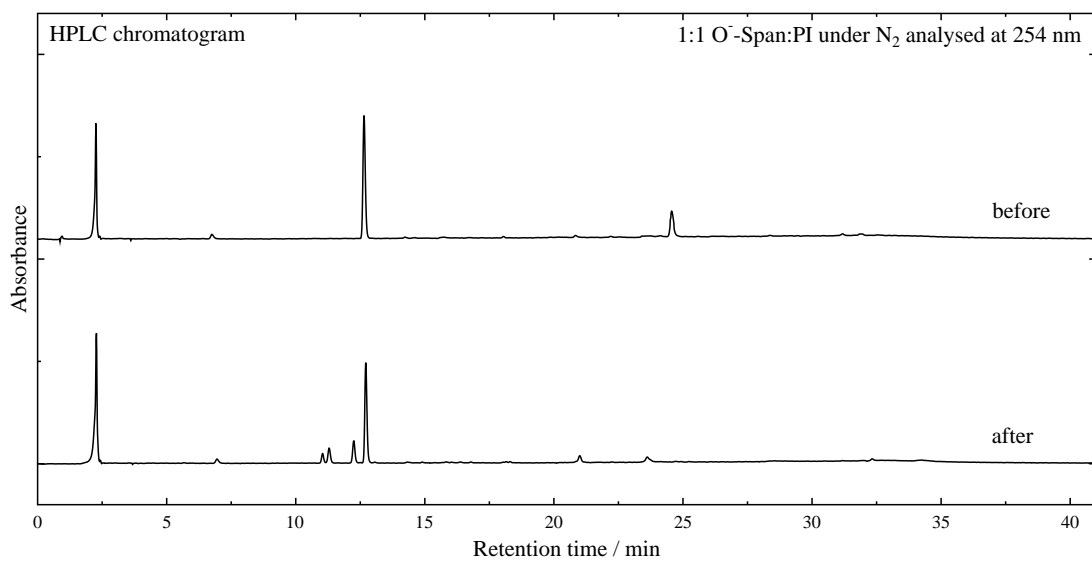


Figure 5.72 HPLC chromatogram of 1:10 O⁻-Span:photoinitiator (5×10^{-5} mol dm⁻³ dye concentration) under nitrogen before (top) and after (bottom) 30 light pulses.

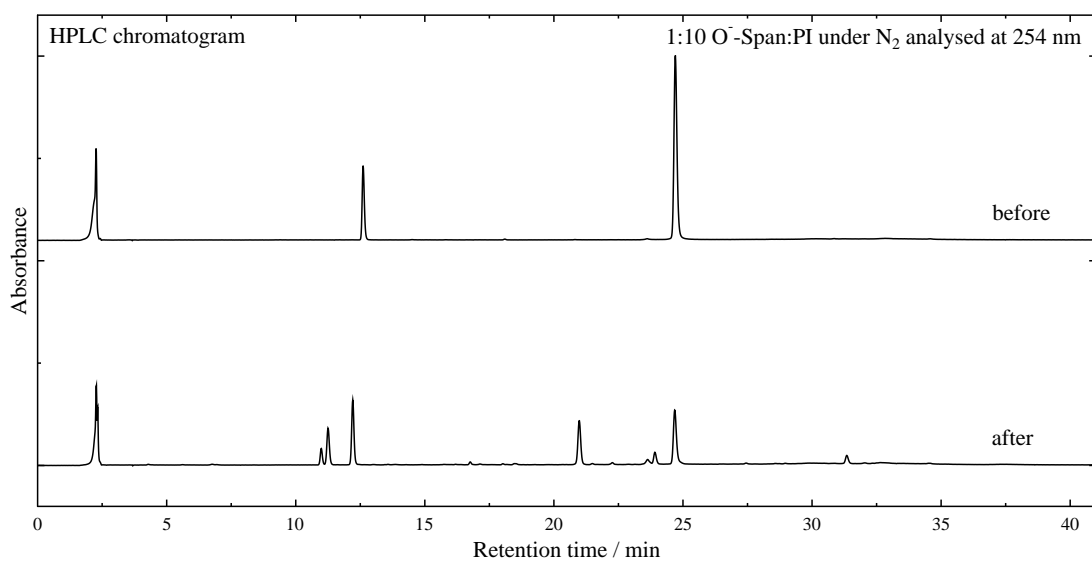


Figure 5.73 HPLC chromatogram of 1:10 O⁻-Span:photoinitiator (5×10^{-5} mol dm⁻³ dye concentration) under nitrogen before (top) and after (bottom) 30 light pulses.

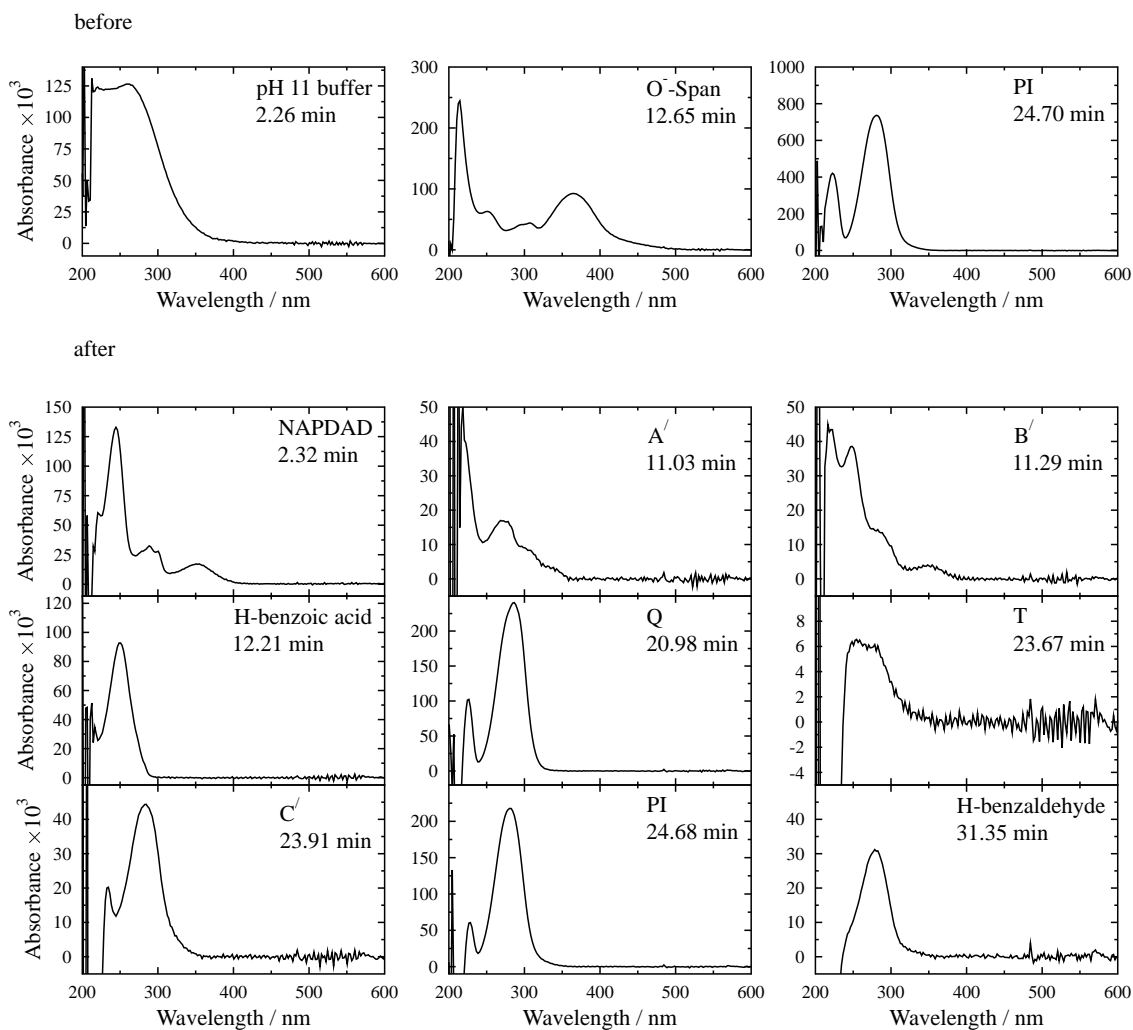


Figure 5.74 UV/Visible absorption spectra of each component formed from 1:10 O⁻-Span:photoinitiator (5×10^{-5} mol dm⁻³ dye concentration) under nitrogen after 30 light pulses.

Table 5.11 Retention times (RT / min), peak integrations (PI), concentrations (Concn / 10^{-5} mol dm⁻³) and UV/Visible absorption band positions (λ / nm) of each component before and after 30 light pulses for 1:1 and 1:10 O⁻-Span:photoinitiator under nitrogen.

Component	1:1			1:10			λ
	RT	PI	Concn ^a	RT	PI	Concn ^a	
<i>Before</i>							
Phosphate buffer	2.15	14.06	-	2.19	14.00	-	273
O ⁻ -Span ¹	12.64	10.32	5.00	12.64	10.21	5.00	215, 251, 294, 308, 363
Photoinitiator	24.64	3.42	5.00	24.68	34.25	50.00	217, 279
<i>After</i>							
O ⁻ -Span ¹	12.73	7.17	2.79	-	-	-	215, 251, 294, 308, 363
Phosphate buffer	2.15	14.22	-	2.19	14.00	-	273
NAPDAD	-	-	-	2.28	2.45	0.88	217, 244, 288, 299, 353
A ¹	11.05	0.73	-	10.96	2.10	-	220, 273, 308, 336
B ¹	11.29	1.32	-	11.31	5.83	-	220, 248, 290, 352
H-benzoic acid	12.21	1.71	-	12.17	9.25	-	217, 249
Q	20.98	0.80	-	20.94	7.71	-	243, 281
T	23.67	0.78	-	23.64	1.18	-	254, 281
C ¹	-	-	-	23.95	1.97	-	234, 283
Photoinitiator ²	-	-	-	24.59	10.37	15.13	217, 279
H-benzaldehyde	32.33	0.17	-	31.42	1.46	-	217, 300

^a Concentration of NAPDAD calculated using the calibration curve in Appendix A2.4,

¹ Converted to OH-Span under a pH 5.2 sodium acetate buffer mobile phase used in HPLC,

² concentration of residual photoinitiator calculated from peak integration.

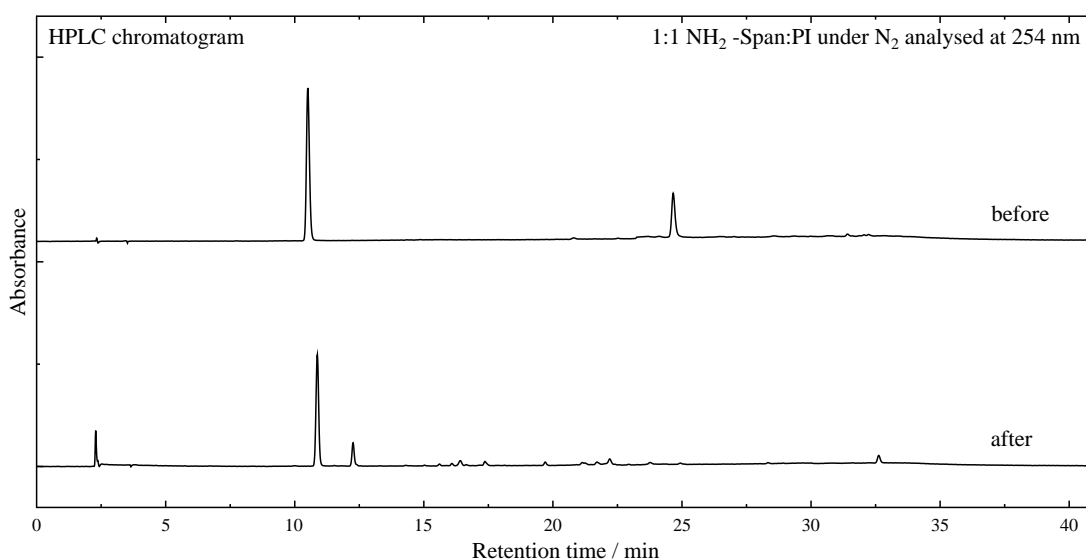


Figure 5.75 HPLC chromatogram of 1:1 NH₂-Span:photoinitiator (5×10^{-5} mol dm⁻³ dye concentration) under nitrogen before (top) and after (bottom) 30 light pulses.

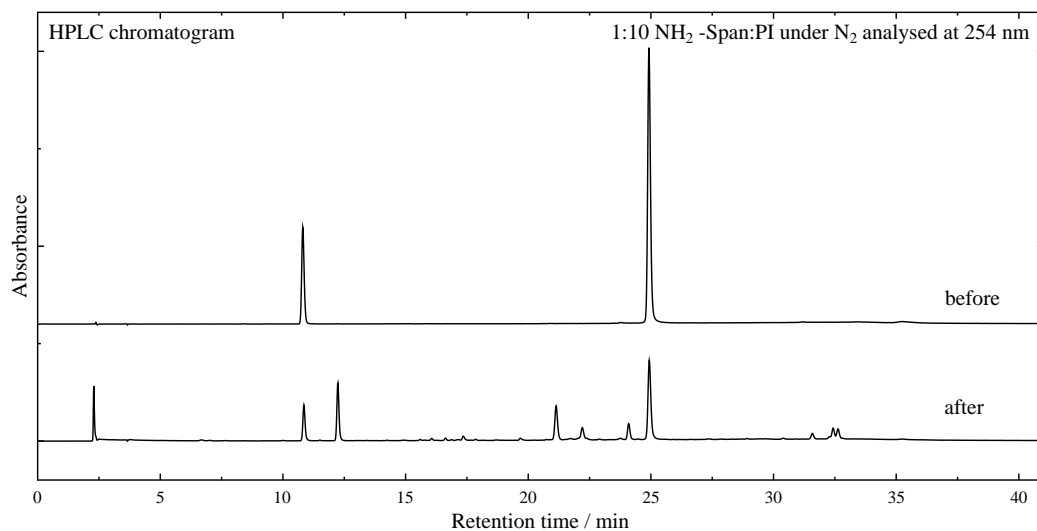


Figure 5.76 HPLC chromatogram of 1:10 NH₂-Span:photoinitiator (5×10^{-5} mol dm⁻³ dye concentration) under nitrogen before (top) and after (bottom) 30 light pulses.

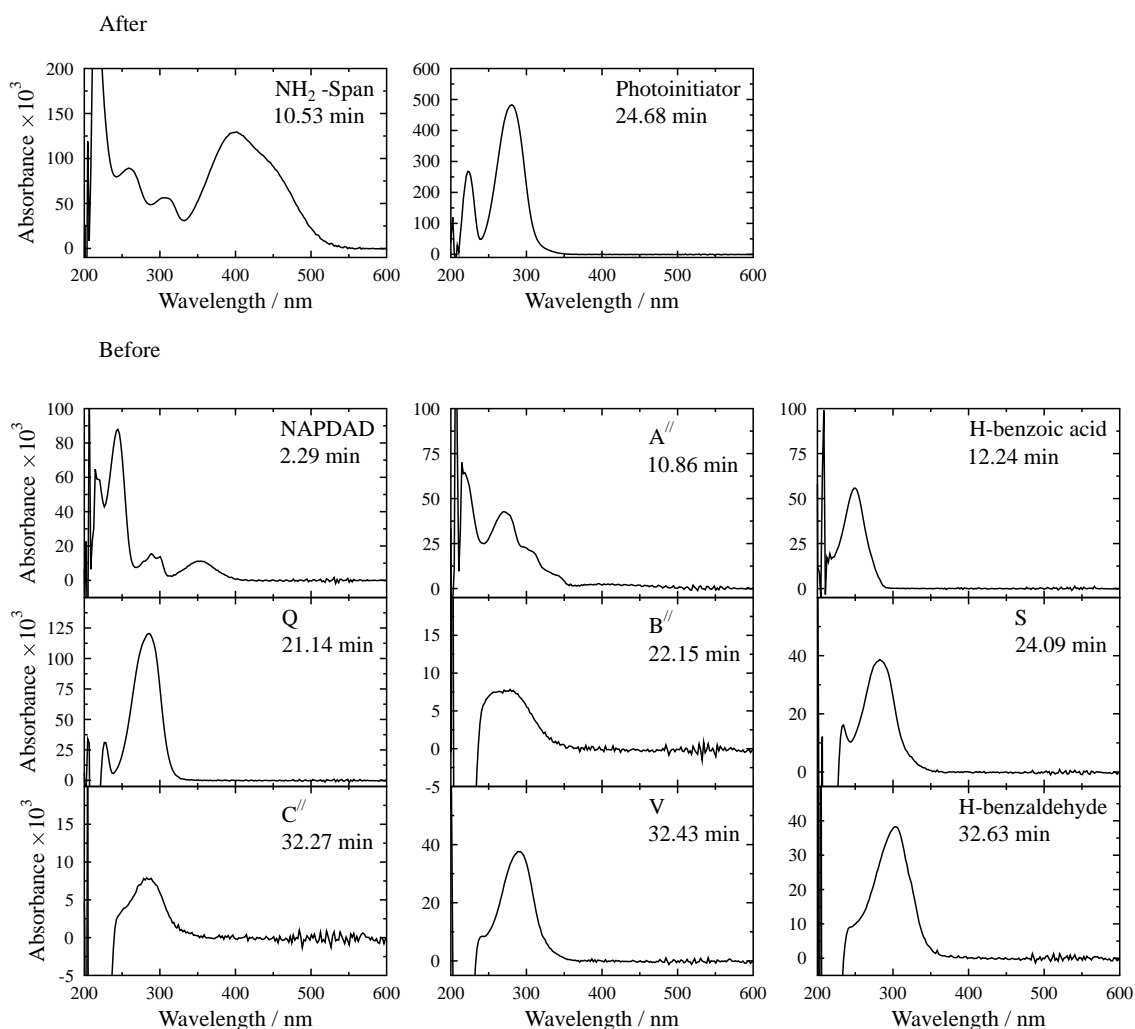


Figure 5.77 UV/Visible absorption spectra of each component formed from 1:10 NH₂-Span:photoinitiator (5×10^{-5} mol dm⁻³ dye concentration) under nitrogen after 30 light pulses.

Table 5.12 Retention times (RT / min), peak integrations (PI), concentrations (Concn / 10^{-5} mol dm $^{-3}$) and UV/Visible absorption band positions (λ / nm) of each component before and after 30 light pulses for 1:1 and 1:10 NH $_2$ -Span:photoinitiator under nitrogen.

Component	1:1			1:10			λ
	RT	PI	Concn ^a	RT	PI	Concn ^a	
<i>Before</i>							
NH $_2$ -Span	10.53	10.32	5.00	10.53	10.21	5.00	213, 260, 311, 401
Photoinitiator	24.68	3.42	5.00	24.68	34.57	50.00	217, 279
<i>After</i>							
NH $_2$ -Span	10.86	5.78	2.79	-	-	-	213, 260, 311, 401
NAPDAD	2.28	1.05	0.37	2.28	2.68	0.97	217, 244, 288, 299, 353
A ^{//}	-	-	-	10.86	3.49	-	213, 271, 300, 308, 342
H-benzoic acid	12.26	1.26	-	12.26	5.39	-	217, 249
Q	21.14	0.23	-	21.14	3.91	-	217, 279
B ^{//}	22.16	0.45	-	22.19	1.58	-	280
S	-	-	-	24.09	1.72	-	234, 283
Photoinitiator ¹	-	-	-	24.99	10.14	14.67	217, 279
C ^{//}	-	-	-	31.62	0.68	-	217, 280
G	-	-	-	32.42	0.88	-	217, 300
H-benzaldehyde	32.63	0.48	-	32.63	0.77	-	217, 300

^a Concentration of NAPDAD calculated using the calibration curve Appendix A2.4,

¹ concentration of residual photoinitiator calculated from peak integration.

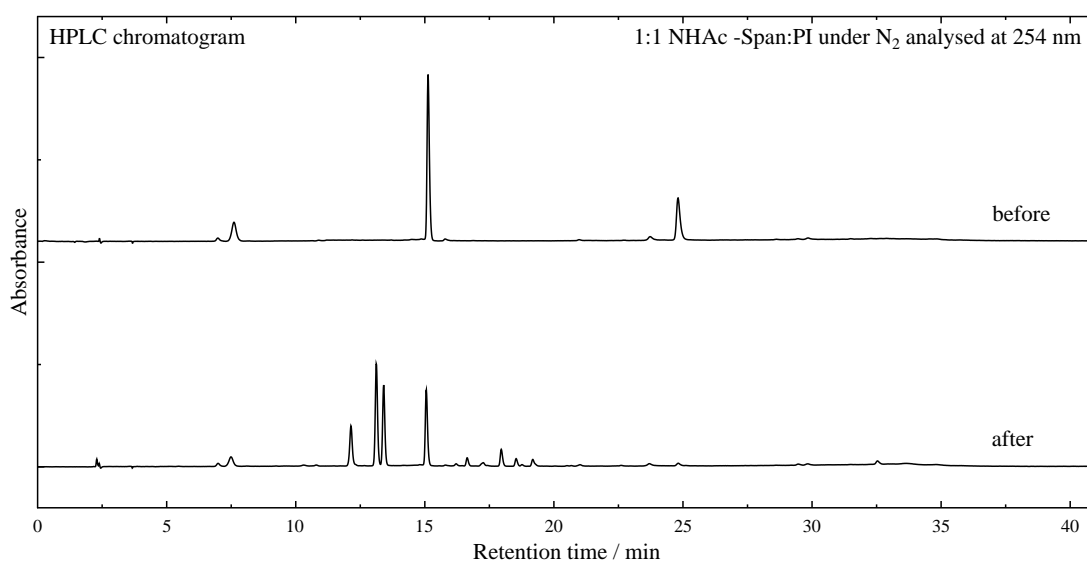


Figure 5.78 HPLC chromatogram of 1:11 NHAc-Span:photoinitiator (5×10^{-5} mol dm $^{-3}$ dye concentration) under nitrogen before (top) and after (bottom) 30 light pulses.

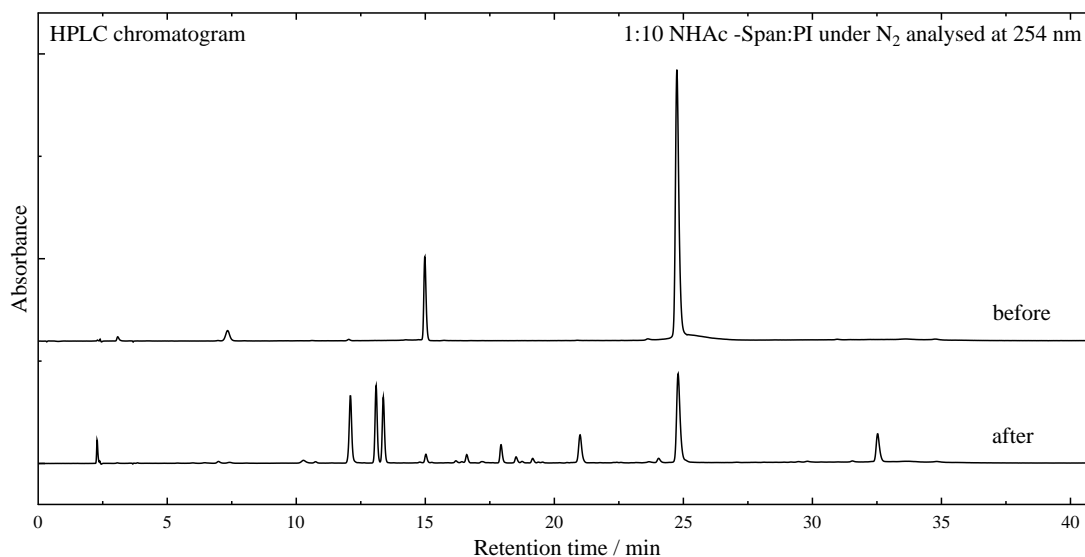


Figure 5.79 HPLC chromatogram of 1:10 NHAc-Span:photoinitiator (5×10^{-5} mol dm $^{-3}$ dye concentration) under nitrogen before (top) and after (bottom) 30 light pulses.

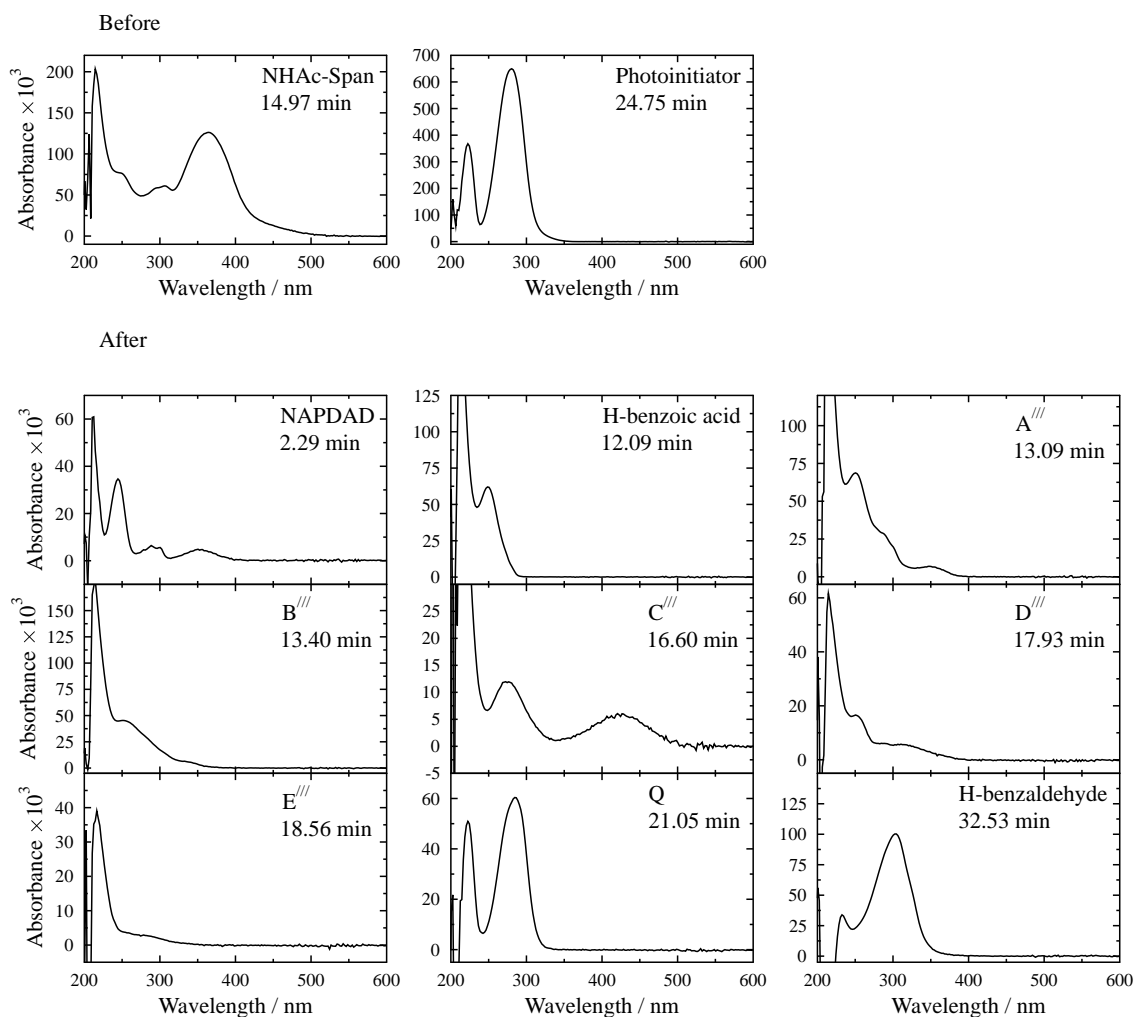


Figure 5.80 UV/Visible absorption spectra of each component formed from 1:10 NHAc-Span:photoinitiator (5×10^{-5} mol dm $^{-3}$ dye concentration) under nitrogen after 30 light pulses.

Table 5.13 Retention times (RT / min), peak integrations (PI), concentrations (Concn / 10^{-5} mol dm⁻³) and UV/Visible absorption band positions (λ / nm) of each component before and after 30 light pulses for 1:1 and 1:10 NHAc-Span:photoinitiator under nitrogen.

Component	1:1			1:10			λ
	RT	PI	Concn ^a	RT	PI	Concn ^a	
<i>Before</i>							
NHAc-Span	14.97	7.95	5.00	14.97	8.04	5.00	214, 247, 294, 308, 364
Photoinitiator	24.75	3.59	5.00	24.75	35.50	50.00	217, 279
<i>After</i>							
NHAc-Span	15.08	3.79	2.38	15.03	0.85	0.52	214, 247, 294, 308, 364
NAPDAD	2.37	0.26	0.09	2.29	1.17	0.42	217, 244, 288, 299, 353
H-benzoic acid	12.12	2.37	-	12.09	6.86	-	217, 249
A ^{///}	13.11	5.24	-	13.09	6.63	-	213, 250
B ^{///}	13.46	4.01	-	13.40	5.53	-	212, 250, 288, 301, 350
C ^{///}	16.68	0.39	-	16.60	0.73	-	214, 253, 340
D ^{///}	17.93	0.88	-	17.93	1.64	-	220, 250, 314
E ^{///}	18.53	0.40	-	18.56	0.49	-	280
Q	-	-	-	21.05	3.37	-	217, 279
Photoinitiator ¹	-	-	-	24.79	12.62	17.77	217, 279
H-benzaldehyde	32.63	0.24	-	32.53	3.71	-	217, 300

^a Concentration of NAPDAD calculated using the calibration curve in Appendix A2.4,

¹ concentration of residual photoinitiator calculated from peak integration.

5.2.3 Summary

Two areas of interest that have arisen from making the current studies on the photochemistry of the R-Span dyes are that *cis-trans* isomerisation is important and that the extensive product analysis on the photoinitiator-generated radical reactions with OH-Span show that the process is complex.

In terms of isomerisation, *trans-cis* photoisomerisation occurs for the R-Span dye series, with the rate of the *cis-trans* thermal back reaction of NH₂-, OH-, OMe- and NHAc-Span differing considerably. The rate constants for the *cis-trans* thermal back reaction are given in Table 5.14 along with their R Hammett σ_p and σ_p^- constants: the rate from quickest to slowest is in the order of -OH > -NH₂ >> -NHAc > OMe. The faster rate of the OH-Span *cis-trans* thermal back reaction has shown that it was the best dye to study in the presence of radicals to explore the mechanisms, because the time-resolved studies have shown that the radical reactions can be attributed predominately to the *trans* isomer. The rate constants obtained for OMe- and NHAc-Span are of the order of ca. 10¹¹ smaller than that for OH-Span, indicating that the barriers between the *cis* and *trans* isomers of OMe- and NHAc-Span are significantly higher, and seen likely to arise from either electronic or steric effects.

Table 5.14 Hammett σ_p and σ_p^- constants⁷³ and rate constants (k / s^{-1}) for the *cis-trans* thermal back reaction of NH₂-, OH-, OMe and NHAc-Span.

R-Span	-NH ₂	-OH	-OMe	-NHAc
σ_p	-0.66	-0.37	-0.27	0.00
σ_p^-	-0.15	-0.37	-0.26	-0.46
k	1.40×10^2	1.50×10^6	4.20×10^{-6}	3.70×10^{-5}

In terms of the products from reactions of the R-Span dyes with photoinitiator-generated radicals under reducing conditions, the naphthyl half of the dye NAPDAD has been identified consistent with the electrochemical studies (Chapter 4), showing that the reduction mechanism leads to N=N bond cleavage. The use of HPLC, LC-MS and NMR product analyses has indicated that the reactions with photoinitiator-generated radicals are complicated and that these may lead to stable dye-photoinitiator products. The main purpose of using the photoinitiator was to generate radicals quickly that allow the formation of the dye radical anion and its subsequent decay to be observed and these

studies were successful. Using kinetic modelling, a rate constant of $k_2 = 6.00 \times 10^9 \text{ dm}^3 \text{ mol}^{-1} \text{ s}^{-1}$ was obtained for $\cdot\text{C}(\text{CH}_3)_2\text{OH}$ reducing OH-Span to give Dye^\cdot , and a value of $k_3 = 5.00 \times 10^8 \text{ dm}^3 \text{ mol}^{-1} \text{ s}^{-1}$ was obtained for its subsequent disproportionation to reform OH-Span and a hydrazine intermediate. The comparative results to other dyes in the literature and the fit of this model to the experimental data indicate that if further reactions are occurring in the dye:photoinitiator solution, they may proceed on longer timescales as reported for Orange II;⁵⁵ hence, the photoinitiator generates radicals which provide a good experimental method to study one-electron reduction to mimic dye fading. Therefore the modelling has provided a good initial kinetic fit for the 1:10 solution, where the analytical techniques have shown that NAPDAD and APOL are products which can be attributed to cleavage across the azo group consistent with the proposed disproportionation reduction mechanism (Figure 5.45). For any further time-resolved studies on the other R-Span dyes, consideration of the presence of the *cis* isomer would become important, where it would be interesting to know if reduction of the *cis* isomer and subsequent reactions would in fact change the mechanism at all, beyond the individual rate constants for reduction. In most reported studies of photoinitiator-generated radical reactions with azo dyes this has not been a consideration because the studies have been performed on hydrazone tautomers locked in the *trans* form.

The DOSY technique when applied to analysing products after CPE reduction of the R-Span dyes gave very clear data (Chapter 4). In its application to the products formed after the irradiation of OH-Span:photoinitiator solutions it has given a very complex test case for the use of the technique. However it has provided useful information and it has give consistent results with LC-MS proposing that structures have formed that have a higher mass than either the dye or the photoinitiator.

5.3 Conclusions

The lack of emission observed from aqueous solutions of the pure R-Span dyes indicates that their excited states decay predominately by non-radiative photophysical processes or undergo photochemical reactions. *trans-cis* photoisomerisation followed by *cis-trans* thermal back reaction was observed and quantified for several dyes in the R-Span series. NH₂- and OH-Span have shown *cis-trans* thermal back reactions on a much shorter timescale (< 30 ms) than those of OMe- and NHAc-Span (1 – 11 days). This result indicates that the ground-state *cis* to *trans* energy barriers are much larger for OMe- and NHAc-Span. Apart from the reversible isomerisation reactions, the R-Span dyes were relatively stable to light with little fading observed on direct irradiation.

The steady-state irradiation studies of NH₂-, OH-, NHAc- and O⁻-Span in the presence of photoinitiator under nitrogen all showed irreversible bleaching of the main dye absorption band, which can be attributed to the dye reaction with 2-hydroxy-2-propyl radicals. This loss of colour is consistent with the destruction of the chromophore, comparable to that observed under electrochemical reduction which occurred due to cleavage across the azo linkage. Detailed product analysis by HPLC, LC-MS and NMR spectroscopy confirmed that cleavage across the azo linkage occurs showing that the naphthyl half of the dye NAPDAD was formed.

The time-resolved experimental data for OH-Span in the presence of photoinitiator gave a good fit to kinetic modelling of a one-electron reduction process in which reaction of the dye with 2-hydroxy-2-propyl radicals gave a k_2 rate constant close to the diffusion-controlled limit. The k_3 value associated with dye radical anion disproportionation was found to be comparable to those from other dyes showing that disproportionation is a key step in the reduction mechanism of OH-Span, which would ultimately lead to the formation of NAPDAD. The formation of NAPDAD in the other R-Span:photoinitiator solutions indicates also that disproportionation occurs in the one-electron reduction mechanisms of the other R-Span dyes.

5.4 References

1. Oakes, J. *Rev. Prog. Col.*, **2001**, *31*, 21-28.
2. Christie, R. M. *Colour Chemistry*. RSC Paperbacks: Cambridge, 2001.
3. Rau, H. *Photochemistry and photophysics*. Volume 2; CRC Press: Boca Raton, 1990, Chapter 4, 119-140.
4. Rau, H. in *Photochromism. Molecules and systems*: Durr, H., Bouas-Laurent, H., Eds.; Elsevier: Amsterdam, 1990, Chapter 4, 65-192.
5. Lednev, I. K.; Ye, T.-Q.; Hester, R. E.; Moore, J. N. *J. Phys. Chem.* **1996**, *100*, 13338-13341.
6. Lednev, I. K.; Ye, T.-Q.; Abbott, L. C.; Hester, R. E.; Moore, J. N. *J. Phys. Chem A* **1998**, *102*, 9161-9166.
7. Wildes, P. D.; Pacifici, J. G.; Irick, G.; Whitten, D. G. *J. Am. Chem. Soc.* **1971**, *93*, 2004-2008.
8. Fujino, T.; Arzhantsev, S. Y.; Tahara, T. *J. Phys. Chem. A* **2001**, *105*, 8123-8129.
9. Crecca, C. R.; Roitberg, A. E. *J. Phys. Chem. A* **2006**, *110*, 8188-8203.
10. Lu, Y. C.; Diau, E. W. G.; Rau, H. *J. Phys. Chem. A* **2005**, *109*, 2090-2099.
11. Wachtveitl, J.; Nägele, T.; Puell, B.; Zinth, W.; Kruger, M.; Rudolph-Böhner, S.; Oesterhelt, D.; Moroder, L. *J. Photochem. Photobiol., A* **1997**, *105*, 283-288.
12. Tait, K. M.; Parkinson, J. A.; Bates, S. P.; Ebenezer, W. J.; Jones, A. C. *J. Photochem. Photobiol., A* **2003**, *154*, 179-188.
13. Magennis, S. W.; Mackay, F. S.; Jones, A. C.; Tait, K. M.; Sadler, P. J. *Chem. Mat.* **2005**, *17*, 2059-2062.
14. Michalski, J.; Kucharska, E.; Wandas, M.; Hanuza, J.; Waskowska, A.; Maczka, M.; Talik, Z.; Olejniczak, S.; Potrzebowski, M. J. *J. Mol. Struct.* **2005**, *744*, 377-392.
15. Yoshida, K.; Koujiri, T.; Horii, T.; Kubo, Y. *Bull. Chem. Soc. Jpn.* **1990**, *63*, 1658-1664.
16. Zhang, A. D.; Qin, J. G. *Supramol. Sci.* **1998**, *5*, 573-576.
17. Tait, K. M.; Parkinson, J. A.; Gibson, D. I.; Richardson, P. R.; Ebenzer, W. J.; Hutchings, G. H.; Jones, A. C. *Photochem. Photobiol. Sci.* **2007**, *6*, 1010-1018.
18. Allen, N. S. *Rev. Prog. Col.*, **1987**, *17*, 61-71.
19. Allen, N. S.; Binkley, J. P.; Parsons, G. O.; Tennent, N. H. *Dyes Pigm.* **1984**, *5*, 209-223.

20. Jansen, L. M. G.; Wilkes, I. P.; Wilkinson, F.; Worrall, D. R. *J. Photochem. Photobiol. A*, **1999**, *125*, 99-106.
21. Joshua, C. P.; Pillai, V. N. R. *Tetrahedron Lett.* **1972**, 2493-2494.
22. Zhang, S. J.; Yi, H. Q.; Li, Q. R. *Chemosphere* **2005**, *61*, 1003-1011.
23. Zielonka, J.; Podsiadly, R.; Czerwinska, M.; Sikora, A.; Sokolowska, J.; Marcinek, A. *J. Photochem. Photobiol. A*, 2004, *163*, 373-379.
24. Dajka, K.; Takács, E.; Solpan, D.; Wojnárovits, L.; Güven, O. *Radiat. Phys. Chem.* **2003**, *67*, 535-538.
25. Das, S.; Kamat, P. V.; Padmaja, S.; Au, V.; Madison, S. A. *J. Chem. Soc., Perkin Trans. 2*, **1999**, 1219-1224.
26. Wojnárovits, L.; Pálfi, T.; Takács, E.; Emmi, S. S. *Radiat. Phys. Chem.* **2005**, *74*, 239-246.
27. Coen, J. J. F.; Smith, A. T.; Candeias, L. P.; Oakes, J. J. *J. Chem. Soc., Perkin Trans. 2*, **2001**, 2125-2129.
28. Nasr, C.; Vinodgopal, K.; Hotchandani, S.; Chattopadhyay, A. K.; Kamat, P. V.; *Radiat. Phys. Chem.*, **1997**, *49*, 159-166.
29. Oakes, J. *Rev. Prog. Col.*, **2003**, *33*, 72-84.
30. Griffiths J.; Hawkins, C. *J. Chem. Soc., Perkin Trans. 2*, **1977**, 747-751.
31. Aranyosi, P.; Csepregi, Z.; Rusznák, I.; Töke, L.; Víg, A. *Dyes Pigm.* **1998**, *37*, 33-45.
32. Ruyffelaere, F.; Nardello, V.; Schmidt, R.; Aubry, J. M. *J. Photochem. Photobiol. A*, **2006**, *183*, 98-105.
33. Yamaguchi S.; Sasaki, Y. *J. Photochem. Photobiol. A*, **2001**, *142*, 47-50.
34. Batchelor, S. N.; Carr, D.; Coleman, C. E.; Fairclough, L.; Jarvis, A. *Dyes Pigm.* **2003**, *59*, 269-275.
35. Bandara J.; Kiwi, J. *New. J. Chem.* **1999**, *23*, 717-724.
36. Hihara, T.; Okada, Y.; Morita, Z. *Dyes Pigm.* **2007**, *73*, 141-161.
37. Bilgi S.; Demir, C. *Dyes Pigm.* **2005**, *66*, 69-74.
38. Hihara, T.; Okada, Y.; Morita, Z. *Dyes Pigm.* **2004**, *60*, 23-48.
39. Morley, J. O.; Guy, O. J.; M. H. Charlton, *J. Phys. Chem. A*, **2004**, *108*, 10542-105550.
40. Csepregi, Z.; Aranyosi, P.; Rusznák, I.; Töke, L.; Frankl, J.; Víg, A.; *Dyes Pigm.* **1998**, *37*, 1-14.

41. Jockusch, S.; Landis, M. S.; Freiermuth, B.; Turro, N. J. *Macromolecules* **2001**, *34*, 1619-1626.
42. Eichler, J.; Herz, C. P.; Naito, I.; Schnabel, W. *J. Photochem.* **1980**, *12*, 225-234.
43. Eichler, J.; Herz, C. P.; Schnabel, W. *Angew. Makromol. Chem.* **1980**, *91*, 39-54.
44. Fouassier, J. P.; Ruhlmann, S.; Graff, B.; Morlet-Savary, F.; Wieder, F. *Prog. Org. Coatings* **1995**, *25*, 235-271.
45. Lalevée, J.; Allonas, X.; Jradi, S.; Fouassier, J. P. *Macromolecules* **2006**, *39*, 1872-1879.
46. Ye, G.; Ke, Z.; Yang, J.; Zhao, T.; Zheng, Z.; Chen, Y. *Polymer* **2006**, *47*, 4603-4612.
47. Fouassier, J. P.; Ruhlmann, S.; Graff, B.; Wieder, F. *Prog. Org. Coatings* **1995**, *25*, 169-202.
48. Hunt, P.; Worrall, D. R.; Wilkinson, F.; Batchelor, S. N. *Photochem. Photobiol. Sci.* **2003**, *2*, 518-523.
49. Kunanandam, S. PhD Thesis, University of York, 2004.
50. Atkinson, D. PhD Thesis, University of York, 2007.
51. Yadav, P.; Rao, B. S. M.; Batchelor, S. N.; O'Neill, P. *J. Phys. Chem. A* **2005**, *109*, 2039-2042.
52. Batchelor, S. N.; Shushin, A. I. *J. Phys. Chem. B* **2001**, *105*, 3405-3408.
53. Jockusch S.; Turro, N. J. *J. Am. Chem. Soc.* **1999**, *121*, 3921-3925.
54. Batchelor, S. N. *New. J. Chem.* **2004**, *28*, 1200-1203.
55. Abbott, L. C.; Batchelor, S. N.; Lindsay Smith, J. R.; Moore, J. N. *J. Phys. Chem. A* **2009**, *113*, 6091-6103.
56. Isak, S. J.; Eyring, E. M.; Spikes, J. D.; Meekins, P. A. *J. Photochem. Photobiol. A* **2000**, *134*, 77-85.
57. Huggenburger, C.; Lipscher, J. Fischer, H. *J. Phys. Chem.* **1980**, *84*, 3467-3471.
58. Littleford, R. E.; Matousek, P.; Towrie, M.; Parker, A. W.; Dent, G.; Lacey, R. J.; Smith, W. E. *Analyst* **2004**, *129*, 505-506.
59. Vikman, K.; Iitti, H.; Matousek, P.; Towrie, M.; Parker, A. W.; Vuorinen, T.; *Vib. Spectrosc.* **2005**, *37*, 123-131.
60. Yamaki, S. B.; Barros, D. S.; Garcia, C. M.; Socoloski, P.; Oliveira, O. N.; Atvars, T. D. Z. *Langmuir* **2005**, *21*, 5414-5420.
61. Karpicz, R.; Gulbinas, V.; Stanishauskaite, A.; Undzenas, A. *Chem. Phys.* **2001**, *269*, 357-366.

62. Gottlieb, H. G.; Kotlyar, V.; Nudelman, A. *J. Org. Chem.* **1997**, *62*, 712-7515.
63. Neta, P.; Grodowski, J.; Ross, A. B. *J. Phys. Chem. Ref. Data* **1996**, *25*, 709.
64. Neta, P.; Lavanon, H. *J. Phys. Chem.* **1977**, *81*, 2288-2292
65. Sharma, K. K.; O'Neill, P.; Oakes, J.; Batchelor, S. N.; Rao, B. S. M. *J. Phys. Chem. A*, **2003**, *107*, 7619-7620.
66. Le Févre, R. J. W.; Northcott, J. *J. Chem. Soc.* **1953**, 867-870.
67. Nishimura, N.; Sueyoshi, T.; Yamanaka, H.; Imai, E.; Yamamoto, S.; Hasegawa, S. *Bull. Chem. Soc. Jpn.* **1976**, *49*, 1381-1387.
68. Norikane, Y.; Katoh, R.; Tamaoki, N. *Chem. Commun.* **2008**, 1898-1900.
69. Norikane, Y.; Tamaoki, N. *Eur. J. Org. Chem.* **2006**, 1296-1302.
70. De Maria, P.; Fontanna, A.; Gasbarri, C.; Siani, G.; Zanirato, P. *ARKIVOC* **2009**, 16-29.
71. Qi, W.; Shuang, G.; Kai, Z.; Wenbin, C.; Congwei, N.; Zhen, X. *Chin. J. Chem.* **2009**, *27*, 1582-1588.
72. Magennis, S. W.; Mackay, F. S.; Jones, A. C.; Tait, K.; Sadler, P. J. *Chem. Mater.* **2005**, *17*, 2059-2062.
73. Hansch, C.; Leo, A.; Taft, R. W. *Chem. Rev.* **1991**, *91*, 165-195.

Chapter 6 Conclusions and future work

Section 6.1 reports on the main conclusions of the work reported in this thesis by, firstly, giving an assessment of the techniques used to study aqueous solutions of the R-Span dyes and, secondly as to dye structure and reactivity. Section 6.2 suggests future work which could be carried out to learn more about the structure and reactivity of the R-Span dye series which could also be applied to other azo dyes.

6.1 Conclusions

6.1.1 Techniques

UV/Visible absorption spectroscopy has been used as a valuable tool in studying the aqueous samples of the R-Span dyes. The spectra recorded were sensitive to dye structure showing changes in dye absorption wavelength and molar absorption coefficient as a result of changing the R substituent and giving an indication of the electronic properties of the dyes. The UV/Visible absorption spectra were also sensitive to pH, allowing pK_a values to be determined; spectra were also successfully used to monitor changes that occur upon reductive and oxidative processes induced by electrochemical and photochemical techniques, and upon isomerisation by direct irradiation of the dyes. The spectra have also been used in product elucidation, particularly in combination with HPLC separation, as a result of the distinct band features being observed.

UV/Visible emission spectroscopy has not been widely used in this work, but has successfully shown that the excited states of the R-Span dyes do not decay significantly through radiative routes.

Raman spectroscopy has been successfully used to report on the vibrational spectra of the R-Span dyes, in which resonance and off-resonance Raman spectra conditions gave comparable spectra for the pure dyes. IR spectroscopy has been used in a more limited way but has been used successfully in assigning bands in the Raman spectrum of OH-Span where assignments were ambiguous.

Electrochemical techniques have been successfully used to understand electron transfer processes that occur in the R-Span dyes. Cyclic voltammetry has proved unsuccessful in studying the aqueous R-Span samples here. Spectroelectrochemistry has proved to be a valuable technique in following the spectral changes that occur upon electrochemical reduction and oxidation, and has provided estimates of the reduction and oxidation potentials. Controlled potential electrolysis has been employed to obtain the number of electrons transferred during the reduction of NH₂-, OH- and NHAc-Span, subsequently these solutions were studied by various analytical techniques to elucidate products quantitatively.

Steady-state studies, using flash gun irradiation, have provided a way of assessing the stability of the dyes alone and in the presence of photoinitiator-generated radicals. As with CPE, this provided solutions which could be analysed by various analytical techniques to elucidate products. Steady-state studies allied with UV/Visible absorption spectroscopy allowed the long term thermal *cis-trans* isomerisation of OMe- and NHAc-Span to be studied.

TRVIS provided a time-resolved laser technique that allowed the short term photochemical effects due to photoisomerisation to be studied, where kinetic data allowed the determination of rate constants. TRVIS also provided an effective way of studying the short time scale reaction of OH-Span with photoinitiator-generated radicals. The technique has shown that the photolysis of the photoinitiator used in this work provides an effective method to study dye fading by one-electron reduction, even though detailed analytical techniques show that some products are formed on a long time scale that are not important to mimicking the initial stages of reduction.

NMR spectroscopy has proved to be an extremely valuable technique throughout this study. A combination of ¹H, ¹³C, COSY, NOESY, HSQC and HMBC has successfully been used to characterise the structure of the R-Span dyes, with all proton and carbon assignments made. The technique has also provided a quantitative way of determining products from the electrochemical and photochemical techniques used to study dye stability. DOSY NMR spectroscopy has been used in this study in part to test its general suitability for the separation of components in a complicated mixture allowing for their elucidation. As is consistent with the literature, simple mixtures of OH-Span, and

authentic samples of NAPDAD and APOL gave distinct diffusion coefficients for their components. Upon CPE reduction of OH-Span, the diffusion coefficients obtained for the products NAPDAD and APOL were comparable to those of the authentic components. The DOSY spectrum recorded for irradiated solutions of OH-Span:photoinitiator solution gave a complex spectrum in which many products have been observed. The range of diffusion coefficients obtained can be attributed to the mass range of the products formed. It should also be noted that NMR product analysis has identified extra products which would not have been observed otherwise by the other analytical techniques used in this work.

As with NMR spectroscopy, HPLC and LC-MS analysis have been valuable in identifying products that have formed as a result of carrying out various electrochemical and photochemical techniques to study dye stability. HPLC has provided further quantitative analysis on these products that in general has matched the NMR analyses. The LC-MS analysis, like the DOSY NMR analysis, has shown that upon the irradiation of OH-Span:photoinitiator solutions products have formed of higher masses than either OH-Span or photoinitiator, which again would not have been detected otherwise.

Computational calculations using DFT have provided optimised structures for all seven core R-Span dyes and the protonated forms of NH₂-Span. These optimisations, although calculated for the gas phase, give an estimate as to the structure and bonding for these dyes, by providing bond lengths and angles. Using these optimisations, electronic transitions, charge distributions, NMR, IR and Raman information were obtained. In general there is a good match of the experimental NMR resonances and vibrational bands to those calculated indicating that these optimisations, with the sulfonates protonated, provide a good mimic of the structure of the R-Span dyes in water. The good match has allowed the experimental vibrational bands recorded for all the R-Span dyes to be assigned to calculated normal modes, which are comparable across the R-Span dye series.

6.1.2 Dye Structure

The R-Span dye series studied here is a set of true azo dyes, unlike much of the reported work carried out on azo dyes which predominately exist as the hydrazone tautomer. Figure 6.1 shows the R-Span dyes studied in this work with the R group representing the only differences between them.

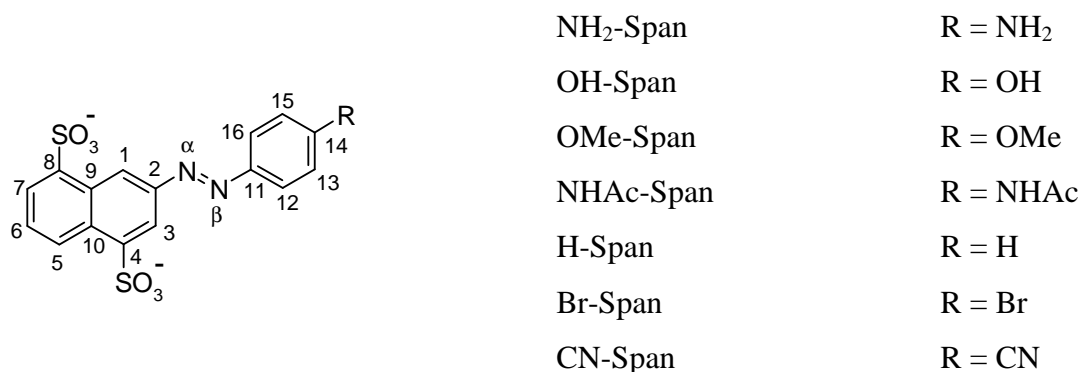


Figure 6.1 Structure of the R-Span dyes.

Studies on this set of R-Span dyes have shown that aggregation and intramolecular hydrogen bonding are not important in comparison to azo dyes that exist predominately as the hydrazone tautomer. What is important in these dyes are pH dependence, *trans-cis* photoisomerisation (section 6.1.3.3) and the effect of the R substituent on their properties.

The pH dependence observed for OH-Span is due to deprotonation of the OH substituent with a pK_a of 7.98. For NH₂-Span, a pK_a of 2.88 for protonation has been determined and extensive studies by UV/Visible absorption, NMR and Raman spectroscopy and DFT calculations indicate that it could be occurring at the azo linkage to give an azonium tautomer or at the terminal R group leading to give an ammonium tautomer, with mixtures of the two species indicated by some of the experimental data. In general this is the same interpretation that has been made on protonated aminoazobenzenes in the literature. No pH dependence was observed for the other R-Span dyes indicating that any protonation or deprotonation occurs outside the range of pH 2 – 12.

Computational calculations using DFT have given calculated NMR and vibrational data which show good correspondence to experimental data, indicating that the optimisations report a good mimic to the structure in solution. The optimisations of all the R-Span dyes show that a planar structure exists in the *trans* form. UV/Visible absorption, NMR and Raman spectroscopy have provided spectra of the *trans* form of the dye, with the UV/Visible absorption and NMR spectra obtained upon irradiation of OMe- and NHAc-Span corresponding to the *cis* form being clearly different.

The Hammett σ_p constants have provided one way to consider the R substituent effect, with the wavelength of the main absorption band and NMR chemical shifts showing a good matching trend to σ_p . With an increasingly electron donating substituent there is a shift to longer wavelength of the main absorption band and an upfield shift of resonances from protons adjacent to the R group.

6.1.3 Dye reactivity

The main focus of work on dye reactivity has been the study of reduction, and the most detailed studies cover OH-Span with comparative studies made on the other R-Span dyes. Some initial studies of oxidation and on photoisomerisation have also been made.

6.1.3.1 Reduction

Spectroelectrochemistry has shown that all the R-Span dyes undergo electrochemical reduction as an irreversible process, where in general a more negative potential is required for reduction, with increasing R substituent electron-donating capacity indicating a greater stability to reduction. Although the initial steps of the electrochemical reduction process have not been resolved, by using calculated atomic charges, N_β is predicted to have a lower charge density than N_α which may be indicative of N_β being the initial site of reduction; however, this is dependent also on the energetics of species formed on reduction which have not been studied in this work.

CPE reduction studies on OH-Span show a clean reduction producing the naphthyl half of the dye, NAPDAD, and the phenyl half of the dye, APOL, in which four electrons are consumed, consistent with the reported hydrazine formation consuming two

electrons followed by irreversible N-N bond scission consuming a further two electrons. The identification of NAPDAD after the electrochemical reduction of the other R-Span dyes shows that a similar reduction process occurs for all the dyes. However, the additional number of electrons and products identified after electrochemical reduction of NHAc-Span and additional products observed after electrochemical reduction of OMe-Span indicate that other processes are also occurring.

Direct photoirradiation of the R-Span dye solutions alone showed little fading, but significant fading occurred in the presence of a photoinitiator. Reduction studies were carried out on the R-Span dyes by generating 2-hydroxy-2-propyl radicals from the photoinitiator, and a detailed analysis of the products formed from OH-Span has shown that NAPDAD and APOL were produced, consistent with a reduction process with N-N bond scission. The TRVIS studies on OH-Span:photoinitiator solutions have enabled the spectral identification of the OH-Span radical anion species to be made; the electron transfer from radical to dye occurs at a near diffusion controlled rate constant of $6.00 \times 10^9 \text{ dm}^3 \text{ mol}^{-1} \text{ s}^{-1}$ followed by disproportionation of the OH-Span radical anion with a rate constant of $5.00 \times 10^8 \text{ dm}^3 \text{ mol}^{-1} \text{ s}^{-1}$. The identification of NAPDAD formed after steady-state irradiation of other R-Span:photoinitiator solutions is consistent with the key reduction mechanism for the R-Span dyes series occurring via disproportionation.

6.1.3.2 Oxidation

Although the work carried out on oxidation was preliminary, the absence of electrochemical oxidation for those dyes containing an electron-withdrawing substituent indicate that CN and Br offer resistance to oxidation. For those R-Span dyes irradiated with photoinitiator under air, an irreversible bleach of the main absorbance band was observed showing degradation of the chromophore occurs.

6.1.3.3 Photoisomerisation

Although direct photoirradiation of R-Span dye solutions alone showed no fading, *trans-cis* photoisomerisation was observed by steady-state and time-resolved irradiation techniques, after which the thermal *cis-trans* back reaction was studied. This back

reaction was observed for NH₂-, OH-, OMe- and NHAc Span with rate constants of 1.5×10^6 , $1.4 \times 10^2 \text{ s}^{-1}$, 4.20×10^{-6} , and $3.70 \times 10^{-5} \text{ s}^{-1}$ (all at 21°C), respectively. The difference between the rates of the thermal back reaction of NH₂- and OH-Span dyes and the OMe- and NHAc-Span dyes shows a huge effect (ca. 10^{12} between NH₂- and OMe-Span) indicating that there must be a much greater *cis* to *trans* energy barrier in the latter two.

6.2 Future work

The most interesting work has come from studying R-Span photoisomerisation and stability and there is a significant amount of further work that could be carried out.

Firstly it would be interesting to explore the substituent effect further by obtaining further samples of H-, Br- and CN-Span. The irradiation studies performed on the sample of CN-Span are very speculative due to impurities being present in the sample and it would be interesting to study the irradiation further as this would give a clear indication as to the influence of the electron withdrawing effect and whether *trans-cis* photoisomerisation and *cis-trans* thermal isomerisation occur. Thereafter the effects of temperature and solvent on the rate of the thermal *cis* to *trans* back reaction could be studied. As well as using UV/Visible absorption spectroscopy, NMR irradiation techniques could be explored in which the peaks giving rise to the *cis* and *trans* forms could be studied as a function of time, especially in the case of OMe-Span and NHAc-Span. It would be interesting to understand why the *cis* isomers of OMe-Span and NHAc-Span are so much more stable than those of the other R-Span dyes studied here. A series of computational DFT calculations could be set up in which several structures of the *cis* form could be proposed to understand the steric effects of the R substituents, for example to equate whether there are significant interactions between the R and sulfonate groups, with structures arising from transition states giving an indication as to the energy barriers involved in isomerisation.

In terms of dye reactivity, electrochemical oxidation could be explored further for NH₂-, OH- and NHAc-Span where oxidation was observed by spectroelectrochemistry. CPE oxidation could be carried out on these dyes to give a measure of the number of

electrons transferred and thereafter the resulting solutions could be analysed by the various analytical techniques used in this thesis. CV could be carried out in a non-aqueous solvent in which the initial reversible step in the reduction mechanism may become identifiable. It would be interesting to study after irradiation the *cis* and *trans* contributions to the redox reactions.

Again by obtaining further samples of H-, Br and CN-Span, the effect of the photoinitiator-generated radical reactions could be explored further, giving a more conclusive way of assessing substituent effects on fading. Further studies using TRVIS on other R-Span:photoinitiator solutions would give a comparative set of rate constants for the electron transfer to produce the dye radical anion, k_2 and subsequent disproportionation, k_3 . Modelling of the reduction mechanism itself could be explored in more detail, by varying laser pump energies and sample concentrations. EPR spectroscopy could be used to provide information on the structure of the R-Span radicals formed.

In addition to all the studies carried out in solution, comparative studies could be made of dyes in cellophane, a mimic of paper, allowing for further structural and reactivity data to be obtained.

Further DFT calculations could be explored on O⁻-Span, where solvent field calculations could be applied, and thereafter compared with the experimental data. For example, O⁻ offers a more electron donating substituent than others in the R-Span dye series, in which the experimental Raman spectrum showed substituent effects which could be identified in the calculated normal modes. Other calculations of interest would be the energy changes that occur on the structures during an electron transfer process like reduction, where the structures of the dye radical anion and hydrazine forms could be optimised. This would also allow for a further consideration of the charge distribution across the molecule.

Appendices

Appendix 1 Structure

A1.1 Non-linear regression analysis on spectrophotometric pH titration data

Single pK_a system

The deprotonation of an acid is given by equation A1.1, where the equilibrium constant are given by equation A1.2, where [HA] and [A⁻] are the concentrations of the protonated and unprotonated species, respectively, and [H⁺] is the concentration of protons released.



$$K_a = \frac{[\text{A}^-][\text{H}^+]}{[\text{HA}]} \quad (\text{A1.2})$$

The mole fractions α_{HA} and α_{A^-} of the protonated and unprotonated species are given by equations A1.3-A1.4, where C_{tot} (mol dm⁻³) is the total concentration.

$$\alpha_{\text{HA}} = \frac{[\text{HA}]}{C_{\text{tot}}} = \frac{[\text{H}^+]}{[\text{H}^+] + K_a} \quad (\text{A1.3})$$

$$\alpha_{\text{A}^-} = \frac{[\text{A}^-]}{C_{\text{tot}}} = \frac{K_a}{[\text{H}^+] + K_a} \quad (\text{A1.4})$$

For a mixture of species the total absorbance A can be expressed as the sum of the absorbance of HA and A⁻ as given by equation A1.5. The Beer-Lambert law can be applied to the mixture of species as expressed in equation A1.6, where ϵ_{HA} and ϵ_{A^-}

($\text{dm}^3 \text{ mol}^{-1} \text{ cm}^{-1}$) are the absorption coefficients of the protonated and unprotonated species, respectively, and l is the pathlength of the cell (cm).

$$A = A_{\text{HA}} + A_{\text{A}^-} \quad (\text{A1.5})$$

$$A = \epsilon_{\text{HA}}[\text{HA}]l + \epsilon_{\text{A}^-}[\text{A}^-]l \quad (\text{A1.6})$$

Substitutions of equations A1.3-A1.4 into A1.6 give an expression for A in terms of K_a and $[\text{H}^+]$ as shown in equation A1.7.

$$A = \frac{C_{\text{tot}}l(\epsilon_{\text{HA}}[\text{H}^+] + \epsilon_{\text{A}^-}K_a)}{[\text{H}^+] + K_a} \quad (\text{A1.7})$$

The total concentration, C_{tot} is given by equation A1.8 where n_{tot} (mol) is the total number of moles of species in solution and V (dm^3) is the solution volume.

$$C_{\text{tot}} = \frac{n_{\text{tot}}}{V} \quad (\text{A1.8})$$

Substitution of equation A1.7 by equation A1.8 gives an expression for the experimental data in terms of K_a and $[\text{H}^+]$ as shown by equation A1.9.

$$\frac{AV}{n_{\text{tot}}l} = \frac{\epsilon_{\text{HA}}[\text{H}^+] + \epsilon_{\text{A}^-}K_a}{[\text{H}^+] + K_a} \quad (\text{A1.9})$$

Using equations A1.10-A1.11, equation A1.9 can be expressed in terms of pH and $\text{p}K_a$ and used for analysis as given by equation A1.12.

$$[\text{H}^+] = 10^{-\text{pH}} \quad (\text{A1.10})$$

$$K_a = 10^{-\text{p}K_a} \quad (\text{A1.11})$$

$$\frac{AV}{n_{\text{tot}}l} = \frac{\epsilon_{\text{HA}} 10^{-\text{pH}} + \epsilon_{\text{A}^-} 10^{-\text{pK}_a}}{10^{-\text{pH}} + 10^{-\text{pK}_a}} \quad (\text{A1.12})$$

Double pK_a system

The deprotonation of a diprotic acid is given by equation A1.13, where the equilibrium constants K_{a1} and K_{a2} are given by equations A1.14-A1.15 where $[\text{H}_2\text{A}]$, $[\text{HA}^-]$ and $[\text{A}^{2-}]$ are the concentrations of the diprotonated, protonated and unprotonated species, respectively, and $[\text{H}^+]$ is the concentration of protons released.



$$K_{a1} = \frac{[\text{HA}^-][\text{H}^+]}{[\text{H}_2\text{A}]} \quad (\text{A1.14})$$

$$K_{a2} = \frac{[\text{A}^{2-}][\text{H}^+]}{[\text{HA}^-]} \quad (\text{A1.15})$$

The mole fractions, $\alpha_{\text{H}_2\text{A}}$, α_{HA^-} and $\alpha_{\text{A}^{2-}}$ for each of the diprotonated, protonated and unprotonated species are given by equations A1.16-A1.17, where C_{tot} (mol dm^{-3}) is the total concentration.

$$\alpha_{\text{H}_2\text{A}} = \frac{[\text{H}_2\text{A}]}{C_{\text{tot}}} = \frac{[\text{H}^+]^2}{[\text{H}^+]^2 + [\text{H}^+]K_{a1} + K_{a1}K_{a2}} \quad (\text{A1.16})$$

$$\alpha_{\text{HA}^-} = \frac{[\text{HA}^-]}{C_{\text{tot}}} = \frac{[\text{H}^+]K_{a1}}{[\text{H}^+]^2 + [\text{H}^+]K_{a1} + K_{a1}K_{a2}} \quad (\text{A1.17})$$

$$\alpha_{\text{A}^{2-}} = \frac{[\text{A}^{2-}]}{C_{\text{tot}}} = \frac{K_{a1}K_{a2}}{[\text{H}^+]^2 + [\text{H}^+]K_{a1} + K_{a1}K_{a2}} \quad (\text{A1.18})$$

For a mixture of species the total absorbance, A can be expressed as the sum of the absorbance of H_2A , HA^- and A^{2-} as given by equation A1.19. The Beer-Lambert law can be applied to the mixture as expressed in equation A1.20, where ϵ_{H_2A} , ϵ_{HA^-} and $\epsilon_{A^{2-}}$ ($dm^3 mol^{-1} cm^{-1}$) are the absorption coefficients of the diprotonated, protonated and unprotonated, respectively, and l is the pathlength of the cell (cm).

$$A = A_{H_2A} + A_{HA^-} + A_{A^{2-}} \quad (A1.19)$$

$$A = \epsilon_{H_2A} [H_2A]l + \epsilon_{HA^-} [HA^-]l + \epsilon_{A^{2-}} [A^{2-}]l \quad (A1.20)$$

Substitutions of equations A1.16-A1.18 into A1.20 gives an expression for A in terms of K_{a1} , K_{a2} and $[H^+]$ as shown in equation A1.21.

$$A = \frac{C_{tot}l(\epsilon_{H_2A}[H^+]^2 + \epsilon_{HA^-}[H^+]K_{a1} + \epsilon_{A^{2-}}K_{a1}K_{a2})}{[H^+]^2 + [H^+]K_{a1} + K_{a1}K_{a2}} \quad (A1.21)$$

The total concentration, C_{tot} is given by equation A1.22 where n_{tot} (mol) is the total number of moles of species in solution and V (dm^3) is the solution volume.

$$C_{tot} = \frac{n_{tot}}{V} \quad (A1.22)$$

Substitution of equation A1.21 by equation A1.22 gives an expression for the experimental data in terms of K_{a1} , K_{a2} and $[H^+]$ as shown by equation A1.23.

$$\frac{AV}{n_{tot}l} = \frac{\epsilon_{H_2A}[H^+]^2 + \epsilon_{HA^-}[H^+]K_{a1} + \epsilon_{A^{2-}}K_{a1}K_{a2}}{[H^+]^2 + [H^+]K_{a1} + K_{a1}K_{a2}} \quad (A1.23)$$

Using equations A1.24-A1.25, equation A1.23 can be expressed in terms of pH and pK_a and used for analysis as given by equation A1.26.

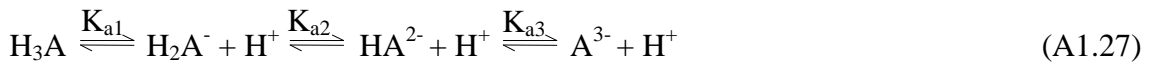
$$[H^+] = 10^{-pH} \quad (A1.24)$$

$$K_a = 10^{-pK_a} \quad (\text{A1.25})$$

$$\frac{AV}{n_{\text{tot}}l} = \frac{\epsilon_{\text{H}_2\text{A}} 10^{-2\text{pH}} + \epsilon_{\text{HA}^-} 10^{-\text{pH}-\text{pK}_{a1}} + \epsilon_{\text{A}^{2-}} 10^{-\text{pK}_{a1}-\text{pK}_{a2}}}{10^{-2\text{pH}} + 10^{-\text{pH}-\text{pK}_{a1}} + 10^{-\text{pK}_{a1}-\text{pK}_{a2}}} \quad (\text{A1.26})$$

Triple pK_a system

The deprotonation of a triprotic acid is given by equation A1.27 where the equilibrium constants K_{a1} , K_{a2} and K_{a3} are given by equations A1.28-A1.30 where $[\text{H}_3\text{A}]$, $[\text{H}_2\text{A}^-]$, $[\text{HA}^{2-}]$, $[\text{A}^{3-}]$ are the concentrations of the triprotonated, diprotonated, protonated and unprotonated species, respectively, and $[\text{H}^+]$ is the concentration of protons released.



$$K_{a1} = \frac{[\text{H}_2\text{A}^-][\text{H}^+]}{[\text{H}_3\text{A}]} \quad (\text{A1.28})$$

$$K_{a2} = \frac{[\text{HA}^{2-}][\text{H}^+]}{[\text{H}_2\text{A}^-]} \quad (\text{A1.29})$$

$$K_{a3} = \frac{[\text{A}^{3-}][\text{H}^+]}{[\text{HA}^{2-}]} \quad (\text{A1.30})$$

The mole fractions, $\alpha_{\text{H}_3\text{A}}$, $\alpha_{\text{H}_2\text{A}^-}$, $\alpha_{\text{HA}^{2-}}$ and $\alpha_{\text{A}^{3-}}$ for each of the triprotonated, diprotonated, protonated and unprotonated species are given by equations A1.31-A1.34, where C_{tot} (mol dm⁻³) is the total concentration.

$$\alpha_{\text{H}_3\text{A}} = \frac{[\text{H}_3\text{A}]}{C_{\text{tot}}} = \frac{[\text{H}^+]^3}{[\text{H}^+]^3 + [\text{H}^+]^2 K_{a1} + [\text{H}^+] K_{a1} K_{a2} + K_{a1} K_{a2} K_{a3}} \quad (\text{A1.31})$$

$$\alpha_{\text{H}_2\text{A}^-} = \frac{[\text{H}_2\text{A}^-]}{C_{\text{tot}}} = \frac{[\text{H}^+]^2 K_{a1}}{[\text{H}^+]^3 + [\text{H}^+]^2 K_{a1} + [\text{H}^+] K_{a1} K_{a2} + K_{a1} K_{a2} K_{a3}} \quad (\text{A1.32})$$

$$\alpha_{\text{HA}^{2-}} = \frac{[\text{HA}^{2-}]}{C_{\text{tot}}} = \frac{[\text{H}^+] K_{a1} K_{a2}}{[\text{H}^+]^3 + [\text{H}^+]^2 K_{a1} + [\text{H}^+] K_{a1} K_{a2} + K_{a1} K_{a2} K_{a3}} \quad (\text{A1.33})$$

$$\alpha_{\text{A}^{3-}} = \frac{[\text{A}^{3-}]}{C_{\text{tot}}} = \frac{K_{a1} K_{a2} K_{a3}}{[\text{H}^+]^3 + [\text{H}^+]^2 K_{a1} + [\text{H}^+] K_{a1} K_{a2} + K_{a1} K_{a2} K_{a3}} \quad (\text{A1.34})$$

For a mixture of species the total absorbance A can be expressed as the sum of the absorbance of H_3A , H_2A^- , HA^{2-} and A^{3-} as given by equation A1.35. The Beer-Lambert law can be applied to the mixture as expressed in equation A1.36, where $\epsilon_{\text{H}_3\text{A}}$, $\epsilon_{\text{H}_2\text{A}^-}$, $\epsilon_{\text{HA}^{2-}}$ and $\epsilon_{\text{A}^{3-}}$ ($\text{dm}^3 \text{mol}^{-1} \text{cm}^{-1}$) are the absorption coefficients of the triprotonated, diprotonated, protonated and unprotonated, respectively, and l is the pathlength of the cell (cm).

$$A = A_{\text{H}_3\text{A}} + A_{\text{H}_2\text{A}^-} + A_{\text{HA}^{2-}} + A_{\text{A}^{3-}} \quad (\text{A1.35})$$

$$A = \epsilon_{\text{H}_3\text{A}} [\text{H}_3\text{A}]l + \epsilon_{\text{H}_2\text{A}^-} [\text{H}_2\text{A}^-]l + \epsilon_{\text{HA}^{2-}} [\text{HA}^{2-}]l + \epsilon_{\text{A}^{3-}} [\text{A}^{3-}]l \quad (\text{A1.36})$$

Substitutions of equations A1.31-A1.34 into A1.36 gives an expression for A in terms of K_{a1} , K_{a2} and K_{a3} and $[\text{H}^+]$ as shown in equation A1.37.

$$A = \frac{C_{\text{tot}} l \left(\epsilon_{\text{H}_3\text{A}} [\text{H}^+]^3 + \epsilon_{\text{H}_2\text{A}^-} [\text{H}^+]^2 K_{a1} + \epsilon_{\text{HA}^{2-}} [\text{H}^+] K_{a1} K_{a2} + \epsilon_{\text{A}^{3-}} K_{a1} K_{a2} K_{a3} \right)}{[\text{H}^+]^3 + [\text{H}^+]^2 K_{a1} + [\text{H}^+] K_{a1} K_{a2} + K_{a1} K_{a2} K_{a3}} \quad (\text{A1.37})$$

The total concentration, C_{tot} is given by equation A1.35 where n_{tot} (mol) is the total number of moles of species in solution and V (dm^3) is the solution volume.

$$C_{\text{tot}} = \frac{n_{\text{tot}}}{V} \quad (\text{A1.38})$$

Substitution of equation A1.37 by equation A1.38 gives an expression for the experimental data in terms of K_{a1} , K_{a2} and K_{a3} and $[H^+]$ as shown by equation A1.39.

$$\frac{AV}{n_{\text{tot}}l} = \frac{\epsilon_{H_3A}[H^+]^3 + \epsilon_{H_2A^-}[H^+]^2 K_{a1} + \epsilon_{HA^{2-}}[H^+] K_{a1} K_{a2} + \epsilon_{A^{3-}} K_{a1} K_{a2} K_{a3}}{[H^+]^3 + [H^+]^2 K_{a1} + [H^+] K_{a1} K_{a2} + K_{a1} K_{a2} K_{a3}} \quad (\text{A1.39})$$

Using equations A1.40-1.41, equation A1.39 can be expressed in terms of pH and pK_a and used for analysis as given by equation A1.42.

$$[H^+] = 10^{-\text{pH}} \quad (\text{A1.40})$$

$$K_a = 10^{-pK_a} \quad (\text{A1.41})$$

$$\frac{AV}{n_{\text{tot}}l} = \frac{\epsilon_{H_3A} 10^{-3\text{pH}} + \epsilon_{H_2A^-} 10^{-2\text{pH}-pK_{a1}} + \epsilon_{HA^{2-}} 10^{-\text{pH}-pK_{a1}-pK_{a2}} + \epsilon_{A^{3-}} 10^{-pK_{a1}-pK_{a2}-pK_{a3}}}{10^{-3\text{pH}} + 10^{-2\text{pH}-pK_{a1}} + 10^{-\text{pH}-pK_{a1}-pK_{a2}} + 10^{-pK_{a1}-pK_{a2}-pK_{a3}}} \quad (\text{A1.42})$$

A1.2 Solvent dependence data

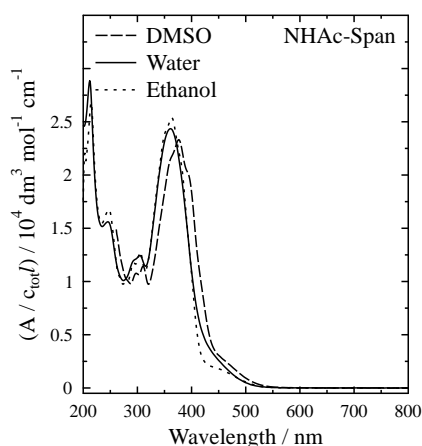


Figure A1.1 Profile of NHAc-Span in DMSO, water and ethanol at $5 \times 10^{-5} \text{ mol dm}^{-3}$.

A1.3 DFT calculations

A1.3.1 Optimisations

Table A1.1 Bond lengths (Å) of the optimised structures; differences (Δ) given for bond lengths (10^{-3} Å) from the values of H-Span.

Bond	H-	NH ₂ -	Δ (NH ₂)	OH-	Δ (OH)	OMe-	Δ (OMe)	NHAc-	Δ (NHAc)	Br-	Δ (Br)	CN	Δ (CN)
C1-C2	1.380	1.381	+1	1.381	+1	1.381	+1	1.381	+1	1.380	0	1.380	0
C2-C3	1.420	1.421	+1	1.421	+1	1.421	+1	1.421	0	1.420	0	1.420	0
C3-C4	1.370	1.370	0	1.370	0	1.370	0	1.370	0	1.370	0	1.370	0
C4-C10	1.436	1.436	0	1.436	0	1.436	0	1.436	0	1.436	0	1.436	0
C10-C5	1.420	1.419	0	1.419	0	1.419	-1	1.419	0	1.420	0	1.420	0
C5-C6	1.377	1.377	0	1.377	0	1.377	0	1.377	0	1.377	0	1.377	0
C6-C7	1.409	1.409	0	1.409	0	1.409	0	1.409	0	1.409	0	1.410	0
C7-C8	1.378	1.378	0	1.378	0	1.378	0	1.378	0	1.378	0	1.377	0
C8-C9	1.431	1.431	0	1.431	0	1.431	0	1.431	0	1.431	0	1.431	0
C9-C10	1.439	1.439	0	1.439	0	1.439	0	1.439	0	1.439	0	1.439	0
C1-C9	1.419	1.418	-1	1.419	0	1.419	0	1.419	0	1.419	0	1.419	0
C1-H1	1.082	1.082	0	1.082	0	1.082	0	1.082	0	1.082	0	1.082	0
C7-H7	1.084	1.084	0	1.084	0	1.084	0	1.084	0	1.084	0	1.084	0
C6-H6	1.085	1.085	0	1.085	0	1.085	0	1.085	0	1.085	0	1.085	0
C5-H5	1.082	1.082	0	1.082	0	1.082	0	1.082	0	1.082	0	1.082	0
C4-S4	1.799	1.798	-1	1.799	0	1.799	-1	1.798	-1	1.799	0	1.800	-1
C3-H3	1.083	1.083	0	1.083	0	1.083	0	1.083	0	1.083	0	1.083	0
C8-S8	1.796	1.795	-1	1.795	-1	1.795	-1	1.795	0	1.796	0	1.797	+1
S8-O	1.462	1.463	+1	1.462	0	1.462	0	1.462	0	1.462	0	1.462	0
S8-O	1.455	1.455	0	1.455	0	1.455	0	1.455	0	1.455	0	1.455	0
S8-O	1.648	1.649	+1	1.649	0	1.649	+1	1.649	0	1.648	0	1.648	0
S4-O	1.650	1.650	+9	1.650	+4	1.650	+4	1.650	+4	1.462	0	1.648	-1
S4-O	1.455	1.456	+3	1.455	+1	1.455	+1	1.455	+1	1.455	0	1.455	0
S4-O	1.461	1.461	+4	1.461	+1	1.461	+1	1.461	+1	1.648	0	1.461	0
C2-N α	1.416	1.413	-3	1.414	-2	1.414	-2	1.415	-1	1.415	-1	1.415	-2
N α -N β	1.261	1.268	+7	1.264	+3	1.265	+4	1.264	+3	1.262	0	1.261	0
N β -C11	1.414	1.399	-15	1.405	-9	1.405	-9	1.406	-8	1.413	-1	1.416	+2
C11-C16	1.407	1.411	+4	1.408	+1	1.406	-1	1.407	0	1.407	0	1.407	0
C16-C15	1.389	1.381	-8	1.385	-4	1.388	-1	1.386	-3	1.388	-1	1.386	-3
C15-C14	1.402	1.415	+14	1.407	+5	1.408	+6	1.411	+9	1.400	-2	1.410	+8
C14-C13	1.396	1.409	+13	1.401	+5	1.405	+9	1.407	+11	1.394	-2	1.405	+8
C13-C12	1.393	1.385	-8	1.387	-6	1.384	-9	1.386	-7	1.392	-1	1.390	-4
C12-C11	1.402	1.406	+4	1.405	+3	1.407	+5	1.403	+1	1.402	0	1.402	0
C12-H12	1.086	1.086	0	1.086	0	1.086	0	1.085	-1	1.086	0	1.085	0
C13-H13	1.086	1.087	+1	1.085	-1	1.085	-1	1.088	+2	1.084	-2	1.085	-1
C15-H15	1.087	1.088	+1	1.089	+2	1.084	-3	1.081	-6	1.084	-2	1.085	-1
C16-H16	1.084	1.084	0	1.084	0	1.084	0	1.084	0	1.084	0	1.084	0
C14-H14	1.087	-	-	-	-	-	-	-	-	-	-	-	-
C14-O14	-	-	-	1.360	-	1.356	-	-	-	-	-	-	-
C14-N γ	-	1.381	-	-	-	-	-	1.403	-	-	-	-	-
C14-Br	-	-	-	-	-	-	-	-	-	1.906	-	-	-
C14-C17	-	-	-	-	-	-	-	-	-	-	-	1.433	-
C17-N γ	-	-	-	-	-	-	-	-	-	-	-	1.163	-
O14-H14	-	-	-	0.970	-	-	-	-	-	-	-	-	-
O14-C18	-	-	-	-	-	1.423	-	-	-	-	-	-	-
C18-N γ	-	-	-	-	-	-	-	1.386	-	-	-	-	-
C17-O17	-	-	-	-	-	-	-	1.220	-	-	-	-	-
C17-C18	-	-	-	-	-	-	-	1.522	-	-	-	-	-
C18-H18	-	-	-	-	-	1.091	-	1.092	-	-	-	-	-
C18-H18	-	-	-	-	-	1.097	-	-	-	-	-	-	-
C18-H18	-	-	-	-	-	1.097	-	-	-	-	-	-	-
N γ -H	-	1.011	-	-	-	-	-	1.011	-	-	-	-	-

Table A1.2 Bond angles (°) of the optimised structures; differences (Δ) given for angles (°) from the values of H-Span.

Angle	H-	NH ₂ -	Δ (NH ₂)	OH-	Δ (OH)	OMe-	Δ (OMe)	NHAc-	Δ (NHAc)	Br-	Δ H(Br)	CN	Δ (CN)
C1-C2-C3	120.2	119.9	-0.3	120.1	-0.1	120.1	-0.2	120.1	-0.1	120.3	0.0	120.4	0.0
C2-C4-C4	119.5	119.6	+0.2	119.5	+0.1	119.5	+0.1	119.6	+0.1	119.4	0.0	119.3	0.0
C3-C4-C10	122.6	122.7	+0.1	122.6	0.0	122.6	0.0	122.6	0.0	122.6	0.0	122.6	0.0
C4-C10-C9	117.1	116.9	-0.1	117.0	-0.1	117.0	-0.1	117.0	-0.1	117.1	0.0	117.2	0.0
C10-C9-C1	119.4	119.4	+0.1	119.4	0.0	119.4	0.0	119.4	+0.1	119.3	0.0	119.3	0.0
C10-C5-C6	121.3	121.4	+0.2	121.4	+0.1	121.4	+0.1	121.3	0.0	121.3	0.0	121.2	0.0
C5-C6-C7	120.9	121.0	+0.1	121.0	0.0	121.0	0.0	121.0	0.0	120.9	0.0	120.9	0.0
C6-C7-C8	120.6	120.6	-0.1	120.6	0.0	120.6	0.0	120.6	0.0	120.6	0.0	120.7	0.0
C7-C8-C9	119.7	119.7	0.0	119.7	0.0	119.7	0.0	119.7	0.0	119.7	0.0	119.7	0.0
C8-C9-C10	122.0	122.1	+0.1	122.1	0.0	122.1	+0.1	122.1	0.0	122.0	0.0	122.0	0.0
C9-C10-C5	117.3	117.2	-0.1	117.3	0.0	117.3	-0.1	117.3	-0.1	117.4	0.0	117.4	0.0
C1-C2-N α	119.4	119.4	0.0	119.4	0.0	119.4	0.0	119.4	+0.1	119.4	0.0	119.3	0.0
N α -C2-C3	123.8	123.9	+0.1	123.9	+0.1	123.8	0.0	123.8	-0.1	123.8	0.0	123.9	0.0
C2-C3-H3	119.2	119.1	-0.1	119.2	0.0	119.2	0.0	119.2	-0.1	119.4	+0.1	119.5	+0.1
H3-C3-C4	121.3	121.3	0.0	121.3	-0.1	121.3	-0.1	121.3	0.0	121.2	-0.1	121.2	-0.1
C3-C4-S4	115.7	115.7	0.0	115.7	0.0	115.7	0.0	115.7	0.0	115.7	0.0	115.7	0.0
S4-C4-C10	121.7	121.6	0.0	121.6	0.0	121.6	-0.1	121.7	0.0	119.8	-1.8	121.7	-1.8
C4-C10-C5	123.5	123.6	+0.1	123.6	0.0	123.6	0.0	123.6	0.0	123.5	0.0	123.5	0.0
C10-C5-H5	119.6	119.6	0.0	119.6	0.0	119.6	0.0	119.6	0.0	119.7	0.0	119.7	0.0
H5-C5-C6	119.4	119.4	0.0	119.4	0.0	119.4	0.0	119.4	0.0	119.4	0.0	119.4	0.0
C5-C6-H6	119.9	120.0	0.0	119.9	0.0	120.0	0.0	120.0	0.0	119.9	0.0	119.9	0.0
H6-C6-C7	119.5	119.5	0.0	119.5	0.0	119.5	0.0	119.5	0.0	119.4	0.0	119.4	0.0
C6-C7-H7	120.7	120.7	0.0	120.7	0.0	120.8	0.0	120.7	0.0	120.8	0.0	120.8	0.0
H7-C7-C8	119.6	119.5	0.0	119.6	0.0	119.5	0.0	119.6	0.0	119.6	0.0	119.6	0.0
C7-C8-S8	116.0	116.0	-0.1	116.0	0.0	116.0	0.0	116.0	0.0	116.1	0.0	116.1	0.0
S8-C8-C9	122.0	122.0	0.0	121.9	0.0	121.9	0.0	122.0	0.0	121.9	0.0	121.9	0.0
C8-C9-C1	123.3	123.4	+0.1	123.3	0.0	123.3	0.0	123.3	0.0	123.3	0.0	123.3	0.0
C9-C1-H1	121.0	121.0	0.0	121.0	0.0	121.0	0.0	121.0	0.0	121.0	0.0	121.0	0.0
H1-C1-C2	117.7	117.6	-0.2	117.6	-0.1	117.7	-0.1	117.7	0.0	117.7	0.0	117.8	0.0
C8-S8-O	108.6	108.6	0.0	108.6	0.0	108.6	0.0	108.6	0.0	108.6	0.0	108.6	0.0
C8-S8-O	109.8	109.9	+0.2	109.9	+0.1	109.9	+0.1	109.8	0.0	109.7	0.0	109.6	0.0
O-S8-O	102.0	102.2	+0.2	102.1	+0.1	102.0	+0.1	101.9	0.0	101.9	-0.1	101.8	-0.1
O-S8-O	121.8	121.7	-0.1	121.8	0.0	121.8	-0.1	121.8	-0.1	121.9	0.0	121.9	0.0
O-S8-O	106.7	106.6	-0.1	106.7	0.0	106.7	-0.1	106.7	-0.1	106.8	0.0	106.8	0.0
O-S8-O	106.1	105.9	-0.1	106.0	-0.1	106.0	-0.1	106.2	+0.1	106.1	+0.1	106.2	+0.1
C4-S4-O	109.7	109.8	+0.1	109.7	0.0	109.8	+0.1	109.8	+0.1	109.7	0.0	109.6	0.0
C4-S4-O	108.8	108.9	+0.1	108.8	0.0	108.9	0.0	108.8	0.0	108.8	0.0	108.8	0.0
C4-S4-O	101.8	101.9	+0.1	101.8	0.0	101.8	0.0	101.9	0.0	101.7	-0.1	101.6	-0.1
O-S4-O	121.9	121.8	-0.1	121.8	0.0	121.8	-0.1	121.8	-0.1	121.9	0.0	121.9	0.0
O-S4-O	105.9	105.8	-0.2	105.9	0.0	105.9	0.0	105.9	0.0	106.1	+0.1	106.2	+0.1
O-S4-O	106.8	106.7	-0.1	106.8	0.0	106.8	0.0	106.7	-0.1	106.8	0.0	106.8	0.0
C2-N α -N β	114.1	114.0	-0.1	114.1	0.0	114.0	-0.1	113.9	-0.2	114.2	+0.1	114.4	+0.1
N α -N β -C11	115.2	115.6	+0.4	115.4	0.2	115.5	+0.3	115.4	+0.3	115.0	-0.2	114.7	-0.2
N β -C11-C16	124.7	125.1	+0.4	124.8	+0.1	125.0	+0.3	125.3	+0.6	124.7	0.0	124.6	0.0
C11-C16-C15	119.4	120.3	+0.9	120.0	+0.6	120.5	+1.1	120.9	+1.4	119.9	+0.5	119.7	+0.5
C16-C15-C14	120.4	120.8	+0.4	120.1	-0.3	119.8	-0.6	119.7	-0.7	119.4	-1.0	120.1	-1.0
C15-C14-C13	120.2	118.8	-1.4	120.3	+0.1	119.9	-0.2	119.5	-0.7	121.4	+1.2	120.1	+1.2
C14-C13-C12	119.8	120.2	+0.4	119.3	-0.4	119.8	+0.1	120.4	+0.6	118.8	-0.9	119.6	-0.9
C13-C12-C11	120.1	121.0	+0.9	120.9	+0.8	120.7	+0.6	120.4	+0.3	120.5	+0.4	120.3	+0.4
C12-C11-C16	120.1	118.9	-1.2	119.4	-0.8	119.2	-0.9	119.1	-1.0	118.5	-1.6	120.1	-1.6
C11-C16-H16	119.0	118.8	-0.3	119.0	-0.1	118.8	-0.2	118.8	-0.2	119.1	+0.1	119.1	+0.1
H16-C16-C15	121.5	120.9	-0.6	121.0	-0.5	120.7	-0.9	120.3	-1.2	120.9	-0.6	121.1	-0.6
C16-C15-H15	119.8	120.1	+0.3	120.2	+0.4	119.4	-0.3	121.1	+1.4	120.7	+0.9	120.5	+0.9
H15-C15-C14	119.8	119.2	-0.7	119.7	-0.1	120.7	+0.9	119.2	-0.7	119.9	+0.1	119.4	+0.1
C15-C14-H14	119.8	-	-	-	-	-	-	-	-	-	-	-	-
H14-C14-C13	120.0	-	-	-	-	-	-	-	-	-	-	-	-
C14-C13-H13	120.2	119.6	-0.7	119.0	-1.2	118.6	-1.7	119.8	-0.4	120.3	+0.1	119.8	-0.5
H13-C13-C12	120.0	120.3	+0.3	121.6	+1.6	121.6	+1.6	119.9	-0.1	120.9	+0.9	120.7	+0.7
C13-C12-H12	121.6	120.8	-0.8	120.9	-0.7	121.0	-0.6	121.1	-0.5	120.9	-0.6	121.2	-0.4
H12-C12-C11	118.3	118.2	-0.2	118.2	-0.1	118.3	0.0	118.5	+0.2	118.5	+0.2	118.5	+0.2
C12-C11-N β	115.2	116.0	+0.8	115.8	+0.6	115.8	+0.6	115.6	+0.4	115.4	+0.3	115.3	+0.1
C15-C14-O14	-	-	-	122.4	-	124.4	-	-	-	-	-	-	-
O14-C14-C13	-	-	-	117.4	-	115.6	-	-	-	-	-	-	-
C14-O14-H	-	-	-	109.4	-	-	-	-	-	-	-	-	-
C14-O14-C17	-	-	-	-	-	118.9	-	-	-	-	-	-	-
O14-C17-H	-	-	-	-	-	105.7	-	-	-	-	-	-	-
O14-C17-H	-	-	-	-	-	111.4	-	-	-	-	-	-	-
O14-C17-H	-	-	-	-	-	111.4	-	-	-	-	-	-	-
H-C17-H	-	-	-	-	-	109.4	-	-	-	-	-	-	-
H-C17-H	-	-	-	-	-	109.4	-	-	-	-	-	-	-
H-C17-H	-	-	-	-	-	109.4	-	-	-	-	-	-	-
C15-C14-C17	-	-	-	-	-	-	-	-	-	-	-	119.9	-
C17-C14-C15	-	-	-	-	-	-	-	-	-	-	-	120.0	-
C14-C17-N γ	-	-	-	-	-	-	-	-	-	-	-	179.9	-
C15-C14-Br	-	-	-	-	-	-	-	-	-	119.2	-	-	-
Br-C14-C13	-	-	-	-	-	-	-	-	-	119.4	-	-	-
C15-C14-N γ	-	120.3	-	-	-	-	-	123.2	-	-	-	-	-
N γ -C14-C13	-	120.8	-	-	-	-	-	117.3	-	-	-	-	-
C14-N γ -H	-	117.2	-	-	-	-	-	-	-	-	-	-	-
C14-N γ -H	-	117.3	-	-	-	-	-	-	-	-	-	-	-
H-N γ -H	-	113.6	-	-	-	-	-	-	-	-	-	-	-
C14-N γ -H	-	-	-	-	-	-	-	114.8	-	-	-	-	-
C14-N γ -C17	-	-	-	-	-	-	-	129.2	-	-	-	-	-
H-N γ -C17	-	-	-	-	-	-	-	115.9	-	-	-	-	-
N γ -C17-O17	-	-	-	-	-	-	-	123.8	-	-	-	-	-
N γ -C17-C18	-	-	-	-	-	-	-	114.0	-	-	-	-	-
O17-C17-C18	-	-	-	-	-	-	-	122.2	-	-	-	-	-
C17-C18-H	-	-	-	-	-	-	-	108.4	-	-	-	-	-
C17-C18-H	-	-	-	-	-	-	-	113.6	-	-	-	-	-
C17-C18-H	-	-	-	-	-	-	-	109.2	-	-	-	-	-
H-C18-H	-	-	-	-	-	-	-	107.8	-	-	-	-	-
H-C18-H	-	-	-	-	-	-	-	109.3	-	-	-	-	-
H-C18-H	-	-	-	-	-	-	-	108.4	-	-	-	-	-

A1.4.2 Electronic structure

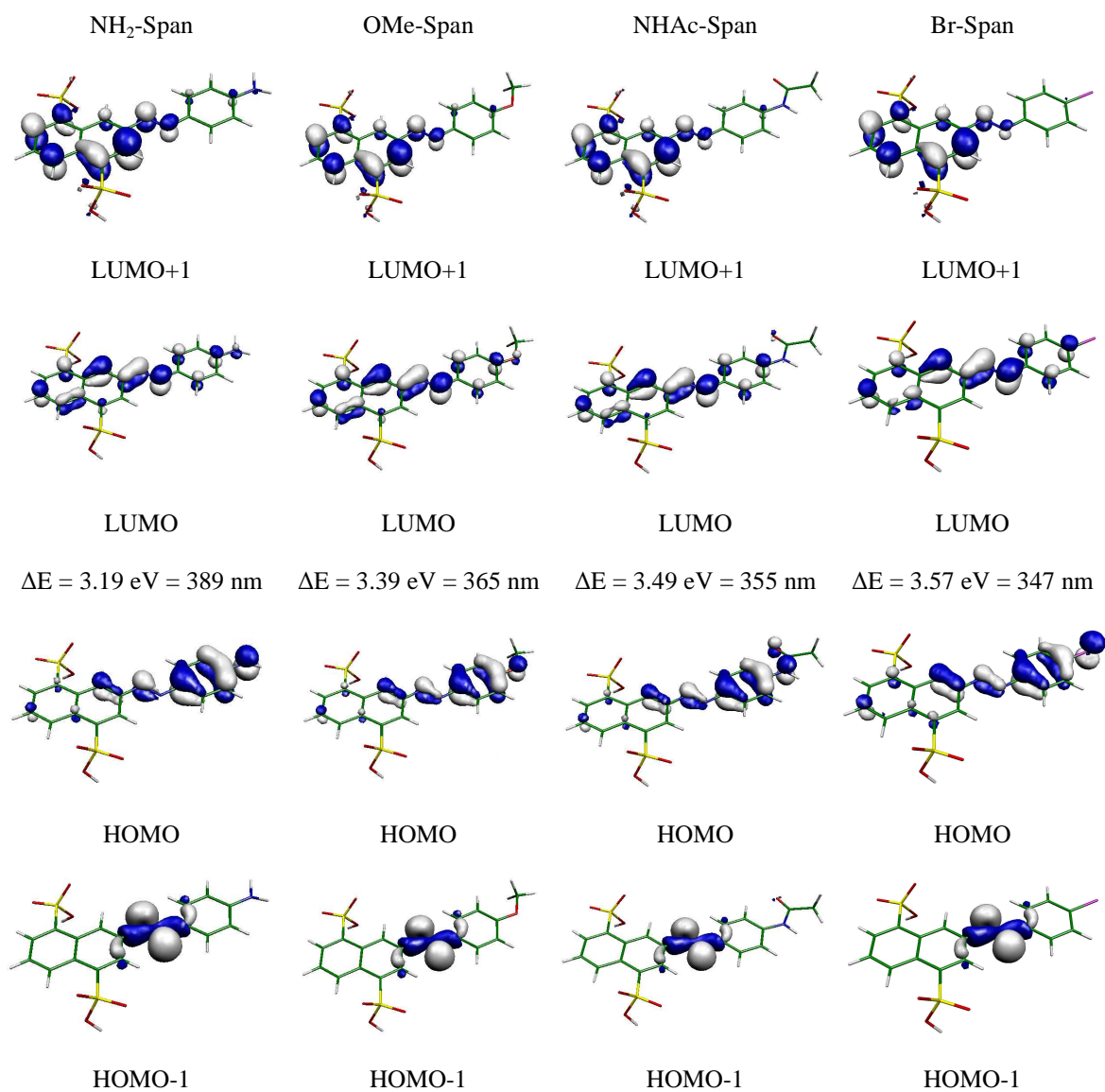


Figure A1.2 Calculated HOMO-1, HOMO, LUMO, LUMO+1 and energy difference for NH₂-Span, NHAc-Span, OMe-Span and Br-Span. (*Original in colour*)

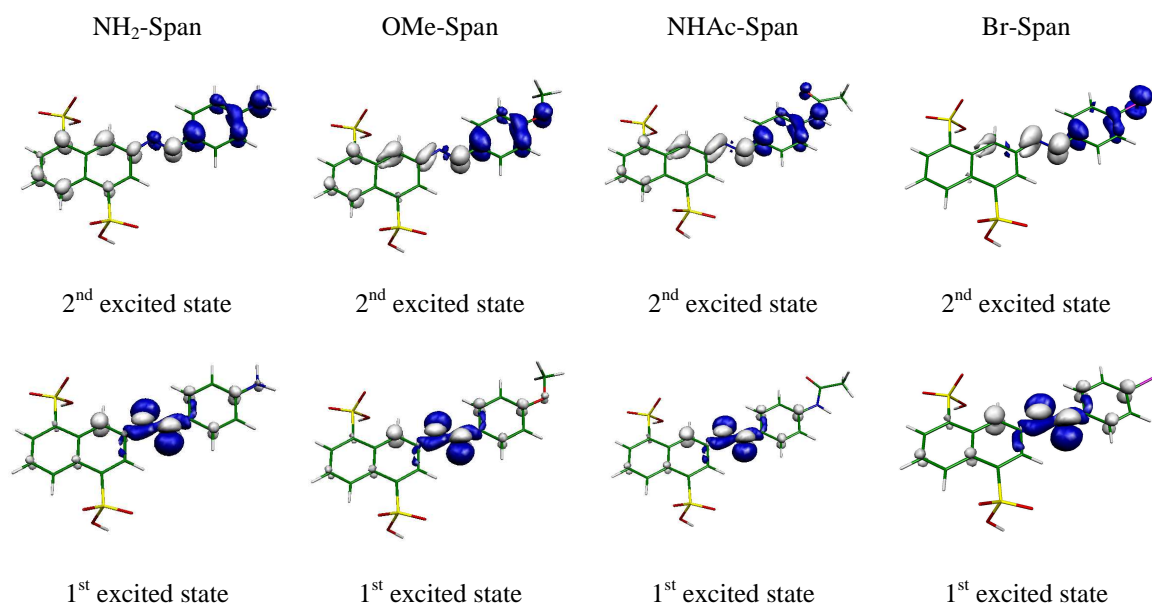


Figure A1.3 Calculated changes in electron density on excitation of the first (top) and second (bottom) excited states for H-Span (left) and OH-Span (middle) and NH₂-Span (right). Blue and white regions represent a decrease and increase in electron density on excitation, respectively. (*Original in colour*)

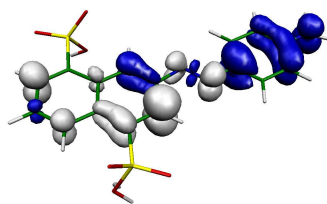


Figure A1.4 3rd excited state of NH₂-Span. (*Original in colour*)

Table A1.3 Calculated transition energies (E), wavelengths (λ), and oscillator strengths (f) for the excited states of NH₂-Span.

Excited state	E / eV	λ / nm	f
1 st	2.57	483	0.0001
2 nd	3.04	407	0.8002
3 rd	3.39	366	0.3187
4 th	3.56	349	0.0003
5 th	3.96	313	0.0787
6 th	4.06	305	0.0128
7 th	4.23	293	0.0512
8 th	4.55	273	0.1747
9 th	4.67	266	0.0022
10 th	4.78	259	0.0398

Table A1.4 Calculated transition energies (E), wavelengths (λ), and oscillator strengths (f) for the excited states of OH-Span.

Excited state	E / eV	λ / nm	f
1 st	2.56	484	0.0001
2 nd	3.27	379	0.8843
3 rd	3.58	347	0.1305
4 th	3.63	342	0.0022
5 th	3.98	311	0.1238
6 th	4.06	305	0.0461
7 th	4.03	288	0.0254
8 th	4.67	266	0.1678
9 th	4.86	255	0.0096
10 th	4.87	254	0.0012

Table A1.5 Calculated transition energies (E), wavelengths (λ), and oscillator strengths (f) for the excited states of OMe-Span.

Excited state	E / eV	λ / nm	f
1 st	2.54	487	0.0002
2 nd	3.20	388	0.9052
3 rd	3.54	350	0.1505
4 th	3.61	344	0.0022
5 th	3.96	314	0.0907
6 th	4.06	308	0.0760
7 th	4.28	289	0.0315
8 th	4.59	270	0.1727
9 th	4.63	268	0.0115
10 th	4.81	257	0.0006

Table A1.6 Calculated transition energies (E), wavelengths (λ), and oscillator strengths (f) for the excited states of NHAc-Span.

Excited state	E / eV	λ / nm	f
1 st	2.52	492	0.0000
2 nd	3.16	392	1.0945
3 rd	3.54	350	0.1135
4 th	3.62	343	0.0002
5 th	3.92	316	0.1119
6 th	3.94	314	0.0306
7 th	4.01	309	0.0004
8 th	4.22	293	0.0527
9 th	4.59	270	0.2139
10 th	4.78	259	0.0007

Table A1.7 Calculated transition energies (E), wavelengths (λ), and oscillator strengths (f) for the excited states of H-Span.

Excited state	E / eV	λ / nm	f
1 st	2.51	495	0.0001
2 nd	3.51	353	0.8963
3 rd	3.65	340	0.0002
4 th	3.71	334	0.0001
5 th	3.80	327	0.0410
6 th	4.11	301	0.2779
7 th	4.44	279	0.0056
8 th	4.63	268	0.0075
9 th	4.79	259	0.1291
10 th	4.94	251	0.0020

Table A1.8 Calculated transition energies (E), wavelengths (λ), and oscillator strengths (f) for the excited states of Br-Span.

Excited state	E / eV	λ / nm	f
1 st	2.51	493	0.0001
2 nd	3.34	371	1.0520
3 rd	3.64	340	0.0025
4 th	3.72	333	0.0002
5 th	3.97	313	0.0296
6 th	4.01	309	0.1718
7 th	4.25	291	0.0396
8 th	4.56	272	0.0000
9 th	4.67	265	0.1902
10 th	4.87	254	0.0093

Table A1.9 Calculated transition energies (E), wavelengths (λ), and oscillator strengths (f) for the excited states of CN-Span.

Excited state	E / eV	λ / nm	f
1 st	2.45	506	0.0001
2 nd	3.38	366	0.9553
3 rd	3.63	342	0.1983
4 th	3.81	325	0.0004
5 th	3.93	315	0.0296
6 th	4.17	302	0.2338
7 th	4.29	289	0.0002
8 th	4.69	264	0.1214
9 th	4.77	259	0.0023
10 th	4.83	256	0.0004

Table A1.10 Calculated dipole moments (D) for the ground state, 1st and 2nd excited states of the R-Span dye series.

Dye	Dipole moment / D		
	Ground state	1 st excited state	2 nd excited state
NH ₂ -Span	6.42	7.90	25.50
OH-Span	5.31	6.23	17.19
OMe-Span	5.69	6.76	19.15
NHAc-Span	6.96	7.93	19.08
H-Span	4.81	5.82	6.85
Br-Span	4.63	4.82	9.91
CN-Span	6.36	6.29	10.82

A1.4 NMR spectroscopy

Table A1.11 HSQC and HMBC of NH₂-Span in DMSO-d₆, ● direct attachment ○ adjacent attachment.

		Proton														
		1	3	5	6	7	12	13	15	16						
Carbon	1	●	○													
	2	○														
	3	○	●													
	4			○												
	5			●		○										
	6			○	●											
	7			○	○	●										
	8				○											
	9	○					○									
	10		○	○	○											
	11							○								○
	12						●	○	○							○
	13							●	○							
	14							○	○							
	15							○	●							
	16							○								●

Table A1.12 HSQC and HMBC of NH₂-Span in D₂O, ● direct attachment ○ adjacent attachment.

		Proton														
		1	3	5	6	7	12	13	15	16						
Carbon	1	●														
	2	○														
	3	○	●													
	4			○												
	5			●	○											
	6			○	●											
	7				○	●										
	8				○	○										
	9	○	○													
	10		○		○	○										
	11							○								○
	12						●	○	○							○
	13							●	○							
	14							○	○	○						○
	15							○	○	●						
	16							○								●

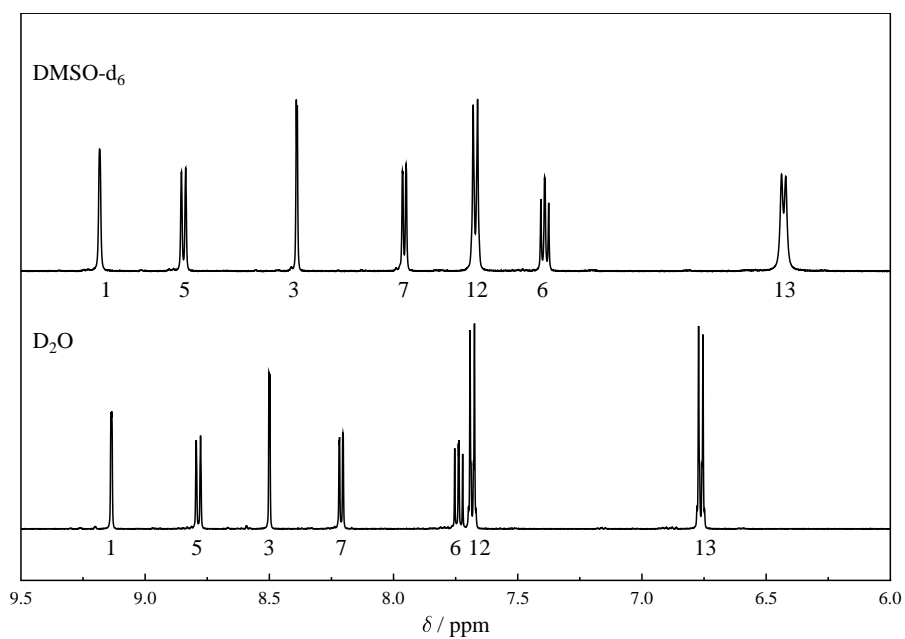


Figure A1.5 Aromatic region ^1H NMR spectrum of OH-Span in DMSO- d_6 (top) and D_2O (bottom).

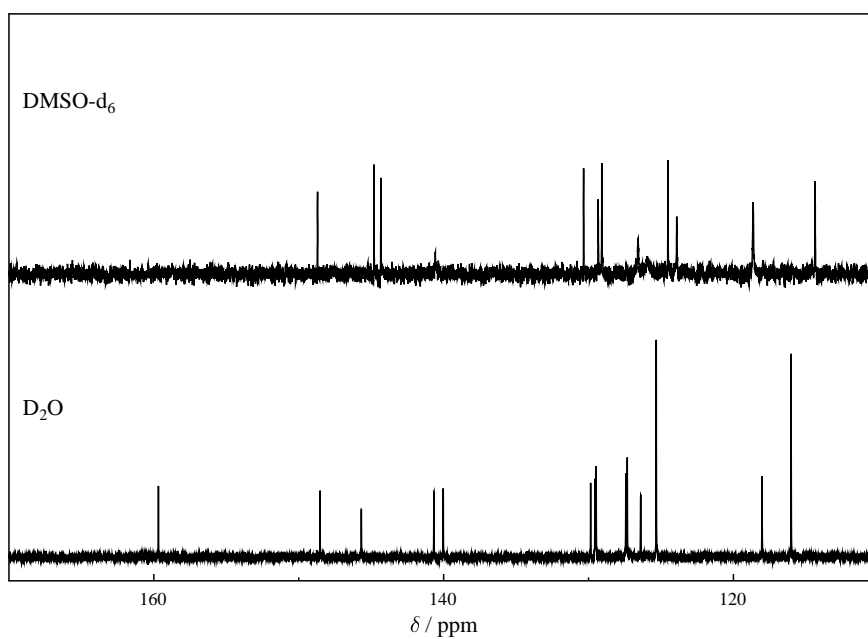


Figure A1.6 ^{13}C NMR spectrum of OH-Span in DMSO- d_6 (top) and D_2O (bottom).

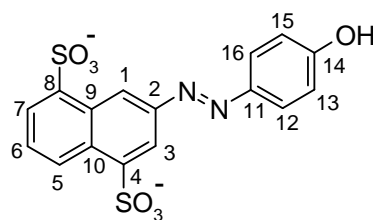


Figure A1.7 Structure of OH-Span with the numbering system used for NMR assignments.

Table A1.13 ^1H and ^{13}C NMR chemical shifts (ppm) of OH-Span in DMSO - d_6 and D_2O .

atom	Experimental								Calculated	
	DMSO				D ₂ O				^1H	^{13}C
	$^1\text{H}^a$		^{13}C		$^1\text{H}^a$		^{13}C			
1	9.18	1 d	1.0	126.6	9.14	1 d	1.0	126.4	9.29	130.0
2				148.7				148.5		143.0
3	8.39	1 d	2.0	114.3	8.50	1 d	2.0	118.0	8.60	111.6
4				144.8				140.7		136.8
5	8.84	1 d	8.5	129.1	8.79	1 d	8.0	129.5	8.77	127.0
6	7.74	1 t	8.5	123.9	7.74	1 t	8.0	127.4	7.58	119.9
7	7.96	1 d,d	7.0, 1.0	124.5	8.21	1 d,d	7.0, 1.0	127.3	8.01	122.4
8				144.3				140.0		136.1
9				129.4				129.9		124.4
10				130.4				129.6		123.8
11				140.5				145.7		139.7
12/16	7.67	2 d	9.0	125.9	7.68	2 d	9.0	125.3	8.04 ¹² , 7.95 ¹⁶	132.1 ¹² , 110.7 ¹⁶
13/15	6.43	2 d	9.0	118.6	6.76	2 d	9.0	116.0	6.95 ¹³ , 6.29 ¹⁵	109.3 ¹³ , 108.2 ¹⁵
14				140.6				159.7		152.6

^a Integration, multiplicity (s = singlet; d = doublet; t = triplet), splitting (Hz)

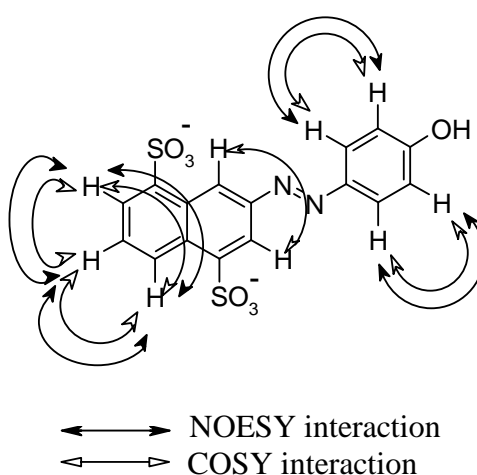


Figure A1.8 COSY and NOESY interactions for OH-Span in DMSO- d_6 and D_2O .

Table A1.14 HSQC and HMBC of OH-Span in DMSO-d₆, ● direct attachment ○ adjacent attachment.

Carbon	Proton								
	1	3	5	6	7	12	13	15	16
1	●	○							
2		○							
3	○	●							
4		○	○						
5			●		○				
6				●	○				
7			○	○	●				
8	○			○	○				
9		○		○					
10			○		○				
11									
12						●			
13							●	○	
14									
15							○	●	
16									●

Table A1.15 HSQC and HMBC of OH-Span in D₂O, ● direct attachment ○ adjacent attachment.

Carbon	Proton								
	1	3	5	6	7	12	13	15	16
1	●	○							
2	○	○							
3	○	●							
4		○							
5			●		○				
6			○	●					
7				○	●				
8	○			○					
9	○			○					
10			○		○				
11									
12						●			○
13							●	○	
14									
15							○	●	
16						○			●

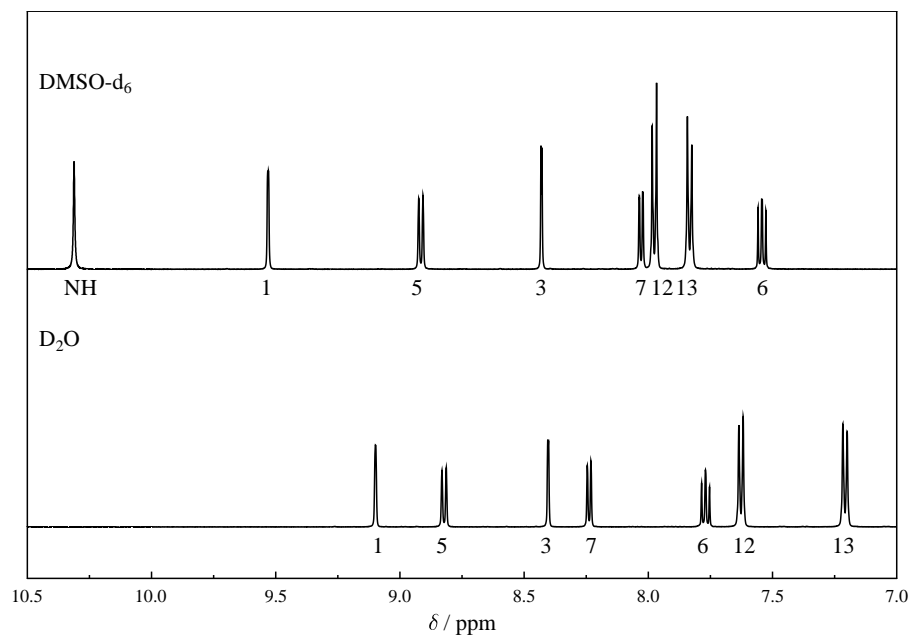


Figure A1.9 Aromatic region ^1H NMR spectrum of NHAc-Span in DMSO- d_6 (top) and D_2O (bottom).

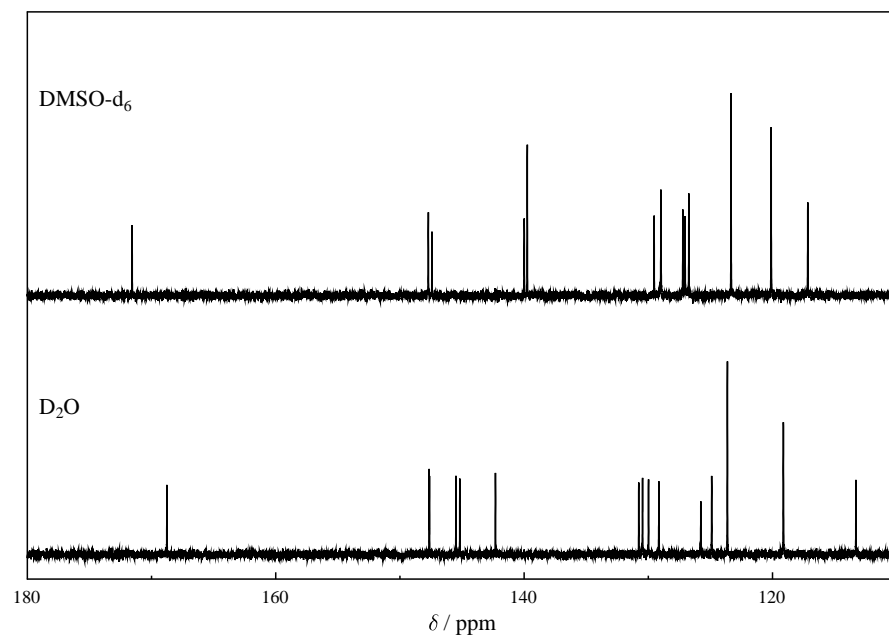


Figure A1.10 ^{13}C NMR spectrum of NHAc-Span in DMSO- d_6 (top) and D_2O (bottom).

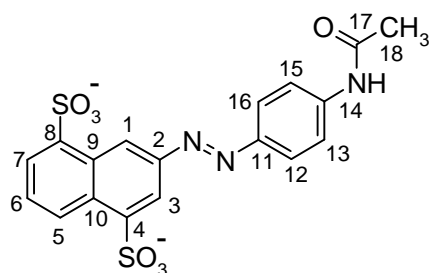


Figure A1.11 Structure of NHAc-Span with the numbering system used for NMR assignments.

Table A1.16 ^1H and ^{13}C NMR chemical shifts (ppm) of NHAc-Span in DMSO- d_6 and D_2O .

Atom	Experimental				Calculated			
	DMSO		D ₂ O		^1H	^{13}C		
	$^1\text{H}^a$	^{13}C	$^1\text{H}^a$	^{13}C				
1	9.53	1 s -	127.2	9.09	1 s -	130.8	9.32	130.4
2			147.7			147.6		143.1
3	8.43	1 s -	117.2	8.41	1 s -	113.3	8.59	111.6
4			140.0			145.5		136.6
5	8.92	1 d 9.0	129.0	8.83	1 d 9.0	129.2	8.75	126.8
6	7.54	1 t 8.0	127.0	7.77	1 t 8.0	125.9	7.58	120.0
7	8.03	1 d 7.0	126.7	8.24	1 d 8.0	124.9	8.03	122.3
8			139.7			145.2		136.2
9			129.4			130.5		124.5
10			129.0			130.0		123.8
11			139.7			142.3		141.0
12/16	7.98	2 d 9.0	123.3	7.64	2 d 9.0	123.6	7.92 ¹² , 8.02 ¹⁶	129.8 ¹² , 111.3 ¹⁶
13/15	7.83	2 d 9.0	120.1	7.21	2 d 9.0	119.1	6.43 ¹³ , 8.80 ¹⁵	109.7 ¹³ , 112.8 ¹⁵
14			147.4			147.6		137.0
NH	10.32	2 s -					6.03	
17			171.6			168.8		156.5
18	2.11	3 s -	22.6	1.86	3 s -	24.1	1.51, 1.98, 2.32	24.1

^a Integrations, multiplicity (s = singlet; d = doublet; t = triplet), splitting (Hz)

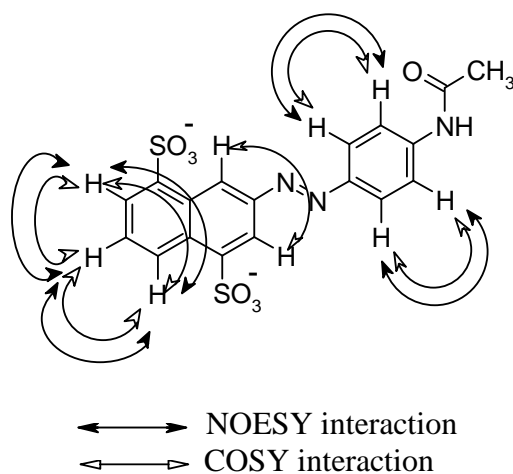


Figure A1.12 COSY and NOESY interactions for NHAc-Span in DMSO- d_6 and D_2O .

Table A1.17 HSQC and HMBC of NHAc-Span in DMSO-d₆, ● direct attachment ○ adjacent attachment.

Carbon	Proton											
	1	3	5	6	7	12	13	15	16	18	NH	
1	●	○										
2	○											
3	○	●										
4	○	○	○									
5			●	○	○							
6				●								
7			○	○	●							
8	○			○								
9	○		○		○							
10			○	○	○							
11						○	○	○	○			
12						●	○	○	○			
13						○	●	○	○			
14						○	○	○	○			
15								●				
16									●			
17												
18												●

Table A1.18 HSQC and HMBC of NHAc-Span in D₂O, ● direct attachment ○ adjacent attachment.

Carbon	Proton											
	1	3	5	6	7	12	13	15	16	18		
1	●	○										
2	○											
3	○	●			○							
4			○									
5			●	○	○							
6			○	●								
7			○		●							
8	○			○								
9												
10		○	○	○								
11						○	○	○	○			
12						●	○	○	○			
13						○	●	○	○			
14						○	○	○	○			
15								●				
16									●			
17												
18												●

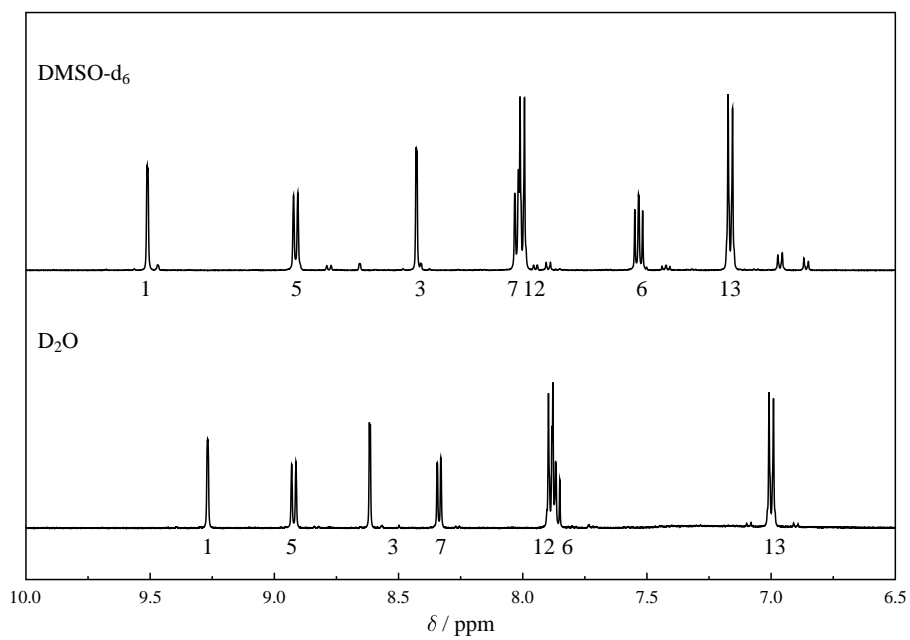


Figure A1.13 Aromatic region ¹H NMR spectrum of OMe-Span in DMSO-d₆ (top) and D₂O (bottom).

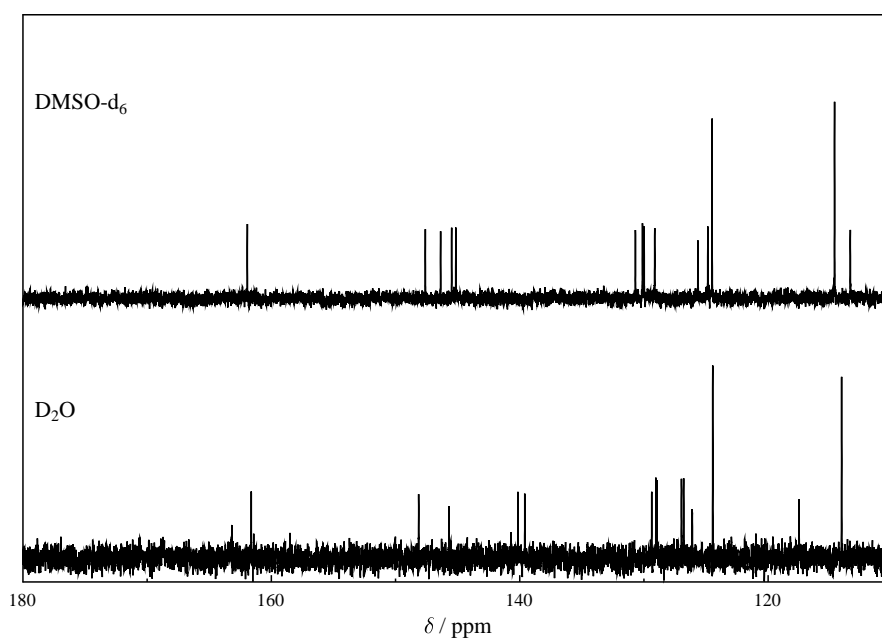


Figure A1.14 ¹³C NMR spectrum of OMe-Span in DMSO-d₆ (top) and D₂O (bottom).

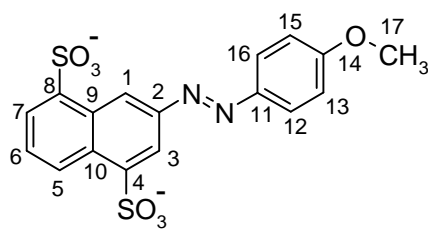


Figure A1.15 Structure of OMe-Span with the numbering system used for NMR assignments.

Table A1.19 ^1H and ^{13}C NMR chemical shifts (ppm) of OMe-Span in DMSO- d_6 and D_2O .

Atom	Experimental								Calculated	
	DMSO				D_2O				^1H	^{13}C
	$^1\text{H}^a$		^{13}C		$^1\text{H}^a$		^{13}C			
1	9.50	1 d	2.0	130.0	9.28	1 d	1.0	126.1	9.29	129.8
2				147.6				148.1		143.1
3	8.42	1 d	2.0	113.4	8.62	1 d	1.0	112.5	8.60	111.7
4				130.7				140.2		136.8
5	8.91	1 d	8.5	129.1	8.92	1 d	8.5	129.0	8.77	126.9
6	7.52	1 t	7.0	125.7	7.87	1 t	8.5	127.0	7.57	119.8
7	8.01	1 d	7.0	124.9	8.34	1 d,d	1.0 7.5	126.8	8.01	122.3
8				130.1				139.6		136.2
9				145.2				129.4		124.5
10				145.5				129.0		123.7
11				146.4				145.7		139.6
12/16	8.00	2 d	9.0	124.5	7.90	2 d	9.0	124.5	8.00 ¹² , 8.03 ¹⁶	131.0 ¹² , 110.6 ¹⁶
13/15	7.16	2 d	9.0	114.7	7.02	2 d	9.0	114.1	6.95 ¹³ , 6.55 ¹⁵	112.0 ¹³ , 104.2 ¹⁵
14				161.9				161.6		155.5
17	3.89	3 s	-	55.6	3.80	3 s	-	55.04		52.7

^a Integration, multiplicity (s = singlet; d = doublet; t = triplet), splitting (Hz)

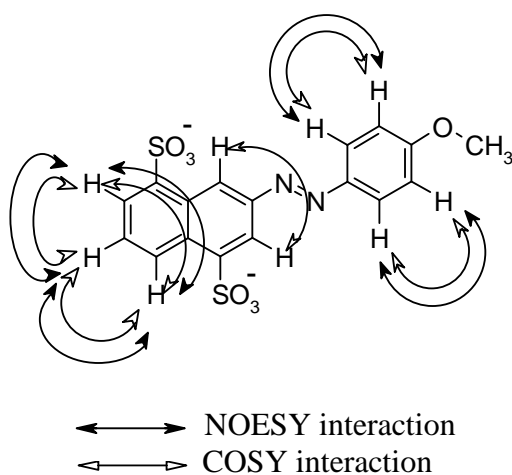


Figure A1.16 COSY and NOESY interactions for OMe-Span in DMSO- d_6 and D_2O .

Table A1.20 HSQC and HMBC of OMe-Span in DMSO-d₆, ● direct attachment ○ adjacent attachment.

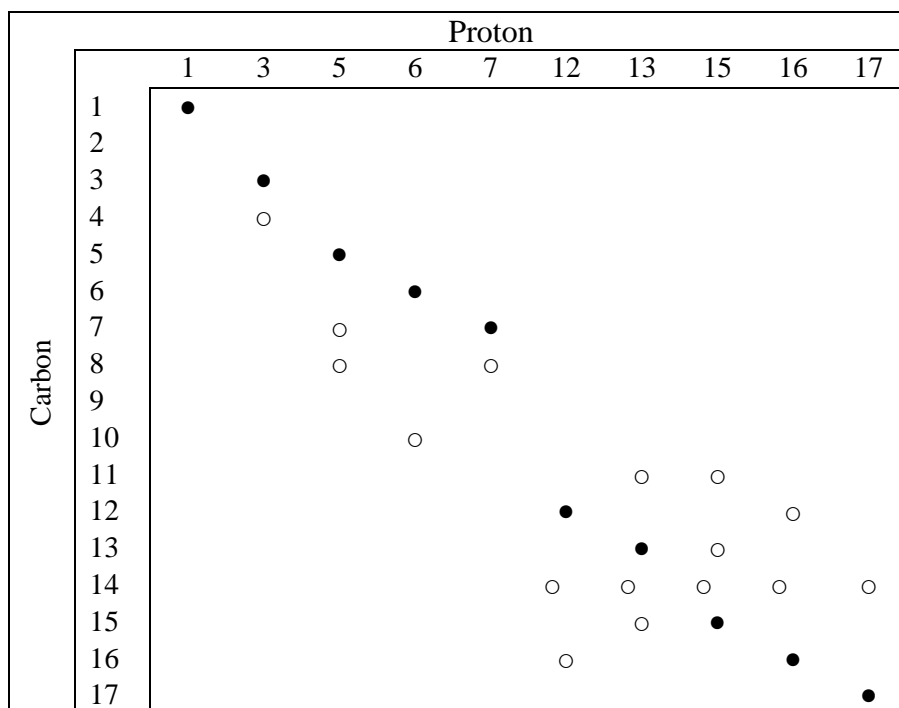
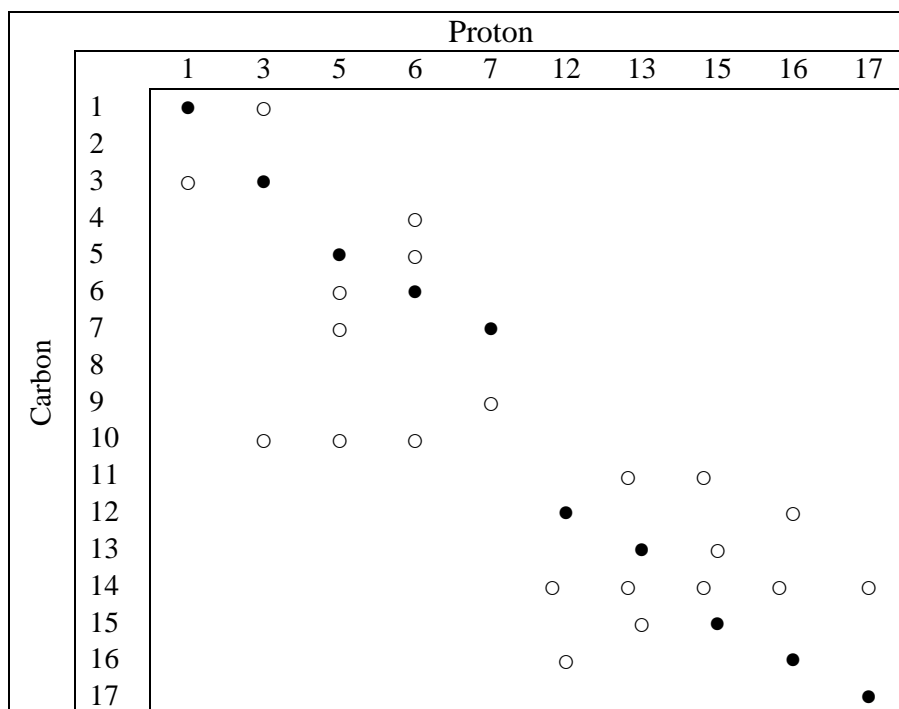


Table A1.21 HSQC and HMBC of OMe-Span in D₂O, ● direct attachment ○ adjacent attachment.



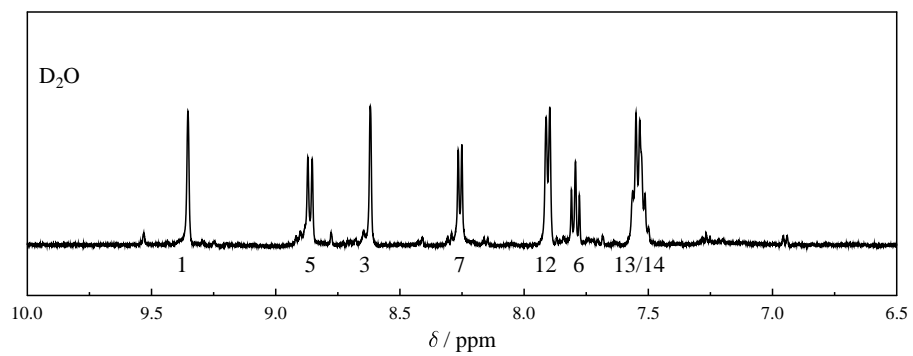


Figure A1.17 Aromatic region ^1H NMR spectrum of H-Span in D_2O .

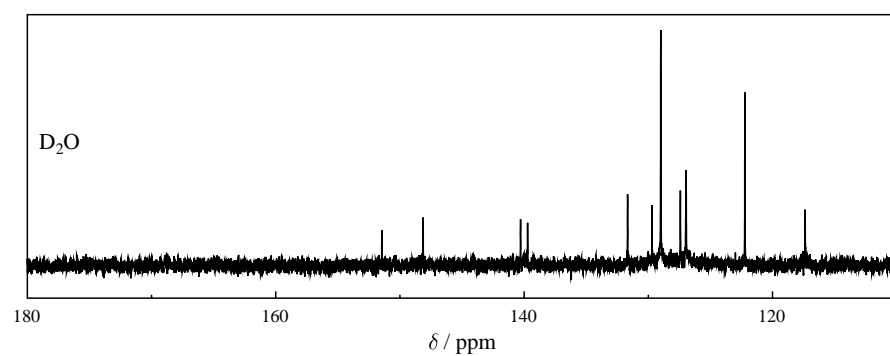


Figure A1.18 ^{13}C NMR spectrum of H-Span D_2O .

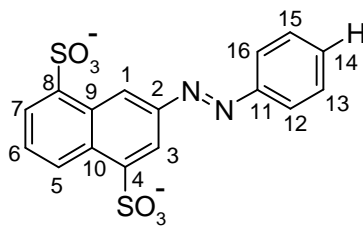


Figure A1.19 Structure of H-Span with the numbering system used for NMR assignments.

Table A1.22 ^1H and ^{13}C NMR chemical shifts (ppm) of H-Span in D_2O .

Atom	D_2O		Calculated		
	$^1\text{H}^a$	^{13}C	^1H	^{13}C	
1	9.351 s	-	127.0	9.43	131.4
2			151.5		142.7
3	8.621 s	-	117.4	8.64	111.4
4			140.3		136.9
5	8.861 d	9.0	129.0	8.80	127.0
6	7.791 t	8.5	127.5	7.62	120.5
7	8.261 d	7.0	127.0	8.06	122.4
8			139.7		136.5
9			129.7		124.4
10			129.0		124.1
11			148.2		144.7
12/16	7.902 d	7.5	122.3	8.12 ¹² , 8.00 ¹⁶	129.7 ¹² , 108.3 ¹⁶
13/15	7.542 d	7.5	129.0	7.55 ¹³ , 7.40 ¹⁵	122.6 ¹³ , 122.2 ¹⁵
14	7.541 t	8.5	131.7	7.47	126.8

^a Integration, multiplicity (s = singlet; d = doublet; t = triplet), splitting (Hz)

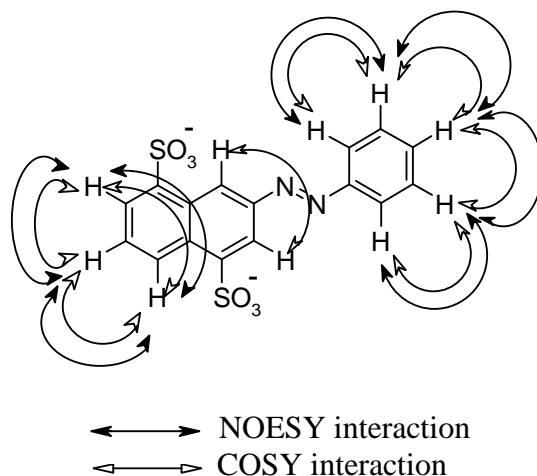


Figure A1.20 COSY and NOESY interactions for H-Span in D_2O .

Table A1.23 HSQC and HMBC of H-Span in D₂O, ● direct attachment ○ adjacent attachment.

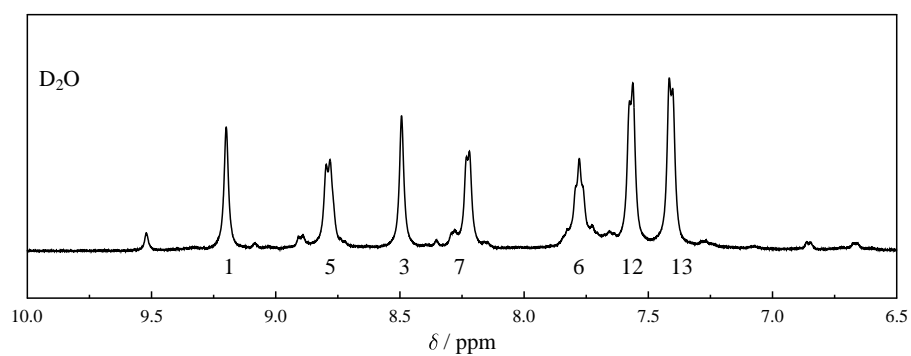
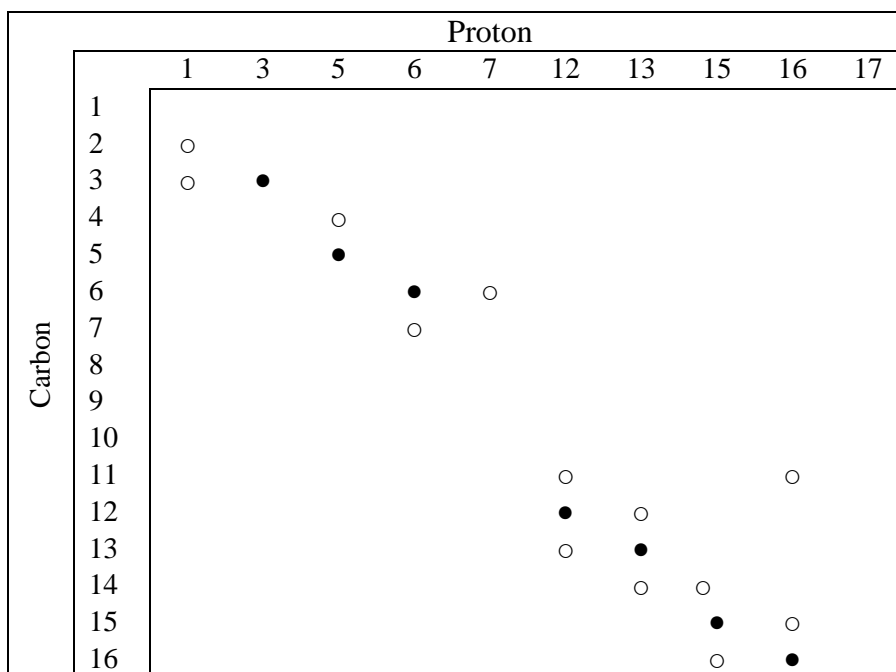


Figure A1.21 Aromatic region ¹H NMR spectrum of Br-Span in D₂O.

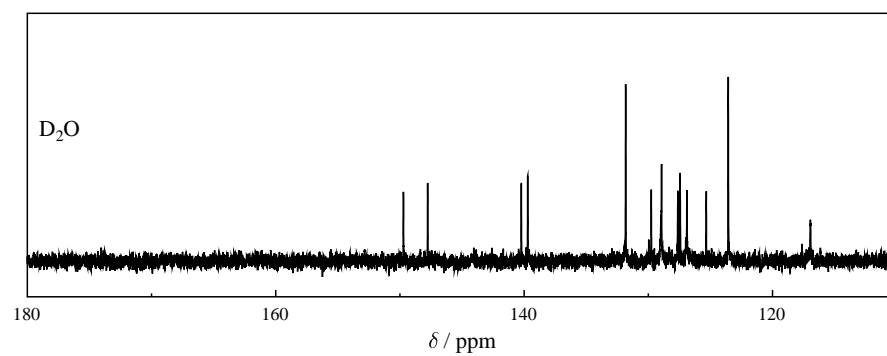


Figure A1.22 ¹³C NMR spectrum of Br-Span D₂O.

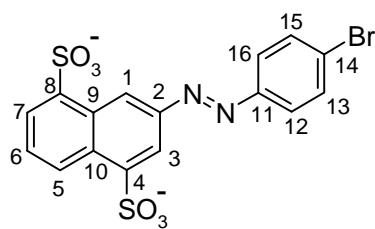


Figure A1.23 Structure of Br-Span with the numbering system used for NMR assignments.

Table A1.24 ^1H and ^{13}C NMR chemical shifts (ppm) of Br-Span in D_2O .

Atom	D_2O		Calculated		
	$^1\text{H}^a$	^{13}C	^1H	^{13}C	
1	9.201 s	-	127.6	9.40	131.7
2			147.8		142.6
3	8.491 s	-	117.0	8.58	111.2
4			139.7		137.1
5	8.791 d	7.5	128.9	8.80	127.0
6	7.781 t	7.5	127.4	7.64	120.8
7	8.231 d	7.5	126.9	8.06	122.5
8			140.2		136.5
9			129.9		124.4
10			129.8		124.3
11			139.6		143.5
12/16	7.572 d	7.0	123.6	7.98 ¹² , 7.88 ¹⁶	129.5 ¹² , 109.0 ¹⁶
13/15	7.412 d	7.0	131.8	7.48 ¹³ , 7.30 ¹⁵	126.2 ¹³ , 126.0 ¹⁵
14			149.7		142.3

^a Integration, multiplicity (s = singlet; d = doublet; t = triplet), splitting (Hz)

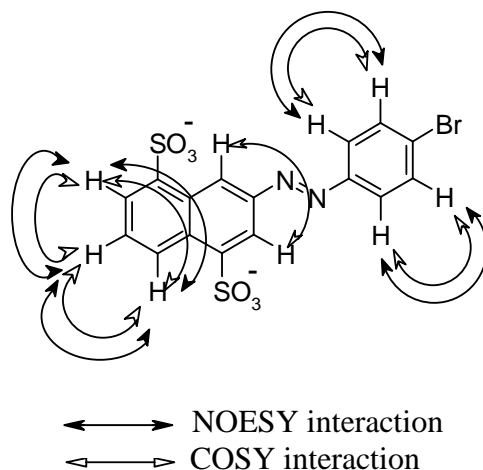


Figure A1.24 COSY and NOESY interactions for Br-Span in D_2O .

Table A1.25 HSQC and HMBC of Br-Span in D₂O, ● direct attachment ○ adjacent attachment.

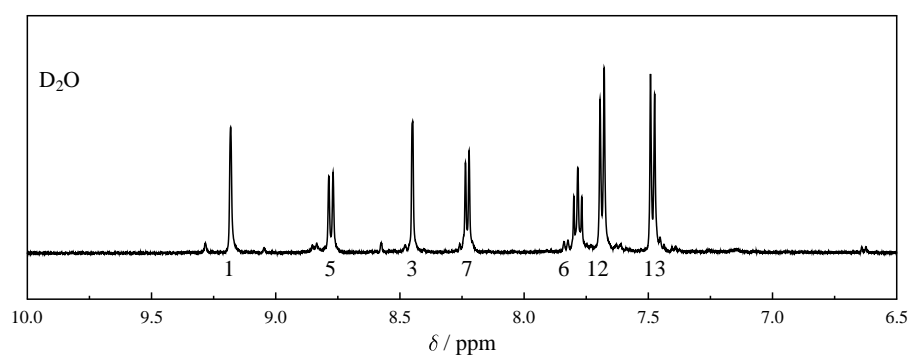
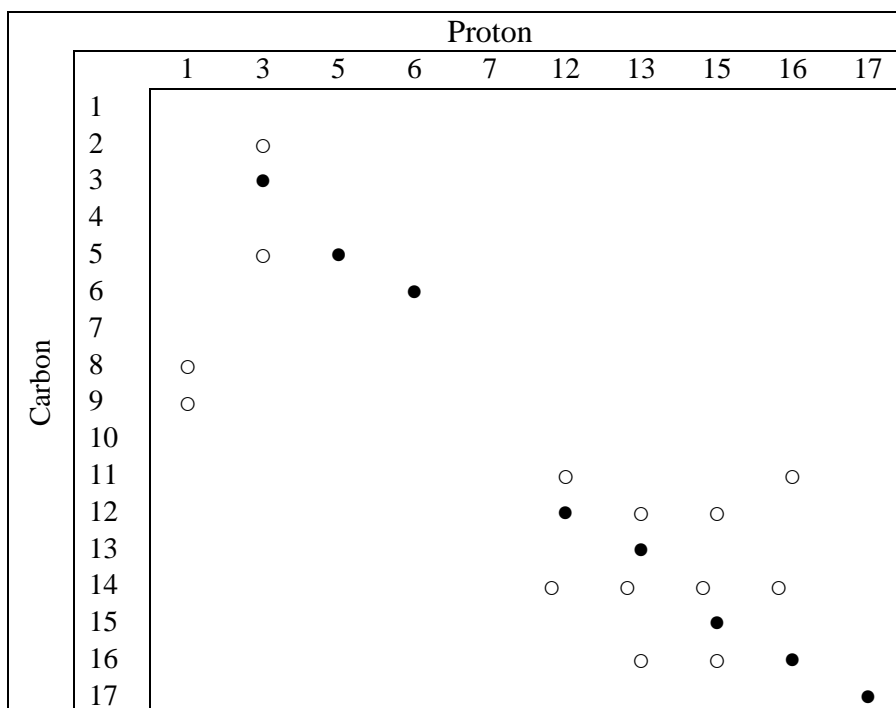


Figure A1.25 Aromatic region ¹H NMR spectrum of CN-Span in D₂O.

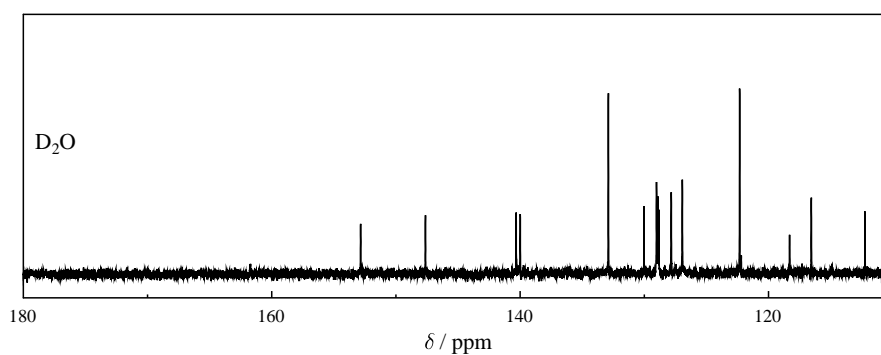


Figure A1.26 ¹³C NMR spectrum of CN-Span D₂O.

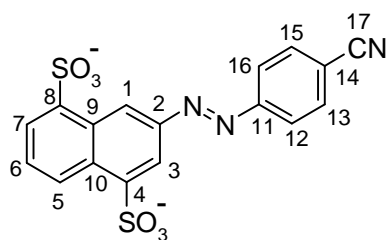


Figure A1.27 Structure of CN-Span with the numbering system used for NMR assignments.

Table A1.26 ^1H and ^{13}C NMR chemical shifts (ppm) of CN-Span in D_2O .

Atom	D_2O		Calculated		
	$^1\text{H}^a$	^{13}C	^1H	^{13}C	
1	9.18 1 s	-	129.0	9.52	133.1
2			147.7		142.5
3	8.45 1 s	-	116.5	8.58	110.7
4			140.0		137.4
5	8.78 1 d	8.0	128.9	8.82	127.0
6	7.78 1 t	8.0	127.8	7.70	121.5
7	8.23 d d	8.0	126.9	8.08	122.7
8			140.3		136.9
9			130.6		124.3
10			128.8		124.8
11			152.8		145.7
12/16	7.69 d d	8.5	122.4	8.15 ¹² , 7.97 ¹⁶	128.7 ¹² , 108.5 ¹⁶
13/15	7.48 d d	8.5	132.9	7.75 ¹³ , 7.58 ¹⁵	127.9 ¹³ , 127.3 ¹⁵
14			118.3		112.6
17			112.2		107.4

^a Integration, multiplicity (s = singlet; d = doublet; t = triplet), splitting (Hz)

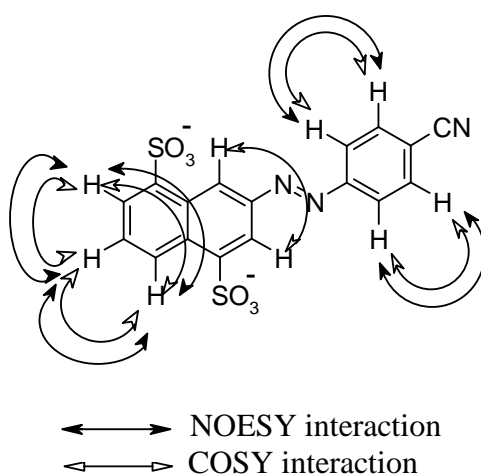
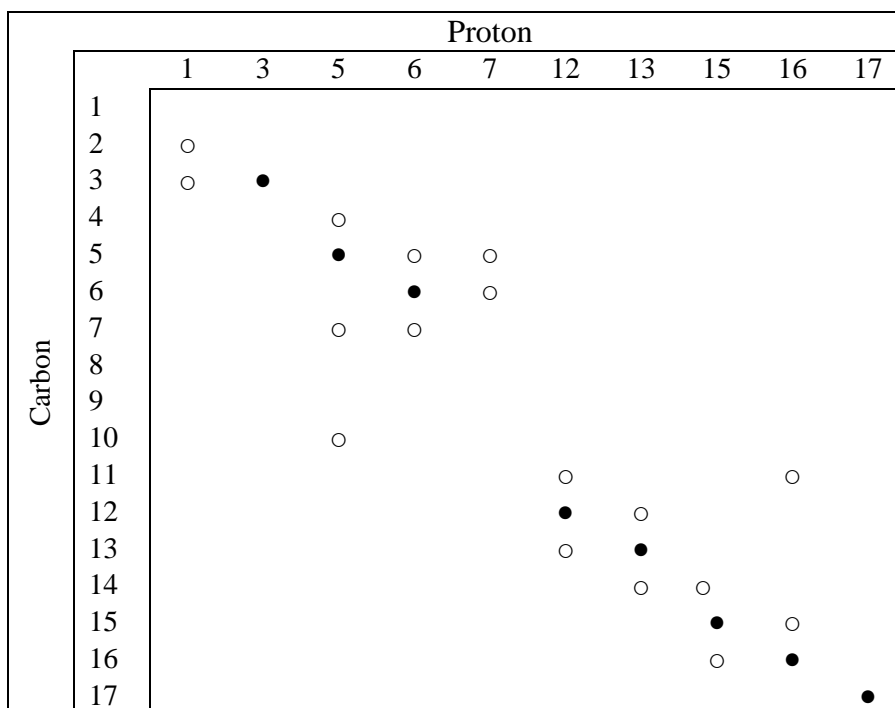


Figure A1.28 COSY and NOESY interactions for CN-Span in D_2O .

Table A1.27 HSQC and HMBC of CN-Span in D₂O, ● direct attachment ○ adjacent attachment.



A1.5 Vibrational spectroscopy

A1.5.1 Short-term photoalteration

A Raman signal of S_0 from a sample that is not photoaltered will reduce to give a signal intensity S_F on photoalteration within the laser beam, and the photoalteration effect can be considered by calculating the normalised Raman signal S' as shown in equation A1.43, where $S' = 1$ shows no photoalteration and $S' = 0$ shows total photoalteration. The photoalteration parameter, F as expressed by equation A1.44 for an experimental Gaussian laser beam can be related to a theoretical square beam model by equation A1.45, which relates F to S' and which has been shown to be a good model and is graphically shown in Figure A1.31.⁹⁸

$$S' = \frac{S_0}{S_F} \quad (\text{A1.43})$$

$$F = \frac{P\lambda\epsilon\phi}{\omega\nu} 1.086 \times 10^{-4} \quad (\text{A1.44})$$

$$S' = \frac{1}{F} [1 - \exp(-F)] \quad (\text{A1.45})$$

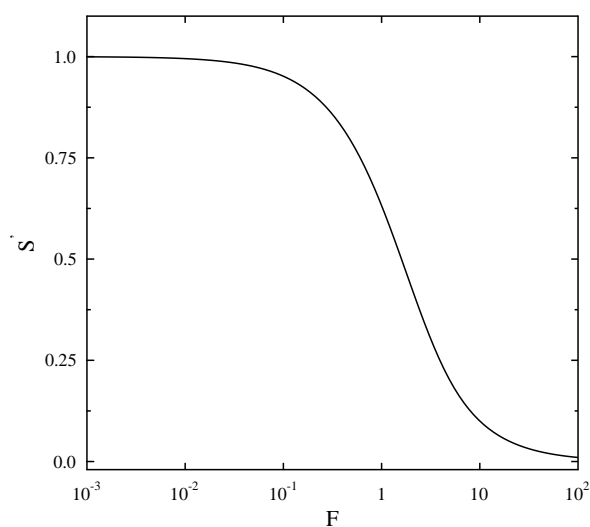


Figure A1.29 Dependence on the normalised Raman intensity S' for a square beam model on the photoalteration factor F .

Using equation A1.45 to calculate F and S' along with the experimental conditions used as given in Table A1.28 for the laser power, beam radius, sample flow rate and molar absorption coefficient for OH-Span at the laser excitation wavelength ($\lambda_{\text{ex}} = 514.5 \text{ nm}$), assuming $\Phi = 0.5$, theory predicts that under highly photoaltering conditions that ca. 10 % of the Raman intensity will be observed (Figure A1.31).

Table A1.28 Experimental conditions, laser power (P / mW), beam radius (ω / μm), sample flow rate (v / cm s^{-1}) and molar absorption (ϵ / $\text{dm}^3 \text{ cm}^{-1} \text{ cm}^{-1}$) coefficient for assessment of photoalteration on Raman spectra with an excitation wavelength of 514.5 nm and a total collection time of 3600 s by calculating F and S' as given in equation A1.45.

P	ω	v	ϵ	F	S'
1	130	250	5500	0.0047	0.99
50	10	415	5500	1.84	0.46
250	10	415	5500	9.15	0.11

Experimentally, the Raman profiles recorded for all R-Span dyes under all conditions were identical showing that no change or degradation of the sample occurred on passing through the laser beam on the timescale of observation, hence no short-term photoalteration was observed under these conditions. It should be noted that Φ for azobenzene is ca. 0.1- 0.5 which is dependent on solvent and wavelength.⁹⁸ Therefore photoalteration in the laser beam was not important for the R-Span dyes.

A1.5.2 Supplementary figures

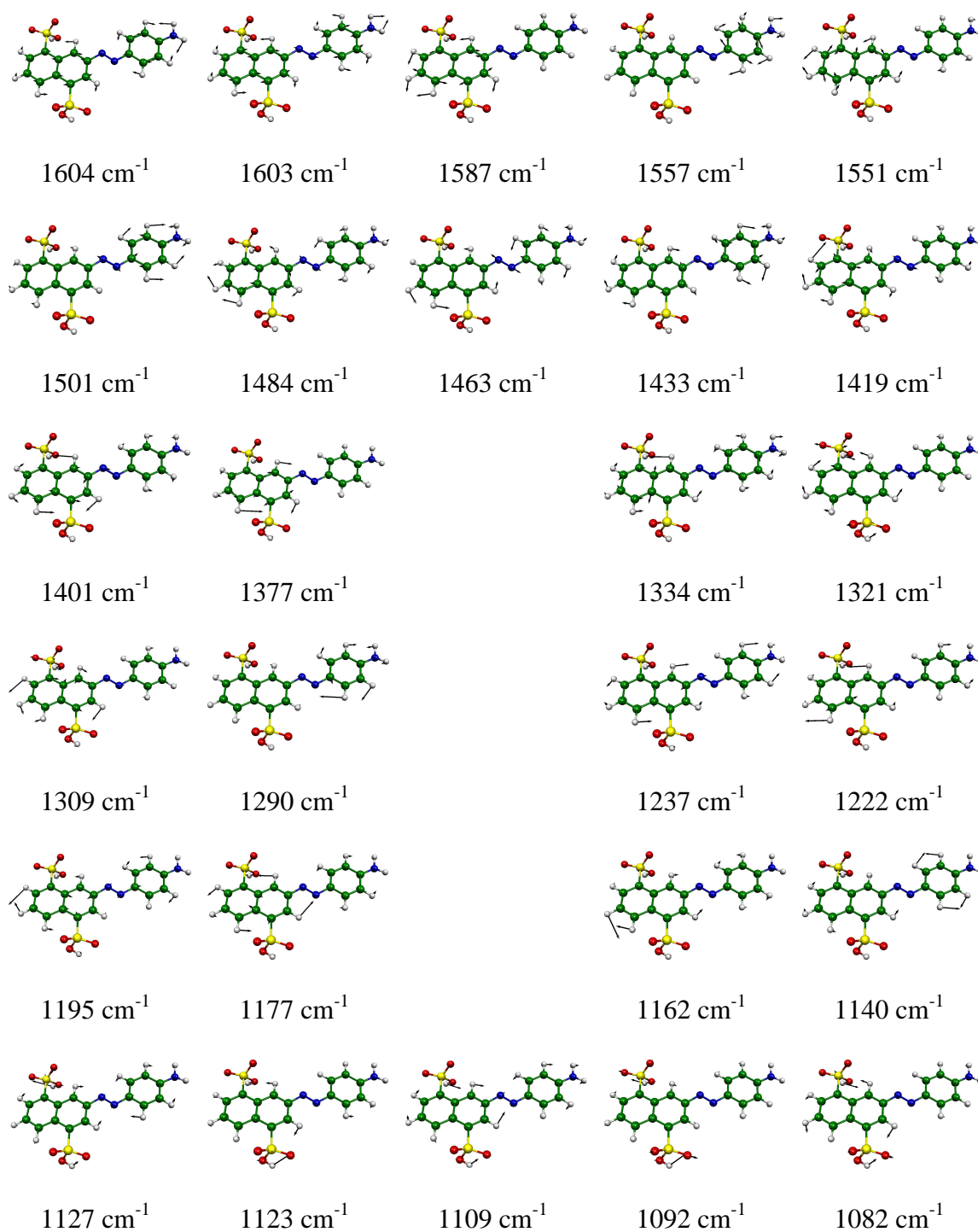


Figure A1.30 Selected calculated normal mode vibrations of $\text{NH}_2\text{-Span}$. (Original in colour)

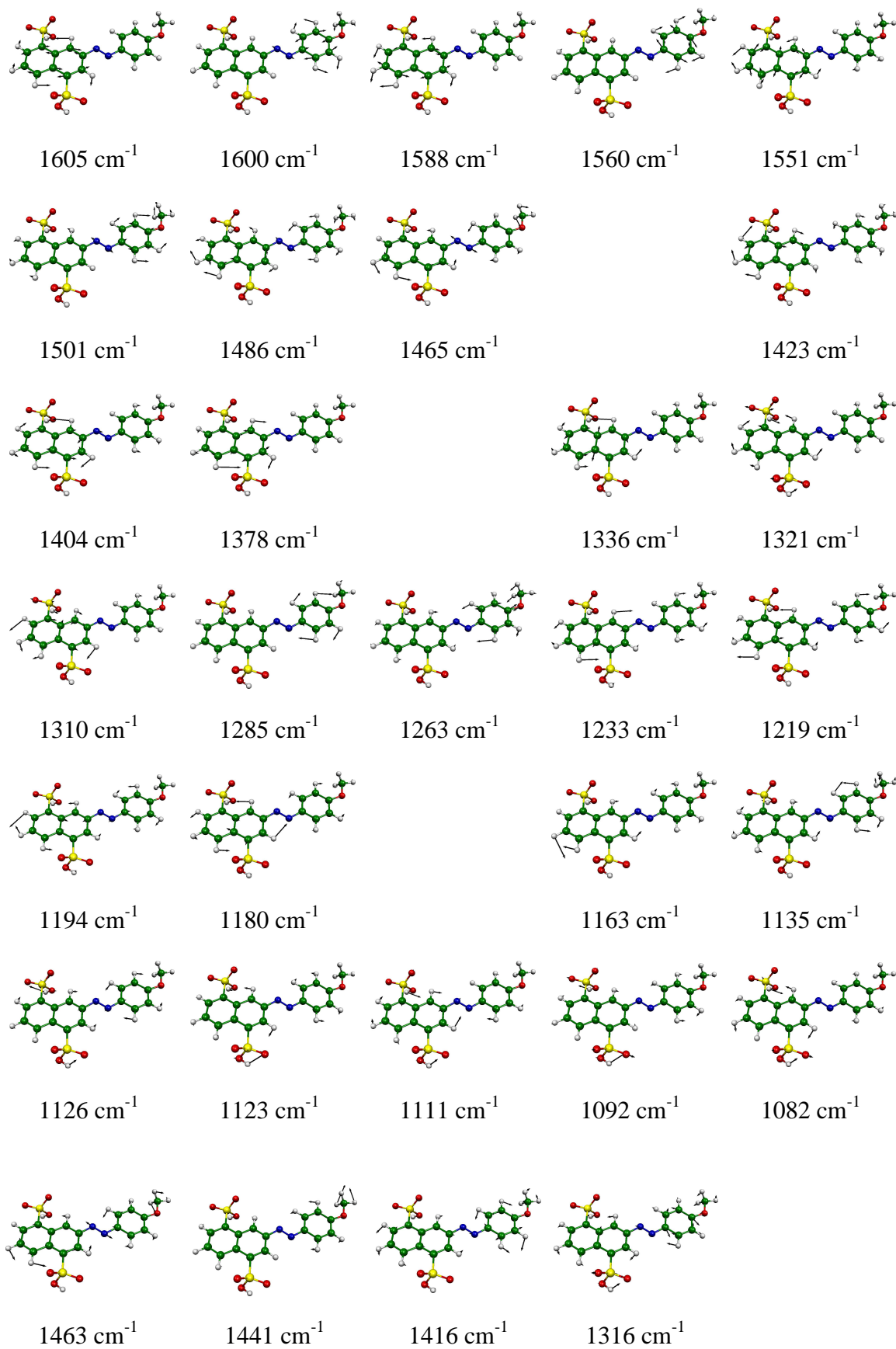


Figure A1.31 Selected calculated normal mode vibrations of OMe-Span. (*Original in colour*)

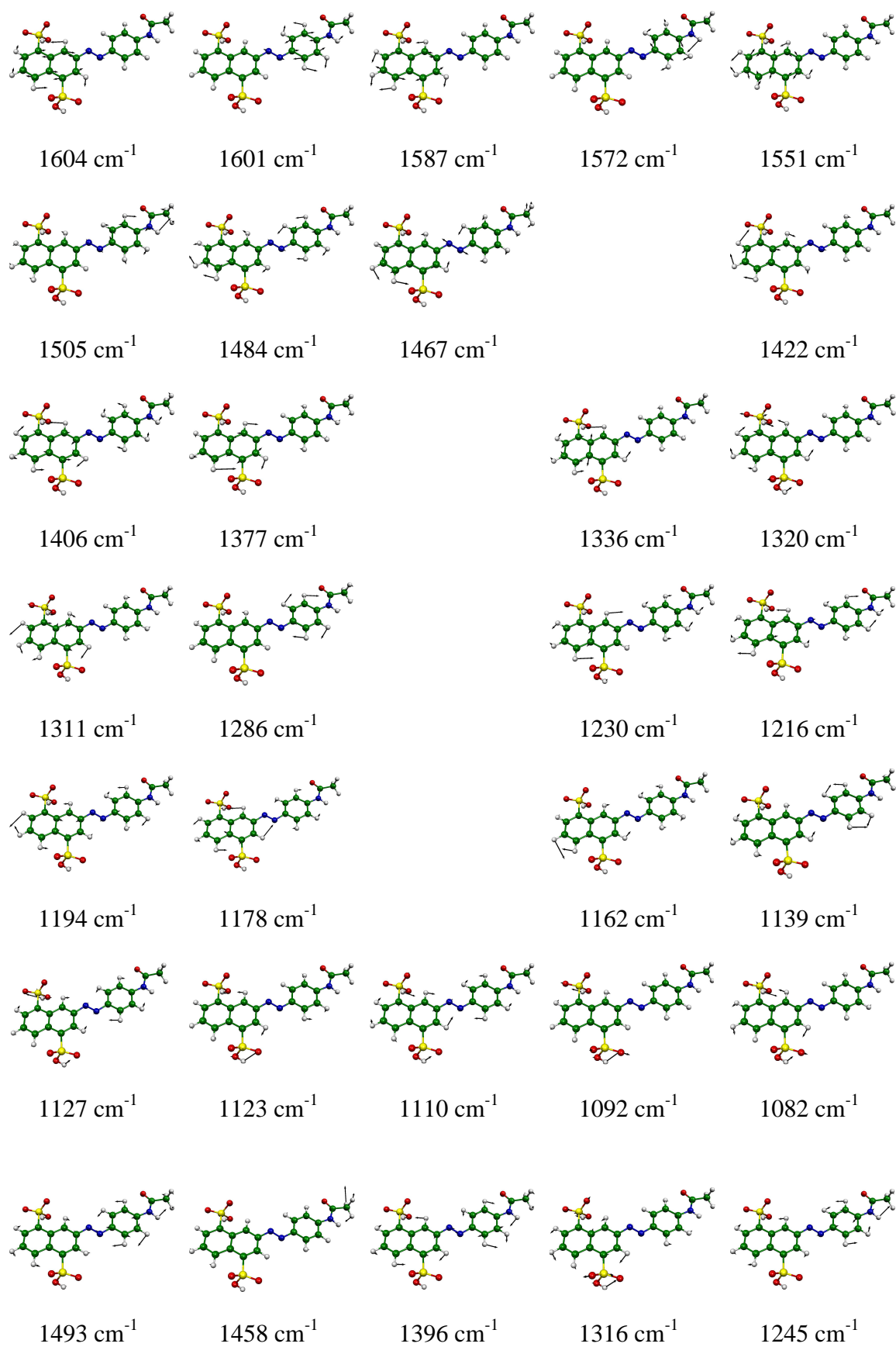


Figure A1.32 Selected calculated normal mode vibrations of NHAc-Span. (*Original in colour*)

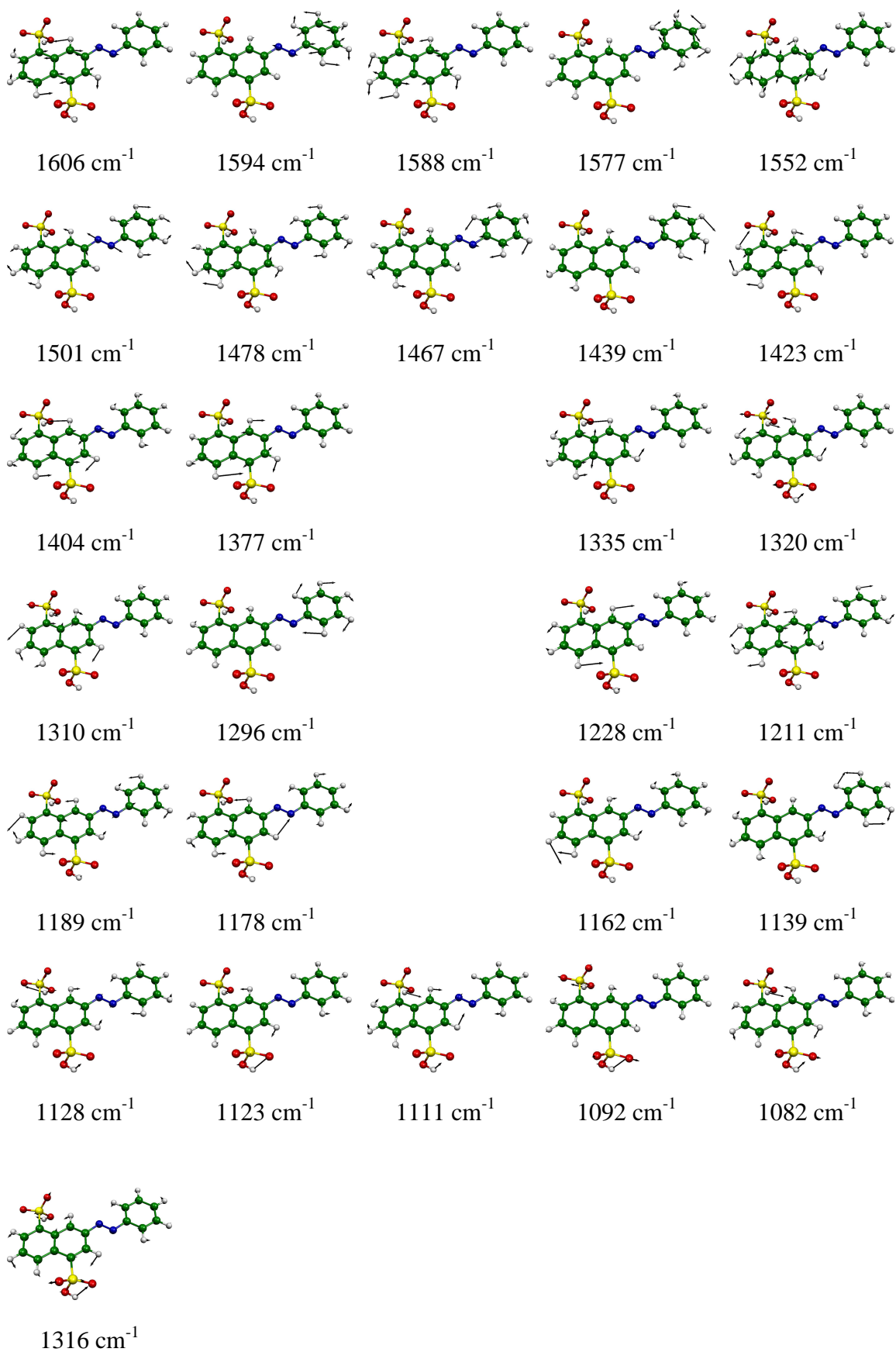


Figure A1.33 Selected calculated normal mode vibrations of H-Span. (Original in colour)

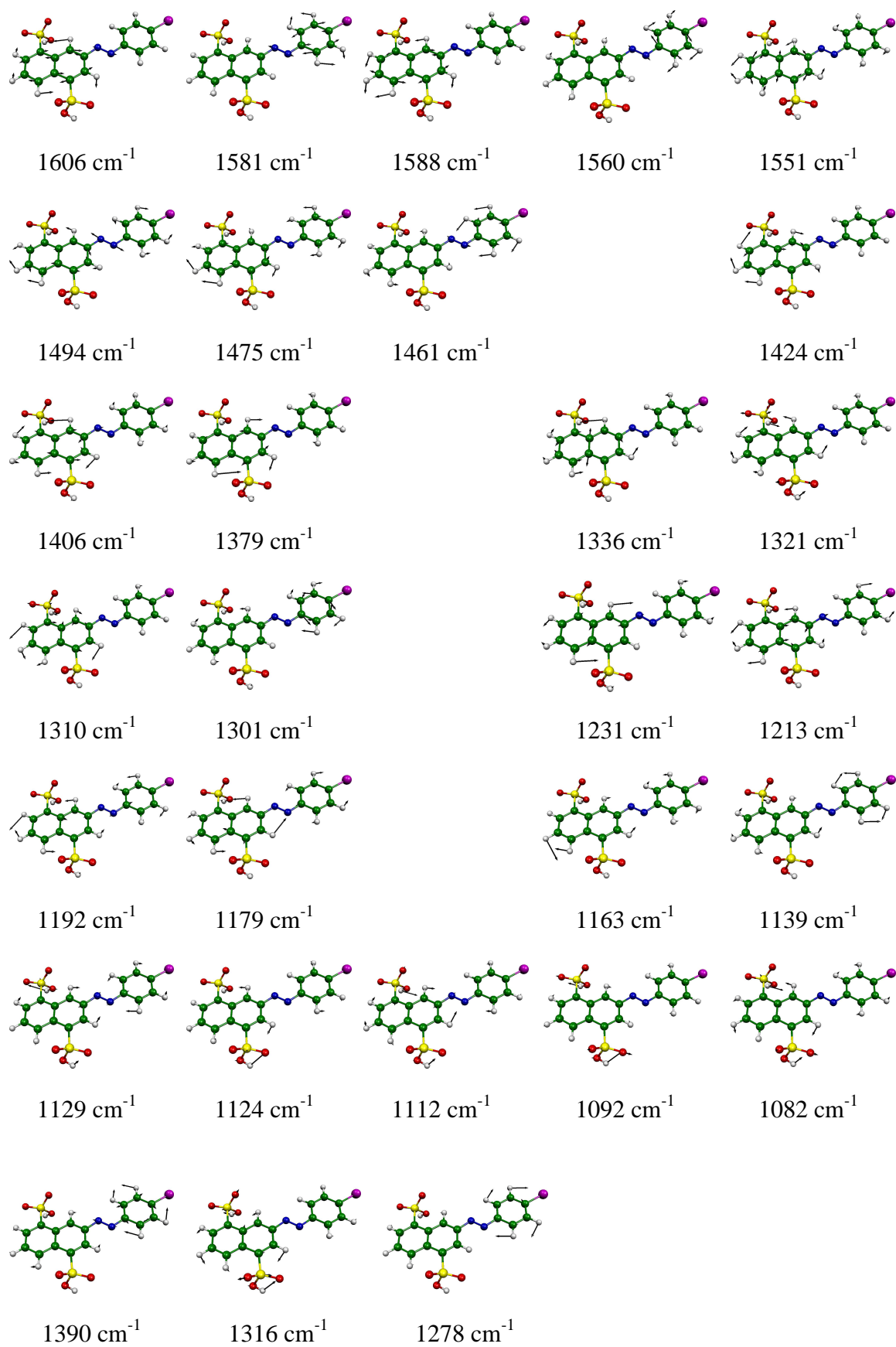


Figure A1.34 Selected calculated normal mode vibrations of Br-Span. (*Original in colour*)

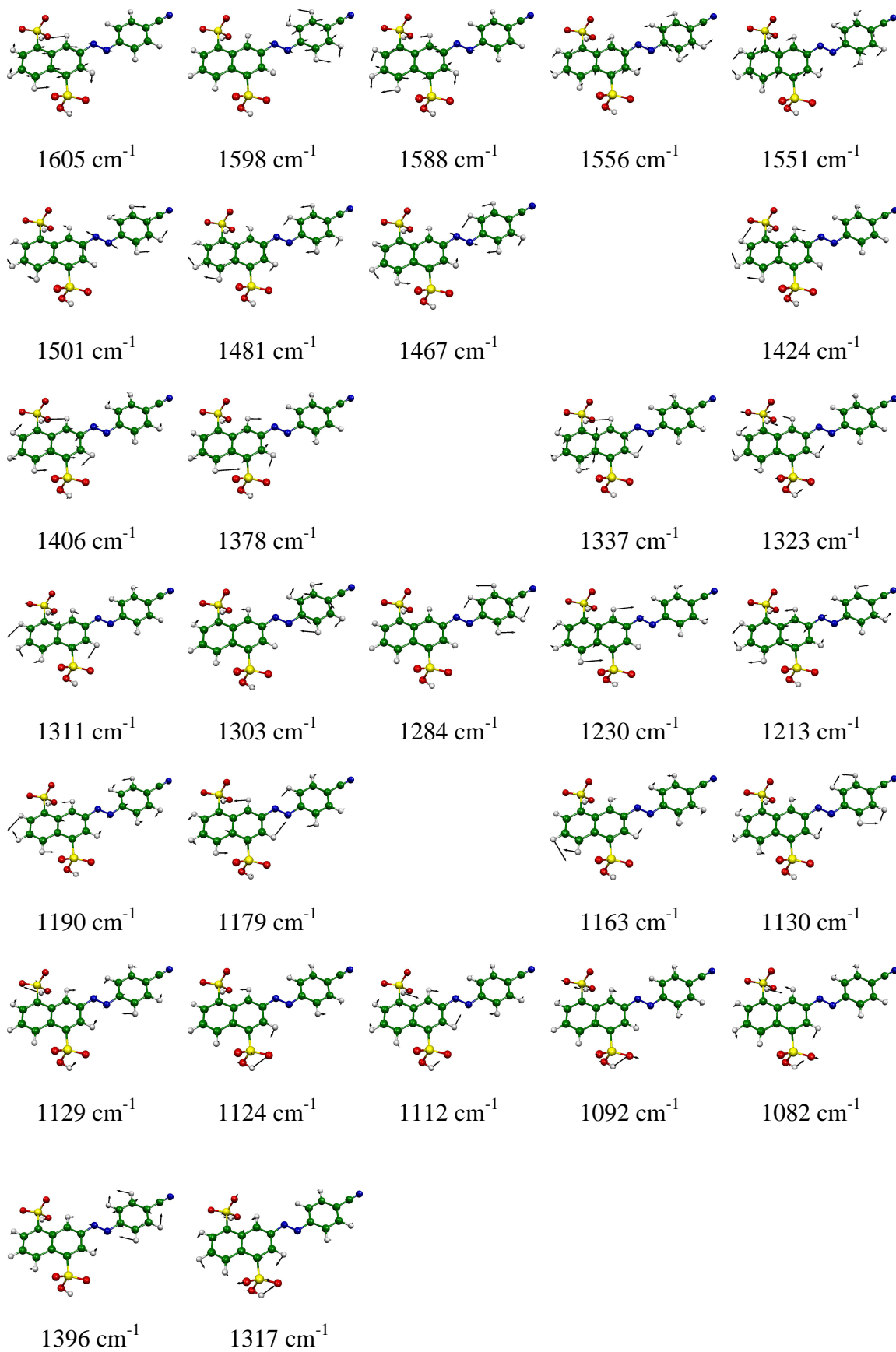


Figure A1.35 Selected calculated normal mode vibrations of CN-Span. (*Original in colour*)

A1.6 Protonation of NH₂-Span

Table A1.29 Calculated transition energies (E), wavelengths (λ), and oscillator strengths (f) for the excited states of the Hydrazone tautomer of P-NH₂-Span.

Excited state	E / eV	λ / nm	f
1 st	2.45	506	0.4126
2 nd	2.85	434	0.6552
3 rd	3.57	347	0.1254
4 th	3.66	339	0.0082
5 th	3.72	333	0.0010
6 th	3.82	325	0.0189
7 th	3.90	319	0.1678
8 th	4.00	310	0.0426
9 th	4.04	306	0.0567
10 th	4.19	296	0.0020

Table A1.30 Calculated transition energies (E), wavelengths (λ), and oscillator strengths (f) for the excited states for the Azo tautomer of P-NH₂-Span.

Excited state	E / eV	λ / nm	f
1 st	2.40	517	0.0005
2 nd	2.91	426	0.2335
3 rd	3.38	366	0.6150
4 th	4.07	305	0.0827
5 th	4.16	298	0.0017
6 th	4.18	297	0.0019
7 th	4.19	296	0.0029
8 th	4.30	288	0.1458
9 th	4.32	286	0.0164
10 th	4.37	283	0.0072

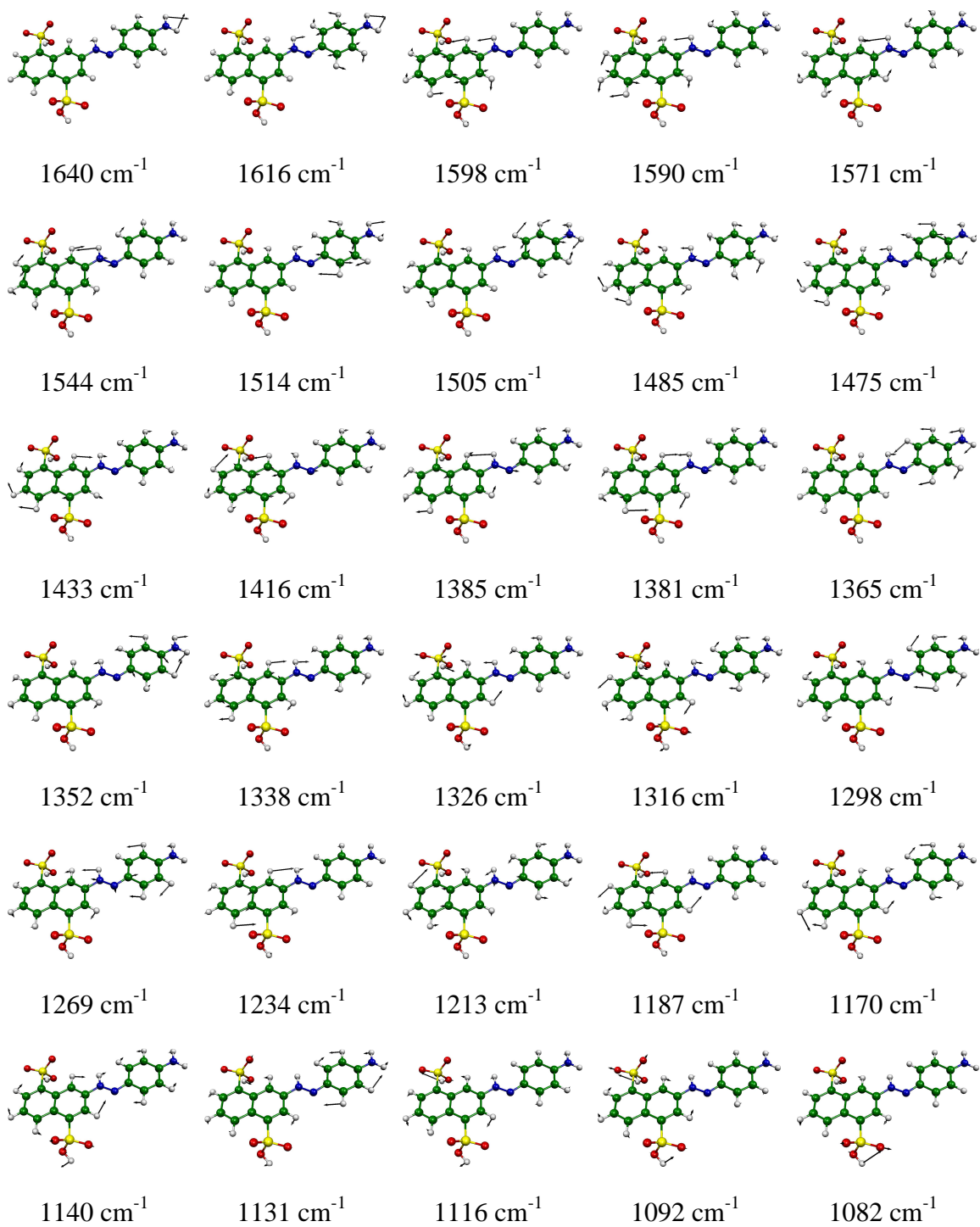


Figure A1.36 Selected calculated normal mode vibrations of the azonium tautomer of P-NH₂-Span. (*Original in colour*)

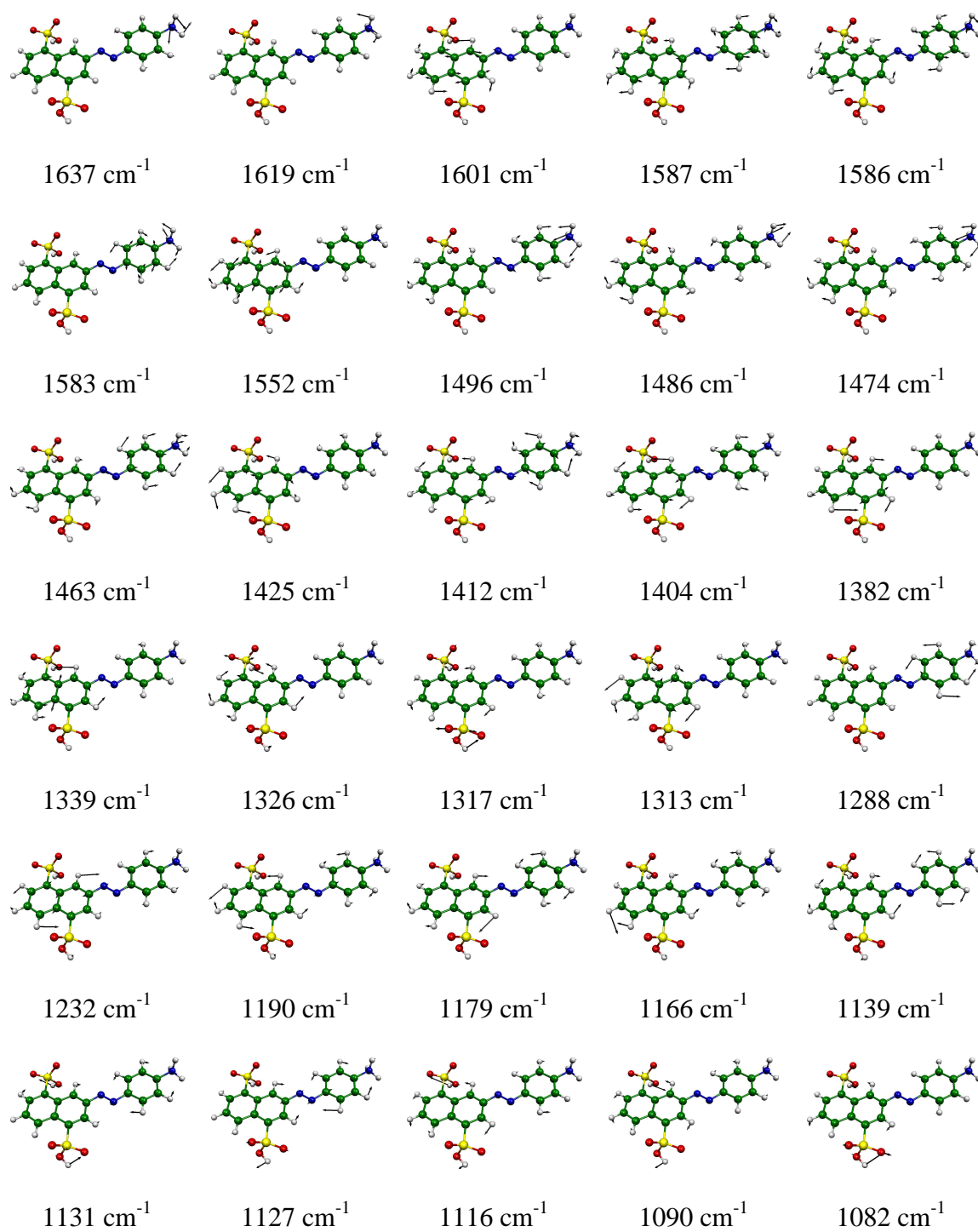


Figure A1.37 Selected calculated normal mode vibrations of the ammonium tautomer of P-NH₂-Span. (*Original in colour*)

Appendix 2 Electrochemistry

A2.1 Supplementary CV data

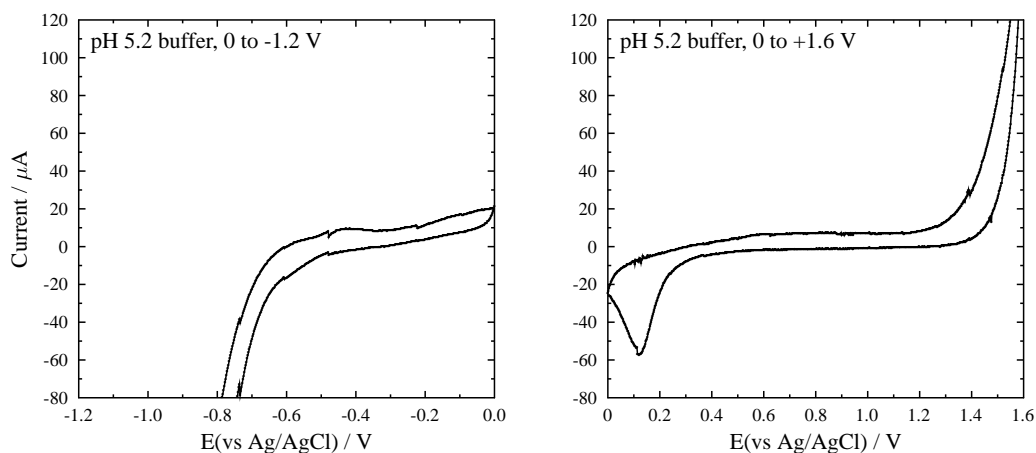


Figure A2.1 Cyclic voltammograms of 0.5 mol dm⁻³ sodium acetate pH 5.2 buffer solution recorded with a sweep rate of 10 mV s⁻¹; Left: Reduction, Right: Oxidation.

A2.2 Spectroelectrochemical fit

The Nernst equation as shown in equation A2.1, relates the applied potential E to the potential of the electrochemical reaction E^\ominus , where R (8.314 J K⁻¹ mol⁻¹) is the molar gas constant, T (K) is the temperature, n is the number of electrons transferred in the electrochemical process, F (96485 C mol⁻¹) is the Faraday constant and Q is the reaction quotient.

$$E = E^\ominus - \left(\frac{RT}{nF} \right) \ln Q \quad (\text{A2.1})$$

Assume $Q = \frac{[\text{Red}]}{[\text{Ox}]}$ from the equilibrium $[\text{Ox}] \rightleftharpoons [\text{Red}]$

$$\therefore E = E^\ominus - \frac{RT}{nF} \ln \frac{[\text{Red}]}{[\text{Ox}]} \quad (\text{A2.2})$$

Rearrangement of equation A2.2 yields the concentration of the reduced species given in equation A2.3.

$$[\text{Red}] = [\text{Ox}] e^{\left(\frac{nF(E^\ominus - E)}{RT}\right)} \quad (\text{A2.3})$$

The total concentration c_{tot} is the sum of the concentration of the oxidised and reduced species.

$$\therefore [\text{Red}] = c_{\text{tot}} - [\text{Ox}] \quad (\text{A2.4})$$

Substitution of equation A2.4 into A2.3 gives equation A2.5.

$$[\text{Ox}] = \frac{c_{\text{tot}}}{1 + e^{\left(\frac{nF(E^\ominus - E)}{RT}\right)}} \quad (\text{A2.5})$$

Substitution of equation A2.5 into A2.3 gives equation A2.6.

$$[\text{Red}] = \frac{c_{\text{tot}} e^{\left(\frac{nF(E^\ominus - E)}{RT}\right)}}{1 + e^{\left(\frac{nF(E^\ominus - E)}{RT}\right)}} \quad (\text{A2.6})$$

The Beer-Lambert law can be applied to relate absorbance A to the concentration of the oxidised and reduced species by the substitution of equations A2.7 and A2.8 into A2.9 to give equation A2.10, where A_{ox} and A_{red} are the absorbance of the oxidised and reduced species, ϵ_{ox} and ϵ_{red} ($\text{dm}^3 \text{mol}^{-1} \text{cm}^{-1}$) are the absorption coefficients of the oxidised and reduced species, respectively, $[\text{Ox}]_0$ and $[\text{Red}]_\infty$ are their respective concentrations at full oxidation and reduction, respectively, and l is the pathlength of the cell (cm).

$$A_{\text{ox}} = \epsilon_{\text{ox}} [\text{Ox}]_0 l \quad \text{where} \quad \epsilon_{\text{ox}} = \frac{A_0}{[\text{Ox}]_0 l} \quad (\text{A2.7})$$

$$A_{\text{red}} = \epsilon_{\text{Red}} [\text{Red}]_{\infty} l \text{ where } \epsilon_{\text{Red}} = \frac{A_{\text{Red}}}{[\text{Red}]_{\infty} l} \quad (\text{A2.8})$$

$$A = \epsilon_{\text{Ox}} [\text{Ox}] l + \epsilon_{\text{Red}} [\text{Red}] l \quad (\text{A2.9})$$

$$A = \frac{A_0 [\text{Ox}]}{[\text{Ox}]_0} + \frac{A_{\infty} [\text{Red}]}{[\text{Red}]_{\infty}} \quad (\text{A2.10})$$

Substitution of equations A2.5 and A2.6 into equation A2.10 and assuming that $[\text{Ox}]_0 = [\text{Red}]_{\infty} = c_{\text{tot}}$ gives equation A2.11 used for the analysis of spectroelectrochemical data.

$$A = \frac{A_0 + A_{\infty} e^{\left(\frac{nF(E^{\ominus} - E)}{RT}\right)}}{1 + e^{\left(\frac{nF(E^{\ominus} - E)}{RT}\right)}} \quad (\text{A2.11})$$

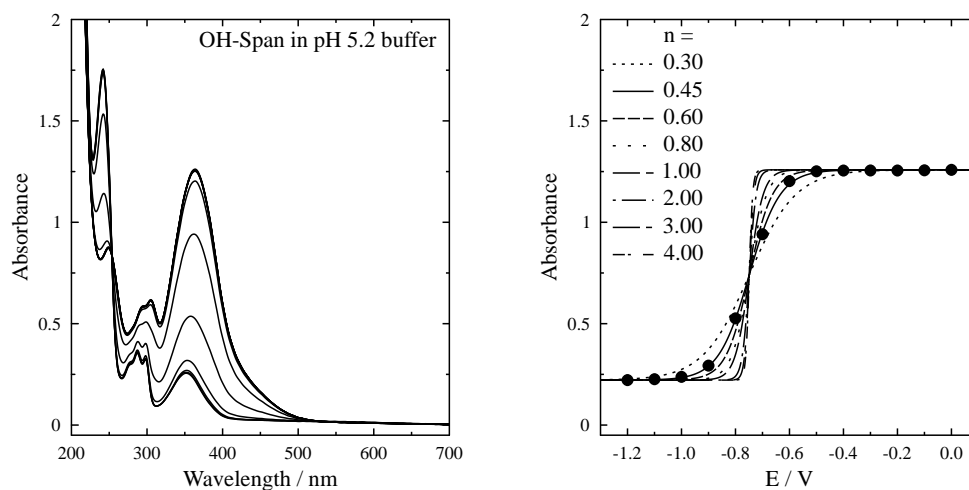


Figure A2.2 Left: UV/Visible absorption spectra of OH-Span ($5 \times 10^{-4} \text{ mol dm}^{-3}$) in pH 5.2 sodium acetate buffer solution. Right: Potential curve analysed using equation A2.11 at 363 nm with different values of n , where E^{\ominus} is set at -0.749 V .

A2.3 Supplementary CPE data

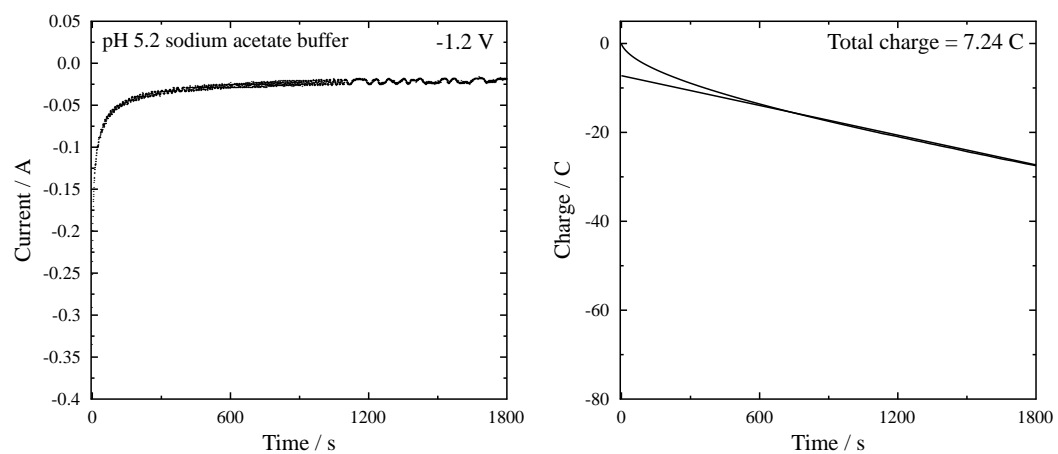


Figure A2.3 CPE reduction on pH 5.2 sodium acetate buffer solution (0.5 mol dm^{-3}) over 30 min at a potential of -1.2 V (vs Ag/AgCl) Left: Current-time profile, Right: Charge-time profile.

A2.4 Supplementary HPLC data

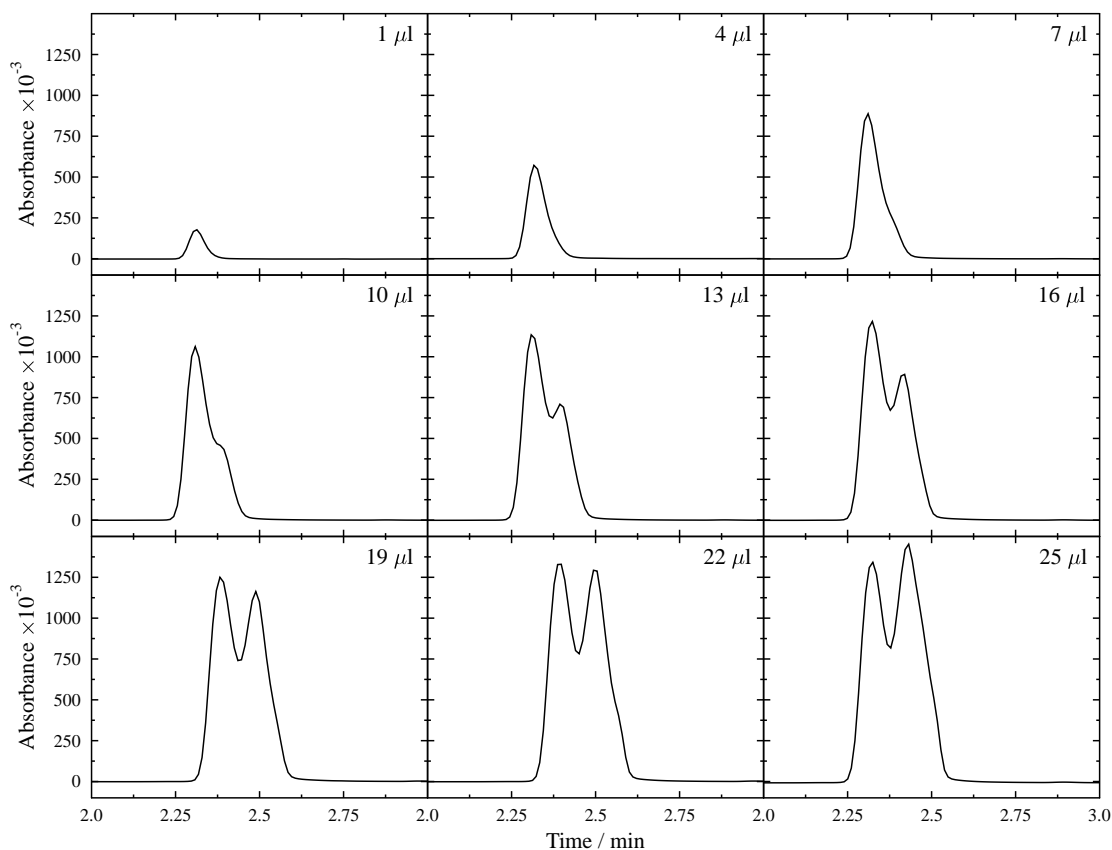


Figure A2.4 HPLC chromatograms of NAPDAD ($1 \times 10^{-3} \text{ mol dm}^{-3}$) over a injection volume range of between 1 and 25 μl analysed at 254 nm.

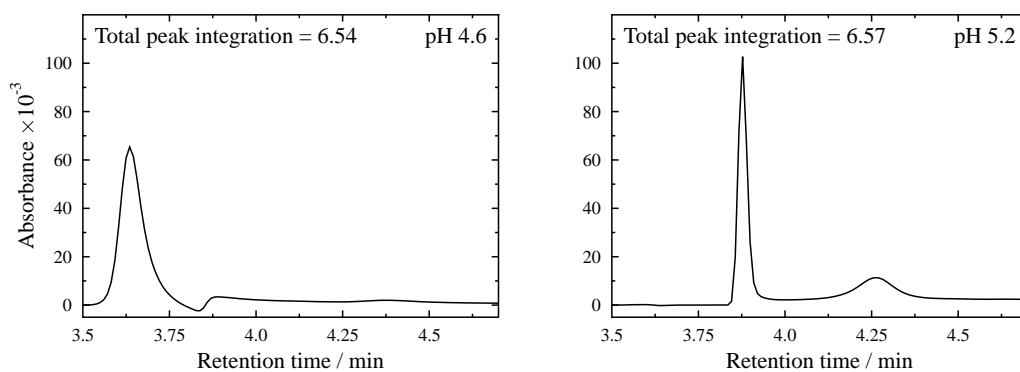


Figure A2.5 HPLC chromatograms of APOL ($1 \times 10^{-3} \text{ mol dm}^{-3}$) analysed at 254 nm with both the sample and eluting system of pH 4.6 (left) and pH 5.2 (right).

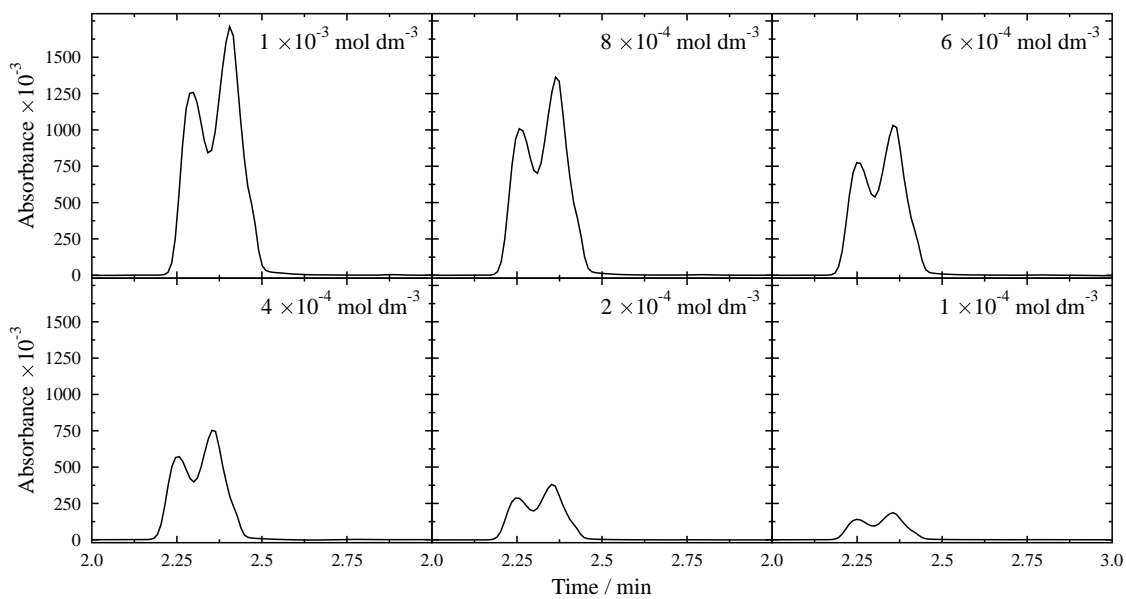


Figure A2.6 HPLC chromatograms of NAPDAD over a concentration range of between 1×10^{-3} and 1×10^{-4} mol dm⁻³ analysed at 254 nm with 25 μ l injection.

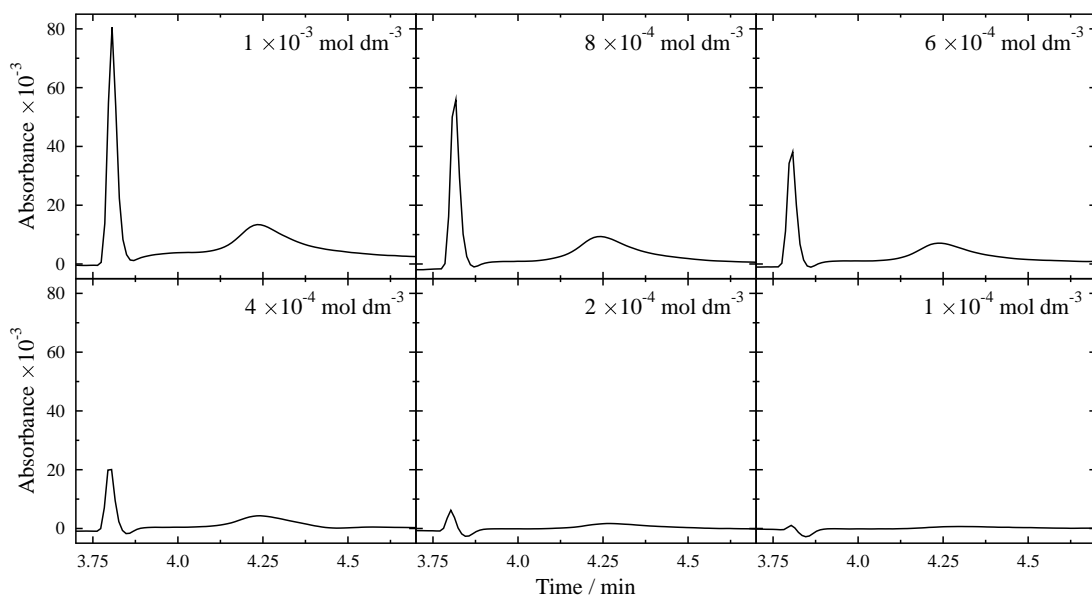


Figure A2.7 HPLC chromatograms of APOL over a concentration range of between 1×10^{-3} and 1×10^{-4} mol dm⁻³ analysed at 254 nm with 25 μ l injection.

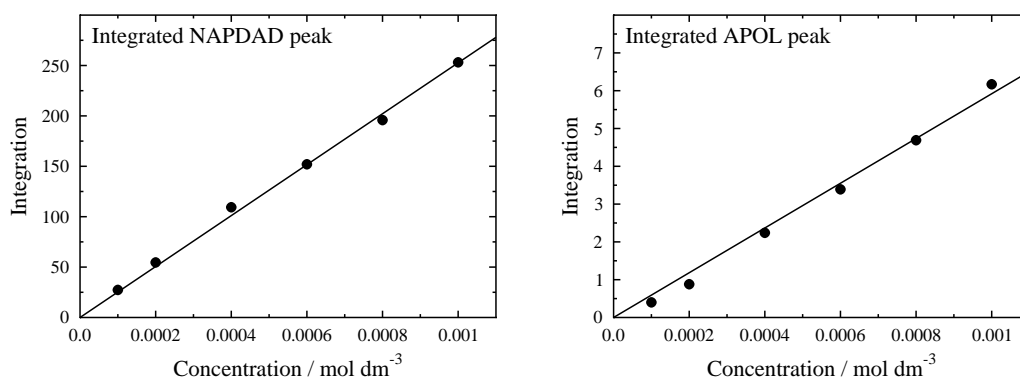


Figure A2.8 Concentration calibration curve for NAPDAD (left) and APOL (right) over a concentration range of between 1×10^{-3} and 1×10^{-4} mol dm⁻³ analysed at 254 nm both with 25 μ l injection volumes.

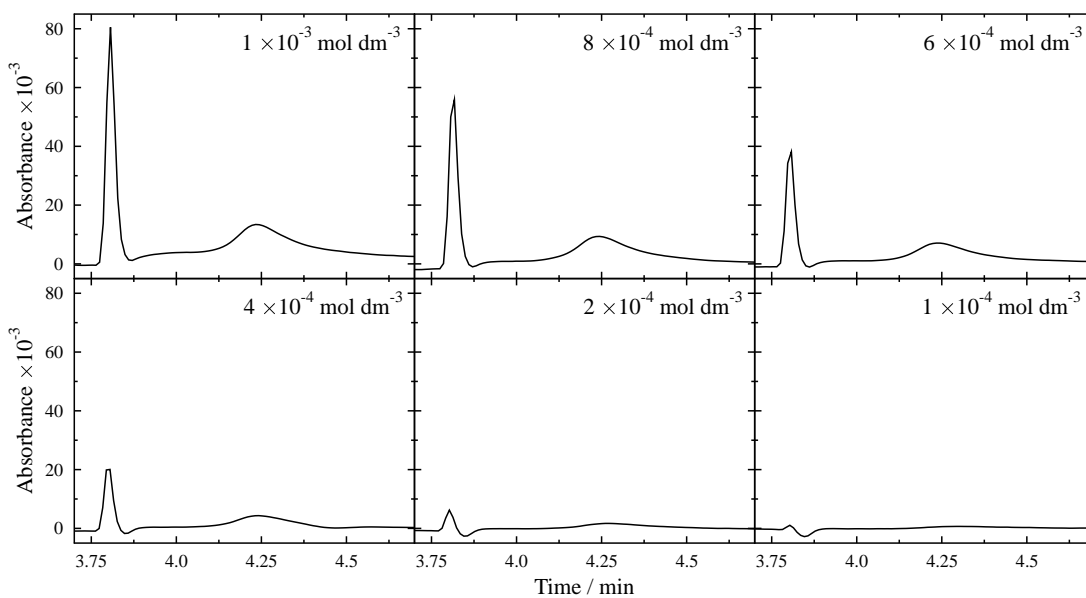


Figure A2.9 HPLC chromatograms of DAB over a concentration range of between 1×10^{-3} and 1×10^{-4} mol dm⁻³ analysed at 254 nm.

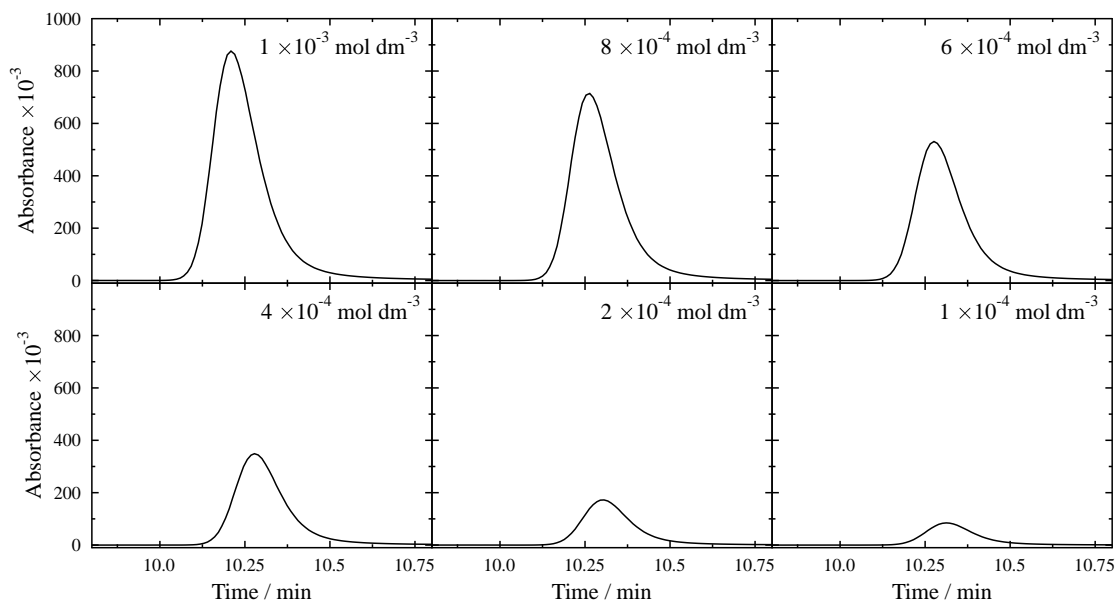


Figure A2.10 HPLC chromatograms of APA over a concentration range of between 1×10^{-3} and 1×10^{-4} mol dm⁻³ analysed at 254 nm.

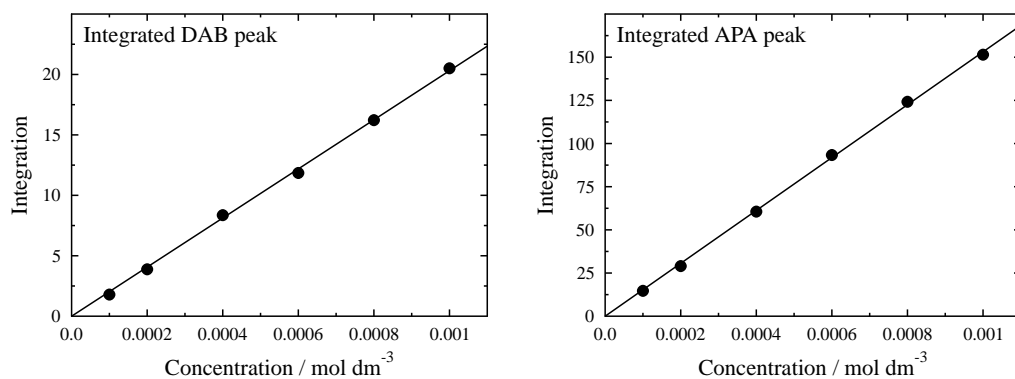


Figure A2.11 Concentration calibration curve for DAB (left) and APA (right) over a concentration range of between 1×10^{-3} and 1×10^{-4} mol dm⁻³ analysed at 254 nm both with 25 μ l injection volumes.

Appendix 3 Photochemistry

A3.1 Kinetic rate laws

$$\frac{d[\text{Photoinitiator}]}{dt} = -k_1[\text{Photoinitiator}] + k_7[\text{ArCO}\cdot][\cdot\text{C}(\text{CH}_3)_2\text{OH}]$$

$$\begin{aligned} \frac{d[\cdot\text{C}(\text{CH}_3)_2\text{OH}]}{dt} = & k_1[\text{Photoinitiator}] - k_2[\cdot\text{C}(\text{CH}_3)_2\text{OH}][\text{Dye}] - 2k_4[\cdot\text{C}(\text{CH}_3)_2\text{OH}]^2 \\ & - k_5[\cdot\text{C}(\text{CH}_3)_2\text{OH}][\text{Dye}^{\cdot-}] - k_7[\cdot\text{C}(\text{CH}_3)_2\text{OH}][\text{ArCO}\cdot] \end{aligned}$$

$$\frac{d[\text{Dye}]}{dt} = -k_2[\cdot\text{C}(\text{CH}_3)_2\text{OH}][\text{Dye}] + k_3[\text{Dye}^{\cdot-}]^2$$

$$\frac{d[\text{Dye}^{\cdot-}]}{dt} = k_2[\cdot\text{C}(\text{CH}_3)_2\text{OH}][\text{Dye}] - 2k_3[\text{Dye}^{\cdot-}]^2 - k_5[\cdot\text{C}(\text{CH}_3)_2\text{OH}][\text{Dye}^{\cdot-}] - k_6[\text{Dye}^{\cdot-}][\text{ArCO}\cdot]$$

$$\frac{d[\text{Dye}^{2-}]}{dt} = k_3[\text{Dye}^{\cdot-}]^2$$

$$\frac{d[\text{ArCO}\cdot]}{dt} = k_1[\text{Photoinitiator}] - k_6[\text{Dye}^{\cdot-}][\text{ArCO}\cdot] - k_7[\cdot\text{C}(\text{CH}_3)_2\text{OH}][\text{ArCO}\cdot] - 2k_8[\text{ArCO}\cdot]^2$$

A3.2 Supplementary TRVIS data

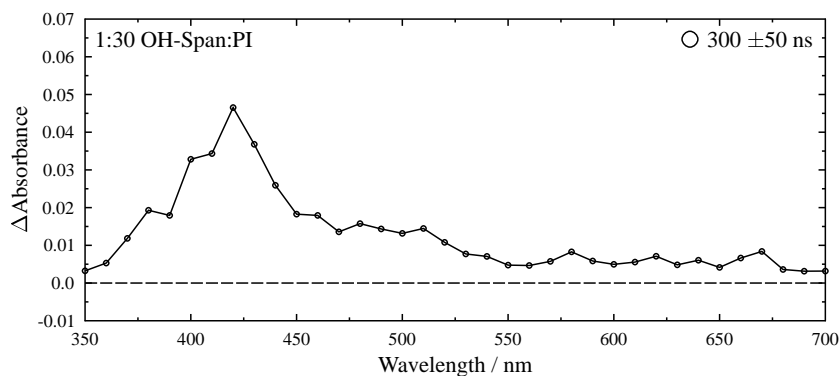


Figure A3.1 TRVIS spectra of 1:30 OH-Span:photoinitiator (1×10^{-4} mol dm⁻³ dye concentration) in pH 5.2 sodium acetate buffer solution, 300 ns after excitation.

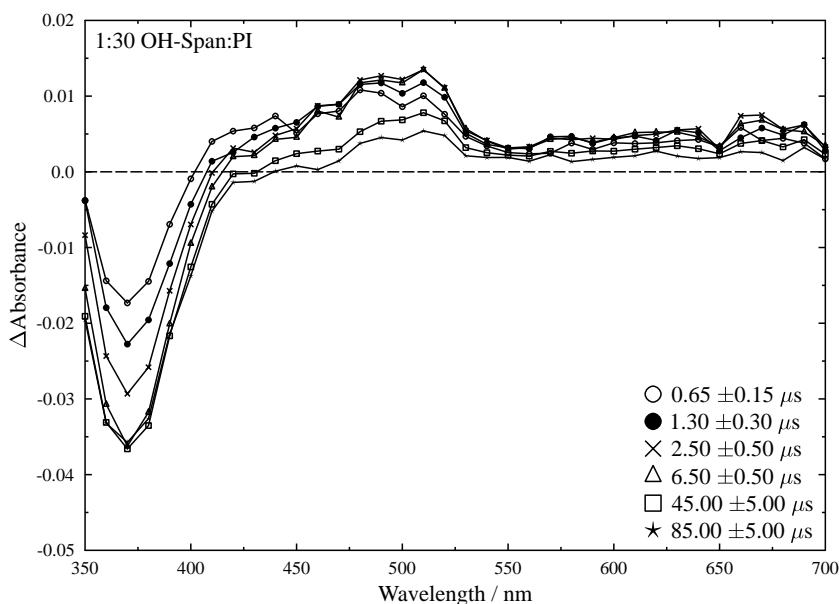


Figure A3.2 TRVIS spectra of 1:30 OH-Span:photoinitiator (1×10^{-4} mol dm⁻³ dye concentration) in pH 5.2 sodium acetate buffer solution, 0.65, 1.30, 2.50, 6.50, 45.00 and 85.00 μ s after excitation.

Appendix 4 Computational data CD

The output files for all DFT optimisations, excited state and NMR calculations for all R-Span dyes and the model compounds APOL and NAPDAD are included in the CD attached to the back of this thesis. All “*.log” files may be opened using Molekel. Data for each dye is contained within its own directory, which are described below. Unscaled vibrations can be viewed for all files ending with “*opt.log”, scaled vibrations together with IR and Raman are shown for all modes in files ending with “*vibs.xml” which can be opened with Microsoft Excel.

H-Span

trans

h-span_topt_dft.log	Optimisation of H-Span
h-span_td_exstat.log	Excited states of H-Span
h-span_nmr.log	NMR of H-Span
h-span_vibs.xml	Scaled vibrations and IR and Raman intensities

NH₂-Span

trans

nh ₂ -span_topt_dft.log	Optimisation of NH ₂ -Span
nh ₂ -span_td_exstat.log	Excited states of NH ₂ -Span
nh ₂ -span_nmr.log	NMR of NH ₂ -Span
nh ₂ -span_vibs.xml	Scaled vibrations and IR and Raman intensities

OH-Span

trans

oh-span_topt_dft.log	Optimisation of OH-Span
oh-span_td_exstat.log	Excited states of OH-Span
oh-span_nmr.log	NMR of OH-Span
oh-span_vibs.xml	Scaled vibrations and IR and Raman intensities

OMe-Span

trans

ome-span_topt_dft.log	Optimisation of OMe-Span
ome-span_td_exstat.log	Excited states of OMe-Span
ome-span_nmr.log	NMR of OMe-Span
ome-span_vibs.xml	Scaled vibrations and IR and Raman intensities

cis

ome-span_copt_dft.log	Optimisation of OMe-Span
-----------------------	--------------------------

NHAc-Span

trans

nhac-span_topt_dft.log	Optimisation of NHAc-Span
nhac -span_td_exstat.log	Excited states of NHAc -Span
nhac -span_nmr.log	NMR of NHAc -Span
nhac -span_vibs.xml	Scaled vibrations and IR and Raman intensities

cis

nhac-span_copt_dft.log	Optimisation of NHAc-Span
------------------------	---------------------------

Br-Span

trans

br-span_topt_dft.log	Optimisation of Br-Span
br-span_td_exstat.log	Excited states of Br-Span
br-span_nmr.log	NMR of Br-Span
br-span_vibs.xml	Scaled vibrations and IR and Raman intensities

CN-Span

trans

cn-span_topt_dft.log	Optimisation of CN-Span
cn-span_td_exstat.log	Excited states of CN-Span
cn-span_nmr.log	NMR of CN-Span
cn-span_vibs.xml	Scaled vibrations and IR and Raman intensities

P-NH₂-Span

Azoinium

pnh2-span_azo_topt_dft.log	Optimisation of azonium P-NH ₂ -Span
pnh2-span_azo_td_exstat.log	Excited states of azonium P-NH ₂ -Span
pnh2-span_azo_nmr.log	NMR of azonium P-NH ₂ -Span
pnh2-span_azo_vibs.xml	Scaled vibrations and IR and Raman intensities

Ammonium

pnh2-span_amm_topt_dft.log	Optimisation of ammonium P-NH ₂ -Span
pnh2-span_amm_td_exstat.log	Excited states of ammonium P-NH ₂ -Span
pnh2-span_amm_nmr.log	NMR of ammonium P-NH ₂ -Span
pnh2-span_amm_vibs.xml	Scaled vibrations and IR and Raman intensities

NAPDAD

napdad_dft.log	Optimisation of NAPDAD
napdad_vibs.xml	Scaled vibrations and IR and Raman intensities

APOL

apol_dft.log	Optimisation of APOL
apol_vibs.xml	Scaled vibrations and IR and Raman intensities